USF UNIVERSITY OF SOUTH FLORIDA

Civil & Environmental Engineering

PUBLICATIONS 2001 - 1996

GRAY MULLINS, PH.D., P.E.






Acknowledgments

This collection of works was made possible by the dedication of many co-authors comprised of university colleagues, state and federal agency officials, graduate researchers, and various contributors from industry.

Aguilar, J.
Ashford, S.
Bermingham, P.
Brown, D.
Dapp, S.
Deese, G.
Dibb, E.
Ealy, C.
Echelberger, W.
Engebretson, d.
Fischer, J.
Garbin, E.
Gunaratne, M.
Hajduk, E.
Hartley, A.
Hourani, N.
Issa, M.
Issa, M.
Jacobsen, L
Johnson, K.
Jory, B.
Justason, M.
Khouri, B.
Knight, W.
Kranc, S.
Kuo, C.
Lane, D.
Lewis, C.
Liby, L.
Meloy, N.
Muchard, M.
Pai, N.
Paikowski, S.
Patel, P.
Pierresaint, V.
Race, R.
Ranganath,
Robertson, D.
Rollins, K.
Salem, T.
Schrader, A.
Sen, R.
Shahawy, M.
Sosa, R.
Spain, J.
Stanley, B.
Stevens, K.
Stinnette, P.
Stokes, M.
Suh, K
Thilikasiri, H.
Weinmann, T.
Winters, D.

Table of Contents

Mullins, G., Lewis, C., and Justason, M., (2002). "Advancements in Statnamic Data Regression Techniques," *Deep Foundations 2002: An International Perspective on Theory, Design, Construction, and Performance*, ASCE Geo Institute, GSP No.116, Vol II, pp. 915-930. 438

Sen, R., Mullins, G., and Salem, T., (2002)."Durability of E-Glass/Vinylester Reinforcement in Alkaline Solution," *ACI Structural Journal*, Vol 99, No. 3, pp. 369-375. 454

Mullins, G., Sosa, R., and Sen, R., (2001). "Seal Slab Prestressed Pile Interface Bond from Full-scale Testing," *ACI Structural Journal*, Vol 98, No. 5, pp. 743-751. 461

Fischer, J., Mullins, G., Sen, R., Issa, M. (2001). "Studies on the Use of Powder Actuated Nails in Pile Repair," Proceedings of the Construction Institute Sessions ASCE Conference, Houston, TX, October 10-13, pp. 10-15. 470

Sen, R., Shahawy, M., Mullins, G. and Spain, J. (2001). "Effect of Environment on the Integrity of CFRP/Concrete Bond. Proceedings of the Eleventh International Offshore and Polar Engineering Conference, Stavanger, Norway, June17-22, (2001), Vol. 4, pp. 222-226. 476

Sen, R., Liby, L., and Mullins, G., (2001). "Strengthening Steel Bridge Sections using CFRP Laminates," *COMPOSITES Part B: Engineering International Journal*, Vol. 32, No. 4, pp. 309-322. 483

Thilakasiri, H., Gunaratne, M., Mullins, G., Stinnette, P. and Kuo, C., (2001)."Implementation Aid for Dynamic Replacement of Organic Soils with Sand," Journal of Geotechnical and Geoenvironmental Engineering, Vol. 127, No. 1, pp. 25-35. 497

Mullins, G., Dapp, S., and Lai, P., (2000). "Pressure Grouting Drilled Shaft Tips in Sand". *New Technological and Design Developments in Deep Foundations*, Dennis, N. D., et al. (ed.), ASCE, Geo Institute, GSP Vol. 100, pp 1-17. 508

Mullins, Gunaratne, Stinnette, and Thilakasiri, (2000). "Prediction of Dynamic Compaction Pounder Penetration," *Soils and Foundations*, Japanese Geotechnical Society, Vol. 40, No. 5, pp. 91-97. 525

Mullins, G., Hartley, A., Engebretson, D., and Sen, R. (2000). "Settlement Repair of Lightly Reinforced Concrete Block Walls Using CFRP," Proceedings of Second Conference of Seismic Repair & Rehabilitation of Structures (SRRS2), Mosallam, A. (ed), Fullerton, CA, March 21-22, pp. 171-180. 532

Sen, R., Shahawy, M., Mullins, G., and Spain, J., (1999). "Durability of Carbon Fiber-Reinforced Polymer/Epoxy/Concrete Bond in Marine Environment,".*ACI Structural Journal*, Vol. 96, No. 6, pp. 906-914. 542

Mullins, G., Race, R. and Sen, R. (1999). "A New Device for In-Situ Testing of FRP/Concrete Adhesion". Fourth International Symposium, ACI SP-188 (Ed. C. Dolan, S. Rizkalla and A. Nanni), Farmington Hills, MI, pp. 383-391. 551

Muchard, M., Robertson, D., Mullins, G., and Stanley, B. (1998) "Statnamic and Dynamic Load Testing of an Instrumented Drilled Shaft at an I-35/I-80 Bridge in Des Moines, Iowa", *Second International Statnamic Seminar*, Tokyo, Japan, October 28-30 ISBN: 90-5809-13-17 pp. 83-98 560

Mullins, G., Garbin, E., Lewis, C., and Ealy, C. (1998) "Statnamic Testing: University of South Florida Research", *Second International Statnamic Seminar*, Tokyo, Japan, October 28-30, ISBN: 90-5809-13-17 pp. 117-132. 576

Hajduk, E., Paikowski, S., Mullins, G., Ealy, C., Lewis, C., and Hourani, N.M., (1998) "The Behavior of Piles in Clay During Statnamic, Dynamic, and different Static Load Testing Procedures", *Second International Statnamic Seminar*, Tokyo, Japan, October 28-30, ISBN: 90-5809-13-17, pp. 59-74. 592

Justason, M., Mullins, G., Robertson, D., and Knight, W. (1998) "A Comparison of Static and Statnamic Load Tests in Sand: A Case Study of the Bayou Chico Bridge in Pensacola, Florida," Presented to *The North American Deep Foundation Institute*, October 15-17, ISBN: 90-5809-13-17 pp. 43-54. 607

Robertson, D., Muchard, M., Mullins, G., and Brown, D. (1998) "Lateral Statnamic Load Testing: A new method for evaluating lateral load capacity", *Second International Statnamic Seminar*, Tokyo, Japan, October 28-30, ISBN: 90-5809-13-17 pp. 619

Mullins, G., Sen, R. and Spain, J. (1998). "Testing of CFRP/Concrete Bond,", in "Fiber Composites in Infrastructure (Ed. H. Saadatmanesh and M. Ehsani)", Vol II, University of Arizona, Tucson, pp. 211-218. 629

Gunaratne, M., Stinnette, P., Mullins, G., Kuo, L., and Echelberger, W. Jr., (1998). "Compressibility Relations for Peat and Organic Soil," *Journal of Testing and Evaluation*, ASTM, Vol. 26, No. 1, pp. 1-9. 637

Stinnette, P., Gunaratne, M., Mullins, G., and Thilakasiri, S., (1997). “A Quality Control Programme for Performance Evaluation of Dynamic Replacement of Organic Soil Deposits,” Geotechnical and Geological Engineering, Vol.15, No. 4, pp. 283-302. 646

Thilakasiri, S., Mullins, G., Stinnette, P., Gunaratne, M., and Jory, B., (1996). “Analytical and Experimental Investigation of Dynamic Compaction Induced Stresses.” *International Journal of Numerical and Analytical Methods in Geomechanics*, Vol. 20, No. 10, pp. 753-767. 666

Thilikasiri, H., Gunaratne, M., Mullins, G., Stinnette, P., and Jory, B., (1996). “Investigation of Impact Stresses Induced in Laboratory Dynamic Compaction of Soft Soils,” *International Journal for Numerical and Analytical Methods in Geomechanics*, Vol. 20., pp.753-767. 681

Thilakasari, S., Mullins, G., Stinnette, P., and Gunaratne, M., (1996). “Discussion of Impact of Weight Falling Onto the Ground,” Paper No. 5957, *ASCE Journal of Geotechnical Engineering, pp*. 415-416. 696

Gunaratne, Ranganath, Thilikasiri, Mullins, Stinnette, and Kuo, (1996). “Study of Pore Pressures Induced in Laboratory Dynamic Consolidation,” *Computers and Geotechnics*, Vol 18., No. 2, pp.127-143. 698

Sen, R., Rosas, J., Mullins, G., Liby, L., Sukumar, S. and Spillett, K. (1996) "Field Measurement of Transfer Length" in *Fiber Composites in Infrastructure ICCI'96*, First International Conference on Composites in Infrastructure (Ed. H. Saadatmansh & M. Ehsani), Tucson, AZ, pp. 536-547. 715

Engebretson, D., Sen, R., Mullins, G. and Hartley, A., (1996). “Strengthening Concrete Block Walls with Carbon Fiber”. *Materials for the New Millennium, Proceedings of the Materials Engineering Conference Volume 2*, ASCE, New York, NY, pp. 1592-1600. 727

Hartley, A., Mullins, G. and Sen, R. (1996) "Repair of Concrete Masonry Block Walls using Carbon Fiber", *Advanced Composite Materials in Bridges and Structures* (Editor M.El-Badry), Canadian Society of Civil Engineers, Montreal, P.Q. pp. 795-802. 736

Sen, R., Liby, L., Mullins, G. and Spillett, K., (1996). “Strengthening Steel Composite Beams with CFRP Laminates”. *Materials for the New Millennium, Proceedings of the Materials Engineering Conference Volume 2*, ASCE, New York, NY, pp. 1601-1607. 744

ACI STRUCTURAL JOURNAL TECHNICAL PAPER

Title no. 99-S39

Durability of E-Glass/Vinylester Reinforcement in Alkaline Solution

by Rajan Sen, Gray Mullins, and Tom Salem

This paper presents results from a 9-month experimental study to evaluate the durability of E-glass/vinylester reinforcement used by the U.S. Navy in the construction of the MRI Pier in San Diego, Calif. A total of 36 specimens were tested. These were split into four groups of 9 specimens each that were exposed to simulated pore solution (SPS) with a pH ranging between 13.35 to 13.5 for periods of 1, 3, 6, and 9 months. Of the nine specimens in each group, a third were unstressed, a third stressed to 10%, while the remaining third were stressed to either 15 or 25% of their ultimate short-term tensile strength. At the end of the designated exposure periods, surviving specimens were tested to failure to determine their residual tensile strength.

The results showed that the E-glass/vinylester bars tested had very limited durability in this environment, especially at stress levels of 15% or higher. All six specimens stressed to 25% failed within 25 days of exposure. Five of six specimens stressed to 15% failed within 180 days. Specimens stressed to 10% lost 70% of their original strength after 9 months of exposure. Even unstressed specimens lost 63% of their original strength after 9 months, indicating that diffusion of the alkaline solution through the resin matrix was largely responsible for their degradation. The faster deterioration of the stressed specimens indicated that resin cracking also played a significant role in the degradation.

Prediction of remaining life for the test specimens based on a Fickian (diffusion) model was between 1.6 to 4.6 years (unstressed) and between 0.5 to 1.7 years for the specimens stressed to 10%. Overall, the results confirm the unsuitability of first-generation glass fiber-reinforced polymer bars as structural reinforcement in concrete members.

Keywords: alkali; concrete; durability; polymer; reinforcement.

INTRODUCTION

The U.S. Navy used E-glass/vinylester reinforcing bars in the construction of the MRI Pier, San Diego, Calif., in 1993. Glass fiber-reinforced polymer (GFRP) bars ranging in size from No. 3 to No. 5 bars were used as the main reinforcement for pile caps and the concrete deck.

A legitimate concern regarding the use of GFRP reinforcing bars in concrete is their long-term durability. This arises because of glass fibers' well-known vulnerability in alkalis.[1] Because the resin matrix protects glass fibers from direct contact in the GFRP composite, this vulnerability is believed to be reduced. However, reliable data substantiating this was unavailable at that time. Given the uncertainty, the U.S. Navy arbitrarily limited stresses to 10% of the maximum short-term tensile strength.[2]

This paper summarizes the results of a 9-month experimental investigation to evaluate the validity of this limit. In the tests, E-glass/vinylester reinforcing bars identical to those used in the construction of the MRI Pier were exposed to simulated pore solution. The study was completed in 1996 and additional information may be found in the final report.[3]

BACKGROUND

Silica constitutes 55% of E-glass fibers.[4] In alkalis, silica reacts chemically with the hydroxyl ions that dissolve its basic silicon-oxygen-silicon structure as

$$-Si - O - Si - + OH^- \rightarrow -Si - OH + SiO^- \text{ (in solution)} \quad (1)$$

This dissolution of silica results in rapid and severe strength loss.

Because concrete has billions of microscopic voids distributed throughout its mass, for example, due to the use of air-entraining admixtures to improve freezing-and-thawing resistance and other factors, any capillary water present in these voids due to exposure to wet/dry conditions has a pH value ranging from 12.5 to 13.5. This represents a caustic or highly alkaline solution.[5] If this alkaline solution can cross the resin barrier, the durability of the GFRP composite will be in jeopardy.

Two mechanisms that allow passage of the alkaline pore solution in concrete to attack glass fibers in GFRP composites are (a) resin cracking under load, and (b) diffusion through the resin. Tests on E-glass/polyester pultruded rods conducted by Canadian researchers[6] indicate that even at stress levels as low as 10% of the ultimate short-term tensile strength of GFRP, the resin matrix can crack at locations where the fibers are not aligned. Misalignment may occur during fabrication and may also be present due to the use of helical wrap for improving bond with concrete. Diffusion is always present and was identified as the mechanism by which alkaline pore solution attacked S-2 glass fibers.[7]

OBJECTIVES

The primary aims of the study were:

- to determine the performance of the E-glass/vinylester reinforcing bars in simulated concrete pore solution at the arbitrarily imposed 10% stress level;
- to assess whether the 10% stress limit was unduly conservative or if it could be increased; and
- to quantify durability in terms of residual strength following exposure in simulated concrete pore solution.

RESEARCH SIGNIFICANCE

Information on the laboratory performance of GFRP used in a demonstration project is important for future calibration. Many innovative features developed in the exposure setup and the testing are presented. Data on the performance of

ACI Structural Journal, V. 99, No. 3, May-June 2002.
MS No. 01-234 received August 7, 2001, and reviewed under Institute publication policies. Pertinent discussion will be published in the March-April 2003 *ACI Structural Journal* if received by November 1, 2002.

ACI member **Rajan Sen** *is the Samuel and Julia Flom Professor in the Department of Civil and Environmental Engineering at the University of South Florida, Tampa, Fla. He is a member of ACI Committees 215, Fatigue of Concrete; 440, Fiber Reinforced Polymer Reinforcement; and 444, Experimental Analysis for Concrete Structures. His research interests include masonry, prestressed concrete, steel, and the application of advanced composite materials.*

Gray Mullins *is an assistant professor in the Department of Civil and Environmental Engineering at the University of South Florida. He received his BSCE, MSCE, and PhD from the University of South Florida. His research interests include full-scale instrumentation and testing in geotechnical structures and the application of advanced composite materials.*

Tom Salem *received his BSCE and MSCE from the University of South Florida.*

GFRP bars subjected to high pH levels at different stress levels is useful for evaluation of structures constructed using this material.

EXPERIMENTAL PROGRAM

The aim of the durability study was to evaluate the appropriateness of the 10% stress limit for the E-glass/vinylester bar used in the construction of the MRI Pier, San Diego, Calif. In view of this, test specimens were investigated at stress levels both above and below this 10% limit to allow for possible increases (or decreases) in the allowable stress.

Four series of tests were carried out in which specimens were tested to determine residual strength after exposure periods of 1, 3, 6, and 9 months. In each series, a total of nine specimens was tested—three each at stress levels of 0, 10, and 25%. The upper limit was later reduced to 15% for the 6- and 9-month series—possible because these tests commenced only after the 1- and 3-month series had been concluded. In all, a total of 36 specimens was tested.

Specimen details

Thirty 3.05 m (10 ft) long No. 3 E-glass/vinylester bars were used in the experimental investigation. Because each test specimen was approximately 1.12 m (44 in.) long, each reinforcing bar provided two specimens and a remnant that was approximately 0.81 m (32 in.) in length. The two specimens were identified by the reinforcing bar number from which it was cut followed by the letter (a) or (b); for example, Specimen 21(b) indicated it was the second bar cut from the reinforcing bar labeled as No. 21. The remnant was similarly identified by the reinforcing bar number followed by the letter (c); for example, 10(c) is the remnant from reinforcing bar No. 10. The remnants were used to evaluate the short-term mechanical properties, that is, tensile strength and elastic modulus as summarized in Table 1.

University of South Florida (USF) anchor

A resin sleeve-type anchor using a steel pipe and a low viscosity epoxy was developed for this study (Fig. 1). This used readily available, inexpensive pipes used in plumbing. The resin used was a high-modulus, low-viscosity epoxy. A polyvinyl chloride (PVC) plug was used to seal the open end.

Three sizes: 0.5, 0.75, and 1.0 in. (12.7, 19.05, and 25.4 mm) diameter, respectively, galvanized steel nipples were evaluated. The length of the anchor was based on the typical dimension of commercially available pipe. Couplers were provided at each end to extend its length. The threaded inside provided greater contact area with the epoxy and improved performance.

The 0.75 in. (19.05 mm) diameter pipe was selected based on the 0.1875 in. (4.7625 mm) clearance on each side between the reinforcing bar and the pipe. The 0.5 in. (12.7 mm) diameter pipe was found to be too narrow. The 1.0 in. (25.4 mm) diameter pipe, although successfully tested, was discarded because of its extra cost and also concerns of possible shrinkage separation between the epoxy and the pipe wall.

Table 1—Average properties of No. 3 E-glass/vinylester bars tested

Properties	U.S. units	SI units
Effective area*	0.078 in.^{2}	50.3 mm^2
Ultimate load	9260 lb	41.1 kN
Failure stress	119 ksi	821 MPa
Tensile modulus	6440 ksi	44.4 GPa
Failure strain, %	1.84	1.84

*Manufacturer's data.

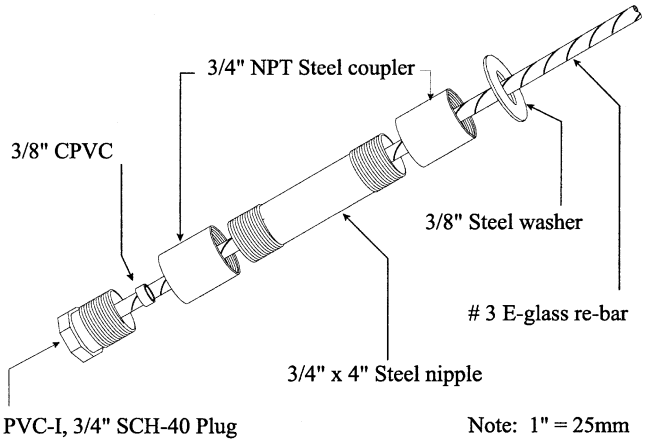

Fig. 1—USF anchor assembly.

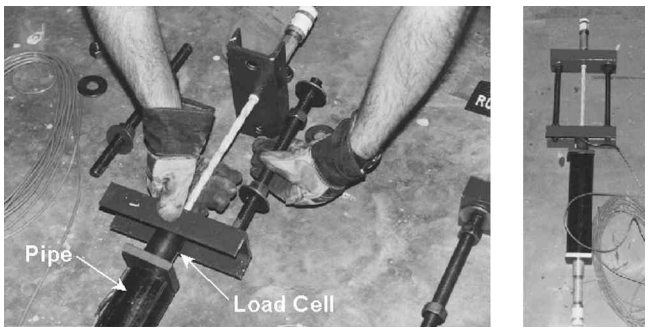

Fig. 2—Assembly of exposure unit (left); assembled unit with stress GFRP bar (right).

Exposure setup

The exposure setup was designed so that it met three key requirements: 1) the method for monitoring and controlling load levels in each specimen was simple; 2) the procedure for determining residual tensile strength was in-built; and 3) it had the facility to circulate (and replace, if necessary) the simulated pore solution (SPS). More importantly, the system devised had to be very inexpensive because of the limited funding available.

A self-straining, portable setup was developed. Its essential components are shown in Fig. 2. A 1.12 m (44 in.) long E-glass/vinylester No. 3 bar provided with a permanent USF anchor at one end was inserted through openings in two

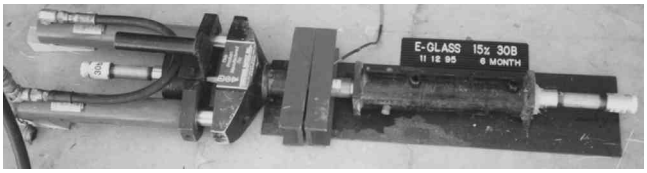

Fig. 3—Residual strength test setup.

channel sections, a load cell, spacer plates, and a steel pipe. A second anchor was subsequently provided at the free end.

The threaded rods were bolted to the channel sections and were tightened against the steel pipe to provide the required preload. The force in the GFRP bar was measured by a load cell sandwiched between the lower channel section and the steel pipe. Removal of the threaded rod released the preload and also freed up space that was utilized by a prestressing jack to determine the residual tensile strength (Fig. 3). The pipe was used as a receptacle for the simulated concrete pore solution (SPS) but also served as part of the reaction frame in resisting the force applied by the prestressing jack.

As the pipe housed the SPS, its bottom was sealed to prevent leakage. Two sets of holes were drilled 200 mm (8 in.) apart along the sides of the steel pipe to serve as an inlet and an outlet to facilitate circulation and replacement of the pore solution. This meant that in the absence of wicking, failure of the GFRP bar would be confined to this 200 mm (8 in.) region.

A total of 18 units were built. As there were 36 specimens, this required the tests to be carried out in sequence. Thus, the 6- and 9-month exposure series commenced after the 1- and 3-month series had been concluded. The 18 units were placed vertically in a rack shown in Fig. 4. Plastic tubing connected the 18 pipes to each other and to a pump that constantly circulated the SPS. As a result, all specimens were exposed to the same solution. The top plastic tube connecting all 18 specimens fed into an upright cylindrical plastic container with a screw-on lid. This was used for daily monitoring of the pH of the circulating solution.

A plexiglass tank was provided below the specimens to capture any SPS that spilled over when the specimens failed or had to be removed for testing. Special solid piping of the same diameter was used to seal the pipes in this case. Thus, the system was flexible enough to permit draining or replacing the SPS as needed.

Considerable attention was paid to the pH of the SPS used. Several alternative pore solutions proposed in the literature were reviewed. In the end, an SPS developed by Sagüés[8] was selected because of its high pH. This solution consisted of 8.33 g of sodium hydroxide, 23.3 g of potassium hydroxide, and 10 g of calcium hydroxide (saturated) in 1 L of distilled water. The pH was monitored daily and average measured values were 13.55, 13.52, 13.35, and 13.41 for the 1-, 3-, 6-, and 9-month studies, respectively. It is important to note that a pH of 13.5 is five times ($10^{0.7} = 5$) higher than the final pH of 12.8 used to test newer GFRP bars.[9]

The applied load was monitored daily throughout the study. A wrench was used to make appropriate adjustments so that constant loads were maintained. The 18 load cells from the specimens were hooked to a strain indicator box through two switch-and-balance units. The channel sections were color-coded for convenience to identify the three different stress levels investigated. Blue corresponded to the lowest limit (0%) and red to the highest limit (25%—later reduced to 15%). Green was used for the intermediate stress limit of 10%.

Fig. 4—Durability setup.

Residual tensile strength

Following completion of the predesignated periods of 1, 3, 6, or 9 months, specimens were removed from the exposure setup for residual tensile strength testing. Because a maximum of nine of the 18 specimens was removed, it was important that the circulating SPS solution was not drained. For this reason, as the specimens were individually detached from the plastic tubing (Fig. 4), the free ends were replaced by identical solid sections that sealed the openings.

The pre-existing tensile force was released by loosening and removing the threaded rods completely. The resulting space was taken up by a twin-cylinder, 20-ton prestressing jack. Tension force was applied by jacking against the pipe (Fig. 3). The applied load was increased at an approximately constant stress rate of 175 MPa/min. The same load cell that monitored the load during exposure was hooked to a strain indicator box to provide the failure load. Following completion of the testing, the load cells were recalibrated against a computer-controlled material testing machine. These results confirmed the accuracy of the strain indicator box readings.

RESULTS

One-month exposure

Table 2 summarizes the test results. The 9 specimens tested were 1(a) to 3(a), all unstressed; 7(a) to 9(a), all stressed to 10%; and 13(a) to 15(a), all stressed to 25%. Only the unstressed specimens and those stressed to 10% of their ultimate short-term tensile strength survived the exposure period. All three specimens stressed to 25% ruptured within 25 days of exposure (Fig. 5). The earliest specimen to fail (15(a)) failed after 15 days; the last to fail (14(a)) failed at 25 days. The average time-to-failure of all three specimens was only 19 days. All failures occurred within the part of the specimen constantly exposed to the alkaline solution, indicating that alkali attack of the glass fibers was primarily responsible for the failure. The six surviving specimens, that is, the unstressed specimens and the ones stressed to 10% of their short-term tensile strength, were tested to failure to determine their residual strength as described previously. The results of these tests indicated very substantial strength losses that averaged from 50% for the three unstressed specimens (Specimens 1(a) to 3(a)), to 60% for those stressed to 10% (Specimens 7(a) to 9(a)).

The reduction in capacity of the unstressed specimens clearly indicated that diffusion of the hydroxyl ion through

Table 2—Percent strength reduction with exposure (1 month)

Specimen no.	Load, %	Time to failure, days	Residual strength		Strength reduction, %	
			kN	lb	Nominal	Average
1(a)	0	—	23.6	5310	41	50
2(a)	0	—	19.3	4315	52	50
3(a)	0	—	16.9	3807	58	50
7(a)	10	—	17.9	4006	56	60
8(a)	10	—	12.1	2724	70	60
9(a)	10	—	18.4	4130	55	60
13(a)	25	17	—	—	100	100
14(a)	25	25	—	—	100	100
15(a)	25	15	—	—	100	100

Table 3—Percent strength reduction with exposure (3 months)

Specimen no.	Load, %	Time to failure, days	Residual strength		Strength reduction, %	
			kN	lb	Nominal	Average
4(a)	0	—	15.5	3474	61	63
5(a)	0	—	14.1	3160	65	63
6(a)	0	—	14.6	3280	63	63
10(a)	10	—	10.7	2407	73	72
11(a)	10	—	10.6	2380	73	72
12(a)	10	—	11.5	2589	71	72
16(a)	25	20	—	—	100	100
17(a)	25	14	—	—	100	100
18(a)	25	19	—	—	100	100

the vinylester resin was primarily responsible for the degradation of the E-glass/vinylester bars. The greater reduction in load capacity of the stressed bars is indicative of the added contribution due to resin cracking.

Since the applied load was 10 and 25% of the short-term tensile strength, the strain in the E-glass/vinylester bars varied between 0.18 to 0.45% obtained from values for effective area and tensile modulus in Table 1. The results indicate that even at such low strains resin can crack, possibly because of misalignment of fibers.

Three-month exposure

Table 3 summarizes the test results for this series. The nine specimens tested were 4(a) to 6(a), all unstressed; 10(a) to 12(a), all stressed to 10%; and 16(a) to18(a), all stressed to 25%. As for the 1-month series, all unstressed specimens and those stressed to 10% survived the exposure period, whereas all the specimens stressed to 25% failed within 20 days of exposure—Specimen 17(a) was the first to fail after 14 days. As before, all failures occurred within the part of the bar that was constantly exposed to the alkali solution, indicating that failure was due to alkali attack.

The six surviving specimens were tested in the manner described previously to determine their residual strength. The results of these tests indicated strength losses averaging 63% for the three unstressed specimens, and 72% for those stressed to 10% of their short-term tensile strength. As stated in the previous section, this difference is indicative of resin cracking in the stressed specimens that provided an additional pathway for the hydroxyl ion to attack the E-glass fibers. The overall reduction in capacity after two additional months of exposure, however, was relatively modest—13% for the unstressed specimens, and 12% for the specimens stressed to 10%.

Table 4—Percent strength reduction with exposure (6 months)

Specimen no.	Load, %	Time to failure, days	Residual strength		Strength reduction, %	
			kN	lb	Nominal	Average
4(b)	0	—	17.5	3874	57	64
5(b)	0	—	12.7	2895	68	64
6(b)	0	—	13.5	3080	66	64
25(b)	10	—	13.7	3254	64	69
26(b)	10	—	10.6	2391	73	69
27(b)	10	—	13.1	2779	69	69
28(b)	15	108	—	—	100	92
29(b)	15	173	—	—	100	92
30(b)	15	—	10.1	2240	75	92

Table 5—Percent strength reduction with exposure (9 months)

Specimen no.	Load, %	Time to failure, days	Residual strength,		Strength reduction, %	
			kN	lb	Nominal	Average
1(b)	0	—	—	4314	52	63
2(b)	0	—	—	2396	74	63
3(b)	0	—	—	3216	64	63
19(a)	10	—	—	3673	59	70
20(a)	10	—	—	1788	80	70
21(a)	10	—	—	2507	72	70
22(a)	15	42	—	—	100	100
23(a)	15	80	—	—	100	100
24(a)	15	100	—	—	100	100

Six-month exposure

Table 4 summarizes the test results for specimens tested in this series. Because all six specimens loaded to 25% of their short-term tensile strength failed within 25 days in the two earlier series, the maximum load was reduced to15% for the remaining series. The nine specimens tested in this series were 4(b) to 6(b), all unstressed; 25(b) to 27(b), all stressed to 10%; and 28(b) to 30(b), all stressed to 15%. As in the two previous series, all unstressed and specimens stressed to 10% of their short-term tensile strength survived the exposure period. Of the three specimens stressed to 15%, only one survived. The remaining two failed within 173 days of exposure, with 28(b) being the first to fail after 108 days. As with previous failures, they occurred within the part of the specimen constantly exposed to the alkali solution, confirming the vulnerability of glass fibers in this environment.

The seven surviving specimens were tested to determine their residual strength. The results of these tests indicated strength losses that averaged 64% for the three unstressed specimens, and 69% for those stressed to 10% of their short-term tensile strength. The relatively small difference suggests that resin cracking plays a limited role, especially at low strain levels.

Nine-month exposure

Table 5 summarizes the test results the nine specimen tested in this series. These were 1(b) to3(b), all unstressed; 19(a) to 21(a), all stressed to 10%; and 22(a) to 24(a), all stressed to

Table 6—Strength reduction prediction[10]

Test series	Load, %	Diffusion coefficient k mm^2/h	Three month percent reduction		Six month percent reduction		Nine month percent reduction		Predicted life, years
			Experimental	Theoretical	Experimental	Theoretical	Experimental	Theoretical	
One month	0	1.80E-3	63	75	64	91	63	—	—
	10	2.80E-3	60	87	69	99	70	—	—
	25	34.7E-3	100	—	—	—	—	—	—
Three months	0	1.06E-3	—	—	69	80	70	89	1.60
	10	1.54E-3	—	—	69	88	70	96	0.50
	25	34.0E-3	100	—	100	—	—	—	—
Six months	0	0.55E-3	—	—	—	—	70	74	2.36
	10	0.73E-3	—	—	—	—	70	80	1.17
	15	3.04E-3	—	—	92	—	—	—	—
Nine months	0	0.320E-3	—	—	—	—	—	—	4.60
	10	0.38E-3	—	—	—	—	—	—	1.70
	15	7.07E-3	—	—	—	—	100	—	—

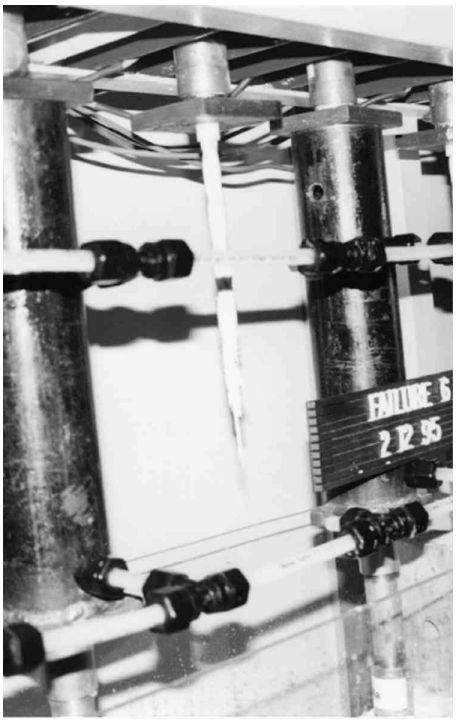

Fig. 5—Failed GFRP bar.

15%. As in all the preceding series, the unstressed specimens, and those stressed to 10% of their short-term tensile strength, survived the exposure period. All three specimens stressed to 15% of their short-term tensile strength failed, however, within 100 days of exposure, with 22(a) being the first to fail after 42 days. This contrasts with similarly loaded specimens in the previous series where specimens lasted much longer and one survived 180 days of exposure. As before, all failures occurred within the part of the specimen that was constantly exposed to the alkali solution.

The six surviving specimens were tested in the manner described previously to determine their residual strength. The results of these tests indicated strength reductions averaged 63% for the three unstressed specimens, and 70% for those stressed to 10%. These results confirm the trend observed in the previous series where the rate of reduction in strength dropped off with time for specimens stressed to relatively low levels.

RESIDUAL LIFE PREDICTION

Katsuki and Uomoto[10] have proposed a simplified procedure to predict the deterioration of GFRP rods immersed in alkali solution that is based on Fick's First Law of Diffusion. The model allows the residual tensile stress σ_t, to be predicted from four parameters: a) diffusion coefficient k (mm^2/h); b) the alkaline concentration C (mol/L); c) exposure time t in hours; and d) initial conditions, that is, radius, R_0, and initial tensile strength σ_0.

To utilize this model, experimental results of strength reduction over a given time frame were used to evaluate an average diffusion coefficient. This value was then used to predict the strength retained after different exposure times, that is, the 3-month diffusion coefficient was used for predicting strength retained after 6 months' exposure. In the case of stressed specimens, the predicted life was obtained by setting the strength retained to just below that needed to sustain the applied stress.

The results from the 1-month study were used to predict the residual strength after 3, 6, and 9 months, and also the remaining life. Similar calculations were carried out using results from the 3-, 6-, and 9-month series.

The results obtained are summarized in Table 6. This table also lists the calculated diffusion coefficients for each of the cases. Because strength reductions in the unstressed bars were smaller, the calculated average diffusion coefficients were also smaller.

Inspection of Table 6 shows that the use of results from the 1-month study for predicting the remaining life of both stressed and unstressed bars is unduly pessimistic, that is, failure is predicted much earlier. This is probably because resin cracking leads to a higher average initial diffusion value. The agreement gets better where results of later tests—for example, those done at 3 months—are used.

Because the model was calibrated for unstressed bars, predictions for these bars is of particular interest.The agreement is fair, however, except for predictions using the 6-month diffusion coefficient where the predicted reduction of 74% compares very favorably with the observed reduction of 70% after 9 months of exposure.

The predicted remaining life for the unstressed specimens ranges from 1.6 to 4.6 years. For the specimen stressed to 10%, it ranges from 0.5 to 1.7 years. The lower limit is based on results from the 3-month tests and the upper limit from the results of the 9-month tests. These predictions, of course,

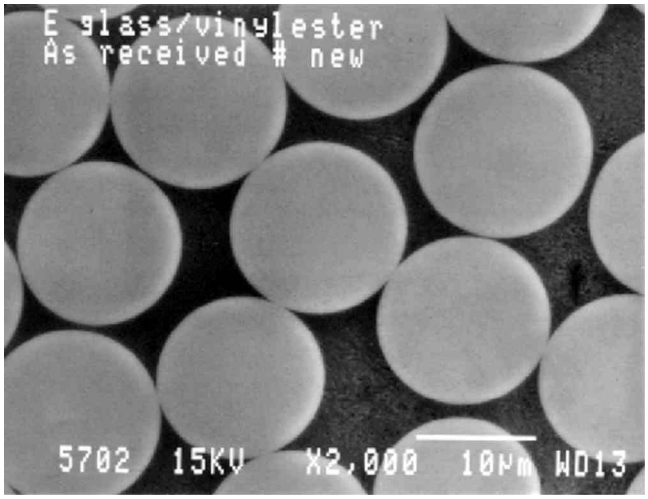

Fig. 6—As-received micrograph.

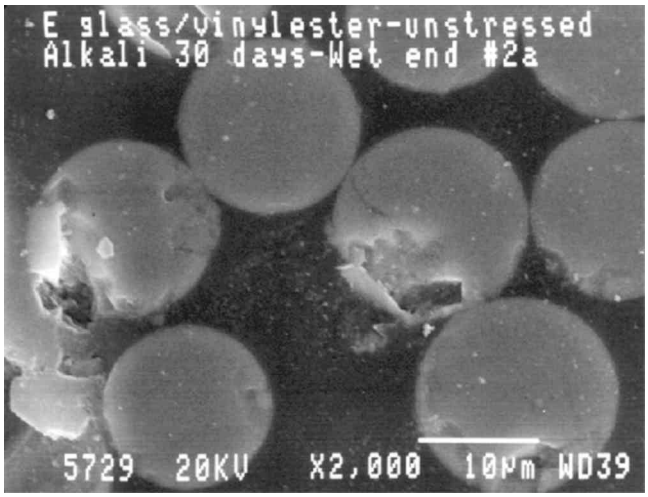

Fig. 7—Unstressed after 30 days.

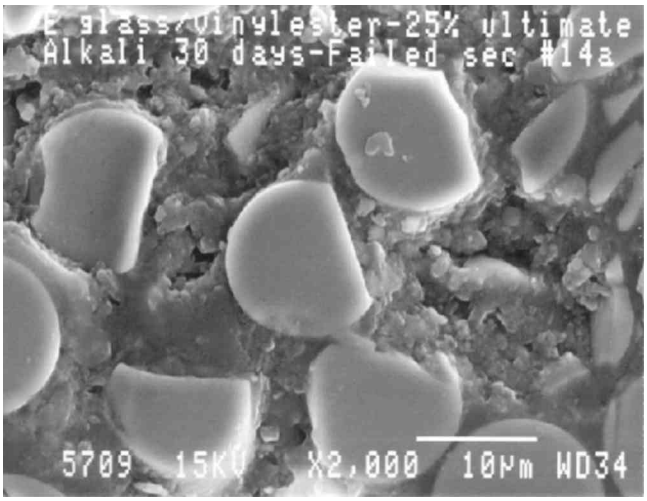

Fig. 8—25% stress after 30 days.

relate to the experimental conditions where the pH concentration remains the same throughout this time frame.

DISCUSSION

The aim of this investigation was to assess the durability of the E-glass/vinylester bars used in the construction of the

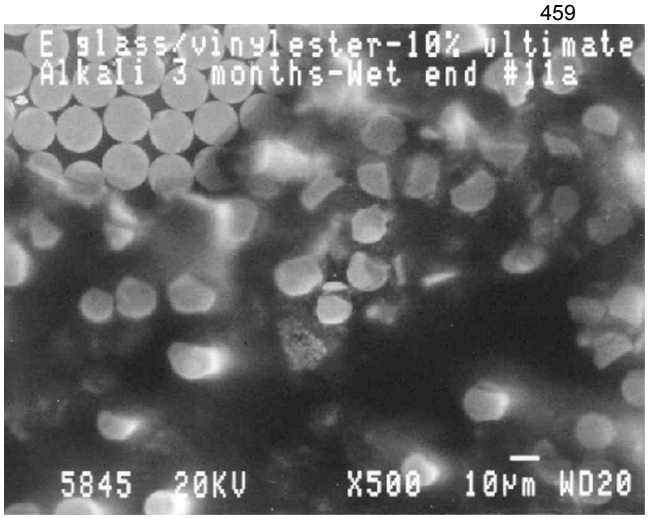

Fig. 9—10% stress after 3 months.

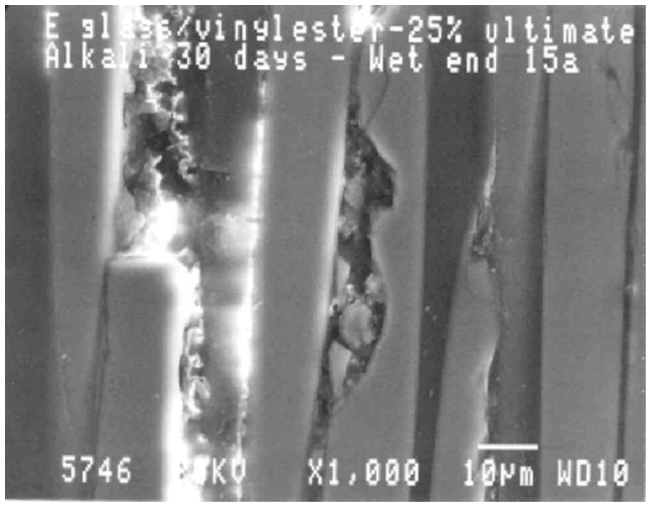

Fig. 10—Longitudinal failed section, 25% load.

MRI Pier, San Diego, Calif., at a sustained stress of 10% of its short-term tensile strength. In the study, an accelerated test was carried out in which these reinforcing bars were exposed to a highly alkaline solution that served to simulate concrete pore solution.

The results from the study convincingly demonstrate the lack of durability of the E-glass/vinylester bars tested. All specimens stressed to 25% failed within 25 days of exposure (Table 2). Five of the six specimens stressed to 15% failed within 180 days, and only one survived (Table 4 and 5). Only the unstressed specimens and the ones stressed to 10% survived the entire duration of the study. Even these specimens sustained substantial strength reductions. For unstressed specimens exposed for 9 months, the reduction averaged 63%, while for those stressed to 10%, the reduction was 70%.

Confirmation of alkali attack may be found from the scanning electron micrographs taken from the as-received specimen (Fig. 6) and from the failed sections of some of the exposed specimens (Fig. 7 to 9). For unstressed specimens, the process of dissolution may be seen in Fig. 7.

For specimens stressed to greater levels, missing cross sections, indicative of fibers that have dissolved, may be seen in Fig. 8 and 9 (the sharp edges of the surviving fibers in this plate are probably the result of cuts made to obtain a

sample and should be disregarded). The degradation can also be seen in the longitudinal section shown in Fig. 10.

The reduction in strength of the unstressed specimens shows that the alkali solution could readily diffuse through the vinylester resin that was used in the pultrusion process. The greater reduction in stressed specimens compared to the unstressed ones is indicative of the role played by resin cracking that provides a passage for additional hydroxyl ions from the alkali solution to attack the E-glass fibers. For specimens stressed to 10%, however, cracking is relatively minor given the small difference in residual strength compared with the unstressed specimens. Clearly, cracking plays a much more significant role for specimens stressed to higher limits, that is, 25% where failure occurred within 25 days, or 15% where failure occurred in five of six specimens within 180 days.

The results relate, of course, to the durability of the E-glass/vinylester bars tested in simulated pore solution. While this does not replicate the conditions the E-glass/vinylester reinforcing bars are exposed to in hardened concrete, they do, however, indicate extremely poor durability. In view of this, the bars tested are considered unsuitable for applications involving fresh concrete where diffusion is likely to be prevalent.

CONCLUSIONS

This study presents results from a focused experimental investigation that evaluated the durability of E-glass/vinylester bars in an alkaline environment. The specimens tested were identical to those used in the construction of the MRI Pier, San Diego, Calif. Four stress levels: 0, 10, 15, and 25% of the ultimate short-term tensile strength were investigated. The pH of the simulated concrete pore solution varied between 13.35 to 13.5 over the duration of the study.

The following conclusions may be drawn:

1. The USF anchor (Fig. 1) provides a very reliable and inexpensive method of gripping the ends of GFRP polymer bars;

2. The exposure setup developed was quite versatile—it successfully allowed maintenance of the stresses in the GFRP bars, the pH level of the simulated pore solution, and permitted determination of the ultimate residual strength (Fig. 2 to 4);

3. The E-glass/vinylester bars tested showed limited durability in simulated concrete pore solution at stress limits above 15% of its short-term tensile strength. All six bars stressed to 25% failed within 25 days of exposure. Of the six bars stressed to 15%, five failed within 180 days. Unstressed specimens, and those stressed to 10% of the ultimate short-term tensile strength, survived the entire 9-month exposure duration. However, the specimens lost strengths ranging from 63% (unstressed) to 70% (10%) of their original strength. The loss in strength of the unstressed specimens indicates that diffusion of the simulated concrete pore solution through the vinylester resin was primarily responsible for the alkali attack of the glass fibers. The difference in the durability of stressed and unstressed specimens indicates that resin cracking played an important role in the degradation process, particularly at higher stress levels;

4. The predicted life of the bars stressed to 10%, based on a model that only considers diffusion and disregards the effect of resin cracking, is between 0.5 to1.7 years. The same model predicted a remaining life of between 1.6 to 4.6 years for the unstressed bars (Table 6); and

5. Given the experimental findings, the U.S. Navy's decision to select a 10% limit in a demonstration structure appears to be a judicious one, especially if conditions in the hardened concrete are less severe. The bar tested, however, is not durable and should not be used to reinforce concrete.

It is important to recognize that the above conclusions are only valid for the E-glass/vinylester bar tested. Newer GFRP bars developed are reputed to have much better alkaline resistance, though testing was carried out at lower pH levels, that is, 12.8[9] versus the 13.35 to13.5 pH levels used in this study. Note that a pH of 12.8 is only 20% as strong as a pH of 13.5. Recent pH measurements[11] appear to validate the higher range used in this study because a pH of 13.5 is not uncommon. The profession needs to pay careful attention to the pH level specified in tests if GFRP is to be used as the primary structural reinforcement with confidence.

ACKNOWLEDGMENTS

This investigation was carried out with the financial support of the U.S. Army Corps of Engineers. The authors wish to thank Edward O'Neil, program manager, and M. Chawla, of the Materials Engineering Naval Facilities Engineering Service Center, for their contribution. However, the opinions, findings, and conclusions expressed in this publication are those of the authors and not necessarily those of the U.S. Army Corps of Engineers.

REFERENCES

1. Bentur, A., and Mindess, S., *Fiber Reinforced Cementitious Composites*, Elsevier Science Publishers, New York, N.Y., 1990.

2. Chawla, M. S., personal communication with R. Sen, 1993.

3. Sen, R.; Mullins, G.; and Salem, T., "Durability of E-Glass/Vinylester Bars in Alkali Solution," *Final Report* submitted to U.S. Army Corps of Engineers, Aug. 1996.

4. Hartman, D. R.; Grenwood, M. E.; and Miller, D. M., "High Strength Glass Fibers," *39th International SAMPE Symposium*, V. 39, Bk 1, 1994, pp. 521-533.

5. Mehta, P. K., and Monteiro, P., *Concrete: Structure, Properties and Materials*, Prentice-Hall, N.J., Second Edition, 1993, 154 pp.

6. Plumtree, A., and Jessen, S. M., "Damage Development in Composite under Stress in Composite Structures and Materials," *Composite Structures & Materials*, S. V. Hoa and R. Gauvin, eds., Elsevier Applied Science, Barking, England, 1990, pp. 68-75.

7. Sen, R.; Mariscal, D.; and Shahawy, M., "Durability of Fiberglass Pretensioned Beams," *ACI Structural Journal*, V. 90, No. 5, Sept.-Oct., 1993, pp. 525-533.

8. Sagüés, A., "Corrosion of Epoxy Coated Rebar in Florida Bridges," *Final Report* to Florida Department of Transportation, 1994.

9. Benmokrane, B.; Rahman, H.; Minh-Tan Ton-That; and Robert, J., "Improvement of the Durability of FRP Reinforcements for Concrete Structures," *Durability of Fibre Reinforced Polymer (FRP) Composites for Construction*, Montreal, Canada, 1998, pp. 571-585.

10. Katsuki, F., and Uomoto, T., "Prediction of Deterioration of FRP Rods to Alkali Attack," *Proceedings of the Second International RILEM Symposium (FRPRCS-2), Non-Metallic (FRP) Reinforcement for Concrete Structures,* L. Taerwe, ed., E&FN Spon, London, 1995, pp. 83-89.

11. Li, L.; Sagues, A. A.; and Poor, N. D., "In Situ Leaching Investigation of pH and Nitrite Concentration in Concrete Pore Solution," *Cement and Concrete Research*, V. 29, No. 3, 1999, pp. 315-321.

ACI STRUCTURAL JOURNAL TECHNICAL PAPER

Title no. 98-S72

Seal-Slab Prestressed Pile Interface Bond from Full-Scale Testing

by Gray Mullins, Ruben Sosa, Rajan Sen, and Moussa Issa

This paper presents experimental results from a study to assess the interface bond between a cast-in-place concrete seal slab and prestressed concrete piles in cofferdams. Three different seal slab placement conditions—fresh water, salt water, and bentonite slurry—were evaluated and the results compared against controls where no fluid had to be displaced by the concrete. Normal pile surfaces were investigated. Additionally, the situation of soil-caked piles was also investigated. Both model and full-scale tests were conducted. In the model tests, twenty-eight 15 cm square prestressed sections were used with the embedment depth varied between d *and 2*d*, where* d *is the width of the pile. In the full-scale tests, 16 specimens were tested. The prestressed piles were 36 cm square with the embedment varied between 0.5 and 2*d*. Four of the 16 piles were cast with embedded gages located at the top, middle, and bottom of the interface region. The results showed that loads were transferred to the piles over an effective area, not the entire embedded depth. Significant bond stresses developed even for the worst placement condition. Recommendations are made for revising current values in specifications.*

Keywords: concrete; foundation; pile; prestressed; salt water; slab.

INTRODUCTION

Seal slabs are unreinforced concrete slabs cast inside cofferdams to prevent the intrusion of water and provide a dry working surface for subsequent construction (Fig. 1). Concreting is typically carried out by displacing water (or natural slurry in cases where the cofferdam supports the sides of an excavation) using a tremie. A tremie is essentially a funnel with a long pipe that places concrete directly on the bottom of the cofferdam. Because the concrete does not fall through the water, cement is not washed away and there is no segregation of coarse and fine aggregates. A series of tremie pipes is used to limit the flow of concrete in the horizontal direction to prevent the build-up of excessive laitence.[1]

As the function of the seal slab is primarily to provide a dry working surface, its design is relatively unsophisticated. The slab depth is selected so that its weight balances the maximum uplift forces. Thus, a 10 m unbalanced head would require a 4 m thick seal slab because concrete density is approximately 2-1/2 times that of water. Such a calculation neglects the frictional resistance that develops at the interfaces between the seal slab and foundation elements such as piles or drilled shafts.

The Florida Department of Transportation (FDOT) requires[2] the seal slab to cure for at least 72 h before the standing water (or slurry) inside the cofferdam can be pumped out. At that time, the seal slab experiences full uplift pressure due to imbalance in hydrostatic pressure inside and outside of the cofferdam. Rational design therefore requires information on the interface shear corresponding to the 72 h concrete strength. Unfortunately, no published data are available, even though the earliest work on interface shear between two concrete surfaces was reported as early as 1914.[3]

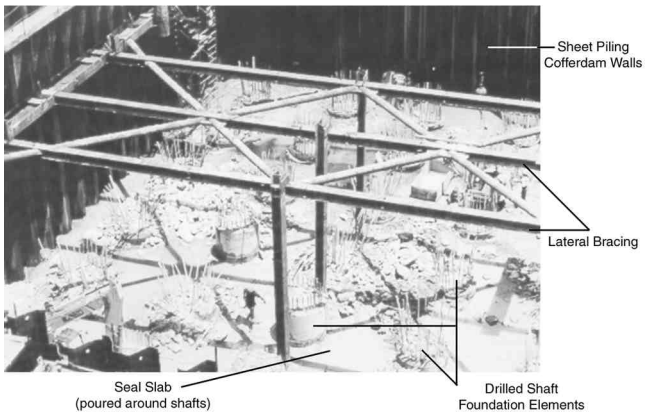

Fig. 1—Seal slab in cofferdam construction (Courtesy Georgia Department of Transportation).

In the absence of experimental data, specifications provide interface shear values that are, by necessity, conservative. For example, AASHTO[4] states that "in seals, the bond between timber, steel, or concrete piles and surrounding concrete may be assumed to be 10 psi (69 kPa)." The 1998 Florida Design Guidelines[5] limited the interface bond between the seal slab and concrete piles to 276 kPa, though it was only set at 34 kPa for steel piles. The larger values permitted in Florida may be due to the local experience associated with the large number of bridges crossing waterways, a relatively high water table, and the predominance of highly pervious cohesionless (sandy) soils that result in excavations quickly filling with inflowing ground water.

In January 1998, the University of South Florida commenced a two-year research program to investigate this problem. Although the goal of the study was to evaluate bond on the basis of full-scale tests, a one-third-scale pilot study was initially carried out to evaluate critical parameters and to develop an efficient method of testing. Following completion of this study, a limited number of full-scale tests were conducted to assess the interface seal slab/pile bond characteristics for prestressed concrete and steel piles, and to recommend suitable values for design. This paper presents results relating to the seal slab/concrete interface bond. A companion paper provides the corresponding results for steel piles.[6] The

ACI Structural Journal, V. 98, No. 5, September-October 2001.
MS No. 00-266 received October 31, 2000, and reviewed under Institute publication policies. Pertinent discussion will be published in the July-August 2002 *ACI Structural Journal* if received by March 1, 2002.

Gray Mullins *is an assistant professor in civil and environmental engineering at the University of South Florida, Tampa, Fla.*

Ruben Sosa *received his BSCE and MSCE from the University of South Florida. He is with GeoSyntec Consultants, Tampa, Fla.*

ACI member **Rajan Sen** *is the Samuel and Julia Flom Professor in Civil and Environmental Engineering at the University of South Florida. He is a member of ACI Committees 215, Fatigue of Concrete; 440, Fiber Reinforced Polymer Reinforcement; and 444, Experimental Analysis for Concrete Structures.*

Moussa Issa *is currently the Chief Structural Engineer, T Y Lin International, Chicago, Ill. He is a member of ACI Committees E 801, Student Activities; 340, Design Aids for ACI Building Codes; and 444, Experimental Analysis for Concrete Structures.*

complete experimental results, as well as the comparative finite element modeling, may be found elsewhere.[7, 8]

RESEARCH SIGNIFICANCE

No studies have previously been carried out to evaluate the seal slab/concrete interface bond for conditions that may be directly used in design specifications. This study provides the first such experimental data from full-scale tests. Results of the study have already led to changes in the latest specifications.[9] Therein, the allowable stresses are greater, permitting thinner seal slabs and bringing about significant savings in construction costs.

OBJECTIVES

The overall goal of the study was to recommend interface bond values for seal slab and piles that could be directly used in FDOT's design specifications. These values were to be based on full-scale tests on specimens prepared in accordance with current FDOT specifications for commonly encountered conditions. Variables examined were the pile embedment depth, pile surface, pile material (steel or concrete), and the type of fluid displaced by the concrete.

EXPERIMENTAL PROGRAM

A seal slab is subject to uplift pressures that are resisted in part by its weight and in part by shear resistance that develops at the pile/slab and sheetpile/slab interfaces, as shown in Fig. 2(a). The same load transfer characteristics can be simulated by applying tensile loads to the pile and compressive loads to the seal slab (Fig. 2[b]). In essence, the determination of the interface bond translated into conducting pullout tests on individual piles embedded in the seal slab; such an equivalent system was used in this study.

The reaction frame required to remove the piles from a seal slab had to meet multiple requirements of capacity, economy, and portability. An adaptable design was also required to accommodate the differing connections for the steel and concrete pile specimens. Additionally, it needed to be integrated with electronic devices that permitted measurement of load and displacement.

A key parameter in the design of the test equipment was capacity. An upper limit could be determined on the basis of the ultimate tensile capacity of the prestressed pile. This depended on the pile size, concrete strength, and the effective prestress. The greater the capacity, the larger and heavier the equipment, which made testing that much more difficult (and expensive).

Uncertainties associated with bond strength predictions were addressed using a comprehensive pilot study with small-sized piles. A scale model study was carried out to develop an efficient testing method and also to identify critical

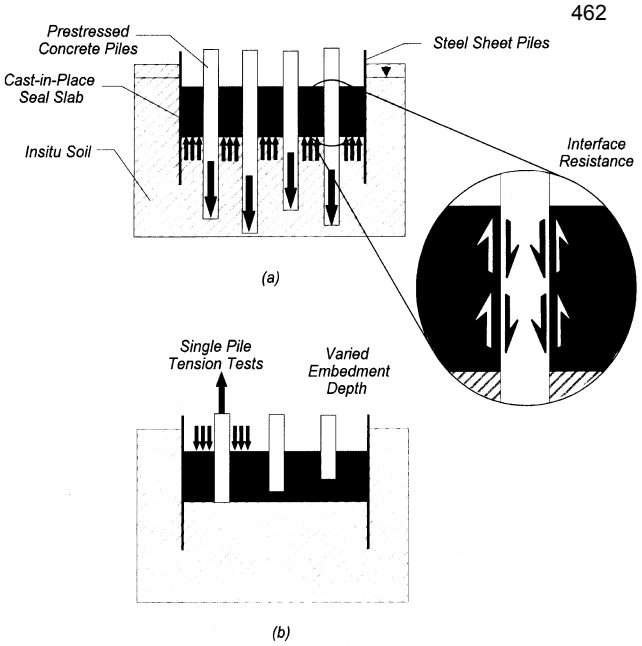

Fig. 2—(a) Field loading; and (b) uplift load simulation.

parameters for the subsequent full-scale program. Brief details from both studies, a complete set of results, and their analysis are presented.

PILOT STUDY

The pilot study simulated three different seal slab placement conditions involving: 1) salt water; 2) fresh water; and 3) drilling fluid. Results were compared against the controls where no fluid was displaced by the concrete. One-third scale was selected since this allowed standard 45 cm prestressed piles to be exactly modeled.[10] Two different surface conditions—natural and soil-caked—were investigated.

Based on results of preliminary trials, the maximum interface bond between the two concrete surfaces was estimated to be approximately 1.7 MPa. This value was used to determine the maximum embedment depth that would not cause tension failure of the prestressed pile. As a result, three different embedment depths—d, 1.5d, and 2d (d is the side of the pile)—were investigated. For each embedment depth, two specimens were tested, that is, 24 tests were conducted (4 conditions × 3 embedment depths × 2 specimens). In addition, four soil-caked specimens were tested—one for each placement condition, and for an embedment depth of 2d.

A total of 28 prestressed piles were tested. Square prestressed piles (1.22 m long, 15 cm wide) were fabricated at a commercial prestressing facility. During fabrication, 3.2 cm threaded bars were embedded centroidally in the specimens to provide a convenient attachment for pulling the specimens (Fig. 3 and 4). Complete details may be found in the final report.[7]

Cofferdam simulation

Four 0.76 m high wood boxes with inside dimensions of 1.4 x 1.4 m were fabricated to simulate the four excavation conditions. Plastic sheeting was used to make the boxes watertight. Wood templates were prepared so that the piles could be accurately positioned inside the form. The piles were spaced at 3 × pile size, that is, the center-to-center distance was 0.45 m (3 × 0.15). The edge distance from the center line was 1.5d or 0.23 m.

As all the specimens were the same length and the seal slab the same thickness, the three different embedment depths of d, 1.5d, and 2d were accommodated by varying the bonded and debonded lengths. For the 15 cm piles, this length varied between 15 cm (d) and 30 cm (2d). All bonded regions were at the bottom of the pile/seal slab. The debonded area was achieved by using bitumen covered with felt paper wrapped in duct tape (Fig. 3). A soil-caked surface was simulated by applying (with a trowel) a paste consisting of a viscous mixture of the clay mineral kaolinite and water. The clay had to be kept moist to prevent it from flaking off when it dried.

Three of the four simulated cofferdams were initially filled with one of the following items

1. Fresh water;
2. 3% salt water; or
3. Drilling fluid.

The latter was made by mixing dry, high-yield bentonite and fresh water to achieve slurry properties similar to those in the FDOT specifications. The final density achieved was 10 kN/m^3 with a pH of 8 and a viscosity of 37 s (Marsh Cone method). The fourth cofferdam was the control and was therefore not filled.

Seal slab placement

Class III seal concrete specified by FDOT[2] was used. This mixture has 332 kg of cement/m^3, a water-cement ratio (w/c) of 0.51, and a specified 28-day strength of 21 MPa. The concrete was purchased from a ready-mix plant and was pumped through a 7.6 cm diameter hose. It was placed from the bottom upwards, keeping the hose tip below the rising level of concrete. This is similar in placement and identical in effect to the tremie method. Figure 3 shows the fresh water cofferdam just after concreting with several inches of free water still present.

Pullout frame

The frame designed for the one-third-scale pilot study is shown in Fig. 4. It consists of two telescopic sections that react against each other via a stiffened beam and a hydraulic jack as shown. A standard nut was used to connect the free end of the threaded rod in the prestressed pile to the base of the tension assembly. Although Fig. 4 conceptually depicts the device assembly, the test procedure was streamlined by leaving it partially assembled between tests. The entire device weighed over 2.2 kN fully assembled and required an overhead chain hoist to assemble and/or move.

Tension loads were measured using a load cell inserted between the top of the jack and the tension assembly. The stiffened beam transferred the load from the base of the jack to a built-up column section which, in turn, applied a uniform compressive stress to the seal slab.

Leveling

As the exposed surface of the seal slab was left uneven from the tremie placement method, a self-leveling grout pad had to be poured around each pile before testing. To further assist in the leveling process, a 12 mm steel bearing plate was placed on the grout immediately afterward. Once the grout had time to cure (approximately 15 min), the tension assembly was connected to the pile and the compression assembly supported on the bearing plate.

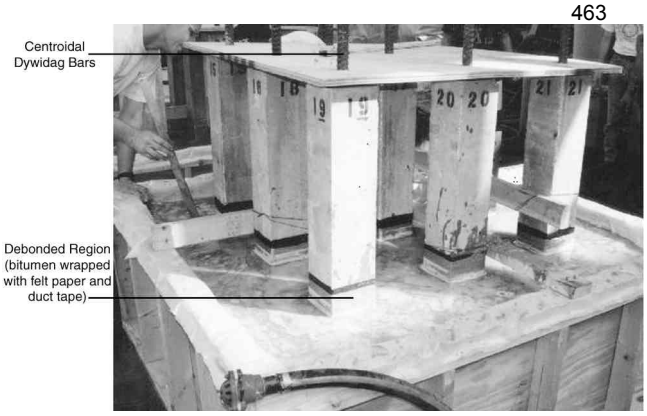

Fig. 3—Pilot study simulated cofferdam.

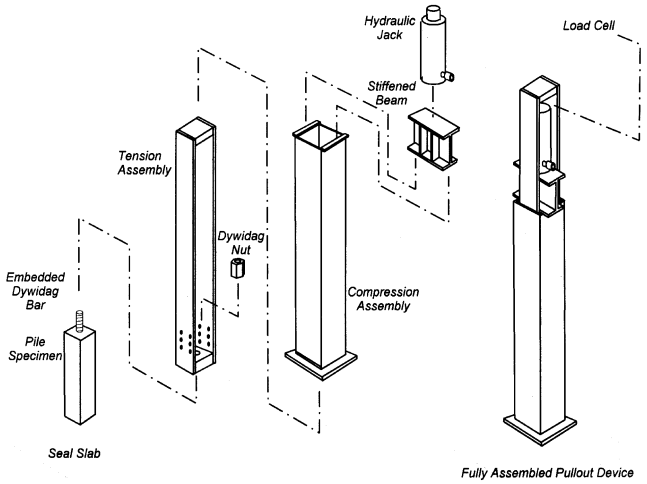

Fig. 4—Pullout equipment in pilot tests.

Instrumentation

A data acquisition system by was used for collecting and recording the test data generated. Loads were measured using a 100 tonne load cell and movement was monitored by two linear variable displacement transducers (LVDTs). One of the LVDTs was magnetically attached to the compression assembly and positioned to record displacement with respect to an external reference beam. This registered any possible seal slab surface crushing or settlement occurring during testing. The other LVDT was attached to the tension assembly and referenced to the top of the compression assembly. This accounted for specimen movement, along with elastic deformation of the frame which was later accounted for in the data reduction.

Test procedure

Tests were initiated after the seal slab had been cured for 72 h. Concrete cylinders were periodically tested to monitor changes in compressive strength during the time it took to complete the tests. The frame was set in position and the pullout test commenced. The tensile load was increased slowly using a manually operated toggle switch, which intermittently engaged the power to a hydraulic pump. The load was increased slowly to reduce any possible dynamic stiffening of the system. Each specimen was displaced upward at least 2.5 cm.

Table 1—Summary of pilot test results

Type	Specimen	f'_c, MPa	Bond length	Pullout load, kN	Bond stress, MPa	Average, MPa
Control	C22	27	1*d*	377	3.9	3.8
	C23	27	1*d*	358	3.8	
	C24	27	1.5*d*	610	4.2	4.3
	C25	27	1.5*d*	632	4.3	
	C26	27	2*d*	630	3.3	3.3
	C27	27	2*d*	625	3.3	
Salt water	C8	29	1*d*	398	4.1	4.1
	C9	29	1*d*	378	4.1	
	C10	29	1.5*d*	631	4.4	4.2
	C11	29	1.5*d*	591	4.1	
	C12	29	2*d*	651	3.3	3.4
	C13	29	2*d*	689	3.6	
Fresh water	C15	29	1*d*	354	3.7	4.0
	C16	29	1*d*	417	4.3	
	C17	29	1.5*d*	620	4.3	4.1
	C18	29	1.5*d*	573	3.9	
	C19	29	2*d*	560	2.9	3.1
	C20	29	2*d*	622	3.2	
Bentonite	C1	29	1*d*	141	1.5	1.5
	C2	29	1*d*	149	1.5	
	C3	29	1.5*d*	557*	3.9	2.8
	C4	29	1.5*d*	237	1.6	
	C5	29	2*d*	206	1.1	1.9
	C6	29	2*d*	543*	2.8	
Soil-caked	Control	27	2*d*	39	0.2	—
	Salt water	31	2*d*	521	2.7	—
	Fresh water	31	2*d*	397	2.0	—
	Bentonite	31	2*d*	49	0.3	—

*Higher values are attributed to scouring action of pumped concrete on piles closest to inflow.

Fig. 5—Postmortem profile view of pilot study specimen during dismantling.

PILOT STUDY RESULTS

A summary of the test results is presented in Table 1. This provides information from all 28 tests and contains details of the compressive strength, the failure load and the computed average bond stress. This was determined as the quotient of the measured failure load and the calculated surface area of the pile in contact with the seal slab. The following observations may be made:

1. Concrete strengths varied between 27 and 31 MPa over the duration of testing;

2. Significant bond stresses developed; the highest value obtained was 4.4 MPa (salt water/1.5*d*), and the lowest was 0.2 MPa soil-caked control. Highest values were for salt water, followed closely by controls and fresh water;

3. Embedment depths above 1.5*d* led to lower average values (Table 1). This suggests that the bond stress distribution is nonuniform and instrumentation would be required to gain an understanding on the stress transfer;

4. Results for salt water and fresh water cofferdam conditions did not differ significantly; and

5. The soil-caked condition did not affect interface bond except in the case of controls and bentonite slurry. For the salt water or fresh water condition, the soil caking was washed off by the water before the installation of the seal slab.

For the larger embedment depths, the prestressed concrete specimens cracked (Fig. 5). This suggested that depths in excess of 1.5*d* may be inappropriate for the full-scale tests. Cracking of the seal slab was also observed during dismantling of the test setup when the sides of the simulated cofferdam were removed. Figure 6 shows a load-slip plot obtained from the pilot study where the pullout capacity did not exceed the tensile capacity. Inspection of this plot indicates that there was continuous slip although minimal up to 50 kN (the elongation of the member was very small.

FULL-SCALE STUDY

The results of the pilot study were used to develop a program for full-scale tests. The principal changes were: 1) elimination of the salt water condition; 2) instrumentation of selected piles to allow evaluation of bond stress distribution with embedment depth; and 3) restriction of the soil-caked surface to bentonite slurry placement. In view of the very high bond stresses that were obtained, the depth of embedment was limited to 1.5*d*, except for bentonite, where the maximum depth was increased to 2*d*. In addition, embedment depths of 0.5*d* were investigated for the control and fresh water placement conditions where the interface bond was expected to be very high.

With three different placement conditions (control, fresh water, and bentonite), two different embedment depths (*d*, 1.5*d*, or 2*d*) and two specimens per test, a total of 12 specimens, were required. Four additional specimens were tested—one each for embedment depth of 0.5*d* (for the control and fresh water condition) and two for investigating the effect of soil caking for the bentonite slurry for an embedment depth of 1*d*. Thus, the controls and the fresh water condition each had five specimens, with six specimens in the bentonite slurry condition.

The bond stresses obtained from the pilot study (Table 1) ranged from a low of 1.1 MPa (bentonite/2*d*) to a high of 4.3 MPa (control/1.5*d*). Because of these large values, 36 cm wide square prestressed piles were used in the full-scale tests. The length of each specimen was limited to 1.5 m. The ends of the strands protruding from the nonpulling end were clinched (flattened) to provide increased anchorage. This would not be required in practice where the pile lengths are much greater and extend beyond the upper surface of the seal slab.

Unlike the pilot tests where a central threaded rod was integrally cast with the specimens, for the full-scale tests the strands were directly attached to the tension frame with prestressing chucks. To ensure that the piles would have a somewhat greater capacity, larger 15 mm strands were used

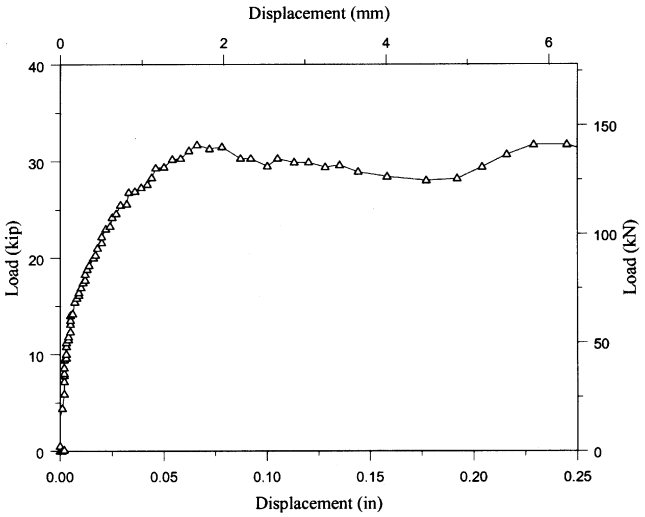

Fig. 6—Load versus displacement: Specimen C1 (1d, bentonite).

instead of the standard 12.5 mm strands, though they were stressed to provide the same effective prestress. The eight 15 mm strands gave an ultimate pulling capacity of $260 \times 8 = 2.1$ MN that exceeded the expected pullout load of the pile. This provided a margin of safety against sudden, dangerous tensile failure of the strands.

A total of 18 specimens were cast at the same commercial prestressing yard. The spacing of the specimens inside the prestressing bed was adjusted so that each specimen had a 0.6 m length of strand projecting from the pulling end that served as a connection point to the pullout frame. Additionally, four specimens were instrumented with embedded sister bar-type strain gages to allow the distribution of bond stresses to be assessed. Figure 7 shows three sister-bar strain gages that consist of a resistive foil strain gage bonded to a short length of 13 mm reinforcing bar. These were located at the bottom, middle, and top of the bonded length of 1*d* (three specimens) or 2*d* (one specimen) (Fig. 7). Complete fabrication details may be found in the final report.[7]

Simulated cofferdam

Three cofferdams had to be constructed for the three conditions investigated. The dimensions of the cofferdams were determined by the number of piles and a 3*d* pile spacing (1.07 m) as in the pilot study. Thus, two of the cofferdams—fresh water and control—were identical in size, but the bentonite slurry-filled cofferdam was larger as it had more specimens.

The cofferdams were constructed using rented steel-reinforced plywood box forms. The forms were connected to form each cofferdam using wedge pins provided by the manufacturer. They were also externally braced using wooden stakes and internally braced with a wooden template that maintained the pile positions. Additionally, each cofferdam was lined with 0.15 mm plastic sheeting. This allowed for the forms to be watertight, preventing the loss of any construction fluid (water or bentonite slurry).

Specimen support

Following the construction of the cofferdam, the specimens were accurately positioned on plywood pads to prevent damage to the plastic lining. Additionally, a polystyrene seal was placed between each concrete pile specimen and the wooden pad to prevent possible bonding between the cast-in-place seal concrete and the bottom of the pile. The specimens were vertically supported by a wooden framework that was secured to the forms (Fig. 8).

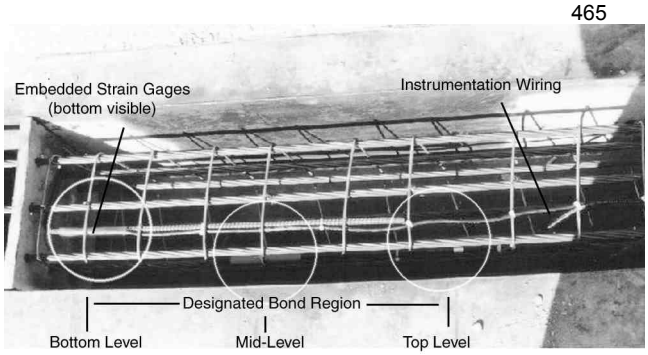

Fig. 7—Prestressing bed for casting 36 cm instrumented piles.

Fig. 8—Overview of cofferdam during concreting.

Debonded surface

As in the pilot study, differing lengths (0.5*d*, 1*d*, 1.5*d* and 2*d*) of the pile surface were bonded or debonded. Debonding was achieved in the identical manner. The bonded concrete surfaces were left in their natural state except for the two specimens that were tested for the soil-caked condition. For this case, an adhesive clay soil, typically used for clay models by artists, was used because it bonded better than the kaolinite paste tested in the pilot study.

The debonded length extended from the boundary of the bonded region to approximately 15 cm above the intended elevation of the finished surface of the seal slab. This included an additional 36 cm depth determined from finite element analysis to ensure uniform distribution of compressive loads to the seal slab (Fig. 2[b]).

Bentonite

The bentonite slurry was made by mixing dry, high-yield bentonite and fresh water. The mixing was accomplished through the use of a shear pump. Enough bentonite clay was added to achieve slurry properties similar to FDOT specifications. The final density achieved was 10.2 kN/m^3 with a viscosity of 40 s (Marsh Cone Method) and a pH of 8. Fig 8 shows the filling and completion of the bentonite slurry filled simulated cofferdam.

Fig. 9—Full-scale pullout device.

Seal slab placement

Seal concrete was placed using a concrete pump truck. The concrete was pumped through a 15 cm diameter hose. It was placed from the bottom upward keeping the hose tip below the rising level of concrete. This procedure is identical to the tremie method commonly used in construction practice.

Testing apparatus

Similar considerations of capacity, economy, and portability dictated the design of the pullout frame. This design incorporated an available double-acting, 3 MN hydraulic jack, a 69 MPa hydraulic pump system, and could accommodate connections for both concrete and steel pile types. Additionally, it provided sufficient clearance for a 4 MN load cell as well as means to record pile displacement.

As with the pilot test, the reaction frame consisted of a tension and compression assembly. The tension assembly was connected directly to the pile using prestress chucks and supported by the hydraulic jack and load cell. The stiffened beam was integrated directly into the compression assembly which applied compressive loads to the seal slab. Fully assembled, the device weighed 16 kN and was placed over each specimen with a straight mast industrial forklift (Fig. 9). Additional information on the design and fabrication may be found elsewhere.[7]

Test setup

The test setup was similar to the pilot study and involved placement of a grout layer, assembly and connection of the hydraulic testing apparatus, attachment of the data acquisition system, and application of loading until failure. Given the requirement that testing be completed quickly following the 72 h cure period, appropriate adjustments were made to expedite testing.

Leveling grout pad

Because concrete vibration is not used in seal slab construction due to possible aggregate segregation in the submerged environment, various degrees of surface roughness developed depending on the placing condition. The bentonite placing condition had the greatest degree of unevenness; the control had the least. The uneven surfaces were leveled using a thin layer of high-strength grout that was placed directly over the seal slab (Fig. 9). The grout was placed and finished two days after the placement of the CIP seal slab. Since the debonded portion of each pile specimen extended well above the CIP slab, there were no difficulties with possible bonding of the grout to the piles.

Frame assembly

Although much heavier than the pilot study device, the full-scale pullout device was easier to use in that it could be left fully assembled between tests. This reduced the number of heavy lifts and expedited testing.

As the entire frame was lowered over the test specimen, the exposed prestressing strands were threaded through the holes in the base of the tension assembly. Standard prestressing chucks that incorporate wedge-type grips were secured on each strand. A 76 mm gap was maintained between the tension assembly and the top of the pile to permit removal of the prestressing chucks after testing. With the chucks in place, the frame was centered and the concrete pile tested.

Data acquisition

As with the pilot study, the data acquisition system was used for collecting and recording the test data generated by the pullout testing. Along with the system, a load cell and two electronic displacement gages (LVDTs) were used to monitor each pile specimen as it was tested. The load cell had a capacity of 4 MN. The electronic displacement gages had a 50 mm range. Additionally, strains were monitored in selected piles that had been cast with embedded resistance-type sister bar strain gages (Fig. 7). For the concrete specimens, one LVDT was magnetically attached to the bottom of the tension assembly and positioned to register displacement with respect to an external reference beam. The other LVDT recorded relative displacement between the tension assembly and the top of the pile specimen. This accounted for any possible slippage of the prestressing chucks.

Test procedure

Once the setup procedure was completed, the pullout testing could be conducted. The tensile load was increased slowly using a manually operated toggle switch which intermittently engaged the power to the hydraulic pump. The load was increased slowly to reduce any possible dynamic stiffening of the system. Each specimen was displaced upward at least 25 mm to ensure that the bond interface had been displaced.

RESULTS

A summary of the test results is presented in Table 2. This provides information from all 16 tests and contains details of the compressive strength, failure load, and the computed average bond stress. Inspection of Table 2 shows that the bond stresses were quite high, ranging between 4.5 MPa for 0.5d embedment in the controls to the lowest value of 1.1

Table 2—Summary of full-scale test results

Type	Specimen	f'_c, MPa	Bond length	Pullout load, kN	Bond stress, MPa	Average, MPa
Control	C0.5	27	0.5*d*	1151	4.5	—
	C1.0A	32	1*d*	1656	3.2	3.2
	C1.0B	32	1*d*	1580	3.1	
	C1.5A	32	1.5*d*	1584	2.1	2.4
	C1.5B	32	1.5*d*	2020	2.6	
Fresh water	W0.5	27	0.5*d*	892	3.5	—
	W1.0A	27	1*d*	1358	2.7	2.7
	W1.0B	27	1*d*	1336	2.6	
	W1.5A	27	1.5*d*	1591	2.1	2.0
	W1.5B	27	1.5*d*	1527	2.0	
Bentonite	B1B	23	1*d*	1338	2.6	2.5
	B1D	23	1*d*	1274	2.5	
	B2A	23	2*d*	1625	1.6	1.5
	B2B	23	2*d*	1438	1.4	
Bentonite (soil-caked)	B1A	23	1*d*	931	1.8	1.5
	B1c	23	1*d*	570	1.1	

MPa for one of the soil-caked bentonite specimens. Trends observed in the pilot tests were repeated: the average bond stresses decreased with increased embedment depth. For example, the average bond stress reduces from 2.7 MPa to 2.0 MPa for fresh water specimens embedded 1.0*d* and 1.5*d*, respectively.

Variations in concrete strength over the duration of the test may also be noted. The lowest compressive strength was for the bentonite series (f'_c = 23 MPa) and the highest for the controls (32 MPa). This was due in part to an increase in strength over the seven-day period it took to complete the testing. A typical load-versus-slip variation plot is shown for each cofferdam condition in Fig. 10 to 12. As previously noted, the plots show continuous displacement with increasing load, initially elastic and then plastic. While measurements included the effect of elongation of the 1.5 m long prestressed pile, calculations show that length increases were minimal even after the pile had cracked. Figure 10 shows no evidence of cracking (bentonite) whereas Fig. 11 and 12 indicate pile cracking at 1044 and 955 kN, respectively. The cracking load was consistently smaller than expected due to the shortened transfer length near the end of the pile and the associated inability to develop effective prestress in the concrete. This was due to the relatively short length of the test piles. In actual construction where longer piles are used, this would not be the case. Additionally, variations in cracking force in nearly identical specimens were attributed to indiscernible alignment errors during testing.

Strain variation

The shear stress distribution within the bonded region of the pile was evaluated using embedded strain gages in four of the specimens: fresh water (1); control (1); and bentonite (2). The bond length was 1*d* for three of the specimens (one in each bed) and 2*d* for an additional specimen in the bentonite. The gages were located at the top, middle, and bottom of the bonded region. Figure 13 shows the axial strain measured at three points along the bond interface during testing of one instrumented pile specimen. Additional results may be found in the final report.[7] The strains recorded at three levels (top, middle, and bottom of the bond interface) define two bonded layers

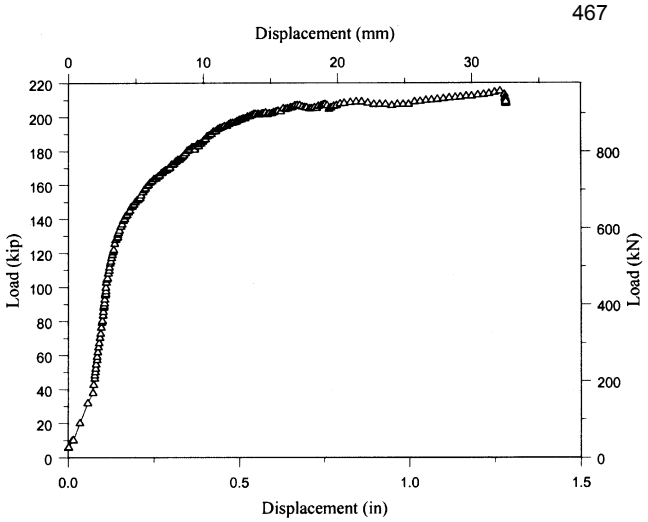

*Fig. 10—Load versus displacement—Specimen B1A (1*d*, bentonite, soil-caked).*

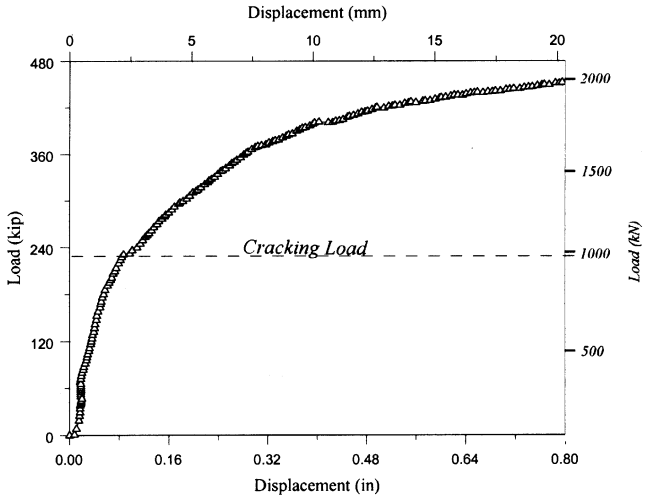

*Fig. 11—Load versus displacement—Specimen W1.5B (1.5*d*, water).*

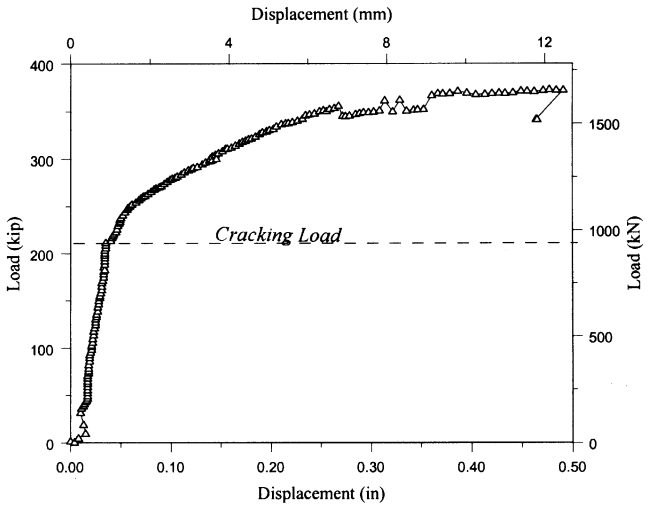

*Fig. 12—Load versus displacement—Specimen C1.0A (1*d*, control).*

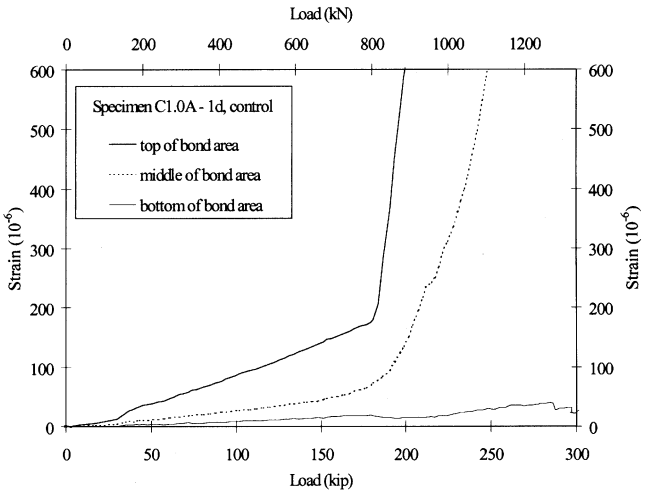

*Fig. 13—Change in strain with respect to load for Specimen C1.0*A *(control, 1*d *embedment).*

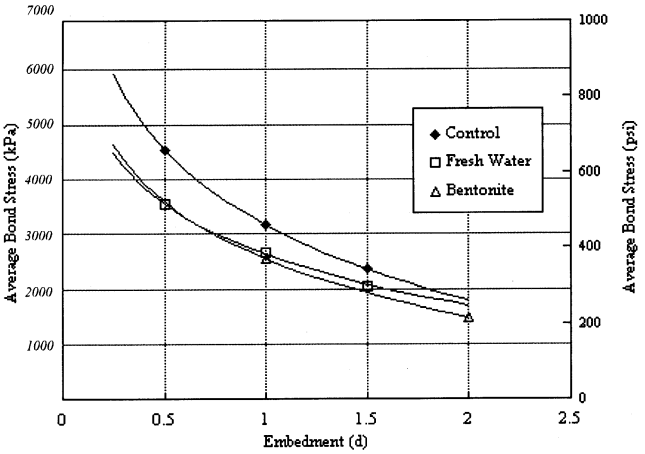

Fig. 14—Average bond stress variation with embedment from full-scale testing.

Table 3—Allowable bond stresses for square piles

Material	Condition	f_b, MPa
Concrete	Salt or fresh water	2.1
	Bentonite	0.7

(upper and lower) separated by the middle gage. The difference between the top and middle gage indicates the load carried by the upper layer. Likewise, the difference between the middle and bottom gage indicates the load carried by the lower bond layer. Inspection of this plot shows the load distribution stayed relatively constant up to the elastic limit of the upper bonded layer (2 MPa); at which time the load was gradually transferred to a lower layer. The top gage reading should linearly relate to the load cell as there is no alternate load path between them. As expected, the gage at the bottom of the bond area registers near zero strains as no additional capacity can be developed below that level. The nonlinear portion of the middle gage indicates the upper layer bond failing and transferring load to the lower layer. Sharp discontinuities are observed in the upper gages due to sudden cracking; whereas less severe strain changes are noticed in the middle gages as the cracked sections reach further into the seal slab.

Fig. 15—Pile cracks during loading.

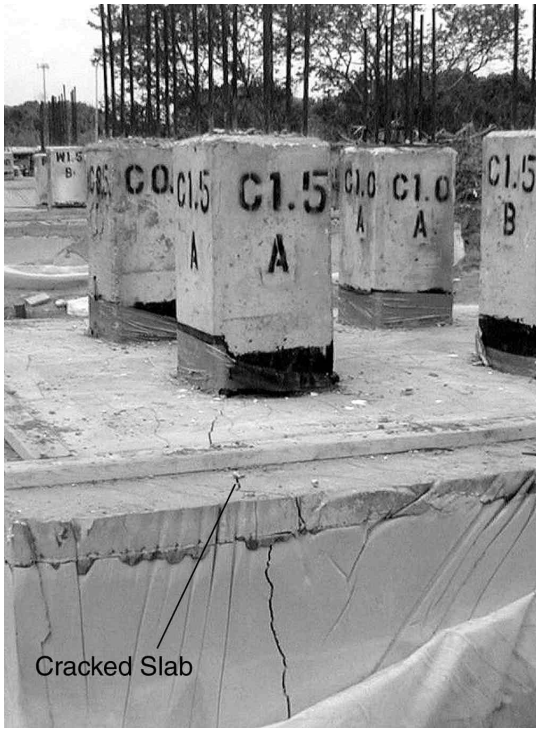

Fig. 16—Seal slab cracks during testing.

The load distribution as measured by the strain gages indicates that the full bond length contributed to its capacity. However, peak bond capacities occurred at different locations and times from top to bottom in that the amount of slippage required to develop peak shear strength is small with respect to elastic elongation. This can also be deduced by evaluating the average bond strengths from Table 2 with respect to embedment (for example, average control values: 0.5*d*, 4.5 MPa; 1.0*d*, 3.2 MPa; and 1.5*d*, 2.4 MPa). As embedment decreases, bond strength approaches an upper limit proportional to the concrete strength as shown in Fig. 14.

As in the pilot study, cracking was observed in both the prestressed piles and in the seal slab. Figure 15 shows a transverse tension crack just above the seal slab. Figure 16 shows a crack that formed in the seal slab originating from the corner of a pullout specimen. These conditions need to be addressed in design.

CONCLUSIONS

This paper presents results from an experimental study that investigated the interface bond stress that developed between seal concrete and prestressed piles in cofferdams. Two series of tests were conducted. In the first series, one-third-scale models were fabricated and tested. Three variables were investigated: 1) displacement of fresh water, salt water, and bentonite slurry; 2) different pile surface conditions; and 3) varied embedment depths expressed as multiples of the pile width *d*. In the second series, full-scale tests were conducted for only two conditions (fresh water and bentonite slurry) as well as varied embedment depths. In all cases, results were compared against controls where no fluid was displaced. Seal slabs were cast using concrete delivered by ready-mix plants that conformed to Class III concrete in current FDOT specifications.[2] The concrete was allowed to cure for 72 h before testing as permitted by existing specifications. The following conclusions may be drawn:

1. Bond stresses determined experimentally were significantly higher than set in current specifications. Average values obtained from the full-scale tests varied between 2.0 to 2.7 MPa for fresh water displacement and from 1.5 to 2.5 MPa for bentonite displacement. The lowest value obtained was 1.1 MPa for piles caked in soil and embedded in bentonite to a depth *d*;
2. Bond stress values from the full-scale tests were generally smaller than those for the model tests excepting for bentonite slurry (Table 1 and 2);
3. Strain data indicated that regardless of the embedment depth, loads were transferred to the pile over an effective depth. For the specimens tested, this depth was the same as the size of the pile *d*;
4. The bond between seal slab and piles caked with mud was largely unaffected when fresh water or salt water was displaced. These effects became important in controls or when bentonite slurry was displaced. This was because the caked soil was washed away by water currents that developed during concreting; and
5. Prestressed piles and seal slabs developed cracks before the full pullout load was developed. Thus, structural failure of the seal slab and/or the piles themselves should be considered in any rational design process.

RECOMMENDATIONS

The buoyancy force generated at the base of a seal slab can be withstood using a combination of both the bond strength formed between the pile and the cast-in-place concrete as well as its self-weight. While using this bond to offset a portion of the upward load, the tensile force developed in the pile cannot be permitted to exceed its cracking strength. The bond capacity developed by an individual pile may be determined using the allowable bond stress f_b listed in Table 3.

This stress f_b may be assumed to act uniformly over an effective surface area A_e, given by

$$A_e = pD \quad \text{if} \quad D < d$$

or

$$A_e = pd \quad \text{if} \quad D > d$$

given the pile width d, pile perimeter p, and the seal slab thickness D. This limits the effective bond length to 1.0d of the pile. Hence, the uplift capacity of the pile P is the lesser of the allowable bond capacity ($P_a = f_b A_e$), or the pile tensile strength (for example, AASHTO [5.6.3.4.1-1]).

In the latest Florida Design Guidelines,[9] allowable bond stress values have been increased from 40 to 250 psi (0.3 to 1.7 MPa) based on the results that are presented in this paper.

ACKNOWLEDGMENTS

This investigation was carried out with the financial support of the Florida Department of Transportation. The authors especially acknowledge the contribution of Hayward Baker, Inc., Tampa, Fla., as well as Rudy in the full-scale testing. Additional thanks are extended to P. V. Liles, Jr. and the Georgia Department of Transportation for providing Fig. 1. The opinions, findings, and conclusions expressed in this publication are those of the authors and not necessarily those of the Florida Department of Transportation.

REFERENCES

1. Tomlinson, M. J., *Foundation Design and Construction*, 5th Edition, Longman Scientific and Technical, Essex, England, 1986.
2. "Standard Specifications for Road and Bridge Construction," Florida Department of Transportation, State Specifications Office, Tallahassee, Fla., 1999.
3. Johnson, L. J., and Nichols, J. R., "Shearing Strength of Construction Joints in Stems of Reinforced Concrete T-Beams as Shown by Tests," Transactions of the American Society of Civil Engineers, Dec. 1914, pp. 1499-1522.
4. "Standard Specifications for Highway Bridges," 13th Edition, American Association of State Highway and Transportation Officials, Washington, D.C., 1983.
5. "Structural Design Guidelines," Florida Department of Transportation, Tallahassee, Fla., July 1998, pp. 4-12.
6. Mullins, G.; Sosa, R.; Sen, R.; and Issa, M., "Seal Slab/Steel Pile Interface Bond from Full-Scale Tests," 2001. (in preparation)
7. Mullins, G.; Sosa, R.; and Sen, R. "A Seal Slab/Pile Interface Bond," *Final Report* submitted to Florida Department of Transportation, June 2000, 151 pp.
8. Wu, Z., "Studies of Bond of Cast-in-Place Concrete to Other Surfaces," MSCE thesis, Department of Civil and Environmental Engineering, University of South Florida, Tampa, Fla., Aug. 1999.
9. "Structural Design Guidelines," Florida Department of Transportation, Tallahassee, Fla., 2000.
10. Fischer, J.; Mullins, G.; and Sen, R., "Strength of Repaired Piles," *Final Report* submitted to Florida Department of Transportation, Mar. 2000.

Studies on the Use of Powder Actuated Nails in Pile Repair

Jeff Fischer[1], Gray Mullins[1], Rajan Sen[1] and Moussa Issa[2]

Abstract

The bond between original and new material is of critical importance in any repair. In an effort to improve bond, the Florida Department of Transportation recently proposed the use of powder actuated nails as shear connectors in the repair of corrosion-damaged prestressed piles. This paper presents results from an experimental study that investigated the efficacy of such repairs. In the study, six one-third scale repaired prestressed columns were tested under concentric axial loads. The repairs were carried out in accordance with current specifications on sections where damage had been simulated during fabrication. Two different shear connector arrangements were investigated. The results indicated that improvement in performance was relatively modest. However, damage caused by the installation of the powder-actuated nails could be problematic.

Introduction

Corrosion damaged piles are commonly repaired by pile jacketing. In this method, jackets consisting of removable or stay-in-place forms are installed around a pile and subsequently filled with concrete, mortar or epoxy. This type of repair is referred to as *non-structural* and is carried out where damage is minor. In case of extreme damage, *structural* repairs are carried out in which a reinforcement cage is incorporated inside the jacket to provide increased capacity.

---

[1] Department of Civil and Environmental Engineering, University of South Florida Tampa, FL 33620
[2] T Y Lin International, Chicago, IL

The efficiency of a repair may be improved by achieving better bond between the pile core and the repair material. Shear connectors are widely used in bridge decks to ensure composite action. The idea of using the same concept in piling applications was first recommended by one of Florida Department of Transportation's districts who proposed the use of powder actuated nails as shear connectors. These are simple to install and have a proven track record for applications involving concrete and steel. In their proposed scheme, the powder actuated nails are fastened to the pile surface in a rectangular grid pattern at 75 mm (3 in.) on centers in the top region of the jacket above the high water level. This arrangement was based on an intuitive understanding of the structural response.

In 1998 the University of South Florida embarked on a study to assess the efficiency of jacketed repairs. As part of this investigation, they chose to conduct experimental studies to assess the effect of using powder actuated nails on the ultimate axial capacity. The repairs were carried out on one-third scale prestressed piles and results evaluated against the ultimate capacity of undamaged controls. This paper presents a brief description of the experimental program and a summary of the test results. Complete test results may be found elsewhere (Fischer et al., 2000).

Experimental Program

Specimen Detail

The test specimens were each 2.44 m long and 15 cm x 15 cm in cross-section. This was established on the basis of a survey of damage in corroded prestressed piles observed statewide. They were prestressed by four 7.9 mm Grade 250 prestressing strands each jacked to 51.5 kN. This provided a jacking stress of 8.9 MPa that is consistent with values of 8.3-9.5 MPa in prototype piles.

To ensure uniformity, accelerated corrosion methods were not used for simulating damage. Instead, damage was artificially formed during fabrication with the help of plywood cutouts. The damage zone had a constant cross-section of 11.4 cm x 11.4 cm that extended over a 45 cm length corresponding to 1.35 m in the prototype. A 3:1 transition slope was provided at each end of the uniformly damaged surfaces to the 15 cm by 15 cm section. As 19 mm plywood was used, this meant the damage length was an additional 11.4 cm. The resulting *formed* surface provided the texture that was used in all the repairs that are reported.

Powder Actuated Nails

In addition to FDOT's scheme in which powder actuated shear connectors are provided in the upper region of the pile jacket above the waterline, an alternate scheme was investigated in which shear connectors extended over the *entire* repair region. The latter scheme is referred to as the *modified* scheme. These two schemes were used in both the non-structural and structural repairs.

Because a limited number of specimens were available, the majority of the specimens tested were non-structural as is generally the case in actual repairs. Thus, only two of the six specimens tested were structural, the remaining four being non-structural. As the modified scheme was anticipated to provide better results, four of the test specimens employed this scheme. These included both structural and non-structural repairs. The original FDOT scheme was limited to non-structural repairs.

Powder actuated nails come in a limited number of sizes and therefore their use in the one-third scale model presented particular problems especially since spacings had to comply with limitations imposed by the manufacturer. As a result, only a single line of 5 cm long fasteners could be used. These had a 7.5 mm head diameter with a shank diameter of 3.6 mm. They were installed with a low velocity, semi-automatic .27 caliber tool. These nails were selected specifically because they were appropriate for the concrete strength of the prestressed piles.

Fig.1 shows the layout of the nails. The first nail was driven along the centerline of the pile 5 cm above mid height. The remaining fasteners were spaced at 7.5 cm intervals. These nails were placed on each of the four faces. In the first (original) scheme, a total of 20 nails were used. In the modified scheme, 40 nails were used since they extended below the waterline.

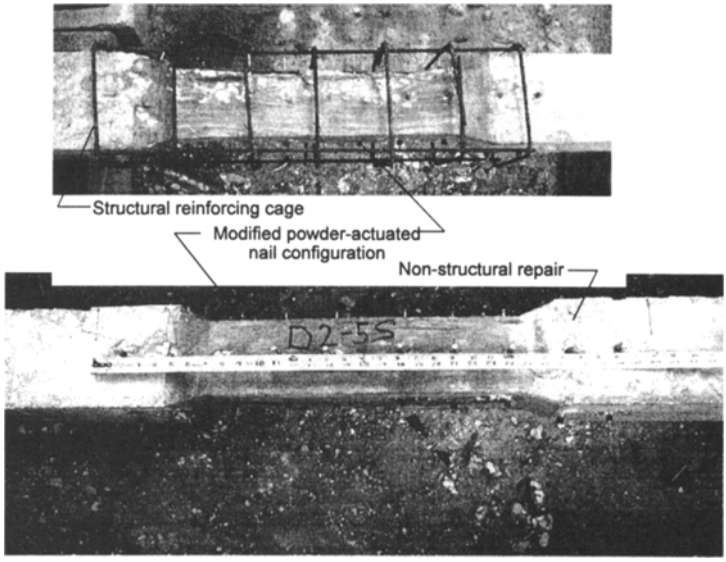

Figure 1. Structural and non-structural repair.

Repair Procedure

Field repairs are carried out on loaded bridges where piles support both service dead and vehicular loads. A special service load simulator was fabricated that permitted sustained loads to be applied to the pile prior to jacketing. This maintained increased stress in the reduced section typical of damaged piles prior to the application of the repair material. In essence it consisted of a pair of steel angles that were clamped in place by high strength bolts (Fig. 2). Two threaded rods were connected to these angles and tensioned to provide the requisite compressive stress in the pile. A calibrated torque wrench was used to maintain desired sustained compressive stress.

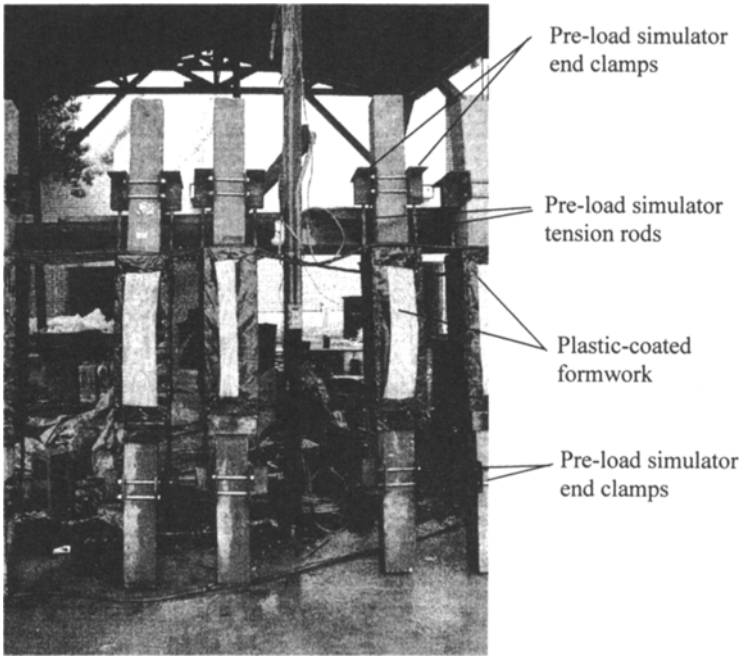

Figure 2. Piles with jackets and pre-load simulator prior to concreting.

A jacket was formed around the pile and filled with water. The forms were drained just prior to the placement of Class IV concrete (FDOT, 1996). The repaired piles were cured at least 28 days with the plastic lined plywood forms in place.

Results

An earlier phase of the study indicated that axial load tests were better at identifying improvements in interface bond between the repair material and the pile core. In view of this, testing of the repaired piles was limited to concentric load tests that were conducted on all six specimens. The results of these tests were compared against those for undamaged controls.

Prior to the test, specimens were instrumented by a number of strain gages that were bonded to the outside surface of the jacket. Additional gages were also attached to the prestressed pile surface. Readings from these gages enabled an assessment to be made of the load transfer characteristics in the jacketed region.

Table 1 provides a summary of the average failure loads from the three series of tests carried out on the six specimens. It also includes information on the debonding load and presents it as a percentile of the ultimate load and that of the undamaged control. Inspection of Table 1 shows that the performance of the structural repair was the best as it reached 73.9% of the capacity of the undamaged control. The performance of the non-structural repairs was surprising; the capacity of the modified repair was lower than that of the original repair in which powder actuated shear connectors were limited only to the top region. This result is believed to be caused by damage that resulted during the installation of the fasteners. As damage was greater, with the installation of more nails, there was greater reduction in capacity.

Table 1 Summary of results from axial load tests.

Test Series	Average Debond Load kN	Average Ultimate Load kN	Debond Percent kN	Percent of Undamaged Control kN
Undamaged controls	n/a	1064	n/a	100%
Structural repairs	774	786	98.3	73.9
Non-Structural *nails at top*	632	674	93.9	63.4
Non-Structural *nails top and bottom*	574	620	92.7	58.3

Inspection of Table 1 also shows that there was little capacity beyond debonding. This was also reflected in the failure modes. In the case of structural repairs where there was a modest 1.7% increase, there was some cracking in the jacket but no separation. In the case of the non-structural repair, the jacket was completely separated where nails were only provided at the top. In the remaining case, the jacket was still held to the pile at the bottom.

Measurement of strain variation across the depth of the pile jacket indicated that the strains were lower at the top than at the bottom. This suggests that bond is poorer at the top than at the bottom. This is probably because of water from the concrete mix rising to the top. It may be noted that ACI 318 imposes a 30% penalty on rebars that have 12 in of concrete below it.

Conclusions

This paper presents results of a study conducted to evaluate the effect of using powder actuated nails to improve composite action in piles. In the testing, repairs were carried out under sustained load that simulated service dead and live loads on a bridge. This meant that additional applied load had to be transferred across the repaired region.

The results of the study showed that improvements in the efficiency of the repairs were quite modest and even declined where powder actuated nails were driven over the entire depth of the repair zone. This was attributed to damage to the concrete core during their installation. As a result, the capacity of original core that was sustaining the service dead and live loads was reduced.

The findings of the study are based on tests on model-scale piles. Given the small size of the piles it was not possible to exactly simulate the layout of powder actuated nails recommended by the Florida Department of Transportation. Thus, whether the same conditions apply to prototype piles is debatable. Nonetheless, it will be prudent to ensure that fasteners chosen do not damage the concrete. Also, as powder actuated nails rely on compression bond for their holding capacity, the bond may deteriorate under eccentric loading that was not tested in this study.

Acknowledgments

The opinions and findings reported in this study are those of the authors and not necessarily those of the Florida Department of Transportation

References

Fischer, J., Mullins, G. and Sen, R. (2000). Strength of Repaired Piles. Final Report submitted to Florida Department of Transportation, Tallahassee, FL.

Florida Department of Transportation (1996). Standard Specifications for Road and Bridge Construction, Tallahassee, FL

Proceedings of the Eleventh (2001) International Offshore and Polar Engineering Conference
Stavanger, Norway, June 17–22, 2001

ISBN 1-880653-51-6 (Set); ISBN 1-880653-55-9 (Vol. IV); ISSN 1098-6189 (Set)

Effect of Environment on the Integrity of CFRP/Concrete Bond

Rajan Sen and Gray Mullins
University of South Florida, Tampa, FL, USA
Mohsen Shahawy
SDR Engineering, Tallahassee, FL, USA
John Spain
PSI Environmental Geotechnical Construction, New Haven, CT, USA

ABSTRACT

The Florida Department of Transportation (FDOT) is one of the leaders in the US on the application of CFRP material for the repair of bridges damaged by vehicular collision or corrosion. As part of an integrated research effort, FDOT sponsored a multi-year experimental study to investigate the long term integrity of the bond between CFRP/epoxy adhesive and concrete. In the study, five competing epoxy systems were evaluated for three disparate exposure conditions representative of Florida's sub-tropical climate. Results were compared with identically prepared specimens kept in a controlled environment. Following completion of exposure, bond integrity was evaluated visually and through destructive testing. The results reaffirmed that bond deterioration was a function of workmanship and surface preparation. It also indicated that visual inspection was limited in its ability to identify degradation. Despite the severity of the exposure, all systems performed satisfactorily.

KEY WORDS: bond; carbon; concrete; durability; tension; torsion; epoxy; FRP.

INTRODUCTION

Carbon fiber reinforced polymers (CFRP) are increasingly used for repair and strengthening of structural elements made of reinforced or prestressed concrete. As the performance of the repaired element depends on the integrity of the epoxy bond between the CFRP and the concrete surface, evaluation of its likely long-term performance is of critical importance.

Bond integrity of particular interest is that encountered under *service* conditions. This varies from application to application depending on the *post-repair* environment. For this reason, satisfactory service performance of CFRP bridge column retrofit in temperate California cannot necessarily be assumed to apply, for instance, to similar repairs carried out in New Hampshire where freeze-thaw cycles are encountered. Consequently, there is a need to evaluate performance for specific service conditions.

This paper is an overview of studies carried out over several years to investigate the likely long-term performance of CFRP repairs carried out by the Florida Department of Transportation (Sen 1997; Sen et al. 1999; 2000). In the experimental investigation, long-term performance was assessed both qualitatively and quantitatively. Qualitative assessment refers to visual and tactile examination while quantitative assessment refers to destructive tests carried out to measure the residual interface bond. This required the development of specialist equipment, Mullins et al. 1998, 1999.

BACKGROUND

In the 1990s the Florida Department of Transportation used CFRP material to repair several busy highway bridges. Such repairs fell into two broad categories (1) emergency repair of bridge superstructures damaged by vehicular collision and (2) repair of corrosion-damaged structural elements. In either case, time and cost considerations led to the selection of the CFRP repair system.

Typical examples of both categories of repair are illustrated in Figs 1-2. Fig. 1 shows a prestressed concrete AASHTO girder bridge on I-75 near Naples, FL that was hit by a construction vehicle carrying a large crane whose boom had not been lowered. This caused severe damage to several of the girders. The need to keep the main highway connecting New York and Miami open necessitated rapid repairs that were carried out using CFRP. Fig. 2 shows corrosion damage in a reinforced concrete bridge on State Road 24 over Indian River, Melbourne FL. As before, speedy repairs were carried out using CFRP.

The service environment for the two repairs is completely different. In the first structure, Fig.1, environmental effects are due to changes in ambient conditions. Thus, the integrity of the bond would have to resist the detrimental effects of a mis-match in the coefficient of thermal expansion between the concrete and the CFRP material (Hancox and Mayer, 1994). In the second structure, Fig. 2, the repaired element is located within tidal waters and therefore subjected to repeated wet/dry cycles in salt water. The water temperature also changes, so it will be subject to combined wet/dry and thermal cycles.

Objectives

The overall goal of the study was to conduct accelerated tests to assess the integrity of the CFRP bond for the disparate conditions repaired structures were exposed to. No formal accelerated tests have yet been developed though methods for evaluating adhesion were recently proposed (ACI Committee 440, 2000). Consequently, acceleration was simulated using exposure conditions more severe than normally encountered in service.

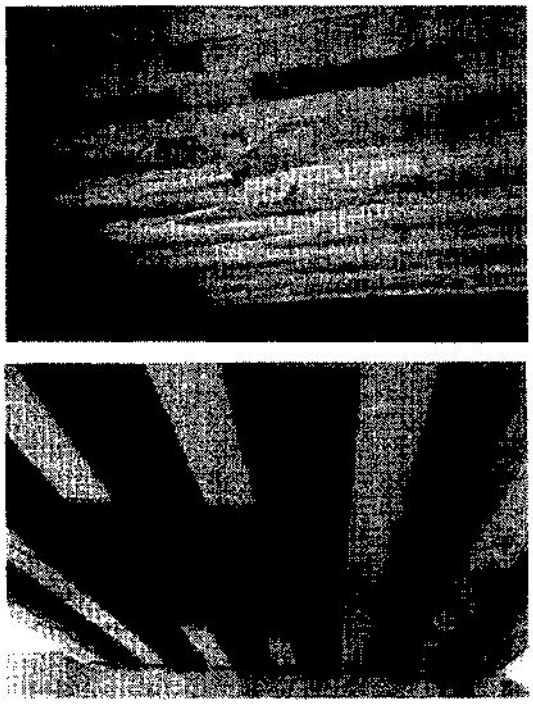

Figure 1. CFRP repair of vehicular damage.

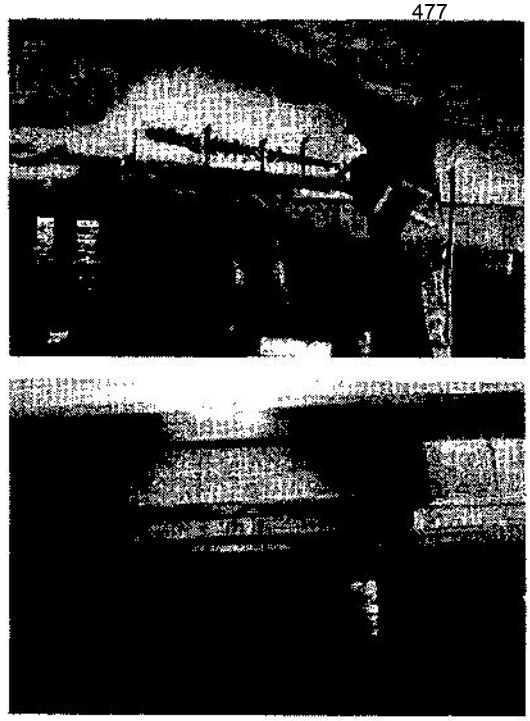

Figure 2. CFRP repair of corrosion damage.

Two factors make the integrity of the bond potentially problematic: *first*, the relatively large temperature range in Florida (see Table 1); *second*, moisture absorption by the epoxy under conditions of high humidity that are characteristic of Florida (Hancox and Mayer 1994). Both effects lead to swelling and potential separation of the CFRP material from concrete.

Table 1. Temperature range and average humidity for Florida cities (1961-90).

City	Maximum, C	Minimum, C	Range, C	Relative Humidity, %
Jacksonville	39	-14	53	81
Key West	34	5	29	76
Miami	37	-1	38	78
Orlando	38	-7	45	79
Pensacola	41	-14	55	78
Tampa	37	-8	45	78

EXPERIMENTAL PROGRAM

Specimens

A total of 24 specimens (19 for exposure and 5 controls) were prepared by the Structural Research Center in Tallahassee, FL and shipped to the University of South Florida campus where the study was conducted. The specimens, each 455 mm square in plan, used uni-directional or bi-directional carbon fibers that were directly bonded to concrete slabs in single or double layers (Table 2). Five different epoxy systems were investigated and these are identified by the roman numerals I-V. The bi-directional carbon fibers used in systems I-III were identical; two different manufacturers made the uni-directional carbon fibers in systems IV and V.

Initial Inspection

All specimens were carefully inspected to identify and catalogue any defects prior to exposure. No evidence of debonding could be detected; however, minor defects were found at the CFRP/concrete corners and edges in four specimens from Systems II and III.

Table 2. Specimen details.

System	Number of Specimens	Fiber Type	Layers
I	6	bi-direct	1 or 2
II	4	bi-direct	2
III	6	bi-direct	1
IV	4	uni-direct	1 or 2
V	4	uni-direct	1 or 2

Exposure

Specimens were exposed to three different environments and the performance compared to that of controls kept in an air-conditioned laboratory. These were (a) outdoor exposure referred to as ***ambient***, (b) wet/dry cycles in 15% salt water referred to as ***tidal***, and (c) combined wet/dry cycles and hot/cold cycles in 5% salt water referred to as ***tidal+thermal***.

Exposure (a) was representative of the environment encountered in vehicular damage repair (Fig. 1). Exposure (b) and (c) simulated conditions representative of the repair of the corrosion–damaged bridge

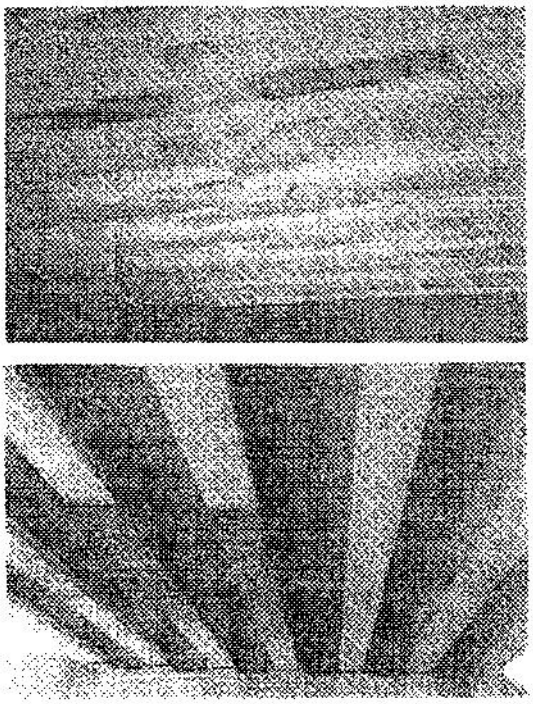

Figure 1. CFRP repair of vehicular damage.

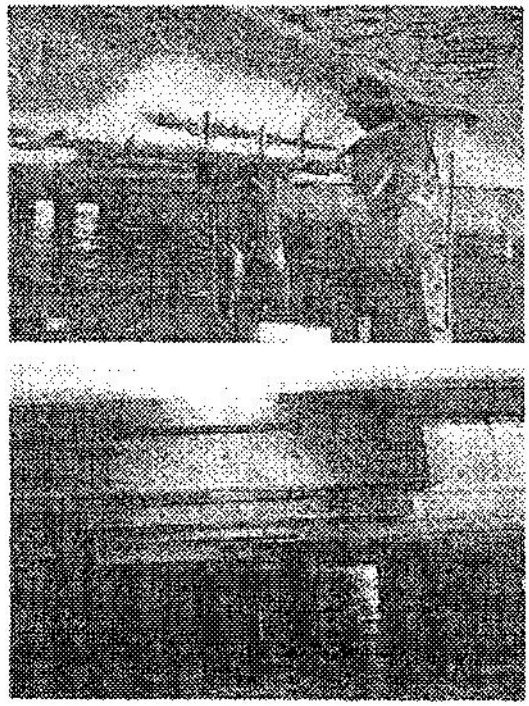

Figure 2. CFRP repair of corrosion damage.

Two factors make the integrity of the bond potentially problematic: *first*, the relatively large temperature range in Florida (see Table 1); *second*, moisture absorption by the epoxy under conditions of high humidity that are characteristic of Florida (Hancox and Mayer 1994). Both effects lead to swelling and potential separation of the CFRP material from concrete.

Table 1. Temperature range and average humidity for Florida cities (1961-90).

City	Maximum, C	Minimum, C	Range, C	Relative Humidity, %
Jacksonville	39	-14	53	81
Key West	34	5	29	76
Miami	37	-1	38	78
Orlando	38	-7	45	79
Pensacola	41	-14	55	78
Tampa	37	-8	45	78

EXPERIMENTAL PROGRAM

Specimens

A total of 24 specimens (19 for exposure and 5 controls) were prepared by the Structural Research Center in Tallahassee, FL and shipped to the University of South Florida campus where the study was conducted. The specimens, each 455 mm square in plan, used uni-directional or bi-directional carbon fibers that were directly bonded to concrete slabs in single or double layers (Table 2). Five different epoxy systems were investigated and these are identified by the roman numerals I-V. The bi-directional carbon fibers used in systems I-III were identical; two different manufacturers made the uni-directional carbon fibers in systems IV and V.

Initial Inspection

All specimens were carefully inspected to identify and catalogue any defects prior to exposure. No evidence of debonding could be detected; however, minor defects were found at the CFRP/concrete corners and edges in four specimens from Systems II and III.

Table 2. Specimen details.

System	Number of Specimens	Fiber Type	Layers
I	6	bi-direct	1 or 2
II	4	bi-direct	2
III	6	bi-direct	1
IV	4	uni-direct	1 or 2
V	4	uni-direct	1 or 2

Exposure

Specimens were exposed to three different environments and the performance compared to that of controls kept in an air-conditioned laboratory. These were (a) outdoor exposure referred to as ***ambient***, (b) wet/dry cycles in 15% salt water referred to as ***tidal,*** and (c) combined wet/dry cycles and hot/cold cycles in 5% salt water referred to as ***tidal+thermal.***

Exposure (a) was representative of the environment encountered in vehicular damage repair (Fig. 1). Exposure (b) and (c) simulated conditions representative of the repair of the corrosion-damaged bridge

(Fig. 2). In both cases, test conditions were more severe than likely to be encountered under service conditions. In the tidal exposure, specimens were placed in a tank in which the water level was raised or lowered every two weeks. In the first week, they were completely submerged simulating high tide; in the following week the water level was lowered below the bond line to simulate low tide. The tanks were covered with a plastic sheet that served to increase humidity. The tanks themselves were placed outdoors to ensure that temperature changes were comparable to those on highway structures.

An identical arrangement was used for the tidal+thermal exposure excepting that the fully-submerged specimens were placed inside a covered, insulated tank in which the water was heated to 60C. At low tide, the heating was stopped and the specimens allowed to cool without the cover. This led to rapid reductions in humidity and temperature that were deemed more critical for degradation of epoxy bond. The hot/cold cycles were repeated every week and as for the tidal exposure, the tanks were kept outdoors. The water temperature inside the tanks was monitored, as was the ambient temperature. During winter when ambient temperatures were low the temperature range was maximized. The temperature range recorded was comparable to that in Table 1 (Sen et al. 1997).

RESULTS

Visual Inspection

After 17 months of exposure the experiment was stopped because of technical problems associated with maintaining the thermal cycles. Visual and tactile inspection of all 24 specimens was then carried out to identify degradation in bond. A thorough examination revealed deterioration in only four of the 24 specimens. These were the very same specimens that had previously been identified as having flaws (System II and III) and were evenly divided between the tidal and tidal+thermal exposures. With the exception of a single specimen shown in Fig. 3 only minor increases in the extent of debonding were observed.

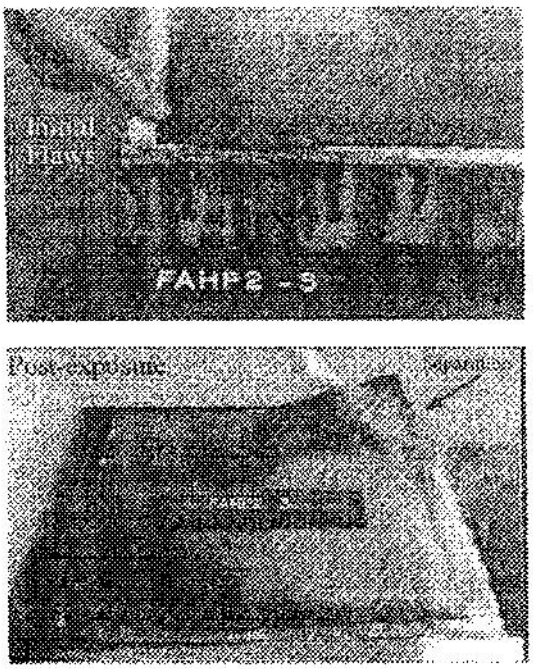

Figure 3. Visual inspection.

The results of the visual inspection were useful in that they provided a measure of the role of workmanship on the integrity of the CFRP concrete bond. However, it was unable to provide information on the changes in the interface epoxy/concrete bond due to exposure.

Destructive Tests

Three devices were developed - one to measure the interface tensile bond and two others to measure the shear bond. Complete details may be found elsewhere (Mullins et al. 1998). The tension test apparatus was similar to commercially available equipment. The shear devices measured the integrity of the bond between CFRP and concrete under *direct* and *torsional* shear. All these devices used a 50 mm diameter metal disk, (called a dolly) that was bonded to the CFRP surface using epoxy. A water-flushed, diamond-tipped core barrel was used to score around the metal disk through the CFRP for the tensile and the torsional shear test. For the direct shear test, a 50 mm diameter core was extracted from the specimen. This cylindrical specimen was inserted inside a special shear box that ensured the failure plane coincided with the location of the CFRP/epoxy bond. Because of the need to extract a core, this test was more time consuming. Moreover, results were inconsistent because of surface defects in the core that led to the introduction of bending stresses along the failure plane. In view of this, only tensile and torsional shear tests were conducted.

Under the action of tensile or shear loads, five different failure modes can occur. These are (1) debonding of the dolly - this means that the strength of the epoxy bond between the dolly and the CFRP material was too low. (2) complete debonding of the CFRP from the concrete - this provides a baseline for the bond strength. (3) partial debonding of the CFRP/concrete bond. (4) separation of the CFRP layers - this indicates that bond between the two CFRP layers was weaker than the epoxy/concrete bond - only possible for Systems I, II, IV or V (see Table 2) where two layers were present and (5) failure in the concrete - this only indicates that the epoxy bond was at least as strong as the concrete.

The tension and torsion tests were conducted on all 24 specimens including the five controls. As the specimens were 455 mm square in plan, several tests could be conducted on the same specimen. On an average, two tension and two torsional shear tests were carried out on each specimen. A total of one hundred tests were carried out altogether.

Tension Tests

Fig. 4 summarizes the results of the 58 tension tests for the four different exposures. The numeric integers in the three segments in this figure specify the numbers of tests relating to a particular mode. It may be seen that a total of 13 (1+5+7) (24%) debonded completely and 18 others (33%) debonded partially. The remaining 24 (43%) did not debond and failure occurred in the concrete.

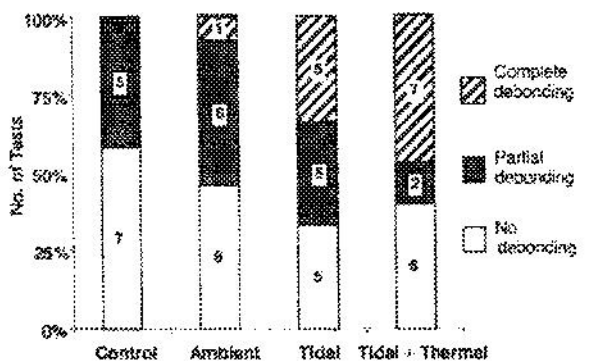

Figure 4. Summary of tensile bond results.

Inspection of Fig. 4 shows that debonding was largely limited to exposure in the wet/dry environment. None of the controls debonded

(Fig. 2). In both cases, test conditions were more severe than likely to be encountered under service conditions. In the tidal exposure, specimens were placed in a tank in which the water level was raised or lowered every two weeks. In the first week, they were completely submerged simulating high tide; in the following week the water level was lowered below the bond line to simulate low tide. The tanks were covered with a plastic sheet that served to increase humidity. The tanks themselves were placed outdoors to ensure that temperature changes were comparable to those in highway structures.

An identical arrangement was used for the tidal+thermal exposure excepting that the fully-submerged specimens were placed inside a covered, insulated tank in which the water was heated to 60C. At low tide, the heating was stopped and the specimens allowed to cool without the cover. This led to rapid reductions in humidity and temperature that were deemed more critical for degradation of epoxy bond. The hot/cold cycles were repeated every week and as for the tidal exposure, the tanks were kept outdoors. The water temperature inside the tanks was monitored, as was the ambient temperature. During winter when ambient temperatures were low the temperature range was maximized. The temperature range recorded was comparable to that in Table 1 (Sen et al. 1997).

RESULTS

Visual Inspection

After 17 months of exposure the experiment was stopped because of technical problems associated with maintaining the thermal cycles. Visual and tactile inspection of all 24 specimens was then carried out to identify degradation in bond. A thorough examination revealed deterioration in only four of the 24 specimens. These were the very same specimens that had previously been identified as having flaws (System II and III) and were evenly divided between the tidal and tidal+thermal exposures. With the exception of a single specimen shown in Fig. 3 only minor increases in the extent of debonding were observed.

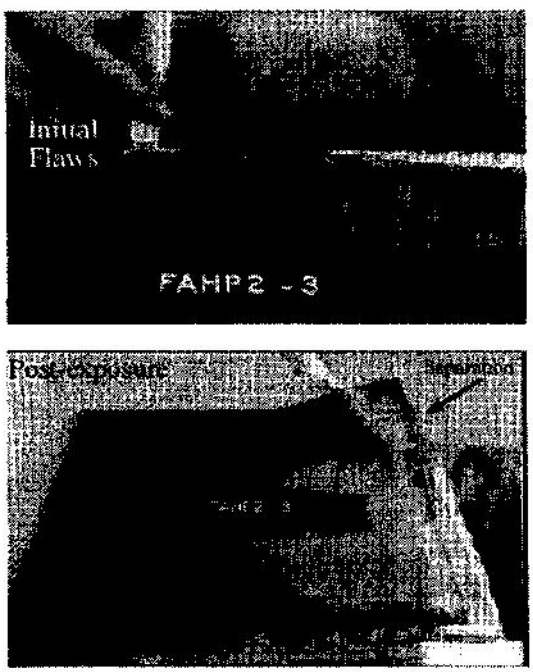

Figure 3. Visual inspection.

The results of the visual inspection were useful in that they provided a measure of the role of workmanship on the integrity of the CFRP concrete bond. However, it was unable to provide information on the changes in the interface epoxy/concrete bond due to exposure.

Destructive Tests

Three devices were developed – one to measure the interface tensile bond and two others to measure the shear bond. Complete details may be found elsewhere (Mullins et al. 1998). The tension test apparatus was similar to commercially available equipment. The shear devices measured the integrity of the bond between CFRP and concrete under *direct* and *torsional* shear. All these devices used a 50 mm diameter metal disk (called a dolly) that was bonded to the CFRP surface using epoxy. A water-flushed, diamond-tipped core barrel was used to score around the metal disk through the CFRP for the tensile and the torsional shear test. For the direct shear test, a 50 mm diameter core was extracted from the specimen. This cylindrical specimen was inserted inside a special shear box that ensured the failure plane coincided with the location of the CFRP/epoxy bond. Because of the need to extract a core, this test was more time consuming. Moreover, results were inconsistent because of surface defects in the core that led to the introduction of bending stresses along the failure plane. In view of this, only tensile and torsional shear tests were conducted.

Under the action of tensile or shear loads, five different failure modes can occur. These are (1) debonding of the dolly - this means that the strength of the epoxy bond between the dolly and the CFRP material was too low (2) complete debonding of the CFRP from the concrete - this provides a baseline for the bond strength (3) partial debonding of the CFRP/concrete bond (4) separation of the CFRP layers - this indicates that bond between the two CFRP layers was weaker than the epoxy/concrete bond - only possible for Systems I, II, IV or V (see Table 2) where two layers were present and (5) failure in the concrete - this only indicates that the epoxy bond was at least as strong as the concrete.

The tension and torsion tests were conducted on all 24 specimens including the five controls. As the specimens were 455 mm square in plan, several tests could be conducted on the same specimen. On an average, two tension and two torsional shear tests were carried out on each specimen. A total of one hundred tests were carried out altogether.

Tension Tests

Fig. 4 summarizes the results of the 55 tension tests for the four different exposures. The numeric integers in the three segments in this figure specify the numbers of tests relating to a particular mode. It may be seen that a total of 13 (1+5+7) (24%) debonded completely and 18 others (33%) debonded partially. The remaining 24 (43%) did not debond and failure occurred in the concrete.

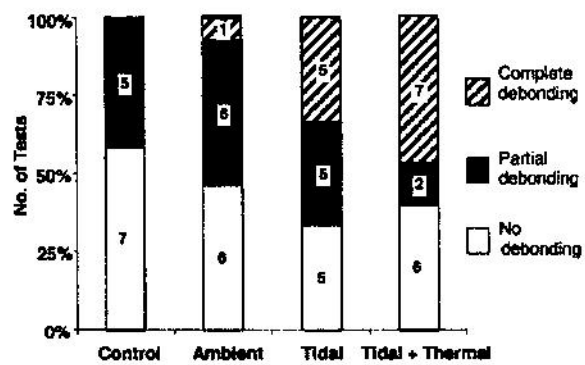

Figure 4. Summary of tensile bond results.

Inspection of Fig. 4 shows that debonding was largely limited to exposure in the wet/dry environment. None of the controls debonded

completely; only one exposed to ambient conditions debonded completely. Thus, constant exposure to wet/dry cycles is more detrimental to the long term CFRP/ concrete bond.

Shear Tests

Fig. 5 summarizes the results from the 45 torsional shear tests. Of these 9 (20%) debonded completely, 12 (27%) partially. Thus, nearly, half the specimens tested debonded partially or completely. The remaining 24 (53%) did not debond. As before, exposure to the wet/dry or a combination of wet/dry and thermal cycles led to the greatest degradation. None of the controls debonded completely; partial debonding was observed in one test.

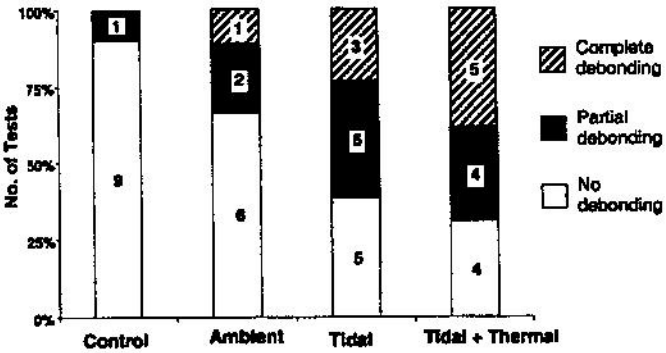

Figure 5. Summary of torsional shear bond results.

The average bond stress from the tensile and torsional shear tests are shown in Fig. 6. The stresses shown in this figure relate only to those tests that led to complete debonding, i.e. 13 tension tests (Fig. 4) and 9 torsional shear tests (Fig. 5).

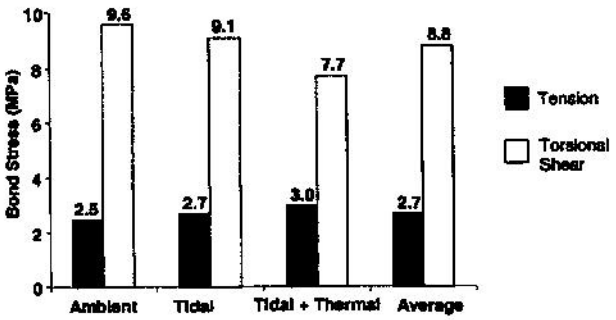

Figure 6. Failure bond stresses in tension and shear.

The tensile debonding stress values range from 2.5-3.0 MPa with an average value of 2.7 MPa. In contrast, the corresponding values for torsional shear are much higher and range between 7.7-9.6 MPa with an average value of 8.8 MPa. These results are consistent with results for plain concrete (Mindess and Young, 1981) where the shear strength is about three times the tensile strength.

When failure occurred in the concrete, no estimate can be made of the extent of degradation in the epoxy/concrete bond. However, where there was partial or complete debonding, a measure of degradation may be obtained by comparing the relative failure loads of the exposed and control specimens. Such an assessment makes the important assumption that all specimens belonging to the same series were identically prepared and were bonded to identical concrete slabs having the same tensile and shear strengths.

Critical Exposure

The residual bond strength may be used to identify the exposure that is most critical for the CFRP/concrete bond. Fig. 7 is a plot of the average residual bond stress from all the 100 tests that were carried out. Exposure to wet/dry cycles or combined wet/dry and thermal cycles led to the greatest degradation in bond while exposure to ambient conditions has relatively minor effect. Surprisingly, the effect of tidal and tidal+thermal were comparable. The researchers had anticipated the latter environment to be more detrimental.

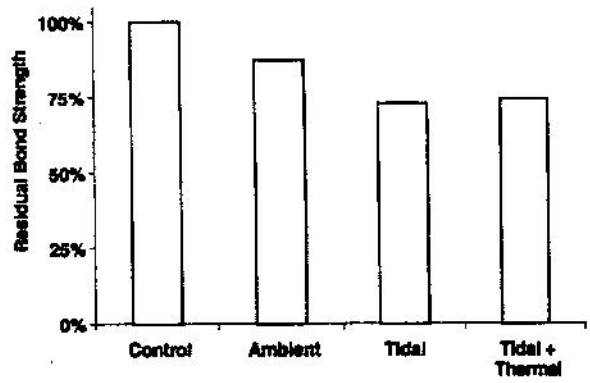

Figure 7. Critical exposures.

System Performance

The relative performance of the five different systems based on the residual bond strength is shown in Fig. 8. For ambient conditions, systems II and IV performed the best and System V the worst. For tidal exposure, System IV was the best but System II was the worst. For tidal plus thermal, System IV was the best and System II the worst. Overall, System IV performed the best showing no deterioration. Systems I and III also performed satisfactorily in all the environments. System II did not perform well in wet/dry environments. System V generally did not perform well in any of the outdoor environments.

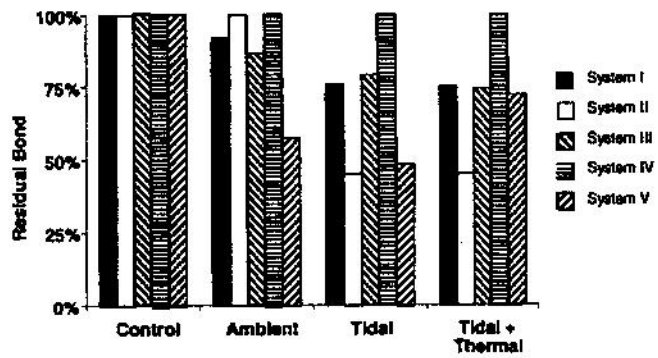

Figure 8. Relative performance.

The relative performance of the five epoxy systems for the exposures are shown in Fig. 9. Tidal exposure shown is the average of tidal and tidal+thermal. It may be seen that the epoxy systems performed better in the ambient rather than the more severe tidal exposure.

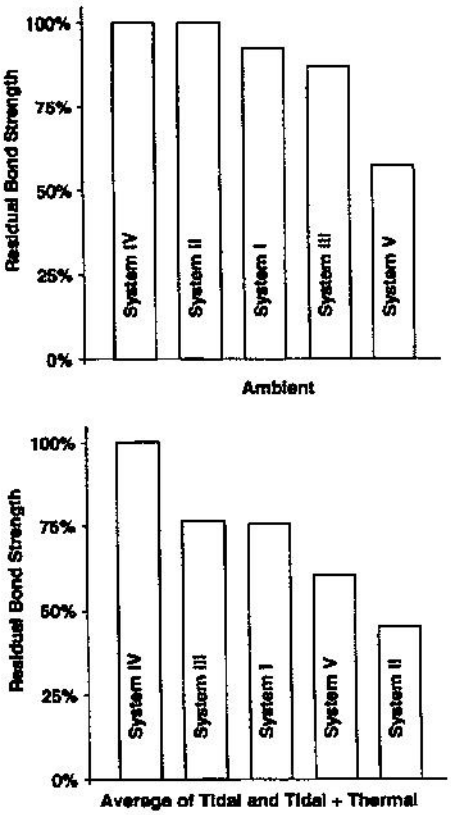

Figure 9. Ranking of systems.

DISCUSSION

The goal of this study was to assess the long-term performance of CFRP/epoxy concrete bond in the disparate environments encountered in Florida. Both qualitative and quantitative measures were used. Visual examination detected degradation in the four specimens that had been initially identified as containing minor defects at the corners and edges. Destructive tension and torsional shear tests detected degradation in an additional 14 of the 24 specimens including controls and those exposed outdoors. Thus, only 6 of the 24 specimens did not degrade. In these six specimens, all failures, i.e. tensile and torsional shear, occurred in the concrete. Visual examination is therefore not very reliable in detecting bond degradation.

The results showed that the average debonding tensile stress was 2.7 MPa, much lower than the corresponding torsional shear bond value of 8.8 MPa. These values were calculated for the 22 tests (9 shear, 13 tensile) in which complete debonding occurred. Partial debonding was observed in 18 tensile tests (Fig. 4) but only 12 torsional shear tests (Fig. 5). As both tests were carried out on the same specimen, it is apparent that the tensile test results provide a lower bound on available strength. Tensile bond failure therefore does not necessarily indicate that the repair will be unable to transfer flexural loads.

CONCLUSIONS

The following conclusions may be drawn:

1. Visual examination alone cannot identify degradation in the epoxy/concrete bond due to exposure. It detected degradation in only 4 of the 24 specimens (19 exposed and 5 controls) instead of the 18 specimens identified by destructive testing.
2. Severe degradation may be expected where CFRP is not properly bonded to concrete at the time of repair (Fig. 3).
3. Tension tests provide a lower bound on the integrity of the bond. Average computed tensile bond for specimens that completely debonded was approximately a third of that obtained from torsional shear (Fig. 6).
4. Exposure to wet/dry cycles was the most critical environment. The addition of thermal cycles did not prove detrimental (Fig. 7)
5. Some epoxy systems performed well in all the environments. Others performed well in selected environments (Fig. 8).

Overall, the results are quite encouraging given the severity of the exposure investigated. The extreme temperature range and humidity exposure greatly exceed conditions that could be reasonably expected under normal service conditions. In spite of this, bond degradation was minimal especially in specimens that had been prepared properly.

ACKNOWLEDGMENTS

This study was funded in part by the Florida Department of Transportation. Additional support was provided by the Department of Civil and Environmental Engineering, University of South Florida,Tampa, FL. This support is gratefully acknowledged. The opinions findings and conclusions expressed in this publication are those of the writers and not necessarily those of the Florida Department of Transportation.

REFERENCES

ACI Committee 440 (2000). "Guidelines for the Selection, Design and Installation of Fiber Reinforced Polymer (FRP) Systems for Externally Strengthening Concrete Structures", Draft Report.

Hancox, N. and Mayer, R. (1994). *Design Data for Reinforced Plastics*, Chapman and Hall, New York, New York.

Mindess, S. and Young, J. (1981). *Concrete*, Prentice-Hall, Englewood Cliffs, NJ, pp. 400-401.

Mullins, G., Sen, R. and Spain, J. (1998). "Testing of CFRP/Concrete Bond,", in *Fiber Composites in Infrastructure (Ed. H. Saadatmanesh and M. Ehsani)*, Vol II, University of Arizona, Tucson, pp. 211-218.

Mullins, G., Race, R. and Sen, R. (1999). "A New Device for In-Situ Testing of FRP/Concrete Adhesion". *Fourth International Symposium, ACI SP-188* (Ed. C. Dolan, S. Rizkalla and A. Nanni), Farmington Hills, MI, pp. 383-391.

Sen, R. (1997). "Durability of Epoxy/Carbon/Concrete Bond in a Marine Environment," *Final Report submitted to Florida Department of Transportation*, January, pp. 67.

Sen, R., Shahawy, M., Mullins, G. and Spain, J. (1999). Durability of CFRP/Epoxy/Concrete Bond in Marine Environment, *ACI Structural Journal*, Vol. 96, No. 6, pp. 906-915.

Sen, R., Shahawy, M., Mullins, G. and Spain, J. (2000). Durability of CFRP/Epoxy Concrete Bond". *Proceedings of the ACUN-2, International Composites Conference Composites in the Transportation Industry* (Ed. S. Bandyopadhyay, N. Gowripalan, N. Drayton and Rik Heslehurst), University of New South Wales, Vol 1, pp. 259-265.

ELSEVIER

Composites: Part B 32 (2001) 309–322

composites
Part B: engineering

www.elsevier.com/locate/compositesb

Strengthening steel bridge sections using CFRP laminates

Rajan Sen[a,*], Larry Liby[b], Gray Mullins[c]

[a]Samuel and Julia Flom Professor, Department of Civil and Environmental Engineering University of South Florida, Tampa, FL 33620, USA
[b]Formerly graduate student, Department of Civil and Environmental Engineering, University of South Florida, Tampa, FL 33620, USA
[c]Assistant Professor, Department of Civil and Environmental Engineering, University of South Florida, Tampa, FL 32620, USA

Received 17 December 2000; accepted 15 February 2001

Abstract

This paper presents results from an experimental investigation to determine the feasibility of using carbon fiber reinforced polymer (CFRP) epoxy laminates to repair steel composite bridge members. Six specimens, each consisting of a 6.1 m long W8 × 24 wide flange A36 steel beam acting compositely with a 0.114 m thick by 0.71 m wide reinforced concrete slab, were first loaded past yield of the tension flange to simulate severe service distress. The damaged specimens were then repaired using 3.65 m lengths of 2 or 5 mm thick CFRP laminates bonded to the tension flange and tested to failure. The results indicated significant ultimate strength gains but more modest improvement in the elastic response. Non-linear finite element analyses were in good agreement with the experimental results. The study suggests that it is feasible to strengthen steel composite members using CFRP laminates.

Keywords: A. Laminates; Carbon fiber reinforced polymer

1. Introduction

Fiber reinforced polymers have been successfully used to strengthen structural elements made of concrete, masonry and wood. Numerous applications have been cited for bridge structures (e.g. repair of prestressed concrete and wood bridges in Switzerland [10], multi-span hollow box girder bridge in Germany [11], slab bridges in Japan [12], and reinforced/prestressed concrete bridges in the United States [13]).

Although there have been some studies which involved strengthening steel members (e.g. Refs. [3,4]), this extension has not been so widespread since it poses a different set of problems. First, the likelihood of lateral buckling makes it necessary to fabricate composite steel sections where the compression flange is continuously supported by a reinforced concrete slab. These sections are much more difficult to fabricate and test in comparison with rectangular concrete or wood sections. Second, steel's high strength and stiffness make it a more difficult material to strengthen especially since carbon fiber reinforced polymers (CFRP) that are commonly used have a smaller modulus. This means that substantial load transfer can only take place *after* the steel has yielded. Finally, for this system, the CFRP/adhesive bond is the weakest link and will always control the mode of failure. Thus, consideration of surface preparation alone will not suffice. Instead, more attention must be paid to augment the capacity of the adhesive through the use of appropriate fasteners.

Successful strengthening of steel bridge sections with CFRP would be particularly useful as steel stringer bridges constitute a large segment of aging bridges in the United States that are nearing the end of their useful service life. If service life could be extended, highway authorities would have access to a lightweight, speedy and therefore economical strengthening method that would minimally disrupt traffic.

The opportunity to use CFRP laminates to strengthen steel came unexpectedly. In 1992, the University of South Florida, Tampa, FL were developing a steel composite bridge model to evaluate the restraint effect of elastomeric bridge bearings [7]. For this study, the girder spacing, slab thickness or the number of shear connectors was not critically important. Consequently, advantage was taken to alter these parameters to boost the ultimate capacity of the slab and to ensure that if the concrete slab were cut longitudinally, three identical steel composite beams would result. In addition, an identical second bridge was fabricated to provide additional specimens.

* Corresponding author. Fax: +1-813-974-2957.
E-mail address: sen@eng.usf.edu (R. Sen).

1359-8368/01/$ - see front matter
PII: S1359-8368(01)00006-3

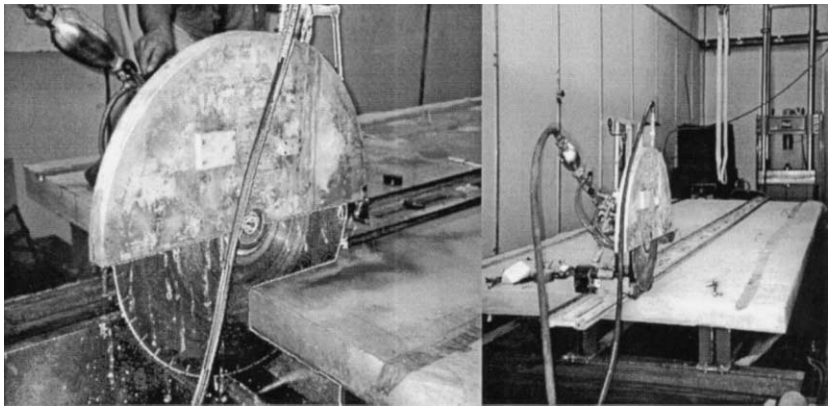

Fig. 1. Cutting bridge into three composite beam sections.

Following completion of the experimental phase of the bearing restraint study, the concrete slabs of the two bridges were cut (Fig. 1) to obtain the six test specimens used in this study. This paper presents a brief summary of the technical problems that were overcome and highlights some of the principal findings. A comprehensive report describing all aspects of the research is available [6].

2. Objectives

The overall goal of the study was to assess the feasibility of using CFRP laminates for strengthening steel composite bridge members. Since only distressed sections would be strengthened it was necessary to simulate such damage prior to any strengthening. The main objectives of the study may be summarized as follows:

1. To develop a procedure that could be used for strengthening steel composite members using CFRP laminates.
2. To evaluate the potential benefit of strengthening damaged steel composite specimens using CFRP laminates.
3. To assess the extent to which experimental results may be predicted using available non-linear finite element computer programs.

3. Specimen details

As mentioned already, the six specimens used in the study were obtained by cutting each of two concrete/steel composite bridge models into three parts (Fig. 1). The resulting cross-section is shown in Fig. 2. It consisted of a 114 mm thick, 710 mm wide reinforced concrete slab that was attached to a W8 × 24 steel section by 36 shear connectors. The spacing of the 50 mm long, 19 mm diameter stud-type shear connectors was varied — they were more closely spaced near the supports than at mid-span. The concrete slab deck was reinforced top and bottom in the longitudinal and transverse directions by 20M (#6 bars). These were spaced at 230 mm in the transverse direction and 280 mm in the longitudinal direction.

The specimens were identified as *North*, *Center* or *South* depending on their location in the original bridge deck. Although the six specimens were geometrically identical, test coupons provided by the fabricator indicated that the yield strength of the A36 steel in the two bridge models were 310 and 370 MPa. Thus, three of the specimens had wide flange beams with a yield stress of 310 MPa and three others had a yield stress of 370 MPa. In the following, specimens are identified by their position in the original bridge deck and the yield stress that is used as a suffix, e.g. *North*-310 MPa, *Center*-370 MPa, etc.

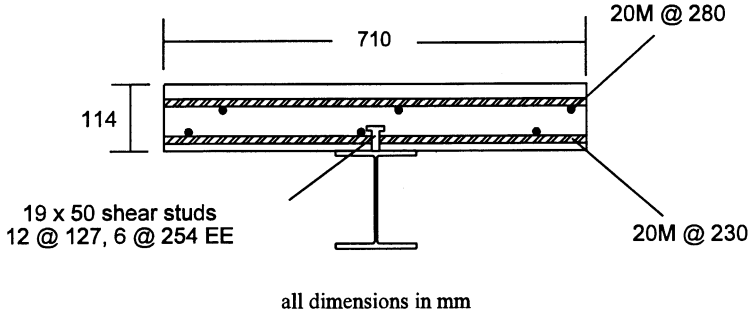

Fig. 2. Slab reinforcement details.

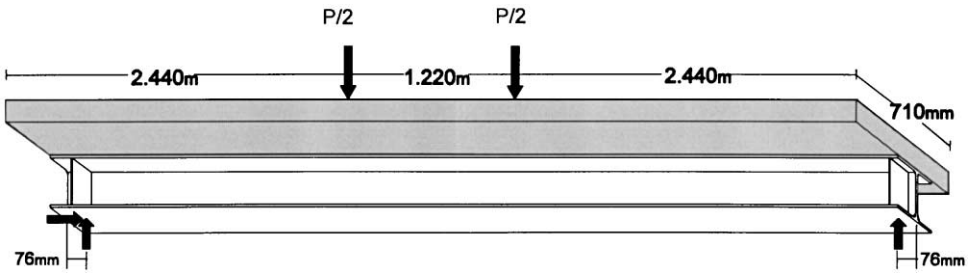

Fig. 3. Loading of simply supported steel composite bridge section.

4. Materials

4.1. Concrete

Normal weight concrete used in casting the bridge deck was supplied locally and was selected to satisfy Florida Department of Transportation's specifications for Class II concrete. Specialist help was used for pouring, screeding and finishing. The 28 day compressive strength of 43.6 MPa was 40% higher than the 31 MPa design strength. An additional 18% compressive strength gain was realized at the time of testing, which resulted in a compressive strength range of 48.5–52.6 MPa.

4.2. CFRP laminates

The CFRP laminates used were fabricated by Composite Horizons, Covina, CA using a simple hand layup process. Widely available T300 carbon fibers and an epoxy matrix were used. The laminate had a uni-directional elastic modulus of 114 GPa and an average unidirectional tensile strength of 1840 MPa. A linear stress-strain relationship gave an ultimate failure strain of 1.6%. Three of the six laminates were 2 mm thick, the remaining three were 5 mm thick. These thicknesses are considerably greater than those used for strengthening concrete or wood and were established from non-linear finite element analyses to ensure comparable strengthening [9]. The width of the laminate was 0.165 m to match the width of the flange of the W8 × 24 beam but its length was only 3.65 m, being limited by fabrication considerations of the CFRP laminate.

4.3. Adhesive

The two-part epoxy adhesive FR1272 was selected based on the recommendation of the CFRP laminate fabricator. It is relatively inexpensive and is widely available. However, it has a pot life of 10–15 min at 24°C making its field applicability limited.

5. Simulation of damage

In order to meet the objectives of this study, it was first necessary to simulate severe service distress in the specimens. This was achieved by pre-loading each specimen (see Fig. 3 for schematic arrangement) past yield of the tension flange, a much higher stress level than the maximum stress of 55% of yield permitted by the AASHTO Bridge Specifications [1]. As a result of this loading, there was permanent deformation in each member prior to strengthening. A summary of the applied loads, deflections and maximum recorded steel strains for all the specimens appears in Table 1. The applied loads averaged 142 and 187 kN for the 310 and 370 MPa girders, respectively.

6. Repair of damaged specimens

6.1. Beam/CFRP combination

Since there were two different sets of yield strengths (310 and 370 MPa) and two different CFRP laminate thicknesses (2 and 5 mm), several beam/laminate combinations were considered. However, to obtain the most data, each steel type was strengthened using each of the two different CFRP laminate thicknesses.

Two of the three lower capacity 310 MPa steel composite beams were strengthened using thicker 5 mm CFRP laminate since this would provide a measure of the maximum strength gain that was attainable. The remaining specimen was strengthened using the 2 mm laminate. This meant that two of the three 370 MPa specimens were strengthened using 2 mm CFRP laminates (providing a lower bound on strength gain) and one by the 5 mm laminate.

6.2. Adequacy of adhesive

Because the epoxy adhesive is so much weaker than steel, non-linear finite element analyses were carried out to evaluate its adequacy under ultimate conditions. The results of the analyses indicated that the epoxy would fail at the ends of the CFRP laminate due to high peeling stresses. To prevent this type of failure, a three-piece steel clamp was designed so that it could be positioned precisely where needed to withstand the predicted peeling stresses. The clamps were attached to the bottom flange of the W8 × 24 section using two, 19 mm A490 bolts and two smaller 8 mm hardened steel bolts. Only two sets of clamps were needed since they could be re-used. Brief details on the analysis and

Table 1
Summary of results

Specimen ID (CFRP thickness)	Mid-span values							Plain section ultimate capacity (kN)	Strength gain (%)	Comments
	Simulating service damage			Repaired specimen						
	Load (kN)	Deflection (mm)	Tensile strain ($\mu\epsilon$)	Ult. load (kN)	Deflection (mm)	Concrete strain ($\mu\epsilon$)	CFRP strain ($\mu\epsilon$)			
North 310 (2-mm)	142	40.90	1524	237	102.9	2258	6646	196	21.0	No failure bolts
Center 370 (2-mm)	186	44.96	1744	271	>100.0	2267	8164	249[a]	8.7	No failure no bolts
South 370 (2-mm)	187	44.96	1717	272	>100.0	2284	7811	249[a]	9.1	No failure no bolts
Center 310 (5-mm)	142	39.69	1239[b]	298	96.0	1918	5099	196	52.2	CFRP rupture along bolts
South 310 (5-mm)	142	30.23	1275[b]	169	32.3	786	1538	196	−13.7	Adhesive failure no bolts
North 370 (5-mm)	187	45.72	1695	329	87.9	1778	4859	249[a]	32.0	CFRP rupture along bolts

[a] Predicted value.
[b] indicates gage failure at specified strain (after value).

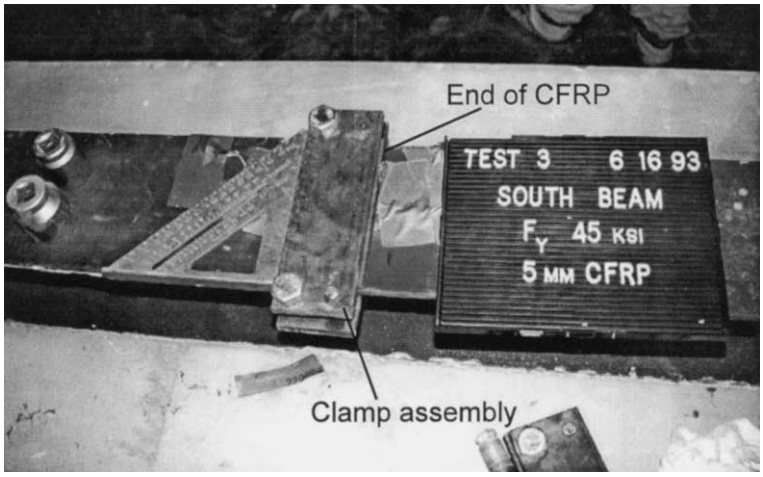

Fig. 4. Clamp assembly used to withstand peeling stresses.

design of the clamps may be found elsewhere [8]. Complete details of the study are presented in Ref. [6].

6.3. Bonding CFRP to steel

Surface preparation is important for ensuring a successful bond between CFRP laminate and steel. Since the steel girders used in the bridges were provided with a protective coat of paint, it was necessary to remove this paint. The specimens were turned over to provide access to the bottom flange where the CFRP was to be bonded and a portable sandblaster was used to obtain the necessary etched surface. The CFRP laminate was bonded to the steel surface using the epoxy adhesive in accordance with the manufacturer's recommendations. After the adhesive cured for 48 h, the specially designed clamps resisting peeling stresses were positioned over the ends of the laminate and secured in place using bolts as shown in Fig. 4.

7. Testing of repaired specimens

7.1. Instrumentation

The test specimens were most heavily instrumented at the quarter and mid-span locations. Strain gages were embedded inside the deck slab during casting and were also attached to the top concrete surface and to the underside of the steel flanges. Strain gages were also affixed to the CFRP laminate at mid-span and at 50 mm from each end of the 3.65 m long CFRP laminate, i.e. 1.27 m from the end of the beam. Additionally, gages were also attached to the bottom flange of the steel beam just beyond the CFRP laminate (1.14 m from the end of the beam). Comparison of strains in the steel beam and that in the CFRP laminate in close proximity allowed slip to be readily detected.

LVDTs were used to measure deflections at the mid-span and quarter-span locations. Load cells were used to measure applied loads and support reactions. All data were automatically recorded by a SYSTEM 4000 data acquisition system.

7.2. Loading

The same four-point loading scheme used for simulating service damage (see Fig. 3) was used for testing the repaired specimens. The applied load was transmitted through two 0.71 m long stiffened spreader beams that were welded to a 1.22 m long stiffened cross beam. The length of the spreader beams was the same as the width of the concrete slab. This meant that the test specimens were subjected to two uniform, transverse line loads spaced 1.22 m apart.

The crossbeam was directly connected to the ram of a 45 ton hydraulic jack using a swivel head that was attached by custom-designed connectors. This ensured that the loads were transferred equally to the two spreader beams. Four 150 mm × 200 mm fabric pads were placed under both spreader beams to ensure uniform distribution.

7.3. Adhesive failure

The first two specimens tested were the *Center*- and *South*-370 MPa steel composite beams strengthened using 2 mm CFRP laminates. The test was stopped when no additional load could be applied (271 and 272 kN) and the deflection exceeded the 100 mm limit of the LVDT (see Table 1). There was no adhesive failure, as was predicted by non-linear analysis.

The third specimen tested was *South*-310 MPa steel composite beam strengthened using 5 mm CFRP laminate. This test ended suddenly with the separation of the CFRP laminate from the steel flange. The clean separation was believed to be adhesive failure due in part to a manufacturing defect that left a small depression on the bonded face of the 5 mm thick CFRP laminate.

To prevent a recurrence of this failure, bolts were used to augment the load transfer capacity of the epoxy adhesive. The configuration and arrangement of bolts was based on

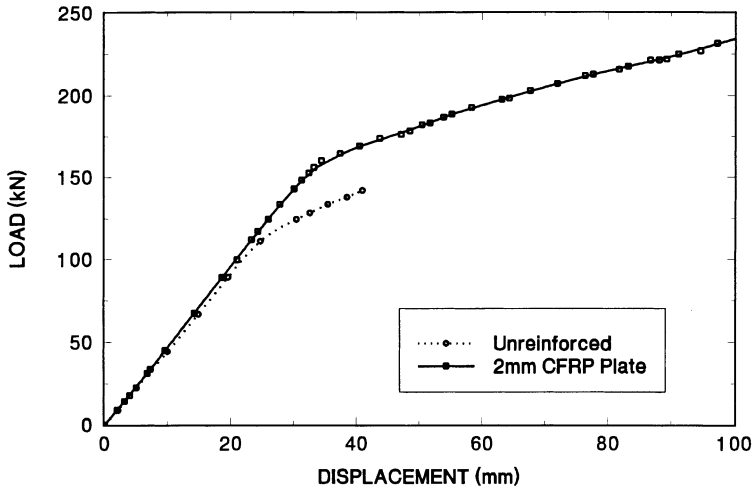

Fig. 5. Load-displacement *North*-310 MPa-2 mm (epoxy + bolted).

non-linear finite element analysis and consisted of two lines of three, 19 mm A490 bolts spaced at 41.9 cm, starting 8.9 cm from the edge of the laminate [6]. In all, a total of 12 steel bolts were used (six at each end) in the two remaining tests involving 5 mm thick CFRP laminates. Although no bolts were needed for the 2 mm CFRP laminate, they were provided nonetheless to assess the effect of load transfer in the presence of bolts. A pair of bolts was provided 8.9 cm from each end of the CFRP in the last specimen strengthened using 2 mm, (for details refer to Ref. [8]).

8. Results for repaired beams

8.1. Strengthening

Load vs displacement plots comparing the responses of the six repaired and plain specimens are presented in Figs. 5–10. The results for specimens repaired with 2 mm CFRP laminates appear in Figs. 5–7, and those for the 5 mm CFRP laminates in Figs. 8–10. A summary of the maximum loads and mid-span deflections and strains in both concrete and the CFRP laminate is presented in Table 1. This table also contains information on the load applied to simulate damage referred to earlier.

Table 1 shows that with one exception *South*-310 MPa, increases in the ultimate strength were substantial. For example, *Center*-310 MPa realized an increase in strength from 142 to 298 kN, a strength gage of 110%. Inspection of Figs. 5–10 shows that the strengthening effect is largely confined to the post-yield region. This is not altogether surprising since the CFRP laminate has a lower elastic modulus −56% that of steel. This meant that prior to yielding, stresses in the composite laminate were lower than those in the bottom steel flange.

The premature local adhesive failure of *South*-310 MPa, enabled it to be re-tested to determine the ultimate capacity of the steel section (see Fig. 9). The results of this test were used to fine-tune the non-linear finite element model to predict the ultimate capacities of all the specimens that

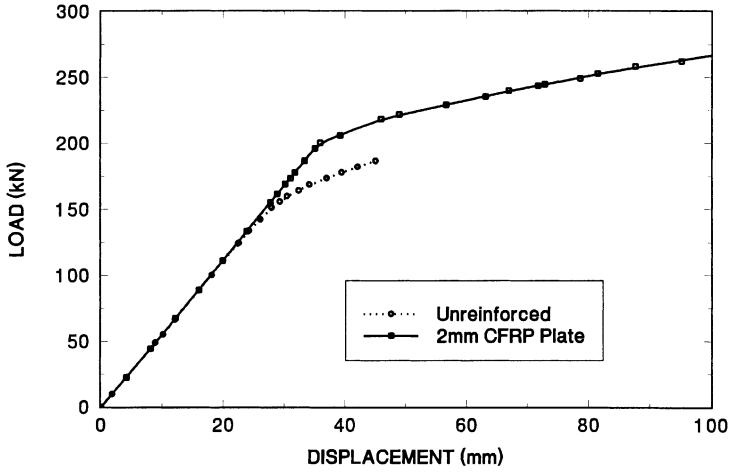

Fig. 6. Load displacement *Center*-370 MPa-2 mm (epoxy only).

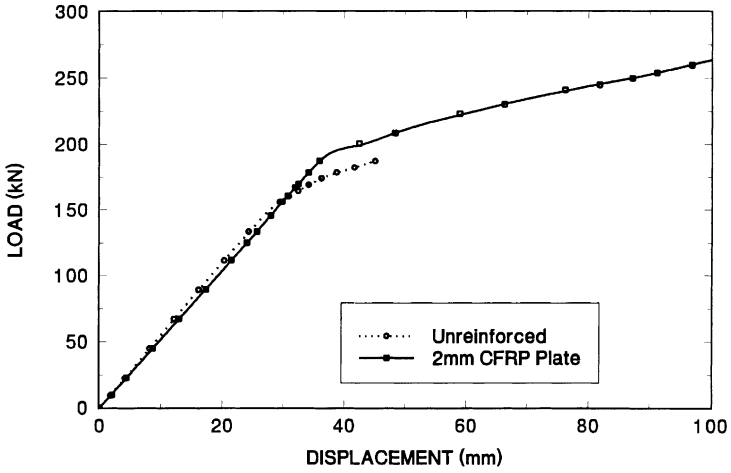

Fig. 7. Load displacement *South*-370 MPa-2 mm (epoxy only).

were tested. The predicted value was found to be 249 kN for the 370 MPa girders. Using the measured and the predicted failure loads, the *absolute* increases in ultimate strength of the strengthened steel beams were found to range between 9 and 52% (Table 1). The smaller increases correspond to the 2 mm laminate and the larger increases to the 5 mm ones.

In addition to increases in ultimate load, the elastic region of the plain section was considerably extended in the repaired specimen. The increases ranged from about 20% for *South*-370 MPa/2 mm (Fig. 7), where the elastic range was extended from 156 to 187 kN, to over 67% in the case of *North*-370 MPa/5 mm (Fig. 10). This increase is particularly encouraging since it suggests that service loads of repaired specimens could be increased using this technique.

8.2. Stiffening

The load vs deflection response of the strengthened and unstrengthened beams also provide a measure of the stiffening effect in the elastic region. This is an important consideration particularly for bridge application where live load deflection limits are very stringent.

Figs. 5–10 show that there is very little stiffening in the elastic region except for specimens strengthened with the 5 mm CFRP laminates (Figs. 8–10). Even for this case, there was practically no stiffening for *Center*-310 MPa specimen (Fig. 8) due to cracking in the slab from the initial loading. For specimens strengthened using 2 mm laminates there is even a reduction in stiffness in the elastic region (Fig. 7). This is probably because the concrete damage in this beam could not be fully offset by repairs and the stiffness lost as a result was not regained by bonding the CFRP laminate.

The lack of increase of stiffness in the elastic range is due to CFRP's smaller elastic modulus compared with steel. The increase in stiffness resulting by bonding a CFRP laminate to the steel surface farthest from the neutral axis is partially offset by this lower modulus. However, with thicker

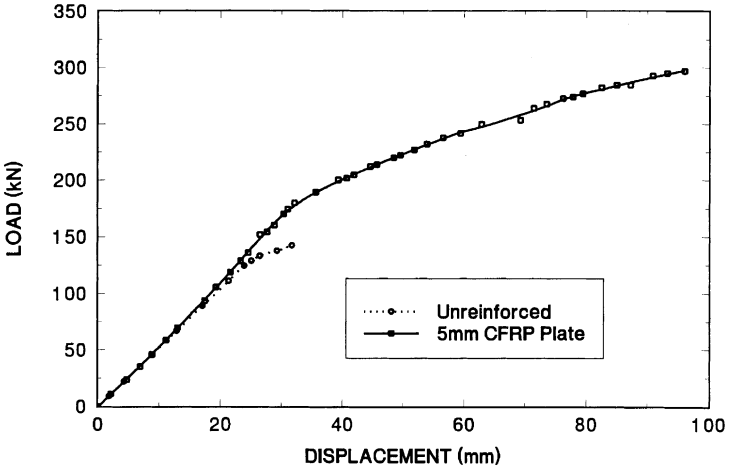

Fig. 8. Load displacement *Center*-310 MPa-5 mm (epoxy + bolted).

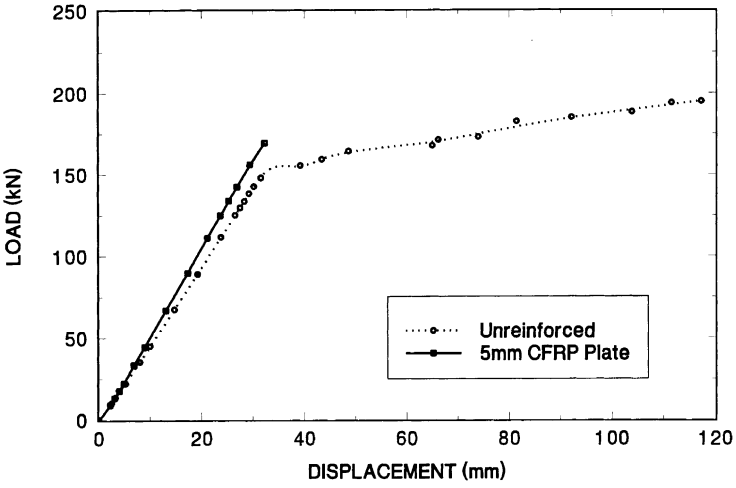

Fig. 9. Load displacement *South*-310 MPa-5 mm (epoxy only).

laminates, increases are larger provided there is no adhesive failure (Fig. 10). If local adhesive failures occur, strengthening cannot be expected (e.g. Fig. 9).

8.3. Failure mode

The load deflection plots in Figs. 5–10 indicate that, in general, there was a considerable amount of deflection when the maximum load was reached (Fig. 11). For the beams strengthened using 2 mm CFRP the test was stopped when no additional load could be applied. As such, there was no failure of the CFRP laminate or its bond with the steel surface. With the beams strengthened using 5 mm CFRP, however, failure occurred due to shearing off the CFRP laminate by the bolts (see Fig. 12).

8.4. Bolted vs bonded

In order to assess the relative performance of bonded and bolted specimens, the strain variations with depth at the critical mid-span locations for different cases are shown in Figs. 13–16. The results for the 2 mm CFRP laminates are shown in Figs. 13 and 14 while those for the 5 mm laminates in Figs. 15 and 16.

Inspection of Figs. 13 and 14 showing the strain variation for the 2 mm CFRP laminate indicate their similarity. This is not surprising since there was no separation of the 2 mm laminates, whether bonded or bolted. In each of these cases, the load was transferred primarily by the adhesive.

The comparison of strain variation along the depth of the specimen strengthened with 5 mm CFRP laminate shown in Figs. 15 and 16 indicate obvious dissimilarities. For the bonded specimen (Fig. 15) there is load transfer to the laminate by the epoxy until adhesive failure. The bolted specimen (Fig. 16) transfers load in the same manner until the CFRP delaminates from the steel at about the same load. The loads hitherto being carried by the epoxy were now transferred to the bolts with commensurate strain relaxation in the CFRP laminate. Failure finally occurred when excessive strain (and therefore deformation) around the bolts led to rupture of the CFRP laminate (Fig. 12). This

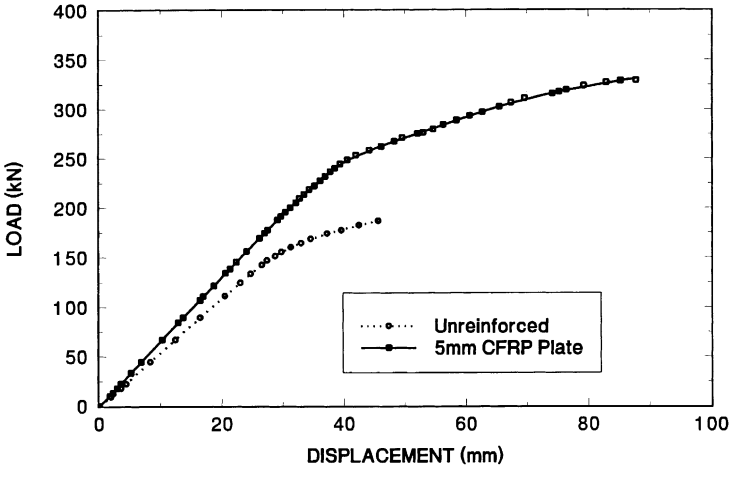

Fig. 10. Load displacement *North*-310 Mpa-5 mm (epoxy + bolted).

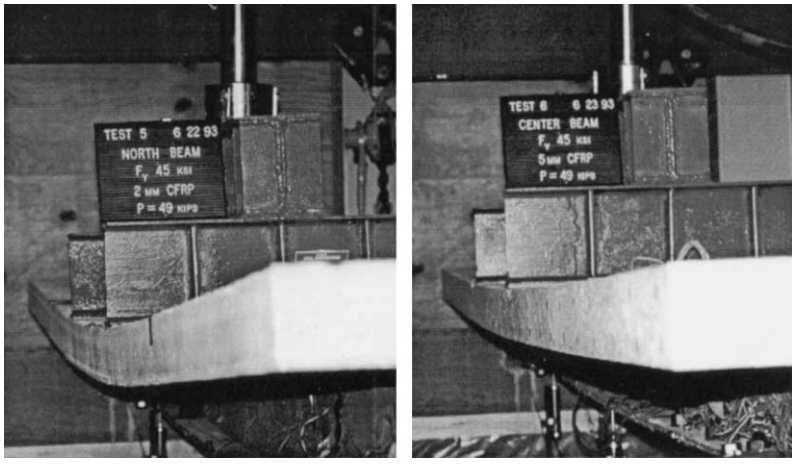

Fig. 11. Deflected shape of repaired 310 MPa beams at 218 kN.

problem may be avoided by using a greater number of bolts, thereby limiting their maximum strain and by using CFRP laminates manufactured with bolt holes and multi-directional carbon fiber reinforcement around such holes.

9. Discussion

The results from the study indicate clearly that it is possible to strengthen steel composite bridge sections using CFRP laminates. Because of the high strength and stiffness of steel the operation is somewhat more complicated than that used for concrete or wood. In this study, a combination of adhesive, fasteners, and clamps were used.

Because T300 carbon fibers were used for cost reasons, strengthening was more pronounced in the post-yield region than in the elastic region. However, if CFRP laminates with higher stiffness are used, an increase in the elastic region may be expected. With the prices of carbon fiber dropping, this may be realizable earlier than previously thought possible.

Since the epoxy adhesive is very weak in comparison with steel, bolting was required especially to assist in the load transfer for the thicker laminates. In configurations that dictate transferring shear using bolts, the use of adhesives would still be recommended to help distribute the load and provide transfer of shear until the bolts become fully loaded in bearing. In this case, the use of adhesives served to secure the CFRP laminate while the bolt holes were drilled. It would be preferable to use a larger quantity of smaller bolts to minimize the magnitude of localized stress concentrations at the bolts and to reduce the tendency for transverse CFRP laminate fractures. The magnitude of the localized stress concentrations may also be reduced by implementing high quality drilling techniques, and by utilizing CFRP laminates which have more plies with varying fiber orientation in the bolt hole regions, or by using CFRP laminates specially manufactured to include reinforced holes for bolting. Installation would be facilitated by such manufactured holes or by pre-drilling the abrasive, drill-resistant CFRP laminates prior to transport to a field site.

Although bolts and clamps were successfully designed, sized, and positioned to aid in shear transfer and to resist peeling stresses at the laminate ends, the use of bolts somewhat negates the time efficiency of CFRP repairs. To ensure effective repairs the bond interface of the CFRP must be free from defects at the onset to maintain uniform adhesive thickness and reduce incidence of local adhesive failures.

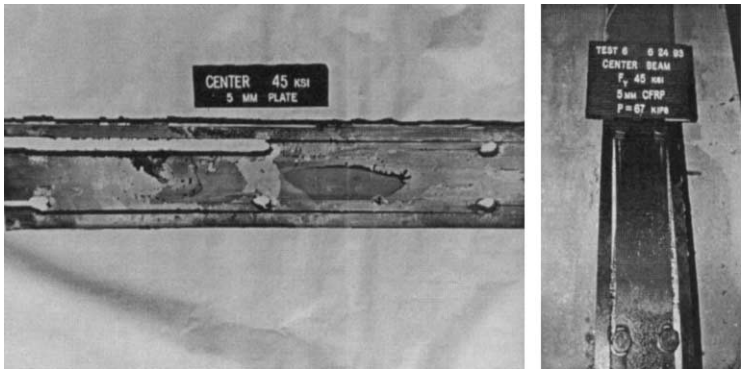

Fig. 12. Rupture of 5 mm CFRP plate (*Center*-310 Mpa).

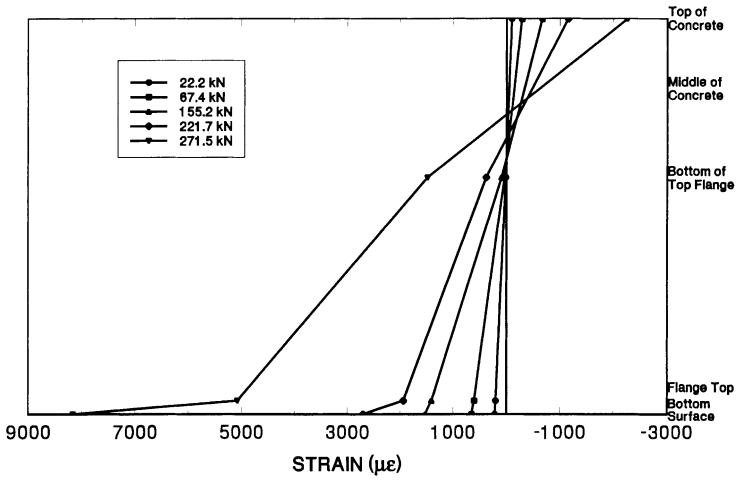

Fig. 13. Strain variation at mid-span *Center*-370 MPa-2 mm (epoxy).

Additionally, tapered laminates in both width and thickness accompanied by a scheme of adhered tapering with an adhesive fillet can reduce the stress concentrations leading to high peeling stresses.

10. Non-linear finite element analysis

The non-linear finite element analysis program PCFRAME [5] was used to predict the response of the six steel composite bridge sections tested. The concrete slab was discretized into 20 layers and the steel reinforcement by two. The wide flange section was modeled as eight steel layers with the CFRP laminate and the adhesive represented by single layers (see Fig. 17). Along the length, each beam was discretized using 41 members.

Figs. 18–20 show comparisons of predictions from the non-linear finite element analysis with test results. The strain variation in the CFRP laminate and concrete strain are shown in these figures. Additional results, including a complete set of comparisons for load vs deflection and steel strains for the unreinforced and strengthened beams tested, may be found elsewhere [2].

Inspection of Figs. 18–20 show excellent correlation between the experimentally measured strains and predictions from the finite element analysis. This is especially true with the 2 mm laminate. The correlation is somewhat poorer for the 5 mm laminate at higher loads. This is not altogether surprising since some of the load taken by the bolts could not be modeled. Use of bolts in the 2 mm specimens proved to have no effect as the adhesive sufficiently transferred the shear forces without causing bearing in the bolts.

Agreement for load vs displacement was not as close with the finite element analysis predicting a stiffer post-yield response. This was because the effect of pre-damage was only approximated in the analysis. The overall agreement between experiment and finite element analysis was generally quite satisfactory.

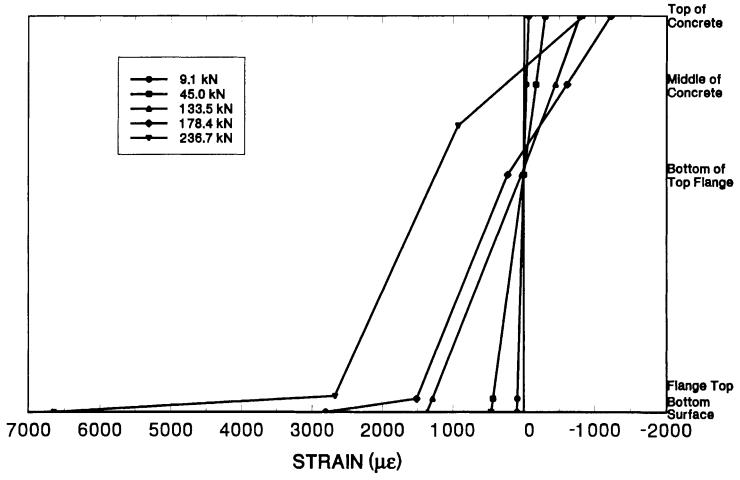

Fig. 14. Strain variation at mid-span *North*-310 MPa-2 mm (epoxy + bolted).

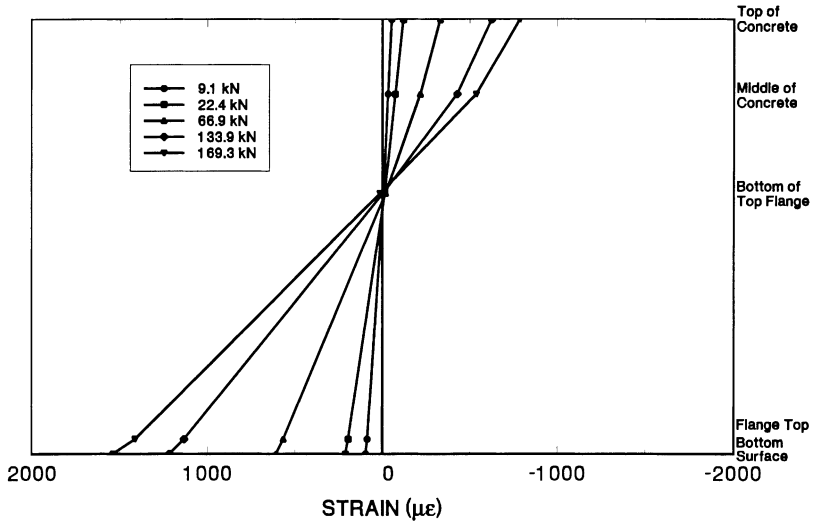

Fig. 15. Strain variation at mid-span *South*-310 MPa-5 mm (epoxy only).

11. Conclusions

On the basis of the experimental and numerical studies presented, the following conclusions may be drawn:

1. Steel composite members may be strengthened by bonding CFRP laminates. However, much thicker laminates are needed to achieve comparable strength and stiffness gains typically obtained in strengthened concrete or wood members. Additionally, the capacity of the epoxy adhesive to transfer loads to the CFRP laminates may need to be augmented, e.g. by clamps or fasteners, to ensure load transfer past yielding of steel.
2. Test results showed significant increases in ultimate capacity of steel composite bridge members strengthened by CFRP laminates. Strength gains for the bridge sections containing 310 MPa wide flange shapes were 21 and 52% for the 2 and 5 mm CFRP laminates, respectively. Corresponding increases for the bridge sections containing 370 MPa wide flange shapes were 9 and 32%, respectively.
3. Increases in the elastic stiffness were relatively modest (see Figs. 5–10) particularly when thinner 2 mm CFRP laminates were used. However, increases in the elastic region of strengthened members were substantial indicating the potential for increases in service loading.
4. The failure mode of the strengthened sections was generally ductile and accompanied by considerable deformation (see Fig. 11). However, where only epoxy adhesive was used for bonding a 5 mm CFRP laminate, adhesive failure led to separation of the CFRP laminate and sudden failure (*South*-310 MPa). No similar separation was observed with 2 mm CFRP laminates bonded using epoxy alone in that smaller tensile forces developed in the thinner CFRP and the associated shear stresses never exceeded the epoxy's shear strength.

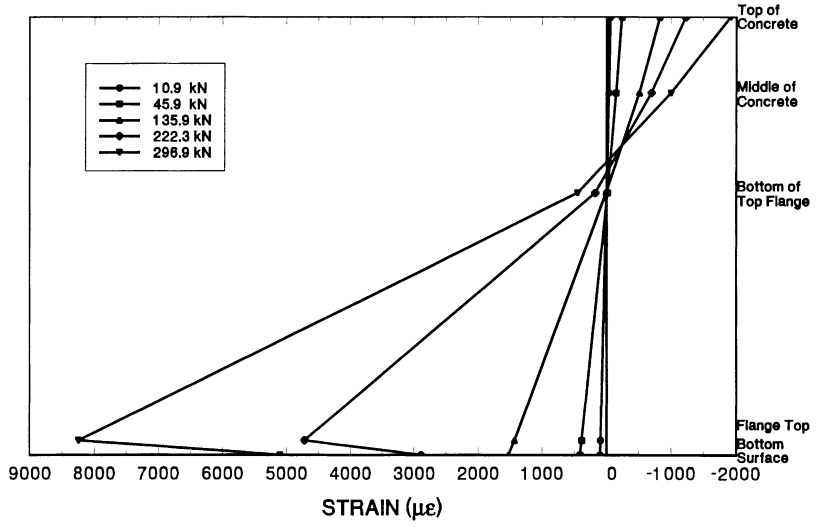

Fig. 16. Strain variation at mid-span *Center*-310 MPa-5 mm (epoxy + bolted).

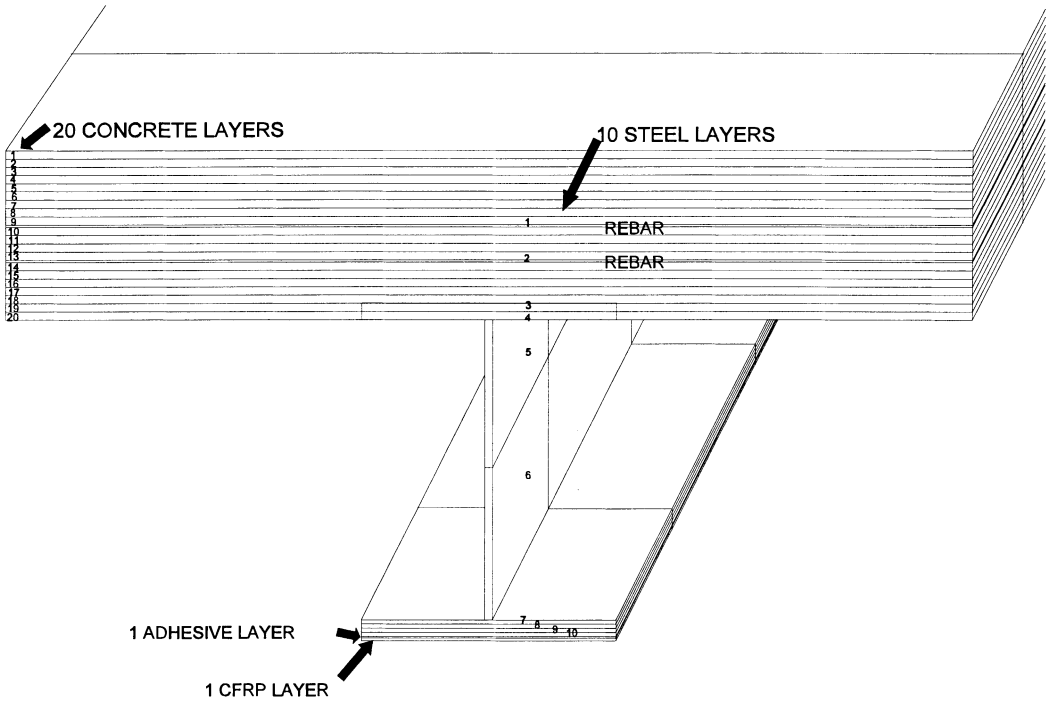

Fig. 17. Discretization of cross-section for finite element analysis.

5. The CFRP laminate must be adequately anchored to the steel flange to prevent peeling failure at the ends. In this study, a re-usable clamp system (see Fig. 4) was developed from non-linear finite element analysis that proved to be simple, efficient and inexpensive. These peeling forces could be minimized by sculpting the ends of the laminates and adhesive to reduce stress concentrations in this region. However, this would probably require ordering the laminates to case-specific lengths and would reduce field installation flexibility.
6. The response of the strengthened specimens was predicted with reasonable accuracy by non-linear finite element analyses.

The study demonstrated the feasibility of using CFRP laminates for strengthening steel composite bridge members. If the intent of the installation is to increase the service load capacity and not to simply restore lost capacity due to damage, both the slab and shear connectors attaching it to the upper steel flange must have the reserve capacity needed for supporting the additional compressive and shear forces.

While clamps and fasteners were both used in the study,

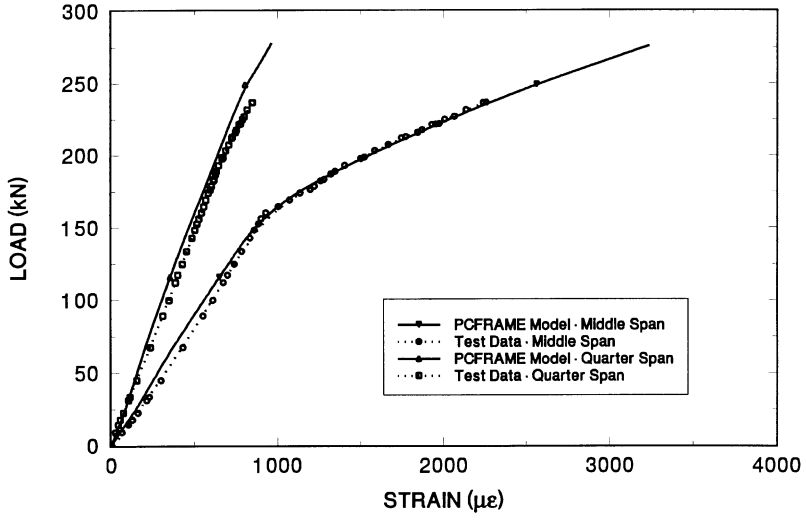

Fig. 18. Comparisons: load vs concrete strain (*North*-310 Mpa-2 mm).

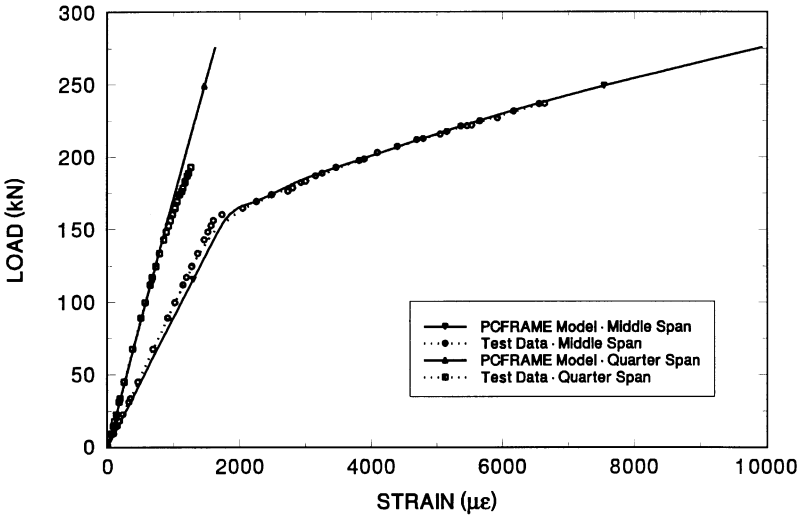

Fig. 19. Comparisons: load vs CFRP strain (*North*-310 Mpa-2 mm).

ideally clamps alone will be more desirable for field installation as it eliminates the need for heavy magnetic drills that will otherwise be needed to secure the CFRP laminates. This will greatly facilitate the speed with which repairs can be carried out particularly in congested urban areas — a very important consideration for using the light-weight CFRP laminates in the first place.

The effects of moisture and humidity on the long-term performance of the adhesive must be evaluated before field applications. However, this issue was not included within the scope of this study. In addition, appropriate measures developed by the aerospace industry should be used to prevent possible galvanic action due to the direct contact of the CFRP laminate with steel in the presence of moisture.

Acknowledgements

The investigations reported were carried out with the financial support of the Florida Department of Transportation and the US Department of Transportation. The authors gratefully acknowledge the contribution of Dr Mohsen Shahawy, Director, Structural Research Center, Florida Department of Transportation and Mr Ken Spillett, formerly a graduate student in the Department of Civil and Environmental Engineering, University of South Florida, currently a Professional Associate, Parsons Brinckerhoff Construction Services, Tampa, FL. They also wish to express their sincerest appreciation to Composite Horizons, Covina, CA for their invaluable advice and assistance. However, the opinions,

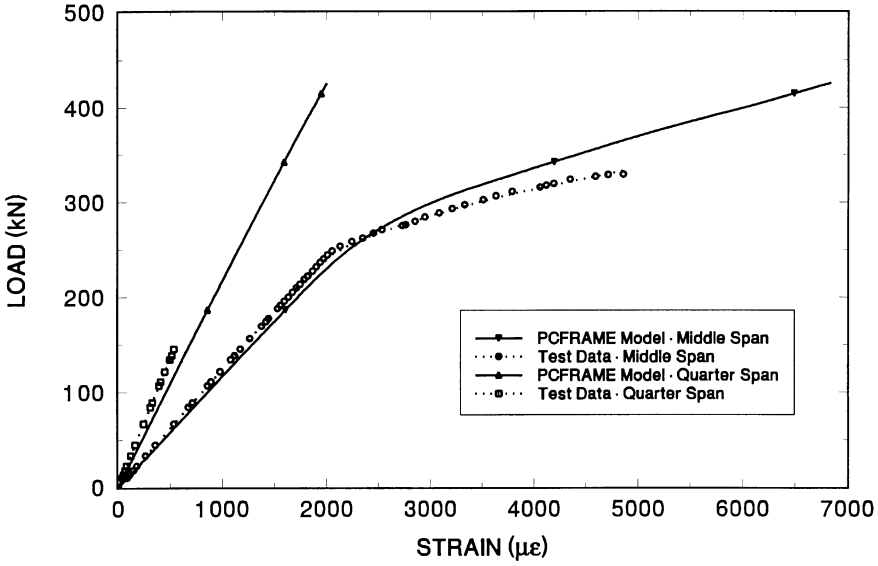

Fig. 20. Comparisons: load vs CFRP strain (*North*-370 Mpa-2 mm).

findings and conclusions expressed in this publication are those of the writers and not necessarily those of the Florida or US Department of Transportation.

References

[1] American Association of State Highway and Transportation Officials. Standard specifications for highway bridges. Washington, DC., 15th ed., 1994.

[2] Liby L. Steel composite bridge sections strengthened by carbon fiber reinforced plastic laminates, MSCE Thesis submitted to Dept. of Civil Engng and Mechanics, University of South Florida, Tampa, FL, November, 1993. 353 p.

[3] Mertz DR, Gillespie JW. Rehabilitation of steel bridge members through the application of advanced composites. Final Report, NCHRP-93-ID01, 1996.

[4] Mosallam AS, Chakrabarti PR. Making the connection, Civil Engineering, ASCE, April, 1999. p. 56–9.

[5] PCFRAME. Computer program for non-linear analysis of reinforced and prestressed concrete frames. Developed by Y. Kang, Ph.D dissertation, University of California, Berkeley, 1977.

[6] Sen R, Liby L. Repair of steel composite sections using CFRP laminates. Final report submitted to Florida and US Department of Transportation, August, National Technical Information Service, VA, 1994.

[7] Sen R, Spillett K. Restraint effect of bridge bearings. Final Report submitted to Florida and US Department of Transportation, January, National Technical Information Service, VA, 1994.

[8] Sen R, Liby L, Spillett K, Mullins G. Strengthening steel composite bridge members using CFRP laminates. In: Taerwe L, editor. Non-metallic (FRP) reinforcement for concrete structures. London, England: E and FN Spon, 1995. p. 551–8.

[9] Wang Y. Bridge strengthening using advanced composites, MSCE thesis submitted to the Department of Civil Engineering and Mechanics, University of South Florida, Tampa, FL, December, 1992.

[10] Meier U, Deuring M, Meier H, Schwegler G. Strengthening of structures with CFRP laminates: research and applications in Switzerland. In: Neale KW, Labossiere P, editors. Advanced Composite Materials in Bridges and Structures. CSCE, Montreal, P.Q., 1992. p. 243–51.

[11] Rostasy FS, Hankers C, Ranisch E-H. Strengthening of R/C and P/C structures with bonded FRP plates. In: Neale KW, Labossiere P, editors. Advanced Composite Materials in Bridges and Structures. CSCE, Montreal, P.Q., 1992. p. 253–63.

[12] Uemura M, Aoyama K, Kliger H. A new reinforcing fiber sheet material and its application in the repair of concrete structures. In: 39th International SAMPE Symposium, April, Vol. 39, 1994. p. 347–54.

[13] Shahawy M. Strengthening highway bridges with carbon fiber materials. In: 74th Annual Meeting of the Transportation Research Board, Washington, D.C., January, 1995.

IMPLEMENTATION AID FOR DYNAMIC REPLACEMENT OF ORGANIC SOILS WITH SAND

By H. S. Thilakasiri,[1] M. Gunaratne,[2] G. Mullins,[3] P. Stinnette,[4] and C. Kuo[5]

ABSTRACT: The objective of this research was to understand the mechanism of dynamic replacement (DR) with the view of identifying the attributes needed to effectively implement it. This was achieved by analytically modeling DR of organic soils with sand using the finite-element method. First, this paper describes briefly the finite-element formulation and the calibration of the finite-element model using common laboratory soil tests. Then, model predictions are compared with observations made during a fully instrumented field DR trial. The respective laboratory tests utilized to extract the model parameters certainly confirmed the applicability of the chosen constitutive models for the relevant geomaterials involved in the field DR test. Furthermore, the analytical predictions of the drop hammer displacement and acceleration, as well as pore pressures and lateral displacements in the drop hammer vicinity, agree reasonably well with those observed during the full-scale field DR. Finally, a parametric study is performed to demonstrate the usefulness of the analytical model in predicting the optimum thickness of the initial sand blanket that would produce the maximum treatment benefits.

INTRODUCTION

Recent research has led to the recognition of relatively new dynamic replacement (DR) as a viable method of weak soil improvement. The literature reports at least two case histories (Kruger et al. 1980; Lo et al. 1990) in which weak soils have been improved by DR. This is essentially an extension of dynamic compaction where the craters formed after each impact are continuously filled with sand to form strong pervious granular columns that penetrate the weak parent soil as shown in Fig. 1. Kruger et al. (1980) and Lo et al. (1990) discovered that when pounding and filling are carried out in an appropriate sequence, it was possible to create a network of such granular columns throughout the weak soil thereby improving not only its consolidation properties but also the shear strength. The optimum sand column depth that can be achieved with a given energy level under specific geological conditions and the spacing of the column grid to achieve the maximum treatment benefits are the major issues associated with effective field implementation of DR. Currently, parameters such as the column depth and spacing are established based on preliminary laboratory or field tests specific to given site conditions (Lo et al. 1990; Stinnette et al. 1996). However, this practice becomes time consuming and even impractical when a wide variation of geological conditions is observed at the same site. Therefore, in the planning stages of a given treatment project, it is invaluable to have a less expensive alternative to ascertain the viability of this technique for the available site.

Hence, the objective of this research is to formulate an analytical methodology that yields the above-mentioned DR parameters based on geology and soil properties of a given site and compare the model predictions with full-scale field DR data. In this paper, the finite-element modeling of the DR process will be described and the applicability of the finite-element model to DR also will be investigated based on laboratory soil tests and a field DR study. The laboratory testing program consisted of the tests necessary to calibrate the material constitutive models, whereas observations from an instrumented full-scale field DR test program were compared with the theoretical predictions of the finite-element model. Parameters involved in the comparative study were the predicted and measured drop hammer acceleration, pore pressure response of the foundation material, and the lateral deformation in the vicinity of the drop hammer. A sensitivity analysis was also carried out to scrutinize the variation of the drop hammer penetration with the mesh size and the time step size in an effort to explore the suitability of the selected mesh configuration and time step size. Finally, to demonstrate the usefulness of the program, a parametric study was conducted to obtain the optimum initial sand blanket thickness required for effective implementation of dynamic replacement.

NUMERICAL SIMULATION

Finite-Element Formulation

As seen in Fig. 1, one realizes that any realistic solution to the dynamic replacement problem must account for such complexities as pore water flow, improvement of soil properties associated with treatment, and, above all, the excessive axial and lateral deformations induced by high energy impact. Hence, consequent to preliminary analysis based on a 1D analytical model (Thilakasiri et al. 1996b), it was seen that the 3D finite-element method had to be adopted in order to appropriately address all of the above issues.

At the first impact point, dynamic replacement is axisymmetric, and, accordingly, a cylindrical coordinate system with updated Lagrangian coordinates will be utilized for the ensuing formulation. Formulation proposed by Kleiber (1989) and Fung (1965) is used to take into account the finite strains in the vicinity of the drop hammer. The equations of motion of

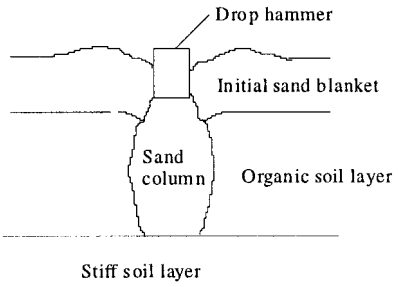

FIG. 1. Dynamic Replacement

[1]Sr. Lect., Dept. of Civ. Engrg., Univ. of Moratuwa, Moratuwa, Sri Lanka.
[2]Assoc. Prof., Dept. of Civ. and Envir. Engrg., Univ. of South Florida, Tampa, FL 33620.
[3]Asst. Prof., Dept. of Civ. and Envir. Engrg., Univ. of South Florida, Tampa, FL.
[4]Asst. Prof., Dept. of Civ. and Envir. Engrg., Hillsboro Community Coll., Plant City, FL 33566.
[5]Chf. Engr., Professional Services Industries, Tampa, FL 33634.

Note. Discussion open until June 1, 2001. To extend the closing date one month, a written request must be filed with the ASCE Manager of Journals. The manuscript for this paper was submitted for review and possible publication on January 9, 1997. This paper is part of the ***Journal of Geotechnical and Geoenvironmental Engineering***, Vol. 127, No. 1, January, 2001. ©ASCE, ISSN 1090-0241/01/0001-0025–0035/$8.00 + $.50 per page. Paper No. 14920.

the solid skeleton and the fluid phase are considered separately while maintaining volume compatibility between the two phases (Zienkiewicz et al. 1988). Subsequently, the finite-element method with four-node, axisymmetric, isoparametric elements is used to spatially discretize the system of equations, and then direct time integration is utilized to integrate the equations of motion in the time domain.

For the explicit form of equilibrium equations, a diagonal mass matrix must be obtained by lumping the element mass at discrete points. However, the numerical convenience of lumping is generally paid off by some loss of accuracy in the solution. For some cases it has been shown that lumping can improve the accuracy by error cancellation, and, in transient approximations, the lumping process introduces additional dissipation of the ''stiffness matrix'' form, thus canceling out numerical oscillation (Zienkiewicz and Taylor 1991). The solution scheme is progressed in the time domain using the direct time integration in which the solution is obtained at discrete time intervals. Of the many time integration schemes available, Newmark's explicit scheme, a popular algorithm for dynamic analysis, is used in the present study. Then, together with a diagonal mass matrix, the algorithm becomes explicit. With Newmark's explicit time integration, the algorithm becomes conditionally stable whereby the size of the time step governs the stability of the solution. It can be shown (Hallquist 1983) that the critical time step size is related to the time taken to propagate an elastic wave across the shortest dimension of the element.

Constitutive Relations

It is a well-known fact that soils exhibit nonlinear behavior even at low strain levels. Therefore, the traditional assumption of linear elasticity is inapplicable for soil at the vicinity of the drop hammer. Considering the implementation ease and their ability to represent most of the soil properties, two constitutive relations are adopted in the present formulation, namely, the elliptical cap model (DiMaggio and Sandler 1971) for granular soil cover (replacement material) and the modified Cam-clay model (Chen and Mizuno 1990) for weak soft organic soil. The cap model consists of a strain hardening elliptical cap and an elastic perfectly plastic Drucker-Prager failure surface that, in the octahedral plane (or π plane), touches the irregular hexagon formed by the Mohr-Coulomb failure surface at its outermost three nodes. Then, following the classical plasticity theory proposed by Zienkiewicz and Taylor (1991), the elastoplastic stress-strain tensor $\mathbf{C}^{ep}_{ijmn}$ can be obtained [(1)] considering a strain hardening yield function $f = f(\boldsymbol{\sigma}_{ij}, \chi(\varepsilon_{ij}))$, where $\boldsymbol{\sigma}_{ij}$ and $\chi(\varepsilon_{ij})$ are, respectively, the stress tensor and the hardening parameter, which is a function of plastic strain tensor $\boldsymbol{\varepsilon}^{p}_{ij}$

$$\mathbf{C}^{ep}_{ijmn} = \left[\mathbf{C}_{ijmn} - \frac{\dfrac{\partial g}{\partial \sigma_{rs}} C_{ijrs} C_{klmn} \dfrac{\partial f}{\partial \sigma_{kl}}}{H' - \dfrac{\partial f}{\partial \sigma_{ab}} C_{abcd} \dfrac{\partial g}{\partial \sigma_{cd}}} \right] \tag{1}$$

where

$$H' = -\frac{\partial f}{\partial \chi} \frac{\partial \chi}{\partial \varepsilon_{ij}} \frac{\partial g}{\partial \sigma_{ij}} \tag{2}$$

and $\mathbf{C}_{ijmn}$ = elastic constitutive matrix.

At each time step, a trial elastic second Piola-Kirchhoff stress increment $d\sigma^e$ is calculated for that time step (Kleiber 1989). Then, $d\sigma^e$ is transformed to the Cauchy stress increment at the end of that time step. Similarly, after the stress at the beginning of the nth time step σ_n is also transformed to the corresponding Cauchy stress at the end of nth time step, the final trial stress $\boldsymbol{\sigma}_{n+1}$ on the current configuration referring to the rotated coordinates at the end of the time step is estimated by adding the stress increment to σ_n (Kleiber 1989). If the trial stress tensor $\boldsymbol{\sigma}_{n+1}$ is outside the current yield surface, then the stress increment is elastoplastic and (3) is used to estimate the stress increment

$$d\boldsymbol{\sigma}_{ij} = \mathbf{C}^{ep}_{ijmn}\, d\varepsilon_{mn} \tag{3}$$

The validity of the approximation in (3) depends on the magnitude of the strain increment. If the strain increment is excessive, it should be divided into smaller increments and passed through the constitutive relations subroutine several times. However, it is possible for such approximations to deviate the stress point from the yield surface even for small strain increments, and such small deviations can become cumulative during several steps, thereby inducing significant errors in the final results. There are a number of methods to relocate the stress point back on the yield surface after each strain increment. The method adopted in the present formulation is known as the radial return method (Chen and Mizuno 1990) where it is assumed that the relocation is done along the direction of the normal to the current yield surface.

Slideline Algorithm

An obvious complexity involved in finite-element modeling of dynamic replacement (or dynamic compaction) procedures is the simulation of the soil punching mechanism. Hence, a unique feature of the current analysis is the development of a specific sideline algorithm to account for the relative displacement between adjacent nodes. In accordance with previous theoretical developments by Thilakasiri et al. (1996b) and Chow et al. (1992) as well as experimental observations, in the present analysis it is assumed that the soil column immediately underneath the hammer punches through the surrounding soil together with the hammer. This punching causes relative displacement between the adjacent nodes on either side of the punching soil column. It is also assumed that whether or not sliding develops between adjacent nodes is determined by the limiting Coulomb friction between them. There is a number of slideline algorithms available to account for various mesh discontinuities in the finite-element or finite-difference formulations (Hallquist et al. 1985). Of those, the model constraints, the penalty, and the distributed parameter methods are widely used; in this formulation the penalty method is adopted.

For all of the slideline algorithms, it is customary to identify one side as the slave side and the other side as the master side. The slideline algorithm employed in this formulation considers the forces transferred from solid to solid and fluid to fluid across the slideline discontinuity. Each slave node is considered in turn, and the effective area for the nth slave node is defined between the center of the $n-1$th slave segment and the center of the nth slave segment. This effective area is indicated for node c in Fig. 2. If the master segment is in contact with the slave side, integrated quantities related to forces corresponding to each slave node are prorated according to the relevant area of contact and transferred to the master node(s) within the effective area.

In the penalty formulation, the nodes are allowed to penetrate the opposite side. Such a situation is shown in Fig. 3, where node $\mathbf{q}$ has penetrated seqment rs of the adjacent element. In this situation, as the node is inside the segment (such as node $\mathbf{q}$ in rs), a new contact point y (on segment rs) and the amount of penetration l_q are found using the relationships given by (4) and (5), respectively.

$$\frac{\partial \mathbf{y}(\eta_c)}{\partial \eta} \cdot [\mathbf{q} - \mathbf{y}(\eta_c)] = 0 \tag{4}$$

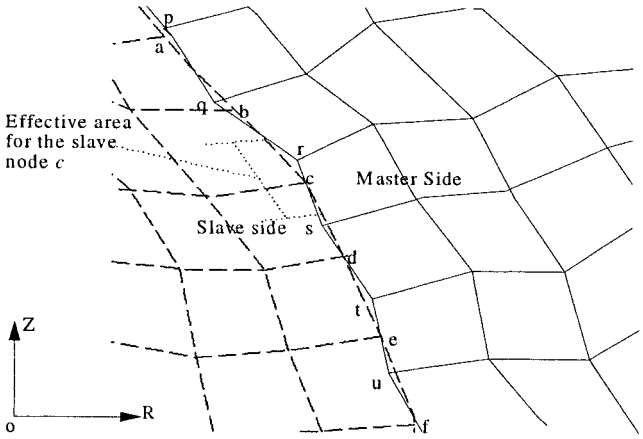

FIG. 2. Typical Mesh Discontinuity with Dotted Lines Showing Slave Side and Solid Lines Showing Master Side

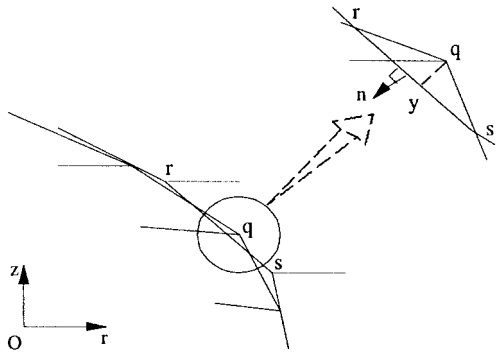

FIG. 3. Penetration of Node *q* through Opposite Side

$$l_q = \eta \cdot [\mathbf{q} - \mathbf{y}(\eta_c)] < 0 \tag{5}$$

where $\mathbf{n}$ = normal vector to segment *rs*; $\mathbf{y}$ = vector *oy*; $\mathbf{q}$ = vector *oq*; and η_c = local coordinate of the contact point with respect to points *r* and *s*. Then, a penalty force f_q [(6)] proportional to the amount of penetration l_q is applied to get the node back onto segment *rs*

$$f_q = -l_q K_q \eta \tag{6}$$

$$K_q = \frac{f_{si} K_b A_i^2}{V_i} \tag{7}$$

where A_i = face area of the element containing segment *rs*; V_i = volume of the element containing segment *rs*; K_b = bulk modulus of the material of the element containing *rs*; and f_{si} = scale factor. The value of the coefficient K_b is generally kept constant, but if excessive penetration is noticed it should be increased to reflect the gradual densification. Then, the master side acceleration is updated for the next time step using the new integrated quantities. As illustrated in (8) and (9), the estimated acceleration is used to determine the respective forces acting on each slave node tangential and normal to the master segment

$$f_{nn} = (a_{rn} \cos\theta + a_{zn} \sin\theta) m_n - f_{rn} \cos\theta - f_{zn} \sin\theta \tag{8}$$

$$f_{tn} = (-a_{rn} \sin\theta + a_{zn} \cos\theta) m_n + f_{rn} \sin\theta - f_{zn} \cos\theta \tag{9}$$

where a_{rn} = acceleration of the *n*th node in the *r*-direction; a_{zn} = acceleration of the *n*th node in the *z*-direction; f_{rn} = internal force at the *n*th node in the *r*-direction; f_{zn} = internal force at the *n*th node in the *z*-direction; m_n = lumped mass at the *n*th node; and θ = inclination of the normal vector $\mathbf{n}$ to the *r*-direction.

For any node, if the normal force is found to be tensile, then the slave node is released, and it is no longer considered to be in contact with the master side. The normal force determined above is used to estimate the shear strength based on Coulomb limiting friction expressed by (10). Then, when the tangential force f_{tn} exceeds the frictional shear strength f_{tn}^s, the slave node slides relative to the master segment

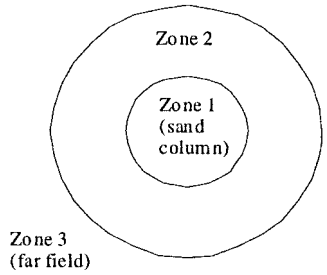

FIG. 4. Vicinity of Impact Location

$$f_{tn}^s = f_{nn} \tan\delta + c \tag{10}$$

where f_{tn}^s = shear strength at the *n*th node tangential to the interface; δ = angle of friction between master and slave sides; and *c* = cohesion between master and slave sides.

When $f_{tn} \geq f_{tn}^s$, a frictional resistive force f_{tn}^f equal to f_{tn}^s is applied on *q* in the tangential direction, and the node is allowed to slide. Then, the direction of the limiting Coulomb frictional force f_{tn}^f applied on the sliding node is determined based on the relative velocity *v* in the tangential direction between the contact node *q* and the point of contact *y* (Fig. 3) as given in (10).

It was observed by Nagger et al. (1994) and Thilakasiri et al. (1996b) that the impact vicinity can be divided into three zones, namely, Zone 1, Zone 2, Zone 3 (Fig. 4) based on the magnitude of the accumulated plastic strains. Furthermore, it was also emphasized that the strains developed in Zone 3 are essentially elastic. Therefore, the boundary traction force vector in the equilibrium equations is determined based on linear elastic material behavior.

CALIBRATION OF CONSTITUTIVE RELATIONS

Estimation of Material Parameters

Calibration of the constitutive models to accurately represent the material behavior is vital to obtaining reliable predictions from finite-element analysis. The bulk modulus *K* and the shear modulus *G* can be constants or stress or strain level dependent elastic material properties. After analyzing the results of a test series carried out on the replacement material (sandy soils), it was concluded that the assumption of constant bulk modulus *G* and shear modulus *K* is reasonable for this material type for the relevant range of pressures. As for the foundation material (organic soil), the bulk modulus is assumed to be a function of the first invariant of the stress tensor (Cam-clay assumption), and the shear modulus is assumed to be constant.

The Cam-clay model requires five material parameters for a complete description of the material (Chen and Mizuno 1990), and the elliptical cap model needs seven independent parameters (Chen and Mizuno 1990). In addition to the material parameters required for the constitutive relations, there are other properties such as density, permeability, and porosity that must be evaluated as well.

The material used for the initial layer and subsequent crater fillings were sandy in nature, and hence they were modeled in the finite-element formulation using the elliptical cap model. In the calibration of the elliptical cap model, isotropic consolidation, consolidated drained, and consolidated undrained triaxial test results were used.

The material parameters obtained during the calibration phase were subsequently used for the prediction of stress-strain and pore pressure-strain response of the respective material during an independent test series, in order to verify the applicability of selected material models, for each material type. The predicted and observed variations are shown in Figs. 5 and 6.

In addition to the volumetric compressibility due to dissipation of pore water pressure (primary consolidation), the long-term settlement due to creep (secondary consolidation) is also excessive for organic soil and persists for a long period under prolonged loading. However, the duration of the impact of a single hammer blow during dynamic replacement is relatively short making it impossible for secondary consolidation to take place. Hollingshead et al. (1971) carried out two 1D consolidation test series on a similar type of material (Canadian muskeg), one with 4-h load increments and the other with 24-h load increments. The results show that the difference in the slope of the e versus log P curve is essentially the same for both test series. Furthermore, another consolidated undrained test series carried out by Hollingshead et al. (1971) showed that the general shapes of the stress-strain curves of these tests are similar to those of insensitive unbound clays. They also showed that the pore pressure response during undrained shearing was similar to what might be expected from an insensitive clayey soil. Hence, a 1D consolidation test series was carried out on the organic material at the study site to estimate the primary consolidation parameters, and these tests were terminated after the primary consolidation phase with the aid of the data acquisition system, which displays the specimen displacement on screen while the test progresses.

The general behavior of Florida organic material under consolidated undrained triaxial conditions resembled the previously mentioned observations of Hollingshead et al. (1972). The stress path plot during one undrained triaxial test is reproduced in Fig. 7. The evaluated material parameters were then utilized in the Cam-clay model to predict the experimental stress path shown in Fig. 7. It is seen that the model predictions agree reasonably well with the experimental results.

1D consolidation test results were also used to investigate the variation of permeability of organic material with the void ratio. Fig. 8 shows permeability versus void ratio trend, and, within the range of values relevant to this study, the following linear fit can be made:

$$\log(k) = 1.9322e - 14.04 \tag{11}$$

where k is measured in centimeters per second. Since it is the direct shear test condition that closely represents the mechanics of shearing taking place at the slideline, the angle of internal friction obtained from a direct shear test is used in the Mohr-Coulomb shear strength expression to get the limiting frictional force.

The compressibility of pore water k_f has a prominent effect on the predicted pore pressure results. It is an accepted fact that the natural pore fluid contains microbubbles and tiny air pockets entrapped in the voids between soil particles (Menard and Broise 1975). When treated as a single substance under a dynamic load, the presence of these air pockets and microbubbles give rise to a high compressibility compared to pure water. The effective elastic bulk modulus of the air-water mixture can be defined as

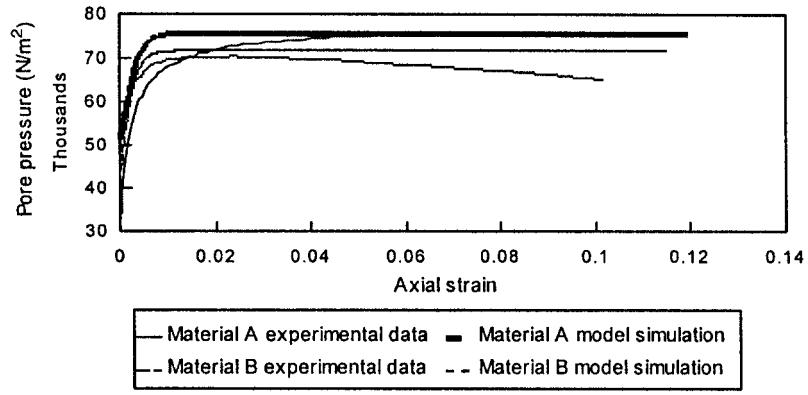

FIG. 5. Experimental Pore Water Pressure versus Strain Variation and Corresponding Elliptical Cap Model Predictions

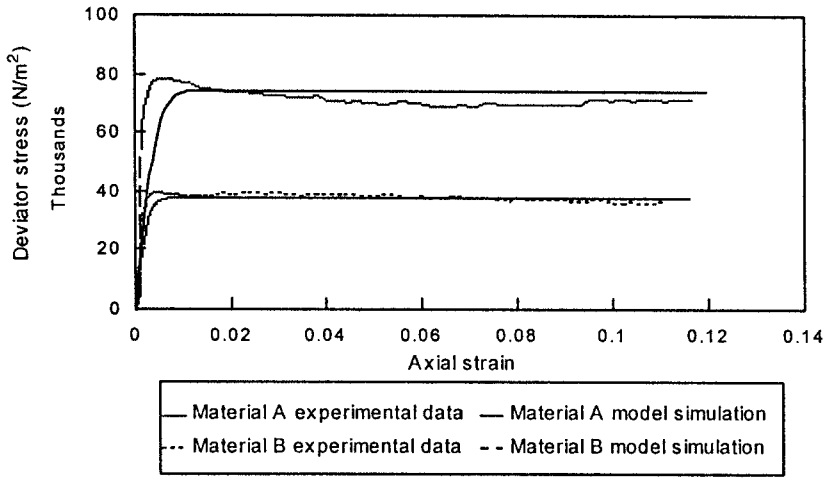

FIG. 6. Experimental Stress versus Strain Curve and Elliptic Cap Model Predictions

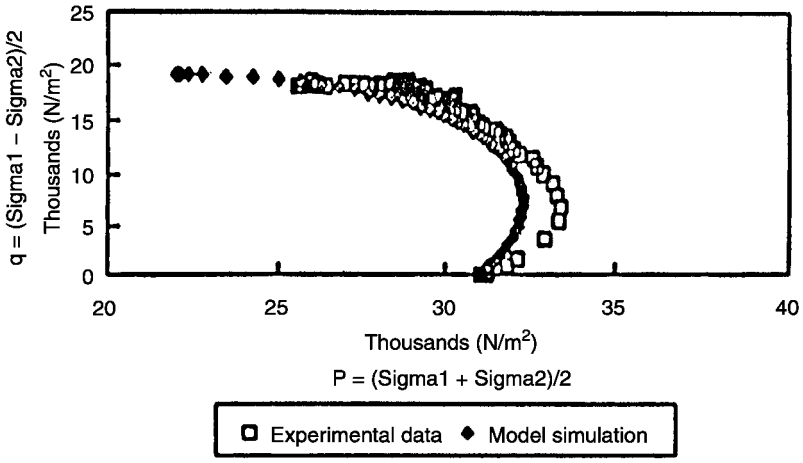

FIG. 7. Experimental and Predicted Stress Paths for Undrained Triaxial Tests on Florida Soils

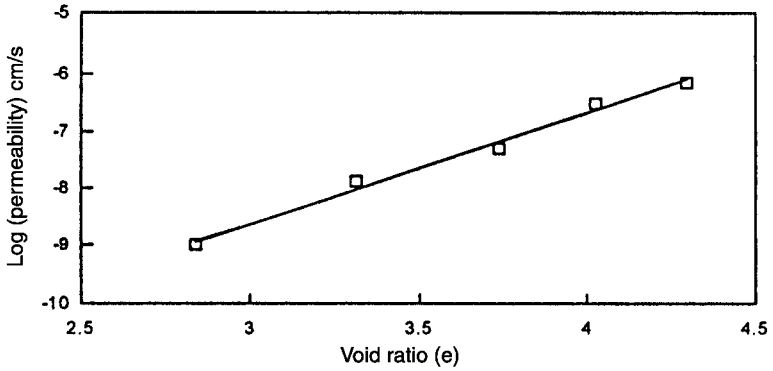

FIG. 8. Variation of Permeability with Void Ratio for Organic Soil

$$\frac{d\rho_w}{\rho_w} = \frac{dp}{K_f} \tag{12}$$

where ρ_w, dp, and K_f are density, pressure change, and bulk modulus of the mixture, respectively. On the other hand, K_f can be related to the bulk modulus of pure water K_{fo} by (Mei and Fonda 1982)

$$\frac{1}{K_f} = \frac{1}{K_{fo}} + \frac{1 - s}{p} \tag{13}$$

in which s = degree of saturation of the soil; and p = absolute pore pressure. The effect of entrapped air on the bulk modulus of the mixture can be illustrated by the following example. Assume that $K_{fo} = 2 \times 10^9$ N/m^2, $S = 95\%$, and $p = 1$ atm = 10^5 N/m^2. Thus, K_f is estimated to be 2×10^6 N/m^2 from (13) clearly showing a magnitude reduction of three orders from K_{fo} due to 5% air. As the order of magnitude of pore pressure p is much less than that of K_{fo}, a constant value of K_f was used assuming the degree of saturation of 95% for air-water mixture.

Computer Program for Finite-Element Formulation

The computer program DYCOM was developed to execute the theoretical procedure outlined above. This program is capable of modeling single or multiple impacts during the dynamic replacement procedure and generating output files of mesh deformation as well as time history data.

Once the main finite-element program was developed, the accuracy of the written subroutines (except the constitutive relations subroutine, the slideline subroutine, and the pore pressure subroutine) were checked against the commercially available dynamic finite-element program DYNA2D. For this purpose, a simple impact load case involving linear elastic material behavior without pore water was analyzed using both DYNA2D and the DYCOM programs. Despite the difference in the number of integration points employed for these two programs (four point integration for DYCOM and one point integration for DYNA2D), excellent agreement was obtained in their predictions. Flowcharts illustrating the organization of the main finite-element program and the constitutive subroutine for the Cam-clay model are shown in Thilakasiri (1996a).

MODELING OF FULL-SCALE FIELD TEST

Field Testing Program

A field testing program was devised to investigate the feasibility of dynamic replacement of Florida organic soil during one phase of the comprehensive research project. The test site is located in Plant City, Florida, adjacent to Interstate 4 (I-4). The subsurface profile at the test consisted of 1.2- to 1.8-m-thick organic soil layer underlain by a dense silty sand deposit. After investigating the thickness of the organic soil layer based on ''muck'' probes, an area of 26 × 18 m was cleared. Then, the cleared area was covered with sand with a layer thickness varying from 1.2 to 2.1 m. The time duration between placing of the surcharge and the beginning of actual dynamic replacement testing was approximately 1 month. Considering the consolidation characteristics of organic soil, it can be reasonably assumed that during that period, the organic soil layer had reached the end of the primary consolidation phase, thus leaving a hydrostatic pressure distribution at the beginning of dynamic replacement. One impact location was selected for the pilot study and instrumented with inclinometers and resistivity type piezometers as shown in Fig. 9.

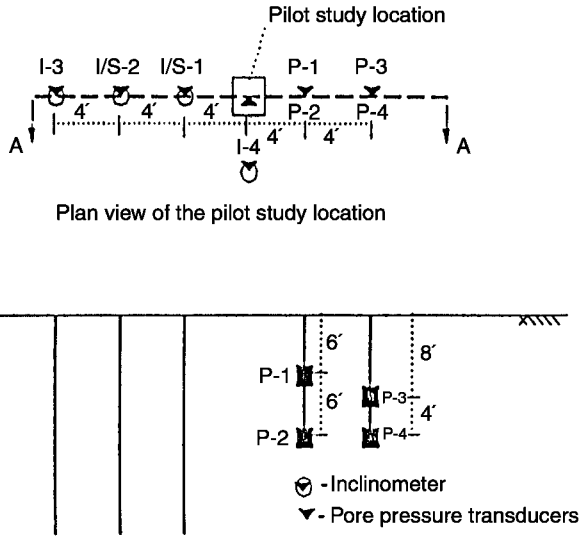

FIG. 9. Instrumentation of Pilot Study

Instrumentation

The instrumentation included inclinometers, resistivity-type electronic piezometers, and an accelerometer. The pressure transducers (6,897 kPa capacity) were first encapsulated in a PVC porous material and then attached to a 19.1 mm schedule 40, PVC standpipe to physically protect the electrical connection to the computer.

The inclinometers were used to measure the lateral deformation of the soil in the vicinity of the drop hammer. Attached to the inclinometers were magnetic rings to measure the vertical settlements. A magnet sensitive probe could descend to facilitate the settlement monitoring. The inclinometer/settlement monitoring system consisted of the inner inclinometer casing surrounded by a flexible corrugated plastic hose to which the magnetic rings were attached. The spacing of the magnetic rings along the casing was kept at 0.61 m.

Fig. 9 shows the plan view and a sectional view of the instrumentation relative to the impact location. In Fig. 9, *I/S* denotes the inclinometer-settlement monitoring system, and *I* denotes only the inclinometer. The typical inclinometer probe, which consists of spring-loaded wheels mounted to an approximately 2-ft-long, 1-in.-diameter rod, was used to measure the position of the inclinometer after the impact.

Apart from the above-mentioned instruments, laser pointers with laser detectors were used to measure the impact velocity of the hammer and trigger the data acquisition system. A drop hammer was also fabricated from 49-mm-thick, 0.61 × 0.61 m square steel plates to a total height of 1.22 m, producing a total weight of 4 tons. Then, an accelerometer was mounted on the top plate of the hammer coinciding with the center of the hammer. A terminal box with receptacles for each of the eight transducers was fabricated to expedite data acquisition during testing.

Comparison of Model Predictions and Field Data

First Blow of Drop Hammer

The aforementioned finite-element program DYCOM was used to model the drop hammer impacts during the field testing program. Then, the predicted displacement and pore pressure fields in the neighborhood of the hammer were compared with the corresponding quantities measured in the field. After conducting a few trials in the area (under similar subsurface conditions) well away from the pilot study location, an initial drop height of 6.1 m was selected. This drop height was verified by the crater prediction method proposed by Mullins et al. (1996).

The soil layer dimensions for the finite-element mesh were selected based on the previously carried out cone penetration test and borehole log results. The mesh boundaries were selected well outside the influence area of the drop hammer. The final mesh configuration was determined after carrying out a sensitivity analysis of the predicted results with respect to the number of elements in the mesh. The ground-water table was observed to be at the top of the organic soil layer. The actual impact velocity of the hammer was estimated by multiplying the free fall velocity by an efficiency factor. Based on the velocity measurement using the laser beam method and videotaping of the free-fall, the efficiency factor was found to be 90%.

The mesh output data were obtained at 20-ms intervals. Fig. 10 shows the initial finite-element mesh, and Figs. 11(a and

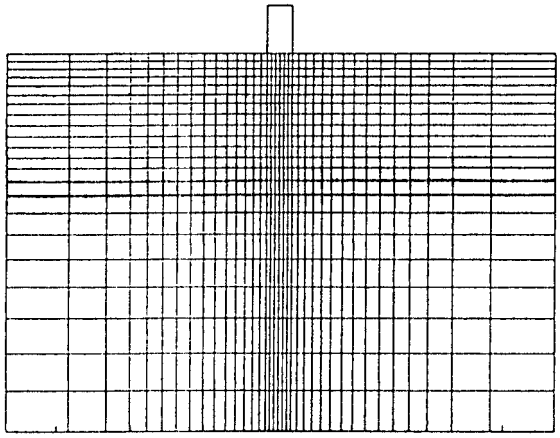

FIG. 10. Initial Mesh

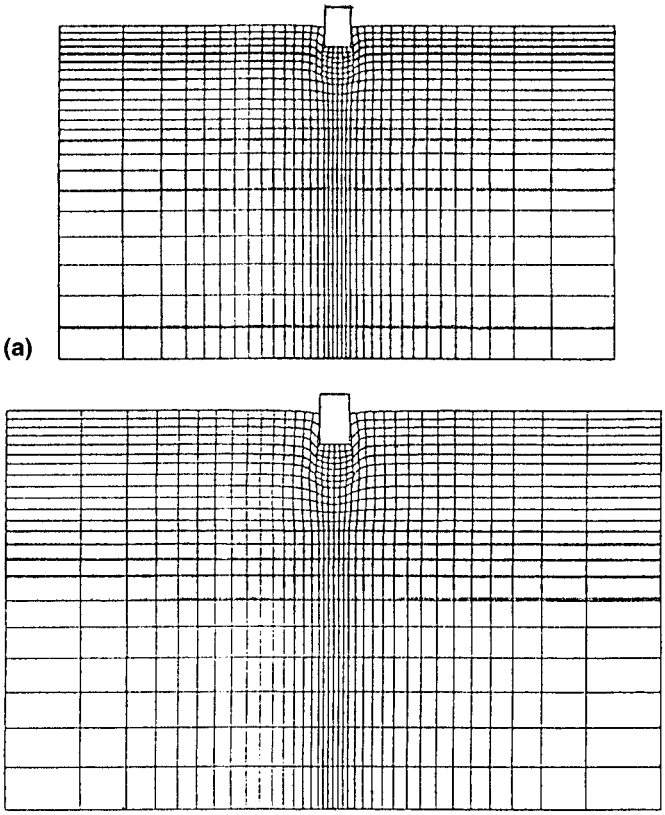

FIG. 11. Hammer Displacement after: (a) 160 ms; (b) 200 ms

b) show the time history of the deformation of the finite-element mesh as predicted by the finite-element model, at 160 and 200 ms after the impact.

The crater depth measured after the first blow was 0.87 m, whereas the theoretical prediction from the model was 0.78 m. In Fig. 12, the rebound portion of the predicted acceleration curve of the drop hammer was of a higher magnitude than the measured negative acceleration, indicating that the rebound velocity of the hammer is less than the rebound velocity predicted by the model. This is probably the reason for the discrepancy between the predicted and the measured crater depths.

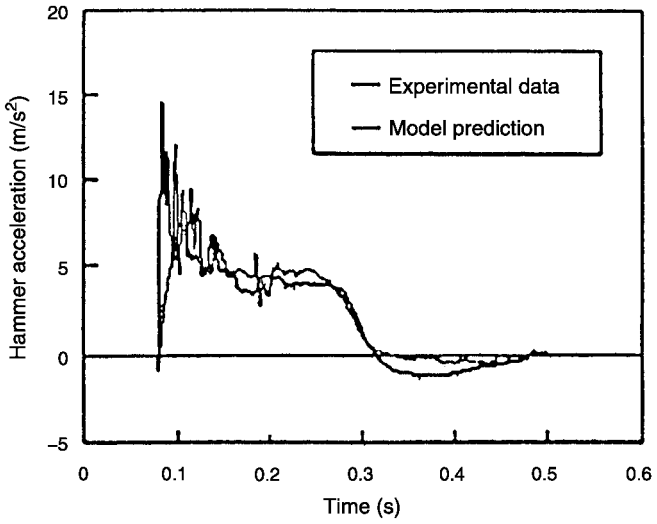

FIG. 12. Acceleration Time History of Drop Hammer

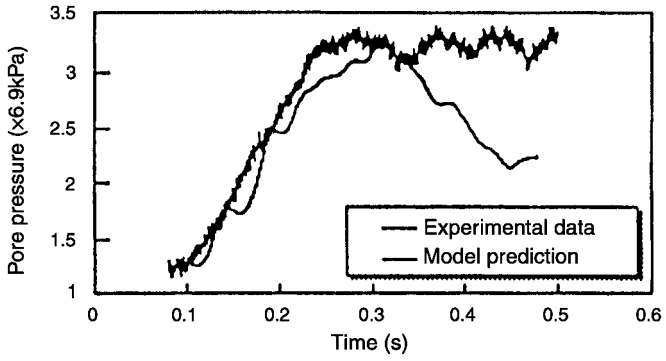

FIG. 13. Measured and Predicted Pore Pressure at Location P-1 of Fig. 9

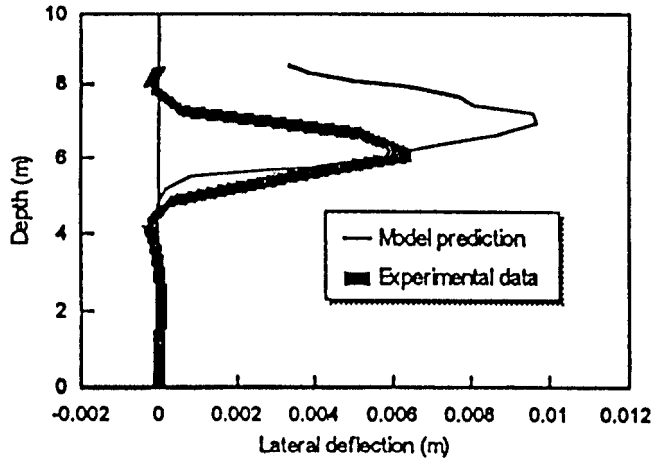

FIG. 14. Measured and Predicted Lateral Displacement at Location I/S-1 of Fig. 9

The model was also utilized to predict the pore pressure responses of the installed piezometers. The results of the comparison of the model and the measured pore pressure response at location P-1 of Fig. 9 is shown in Fig. 13. The comparison of the lateral deformation of the inclinometer I/S-1 with the corresponding model prediction is shown in Fig. 14. Similar comparisons made with other piezometer and inclinometer readings are found in Thilakasiri (1996a).

As mentioned earlier, a convergence study was carried out to select the best mesh configuration and the time step size. For this study, the final hammer penetration was selected as the control parameter. The variations of the control parameter with respect to the number of elements and the time step size are shown in Figs. 15 and 16. In varying the number of elements in the mesh, both the far-field configurations were changed. Accordingly, a time step size of 0.00002 s and a mesh with 464 elements were selected for the field test simulation.

Multiple Blows

The program DYCOM is also capable of modeling multiple blows during dynamic replacement. At the end of a particular hammer blow, the program automatically creates an output file containing the current geometry of the mesh, updated material properties, slip surface information, and other parameters specified by the user in the initial input file. The output file, thus created, acts as the input file for the simulation of the next hammer blow. In addition, the user has to specify the refill material properties together with the re-meshing dimensions for the next hammer blow. For subsequent hammer blows, the program re-meshes only the refilled crater created by the preceding hammer blow and the slave side of the slideline of the previous mesh. On the other hand, the master side of the slideline of the previous mesh is kept unaltered.

Once the re-meshing dimensions and the refill material properties are provided, re-meshing is automatically carried out by taking into account the refilled area and the user specified dimensions. In the process of re-meshing, the updated soil properties at the integration points are determined by linear interpolation of the corresponding quantities from the mesh configuration at the end of the preceding hammer blow. The computational procedure is repeated for the new mesh with the updated material properties.

The first four hammer blows imparted during the field testing program were numerically simulated using the above procedure. Since the hammer acceleration and pore pressure data were not available for comparison, only the lateral displacement measured using the inclinometers are shown in Figs. 17–20 along with predicted values. In addition, the vertical displacement of the top of the organic soil layer predicted and measured with the progression of the treatment process are shown in Fig. 21. Both the predicted and the measured vertical displacement of the bottom of the organic layer was insignificantly small.

If one assumes that the measured displacements are accurate, then it is evident from the comparison of the measured and the predicted lateral displacements (Figs. 17–20) that the model overpredicts the lateral deformation of the organic soil layer. For precise measurement of the lateral deformation, the stiffness of the measuring device should be of the same order of magnitude as that of the surrounding soil. However, the inclinometer pipes were grouted after installation, thus increasing the lateral stiffness of the inclinometer setup. Therefore, it is possible that the inclinometer pipe surrounded by hardened grout may have been stiffer than the weak organic soil, resulting in lower lateral displacement of the inclinometer in the

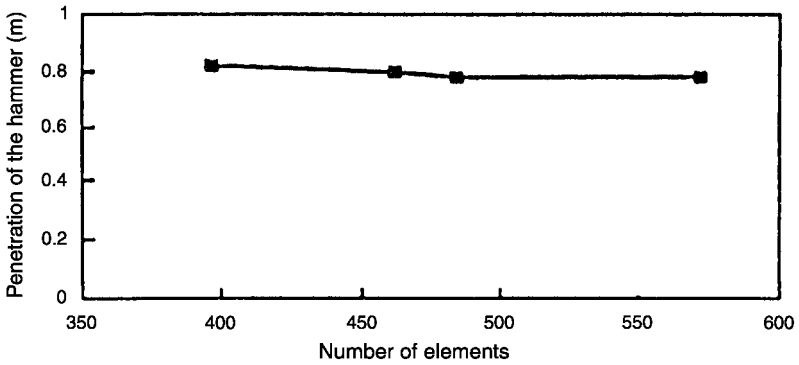

FIG. 15. Variation of Final Hammer Penetration with Number of Elements

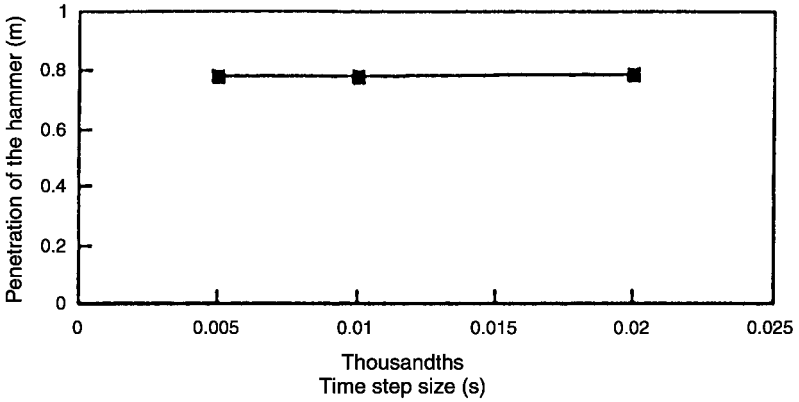

FIG. 16. Variation of Final Hammer Penetration with Time Step Size

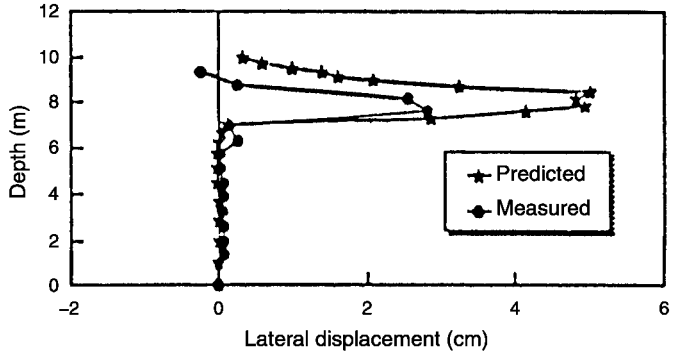

FIG. 17. Lateral Displacement of Inclinometer I/S-1 after Second Blow

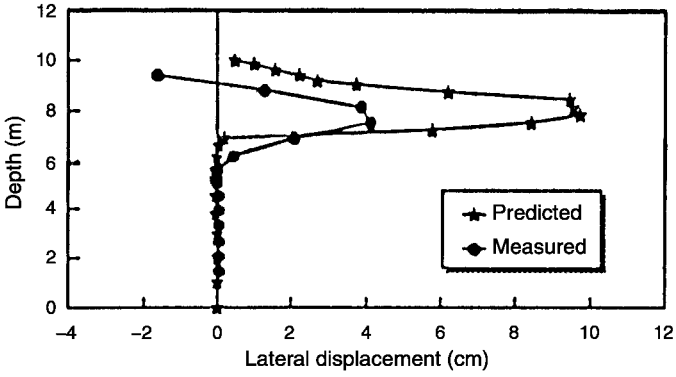

FIG. 18. Lateral Displacement of Inclinometer I/S-1 after Fourth Blow

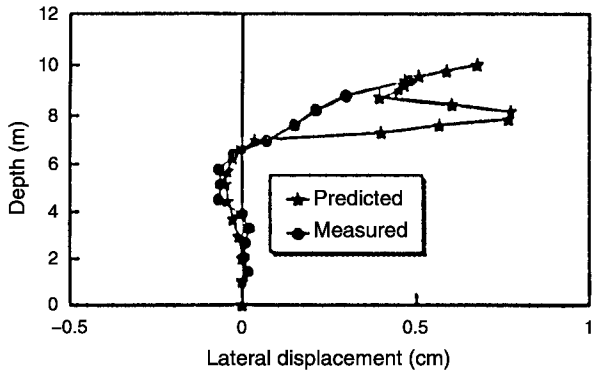

FIG. 19. Lateral Displacement of Inclinometer I/S-2 after Second Blow

organic soil layer. Hence one can also view the results in Figs. 17–20 as indicating a significant limitation of inclinometer measurements rather than an overprediction by the analytical method. This deficiency of the inclinometer systems is hard to overcome when using them in very weak soils.

Parametric Study

The finite-element methodology developed in this study can be effectively utilized in predicting the optimum values of energy level, initial sand blanket thickness, and other significant attributes of dynamic replacement. This would certainly aid in curtailing needless labor and expenses required for field trials needed to assess the impact of each individual attribute. To illustrate this facility, a parametric study was performed using DYCOM to observe the effect of changing the initial sand blanket thickness. The depth of the sand column formation and

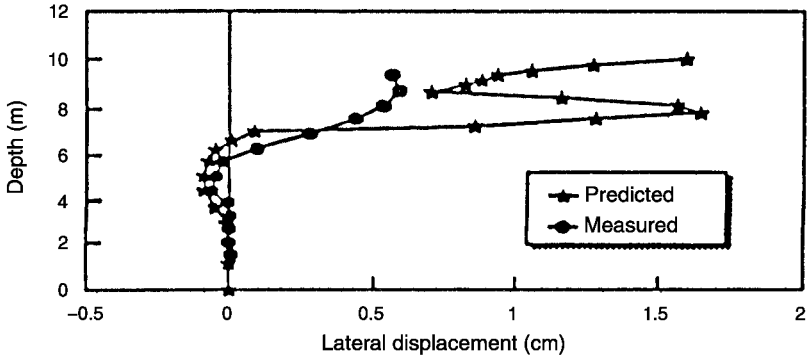

FIG. 20. Lateral Displacement of Inclinometer I/S-2 after 4th Blow

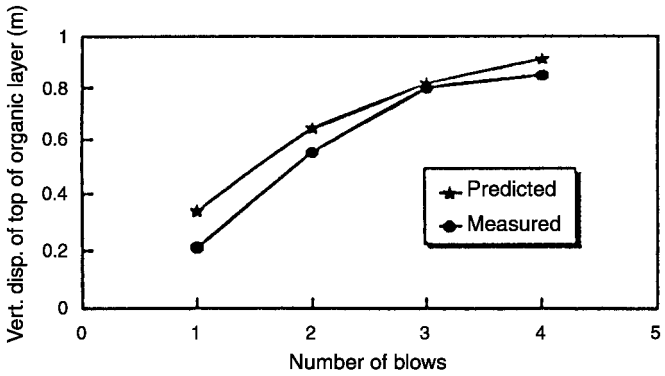

FIG. 21. Vertical Displacement of Top of Organic Layer

the lateral extent of the improvement zone can be regarded as fitting indicators of the effectiveness of dynamic replacement. Hence the parametric study was performed for the test site using three values of the initial sand layer thickness (0.91, 1.22, and 1.53 m), in order to investigate the effect of the initial sand layer thickness on the extent of the column formation and the hammer penetration. The variation of the lateral deformation at a location 1.22 m away form the impact location (I/S-1 of Fig. 9) and the hammer penetration predicted by DYCOM for the first three blows are shown in Figs. 22–25.

As one might expect, the sand column depth and the extent of the lateral influence zone increase with the decrease in the thickness of the initial sand layer thickness. However, thin sand layers create other practical problems such as excessive hammer penetration accompanied by problems of hammer recovery and irregular column formation with intermittent organic soil layers. The latter phenomenon can result from caving-in of organic soil during and after the hammer retrieval, if a significant thickness of the organic soil has been exposed due to a single penetration. The values of hammer penetration after the first blow for each of the layer thicknesses are given in Table 1. If the organic soil layer should not be exposed after the first blow, the maximum hammer penetration must be limited to the thickness of the covering sand layer. Hence, based on the values given in Table 1, a 1.22-m-thick sand layer was selected for the field study.

APPLICABILITY OF STRESS-STRAIN RELATIONS

The main aims of the technique described in this paper are to predict the depth of pounder penetration, depth of compaction influence in organic soil, and the extent of sand column formation. It is apparent that, in terms of these phenomena, the more important deformation behavior is that of the organic soil, which is described adequately by the Cam-clay model. The encouraging computer predictions bear testimony to this statement.

Bishop (1966) stated that the extended von Mises criterion (on which Drucker and Prager failure surface is based) fails to predict meaningful results for cohesionless soils with ϕ' larger than 36.9° in both extension and compression. Bishop (1966) also stated that experimental results strongly support the Mohr-Coulomb failure criterion. In the case of the sand overburden that provides the compaction blanket and refill material for sand columns, the mode of deformation that directly impacts the pounder penetration and vertical influence zone of compaction is compression. Since the triaxial compression tests conducted on the tested sand yielded ϕ' values <36.5° (34° for blanket sand, and 32° for refill sand), the above limitations of the von Mises failure criterion would not have significant implications on the results of this study, especially in the initial stages of dynamic compaction. However, on repeated pounding of the sand columns, as the sand columns become saturated and begin to expand laterally, it is quite possible for the sand in the columns to approach a density that would correspond to the limiting ϕ' value of 36.5°. Under

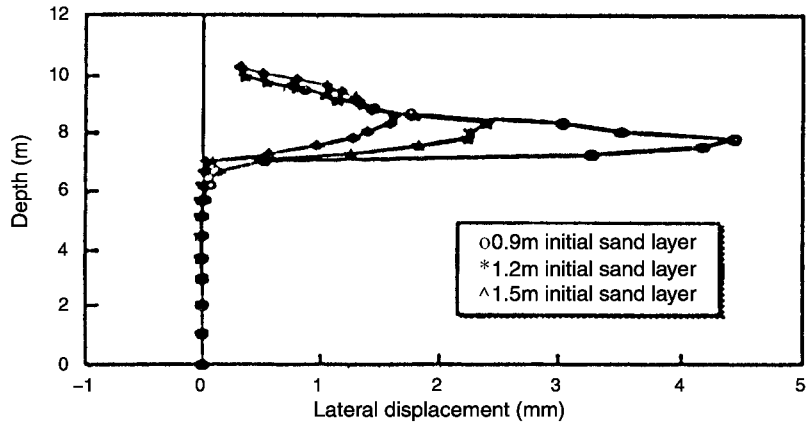

FIG. 22. Lateral Displacement at 1.2 m away from Impact Location after the First Blow

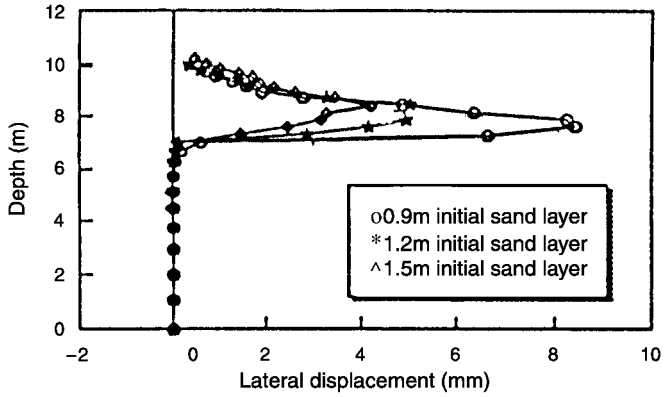

FIG. 23. Lateral Displacement at 1.2 m away from Impact Location after Second Blow

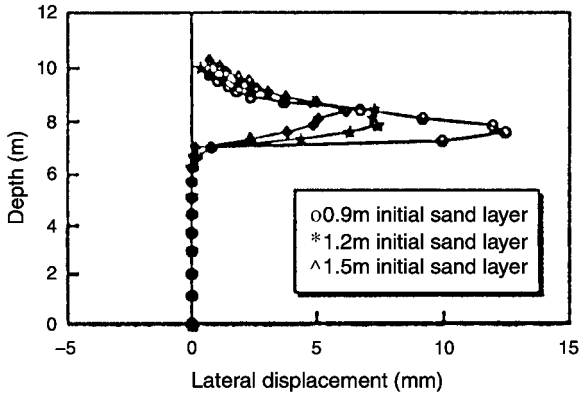

FIG. 24. Lateral Displacement at 1.2 m away from Impact Location after Third Blow

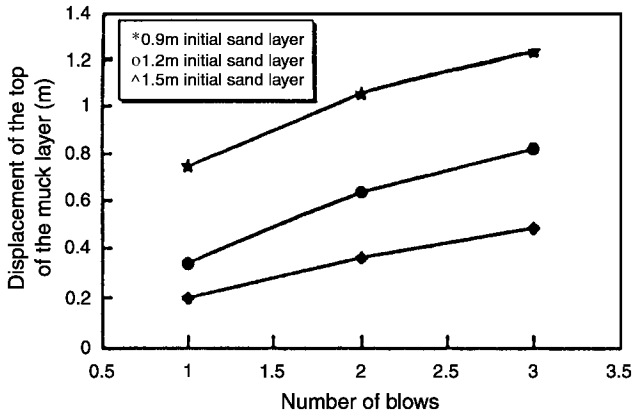

FIG. 25. Variation of Displacement of Top of Organic Layer with Sand Layer Thickness

these conditions, the rates of lateral and even the vertical progression of the sand predicted by the model could be questionable. However, this will not apply to the deformation behavior of the relatively loose refill sand.

CONCLUSIONS

The objective of this study was to develop a finite-element model to explore the significant attributes of the ground modification technique of dynamic replacement and compare model predictions with a full-scale instrumented dynamic replacement test program. As one would anticipate, dynamic impacts produce relatively large strains during dynamic replacement, leading to excessive deformation in the vicinity of the drop hammer. Moreover, at high strain levels, soil exhibits nonlinear characteristics making the linear elastic stress-strain relations unrealistic. Most of the currently available analytical methods used for dynamic compaction analysis assume linear stiffness and damping properties in simulating the dynamic response of the ground. In the current formulation on the other hand, two constitutive relations are used to model the two material types involved: (1) The elliptical cap model for sand; and (2) the modified Cam-clay model for organic soil. The stress is increased in a stepwise manner according the updated Lagrangian method, and the geometrical nonlinearity is considered in the stress incremental process. Hence this analytical methodology can be considered as a significant improvement in the analysis of dynamic stabilization methods. Kinematics of both the solid phase and the pore fluid are considered separately, whereas volumetric compatibility is maintained to ensure the integrity of the two phases. In addition, the complex punching mechanism is also successfully modeled by formulating a comprehensive slideline algorithm. Laboratory drained and undrained triaxial, and isotropic consolidation tests were used to extract the material parameters for the finite-element model. Subsequently, the chosen material parameters were utilized to numerically model the pore pressure and the stress-strain behavior of separate triaxial tests in order to verify the applicability of the selected material models. The agreement between the predicted and the experimental data was reasonable. Then, the hammer acceleration, lateral deformation, and pore pressure generation in the neighborhood of the impact location measured during the test program were compared with the corresponding model predictions. Reasonably good agreement between the measured and the predicted results was observed thereby verifying the applicability of the proposed finite-element methodology for field dynamic replacement. Furthermore, the usefulness of the finite-element program in determining the optimum sand layer thickness was also demonstrated by a parametric study. Hence in field construction situations where field pilot DR studies are impractical due to highly variable site geology or when a preliminary DR viability study is needed, this analytical tool can be expediently employed to determine the optimum DR depth and spacing of the DR column grid to achieve maximum treatment benefits.

TABLE 1. Hammer Penetration after First Blow

Initial sand layer thickness (m) (1)	Penetration of hammer after first blow (m) (2)
0.91	0.91
1.22	0.73
1.53	0.55

ACKNOWLEDGMENT

Funding provided by Florida Department of Transportation is gratefully acknowledged.

APPENDIX. REFERENCES

Bishop, A. W. (1966). "The strength of soils as engineering materials." *Sixth Rankine Lecture, Géotechnique*, London, 16, 91–130.
Chen, W. F., and Mizuno, E. (1990). *Nonlinear analysis in soil mechanics—Theory and implementation*, Elsevier Science Publishing Company Inc., New York.
Chow, Y. K., Yong, D. M., Yong, K. Y., and Lee, S. L. (1992). "Dynamic compaction analysis." *J. Biotech. Engrg.*, ASCE, 118(8), 1141–1157.
DiMaggio, F. L., and Sandler, I. S. (1971). "Material model for granular soils." *J. Engrg. Mech.*, ASCE, 97(3), 935–950.
Fung, Y. C. (1965). *Foundations of solid mechanics*, Prentice-Hall, Englewood Cliffs, N.J.
Hallquist, J. O. (1983). *Theoretical manual for DYNA3D*, Lawrence Livermore National Laboratory, University of California, Calif.

Hallquist, J. O., Goudreau, G. L., and Benson, D. J. (1985). ''Sliding interface with contact-impact in large scale Lagrangian computations.'' *J. Comp. Meth. Appl. Mech. and Engrg.*, South Africa, 51, 107–137.
Hollingshead, G. W., and Raymond, G. P. (1971). ''Field loading tests on muskeg.'' *Civ. Engrg. Res. Rep. 71-7*, Royal Military College of Canada, Kingston, Ontario, Canada.
Kleiber, M. (1989). *Incremental finite element modelling in non linear solid mechanics*, Ellis Horwood Ltd., Chichester, England.
Kruger, J. J., Guyot, C., and Morizot, J. C. (1980). ''The dynamic substitution method.'' *Proc., Int. Conf. on Compaction*, Ecole Nationale des Ponts et Chaussées and the Laboratoire Central des Ponts et Chaussées, Editions Anciens ENPC, 339–343.
Lo, K. W., Ooi, P. L., and Lee, S. L. (1990). ''Unified approach to ground improvement by heavy tamping.'' *J. Geotech. Engrg. Div.*, ASCE, 116(3).
Mei, C. C., and Fonda, M. A. (1982). ''Boundary layer theory of waves in a poro-elastic sea bed.'' *Soil mechanics—Transient and cyclic loads*, G. N. Pande and O. C. Zienkiewicz, eds., Wiley, New York, 573.
Menard, L., and Broise, Y. (1975). ''Theoretical and practical aspects of dynamic consolidation.'' *Géotechnique*, London, 25(1), 3–18.
Mullins, G., Gunaratne, M., Stinnette, P., and Thilakasiri, H. S. (1996). ''Prediction of dynamic compaction pounder penetration.'' *Soils and Found.*, 40(5), 91–97.
Nagger, M. H. El, and Novak, M. (1994). ''Non-linear model for dynamic axial pile response.'' *J. Soil Mech. and Found. Div.*, ASCE, 120(2).
Thilakasiri, H. S. (1996a). ''Analytical simulation of dynamic replacement of Florida organic soil.'' PhD dissertation, University of South Florida, Tampa, Fla.
Thilakasiri, H. S., Gunaratne, M., Mullins, G., Stinnette, P., and Jory, B. (1996b). ''Analytical and experimental investigation of dynamic compaction induced stresses.'' *Int. J. Numer. and Analytical Methods in Geomech.*, 20, 753–767.
Zienkiewicz, O. C., Humpheson, C., and Lewis, R. W. (1977). ''A unified approach to soil mechanics problems (including plasticity and viscoplasticity).'' *Finite element in geomechanics*, G. Gudehus, ed., Wiley, New York, 573.
Zienkiewicz, O. C., Leung, K. H., Hinton, E., and Chang, C. T. (1982). ''Liquefaction and permanent deformation under dynamic condition—numerical solution and constitutive relations.'' *Soil mechanics—Transient and cyclic loads*, G. N. Pande and O. C. Zienkiewicz, eds., Wiley, New York, 627.
Zienkiewicz, O. C., and Taylor, R. L. (1988). *The finite element method*, Vol. 1, McGraw-Hill, New York.
Zienkiewicz, O. C., and Taylor, R. L. (1991). *The finite element method*, Vol. 2, McGraw-Hill, New York.

Pressure-Grouting Drilled Shaft Tips in Sand

Gray Mullins[1], Steven D. Dapp[2], and Peter Lai[3]

Abstract

Considering the strain incompatibility between end bearing and side friction of drilled shafts, tip capacity is often discounted from total shaft capacity. This is due to the relatively large displacements required to mobilize the tip which often exceed service load displacement criteria. Additionally, concerns regarding shaft tip soil disturbance (i.e. insitu stress relief) and toe cleanliness further discourage designers from using end bearing as available capacity. As a method of mitigating these conditions, pressure-grouting the shaft tip after its construction has been successfully employed throughout the world. With very few exceptions, the benefits of tip-grouting have been disregarded in the United States. Sources of skepticism arise from the uncertainty of the grout formation beneath the tip and the lack of rational design procedures for its use. In cooperation with the Florida Department of Transportation, the University of South Florida is researching the effects of post-grouting on shaft capacity in loose to medium dense sands. This paper presents a review of past and present base-grouting methods used throughout the world and the scope of on-going full-scale load test programs.

Introduction

The use of drilled shafts as structural support has recently increased due to heightened lateral strength requirements for bridge foundations and the ability of drilled shafts to resist such loads. They are particularly advantageous where enormous lateral loads from extreme event limit states govern bridge foundation design (i.e. vessel impact

[1]Assistant Professor, Department of Civil and Environmental Engineering, University of South Florida, Tampa, FL 33620

[2]Graduate Researcher, University of South Florida, Tampa, FL 33620

[3]State Geotechnical Engineer, Florida Department of Transportation, Tallahassee, FL

loads). Additional applications include high mast lighting, cantilevered signs, and most recently, cellular phone and communication towers. With respect to bridge construction, design procedures, both axial and lateral, have been additionally impacted where increased unsupported pile lengths are mandated by scour depth predictions based on 100 year storm events. This dramatically changes driven pile construction where piles cannot be driven deep enough without overstressing the concrete or without pre-drilling dense surficial layers. In contrast, drilled shaft construction is relatively unaffected by scour depth requirements and the tremendous lateral stiffness has won the appeal of many designers. However, drilled shaft design and construction is plagued with quality control issues (e.g. shaft bottom cleanliness or open excavation time) not experienced during pile driving.

Typically, designers have chosen to significantly reduce end bearing capacity or even discount it altogether to account for soft toe conditions. Even in ideal conditions, full end bearing is typically not mobilized before service load displacement criteria are exceeded. The bulk of the capacity is therefore derived from side friction which can be developed with relatively small displacements. This is especially problematic for larger shafts which must displace even further to fully develop tip capacity in loose to medium dense cohesionless soils where unit side friction values are comparably low with respect to competing foundation systems. Consequently, the end bearing strength component, which may be on the order of up to twenty times the unit side friction, is unavailable to the useful capacity of the shaft (AASHTO, 1997). In an effort to mitigate shaft toe cleanliness and also balance the useful capacity between end bearing and side friction, projects throughout the world have implemented pressure grouted shaft tips after normal shaft construction (sometimes termed "post-grouting"). An overview of pressure grouting considerations will be presented herein as well as efforts underway to develop recommendations for its use by the Florida Department of Transportation (FDOT).

Background

In the early 1960's, efforts began to obtain more usable tip capacity of drilled shafts using pressure grouting below the shaft tip. In 1975, Gouvenot and Gabiax presented results of a test program where post-grouting large diameter piles led to increased ultimate load capacities up to three times in sands and clays. As a result, post-grouting techniques have become a routine construction process in many parts of the world (Bruce, 1986). The post-grouting process entails: (1) installation of grout pipes during conventional cage preparation that run to the bottom of the shaft reinforcement cage, and (2) after the concrete in the shaft has cured, injection of high pressure grout beneath the tip of the shaft which both densifies the insitu soil and compresses any debris left by the drilling process. By essentially preloading the soil beneath the tip, end bearing capacities can be realized within the service displacement limits.

Although the performance of a drilled shaft is bounded by the maximum contribution of end bearing and skin friction components, these values are not fully realized due to flaws introduced by full scale construction techniques. Three

mechanisms, or combinations thereof, are responsible for the excessively large shaft displacements required to develop bearing capacity:

- Strain incompatibilities typically exist between the end-bearing and side friction components in relation to service displacement criteria. The ultimate side frictional component develops with relatively small shaft displacements compared to the displacements required to mobilize ultimate end bearing. Development of the side friction component can be 50% of ultimate at displacements of approximately 0.2% of the shaft diameter (D) (AASHTO, 1997), and fully developed in the range of 0.5 to 1.0 % D (Bruce, 1986). In contrast, mobilization of the end bearing component can be 50% mobilized at 2.0% D (AASHTO, 1997), and fully mobilized in the range of 10 to 15 % D (Bruce, 1986). The end bearing component therefore requires 10 to 30 times more shaft displacement in order to mobilize the same percentage of its ultimate value as the side shear component. This means that the side friction is strained beyond its ultimate strength and into a residual state by the time the end bearing capacity is realized. In addition, the service load deflection criteria is often exceeded long before any significant amount of end bearing can be developed.

- The pile toe zone is often disturbed by normal construction procedures. This disturbance can occur by soil stress relaxation due to excavation of the overburden, inflow of groundwater due to insufficient hydrostatic head or rapid removal of the excavation tool during the construction process. This soil disturbance of the pile toe zone by normal construction procedures is often difficult or nearly impossible to eliminate. Displacements necessary to overcome this disturbance and mobilize end bearing are usually in excess of allowable service limits. In instances of less competent soil, this problem is further compounded.

- Construction methods and processes may leave soft debris/deposits at the bottom of the excavation. Primary contributing factors are: overall shaft bottom cleanliness, a non-uniform distribution of toe debris causing an initially reduced shaft area bearing on the soil, excessive sand content in the drilling fluid, prolonged time for cage and concrete placement, and deposits of drilling fluid itself at the bottom. These construction related factors may then also be the cause of excessive deflections required to mobilize end bearing due to toe inclusions not evident in an otherwise clean excavation.

Depending on soil type and drilling method, any or all of the above mechanisms may occur at a given excavation. However, each scenario can be mitigated by a procedure, relatively unused in the United States, where post-grouting is performed beneath the shaft tips. This grouting concept accommodates the trend towards large diameter drilled shafts due to lateral load considerations, while allowing for the end bearing component to contribute to the useful capacity of the shaft.

Soil Type Applicability

End bearing strata may be grouped into three broad categories in relation to the

process of post-grouting pile tips. These categories are cohesionless soils (sands to silts), cohesive soils (clays), and soft or fractured rock formations. Although all soils can be improved to some degree by grouting techniques, the applicability and effectiveness of grouting, primarily compaction grouting, is many times more effective in cohesionless soils than other soil types (Baker and Broadrick, 1997). Historically, nearly all of the studies and construction projects involving grouting of the pile tips to increase end bearing have been in cohesionless soils.

Sand and Silt. The first effective large scale grouting of pile tips was performed in sandy soils in 1961 at the Maracaibo Bridge (Sliwinski, 1984). Since then many studies and construction projects have proven the extreme benefits of post-grouting the pile tips in cohesionless soils (Piccione in Cairo, 1984; Sliwinski and Fleming, 1984; Logie in Jakarta, 1984; Stocker in Jedda-Mecca Expressway, 1983; and Bauer in Brooklyn, NY, 1988). In general, results have shown that post-grouting the pile tips in cohesionless soils has significantly increased end bearing capacities. Figures 1, 2 and 3 show the effectiveness of post-grouted shafts.

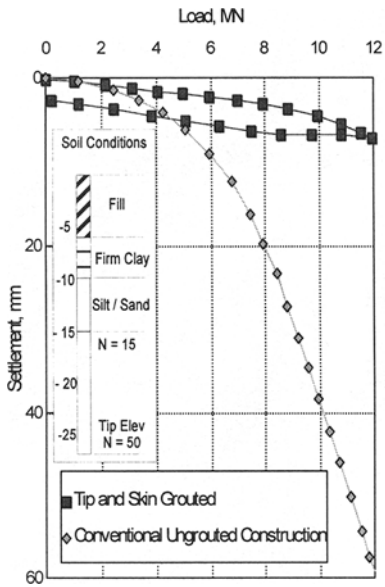

Figure 1. Comparison of two1.5m diameter drilled shafts (Sliwinski, et al., 1984).

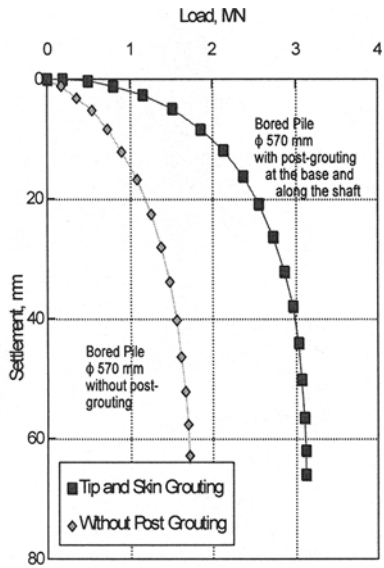

Figure 2. Load-displacement of 570 mm bored piles (Stocker, 1983).

Loose to medium dense sands hold the highest potential for increase in useable shaft end bearing. This is due to this soil profile being the most susceptible to the three mechanisms contributing to lack of pile end bearing as outlined in the previous section.

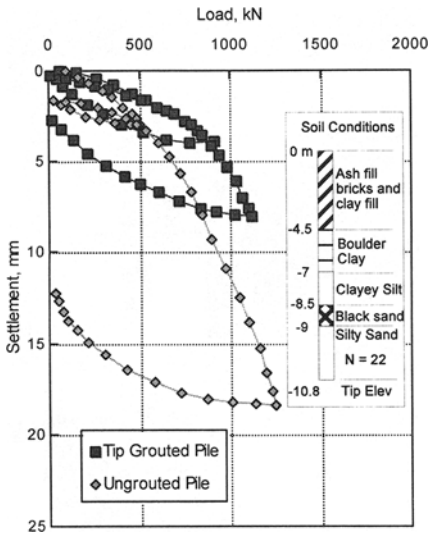

Figure 3. Results from 450 mm shaft load tests (Sliwinski, et al., 1984).

Two different grouting methods, permeation grouting and compaction grouting, are applicable to these soils. The permeation grouting can easily create a very large grout bulb, and compaction grouting can dramatically improve the soil stiffness. Both processes can be done with the use of ordinary cementitious grout.

Dense sands can be both permeation and compaction grouted with cementitious grout in the same manner as loose sands. However, a micro-fine cement may become necessary for permeation grouting, and may not yield significant improvement over compaction grouting alone. The grout volume used in dense sands would be significantly less. Bruce (1986) reviewed many cases to state that there is a direct relationship between ultimate load increase and volume of cement grout injected for all sands; when grouting dense sands the grout volume simply corresponded to the void volume of the gravel pack (discussed later, Figure 8).

Sandy silts can be densified by means of applying effective stresses during compaction grouting with ordinary cementitious grouts, although it is less effective than compaction grouting of clean sands. Permeation grouting in silty soil, however, would involve the use of chemical grouts, such as a silica gel, and is beyond the scope of this paper.

Although disturbance to the shaft toe area during construction is of little practical importance in soft rocks and clays (Sliwinski and Philpot, 1980), Sliwinski and Fleming (1984) concluded that in sands the end bearing contribution to the total load capacity is

extremely sensitive to construction induced soil disturbances. Therein, full scale load testing was used to verify the effectiveness of pressure grouting for mitigating these conditions.

Clay. Post-grouting in clay produces only a minimal gain in end bearing governed by the amount of consolidation that can occur within the set time of the grout. The high pressures introduced by this method may only result in hydrofracture of the soil matrix. Careful consideration would be needed so that the allowable end bearing contribution, even after grouting, would not exceed the creep limit of the clay at the grout bulb/soil interface. The most effective way of grouting in clay material would be to jet-grout, or deep-soil-mix under the shaft tip. While these are certainly viable options for remediating deep foundations in this soil type, it is not the focus of this paper.

Rock. Grouting of fractured and soft rock formations with low strength grout in order to fill voids, fractures, seams, and solution channels is sometimes conducted to alleviate drilling problems associated with karst topography. However, this is usually accomplished prior to drilling, and is not the grouting technique that is discussed herein. These formations typically are incapable of consolidation or densification by effective stresses induced by compaction grouting. Further, permeation grouting of the macro inclusions is effectively accomplished by the concrete head during normal construction, as is evidenced by high concrete over-runs in such cavernous strata.

Although grouting can effectively mitigate soft toe conditions caused by excessive construction debris/deposits at an excavation bottom for all soils, current quality control procedures for drilled shaft production already effectively address shaft bottom cleanliness for clay and rock during normal construction. Thus, only a marginal benefit would be realized in these conditions through the use of post-grouting. An exception may be where shaft bottom cleanliness is problematic due to extreme depths and time requirements such as the My Thuan Bridge Project, Vietnam (Dapp, 1998) or for cases where the capacity of shafts already constructed fall short of adequate (Logie, 1984).

Post-grouting can be effective in all soil types; however, research shows the greatest performance gain in cohesionless soils. As such, an ongoing study at the University of South Florida, Tampa is concentrating on the effectiveness of post-grouting in cohesionless soils (both sands and silt) with an emphasis on identifying the most effective grouting techniques. Effectiveness is evaluated by: (1) the final strain compatibility of the tip and skin friction components, (2) constructability, and (3) overall capacity gain.

Uplift Considerations

In general, upward movement of shafts during compaction grouting should be limited such that the frictional strength of the shaft is not developed beyond its ultimate value and into a lesser residual value. This is most critical in dense sand where there is

a pronounced loss of frictional resistance with large strains (Figure 4). Historically, uplift criteria have been limited to ranges from 2 mm (Stoker, 1983) to 20 mm (Bolognesi and Moretto 1973). Presently, in Taipei, a 3mm uplift criterion is in effect (Mullins, 1999). It is unclear, however, if these criteria were placed only on top-of-shaft movement or if the tip movement associated with elastic compression was also given a maximum permissible movement. Long shafts such as those in Taipei (80 m) can exhibit relatively large displacements at the tip without being detected at the top (and vice versa).

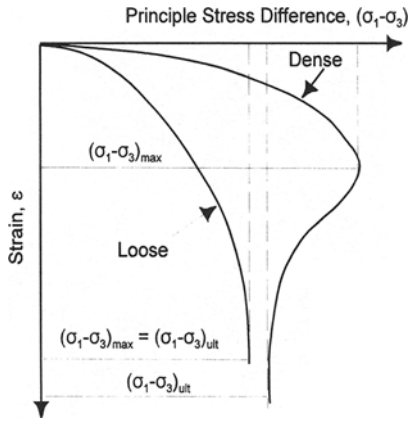

Figure 4. Stress / strain curves for typical loose and dense sands (Holtz and Kovacs, 1981).

Essentially, the maximum amount of end bearing improvement is dependent on how much downward resistance the side friction component of the shaft can provide. As such, post-grouting can also be applied to the sides of the shaft to improve unit side friction values. This aides in providing downward restraint during the tip-grouting process (resisting uplift). This is of particular importance for shorter shafts, and as a consequence skin grouting has been employed to aide in providing reaction (e.g.Bauer system of pile grouting). Additional criteria of maximum grout volume (per stage) and minimum grout pressure are established based on reasonable cavity expansion and the anticipated tip performance, respectively. Figure 5 shows grout pressures that have been used on various sites throughout the world in relation to the shaft tip depth.

Grouting Types

Standard grouting techniques can be divided into two basic categories: permeation grouting and compaction grouting. Staged grouting procedures are often designed which have a combination of these two, first permeation and then compaction. There are also state-of-the-art techniques available for cohesive soils, such as jet grouting or deep soil mixing, which alter the soil type and structure without inducing significant effective stresses.

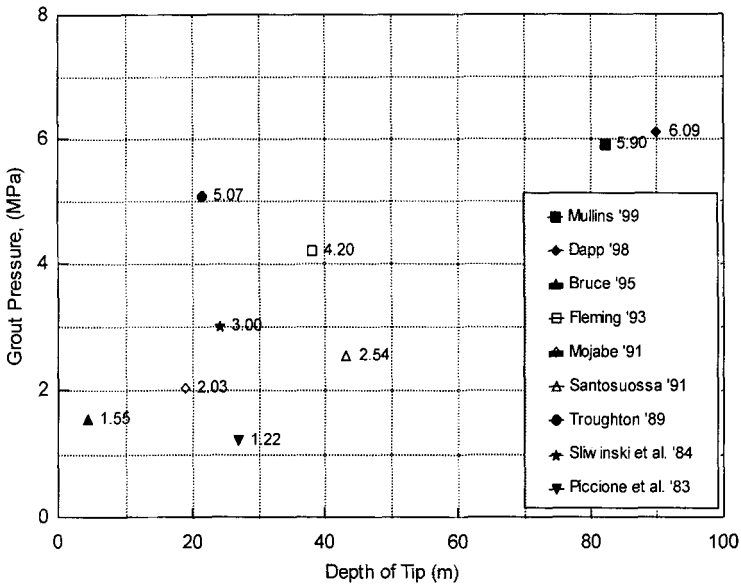

Figure 5. Tip grouting pressures used at various sites worldwide.

Permeation Grouting. Permeation grouting uses a fluid grout which is highly mobile within the soil formation, and therefore travels through the void spaces without providing any significant compaction or densification of the surrounding soils. In this manner a very large zone of improved soil below the pile tip is developed. Careful adjustment of the water-to-cement ratio is used to control the mobility of the grout. The type of grout mix design is also crucial to achieve this mobility. For example Littlejohn (1983), at the Jeddah - Corniche Centre, first tried remediating substandard piles with the use of a cement grout in a dense sand profile interbedded with hard sandy silt. However, grout takes were very low, and the remediation technique failed. Subsequently, a low viscosity resorcinol formaldehyde grout was successfully used.

Compaction Grouting. In contrast to permeation grouting, compaction grouting utilizes a thick, viscous, homogeneous, typically cementitious mass designed to remain together within the soil matrix. Generally there is a distinct interface between the soil and grout material, thus the insitu soil is consolidated and densified by cavity expansion of the grout bulb (Baker and Broderick, 1997). A typical compaction grouting mix design is shown in Table 1. However, this mix is recommended for minimum grout pipe diameters of 100mm.

Table 1. Typical Compaction Grout Mix (Baker and Broderick, 1997)

Description	Quantity	Standard	Comment/Effect
Sand	800-1000 kg	ASTM C-33	Well graded, rounded edge, min. 15% passing 0.075 mm sieve
Cement	110-225 kg	ASTM C-150	Control strength of mix, increase density of mix
Flyash *	90-310 kg	ASTM C-618	Improve pumpability, increase density, reduce cement content required for mix, Class F or Class C
Water	60-160 L		Control slump
Admixtures (optional)	1%-2% of cement		Control set time, control shrinkage

* Depending on the fines available from the sand.

Compaction grouting develops its own "filter cake" at the soil/grout interface which differs from the Bauer system of grouting where a mechanical grouting system uses steel plates and an impermeable cover or a liner embedded between the plates (discussed later). In either case, the mechanism of soil improvement is the same; the grout applies an effective stress to the soil, thus densifying it. A notable difference is that the simple compaction grouting (i.e., with a filter cake) is a uniform stress case at the pile tip, whereas the mechanical compaction system of steel plates provides a uniform strain condition. A potential benefit of compaction grouting the shaft tip is that this procedure could provide a means of proof testing shaft tip capacity during the compaction grouting procedure.

Presently, a testing program is underway to quantify the effectiveness of pile tip grouting to improve end bearing in loose to medium dense sand. Therein, simple compaction grouting will be compared to compaction grouting with a mechanical compaction cell, and a combination of permeation and compaction grouting.

Injection Techniques

Grouting techniques vary in the mechanism by which the grout is dispensed beneath the shaft tip. Variations include whether to use:

- stem, orifice, tube-a-manchette, or mechanical distribution system
- a gravel pack beneath the tip to aide in distribution of grout
- fixed or floating distribution system
- permeation, compaction, or a staged combination.

Two basic distribution systems are mainly used: (1) *simple compaction grouting* in which

the tube-a-manchette system employs a network of exposed grout tips, and (2) the *mechanical grouting system* in which the Bauer-type system of one or two steel plates with an impermeable membrane is used. Although both systems can be used in a wide variety of soils, the membrane-type mechanisms minimize hydro-fracture grout losses more common with tube-a-manchettes used in weakly layered soils.

The tube-a-manchette has several variations, but is primarily a simple pipe network across the bottom of the shaft pre-drilled along its length on the bottom face and connected to grout tubes to the top of shaft. The pipes are wrapped in a rubber membrane at the location of the holes to prevent blockage of grout passage during normal shaft construction where the tubes become completely encased in concrete. A problem with fixed tube-a-manchette systems is that the grouting must be accomplished immediately after the concrete has set (24 to 48 hours), while its strength is still low enough to burst the encapsulation. A simple tube-a-manchette system fixed to the cage and resting on the bottom of the excavation was used in the shafts supporting a major cable stay bridge in Thailand in 1985, as shown in Figure 6. A similar configuration has recently been used for the foundations supporting the cable-stay bridge over the Mekong River in Vietnam (Dapp, 1998). Presently, at the Taipei Financial Center project in Taiwan, an adaptation is being employed that closely contours the pipe network to the shaft bottom (Figure 7). The shape resembles the reverse circulation cutting tool and minimizes the concrete cover between the grout pipes and the shaft bottom.

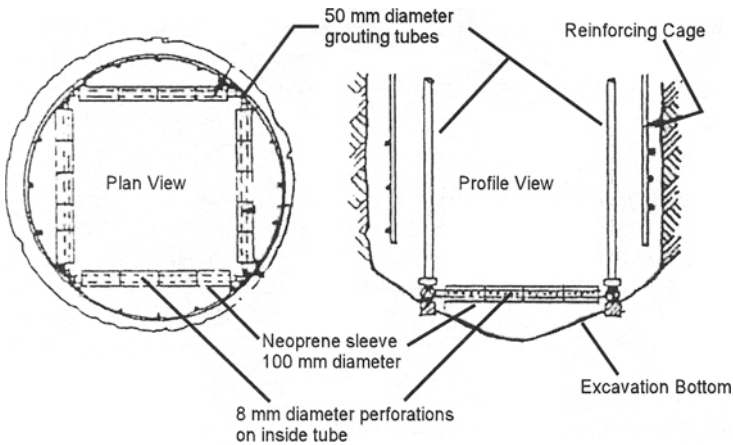

Figure 6. Simple tube-a-manchette compaction grout apparatus (after Bruce, 1986).

Complications can arise if the excavation depth is lower than the tube-a-manchette elevation. In such instances, the grout pressure is unable to break the

encapsulation and modify the soil. Such was the case when the first 90 m deep excavation in Vietnam was inadvertently over-excavated by 0.5m by way of extensive clean out procedures. This caused the tube-a-manchette to be embedded in an extra 0.5m of concrete. To avoid this problem, floating tube-a-manchettes were used for subsequent shafts which used slip joints allowing the distribution system to adjust to the actual bottom of excavation elevation. Other systems have used flexible grout hoses to overcome this problem. It is thus recommended that suspending the tube-a-manchette, by either method, should be considered necessary for proper steel placement of extremely long shafts where cage length and excavation depths may not be consistent.

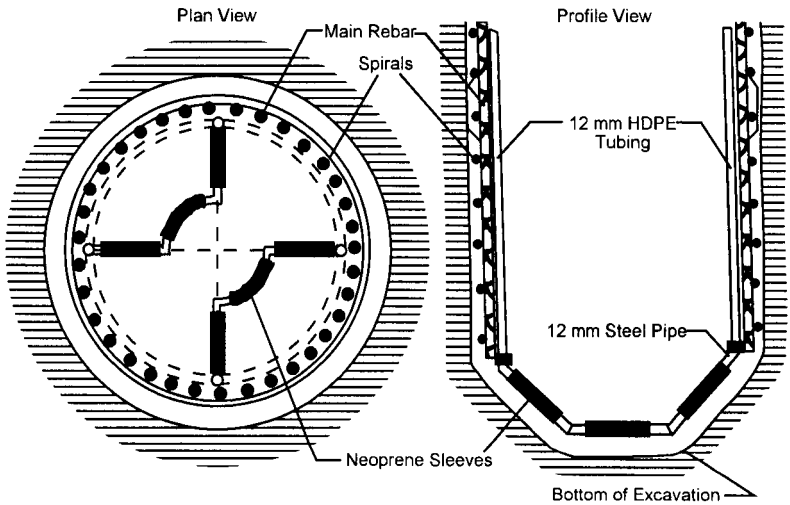

Figure 7. Tube-a-manchette system used in Taipei, Taiwan (Mullins, 1999).

Sliwinski and Fleming (1984) described first placing a gravel plug in the excavation, then the tube-a-manchette with a steel plate above (both suspended from the cage). This configuration is shown in Figure 8. The steel plate has the benefits of isolating the tube-a-manchette and gravel plug from the concrete so that the post-grouting process can take place after the concrete has gained design strength, the tube-a-manchette is protected from the tremie during concreting operations, and the steel plate gravel interface provides a consistent bearing surface for the compaction grouting pressure to act against (important for proof testing aspects). The gravel is beneficial for both permeation and compaction grouting by exposing more soil interface to the grout, as well as providing aggregate to knit the soil bulb together directly below the shaft tip.

Lizzi (1981) discussed a mechanism consisting of two steel plates separated by mechanical spacers (to allow grout pressure to initially act upon the full face of the

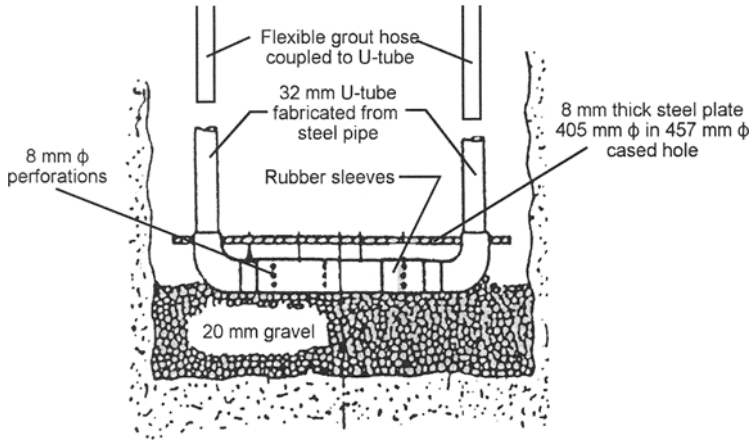

Figure 8. U-shaped grouting cell positioned at bottom of excavation (after Sliwinski and Fleming, 1984).

plates). This technique is similar to the Bauer system of tip grouting used on the Jedda-Mecca Expressway (Bruce, 1983) and the Brooklyn Queen's Expressway (1988). The

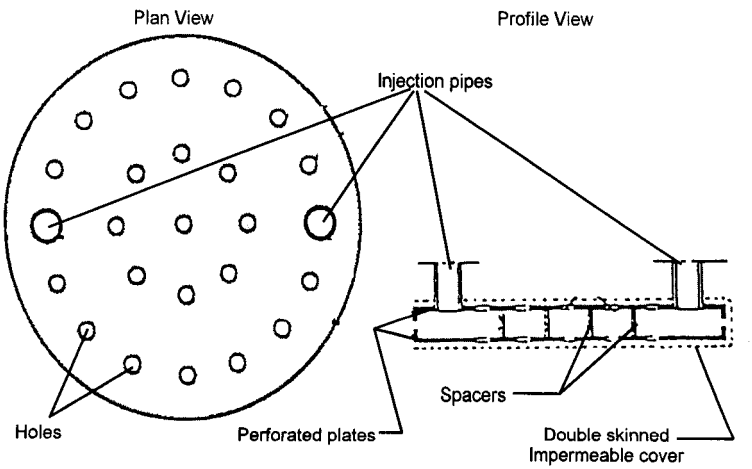

Figure 9. Mechanical compaction grout apparatus (from Lizzi, 1981)

difference is that Lizzi had the plates covered with an impermeable liner to ensure that separation of grout injection ports and concrete was maintained (see Figure 9). The impermeable liner ensured that no permeation into the surrounding soil occurred. Consideration can also be given as to whether a gravel pack should be included between the two plates, as was discussed in the early work by Bolognesi and Moretto in Paranah River (1973), shown in Figure 10. The benefit of the gravel pack again is as stated

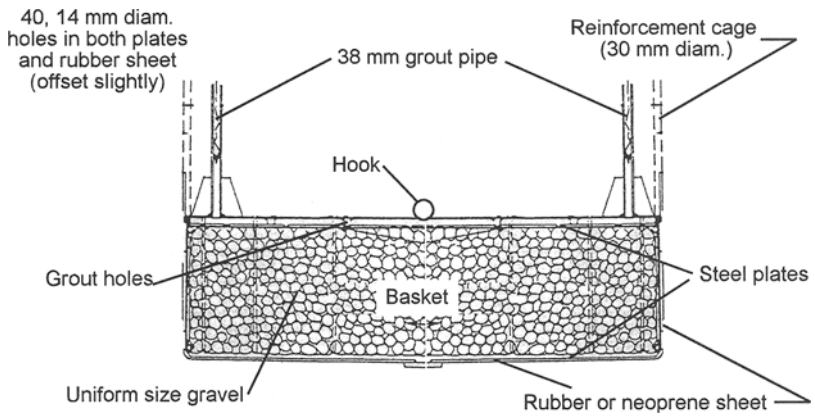

Figure 10. Gravel pack between two steel plates (after Bolognesi and Moretto, 1973).

above; however, this configuration must be suspended from, and lowered into the excavation with the cage which could become extremely cumbersome in a production-oriented setting.

Scope of Testing and Research

To investigate the various mechanisms of post-grouting and evaluate their effects on shaft performance, the University of South Florida, Tampa is presently conducting concurrent laboratory and full-scale testing on post-grouted drilled shafts. The laboratory component is looking at parameters such as: grout bulb formation, strength gains, grout mechanisms, and residual stress states after grouting; whereas the field component is addressing issues such as constructability, applicable mechanisms, mechanism durability, maintaining production, as well as strength gain and design recommendations.

The laboratory testing is being conducted using a relatively new device called a Frustum Confining Vessel (FCV) which provides a method of physically modeling pile-type insitu stresses on small-scale piles without the use of a centrifuge. The device, developed by Berminghammer Foundation Equipment in conjunction with McMaster University (Sedran, 1999), is a conical-shaped steel vessel in which sands are placed and

stressed as shown in Figure 11. The resulting vertical and horizontal stress distributions are reasonably similar to those of full-scale prototype piles. In the control volume portion of the FCV stresses are distributed similar to those encountered in the field. Some significant advantages of the FCV with respect to other physical modeling methods are the simplicity of testing, relatively low cost, and its ability to model relatively large model piles (e.g. 1 m long, 100 mm diameter).

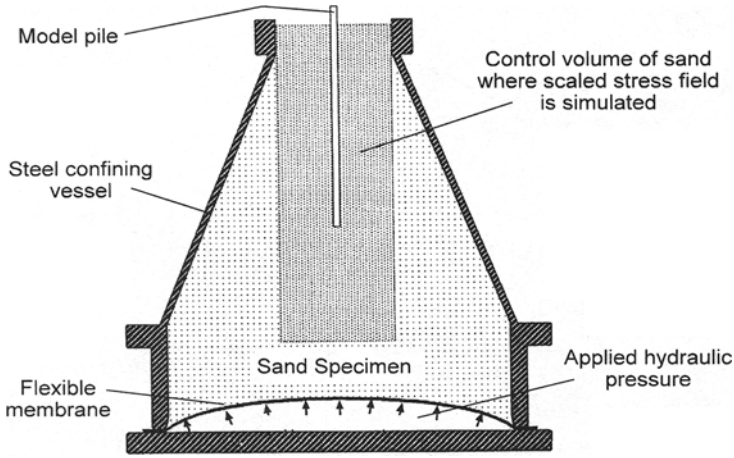

Figure 11. Frustum Confining Vessel used for physical modeling of pile load tests (after Sedran, 1999).

Specifically, post-grouting model piles/shafts requires overburden pressures that provide adequate reaction to pre-load the soil beneath the tip. Furthermore, the effects of scaling the size of the shaft will require additional foundation mass to restrain the upward movement of the shaft. Although scaling parameters require close attention to conduct meaningful load testing, the initial goal is merely to show the formation of the grout bulb at various relative densities for the sand. Subsequent load testing of post-grouted model shafts in the FCV is an added benefit that will afford interesting results.

The performance of post-grouted shafts is largely dependant on the strain compatibility of the tip and skin resistance. Additionally, for post-grouting to be fully beneficial, the soil must be returned to an unstressed state at the completion of the grouting process to remove locked-in stresses from negative skin friction. The benefit from post-grouting is therefore derived from the improved stiffness associated with reloading. The effects of residual stress are being investigated by maintaining various grout pressures during the curing of the grout and then testing the capacity of these model shafts. Instrumentation is included within the model shafts to confirm the state of stress locked into the soil.

The full scale portion of the program presently involves two sites where drilled shafts are being installed with post-grouting mechanisms. The first site has eight relatively short shafts, 5 meters long, installed in loose to medium dense silty sand that will be used to investigate both the effects of tip grouting as well as skin grouting. Four shafts will be installed with only tip grout mechanisms (similar to those in Figures 6, 8, and 9), two with tip and skin grouting, and two with no grouting systems as a controls. Figure 12 shows three variations of grouting mechanisms currently in use at the University of South Florida test site.

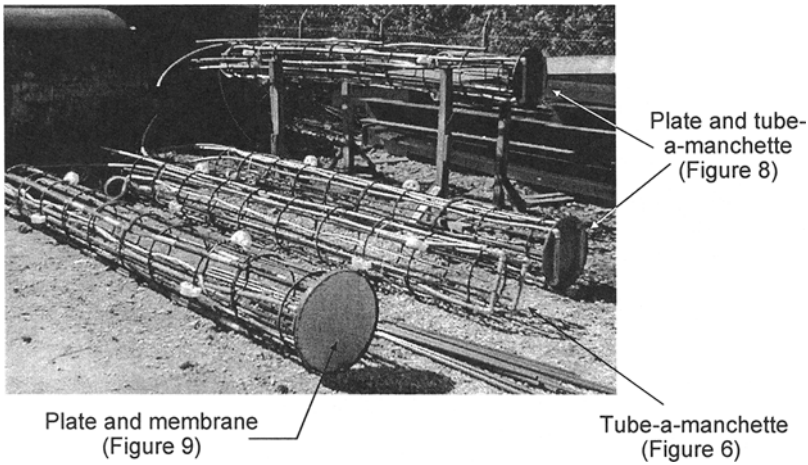

Figure 12. Post grouting mechanism used at the first site.

The second site has three proposed test shafts in sand and limestone involving five 30MN load tests. Due to the variable nature of the site, post-grouting has been selected for shafts tipped in sand to reduce their length. Two of the shafts will be tested prior to post-grouting and then subsequently after post-grouting for direct comparison. The third shaft will only be tested without grout effects. The tip grout mechanism will be selected based on the performance evaluation of the previous site. All shafts from both sites will be fully strain instrumented and continuously monitored to determine the distribution of load and the presence of residual stresses throughout the load test/post-grout/load test procedures.

Summary

Pressure grouting drilled shaft tips (post-grouting) has been successfully employed throughout the world for over thirty years with surprisingly little use within the

United States. Recently, the FDOT has contracted research to investigate the parameters affecting its performance and to develop recommendations and guidelines for its use on Florida roadway projects. The method provides a means by which to mitigate many of the factors that presently exclude the contribution of the end bearing from the useful shaft capacity (e.g. toe cleanliness). Presently, researchers at the University of South Florida are examining many of the considerations designers will need to address for its eventual use. By including significant end bearing contributions into the useful capacity, the design of drilled shafts can be drastically improved. Moreover, this inexpensive procedure could directly provide test results for every shaft installed.

References

AASHTO, LRFD Bridge Design Specifications, SI (1st Edition), American Association of State Highway and Transportation Officials, Washington, D.C., 1994, *w/1996 and 1997 interim revisions.*

Baker, A.C. and Broadrick, R.L., (1997), "Compaction Grouting, a twenty year update and a vision for the 21st century," Proceedings *Florida/South Florida Section Annual Meeting*, Clearwater, FL, September.

Bauer in Brooklyn Queen's Expressway, NY (1988) Bauer inner office Tech Note.

Bolognesi, A. J. L. and Moretto, O. (1973) "Stage Grouting Preloading of Large Piles on Sand" Proceedings of 8th ICSMFE, Moscow.

Bruce, D.A. (1986), "Enhancing the performance of large diameter piles by grouting," Parts 1 and 2, *Ground Engineering,* May and July, respectively.

Bruce, D. A., Nufer, P. J., and Triplett, R. E. (1995) " Enhancement of Caisson Capacity by Micro-Fine Cement Grouting - a Recent Case History" ASCE Special Publication 57, Verification of Geotechnical Grouting.

Dapp, S.D. (1998) "Interviews with engineers during load testing on the My Thuan Bridge" Mekong Delta, Vietnam."

Dhir, V. K., (1984) "Grouting to save money," *Gulf Construction*, July.

Flemming, W. G. K. (1993) "The Improvement of Pile Performance by Base Grouting" Proceedings of the Institution of Civil Engineers, London.

Gouvenot, D. and Gabiax, F. D. (1975), "A new foundation technique using piles sealed by concrete under high pressure," Proceedings, *Seventh Annual Offshore Technical Conference*.

Holtz, R. D., and Kovacs, W. D. (1981), "An Introduction to Geotechnical Engineering," Prentice Hall, New Jersey.

Littlejohn, G. S., Ingle, J., Dadasbilge, K. (1983) "Improvement in Base Resistance of Large Diameter Piles Founded in Silty Sand" Proceedings, *Eighth European Conference on Soil Mechanics and Foundation Engineering,* Helsinki, May.

Lizzi, F., Viggiani, C., Vinale, F. (1983) "Some Experience with Pre-Loading Cells at the Base of Large Diameter Bored Piles" Proceedings of the 7th Asian Regional Conference on Soil Mechanics and Foundation Engineering, Haifa, Israel

Logie, C. V. (1984) "Drilled Pier Foundation Rehabilitation Using Cement Grouting" ACI Publication SP-83, Innovative Cement Grouting.

Mojabe, M.S., and Duffin, M. J. (1991) "Large Diameter, Rock Socket, Base Grouted Piles in Bristol" Proceedings of the 4th International Conference on Piling and Deep Foundations, Stresa, Italy, April

Mullins, A. G. (1999) "Interviews with engineers during load testing on the Taipei Financial Center " Taipei, Taiwan.

Piccione, M., Carletti, G., and Diamanti, L. (1984) "the Piled Foundations of the Al Gazira Hotel in Cairo" Proceedings of the International Conference on Advances in Piling and Ground Treatment for Foundations, Institution of Civil Engineers, London, UK.

Santosuossa, M., Rizzi, G., Diamanti, L. (1991) "Construction of Pile Foundation of the Postal Cittadel in the Direction Center of Naples" Proceedings of the 4th International Conference on Piling and Deep Foundations, Stresa, Italy, April

Sedran, G. (1999) "Experimental and Analytical Study of a Frustum Confining Vessel," Doctoral Dissertation, McMaster University, Hamilton, ON, September.

Sliwinski, Z. J., and Philpot, T. A. (1980) "Conditions for Effective End Bearing of bored Cast in Situ Piles" Proceedings of Recent Developments in the Design and Construction of Piles, Institute of Civil Engineers, London, UK

Sliwinski, Z. J., and Flemming, W. G. K. (1984) "the Integrity and Performance of Bored Piles" Proceedings of the International Conference on Advances in Piling and Ground Treatment for Foundations, Institution of Civil Engineers, London, UK.

Stocker, M.F. (1983), "The influence of post grouting on t he load bearing capacity of bored piles," Proceedings, *Eighth European Conference on Soil Mechanics and Foundation Engineering,* Helsinki, May.

Troughton, V. M. and Platis, A.(1989) "The Effects of Cahnges in Effective Stress on a Base Grouted Pile in Sand" Proceedings of the International Conference on Piling and Deep Foundations, London, UK, May.

SOILS AND FOUNDATIONS Vol. 40, No. 5, 91–97, Oct. 2000
Japanese Geotechnical Society

PREDICTION OF DYNAMIC COMPACTION POUNDER PENETRATION

GRAY MULLINS[i], MANJRIKER GUNARATNE[i], PAMELA STINNETTE[ii]
and SAMAN THILAKASIRI[iii]

ABSTRACT

A semi-empirical computational technique is presented for predicting the depth of craters formed by dynamic compaction (DC) pounders after the first impact. This technique utilizes a correlation developed between the initial shear strength of the soil beneath the pounder, determined by a CPT profile, and the impact energy per unit area (*specific impact energy*). First, the correlation is established by a series of model impact tests involving different drop heights, drop weights and impact areas. Then, the correlation is verified by the results from a full-scale field test performed by the authors. Further, data from a DC project performed elsewhere is also shown to support the predictive technique. An illustrative example is provided to demonstrate how typical CPT data can be adapted to predict the crater depths during DC projects for a given level of applied impact energy. On the other hand, this method can be used to determine the maximum impact energy that can be applied without causing excessive *initial* penetration of pounders and thus preclude the need for trial impacts. Hence well in advance of heavy equipment mobilization, this technique can certainly aid in effective planning of DC projects on particularly weak ground where penetration predominates heave.

Key words: CPT, crater, dynamic compaction, dynamic replacement, organic soil, pounder, specific impact energy (**IGC**: K3/K5)

INTRODUCTION

Dynamic Compaction (DC) is a ground modification technique used to densify loose soil deposits as deep as 10 meters below the surface. The DC process entails dropping a large weight or pounder onto the ground to be compacted. Although dynamic compaction is reported to be effective both above and below the ground water table, certain construction difficulties arise if the water table is not maintained at least 2 m below the ground surface. This is achieved by dewatering or raising the grade (Lukas, 1986). Raising the grade by the addition of a sand layer can aid the ensuing construction by providing a working mat. Moreover, when unusually soft soils are to be modified, the sand furnishes a replacement material that is driven into the underlying soft layer. The latter process, Dynamic Replacement (DR), has been shown effective in stabilizing weak compressible soils that have poor consolidation properties (Ramaswamy et al., 1979; Lo et al., 1990; Chow et al., 1992; Mullins, 1996).

During DC or DR, the first penetration of the pounder is an uncertain parameter that can cause considerable construction difficulties especially in the case of softer soils. A pounder that penetrates too deeply can develop such high suction forces during withdrawal that it cannot be recovered without additional equipment. To prevent this, the common practice is to limit the crater depth to "the height of the pounder plus a few feet" (Lukas, 1986). Because of the uncertainties involved Lukas (1986) states that it is not possible to predict precisely the crater depth, prior to impact and suggests that the information obtained during the first pass be used as a guide to establish a criterion for subsequent passes. However, this exercise involves mobilization of heavy equipment and thus it cannot be utilized for preliminary project surveys.

Typically, the energy application for the first impact on soft soils is governed by experience or general guidelines formulated on the basis of the drop energy (WH). As an example, the National University of Singapore's experience suggests limiting the first impact drop energy to 150 tonne-meter (Chow, 1995). It is evident therefore, that accurate predictions of the crater depths are useful for efficient implementation of DC or DR processes. Chow et al. (1992) proposed a model to predict the penetration depth based on the one-dimensional wave equation. However, since its application involves determining a number of soil parameters from additional laboratory tests, its field applications may be limited. The new method presented herein predicts crater depths on the basis of impact energy per unit contact area and the soil strength obtained from the routinely conducted Cone Penetration Tests. The new technique has been de-

[i] Department of Civil and Environmental Engineering, University of South Florida, Tampa, FL 33620, USA.
[ii] Hillsborough Community College, Plant City, FL 33620, USA.
[iii] Department of Civil Engineering, University of Moratuwa, Moratuwa, Sri Lanka.
Manuscript was received for review on January 28, 1999.
Written discussions on this paper should be submitted before May 1, 2001 to the Japanese Geotechnical Society, Sugayama Bldg. 4F, Kanda Awaji-cho 2-23, Chiyoda-ku, Tokyo 101-0063, Japan. Upon request the closing date may be extended one month.

veloped based on laboratory impact tests and validated by full-scale field studies.

EFFECT OF SPECIFIC IMPACT ENERGY

The effect of the impact area of a pounder has not been adequately addressed in the literature when considering the depth of improvement. Despite Lukas' (1986) realization that contact pressure (W/A) must affect the depth of improvement, the following relationship presented by Menard et al. (1975) is used most commonly:

$$D = n\sqrt{WH} \tag{1}$$

where: D = depth of improvement, m
W = weight of pounder, tonnes
H = drop height, m
n = an empirical coefficient (less than 1)

The empirical coefficient, n, accounts for variability in soil types and layers, contact area of the pounder, and the efficiency of the drop mechanism. The strong correlations that evolved into this relationship exist possibly due to the uniformity of contact pressures for DC pounders (generally 40 to 75 kN/m^2). Lukas (1986) proceeds to advise that pounders with lower contact pressures create a shallow densified crust of soil and are generally used for the ironing pass. Pounders with higher contact pressures can cause excessive penetration or punching failure of the soil surface. However, these considerations qualitatively address drop energy as well as contact pressure and fail to quantitatively incorporate the effects of all pertinent parameters, pounder weight, drop height, contact area, and pounder base width. Another drawback of the current guidelines for determining the crater depths is the absence of soil strength criteria since it is obvious that the crater depth must depend on the soil strength properties. The proposed method addresses these issues by introducing specific impact energy and the soil strength as the key parameters controlling pounder penetration.

PROPOSED METHODOLOGY

In terms of quantifying the soil strength, the Cone Penetration Test (CPT) is preferred over Standard Penetration Test (SPT) especially in soft soils. This is primarily for two reasons: (1) the high sensitivity of an electronic cone penetrometer, and (2) the test provides a continuous record of soil resistance with respect to depth. The proposed approach utilizes the sensitivity and continuity of CPT data and incorporates the *specific impact energy* of the pounder to predict initial impact penetrations.

The *specific impact energy*, E, is defined as the impact energy per unit area as shown in Eq. (2).

$$E = \eta \frac{WH}{A} \tag{2}$$

where E = specific impact energy
A = contact area
η = drop energy reduction factor = $(V_0/V_t)^2$
V_0 = observed impact velocity
V_t = theoretical impact velocity ($\sqrt{(2gH)}$)

The energy reduction factor (η) accounts for the amount of energy lost to cable drag and the spool inertia. For a given soil profile and drop energy (pounder weight and drop height), one would expect deeper crater depths for smaller contact areas and *vice-versa*. Further, the depth of penetration is dependent on the variable soil strength profile as evidenced by different crater depths observed in essentially the same soil profile. Hence the depth of penetration must be a function of the *specific impact energy* (energy per unit area) and the shear strength characteristics of the soil profile. In this regard, one can assume that the cone resistance, q_c, at a given depth, indicates soil shear strength at that elevation. The validity of this assumption is further discussed in the next section.

In an attempt to formulate the above speculated relationship, the authors semi-empirically correlated the *specific impact energy* and the cumulative shear resistance encountered by the pounder up to the depth of penetration. The technical basis for the existence of such a correlation is described below.

If the initial ground heave is insignificant, the *specific impact energy* can be equated to the work done to overcome the shear resistance of the penetrated soil per unit pounder base area as expressed in Eq. (3).

$$E = \int_0^{z_p} q_c dz + \epsilon \tag{3}$$

where E = specific impact energy
q_c = cone resistance at any depth z
z_p = effective depth of penetration
ϵ = error term due to losses.

It has been assumed that the local shearing resistance encountered by the DC pounder at any penetrated point can be expressed by its q_c value. However, since the mechanisms of ground penetration are different in DC and CPT, there are limitations to the applicability of this method. In light of the discussion on penetration resistance of soils offered by Schmertmann (1978), one can visualize two basic differences between these two penetration mechanisms. They differ in (1) the shape of the penetrating object and (2) the rate of penetration. In this newly introduced practical correlation between impact energy and penetration resistance, the authors compute the total penetration resistance encountered by the pounder by integrating the CPT profile from the ground surface to the depth penetrated by the pounder. Hence the shape difference will be insignificant if one assumes that the cone tip is small enough to present data representative of any point under the pounder base, at any depth.

On the other hand, there is a marked difference in the penetration rates especially when the pounder first touches the ground with a free fall penetration rate much higher than the 2 cm/s advancing rate of the cone. Rapidly penetrating objects can impede pore pressure dissipa-

tion thereby lowering the effective stresses and the penetration resistance, in turn. However, this phenomenon is certainly limited to saturated soils with low hydraulic conductivity (k) values. According to Schmertmann (1978), this "k" threshold is around 10^{-5} cm/s. Therefore, the above assumption would be reasonable for dynamic compaction of granular and silty soil deposits as well as unsaturated clays. Unrelated laboratory hydraulic conductivity tests on the tested organic soils revealed k values in the range of 10^{-4}–10^{-5} cm/s. Thus, no significant pore pressure effects were expected in this particular study. Further support for this assumption is offered in the section on Correlation of Results.

Equations (2) and (3) verify common experience that larger-width pounders penetrate less than smaller-width pounders in the same soil for a given impact energy. The integration term in Eq. (3) can be graphically illustrated in Fig. 1 as the area under the q_c profile. However, z_p (in Eq. (3)) cannot be simply the crater depth, but rather the effective depth of the active soil wedge advancing with the pounder as shown in Fig. 2. This is because a part of the impact energy is also utilized in mobilizing some shear resistance in the soil wedge beneath the pounder. If it is assumed that the active soil wedge resembles one that is formed during typical bearing capacity failures, one can approximately determine the effective depth z_p as follows.

Due to the variable cross-sectional area of the active soil wedge and possible variations in cone resistance over the entire depth of the wedge, Eq. (3) can be expanded to differentiate two separate zones: (1) the zone penetrated by the full area of the pounder (A_p), and (2) the zone affected by the varying area of the failure wedge, $A(z)$.

$$E=\int_0^{z_c} q_c dz+\int_{z_c}^{z_c+h} q_c \frac{A(z)}{A_p} dz+\epsilon \tag{4}$$

where z_c = crater depth
h = height of the wedge
$A(z)$ = cross sectional wedge area at depth z
A_p = projected area of the pounder base

The first integral term expresses the energy required to overcome the shear strength of the crater per unit area of the pounder. The second term on the other hand expresses the energy required to mobilize shear strength in the failure wedge per unit area of the pounder.

The depth of the failure wedge will be relatively small for small pounders such as the one used in the model study herein. Hence, q_c will be essentially constant over the entire depth of the failure wedge reducing Eq. (4) to:

$$E=\int_0^{z_c} q_c dz+q_c\int_{z_c}^{z_c+h} \frac{A(z)}{A_p} dz+\epsilon \tag{5}$$

It can be shown that the second integrand in Eq. (5) is mathematically reduced to $h/3$. Then,

$$E=\int_0^{z_c} q_c dz+q_c(z_p)\frac{h}{3}+\epsilon \tag{6}$$

where

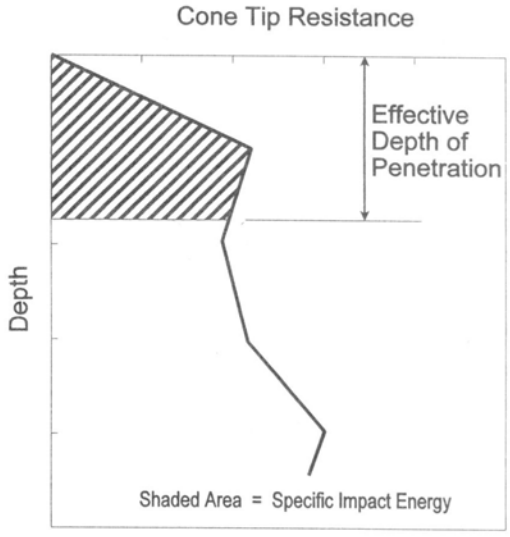

Fig. 1. Penetration calculated from a given specific impact energy

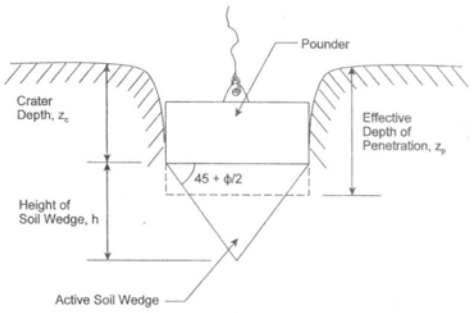

Fig. 2. Effective depth of penetration in advancing soil wedge

$$z_p=z_c+\frac{h}{3} \tag{7}$$

given that from Fig. 2, h can be approximated by

$$h=\frac{B}{2}\tan\left(45+\frac{\phi}{2}\right) \tag{8}$$

and

B = pounder base width
ϕ = angle of internal friction

Therein, the crater depth can be estimated by finding the appropriate z_p to satisfy Eq. (3) and then combining Eqs. (7) and (8) in the following form:

$$z_c\cong z_p-\frac{B}{6}\tan\left(45+\frac{\phi}{2}\right) \tag{9}$$

The angle of internal friction can be approximated by employing any one of the common correlations that are available between q_c and ϕ (Robertson and Campanella, 1983).

For relatively large pounders, the depth of the failure wedge will be significant, possibly penetrating a number

of variable layers. In such situations, one must use Eq. (4) for varying q_c values beneath the pounder. This requires an iterative approach in that z_c depends on $A(z)$, h, and the average ϕ beneath the pounder, and ϕ depends on the depth to which the pounder penetrates, z_c.

Based on Eqs. (3) and (9) and data from a number of model tests, the investigators developed a correlation between the specific impact energy E and the area under the q_c profile as shown in Fig. 1.

MODEL TESTING

A series of DR tests was conducted in order to investigate the effects of pounder weight, drop height, impact area, number of impacts and initial soil strength on the pounder penetration. Although the primary objective was to develop guidelines for efficient implementation of DR in weak soils, the results were used to develop the correlation between impact energy and the pounder penetration.

The tests were conducted in a 2.44 m square, 1.22 m deep test pit. The test pit was equipped with a sand-gravel drain and a 3.5 m high, steel lifting frame shown in Fig. 3. The frame was supported by four rollers which rested on two parallel steel angles serving as guides on opposite sides of the pit. A drop mechanism was attached to the upper I-beam of the frame via a trolley and pulley system. The rollers and trolley provided 2 degrees of freedom allowing the drop mechanism to impact soil at any desired location in the pit. The drop mechanism could deliver free-fall impacts from a maximum height of 3 m. A 1 m deep bed of organic rich soil was prepared in 15 cm lifts and compacted with a WACKER BS-45-Y vibratory rammer. In order to prevent excessive compaction of the soil, the rammer was modified with a larger base. The soil was obtained from a site in Central Florida with an organic content ranging from 50 to 90%. Since organic soils are generally classified based on organic content or the moisture content, the consistency limits were not determined. However, further classification revealed the soil to be silty sands mixed with amorphous organic matter. Although care was taken to prepare a homogeneous bed of soil, a cone penetrometer was used to establish the soil strength profile at 24 locations within the bed to detect local variations. The penetrometer was specifically designed to register low stresses (2200 kPa capacity) such as those typically encountered in organic soils.

Four 177.56 N square pounders were fabricated with base areas ranging from 58 to 232 cm^2. Each of the pounders was dropped from five different heights (H=0.9, 1.2, 1.5, 1.8 and 2.1 m). As a result, 20 specific impact energy levels were analyzed. Figure 4 shows the plan view of the test bed which includes the 20 impact locations, contact areas (A), and the impact energies (WH).

CORRELATION OF RESULTS

The effective depth of penetration for each initial impact was used as the upper limit of numerical integration (Eq. (3)) of the CPT profile from its respective print location. The area estimated from the CPT curve from $z=0$ to $z=z_p$ is shown in Fig. 5 for a typical initial impact (a numerical example of the prediction methodology is presented in Appendix II). The computed areas for each test were then compared to the specific impact energy (E) of the corresponding pounder. Figure 6 shows the plot of E versus 'Area under CPT curve' for impact tests on the organic soil used in the model test. A sandy soil was used in the test pit to provide a blanket for dynamic compaction of the organic soil. As one would expect, punching through the sand blanket with the pounders produced sand columns in the organic soil at the impact locations. Linear regression with a coefficient of correlation of 0.93 confirms the relationship in Eq. (3) with an efficiency of energy transfer (η) of 98%. It is also seen from Fig. 6 that the energy loss term (ϵ) appears to be negligible for the model tests.

The results from impact tests on both the organic and sandy soil were re-evaluated to *predict* z_c based on the pounder drop energy and the q_c profile. Equations (3) and (9) were used in this exercise by assuming zero energy

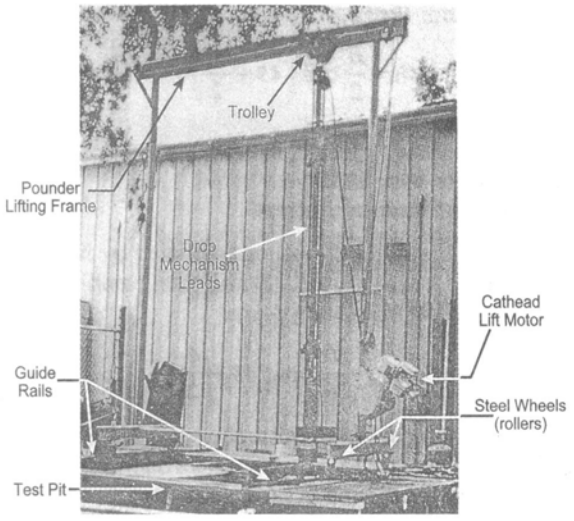

Fig. 3. Frame assembly used to lift and release the pounder over the test pit

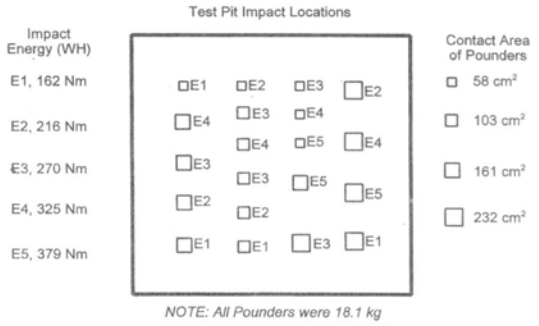

Fig. 4. Layout of test pit showing print locations, contact area, and applied impact energy

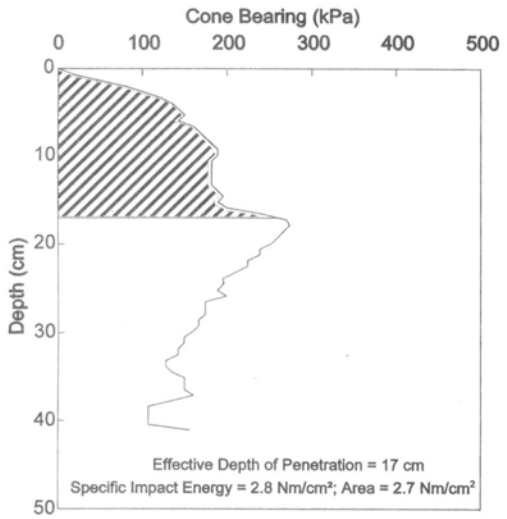

Fig. 5. Typical numerical integration results

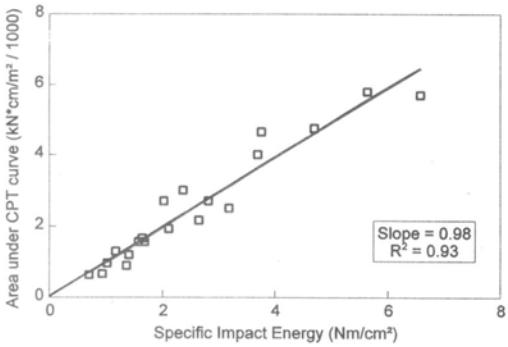

Fig. 6. Comparison of specific impact energy with area under CPT curve

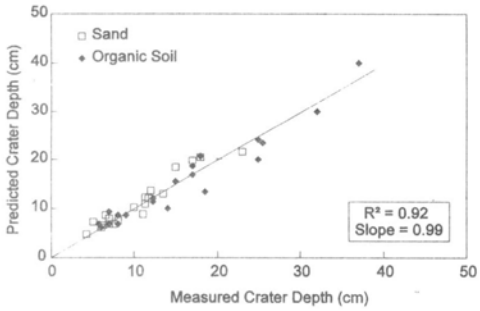

Fig. 7. Crater depth predictions for model test impacts

losses. Figure 7 shows the comparison of predicted penetrations and measured penetrations for all of the model tests. The linear correlation along a slope of 0.99 with a coefficient of correlation of 0.92 indicates the potential of this new method in accurately predicting crater depths.

It is recalled that the crater depth prediction technique advanced in this study stems from the assumption that q_c values represent the shear resistance encountered by the dynamic pounder at every depth. A clear affirmation of the validity of this assumption for many field situations is seen in the results of this study itself. In this respect, Figs. 6 and 7 show that, for the tested organic soil and sand, the difference in the penetration resistance manifested for the cone and the pounder is insignificant *for all practical purposes*.

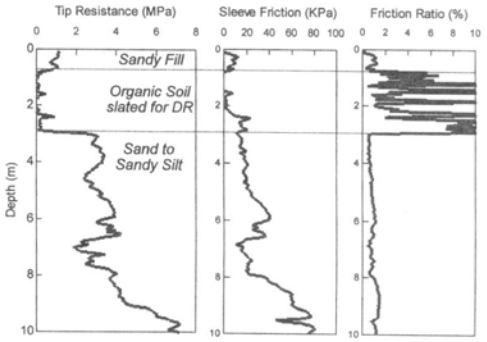

Fig. 8. Cone penetration sounding prior to DR process in Plant City, Florida

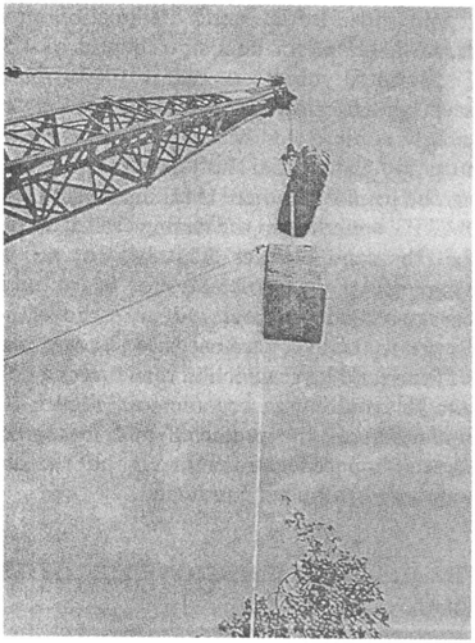

Fig. 9. Pounder (36 kN) designed for DR

FIELD VERIFICATION

The results of the model study predictions were verified during a full-scale Dynamic Replacement project conducted as part of the I-4 expansion project in Plant City, Florida. Therein, a portion of the *Exit 13* westbound on-ramp was set aside for experimental ground modification using DR as an alternative to replac-

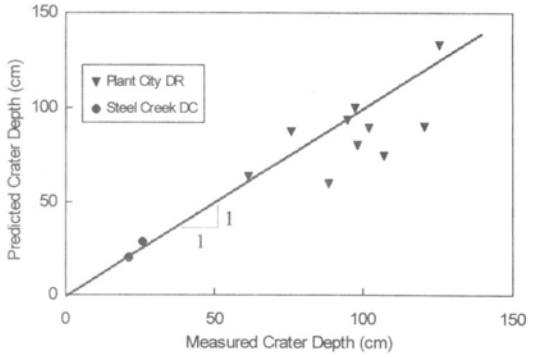

Fig. 10. Comparison of predicted and field measured crater depths

ing organic soils. Initial muck delineation probes revealed a surficial organic deposit to depths of 4.5 meters with an estimated volume exceeding 1000 cubic meters. After clearing and grubbing the site, an 18 meter by 45 meter area was blanketed with approximately one meter of clean sandy fill material. Full details of the entire program can be found elsewhere (Mullins, 1996). Figure 8 is a typical CPT sounding in the testing area after the application of the sand blanket. This type of soil strength profile is particularly problematic for the initial impacts due to excessively deep craters. Figure 9 shows the 36 kN pounder with a 0.6 m square base used to cause punching failure of the sand layer which in turn drives a column of sand into the underlying organic soil. Figure 10 shows the comparison of the predicted and measured crater depths at ten impact locations throughout the site where CPT soundings had been conducted.

CRATER DEPTH PREDICTIONS FOR OTHER DC PROGRAM

Crater depth predictions were also made using CPT data supplied by GKN Hayward Baker, Inc. from the Steel Creek Dam project on the Savannah River south of Augusta, Georgia, USA. This project entailed the construction of a 600 meter-long earthen dam up to 25 meters above the original stream elevation. To alleviate the problem of excessive penetration during DC with a 266.7 kN pounder dropping from a 30 m height, a 168.6 kN pounder dropping from a 15 meter height was used for the first pass in order to densify upper layers enough to withstand blows from the heavier pounder. The two pounders were of cross-sections of approximately 2 m × 1.3 m and 1.3 m × 1.3 m, respectively. The compacted soil was predominantly sandy with a clay layer appearing from about 1 to 3 meters. The entire DC process was performed in four passes totaling over 1300 impact locations (prints). The print pattern and spacing was based on a 15 m square configuration and the crater depths were typically recorded after 5 to 10 drops. In a few locations where initial impacts were recorded and CPT data were available, the predicted crater depths matched reasonably with those recorded in the field (Fig. 10).

CONCLUSIONS

An empirical-mechanistic method is presented for predicting the initial crater depth created by a dynamic compaction pounder after the first impact on a soil. This computational technique will be particularly useful for dynamic compaction projects on weak soil types where the ground heave is expected to be negligible. In this approach, the *specific impact energy* (impact energy per unit area) of dynamic compaction is equated to the cumulative area under the CPT curve between the ground surface and the effective depth of penetration. Hence it certainly addresses shortcomings of the current methods of evaluating the depth of pounder penetration which account for neither the soil strength nor the pounder surface area.

Although the correlations leading to the prediction technique are based on a large number of model tests, full-scale dynamic replacement results are used to verify it. Further, field data obtained from dynamic compaction tests performed elsewhere have been used to corroborate the new technique. Although the methodology is intended for use in uniform soft soils, its application also can be extended to non-uniform soils. A numerical example (Appendix) illustrates how typical CPT data can be adapted to predict the effective depth of penetration and subsequently, the crater depth. The newly developed method is expected to enable engineers to determine approximately the optimum impact energy that can be used in dynamic compaction without causing excessive initial penetrations, based only on cone penetration test results. Furthermore, since the ensuing impacts carried out on refilled craters do not generally cause deeper penetrations than the initial one, the initial crater depth can provide an approximate idea of the influence zone. Hence the predictive technique will furnish an effective planning tool for dynamic compaction programs on sites with weak soils, well before the mobilization of heavy equipment.

ACKNOWLEDGMENTS

The writers would like to thank the following: Hayward Baker, Inc. of Tampa for their collaboration in the Plant City, DR project and for providing the field information from the Steel Creek Dam program; Bob Lukas for clarifying some points concerning crater depths measurements found in Lukas (1986); Rudy; and the Florida Department of Transportation, District I Geotechnical Engineering Group for their extended support in conjunction with ongoing USF research.

REFERENCES

1) Chow, Y. K. et al. (1992): "Dynamic compaction analysis," J. of the Geotech. Engrg. Div., ASCE, Vol. 118, No. 8, pp. 1141–1157.
2) Chow, Y. K. (1995): Personal communication with the second author.
3) Lo, K. W. et al. (1990): "Unified approach to ground improvement

by heavy tamping," J. of the Geotech. Engrg. Div., ASCE, Vol. 116, No. 3, pp. 514–527.
4) Lo, K. W. et al. (1990): "Dynamic replacement and mixing of organic soils with sand charges," J. of the Geotech. Engrg. Div., ASCE, Vol. 116, No. 10, pp. 1463–1482.
5) Lukas, R. G. (1986): "Dynamic compaction for highway construction, Design and construction guidelines, Volume I," Federal Highway Administration Report FHWA-RD-86-133.
6) Menard, L. and Broise, Y. (1975): "Theoretical and practical aspects of dynamic consolidation," Géotechnique, pp. 3–18.
7) Mullins, A. G. (1996): "Field characterization of the dynamic replacement of Florida organic soils," Doctoral Dissertation, Univ. of South Florida, Tampa, FL.
8) Ramaswamy et al. (1979): "Treatment of peaty clay by high energy impact," J. of the Geotech. Engrg. Div., ASCE, Vol. 105, No. GT8, pp. 957–967.
9) Robertson, P. K. and Campanella, R. G. (1989): "Guidelines for use and interpretation of the electronic cone penetration test," UBC, Civil Engrg. Dept., Vancouver, British Columbia; also available from Hogentogler & Company, PO Drawer 2219, Columbia, Maryland 21045, (4th Ed.).
10) Schmertmann, J. H. (1978): "Guidelines for cone penetration test, Performance and design," Federal Highway Administration, Report FHWA-TS-78-209.

APPENDIX

Numerical Example

To illustrate the new method of predicting crater depths, Eq. (3) is rewritten for discrete CPT values in Eq. (10). Assuming the typical depth recording interval of a mechanized cone to be Δz and the average cone resistance q_c over each interval as a discrete value, a cumulative $q_c \Delta z$ is computed as a function of depth (z). Then z_p can be determined as the depth at which the cumulative $q_c \Delta z$ equals the specific impact energy for the given drop configuration.

$$\sum_{0}^{z_p} q_c \Delta z = \eta E \tag{10}$$

where: q_c = average CPT value over that depth interval
Δz = depth recording interval (typically 5 cm)
η = drop efficiency ($\eta \approx 1$, for free-fall)
$E = WH/A$

Assume that CPT data from a site in Central Florida where predictions of crater depths due to free-fall impacts are needed are shown in CPT data below:

Given: $W = 6$ tonnes (58.9 kN)
$H = 20$ meters
$B = 1$ m square ($A = 1$ m^2)
$\phi = 35$ degrees,

predict the initial crater depth.

Cone Penetration Test Data for Numerical Example

SOUNDING DATA IN FILE 6 02/05/95 14:42
ENGINEER: W. R. MCLAUGHLIN LOCATION: 6
CONE ID: 271 JOB #: 99901 1521
FLORIDA DEPARTMENT OF TRANSPORTATION
BARTOW DISTRICT

Depth (meters)	TIP resistance (kPa)	Local friction (kPa)	Friction Ratio (%)	Inclination (deg)	Cumulative area under CPT (z)
0.00	0.01	0.00	0.00	−0.1	0
0.05	512.68	1.08	0.21	−0.2	12.82
0.1	769.01	1.92	0.25	−0.2	44.86
0.15	1412.11	4.24	0.3	−0.2	99.39
0.2	2202.11	8.37	0.38	−0.2	189.74
0.25	2784.74	9.75	0.35	−0.2	314.41
0.3	3356.32	12.08	0.36	−0.2	467.94
0.35	3432.11	11.67	0.34	−0.2	637.65
0.4	3920.21	9.80	0.25	−0.2	821.45
0.45	4052.11	13.37	0.33	−0.2	1020.76
0.5	3927.37	18.46	0.47	−0.2	1220.24
0.55	3905.26	31.24	0.80	−0.2	1416.06
0.6	3773.68	40.38	1.07	−0.2	1608.03
0.65	3695.79	32.15	0.87	−0.2	1794.77
0.7	3737.37	16.44	0.44	−0.2	1980.6
0.75	2001.05	8.80	0.44	−0.2	2124.06
0.8	2511.05	14.06	0.56	−0.2	2236.86

The prediction process involves three steps:

1. Estimate the cumulative area under the CPT curve at different depths.
   This is recorded at each depth in the last column of Table 1.
2. Determine the *specific impact energy* (E) for the given drop mechanism, assuming a free fall.
   The specific impact energy = 58.9*20/1.0 = 1177.2 kN/m.
3. Estimate the effective penetration depth where the cumulative area equals the *specific impact energy*.

Thus, z_p can be estimated to be 49 cm. Then, by using Eq. (9) the crater depth is predicted to be 17 cm.

Settlement Repair of Lightly Reinforced Concrete Block Walls Using CFRP

G. MULLINS, A. HARTLEY, D. ENGEBRETSON and R. SEN

ABSTRACT

This paper presents the results of an experimental study to assess the feasibility of using uni-directional carbon fiber reinforced polymer sheets for repairing lightly reinforced concrete masonry walls that have cracked due to foundation settlement. In the study, two full-sized 8 in. block walls, 8 ft high and 20 ft long were first damaged under simulated settlement loading and then re-tested after being repaired using carbon fiber sheets bonded to one side of the wall. Strength gains of over 50% were recorded. This suggests that carbon fiber reinforced polymers may be suitable for repairing concrete block walls damaged by foundation settlement.

INTRODUCTION

Un-grouted, lightly reinforced concrete block walls are widely used in residential construction in southeastern United States where wind, not earthquake loading, is critical. Until as recently as the early 1990's, walls were vertically reinforced by #5 bars at the corners or every 240 sq. ft. (i.e. every 30 ft, for typical 8 ft high walls) and by a horizontal #5 bar in 8-in. bond beams. This is in stark contrast to masonry construction in seismic regions that are fully grouted with significant reinforcement in both the vertical and horizontal directions.

The vast majority of masonry homes are fortunately not subjected to hurricanes (or even earthquakes) in their lifetime. Instead, they stand a greater chance of being damaged by foundation settlement. Nationwide, foundation subsidence affects an estimated quarter-million homeowners *annually* [1]. Conventional repair of settlement damage can be both time consuming and costly. In contrast, fiber reinforced polymer (FRP) materials offer the prospect of speedy, unobtrusive and inexpensive repairs. This paper describes the results from a pilot study to investigate the feasibility of using FRP material to repair foundation settlement problems in lightly reinforced masonry walls.

Gray Mullins and Rajan Sen, Department of Civil and Environmental Engineering, University of South Florida, Tampa, FL 33620
Alfred Hartley, Carlan Killam Consulting Group Inc., Tampa, FL 33619
Dan Engebretson, Walter P. Moore and Associates, Inc., Tampa, FL 33602

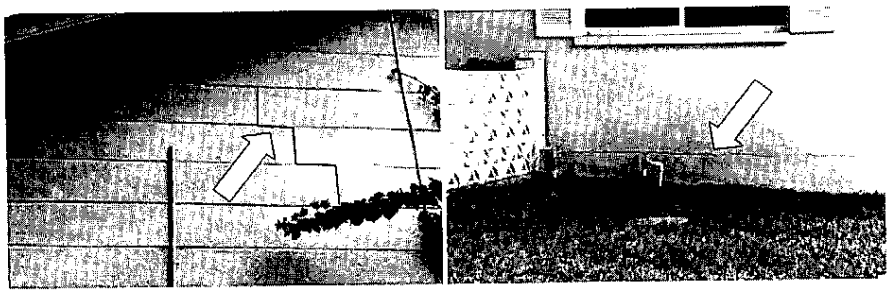

Figure 1. Characteristic Settlement Cracking.

BACKGROUND

Foundations for masonry walls (in the southeast) are commonly reinforced longitudinally by two #5 bars to allow the footing to bridge over soft nonuniform soil. However, improper compaction or the presence of buried compressible material such as tree roots or construction debris can nonetheless lead to excessive settlement. As unreinforced masonry is brittle it has a greater propensity to crack even when the movement is within the allowable limit for the concrete footing.

Characteristic settlement cracks observed in block homes are stair-step mortar cracking or horizontal mortar cracks between the concrete floor slab and the first course of blocks as shown in Fig. 1. The failure is the result of un-grouted masonry's very low tensile strength - allowable values vary between 25-50 psi [2] - compared to modulus of rupture values of over 400 psi for 3000 psi concrete [3].

Typically, repairs involve two steps. *First,* the movement of the foundation is stabilized either through the use of grade beams or a combination of both grade beams and pin piles. *Second*, the wall is transformed to a 'wall-beam' by the introduction of vertical steel reinforcement (Fig. 2) or fully grouting all the cells. The latter option provides a nearly eightfold increase in shear capacity. The cost of repairing an average home with 140 ft length of masonry wall is in the range of $40-45,000 [4].

OBJECTIVES

The primary goal of this study was to investigate the feasibility of using uni-direction fiber-reinforced polymer material to repair walls damaged by foundation settlement. An important element was to examine the performance of as-built walls that conformed to construction standards since the 1960's so that the results of the study would be more widely applicable.

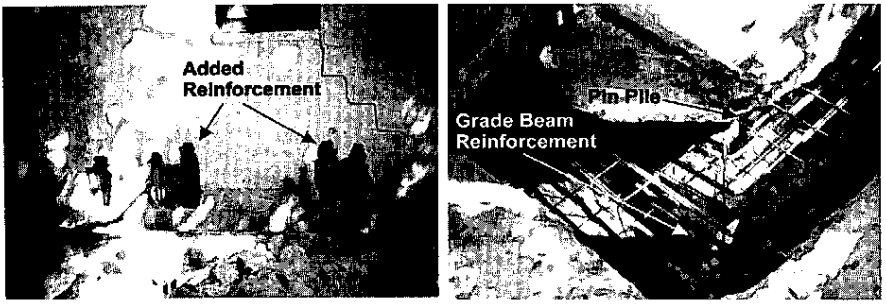

Figure 2. Conventional Repair of Settlement Damage.

SBC PROVISIONS

The governing design code for the southeast is the Standard Building Code (SBC) [5]. As part of this study, a detailed historical review of the relevant masonry and wind provisions of SBC was carried out to identify construction practice since the first edition of the code was published in 1946. The findings may be summarized as follows: (1) no vertical reinforcement - 1940's through 1950's construction; (2) vertical reinforcement only at the corners - 1960's through early 1990's; and (3) intermediate reinforcement required - 1993 to present.

Intermediate reinforcement was actually required starting with the 1969 edition where masonry could "... not exceed 240 square feet without approved vertical and horizontal support..." for walls which were 8 in. thick. However, this revision specifically excluded "one and two family residences". By the 1988 SBC Edition, this exemption was removed but the fact that most single-story masonry walls were only eight feet high meant that intermediate reinforcement was still only required every 30 feet. At best, a continuous masonry wall may have required one intermediate rebar; and this revision had little impact on single-story residential walls. The deemed to comply "Standard for Hurricane Resistant Residential Construction (SSTD 10)," first published in 1993 [6], further reduced the spacing for vertical reinforcement. For example, SSTD 10-93 required that a 44 ft x 8 ft x 8 in masonry wall have intermediate reinforcement at a maximum spacing of four feet and a rebar aside every opening to withstand 110 mph wind velocities.

TEST PROGRAM

A careful survey was made of subsidence damage to masonry block homes in the Tampa Bay area prior to the design of the test specimens. Based on this inspection and interviews with consulting engineers, the representative wall length in testing was determined to be 20 ft. The wall height was taken as 8 ft which is typical for residential construction.

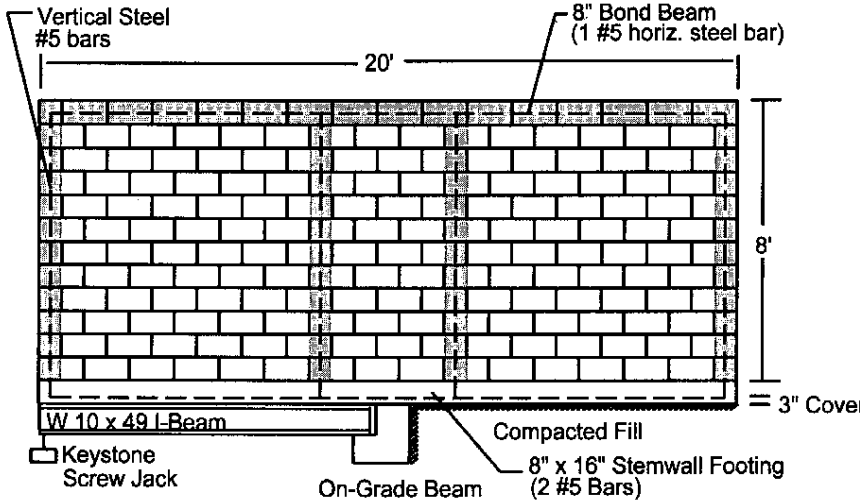

NOTE: Intermediate Vertical Reinforcement Omitted in Wall 3

Figure 3. Reinforcement Details - Wall 2.

A total of four walls were constructed by experienced local masonry contractors to represent the prevailing building standards from the 1960's to the present. Walls 2 and 3 represent construction practice prior to the 1990's that provided vertical reinforcement only at the corners and optionally at intermediate locations; Walls 1 and 4 represent current practice with vertical reinforcement at 4 ft spacing. Wall 2 had intermediate reinforcement spaced at 8 ft from the ends (see Fig. 3) while Wall 3 had no intermediate reinforcement (ends only).

Past and current building practices were represented by two different methods of forming the bond beam. In the older style of construction, a 6 in. wide felt strip was applied to the last course of the masonry unit just prior to the bond beam course. The felt strip covers the open cells of the masonry units and prevents grout from falling through while the bond beam is poured. The felt cap, however, reduces the face shell bedding for the typical 8 in. block from 1.25 in. to only 13/16 in. width for each shell. Current practice is to cover each cell with a thin metal pan. Walls 1 and 4 were constructed with metal fill caps while Walls 2 and 3 were built with a felt cap.

The four walls were built such that they shared a common support wall that was perpendicular to each wall. All of the walls were built on top of a 8 in x 16 in concrete footing reinforced with two #5 bars. Dowels with 90° hooks were provided at the location of the vertical steel to connect wall to the foundation. Each footing was cantilevered approximately 10 ft. 6 in. past a concrete grade beam. This beam served mainly to retain the soil and support the steel beam - the footing did not bear upon the grade beam.

The interface between the test walls and the support wall was a butt rather than an interlocking joint that is typical of actual construction. An interlocking joint would have provided greater support to the test walls at the interface and prevented rotation of the wall panel as a whole. However, the bond beam was poured continuously such that the common grout core shared by all of the walls provided some degree of support. The grouting of the reinforced cells and pouring of the bond beam was performed in one operation.

Test Setup

Differential settlement cracking has been observed to occur only over a portion of a masonry wall. This suggests that part of the wall is continuously supported while the rest is free to subside. This condition was simulated in the test setup by constructing about half the length of the wall on compacted fill. The remainder was supported on a W10x49 steel beam that cantilevered off a grade beam. This steel beam was supported at its free end on a keystone screw jack (see Fig. 3). Plastic sheeting was used to separate the footing from the steel beam and prevent composite action.

Three complete turns of the hex-nut in the screw jack provided 3/8 in. settlement which was sufficient to allow a 10 ft, 6 in. length of the wall to act as a cantilever under its own weight. Additional settlement was induced by applying loading at the top of the wall using a 50-ton ENERPAC hydraulic jack. A steel reaction frame made of W12 x 22 steel beams provided the reaction to the jack. The frame was held down by chains connected to "Chance"anchors bored into the soil. Each was drilled to a depth of 12 ft to 15 ft and was located on both sides of each wall. The reaction frame geometry and the location of the ground anchors permitted loads of up to 15 tons to be applied to the cantilevered end of each wall (see Fig. 4).

Instrumentation

The test specimens were instrumented using load cells, LVDT's, and strain gages. Two load cells were used - one at the free end to measure the self weight when the screw jack was released and the second to measure the magnitude of the simulated roof load. LVDT's measured deflections in both the vertical and horizontal directions; strain gages were used to record strains in both the wall and the footing. A battery powered MEGADAC 3108 DC data acquisition system was used for recording data.

Test Procedure

Two series of tests were carried out. In the first series, the settlement loads consisting of the self weight of the cantilevered wall and simulated roof loads were applied that led to the development of stair-step cracks. Subsequently, the loads were removed and the hex nuts of the screw jack returned to their original position. The

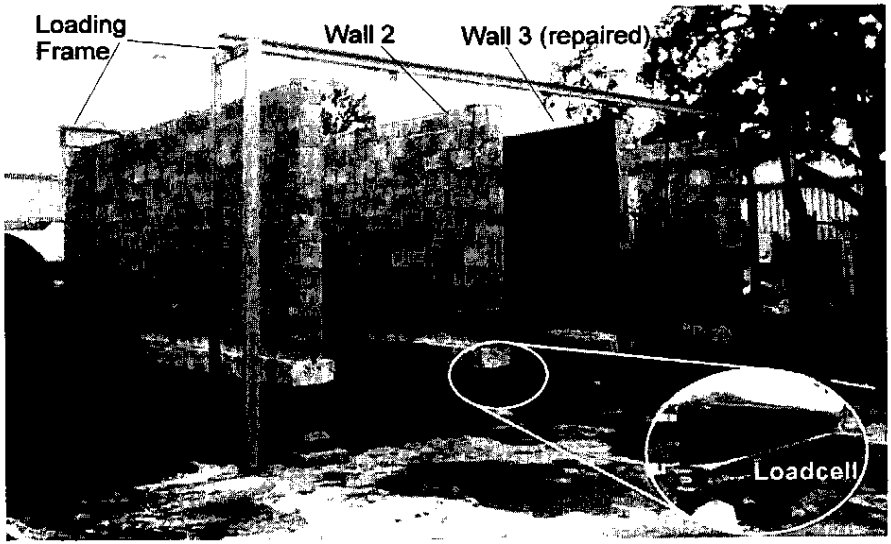

Figure 4. View of Wall Set-Up.

wall was then repaired using carbon fiber reinforced polymer sheeting. As the surface of the walls was smooth, no special surface preparation was deemed necessary and manufacturer's recommendations were generally followed. The ends of the CFRP where secured to the wall with 3 in. steel plates using Tapcon anchors.

Since the uni-directional carbon fiber sheeting (FTS-C1-120) was only intended to increase bending resistance, it was oriented parallel to the length of the wall. Three sheets, each 20 in. wide, were attached *only to one face* as shown in Fig. 4. The intent was to provide additional bending and shear capacity in the zone of the wall that was expected to be in tension. Strain gages were mounted on the CFRP surface and the strengthened wall tested in the same manner as the plain wall. As the specimens were constructed outdoors, all tests were carried out in the pre-dawn hours to ensure constant thermal conditions during the testing.

RESULTS

Two of the four walls constructed have been tested. These were the two weakest walls (#3 with vertical reinforcement at the ends) and (#2 with vertical reinforcement 8 ft from the ends). The results obtained included crack patterns, load deflection and strain variation with depth. Because of space limitations only results relating crack pattern and load deflection are presented.

The crack pattern from the two walls are shown in Figs. 5 and 6. Note the stair step cracking in the supported section of the wall caused by the rotation of the cantilevered

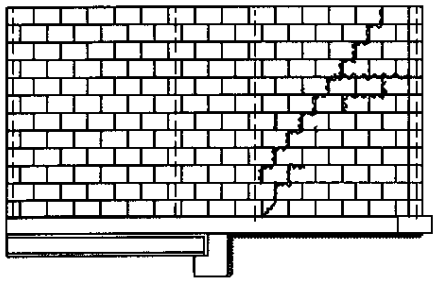

Figure 5. Crack Pattern, Wall 2.

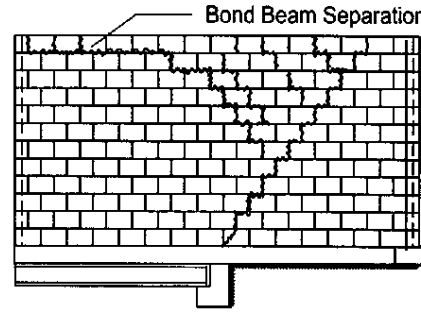

Figure 6. Crack Pattern, Wall 3.

section. The cracking was more pronounced in the weaker wall (#3) as there was no intermediate vertical steel. In contrast, cracking in the stronger wall was confined to the supported region. This is not surprising given that the cantilevered portion of the structure was somewhat longer.

The effect of repair on the capacity of the walls is shown in Figs 7 and 8. Each figure displays the response of plain and strengthened walls. As the weaker wall cracked at a proportionately smaller load, its strength gain was greater (72% vs 57%). Inspection of Figs. 7 and 8 also show improvement in the stiffness of the repaired wall. This was evident in the load vs strain plot. The highest strains were in the bond beam and in the footing. Strains in the remainder of the wall were relatively modest [7].

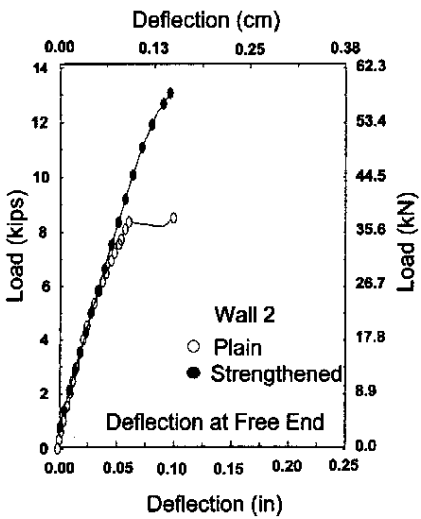

Figure 7. Load-deflection for Wall 2.

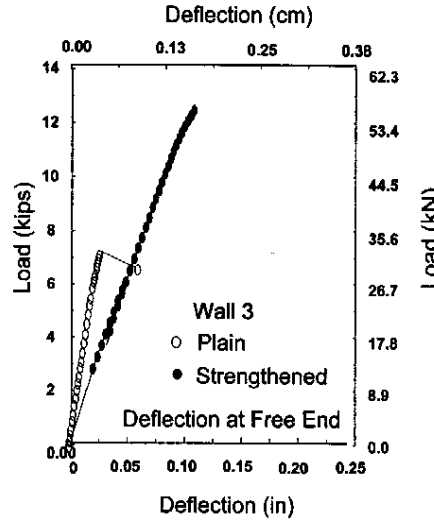

Figure 8. Load-deflection for Wall 3.

DISCUSSION

Masonry walls are subjected to in-plane bending moments and shears due to settlement loading. The bending moment is resisted by a couple formed by the tension steel in the bond beam and compression concrete in the foundation. Due to the very large lever arm, substantial, bending resistance can be realized even by lightly reinforced members. However, the absence of vertical steel, acting as shear reinforcement, causes the wall to crack. In the study, carbon fiber sheets were aligned along the length of the wall to increase the tension capacity of the bond beam. This continuous bonding also improved shear capacity of the wall since resin has a much higher shear capacity than mortar. As a result, significant strength gains were realized and indeed the second specimen, Wall 2 could not be tested to failure.

In the study, three 20 in. wide strips of carbon fiber were used and no attempt was made at material optimization. Finite element analysis carried out [8]indicated that for the walls tested, much narrower strips could be used to provide the same bending resistance. Strips as little as 8 in. or 20 in. would be adequate for most residential repairs though stiffness improvement would be poorer.

The settlement forces that develop in a wall are of course identical regardless of whether it is constructed in a seismic or non-seismic region. However, the repair scheme used in this study will need to be modified to reinforce the wall in both horizontally and vertically and provide greater ductility in seismic regions. It may be convenient to use bi-directional CFRP material for this purpose.

The repair was completed in 1995. After over four years of exposure in Florida's sub-tropical climate there was no discernible deterioration in the CFRP epoxy bond.

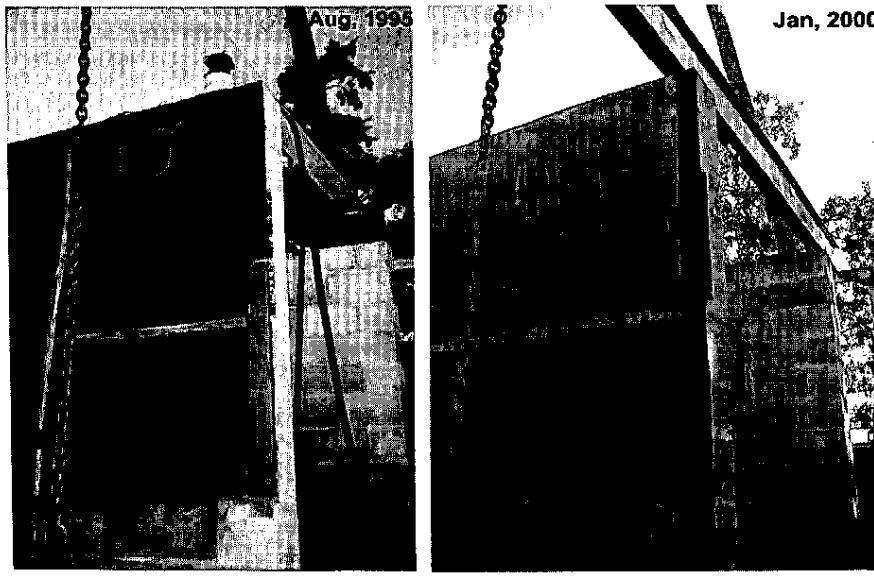

Figure 9. Effect of Exposure on Wall 3.

Fig. 9 compares the wall in its original to its current state. Note the corrosion in the steel that was used to anchor the ends of the CFRP sheeting, and the original sheen in the epoxy coating has lost its luster.

CONCLUSIONS

FRP material has been widely considered for the seismic retrofit of unreinforced masonry. Though devastating, earthquakes are relatively rare. In contrast, damage due to foundation settlement is much more common and affects homes nationwide. This paper presents results from an experimental study to investigate the feasibility of using uni-directional carbon fiber sheets for the repair and rehabilitation of lightly reinforced masonry walls damaged by foundation settlement.

The full-sized test walls were built by experienced masonry contractors in the same manner in which homes have been constructed over the past thirty years. Two of the walls, representative of earlier construction, were tested under simulated foundation settlement before and after strengthening. The CFRP material was applied to one surface to accommodate homeowner preference for minimizing disruption. The results of the tests are very encouraging and suggest that FRP material may be appropriate for repairing some types of foundation damage. Where damage is very severe, it may be also used in conjunction with traditional repairs for strengthening the wall after the foundation settlement has been stabilized using other means (Fig. 3). Moreover, it may be possible to optimize the repair so as to minimize costs.

The study was directed towards applications in southeastern United States where wind loading is more critical. In seismic regions, additional strengthening will be required in the horizontal and vertical directions to comply with ductility requirements for lateral-force resisting systems. In addition, the connections between the masonry walls/ roof framing /foundations will need to be appropriately strengthened. Inadequate anchorage is one of the chief causes of failure of masonry construction during earthquakes. Detailed information on the seismic retrofit of unreinforced masonry may be found elsewhere [9].

ACKNOWLEDGMENTS

The authors gratefully acknowledge the support and contribution of the Tampa Bay Chapter of the Masonry Contractors Association of Florida who donated there services and all materials needed for the fabrication of the walls. We thank Mr. Jack Harrington, P.E. for his contribution in the design of the test setup to simulate settlement. We also wish to thank Dr. Howard Kliger for technical advice and Tonen Corporation, Japan for donating materials used in the testing.

REFERENCES

1. A. B. Chance Company (1995). "Chance Helical Pier System". Bulletin 01-9501, Revised 4/95, Centralia, MO.
2. ACI 530-99 (1999). Building Code Requirements for Masonry Structures, American Concrete Institute, Farmington Hills, MI 48333.
3. ACI 318-99 (1999). Building Code Requirements for Structural Concrete, American Concrete Institute, Farmington Hills, MI 48333.
4. Hungerford, L. (1997). Brown Testing Services, Tampa, FL. Private Communication, March 27.
5. Southern Building Code Congress International (1997). Standard Building Code 1997 Edition, Birmingham, AL.
6. Southern Building Code Congress International (1993). Standard for Hurricane Resistant Residential Construction (SSTD 10-93), Birmingham, AL.
7. Hartley, A., Mullins, G. and Sen, R. (1996). "Repair of Concrete Masonry Block Walls using Carbon Fiber", *Advanced Composite Materials in Bridges and Structures* (Editor M.El-Badry), Canadian Society of Civil Engineers, Montreal, P.Q. pp. 795-802.
8. Engebretson, D., Sen, R., Mullins, G. and Hartley, A. (1996). "Strengthening Concrete Block Walls with Carbon Fiber". *Materials for the New Millennium, Proceedings of the Materials Engineering Conference Volume 2*, ASCE, New York, NY, pp. 1592-1600.
9. Federal Emergency Management Agency (1997). "NEHRP Guidelines for the Seismic Rehabilitation of Buildings", FEMA 273, and "Commentary", FEMA 274, Washington, DC, October.

ACI STRUCTURAL JOURNAL TECHNICAL PAPER

Title no. 96-S99

Durability of Carbon Fiber-Reinforced Polymer/Epoxy/Concrete Bond in Marine Environment

by Rajan Sen, Mohsen Shahawy, Gray Mullins, and John Spain

This paper presents results from a two-year exposure study to evaluate the durability of the epoxy bond formed with concrete and carbon fiber-reinforced polymers (CFRP) in a marine environment. Twenty-four unstressed slab specimens were used to investigate five different epoxy systems exposed to four different environments. Five of the 24 specimens—one for each epoxy system—were controls kept in an air-conditioned laboratory. The remaining 19 slabs were exposed to one of three environments: a) wet/dry cycles in salt water; b) combined wet/dry and thermal cycles in salt water; and c) outdoor. Long-term performance was evaluated both qualitatively, that is, visual inspection, and quantitatively from destructive shear and tension tests conducted at the end of the exposure period. The results showed there was some deterioration in bond, particularly in specimens exposed to wet/dry cycles. This could be more readily detected by destructive testing rather than visual inspection. Overall, the results are promising and suggest that several competing epoxy systems are likely to be durable in Florida's harsh marine environment.

Keywords: bond; carbon; concretes; durability; tension; torsion.

INTRODUCTION

Carbon fiber-reinforced polymer (CFRP) material is increasingly being used for the repair and rehabilitation of flexural concrete elements in buildings and bridges.[1,2] In this method, the CFRP material is bonded to the concrete surface using epoxy adhesives. As the load is transferred to the CFRP material by epoxy, the durability of its bond with concrete is critically important for the integrity and safety of the repaired structure.

Information on the long-term durability of CFRP/epoxy/concrete bond is relatively scarce. Product literature sometimes contains data that purports to provide evidence of satisfactory performance, although testing details are seldom included.[3] Recently, results of exposure tests on CFRP sheeting material were reported at ICCI '98.[4-5] In one of the two studies presented, CFRP sheeting material was exposed to 300 wet/dry cycles (completed in 150 days) and 50 freezing-thawing cycles (completed over 50 days). Tensile tests conducted at the end of the exposure period indicated that there was no degradation in one type of CFRP material tested. The second CFRP type, however, registered a 10% reduction in tensile strength under wet/dry cycles.[4]

The second study provided interim results from a more elaborate on-going investigation.[5] In the study, 12 composite overwrap systems intended for seismic retrofitting were being examined for durability qualification. Of the 12, nine were carbon and three were glass fiber composites. Exposure consisted of several different environments including 100% humidity, salt water, alkali solution, diesel fuel, ultra-violet light, elevated temperature (60 C), and cyclic freezing-thawing conditions. Results presented following 3000 h of a 10,000 h exposure program showed that the majority of the systems tested had excellent durability, although minor reduction in CFRP tensile strength (< 10%) was observed due to saltwater exposure.

Although the two studies provide useful data, their focus was primarily on the effects of exposure on the degradation in material properties, not the bond between concrete, epoxy, and the CFRP sheet material. Indeed, the authors of the second study remarked that "a strong adhesive bond between the composite and the concrete is probably not required" because the wrapping encases the column and its function is largely to provide confinement in the event of an earthquake.[5] Thus, these results are of limited value in flexural applications where the durability of CFRP/epoxy/concrete bond is much more critical.

In 1995, the University of South Florida commenced a 24 month exposure study to evaluate the long-term durability of the CFRP/epoxy bond system in a marine environment. In the study, five different epoxy systems were investigated with specimens exposed to four different environments. At the end of the exposure phase, all specimens were carefully inspected for evidence of bond deterioration. Subsequently, destructive tests were conducted to evaluate the bond under tension and shear. This paper summarizes the principal findings from this study.

PROBLEM STATEMENT

An essential requirement for successful performance of CFRP strengthened structures is the physical and chemical compatibility between concrete and the adhesive material used for bonding. If incompatibilities exist, internal stresses develop that can lead to a weakening of the long-term CFRP/epoxy/concrete bond.

When epoxy is used to bond CFRP material to concrete, both physical and chemical incompatibilities are introduced. Physical incompatibility stems from a mismatch in the coefficient of thermal expansion between epoxy, CFRP, and concrete; for example, the coefficient of thermal expansion for epoxy, reported as 44-120 $\times 10^{-6}$ per C,[6] is several times greater than concrete that varies between 6-13 $\times 10^{-6}$ per C depending on aggregate.[7] This suggests that if a CFRP-strengthened structure is subjected to large temperature variations, its performance may be impaired. Records from the National Climatic Data Center, Asheville, N. C., show that over the past 50 years several regions in Florida have experienced a significant temperature change, such as Pensacola, Fla., recorded a temperature range in excess of 55 C.[8] Thus, temperature variation encountered under normal service conditions can adversely affect the CFRP/epoxy/concrete bond.

Chemical incompatibility can stem from permeability differences between concrete and epoxy. The permeability of concrete depends on a number of factors, most notably its wa-

ACI Structural Journal, V. 96, No. 6, November-December 1999.

Received March 10, 1998, and reviewed under Institute publication policies. Pertinent discussion will be published in the September-October 2000 *ACI Structural Journal* if received by May 1, 2000.

Rajan Sen *is the Samuel and Julia Flom Professor in Civil and Environmental Engineering at the University of South Florida, Tampa, Fla. He is a member of ACI Committee 440, Fiber-Reinforced Polymer Reinforcement.*

Mohsen Shahawy *is the director of the Structural Research Center of the Florida Department of Transportation, Tallahassee, Fla. He is a member of ACI Committee 440, Fiber-Reinforced Polymer Reinforcement.*

Gray Mullins *is an assistant professor in the Department of Civil and Environmental Engineering at the University of South Florida.*

John Spain *is with PSI Environmental Geotechnical Construction, New Haven, Conn. He received his MSCE in civil engineering at the University of South Florida, in 1997.*

ter/cement ratio (w/c).[9] In applications involving flexural members, permeabilities are likely to be much higher because of cracking. Mismatches in permeabilities result in accelerated corrosion of steel in chloride-contaminated concrete. The resulting volume increase can set up internal stresses that can lead to debonding of the CFRP sheet material.

Information on long-term moisture absorption characteristics of CFRP/epoxy/concrete systems in harsh marine environments is very limited. What is known, however, is that moisture absorption increases under wet/dry cycles because of progressive microstructure damage.[10] A measure of absorption levels can be obtained from recently published test results that showed that CFRP/epoxy composites absorbed 1% moisture by weight after 9 years of exposure in outdoor tropical environments.[11]

It is evident that both temperature increase and moisture absorption lead to volume increases at the epoxy/concrete interface. More importantly, under normal service conditions both effects act simultaneously. Therefore, the combined effect of wet/dry cycles and thermal cycles on the CFRP/epoxy/concrete bond is of critical importance and needs to be carefully evaluated. This was an important objective of the study.

OBJECTIVES

The objective of the study was to assess the likely long-term performance of epoxy systems that had actually been used to repair bridge elements in the State of Florida. An equally important objective was to quantify bond deterioration in terms of residual strength so as to provide a measure of the degradation caused by exposure.

The primary objectives of the study can be summarized as follows:

1. To investigate the performance of five different epoxy systems used for bonding CFRP to concrete in conditions characteristic of marine environments.
2. To quantify the degradation in bond strength in terms of changes in tensile and shear resistance relative to that of unexposed controls.

As surface preparation and workmanship are critical parameters for bond integrity, their role in the performance of the CFRP/epoxy/concrete bond was also examined.

RESEARCH SIGNIFICANCE

This paper provides unique results relating to the exposure of five different epoxy systems to different environments characteristic of the application of CFRP for the external repair of highway structures in subtropical environments. The study is believed to be the first to quantify bond degradation in terms of changes in tension/shear strength at the bond line.

EXPERIMENTAL PROGRAM

Specimens

Two different carbon fibers—bidirectional woven fabric and unidirectional carbon fiber prepreg sheets—were investigated in the study. A total of 24 specimens were prepared by bonding the two carbon-fiber types to concrete slabs using five different epoxy systems (Table 1). These systems identified by the Roman numerals I-V comprised commercially developed systems as well as others that were under development.

Although there are subtle differences in the manufacturer's installation procedures, the basic steps are as follows:

1. Grind/abrade the concrete surface to remove debris or coatings, to level the surface, and to form a radius on corners when wrapping CFRP around sharp edges.
2. Coat the dry clean surface with the respective manufacturer-supplied epoxy-based primer.
3. Fill voids with an epoxy-based putty (optional).
4. Roll on an undercoating of epoxy resin to all bond surfaces.

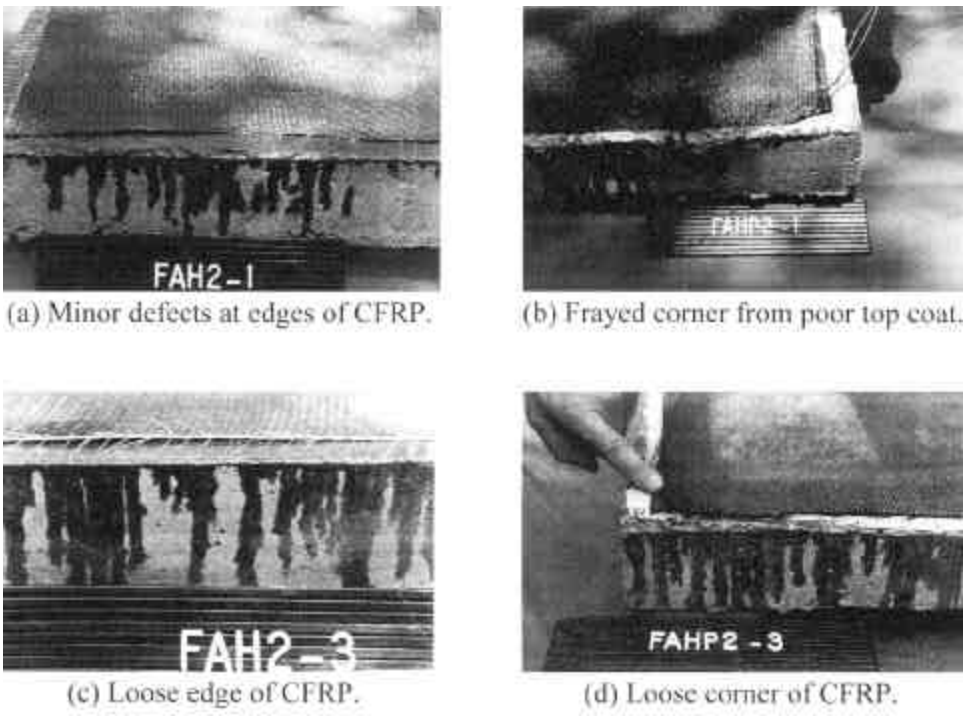

(a) Minor defects at edges of CFRP.
(b) Frayed corner from poor top coat.
(c) Loose edge of CFRP.
(d) Loose corner of CFRP.

Fig. 1—Defects in as-received specimens.

5. Cut-to-size, align, and install the carbon fiber sheets rolling out any entrapped air bubbles (note: keep sheet sizes manageable).

6. Roll on a generous topcoat of epoxy resin to seal in and fully saturate the carbon fiber sheets.

All specimens were prepared by the Florida Department of Transportation in Tallahassee and shipped to the University of South Florida where the testing was carried out. The concrete slabs were each 455 x 455 mm in plan with the thickness varying between 75 and 95 mm. Details of the specimens are summarized in Table 1. Inspection of Table 1 shows that both single-layer and double-layer applications were considered for each type of carbon fiber.

Table 1—Specimen details

Epoxy system	Identifier	No. of specimens	Carbon fiber type	No. of carbon layers
I	FA2	6	Bidirectional	1 or 2
II	FAHP2	4	Bidirectional	2
III	FAH2	6	Bidirectional	1
IV	T2	4	Unidirectional	1 or 2
V	MP2	4	Unidirectional	1 or 2

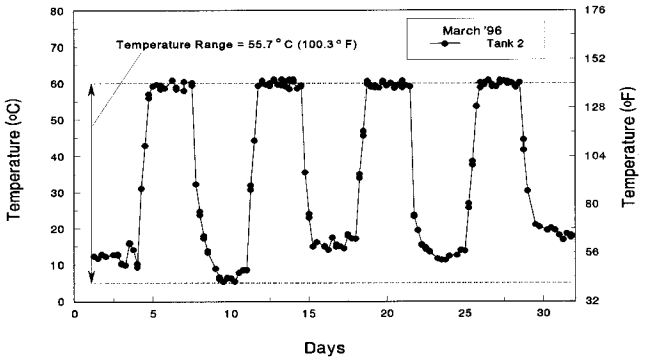

Fig. 2—Typical temperature time history of bond exposure spec-

Initial inspection

Before exposure, all specimens were carefully inspected to identify and catalogue any existing defects. No evidence of debonding could be detected; however, minor defects were found at the CFRP/concrete corners and edges in four specimens from the FAH2 and FAHP2 series. These are shown in Fig. 1.

Exposure

Four different exposures were investigated. These were: a) combined wet/dry cycles and hot/cold cycles in 5% salt-water termed bond; b) wet/dry cycles in 15% salt water termed durability; c) outdoor conditions, termed outdoor; and d) air-conditioned laboratory termed control.

Exposures (a) and (b) were identical to that used recently to investigate the durability of CFRP pretensioned beam elements.[12-13] Unlike the beam specimens, however, there was no splash-zone and the slab specimens were either completely submerged or completely dry during the wet/dry cycles.

In the bond exposure, saltwater in the tanks containing the slab specimens was heated to 60 C at high tide. At low tide, the tank was left uncovered to allow for rapid humidity and temperature change. Figure 2 shows the variation in the saltwater temperature with time. Inspection of Fig. 2 shows that during a cold spell around March 10, the temperature range was at its most extreme. Much smaller ranges were recorded towards the end of the month when ambient temperatures were higher.

RESULTS

The durability and bond exposures had to be terminated after 17 months because of technical problems associated with the hot/cold cycles. At this time, all 24 specimens were reinspected for signs of deterioration of the CFRP/epoxy/concrete bond. This provided a qualitative in-place measure of the state of bond after exposure.

To provide a quantitative measure of degradation, two devices were developed to measure the tensile and shear capacity of the CFRP/epoxy/concrete bond.[14] These devices took six months to perfect, during which time the outdoor and laboratory exposures continued. At the end of this period, all 24 specimens were tested to determine their tensile and shear bond strength. Thus, the qual-

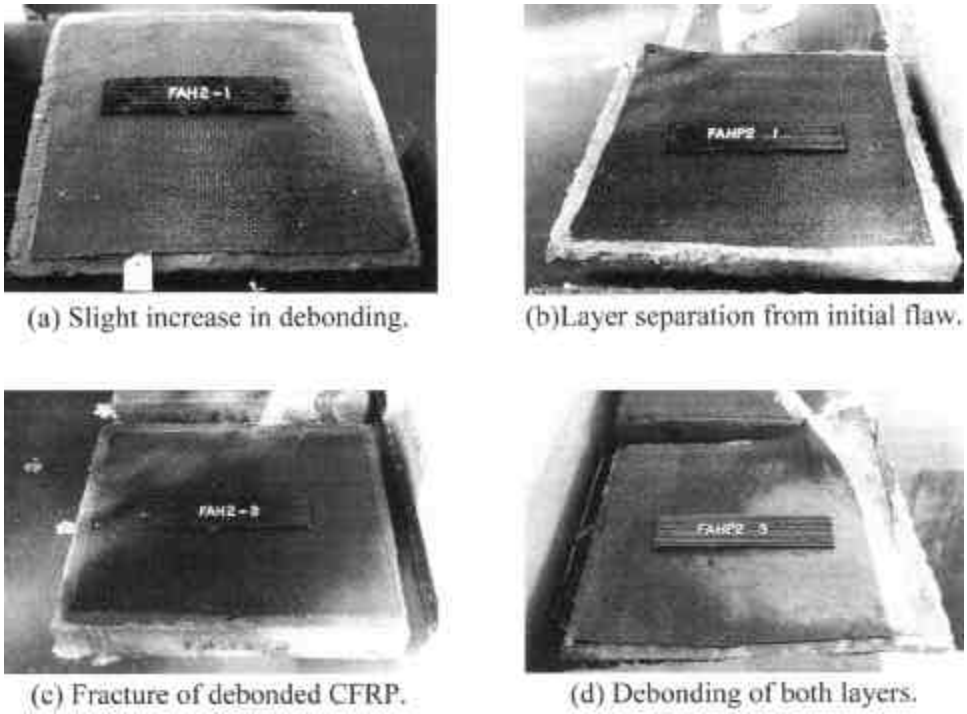

(a) Slight increase in debonding.

(b)Layer separation from initial flaw.

(c) Fracture of debonded CFRP.

(d) Debonding of both layers.

Fig. 3—Deterioration in epoxy bond due to 17 months exposure.

itative results relate to 17 months of exposure for all specimens. The quantitative results, however, relate to 17 months exposure for the durability and bond specimens (with an additional six-month outdoor exposure before testing), and 23 months of continuous exposure for the outdoor and control specimens.

Qualitative observations

Deterioration in bond was only observed in the four specimens identified as having initial defects. Exposure generally resulted in increases in the extent of the initial defect. The most extensive increase was recorded for specimen FAHP2-3 exposed to wet/dry cycles. Only the specimens having bidirectional CFRP fabric experienced deterioration. Details are in Table 2 and Fig. 3.

Quantitative results

To obtain a quantitative measure of bond degradation, destructive torsion and tension tests were conducted on all 24 specimens. In the tests, a 50 mm metal disk called a dolly was bonded to the CFRP surface using epoxy and a water-flushed, diamond-tipped core barrel was used to score around the metal disk through the CFRP (Fig. 4 through 6). Each dolly was either subjected to tension or torsion. Center-drilled and tapped dollies were used for tension tests; all others were equipped with a hexagonal upper surface for torsional shear tests. Figure 4 shows nine dollies bonded to the CFRP-covered concrete. Five of the nine were prepared for tension testing, the other four for torsion testing (hexagonal upper surface).

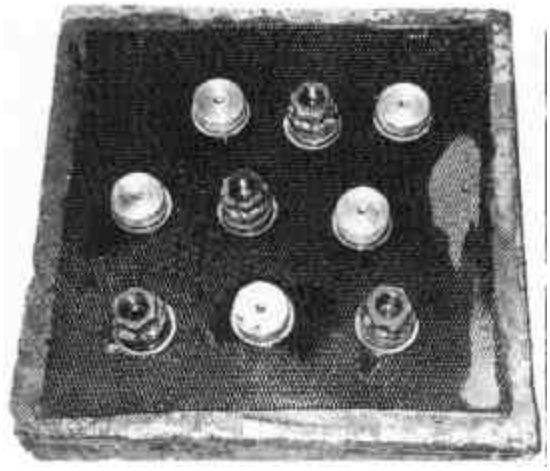

Fig. 4—Tension and torsion dollies bonded to CFRP.

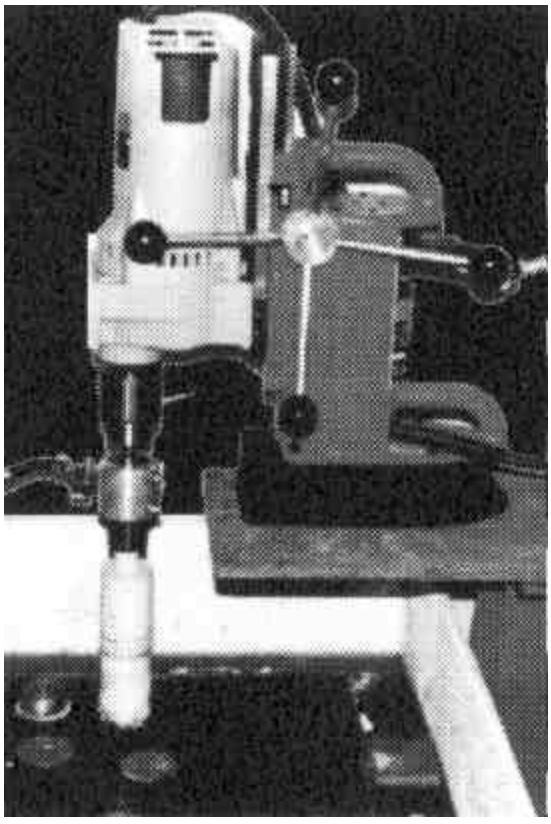

Fig. 5—Scoring CFRP.

The tests were conducted using specialized devices developed at the University of South Florida (Fig. 7 and 8). Torsional shear stresses were induced at the bond line by applying a torque to the dolly via a 25 mm diameter instrumented shaft that was in turn connected to a hydraulically activated lever arm. The torque was continuously monitored with a MEGADAC Series 5100 computerized data acquisition system. The failure torque (T) was then used to determine the maximum torsional shear stress (τ) at the outer radius (r) of the dolly (where $\tau = Tr/J$ and J is the polar moment of inertia of the dolly). Uniaxial tension tests were also monitored in a similar fashion, but used an axial load cell, LVDT, and a portable hand-operated tension frame; the peak axial stress was determined by calculating the quotient of the peak load and the dolly surface area. Complete details on these devices and procedures used may be found elsewhere.[14,15]

Under the action of tensile or shear loads, five different failure modes can occur (see Fig. 9). These are: 1) debonding of the dolly—this means that the strength of the epoxy bond between the dolly and the CFRP material was too low; 2) complete deb-

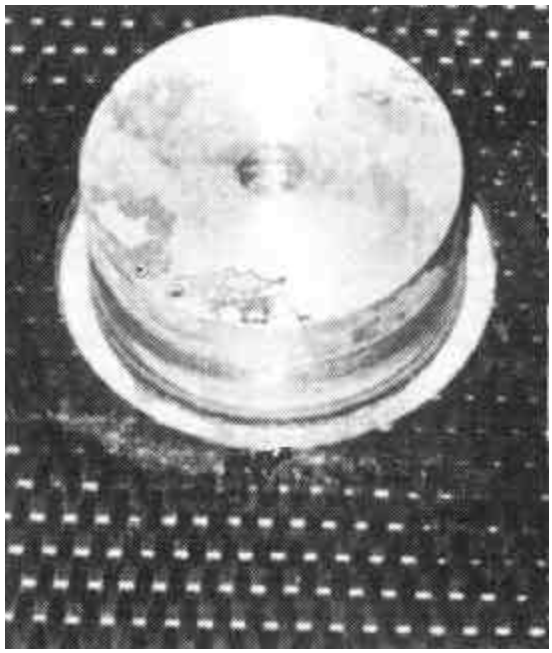

Fig. 6—Bonded dolly and scored CFRP.

Table 2—Summary of 17 months qualitative results

Identifier	Exposure	Epoxy	Defective	Comments
FAH2-1	Durability (Fig. 3(a))	III	Yes	Slight increase in extent of debonding
FAHP2-1	Bond (Fig. 3(b))	II	Yes	Separation of layers from location of initial flaw
FAH2-3	Bond (Fig. 3(c))	III	Yes	Propagation of debonding and fracture of CFRP from location of original defect
FAHP2-3	Durability (Fig. 3(d))	II	Yes	Greatest increase in extent of separation between two layers from location of initial flaw

onding of the CFRP from the concrete—this gives the bond strength; 3) partial debonding of the CFRP/concrete bond; 4) separation of the CFRP layers—this indicates that bond between the two CFRP layers was weaker than the epoxy/concrete bond—only possible for FA2, FAHP2, T2, and MP2 series (see Table 1) where two layers were present; and (5) failure in the concrete—this only indicates that the epoxy bond was at least as strong as the concrete.

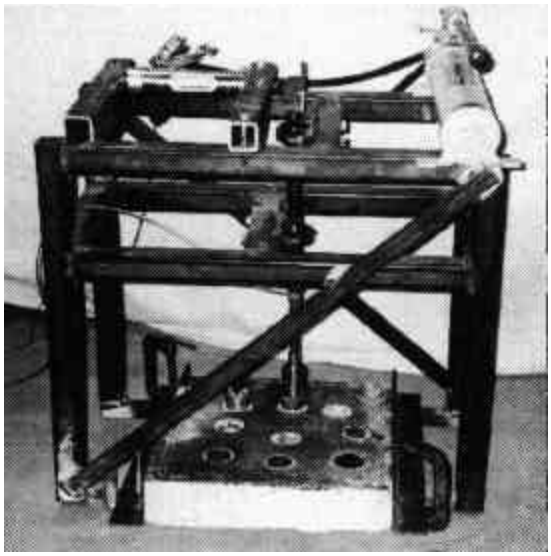

Fig. 7—Torsional shear apparatus.

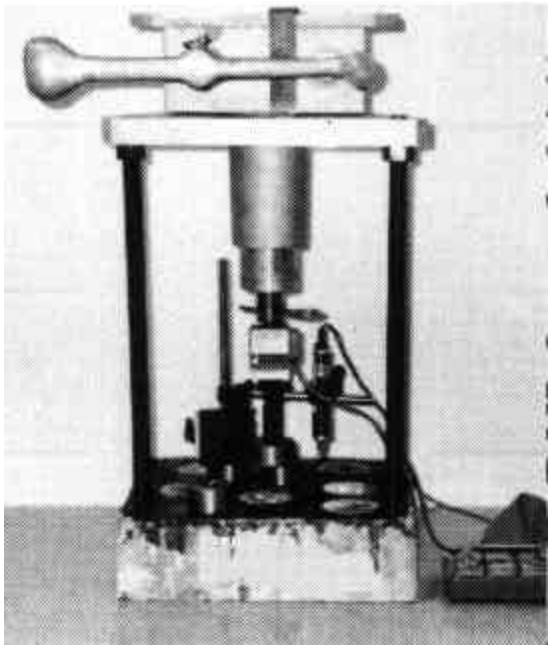

Fig. 8—Tension test apparatus.

Tension and torsion tests were conducted on all 24 specimens including the five controls. On an average, two tension and two torsion tests were carried out on each specimen. Altogether, a total of over 100 tests were carried out. The test results for all the specimens are summarized in Table 3. For each specimen, an estimate of the extent of debonding where partial debonding was observed is provided (see Fig. 9[c]). Additionally, the tensile load, the torsional moment, the corresponding computed stresses at the bond line, and average tensile and shear stress values are also included.

Compared to the qualitative results where degradation was only observed in specimens that were blemished before exposure (see Table 2), the quantitative results provided evidence of deterioration in an additional fourteen specimens. Several specimens from the bond (FA2-1, FA2-3, FAHP2-1) and durability (FAH2-4) exposures debonded completely under both tensile loads and torsional moments. Durability specimen FAHP2-3 completely debonded in tension and would most likely have debonded in torsion; however, the sheets were too badly separated to prepare a torsion sample (see Fig. 3). In addition, one specimen exposed outdoors (FA2-4) also debonded completely under torsion.

None of the five controls debonded completely under shear or torsion. Three control specimens experienced only partial debonding under tension loads (FA2-6, FAHP2-2, MP2-1) and one (FA2-6) under torsional moment. In cases of partial debonding, the surface of the concrete was found to be uneven and the epoxy remained in the debonded locations (Fig. 10). This indicated that partial debonding may have been the result of the CFRP not being bonded to the concrete surface in the first place. In contrast, the exposed concrete surface in cases of complete debonding was found to be smooth (see Fig. 11).

It is evident that where failure occurred in the concrete, no estimate can be made of the extent of degradation in the epoxy/concrete bond. Where there was partial or complete debonding, however, a measure of degradation can be obtained by comparing the relative failure loads of the exposed and control specimens. Such an assessment makes the important assumption that all specimens belonging to the same series were identically prepared and were bonded to identical slabs having the same tensile and shear strengths.

The average results of the tension and torsion tests in Table 3 have been replotted in Fig. 12 through 16 to provide an assessment of the extent of degradation in the epoxy/CFRP bond due to exposure. In these plots, the residual bond strength of the exposed specimens is the ratio of its failure load to that of the control when there was some evidence of debonding, for example, FA2-1 had a residual strength of 86% in tension because it failed at a load of 6.7 kN compared with 7.8 kN for the control. Similarly, its residual torsional resistance is 60% (ratio of 176 N-m to 294 N-m for the control). Where there was no debonding, however, the residual strength was taken as unity, that is, T2-4. In this case, the test results simply showed that the bond strength still exceeded the concrete strength.

Inspection of Fig. 12 through 16 indicates that, compared with the controls, there was some degradation in the epoxy/concrete bond in all exposures with the exception of specimen FAHP2-4

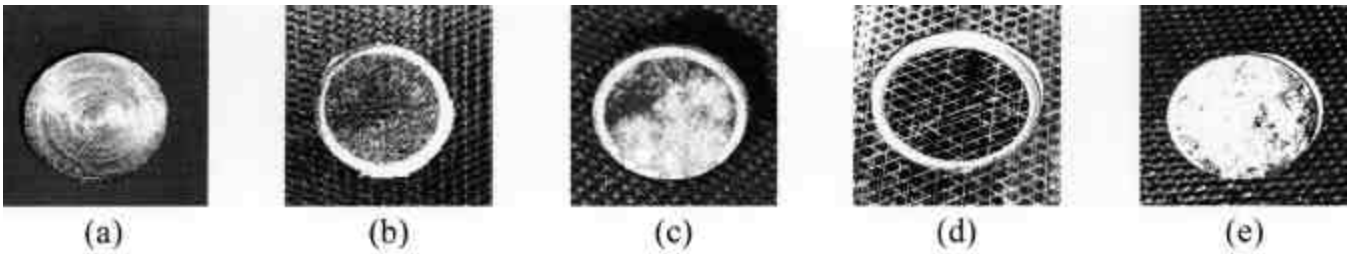

Fig. 9—Possible failure modes: (a) dolly bonded; (b) epoxy bonded; (c) partial debonded; (d) sheet separation; and (e) concrete fail-

(Fig. 13) and all the T2 specimens (Fig. 15). This is in marked contrast to the results from visual inspection where similar degradation could not be discerned.

The overall trend in bond degradation for all the specimens relative to that of the controls is shown in Fig. 17. Inspection of Fig. 17 shows that exposure to wet/dry cycles (in the bond or durability exposures) tended to lead to greater degradation than outdoor exposure. This suggests that moisture absorption, not the mismatch in the thermal expansion coefficients between the CFRP, epoxy, and concrete, was more critical for long-term performance. A similar finding was also made in the exposure tests carried out on CFRP pretensioned beam specimens.[12-13]

DISCUSSION

This paper presents results from a study that attempted to evaluate the extent of degradation in the CFRP/epoxy/concrete bond in five epoxy systems that had been exposed to four different environments simulating a range of indoor and outdoor applications. In the investigation, bond degradation was evaluated on the basis of both visual inspection and destructive testing.

Visual examination led to the detection of degradation in only four specimens—two each from the bond and durability exposures that had been identified as blemished before exposure (Fig. 1). No deterioration was found in any of the controls or the outdoor specimens that had been exposed for a longer period. In contrast, destructive tension and shear tests detected degradation in an additional fourteen specimens including 60% of control and outdoor specimens (Table 3). Bond degradation could not be determined in six of the 24 specimens as the residual bond strength exceeded the concrete strength. It is evident, therefore, that visual examination may not be reliable in identifying bond degradation.

It can be tempting to rank the performance of the various epoxy systems on the basis of the results obtained from the study. Such a ranking would be valid if all specimens tested had been prepared exactly in accordance with the manufacturer's recommendations. Examination of the failure interface obtained from tension and shear tests showing partial debonding and fiber separation provide compelling evidence to the contrary. This indicated that despite laboratory conditions, surface preparation had been improper in some cases; partial debonding was generally the result of an uneven concrete surface and was a di-

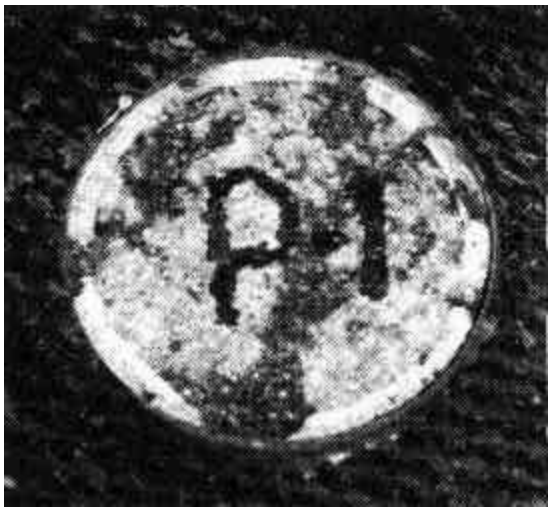

Fig. 10—Partial debonding.

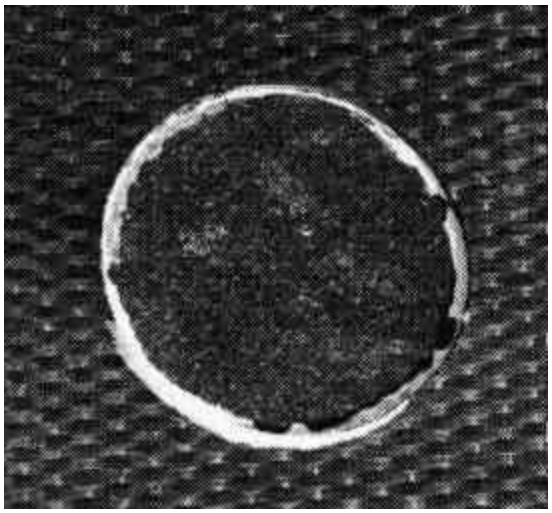

Fig. 11—Complete debonding.

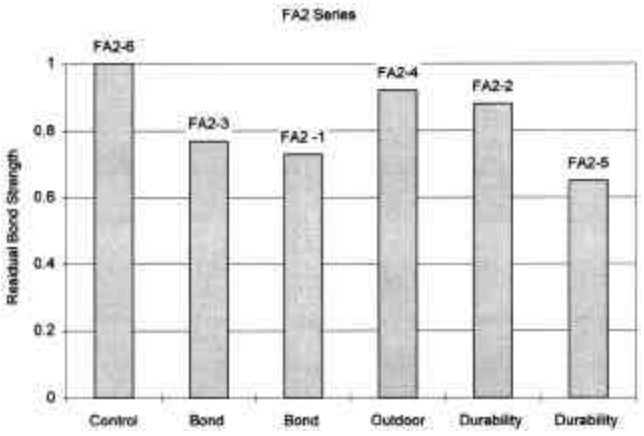

Fig. 12—Performance of epoxy System I.

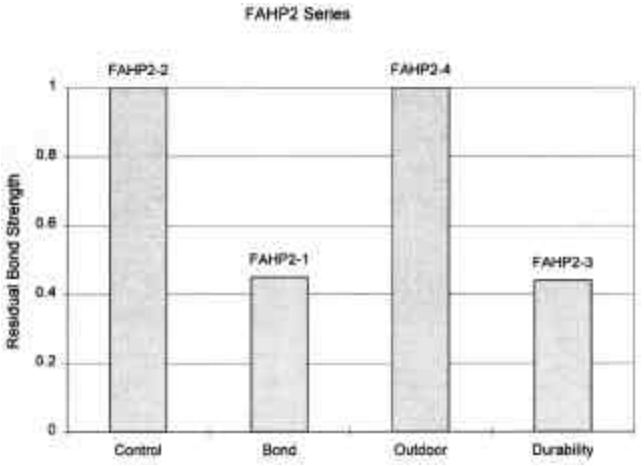

Fig. 13—Performance of epoxy System II.

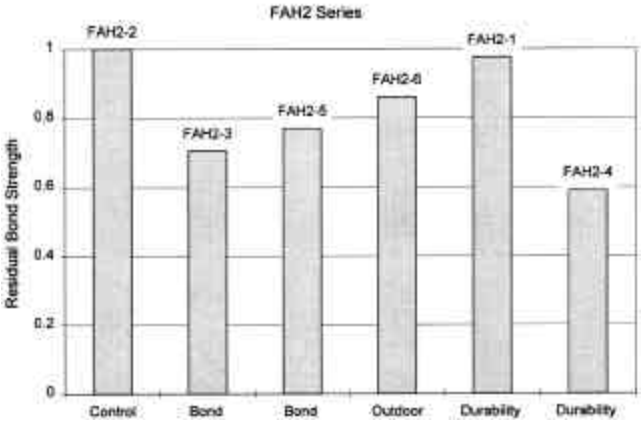

Fig. 14—Performance of epoxy System III.

Table 3—Summary of results

Identifier	Epoxy	Exposure	Tension					Torsion				
			kN	σ^* (MPa)	σ_{avg} (MPa)	% debond	Average % debond	N-m	τ^* (MPa)	τ_{avg} (MPa)	% debond	Average % debond
FA2-6	I	Control	7.7	3.8	3.9	40	33	369	14.3	11.4	0	25
			7.0	3.4		30		220	8.5		50	
			8.8	4.3		30						
FA2-1	I	Bond	5.3	2.6	3.3	100	100	172	6.7	6.8	100	100
			8.2	4.0		100		179	6.9		100	
FA2-3	I	Bond	5.5	2.7	2.8	100	100	248	9.6	9.1	100	100
			6.0	3.0		100		222	8.6		100	
FA2-2	I	Durability	9.1	4.5	4.3	20	30	271	10.5	8.6	70	55
			8.3	4.1		40		174	6.7		40	
FA2-5	I	Durability	1.9	0.9	1.8	100	80	153	6.0	6.8	30	35
			5.5	2.7		60		195	7.6		40	
FA2-4	I	Outdoor	8.9	4.4	3.8	90	77	270	10.5	9.6	100	100
			5.1	2.5		100		222	8.6		100	
			9.2	4.5		40						
FAHP2-2	II	Control	11.8	5.8	5.4	0	25	339	13.2	13.0	0	0
			9.8	4.9		50		331	12.9		0	
FAHP2-1	II	Bond	3.0	1.5	2.1 (4.3)	100	100	168	6.5	6.5	100	100
			5.6	2.8		100						
FAHP2-3	II	Durability	4.2	2.1	2.4	100	100	No sample left to be tested				
			5.3	2.6		100						
FAHP2-4	II	Outdoor	4.9	2.4	3.2	50	17	248	9.6	9.6	0	0
			8.2	4.1		0						
			7.2	3.5		0						
FAH2-2	III	Control	8.6	4.2	3.5	0	0	232	9.0	9.8	0	0
			5.6	2.8		0		274	10.6		0	
FAH2-3	III	Bond	6.8	3.4	3.4	40	13	277	10.7	10.8	50	45
			6.7	3.3		0		281	10.9		40	
			7.4	3.6		0						
FAH2-5	III	Bond	9.3	4.6	4.4	100	95	346	13.4	13.3	60	60
			8.7	4.3		90		340	13.2		60	
FAH2-1	III	Durability	13.2	6.5	6.2	10	5	359	14.0	16.2	0	0
			11.9	5.9		0		475	18.4		0	
FAH2-4	III	Durability	7.2	3.6	3.8	100	100	153	6.0	9.1	100	100
			8.3	4.1		100		226	8.8		100	
								323	12.5		100	
FAH2-6	III	Outdoor	9.2	4.6	4.4	70	60	353	13.7	14.0	0	0
			8.5	4.2		50		370	14.4		0	
T2-2	IV	Control	12.2	6.0	5.8	0	0	452	17.5	16.5	0	0
			11.5	5.7		0		400	15.5		0	
T2-4	IV	Bond	11.4	5.6	6.0	0	0	416	16.2	15.6	0	0
			12.9	6.4		0		388	15.1		0	
T2-3	IV	Durability	13.0	6.5	5.6	0	0	410	15.9	16.3	0	0
			9.6	4.7		0		430	16.7		0	
T2-1	IV	Outdoor	8.3	4.1	4.5	0	0	401	15.6	15.5	0	0
			9.7	4.8		0		397	15.4		0	
MP2-1	V	Control	4.2	2.1	2.4	0	10	258	10.0	9.9	0	0
			6.3	3.1		0		251	9.8		0	
			4.3	2.1		30						
MP2-2	V	Bond	10.2	5.0	3.3	0	0	85	3.3	6.1	0	0
			3.2	1.6		0		231	9.0		0	
MP2-3	V	Durability	3.7	1.8	2.6	0	10	144	5.6	5.9	0	30
			9.2	4.5		30		161	6.3		60	
			3.1	1.5		0						
MP2-4	V	Outdoor	3.5	1.7	2.4	0	0	400	15.5	9.6	0	30
			9.7	4.8		0		94	3.6		60	
			1.4	0.7		0						

*Note: $\sigma = P/A$, where A = 0.001963 m^2; and $t = Tr/J$, where r = 0.025 m, J = 6.14E-7 m^4.

rect consequence of only partial contact between the CFRP and epoxy. It is believed that had a filler material been used to smooth the surface, results would have been better. Similarly, in cases of sheet separation (Fig. 9) observed particularly in the MP2 specimens (Epoxy System V), the carbon fibers in the first layer were dry and had not been properly impregnated with resin.

In the testing, the specimens belonging to the T2 series fared the best with no evidence of bond degradation from any of the exposure schemes (Fig. 15). This, however, was attributed to the visually apparent high quality of workmanship. It is conceivable, however, that longer exposure times could eventually degrade this bond to a detectable level, even though none could be shown herein.

Although both tension and shear tests were conducted, the latter are more representative of stresses that typically need to be transferred by the epoxy to the CFRP. The results indicated that the computed failure stresses under shear were significantly higher than those in tension (see Table 3), a trend observed in similar tests on repaired concrete.[16] As a result, whereas there was partial or complete loss of bond in 18 tension test specimens, only 12 of the same specimens failed in a similar manner in shear (Table 3).

The disparity in failure stresses is not surprising given that concrete's shear strength exceeds its tensile strength. While the tensile strength varies between 8 to 15% of concrete's compressive strength,[17] the shear strength is estimated to be about 20 percent of the same value.[18] Thus, the results of tensile bond tests provide only a lower bound of the available bond strength for flexural applications. For this reason, tensile bond failures do not necessarily imply that bond is impaired for transferring shear.

Although the tension and shear tests carried out are destructive, only a small area of the slab is affected. By reapplying the CFRP to the location where it was removed and providing adequate lap length, the original capacity can be restored.

CONCLUSIONS

This paper presents results from an exposure study in which five different epoxy systems bonding CFRP to concrete were evaluated. Exposure comprised four different environments simulating indoor and outdoor conditions in tropical coastal regions for a period ranging between 17 and 23 months. Both qualitative and quantitative measures were used to evaluate the CFRP/epoxy/concrete bond.

The following conclusions may be drawn:

1. Visual examination cannot recognize the full extent of bond degradation. In the study, only four cases of bond degradation were detected by visual examination, which were limited to specimens that were blemished before exposure. This amounted to only 22% (four out of 18) of the all specimens that were found to have developed bond degradation. With respect to workmanship, visual examination is a primary mechanism for detecting flaws; postmortem inspection of partially and completely debonded test specimens suggested that departures from recommended installation procedures accounted for these failures.

2. Destructive tension and torsion tests provide a more reliable measure of bond degradation not detectable from visual inspection. Tension testing caused debonding in more specimens at lower failure stresses than torsion testing and consequently provided more pessimistic measures of bond degradation. Therefore, torsional shear testing that consistently produced higher stresses at the bond line is more appropriate for detecting bond degradation in flexural applications.

3. Bond degradation was least for outdoor exposure and greatest under wet/dry cycles. This suggests that moisture absorption by the epoxy is potentially more detrimental to bond durability where CFRP is used for repair.

4. Surface preparation and proper application of epoxy following recommended procedures is essential for the long-term integrity of the CFRP/epoxy/concrete bond. In the tests, bond deterioration was compounded at locations where there were initial blemishes. Such damage can be readily detected from careful visual and tactile inspection that should be routinely carried out during repair.

Overall, the results are quite encouraging given the severity of the exposure conditions investigated. The extreme temperature range and humidity the specimens were subjected to are far more severe than could be reasonably expected under normal service conditions. In spite of this, bond degradation was minimal, especially in specimens that had been prepared properly. What is particularly gratifying is the satisfactory performance of all the five disparate epoxy systems that were tested. This indi-

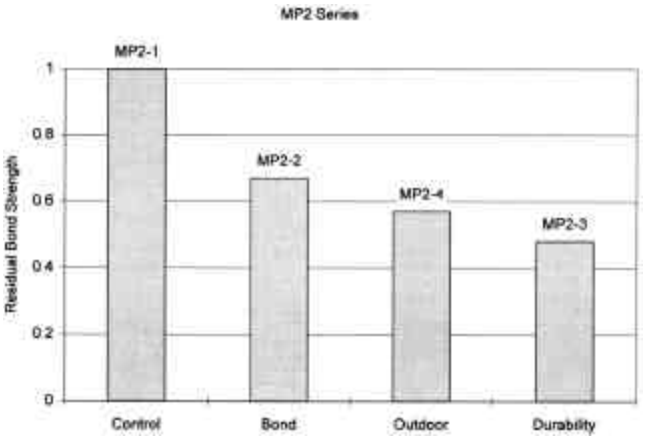

Fig. 16—Performance of epoxy System V.

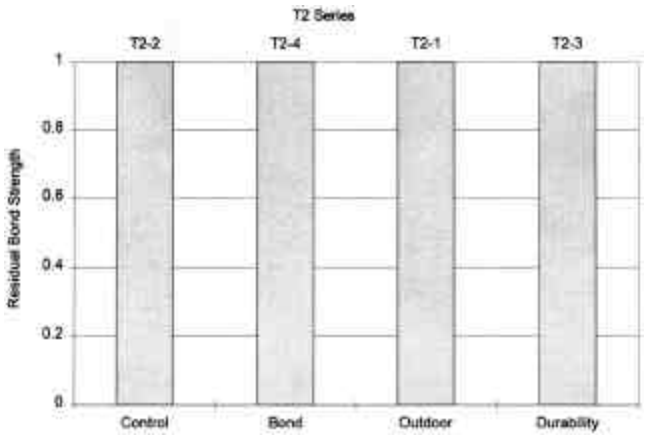

Fig. 15—Performance of epoxy system IV.

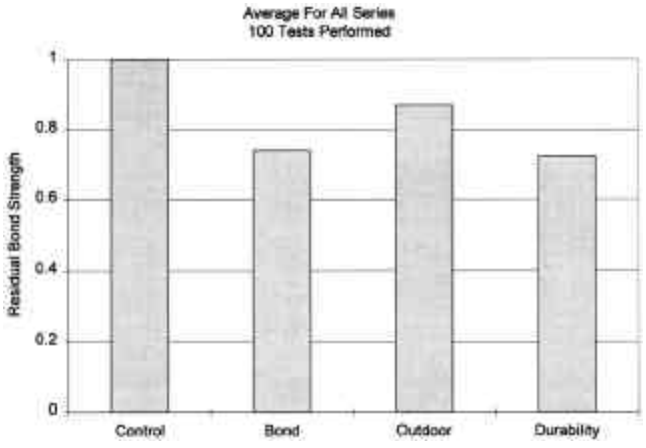

Fig. 17—Results summary.

cates the availability of competing epoxy systems that can lead to equally durable repairs under very harsh environments. Such availability is likely to have a positive long-term effect on the economy of repairs.

The durability of epoxy systems observed in this investigation is not altogether surprising. Epoxy's crosslink structure ensures high chemical resistance and makes it durable in aggressive environments. In bridge applications, epoxy-bonded steel plates have a long history of successful performance.[19]

ACKNOWLEDGMENTS

This study was funded in part by the Florida Department of Transportation. The opinions, findings, and conclusions expressed in this publication are those of the writers and not necessarily those of the Florida Department of Transportation. Additional support was provided by the Department of Civil Engineering, University of South Florida. This support is gratefully acknowledged. The writers acknowledge the contribution of graduate students Al Hartley, Jose Rosas, Hasan Shaffee, and Steve Johnson.

REFERENCES

1. "Non-Metallic Reinforcement for Concrete Structures," *Proceedings* of the Third International Symposium on Non-Metallic (CFRP) Reinforcement for Concrete Structures, Sapporo, Japan, Oct. 1997, Japan Concrete Institute, V. 1, Strengthening Applications, pp. 587-646.

2. "Fiber Composites in Infrastructure," *Second International Conference on Composites in Infrastructure ICCI '98,* V. 1, H. Saadatmanesh and M. Ehsani, eds., Tucson, Ariz., Jan. 1998, Part II, Repair and Retrofit, pp. 113-340.

3. *Revitalizing Concrete Structures*, Replark, Mitsubishi Chemical Corp., Tokyo, Japan, 4 pp.

4. Toutanji, H., and El-Korchi, T., "Tensile Durability Performance of Cementitious Composites Externally Wrapped with FRP Sheets," *Second International Conference on Composites in Infrastructure, ICCI '98*, H. Saadatmanesh and M. Ehsani, eds., Tucson, Ariz., Jan. 1998, V. 2, pp. 410-422.

5. Steckel, G.; Hawkins, G.; and Bauer, J., "Environmental Durability of Composites for Seismic Retrofit of Bridge Columns," *Second International Conference on Composites in Infrastructure, ICCI '98,* H. Saadatmanesh and M. Ehsani, eds., Tucson, Ariz., Jan. 1998, V. 2, pp. 460-475.

6. Hancox, N. L., and Mayer, R. M., *Design Data for Reinforced Plastics*, Chapman and Hall, 1994, London.

7. Priestley, M. J. N., "Thermal Response of Concrete Bridges," *Concrete Bridge Engineering: Performance and Advanced*, R. J. Cope, ed., Elsevier Applied Science, London, 1987, pp. 143-188.

8. National Climatic Data Center, "Climatic Averages and Extreme Temperatures for US Cities," Asheville, 1991.

9. Mindess, S., and Young, J., *Concrete*, Prentice-Hall, Englewood Cliffs, N.J., 1981.

10. Delasi, R. J.; Whiteside, J. B.; and Wolter, W., "Effects of Varying Hygrothermal Environments on Moisture Absorption in Epoxy Composites," *Fibrous Composites in Structural Design*, E. M. Lenoe; D. W. Oplinger; and J. J. Burke, eds., Plenum Press, New York, 1980, pp. 809-818.

11. Chester, R. J., and Baker, A. A., "Environmental Durability of F/A-18 Graphite Epoxy Composite," *Polymers and Polymer Composites*, V. 4, No. 5, 1996, pp. 312-323.

12. Sen, R.; Shahawy, M.; Rosas, J. and Sukumar, S., "Durability of CFRP Pretensioned Elements in Marine Environment," *ACI Structural Journal*, V. 95, No. 5, Sept.-Oct. 1998, pp. 578-587.

13. Sen, R.; Shahawy, M.; Sukumar, S.; and Rosas, J. "Durability of CFRP Pretensioned Elements under Tidal/Thermal Cycles," *ACI Structural Journal*, V. 96, No. 3, May-June 1999, pp. 450-457.

14. Mullins, A. G.; Sen, R.; and Spain, J., "Testing of CFRP/Concrete Bond," ICCI '98, *Second International Conference on Composites in Infrastructure*, H. Saadatmanesh and M. Ehsani, eds., Tucson, Ariz., Jan. 1998, pp. 211-218.

15. Spain, J., "CFRP/Concrete Bond under Shear and Tension," MSCE thesis, University of South Florida, Tampa, Fla., Dec. 1997.

16. Emmons, P. H., *Concrete Repair and Maintenance Illustrated*, R. S. Means, Mass., 1993, 158 pp.

17. MacGregor, J. G., *Reinforced Concrete*, 3rd Edition, Prentice-Hall, Englewood Cliffs, N.J., 1997.

18. Mindess, S., and Young, J., *Concrete*, Prentice-Hall, Englewood Cliffs, N.J., 1981.

19. Meier, U., "Strengthening of Structures with CFRP Laminates," *Advanced Composite Materials in Civil Engineering Structures*, S. Iyer and R. Sen, eds., ASCE, New York, pp. 224-232.

SP 188-35

New Device for In Situ Testing of Fiber Reinforced Polymer/Concrete Adhesion

by G. Mullins, R. K. Race, R. Sen, and J. From

Synopsis:

Fiber reinforced polymer (FRP) is proving to be increasingly cost-effective as a solution for the repair and rehabilitation of substandard concrete structures. As the integrity of the repair is dependent on the FRP/concrete bond, its evaluation for both acceptance and long-term maintenance purposes is of obvious importance.

FRP/concrete adhesion is currently evaluated from the more common tension test or the less used shear test. In either test, a metal disk called a dolly is bonded to the FRP surface. The force needed to separate the dolly under tensile or shear loads is used to determine the FRP-concrete interface adhesion. The similarity of the procedures for the two tests suggests it would be logical to develop a single device that could be used to conduct both in-situ tension and shear tests.

This paper describes the basis and development of a new device that allows both tension and shear tests to be carried out in-situ. The device is simple to use and only requires an instrumented socket wrench to apply the separation load. Preliminary results from tests carried out to assess the role of different surface finishes on the FRP/concrete bond are presented to demonstrate the application of the device.

Keywords: adhesion; bond; carbon; concrete; repair; shear; tension

Gray Mullins is an Assistant Professor in the Department of Civil and Environmental Engineering, University of South Florida, Tampa, FL

Rob Race is a Graduate Student in the Department of Civil and Environmental Engineering, University of South Florida, Tampa, FL

Rajan Sen is the Samuel and **Julia Flom** Professor in the Department of Civil and Environmental Engineering, University of South Florida, Tampa, FL

INTRODUCTION

The increased use of fiber reinforced polymer (FRP) sheets in rehabilitation and retrofit of concrete *flexural* components has made the evaluation of the FRP/concrete bond an important consideration for design. The simplicity of the uniaxial tension test accounts for its widespread use for this purpose (1). In this test, a metal disk (*referred to as a 'dolly'*) is bonded to the FRP surface and the tensile force required for separation measured. The quotient of the separation load and the area of the dolly give the tensile bond stress. Despite its popularity, the results from this test may not be very meaningful since flexural load transfer relies on shear rather than tensile bond (2). More importantly, the low tensile strength of concrete generally leads to failure in the concrete so that the test only provides a *lower bound* on the true FRP/concrete interface bond value.

In 1996, the University of South Florida embarked on a program to develop equipment that would allow the FRP/concrete adhesion to be evaluated under shear loading. In the study, two devices were developed to permit evaluation under both direct and torsional shear. For the direct shear test, a core of the concrete specimen with the FRP material bonded to it was taken and tested in the laboratory using a specially developed direct shear box (3,4). This elaborate procedure made the direct shear test unsuitable for in-situ testing. In the torsional shear test, no coring was required and torque was directly applied to the dolly bonded to the FRP surface. This test was found to give good results. However, the equipment developed required an unwieldy reaction frame that made it less than ideal for in-situ testing.

In view of the similarity in the procedure for conducting tension and torsional shear tests, the possibility of developing a more manageable device to conduct in-situ tests appeared to be a logical extension of the earlier study. This paper describes the development of a simple device that utilizes two dollies and a socket wrench to determine the in-situ FRP/concrete tensile and shear bond. The basis for the equipment developed and the preliminary results are presented herein.

TEST APPARATUS

Typically, devices for evaluating FRP/concrete adhesion consist of several essential components: (a) dollies, (b) a reaction frame, (c) a loading mechanism,

and (d) a load cell. In developing a device that could be used for in-situ shear and tension testing, radical changes were needed to earlier designs to minimize equipment mobilization and the affected testing area. The most significant of these changes was the introduction of an annular tension dolly that served as an alignment frame for the torsion test as well as fulfilling the requirement for the simple tension test. This not only made the device compact but more importantly permitted the use of an instrumented socket wrench for applying both shear and tension loads.

Shear and tension tests require separate dollies and therefore a device that conducts both tests also requires *two* dollies. The shape and dimensions of the dollies must be sized such that excessive force is not required to initiate separation. The choices of shapes conceptually entertained were (a) an inner circular disk, and outer annular disk or (b) two concentric annular disks. The first option was selected in part due to the availability of 50-mm diameter circular dollies (*with a welded hexagonal nut*) from the earlier study, but also it required one less step in scoring the FRP.

Since the concrete shear capacity is almost double its tensile capacity, the 50-mm diameter inner circular dolly was selected for the torsional shear test so that a single operator could manually produce the required separation torque. Due to the enormous mechanical advantage of the tension apparatus, virtually any size annular dolly could have been used. Hence, a commercially available 75-mm diameter, schedule 80 pipe nipple was selected which when cut in half, produced two tension dollies economically. The finished tension dolly had an external radius of 45-mm and an internal radius of 37-mm resulting in an adhesive surface area of 20.2 cm^2. The use of this dolly configuration limited the area affected by destructive testing to less than 85 cm^2.

As noted earlier, the annular tension dolly also serves as an alignment frame for the torsional shear test. To this end, two separate steel caps - one for torsion and one for tension – were fashioned from 75-mm end caps forming the nucleus of each testing device (see Figure 1). Both caps have openings for bolts that incorporate either a bushing to provide alignment during torsion, or threads to apply the required force during tension. For the shear test, a 22-mm bolt is inserted through the adjustable steel bushing of the shear cap and secured in the torsion dolly. Subsequent tightening of this bolt directly transmits torque into the shear dolly.

Once the shear dolly (inner) has failed, the shear cap and dolly are removed and a thrust bearing is seated in the position now vacated by the shear dolly (see Figure 2). The tension cap is then screwed onto the tension dolly. At this point in the testing procedure, the role of the tension dolly is transformed from a torsion alignment frame to a tension test specimen. Tension can now be applied to the outer dolly with a bolt threaded through the tension cap that bears on the thrust bearing assembly. As the bolt is turned, the applied rotation is translated into

linear motion placing the dolly in tension. Hence, the applied force on the tension dolly is indirectly determined from torque measurements. The entire time of testing requires less than five minutes. Figure 1 shows the actual equipment, whereas Figure 2 shows a schematic drawing of its components.

A critical requirement prior to tension testing was the calibration of the socket wrench to correlate applied torque on the bolt with equivalent tensile force on the dolly. For this purpose, strain gages - mounted in a full bridge configuration - were attached to a standard 150-mm long socket extension (see Figure 3). With the tension cap mounted on a reaction frame, the applied torque and corresponding tensile force was measured using the instrumented extension and load cell (see Figure 4). All data was automatically recorded with a MEGADAC computerized data acquisition system during calibration.

For machine design purposes, the tensile forces on the dolly were calculated using Eq. 1 from known values of torque, bolt and thread characteristics and the coefficient of friction of the bolt threads (4).

$$F = M / [r \tan(\theta + \alpha)] \quad (1)$$

In Eq. 1, F is the axial force developed in the bolt, M is the moment needed to impend motion or sustain uniform motion, R is the average of minimum and maximum bolt radii, θ is $\tan^{-1}(\mu)$ where μ is the coefficient of static or kinetic friction and α is the slope of bolt thread.

Several different thread conditions from oxidized, non-lubricated threads to clean, well-lubricated threads were tested. A new, non-lubricated bolt yielded a coefficient of friction value of approximately 0.27 in the first trial. As the threads became conditioned with each trial the coefficient of friction decreased. Lubricating the bolt yielded a coefficient of friction of approximately 0.19 after several trials. Therefore, the importance of using a properly conditioned and lubricated bolt should not be underestimated. Ultimately, the measured torque vs. force function (1.0 N-m torque corresponds to a 447 N tensile force) was regressed from data obtained from numerous calibration cycles.

TEST PROGRAM

A systematic test program was completed to evaluate the effectiveness of the new device in measuring the FRP/concrete bond in shear and tension. Over a hundred tests were conducted during the development of this test mechanism/procedure. Forty-seven of these tests reflect the final testing procedure adopted herein.

Specimen Preparation

Before the dollies can be bonded to the FRP surface, their outline had to be scored. This was carried out in a jig using a laminate trimmer (see Figure 5) fitted

with an 8-mm (5/16-inch) carbide bit. When scoring was complete, the adhesive surface of the CFRP and the dollies were lightly sanded and cleaned with acetone. The dollies were then positioned on the CFRP using Sikadur 32 Hi-Mod epoxy adhesive. All adhesives were cured for a minimum of 7 days prior to testing.

Test Procedure

After the dollies have fully bonded to the FRP surface, the shear device is assembled (Figure 2). A 22-mm bolt is then inserted through the shear cap bolt guide (bushing) and threaded into the shear dolly. Once the bolt is securely threaded into the shear dolly, the bolt guide is tightened in-place to prevent lateral movement or bending during testing. A socket attached to a 13-mm socket wrench via the instrumented extension is placed over the head of the bolt. Using the tension dolly as an alignment anchor, torque is increased on the bolt head smoothly and continuously until shear failure occurs. The output of the instrumented extension is continuously monitored to detect the peak torque applied. Figure 6 shows typical results from the shear testing portion of the procedure.

Upon completion of the torsion test the shear cap, dolly and any debris are removed from the center of the annular tension dolly. The thrust bearing is then inserted as previously described and the tension cap installed. A 19-mm fully-threaded bolt is advanced by hand until it contacts a recess on the top of the thrust bearing assembly. Using the instrumented wrench previously described, a tension force is now applied and recorded by way of torque measurements. As the bolt is tightened, the tension dolly is axially stressed and separates; the tension cap and thrust bearing are removed and the failure mode noted. Curves similar to Figure 6 are also obtained from tensile tests; they differ only in that must be converted from torque to tensile load as previously described.

RESULTS

Table 1 summarizes results obtained from 25 shear and 22 tension tests conducted on a total of 26 specimens. Values reported are *average* from each of the six series reported. Specimen labels identify surface treatment, substrate material, and CFRP type. N denotes no treatment, M - mechanically abraded, and W - water blasted. The two substrate identifiers indicate their nominal strength in ksi for masonry (3) and concrete (5). The CFRP types were either balanced or unbalanced weaves, denoted by B and U, respectively. Water blasted surfaces were prepared using a portable pressure washer while the mechanically abraded surfaces were prepared with a belt sander.

As no instances of complete debonding were recorded, definite pronouncements relating to the magnitude of the CFRP/concrete adhesion cannot be made. However, the results indicate that surface preparation had varied effects dependent on the substrate type. For the masonry substrate, water blasting

consistently produced lower shear values and mechanical abrasion higher values or no effect when compared to the controls with no treatment. Alternately, water blasting produced higher shear values on the concrete substrate whereas mechanical abrasion resulted in lower values.

CONCLUSIONS

This paper describes the basis and development of a new device that may be used to conduct in-situ shear and tension tests to evaluate the integrity of the FRP/concrete bond. The device is compact, inexpensive and light-weight. The prototype only weighed 31 N (7 lbs) making it suitable for outdoor use. Moreover, a single conventional socket wrench is used to apply *both* shear and torsion loads.

Application of the device to shear and tension testing proved to be fairly straightforward. The device was used to investigate the effect of surface preparation on the bond between CFRP and concrete. Both balanced and uni-directional CFRP materials were tested.

Preliminary results suggest that water blasting of the substrate prior to application of the CFRP led to greater bond strength for concrete when compared to mechanical abrading or no treatment. The reverse was true for masonry. These results imply that an optimal surface roughness produces the best bonding condition. This was also noted in the development of the dolly surfaces where surfaces too rough or too smooth would not effectively transfer stress to the FRP.

ACKNOWLEDGEMENTS

The authors gratefully acknowledge the advice and support of Dr. Howard Kliger. Tonen Corporation of Japan donated materials tested. This support is gratefully acknowledged.

REFERENCES

1. Steele, J. 1994. "Testing Adhesion of Concrete Coatings Applied to Concrete," *Materials Performance,* Vol. 33, No. 11, 33-36.

2. Karbhari, V. M. and M Engineer, 1996. "Investigation of Bond Between Concrete and Composites: Use of a Peel Test," *Journal of Reinforced Plastics and Composites,* Vol. 15, Feb. 1996, 208-227.

3. Mullins, G., Sen, R. and Spain, J. 1998. "Testing of CFRP/Concrete Bond," in *Fiber Composites in Infrastructure Vol 2* (Edited H. Saadatmanesh and M.R. Ehsani), Second International Conference on Composites in Infrastructure, ICCI '98, University of Arizona, Tucon, AZ, pp. 211-218.

4. Spain, J., 1997. "Evaluation of CFRP/Concrete Bond Under Shear and Tension," Master's Thesis, University of South Florida, Tampa, FL.

5. Bedford, A. and Wallace L. Fowler, 1995. *"Statics–Engineering Mechanics"* Addison-Wesley Publishing, Reading, MA.

TABLE 1—SUMMARY OF TEST RESULTS.

Label	Number Of Specimens	Shear Stress from Tr/J		Percent Debond	Tension Stress from P/A		Percent Debond
		ksi	MPa		ksi	MPa	
N3U	4	1.86	12.8	40	0.49	3.4	7.5
N3B	4	1.52	10.5	0.0	0.49	3.4	6.7
M3U	4	1.86	12.8	6.3	0.52	3.6	16.5
W3U	4	1.65	11.4	20.0	0.57	3.9	7.5
M5U	4	1.32	9.1	1.3	0.38	2.6	0.0
W5U	6	1.47	10.1	3.0	0.55	3.8	0.0

Fig. 1—Tension/shear setup.

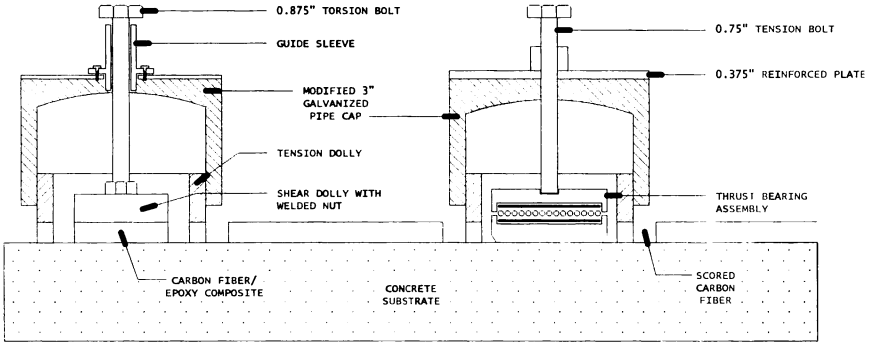

Fig. 2—Schematic drawing of shear (left) and tension (right) test apparatus.

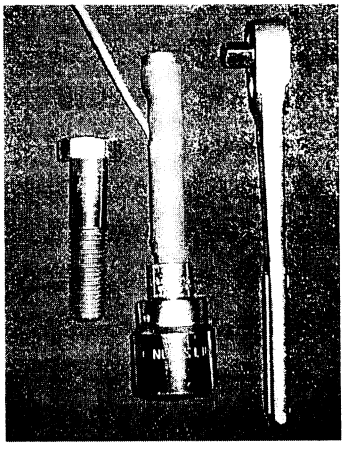

Fig. 3—Instrumented wrench.

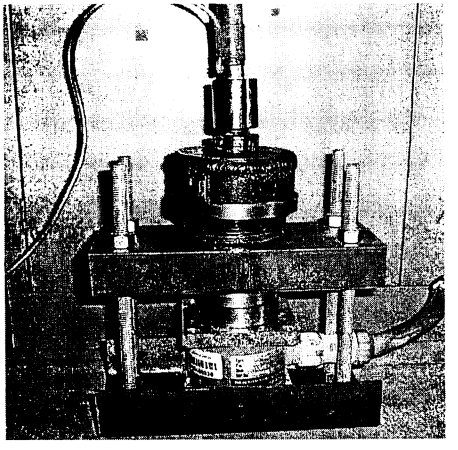

Fig. 4—Tension device calibration.

Fig. 5—CFRP scoring.

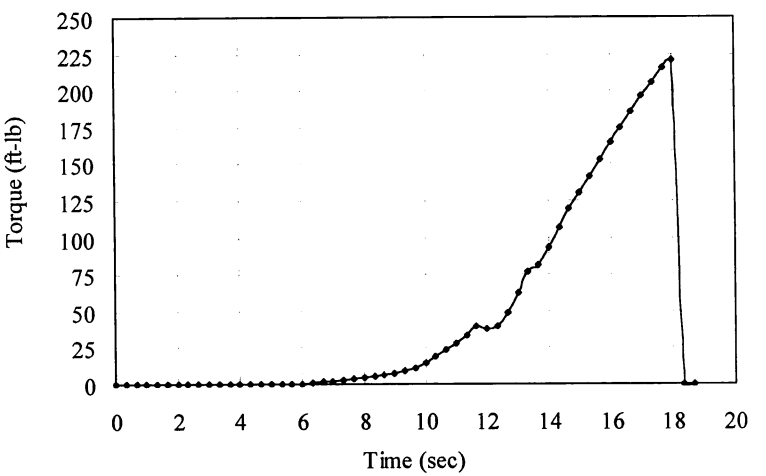

Fig. 6—Torque versus time during shear test.

STATNAMIC Loading Test'98, Kusakabe, Kuwabara & Matsumoto (eds)60
© 2000 Balkema, Rotterdam, ISBN 90 5809 131 7

STATNAMIC and dynamic load testing of an instrumented drilled shaft at an I-35/I-80 bridge in Des Moines, Iowa

M. Muchard & D.T. Robertson
Applied Foundation Testing Incorporated, Green Cove Springs, Fla., USA
G. Mullins
University of South Florida, Tampa, Fla., USA
B. Stanley
Iowa Department of Transportation, Ames, Iowa, USA

ABSTRACT: The Iowa Department of Transportation in conjunction with the Federal Highway Administration performed a design phase Statnamic load test program on a drilled shaft foundation for a series of four new bridges along I-35/I-80 in Des Moines, Iowa. For research purposes, high strain dynamic testing via a drop hammer was also performed. This paper presents the results of Statnamic and high strain dynamic tests conducted at a drilled shaft test site adjacent to the new 2nd Avenue Bridge. Load testing was performed on a single instrumented 1.07 meter diameter drilled shaft 27.3 meters in length. The test shaft was designed predominately for side shear in "Glacial Till", gravelly sands and weathered shale. End bearing in the weathered shale was also considered in the design. Internal instrumentation consisted of 12 resistance strain gages and a toe accelerometer which were monitored during Statnamic and dynamic load testing. The paper discusses the results of each test method and their applicability to drilled shaft load testing.

1 INTRODUCTION

1.1 *Project Background*

A several mile corridor of I-35/I-80 in Des Moines, Iowa is being widened. This construction includes five existing structures that will be replaced with new larger structures four of which will be founded on drilled shafts. The Iowa Department of Transportation in conjunction with the Federal Highway Administration took an approach to this design which incorporated the most contemporary design and construction technics. Recent drilled shaft designs in the area by Iowa Department of Transportation were based on side shear and end bearing in the shale formation. This design was to include side shear in the overburden soils locally termed "Glacial Till" as well as the shale for two of the bridges. Shaft designs for the other two bridges will rely on side shear in the glacial till and will not extend into the shale. The local database of drilled shaft design parameters for glacial till was not specific enough to the construction methods anticipated for this site. Therefore, a full scale load test program was organized and implemented. To take full advantage of the load test program results, it was carried out early in the design phase of the new structures. The test site was selected adjacent to the existing 2nd Avenue Bridge on the north side of Des Moines, Iowa shown Figure 1. The load test program also allowed evaluation of site specific drilled shaft construction intricacies using the "wet hole" method involving polymer slurry admixture. The paper is limited to discussions of the load test methods.

Statnamic load testing was selected for this project for several technical and economical reasons as follows: (1) It requires no special shaft construction procedures so installation is more representative of production shaft construction, (2) The shaft is loaded entirely in downward compression as will occur when the structure is placed on the foundation, thus load and deflection of the shaft top is measured directly, (3) Load distribution within the shaft was directly measured via strain gages mounted on the reinforcement cage, (4) Displacement of the shaft toe was obtainable by casting an accelerometer in the shaft bottom, (5) Statnamic load testing is non destructive, (6) It is set up faster and more economically than static load testing, and (7) To compare this method to the cast in place bi-directional jack method used on an adjacent drilled shaft site. There is an interesting irony to this project in that it was the first Statnamic load test program performed by the Iowa Department of Transportation and it also incorporated many firsts for Statnamic and high and low strain dynamic testing.

The Federal Highway Administration also saw this project as an excellent opportunity for gaining data involving high strain dynamic testing, a testing technique widely used on driven piles, on a fully instrumented drilled shaft. Drop weight testing was monitored concurrently with a PDA/DLT® manufactured by The Netherlands Organization for Building and Construction Research (TNO) and a PDA® manufactured by Pile Dynamics, Inc (PDI). The internal strain and acceleration instrumentation was also measured during the drop weight testing with a MEGADAC® 5100 data acquisition system manufactured by Optim, Inc.

Shaft integrity was evaluated before and after all load testing sequences using several methods including Crosshole Sonic Logging (CSL), Sonic Integrity Testing (SIT) and Pile Integrity Testing (PIT). These test methods will not be discussed in this paper. The results will only be used to backup some of the analysis and conclusions presented in this paper.

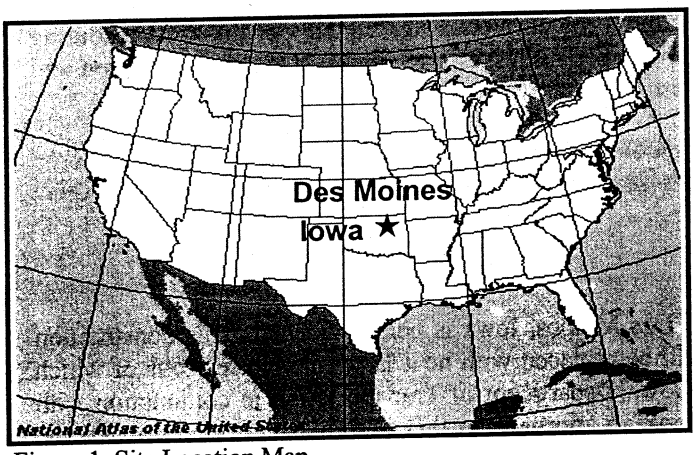

Figure 1. Site Location Map.

1.2 *Soil Conditions*

A comprehensive geotechnical exploration was performed at this site by the Iowa Department of Transportation, part of which included an SPT boring drilled at the precise location of the test shaft. This boring is shown in Figure 2. Soils at this test site generally consist of a surficial layer of silty clay, 5 meters in thickness. The upper 5 meters of silty clay will not be considered as foundation supporting material in the design. Below this, a mottled silty, sandy, clayey soil with intermittent gravel seams and boulders, locally termed glacial till, is present from a depth of 5 meters extending to 19 meters below ground surface. Fine sands, course gravely sands and bouldery gravel was present to 25.75 meters in depth where the top of the shale formation was. SPT "N" values in the shale were 100 blows per 0.27 meters and 72 blows per 0.30 meters. SPT "N" values in the glacial till generally ranged from 10 to 20 blows per 0.30 meters.

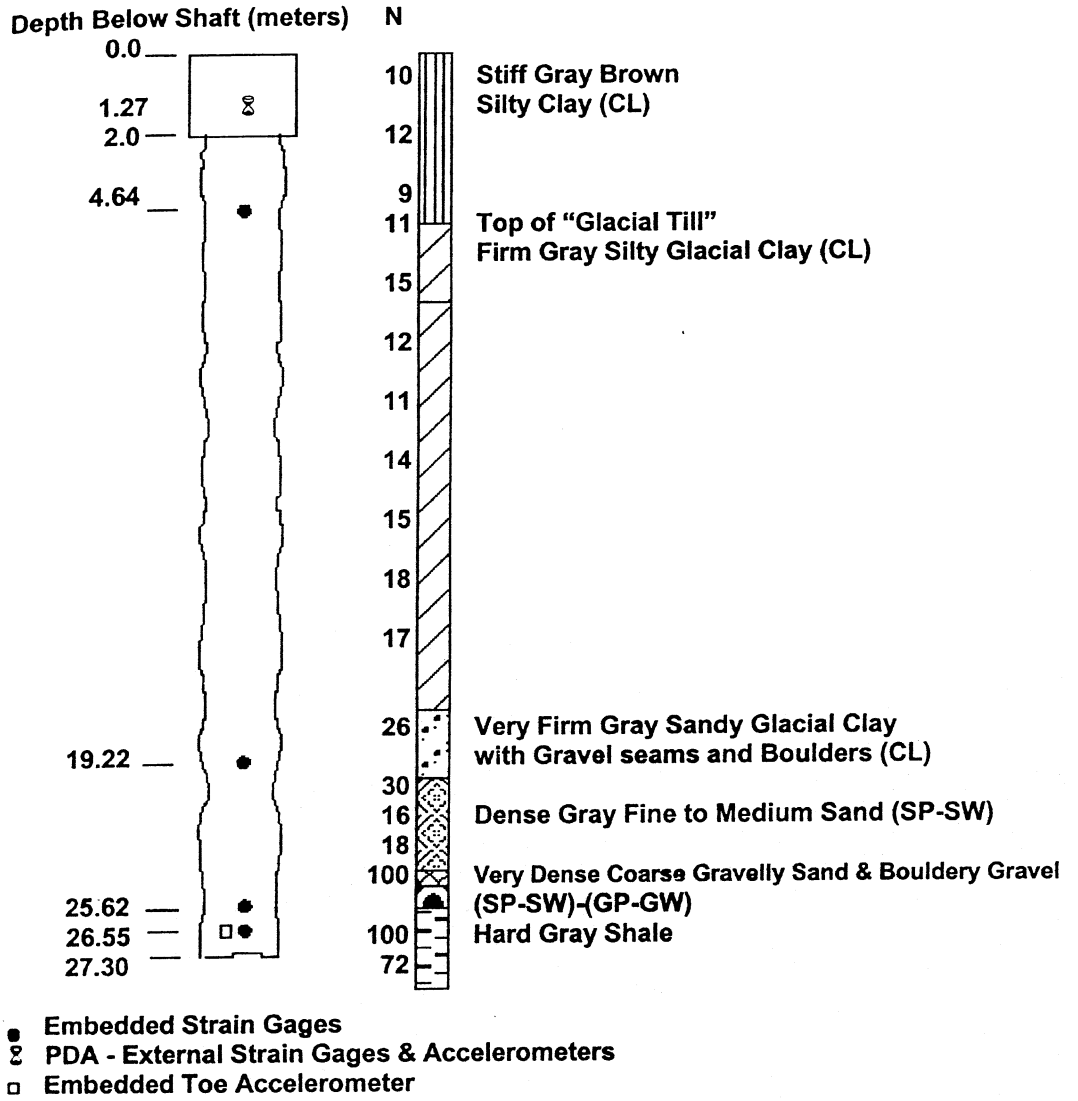

Figure 2. Soil Test Boring.

1.3 *Test Foundation Description*

The test shaft diameter is 1.2 meters for the upper 2 meters as a result of surface casing and assumed to be 1.07 meters in diameter for the remaining length. The overall length is 27.3 meters. Drilled shafts were constructed using the "Wet Hole" technique with polymer slurry admixture to stabilize the hole walls. Longfellow Drilling, Inc. used a Watson crane mounted drill rig to power the cutting tools. Drilling tools with a 1.04 meter diameter were used to excavate the shaft. Several drilling tools were used to excavate the hole consisting of a single flight auger for the glacial overburden soils, a core barrel for penetrating the bouldery material and the single flight auger to excavate the shale material. A clean out bucket with scraper teeth on the bottom was used to clean the shaft bottom prior to placement of the reinforcement cage. Soundings of the shaft bottom were made with a weighted tape for depth determination and estimate cleanliness of the hole bottom. The clean out bucket was used several times until a reasonably sound bottom was felt with the weighted tape. The Contractor decided to install the cage in two parts to closely simulate the methods anticipated for tight space constraints on the upcoming bridge work. Cage placement took approximately 4 hours. Weighted tape soundings

after cage placement (prior to concrete placement) indicated sedimentation on the order of 100 mm in depth on the shaft bottom. Subsequent CSL test results support a soft bottom condition. Load testing results also indicate poor end bearing resistance as a result of not cleaning the bottom. It should be noted that a bottom cleanout procedure such as air lifting or a submersible pump will be implemented for production shafts. Concrete was tremie placed with a pump truck. The tremie pipe was lowered to the shaft bottom and plugged with a "nurf ball". During concreting, the tremie was raised slowly maintaining at least 3 meters below the top level of the concrete. The shaft was over poured until clean concrete was observed at the shaft top. The top of shaft was troweled smooth at the desired top elevation.

The instrumentation scheme consisted of four vertical levels of resistance strain instrumentation installed on the test shaft reinforcement cage with three gages on each plane, 120 degrees apart for a total of 12 strain gages in the shaft. An accelerometer was mounted on the cage adjacent to the lowest level of strain gages (0.6 meters above the shaft toe). The instrumentation locations are shown in Figure 2.

1.4 *Statnamic Test Procedure*

The Statnamic load test system provides a fast and economical method of achieving large downward loads to foundations by "launching" a reaction mass upwards with the test shaft used as a base for the system. During the launching of the mass upwards, an equal and opposite force acts downward on the foundation according to Newton's third law, which states that: "For every action there is an equal and opposite reaction". A mass "m" of 72,398 kg (5 percent of the desired downward load) was used in this case. Upward acceleration "a" of the mass was approximately 20 g's. The theoretical downward load is 20 times the mass. The actual load is measured directly with a calibrated load cell mounted on the shaft top. Shaft top displacements are measured via a photovoltaic sensor mounted to the shaft top, excited with a laser reference beam. Standard instrumentation also includes a shaft top accelerometer. Thus load, displacement, acceleration, and velocity are directly measured at the shaft top. All of these devices are a part of the patented Statnamic testing system and are monitored during a 0.4 to 0.6 second window encompassing the test duration using a high speed data acquisition system sampling at 4000 Hz. A more detailed description of the test methodology and analysis method is provided in references such as Brown (1994) and Middendorp (1992) as well as others.

In this case, as with most, standard Statnamic instrumentation was augmented with strain and accelerometer instrumentation cast inside the foundation for determination of load distribution and shaft toe displacement. The additional instrumentation as well as the Statnamic instruments were monitored with the MEGADAC, which was interfaced with the FPDS Statnamic module. This configuration provides very important redundancy in the measurements and also links the strain gage and toe accelerometer data in time with the other measurements.

The Statnamic load testing was applied in two cycles, first to 5 MN (anticipated design load) and then to 14 MN. This paper only focuses on the larger 14 MN Statnamic test because a greater shaft capacity was mobilized in this test.

1.5 *High Strain Dynamic Test Procedure*

High strain dynamic testing is a method used to quickly and economically evaluate many aspects of a pile driving process including: pile hammer performance, tension and compression driving stresses, pile capacity, and pile integrity. On occasion, the system has been used to test drilled shafts. The test is accomplished by attaching sets of strain gages and accelerometers on opposite sides of the pile near the head using concrete anchors and bolts. During pile driving, measurements of strain and acceleration are made in the region of the pile head for each hammer impact using one of the commercially available data acquisition systems specifically designed for this type of testing. Strain and acceleration signals processed in the field between

each hammer blow are referred to as direct calculations. These calculations are based on simplistic models to perform the calculations in the short time between each hammer impact. Direct calculations of pile capacity are most commonly evaluated using the Case Method approach. The field signals are stored and later subjected to rigorous post processing using commercially available software packages such as TNODLT Signal Matching (TNODLT) and CAse Pile Wave Analysis Program (CAPWAP). In this process, pile and soil data are modeled and a calculation is carried out using the wave equation. The models describe the pile and soil in terms of acceleration, velocity and displacement functions, using empirical parameters which depend on soil properties. Using iterative methods in which the results of each analysis are compared to the actual measured pile behavior, appropriate dynamic parameters are refined and the shaft and toe resistance estimated. The success of this procedure for predicting static capacity is user dependent and the solution is not unique. The margin of error in testing drilled shafts has a potential to be much greater than in driven piles due to the many unknown properties of a cast in place foundation element.

The drop hammer used in this study consisted of two air hammer rams fastened together having a total mass of 9050 kg's (6787 kg's and 2263 kg's). The falling mass was guided by a 0.66 meter width, free swinging box lead section. No provisions for a fixed hammer to shaft alignment were made. A cushion was used to protect the shaft from damaging stresses derived from impact. The cushion was made of three steel disks 50 mm in thickness each over three sheets of plywood 19 mm in thickness for a total thickness of 207 mm. A friction crane with free fall capabilities was used to lift and drop the ram.

The upper 2 meters of the shaft (cased portion) was excavated to allow placement of external strain gages and accelerometers. Eight square holes were cut in the casing to expose the concrete for gage placement. Drop in anchors were installed in the concrete to allow fastening of a total of 6 strain gages and 6 accelerometers from two separate PDA systems. The gages were 1.27 meters below the shaft top.

A total of 7 impacts were monitored varying the drop height from 0.5 meters to 3 meters. The paper focuses on blow number six since this was the highest energy blow.

2 TEST RESULTS

2.1 *Statnamic Results*

The derived static load versus displacement curve shown in Figure 3 was calculated using a variation of the Unloading Point Method (UPM) (Middendorp et. al., 1992) involving the average shaft acceleration and average shaft velocity rather than only the top values typically used. The results indicate a mobilized static capacity of 14.25 MN with a maximum shaft top deflection of 8.8 mm and a permanent set of only 3 mm. In this test case, the load/displacement response is within the elastic realm of the pile/soil system similar to that which would be observed from a static test not run to failure. Because the load/displacement response was within the elastic range and shaft movement was very small, dynamic effects were minimal on the maximum capacity. Correction for the dynamic effects, however, better describes the slope of the elastic region of the pile/soil system.

The shaft bottom load/displacement is also shown in Figure 3 based on toe strain and toe accelerometer measurements. The dynamic effects of inertia are insignificant at the shaft bottom. A maximum load of 1.2 MN is estimated at the shaft toe with a maximum displacement of 3 mm and a permanent displacement of 2.2 mm. The results also indicate residual load and displacement after the test.

Shaft loads at each of the strain gage levels are presented in Figures 4 and 5 and were calculated by the equation:

$$P = \varepsilon AE \qquad (1)$$

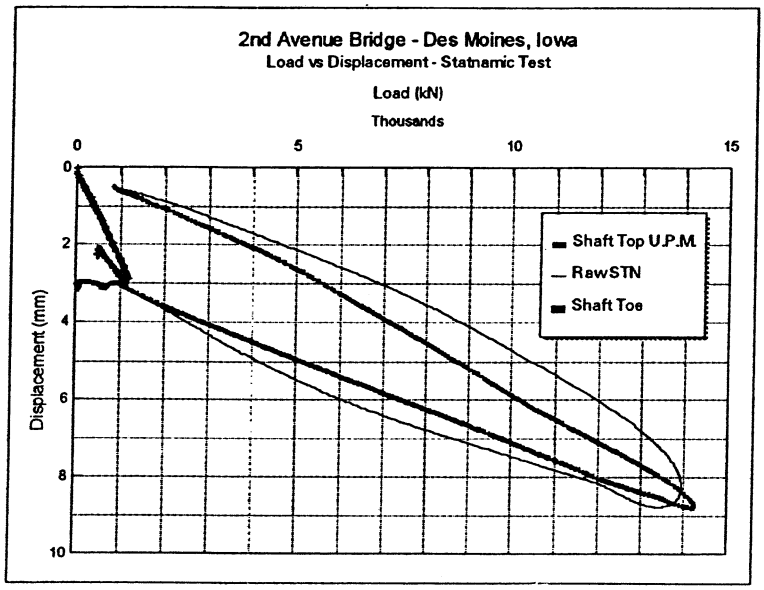

Figure 3. Load vs Displacement.

where P is the load at strain gage location; ε is the average strain of the three gages at each level; A is the assumed shaft cross sectional area; and E is assumed shaft equivalent elastic modulus

This calculation is highly influenced by the shaft diameter and elastic modulus, which must be estimated from as-built information and commonly accepted formula. Shaft top load and displacement are direct measurements thus, not influenced by any of these factors.

Equivalent modulus values for these calculations were based on concrete cylinder break strengths and the weighted average concrete and steel area. The concrete modulus was calculated using the American Concrete Institute (ACI) method:

$$E = 5000(f'c)^{1/2} \quad (2)$$

where E is concrete elastic modulus; and f'c is concrete compressive strength in MPa.

The f'c values were obtained from concrete compressive strength tests performed within two hours of Statnamic testing. An average f'c value of 27.03 MPa was used based on two cylinder tests. The shaft diameter was assumed to be 1.07 meters at the strain gage locations based on the diameter of the drilling tools. The upper 2.0 meters of the shaft was cased and has a diameter of 1.22 meters. The steel area was calculated based on a cage made of ten 25mm vertical reinforcing bars and four 50 mm diameter Schedule 40 steel tubes. A steel modulus of 200 GPa was used. A shaft equivalent modulus of elasticity of 25.91 GPa was calculated for each strain gage location.

The forces from the strain measurements in Figures 4 and 5 were also corrected for dynamic effects by performing a U.P.M. analysis at each level. The load distribution curve in Figure 4 was created by plotting values at various slices in time from Figure 5.

The Statnamic load test produced a compressive load lasting 120 milliseconds as shown in Figure 5 (sign convention is compression negative). The load is applied in a linearly increasing manner then a controlled unloading takes place. Dividing the shaft length of 27.3 meters by an assumed wave speed of 4000 m/s indicates a wave travel time (natural period) of 6.8 milliseconds. For this case, the duration of loading was around 17 to 18 times longer than the natural period of the shaft. This long period dynamic loading has several interesting results. One is that tensile stresses are non existent in a shaft of this length as shown in Figure 5. Tensile

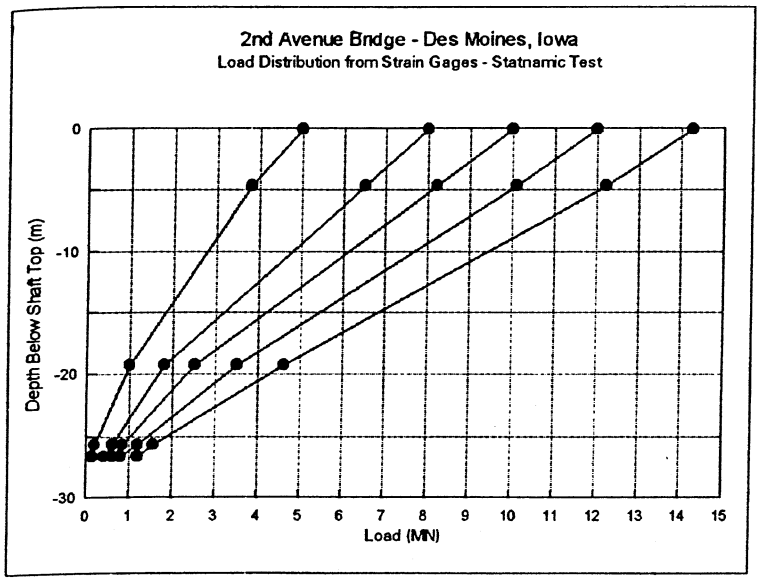

Figure 4. Load Distribution vs Depth.

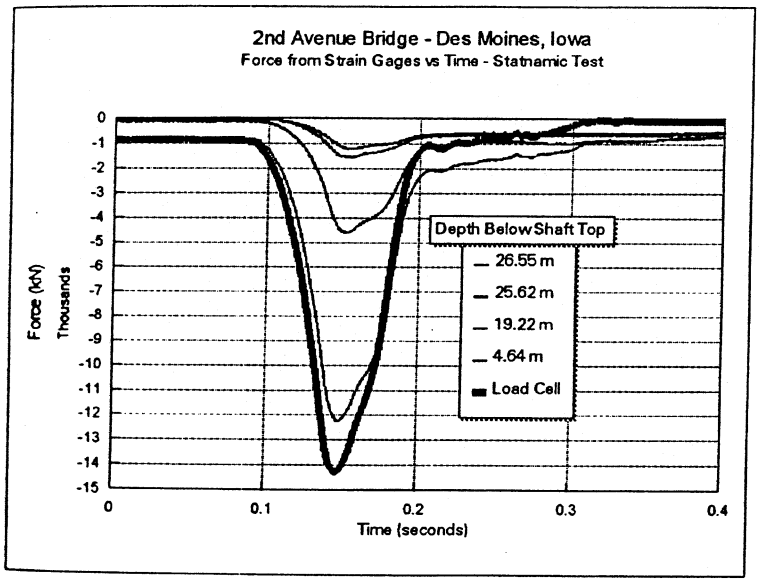

Figure 5. Forces From Load Cell and Strain Gages vs Time.

stress waves are not present with a load duration of more than 12 times the natural period of the shaft (Middendorp, 1995). Secondly, the entire shaft is in compression during the test and moves as a rigid body, like in a conventional static load test. Lastly, the shaft as a whole undergoes translation during the compressive loading, thus minimal shaft accelerations and velocities are present. The measurements of shaft top and bottom accelerations, velocities, and displacements are shown in Figures 6, 7, and 8. Figures 7 and 8 show that the top and bottom accelerations and velocities are relatively small. They are also generally in phase. The slight shift noted is due to the elastic compression of the shaft. The difference in magnitude of the accelerations, and velocities at the top and bottom are due to the soil not being loaded to full plastic deformation. The difference in displacement between top and bottom in Figure 8 is due to the elastic compression of the shaft soil/system. These measurements provide additional support that in evaluation of Statnamic test data, it is correct to consider the mechanics of the pile moving as a rigid body.

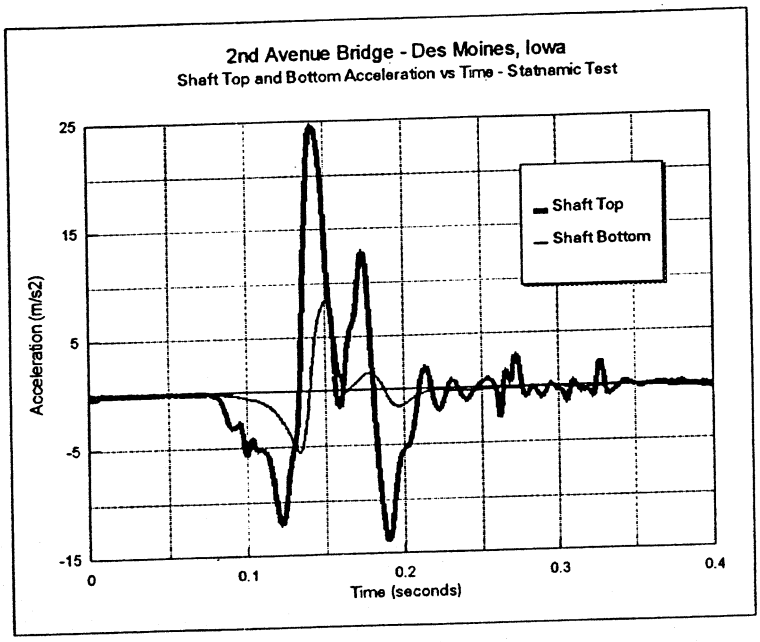

Figure 6. Shaft Top and Bottom Acceleration vs Time.

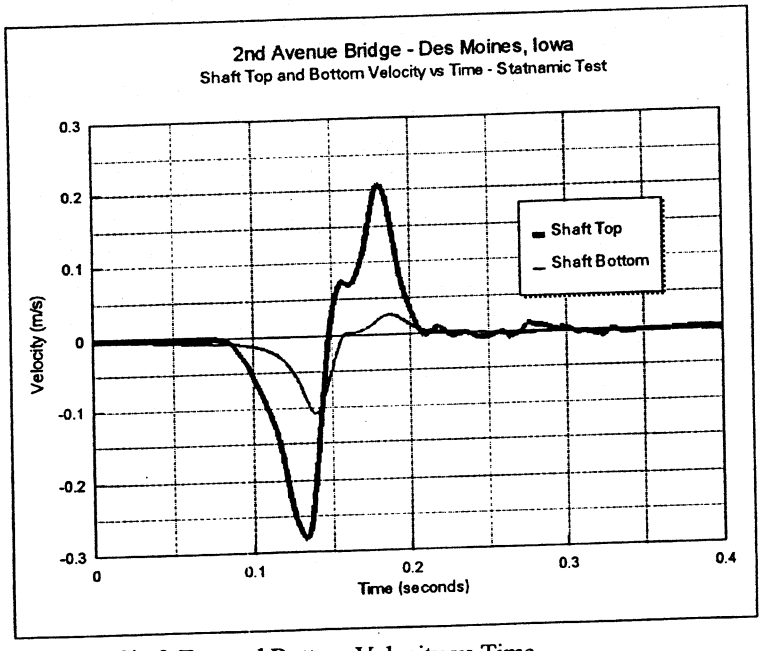

Figure 7. Shaft Top and Bottom Velocity vs Time.

2.2 *High Strain Dynamic Test Results*

2.2.1 *Applicability to Cast in-Situ Piles*

Interpretation of test results in this case is much more difficult for high strain dynamic testing because the element tested was a drilled shaft. For driven piles, results have been shown to be reliable because key pile properties can be determined in a controlled manner. For cast in place foundations like drilled shafts there are several uncertainties for high strain dynamic testing which can lead to considerable error in pile capacity prediction. These include properties such as modulus of elasticity, density, stress wave speed, pile shape and cross section. Further

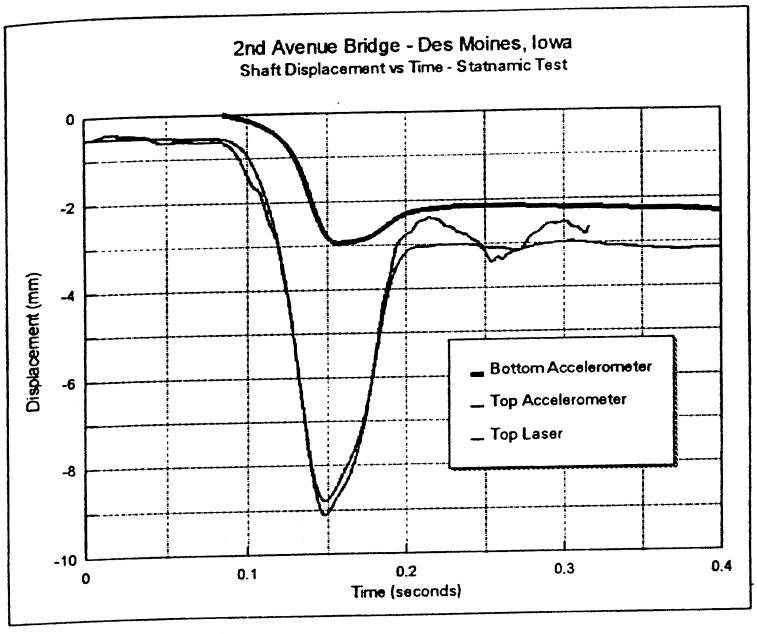

Figure 8. Shaft Top and Bottom Displacement vs Time.

difficulties arise in high strain dynamic testing of cast in-situ piles because tension waves are easily generated. Drilled shafts may become damaged since they are only conventionally reinforced opposed to prestressed concrete piles which are designed to handle tension stresses from driving. Thus, to prevent damage, testing must be stopped prior to mobilizing the large displacements required to fail a drilled shaft. Additionally, the ram to pile alignment is very difficult to control and bending stresses result from eccentric loading. Bending stresses can cause damage and also complicate the analysis method.

With respect to capacity prediction, the only derivation assumption in the Case Method equation is a linearly elastic uniform pile with constant cross section along its length. Therefore, this method alone is not reliable for cast in place foundations. Complex models must be made using TNODLT or CAPWAP to attempt any prediction. These models are also plagued by the same unknown pile properties. The perplexities in assuming pile properties are compounded in these models by unknown dynamic soil parameters such as damping and quakes. Results produced by independent parties do not compare within the same margin of error for driven piles because of these unknowns and the inherent non-unique solution.

2.2.2 *Wave Speed Determination*

The wave speed is one of the most pivotal pile properties and must be correctly determined or large errors may result. A 10 percent error in wave speed results in a 20 percent error in modulus and subsequent pile capacity and stress calculations (Likins, 1996). Wave speed is a function of the following material properties of the pile, elastic modulus and mass density and are related through the equation:

$$c = (E/\rho)^{1/2} \tag{3}$$

where c equals wave speed; E is the elastic modulus; and ρ is the mass density of the concrete.

Several methods of wave speed determination were evaluated for use in the analysis of this data which are: (1) Free Pile Test, (2) Wave Up and Wave Down Method in early driving, (3) Published "standard" values, (4) Inspection of wave up and wave down from current data, (5)

Calculated from laboratory tests, (6) Low strain Sonic Integrity Testing, and (7) Measured from embedded instrumentation.

The two preferred methods to find wave speed are impossible with respect to drilled shafts because they rely on a pile with no shaft resistance from the soil i.e. before driving (Free Pile Test) or during the first blows before the pile significantly penetrates into the ground (Wave Up and Wave Down Method). The free pile test is obviously impossible for cast in-situ piles. In the case of a drilled shaft, which by design and construction method, has large side friction, wave speed determination by WU/WD inspection may be erroneously slow due to high shaft friction. Impact diagrams showing pile top force and velocity times impedance and the resistance wave down and wave up are shown for Blow 6 in Figures 9 and 10. The very soft pile/soil response shown makes wave speed determination difficult. The resistance wave down and wave up shown in Figure 10 illustrates the very rounded area where the toe reflection should be. The best estimates of wave speed from this procedure range from 3962 m/s to 3567 m/s which is as much as 10 percent less than standard published values of 4000 m/s for concrete. Under normal high strain dynamic test circumstances, this would be the only way to determine the shaft wave speed.

Supplementary low strain Sonic Integrity Test (SIT) or Pile Integrity Test (PIT) methods may be used to shed additional light on which wave speed to use. It may also help determine large cross section variations for subsequent signal matching models. But there is also a margin of error associated with low strain test methods which may just confuse matters. The wave speeds reported from the SIT and PIT results are 3600 m/s and 3650 m/s.

The wave speed was also calculated based on laboratory tests. The modulus was calculated by the ACI equation (2) based on concrete cylinder breaks made within 2 hours of the drop hammer test. The concrete compressive strength based on a 10 micro-strain per second loading rate is 27.79 Mpa and the modulus is 26.3 GPa. Loading rate during the drop hammer test was on the order of 200,000 micro-strain per second. It is suggested that the compressive strength is 15 percent greater at a loading rate of 8000 micro-strain per second (Metha, 1986). Therefore, this modulus calculation corrected for loading rate should be somewhat larger, perhaps by 3 to 5 percent. In the laboratory, the unit weight of the cylinder was also determined to be 2195 kg/m^3. The wave speed calculated by (3) is 3465 m/s. If loading rate and reinforcing steel add 5 percent, the wave speed is 3638 m/s.

For this test, internal measurements of strain at four levels and acceleration at the shaft toe were made during the drop hammer test. Using these data is probably the most accurate way to determine the wave speed and pile/soil response. Inspection of the acceleration versus time plot in Figure 12 or any one of Figures 11 through 14 implies a wave travel time of 8 milliseconds over a length of 25.28 meters between the top and bottom accelerometers. Data in Figure 11 also indicates that variations in the wave speed occur over the length of the shaft. The composite wave speed of the shaft from these measurements is 3160 m/s.

So there seams to be an irresolution in the best determination of the wave speed for drilled shaft testing. Values are shown to range from 3962 m/s to 3160 m/s in this case. Capacity variation with wave speed is shown in Table 1.

2.2.3 *Accuracy in Load Measurement*

The elastic modulus also directly influences the accuracy of load measurement, since the load is calculated via strain gages near the pile top by equation (1). Essentially, the shaft cross section at the gage locations is a load cell. Load cells used in static and Statnamic testing are required to be calibrated and traceable back to the National Institute of Standards and Technology (NIST). The shaft concrete curing process near the shaft top is the most unrepresentative of the shaft as a whole. Moreover, the modulus is linearly dependent on the mass density of the pile. What's more, is the elastic modulus is variable over the length of the shaft and over the cross section. Accuracy in load measurement is also influenced by the cross sectional area. In this case, the shaft top was slightly elliptical and the gages were placed 0.7 meters above a transition zone from permanent casing to a smaller diameter uncased shaft.

Table 1. Case Method Capacity Prediction Variation with Wave Speed Value TNO FPDS-5.

Blow Number	c=3963 m/s Static Resistance (MN)	c=3638 m/s Static Resistance (MN)	c=3600 m/s* c=3567 m/s* Static Resistance (MN)	c=3160 m/s Static Resistance (MN)
1	3.1	3.0	2.9	2.5
2	6.5	5.7	5.4	4.9
3	7.2	6.3	6.1	5.3
4	8.7	7.5	7.1	6.5
5	9.1	7.7	7.3	7.4
6	9.3	7.6	7.1	7.5
7	8.4	7.0	6.7	7.4

Table based on a damping constant of JC=0.5.

Table 2. High Strain Dynamic Testing Summary Table (Direct Calculations) from TNO/PDI.

Blow Number	Static Resistance* (MN)	Maximum Compression Stress (MPa)	Maximum Tension Stress (Mpa)	Energy Transfered (kJ)	Drop Height (m)
1	2.9 / 2.3 3 / 3	1 / 1	4 / 4	0.5	
2	5.4 / 4.7 6 / 6	3 / 2	18 / 20	1.3	
3	6.1 / 5.8 8 / 7	2 / 2	27 / 28	1.8	
4	7.1 / 6.5 9 / 9	2 / 2	40 / 41	2.1	
5	7.3 / 6.9 10 / 10	1 / 2	48 / 50	2.5	
6	7.1 / 7.1 11 / 11	2 / 2	55 / 59	2.7	
7	6.7 / 6.7 10 / 10	1 / 2	43 / 47	3.0	

* Maximum Case Method with JC=0.5 & a wave speed of 3600 m/s.
* TNO/PDI data.

2.2.4 *Discussion of Results*

The data contained in Table 2 summarize the results of the high strain dynamic testing. The values shown are direct calculations based on the maximum CASE Method (closed form solution) approach. Since the only derivation assumption in the Case Method equation is a linearly elastic uniform pile with constant cross section along its length, this method is not totally reliable for cast in place foundations. This is a simplistic approach compared to signal matching, but may very well be the best, just because of its simplicity and repeatability. The maximum Case Method capacity independently reported from the TNO and PDI systems were nearly identical in Table 2. Supplemental information such as driving stresses and energy are also reported in Table 2.

Independent evaluations on blow number 6 made by GRL researchers with CAPWAP show a capacity prediction of 10.2 MN with 3.8 MN of end bearing and 6.4 MN of skin friction. GRL researchers performing the CAPWAP analysis were not provide the embedded strain gage and toe accelerometer data. Their analysis was based on shaft top data only.

Signal matching analysis TNODLT of blow 6 performed by the authors produced variable results depending on various permutations of pile properties. Predicted capacities from TNODLT ranged from 6.1 MN to 8.85 MN. A common denominator in these variations was the very low predicted end bearing of only 0.1 MN.

If the embedded strain and accelerometer data was used to back fit a TNODLT model to these internal measurements, a total mobilized pile capacity of 7.8 MN with 7.7 MN in skin friction and 0.1 MN in end bearing was estimated.

Statnamic load test results shown in Figure 38 indicates 0.5 MN to 0.8 MN of end bearing at comparable loads. CAPWAP using only shaft top data over estimated end bearing by 375%.

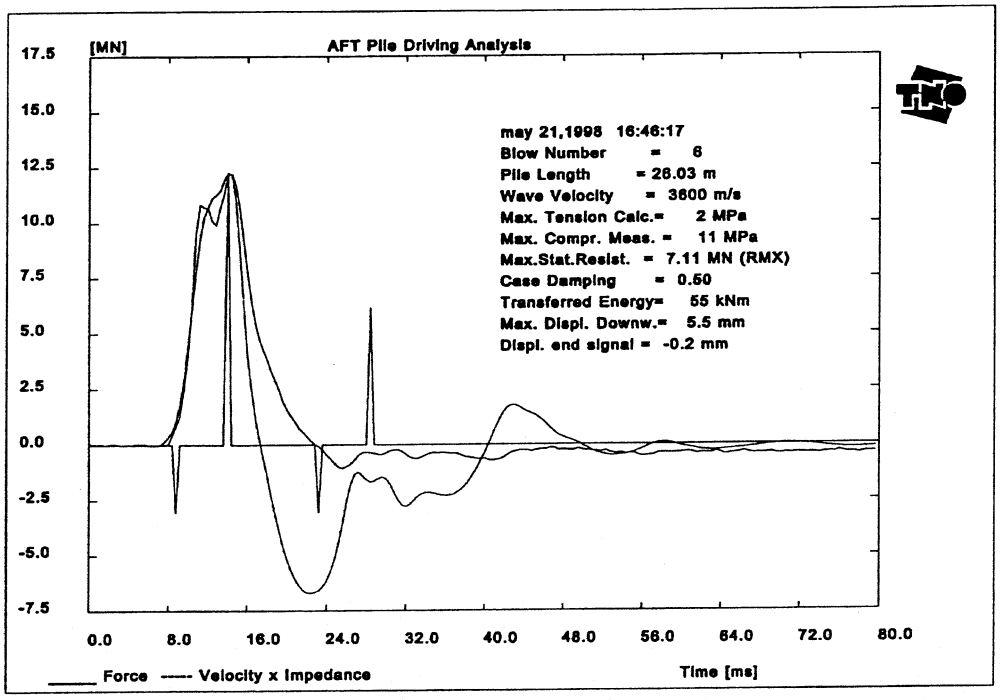

Figure 9. Shaft top force and velocity times impedance - Blow 6.

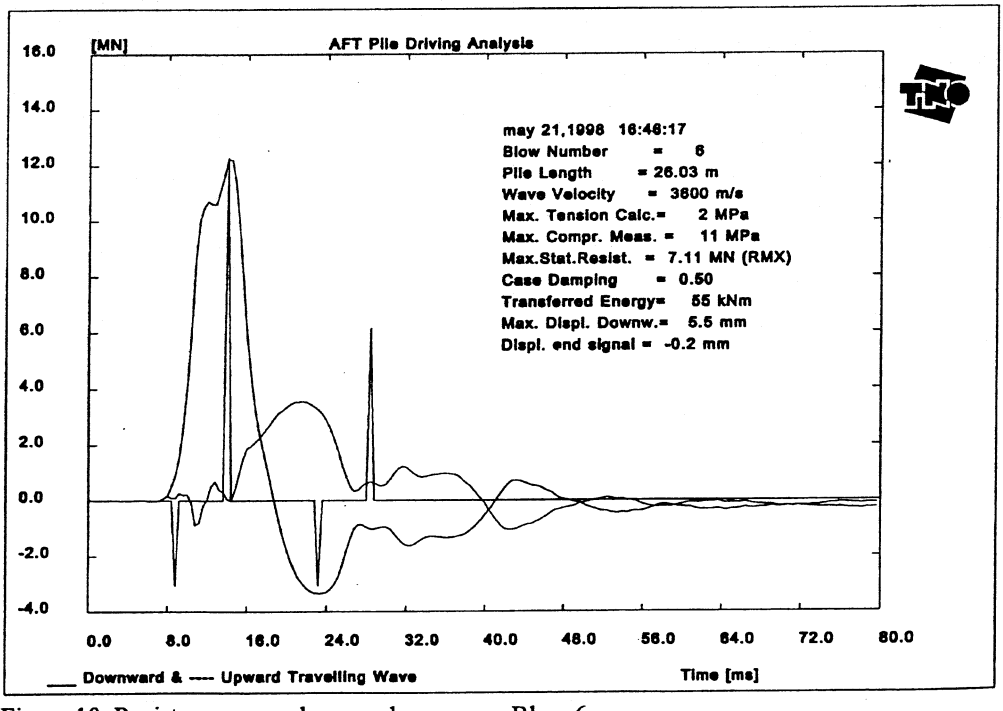

Figure 10. Resistance wave down and wave up - Blow 6.

TNODLT under estimated end bearing by 88 %. Poor end bearing resistance is supported by weighted tape soundings of the shaft bottom prior to concrete placement and subsequent Cross Hole Sonic Logging.

It appears that the more detailed the signal match model becomes, by using measured quantities, the more difficult the match becomes. This is largely due to the uncertainties associated with pile properties previously discussed. Variations in cross section cause stress

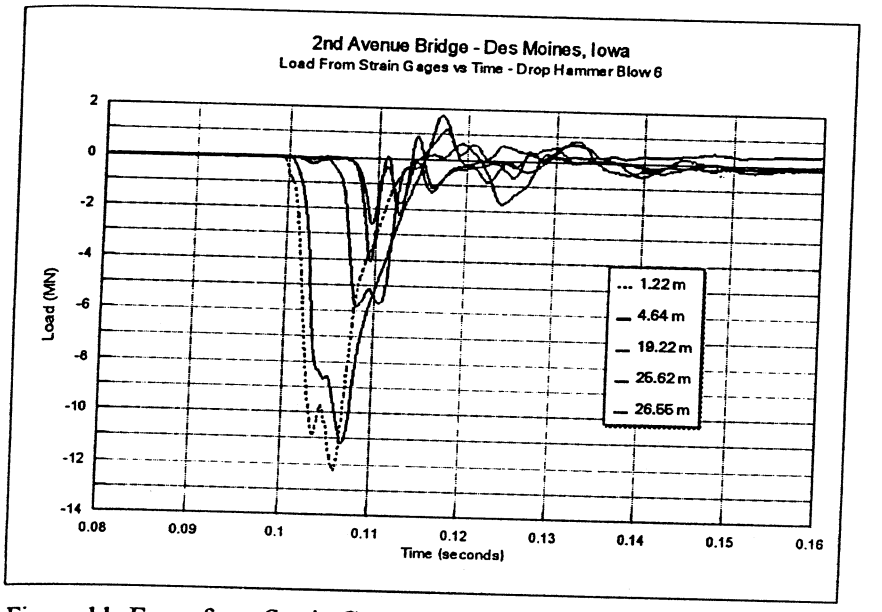

Figure 11. Force from Strain Gages - Blow 6.

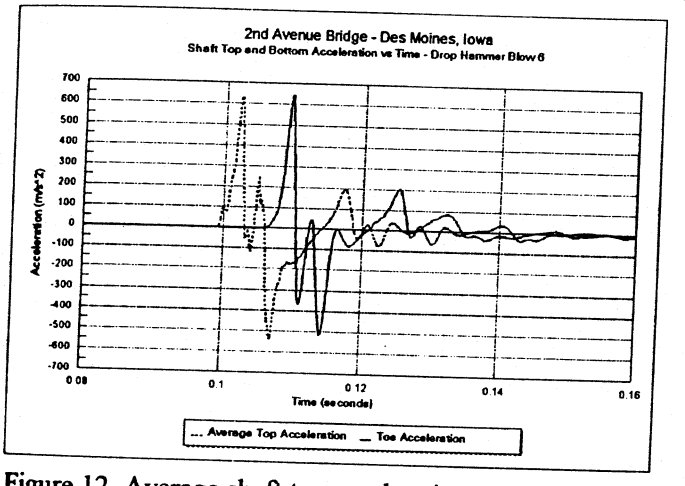

Figure 12. Average shaft top acceleration and shaft toe acceleration.

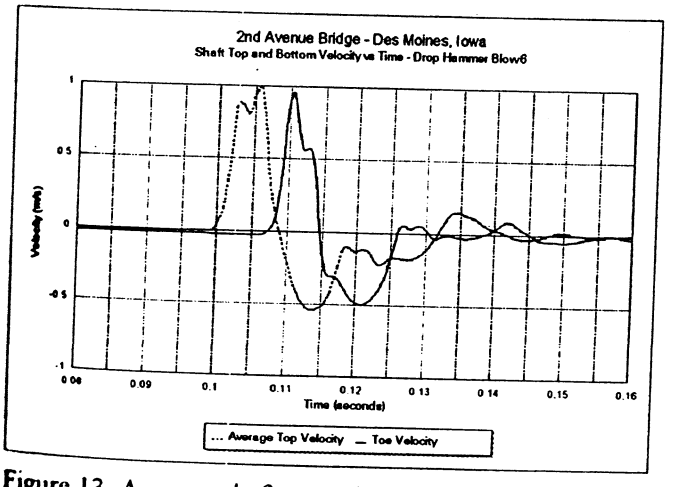

Figure 13. Average shaft top velocity and shaft toe velocity.

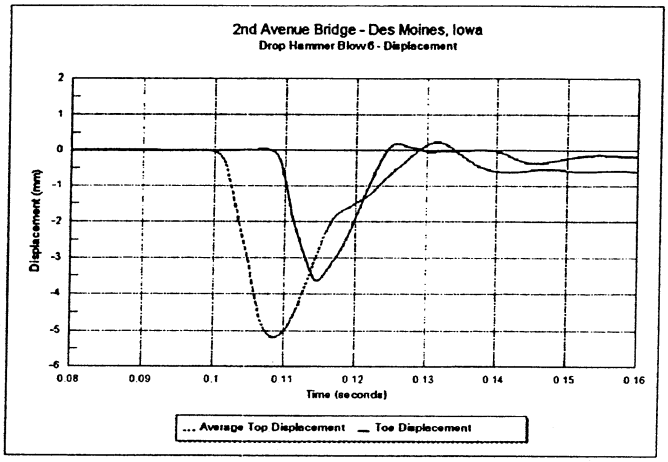

Figure 14. Average shaft top displacement and shaft toe displacement.

wave reflections that can easily be mistaken for soil resistance reflections. A bulge in the shaft can be characterized as high soil resistance and a neck can be taken as low soil resistance. Models cannot adequately describe these complex field conditions. Unknown properties have been shown to seriously influence capacity predictions.

Embedded strain measurements shown in Figure 11 were converted to load via equation (1). The internal measurements clearly indicate the effects of stress wave propagation. Due to this wave propagation, drilled shaft side shear values can not be directly interpreted from these data. The data also shows the presence of tension waves with the maximum tension force of 1.8 MN at 4.64 meters below the shaft top. This corresponds precisely to the maximum calculated tension from the FPDS and PDA. This tension was approaching the maximum allowable value for a non prestressed concrete element. Integrity testing schemes before any load testing indicated an impedance change around 21 to 22 meters below shaft top. This impedance change appeared more prevalent after each test method but was still not a major defect. Figure 11 also shows variation of wave speed over the shaft based on wave arrival times from gage to gage.

The measured acceleration presented in Figure 12 was integrated to velocity in Figure 13 and then to displacement shown in Figure 14. The measurements in these figures are out of phase by the magnitude of the wave travel time. The maximum displacement of the shaft top is shown to be 5.3 mm with a final set of 0.6 mm. The shaft top displacement was also checked with standard survey equipment and reported to have a permanent set of 1.4 mm for this blow. Note that displacement recorded with the survey equipment was a total of 6 mm for the 7 blows. The accuracy of the survey equipment was ±2 mm. As shown in Figure 14, the shaft toe had a maximum displacement of 3.6 mm and a final set of 0.2 mm indicating some residual stress. With displacements of this magnitude, only a fraction of the full shaft capacity was mobilized.

3 LOAD TEST PROGRAM REMARKS

The short coming to the program was that the test shaft was over designed so its ultimate capacity was not measured with the 14 MN Statnamic device. The test shaft at the adjacent site was not loaded to failure either using the bi-directional jack method. Conditions were quite different for that site although it was only a few miles away. The jack was placed in the shaft bottom and loading was from the bottom up. The substantial strength of the shale socket was not overcome and the shaft was permanently cased through the overlying soils. It was just the opposite for the Statnamic test which did not fail the shale. Thus, the two methods complimented each other.

Drilled shaft foundation designs on two of the four bridges will rely entirely on side shear in the glacial till and will not be extended into the shale. Zero end bearing will be used in this

scenario. Larger structural loads will be required for the other two bridges therefore, design criteria includes side shear and end bearing in the shale as well as side shear in the glacial till.

Load test results indicate poor end bearing resistance as a result of not cleaning the shaft bottom. The subsequent construction specifications will require a bottom clean out procedure such as an airlift or submersible pump. A nominal end bearing value in the shale will be used in light of the bottom clean out specification.

Design values for the new structures were based on a combination of both test methods. Statnamic load test results were used for the glacial till and upper soils. Design values in shale were used from the cast in place bi-directional jack method results as well as local data base shale values. The design team felt that a safety factor of 2.5 on the ultimate side shear was appropriate for sizing shafts to match the required structural service loads.

The load test program performed during the design phase is a very innovative approach since the information may be directly incorporated into these designs.

4 CONCLUSIONS

4.1 *Statnamic*

- Statnamic is not effected by uncertainties in pile properties because top load and displacement are measured directly with a calibrated load cell and displacement sensor.
- Embedded strain and accelerometer instrumentation allows direct interpretation of load distribution and toe displacement in Statnamic testing.
- Embedded toe accelerometer instrumentation verified rigid body motion in Statnamic and improved the Unloading Point Method in the elastic range by using average shaft acceleration.
- The duration of the Statnamic load is 10 times longer than high strain dynamic testing, therefore no tensile forces exist in the shaft and the soil is loaded as a rigid body like in a static test.
- Statnamic can safely mobilize greater capacity than dynamic testing.
- It requires no special shaft construction procedures so installation is more representative of actual production shaft construction.
- Comparisons between Statnamic and bi-directional cast in place jack results could not be made since neither test was run to failure.
- Poor end bearing resistance resulted from not cleaning the shaft bottom.

4.2 *High Strain Dynamic Testing*

- High strain dynamic testing has inaccuracy in load measurement on drilled shafts because of unknown pile properties.
- Displacement is not measured directly.
- Capacity prediction from high strain dynamic testing depends on wave speed which has been shown to vary from 3962 to 3160 m/s in this case resulting in considerable variation in capacity estimates.
- High strain dynamic testing is also effected by non-uniform shaft cross section. Unknown cross section variations cause stress wave reflections which can be easily mistaken for soil resistance.
- The Case method is based on a linearly elastic uniform pile with constant cross section along its length, this assumption is not totally reliable for cast in place foundations. This is a simplistic approach compared to signal matching, but may very well be the best, just because of its simplicity and repeatability.
- Capacity estimated from complex signal match models had variations of over 4 MN due to unknown soil properties. Independent CAPWAP analysis based on pile top measurements only indicated a capacity of 10.2 MN while analysis back fit to match embedded strain gages

and toe accelerometer data showed a capacity of 7.8 MN.

- Measurements from internal strain gages may not be directly interpreted in high strain dynamic testing. A signal match must be back fit for prediction of side shear and end bearing.
- To prevent damage, high strain dynamic testing must be stopped prior to mobilizing the large displacements required to fail a drilled shaft. Additionally, the ram to pile alignment is very difficult to control and bending stresses result from eccentric loading. Bending stresses can cause damage and also complicate the analysis method.
- High strain dynamic testing is an excellent tool for driven piles because key pile properties can be determined in a controlled manner.

ACKNOWLEDGMENTS

The authors wish to thank all parties involved including Mr. Carl Ealy of the Federal Highway Administration, the Iowa Department of Transportation, Mr. Dick Longfellow of Longfellow Drilling, Inc., Mr. Scott Webster and Mr. Frank Rauche of GRL/PDI for performing independent field measurements and data analysis.

REFERENCES

Applied Foundation Testing, Inc. 1997. *Report of Statnamic Load Testing - I-35/I-80 Bridge over Second Avenue*. For Soil and Land Use Technology, Inc. on behalf of the Iowa Department of Transportation and Federal Highway Administration.

Brown, D.A. 1994. Evaluation of Static Capacity of Deep Foundations from Statnamic Testing. *Geotechnical Testing Journal*, December, 1994.

GRL & Associates, Inc. 1997. *Summary Report for Dynamic Testing and Analysis - Second Avenue Bridge Test Shaft Project*. For Soil and Land Use Technology, Inc. on behalf of the Iowa Department of Transportation and Federal Highway Administration.

Likins, G. 1996. Helpful Hints for Field Testing and Data Interpretation using the Pile Driving Analyzer. *PDA Users Day*, Orlando, Florida, 1996.

Metha. 1986. *Concrete Materials and Properties*. McGraw Hill.

Middendorp, P. 1995. Statnamic Load Testing and the Influence of Stress Wave Phenomena. *Proceedings of the First International Statnamic Seminar*, Vancouver, September 1995.

STATNAMIC Loading Test'98, Kusakabe, Kuwabara & Matsumoto (eds)
© 2000 Balkema, Rotterdam, ISBN 90 5809 131 7

STATNAMIC testing: University of South Florida research

G. Mullins, E.J.Garbin, Jr. & C.Lewis
University of South Florida, Tampa, Fla., USA
C.Ealy
Federal Highway Administration, McLean, Va., USA

ABSTRACT: Over the past two years researchers at the University of South Florida in Tampa, Florida have conducted over 150 Statnamic tests in conjunction with privately and federally funded test programs. In this time a research program has been developed exploring further applications for its use. This paper will describe some of the areas of research presently under investigation, developments in instrumentation and testing procedures, and preliminary findings.

1. INTRODUCTION

Since its inception in 1988, Statnamic testing has gained acceptance in more than 15 countries and in 6 continents, and it is estimated that over 500 tests have been conducted worldwide. With its growth has come the exploration of new avenues for its application. Although typically considered an axial deep foundation test procedure, it was expanded into lateral load testing in North Carolina (1994) and most notably, in Mississippi (1998), where lateral loads exceeded 7 MN. Additionally, developments such as the hydraulic catching mechanisms, shallow foundation applications, and under water reaction masses continue to emerge. Although some of the most recent developments have yet to be released for production, they promise to be equally beneficial to the full-scale testing arena.

Over the past two years researchers at the University of South Florida have conducted over 150 Statnamic tests on both deep and shallow foundations. These tests were performed in conjunction with production and research oriented projects in cooperation with *Applied Foundation Testing Inc.*, *Auburn University*, *Berminghammer Foundation Equipment*, the *Federal Highway Administration*, *Hayward Baker Inc.*, *University of Massachussetts*, and eight different state departments of transportation. The Statnamic test programs have included: (1) axial load tests on piles and shafts in sands, clays, or rock-sockets, (2) lateral load tests on pile groups and shafts, and (3) plate load tests on sands and full-scale spread footings on sands and vibro-compacted soils (stone columns). This paper will describe some of the research areas presently under investigation, developments in instrumentation and testing procedures, and preliminary findings.

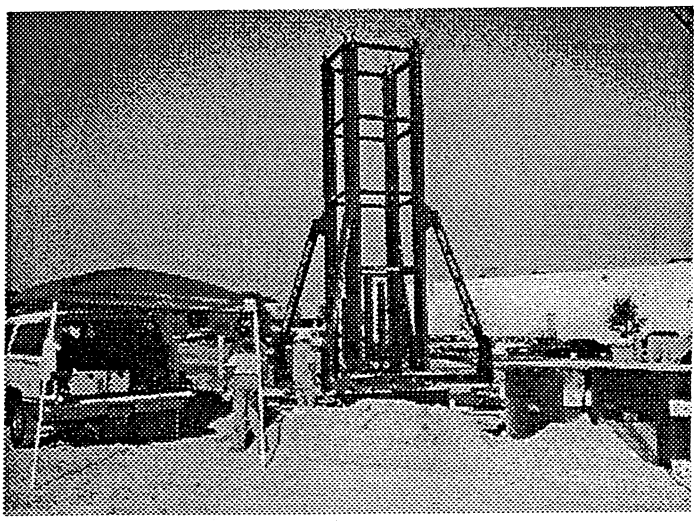

Figure 2.1 Level frame using hydraulic legs.

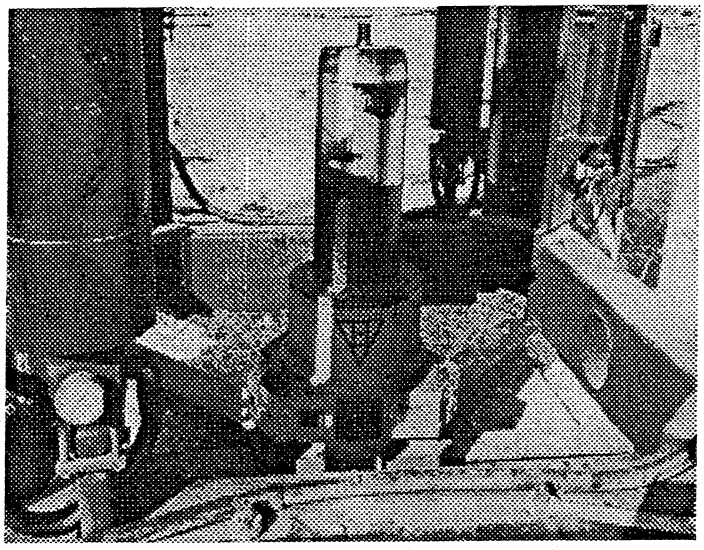

Figure 2.2 Secure piston to foundation.

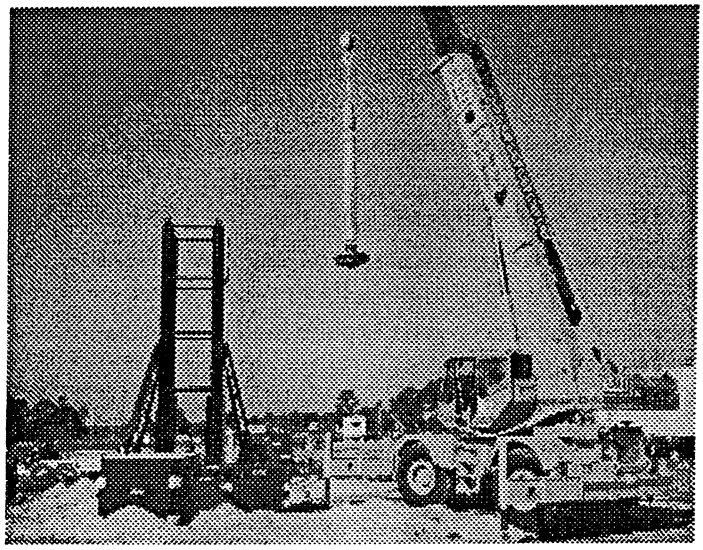

Figure 2.3 Install silencer. *NOTE: fuel basket can be installed after assembly is complete.*

2. HYDRAULIC CATCHING MECHANISM

By means of a grant with the Federal Highway Administration, USF purchased a 4 MN hydraulic catching mechanism (HCM), the largest-capacity hydraulic catching mechanism to date. Although not used exclusively, this device serves as the primary core of the university's Statnamic research program. This catch mechanism provides the luxury of multiple load cycles within a matter of minutes, the ability to inspect the ignition circuit without disassembly, the benefit of single-truck mobilization, and it avoids the environmental problems with gravel retrieval when testing over water.

Hydraulic catching systems eliminate the need for gravel and gravel structure since the upward moving reaction masses are caught at the top of their flight by four hydraulic actuators (or rams). These 3.2 m stroke rams are activated by four low pressure (1500 psi) nitrogen accumulators which store compressed nitrogen gas over hydraulic oil. As the weight on the rams is released during a test, the compressed nitrogen quickly expands to force hydraulic oil into the rams causing them to chase the reaction masses to the apex of their flight. The hydraulic oil is routed (in series) through one-way valves at the base of each ram which restricts reverse flow and thus the downward movement of the masses. Each of the four rams is independent of the others providing redundancy and safety. The masses remain at this position until the user redirects the additional fluid in the rams back into the accumulators. At which time, a subsequent load cycle can be performed.

By transferring the initial weight of the masses to the rams at the onset of the test it is possible to perform Statnamic testing without a pre-load condition. Additionally, hydraulic catching systems have no minimum required jump-height for the silencer/reaction mass assembly which is a concern for gravel catching systems. By removing this restriction, low load tests can be performed with much greater than 5% reaction mass. Such tests can produce long duration load pulses greater than 0.5 seconds, thus reducing inertial and damping forces for large portions of the test.

Although the set-up time for a 4MN gravel or hydraulic catching systems is comparable, multiple cycles can be performed in a matter of minutes when using the latter. Further, the break-down typically takes less time. In using gravel catching systems, great care is exercised in the preparation of the ignition circuitry. An inadequate ignitor connection could cost a project as much as a day of delay time. This of little concern when using the hydraulic catching system due to the ability to raise the entire stack of reaction masses with the hydraulic rams so as to access the fuel basket.

A substantial portion of all Statnamic testing costs stems from the mobilization of equipment. Typically, a 4 MN test requires two tractor-trailers to ship the combined weight of the equipment and reaction masses (27,000 kg total) where only 20,000 kg is permitted per truck. The USF device is equipped with two reaction mass options: (1) an entire set of six concrete-filled steel masses which requires two trucks to ship, or (2) an optional set of two empty, structurally-reinforced steel cans that replace five of the concrete-filled steel masses. The empty can option allows single truck mobilization to distant sites with a total shipped mass of 19,000 kg. Once at the site the cans can be filled with sand, gravel, water or any combination to attain the required mass. Lower loads (up to 2.3 MN) can be attained by using just the empty cans without any fill material. Option 2 has the added advantage of using only three reaction masses which translates into time savings in crane usage. Figures 2.1 - 2.10 illustrate typical assembly of the device.

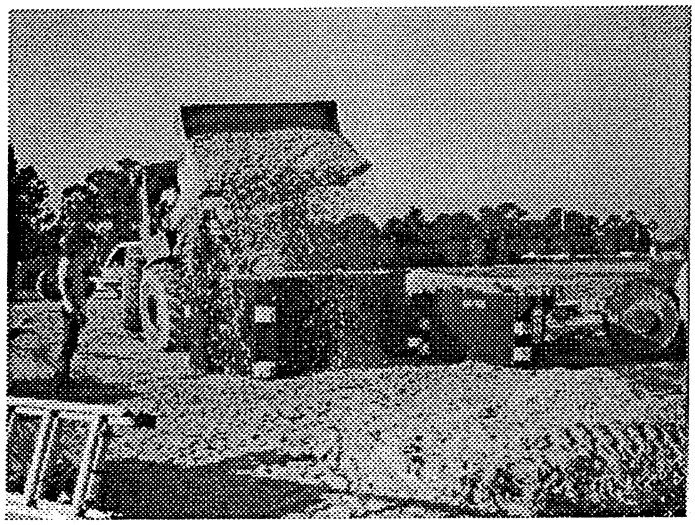

Figure 2.4 Filling cans with gravel (Option 2).

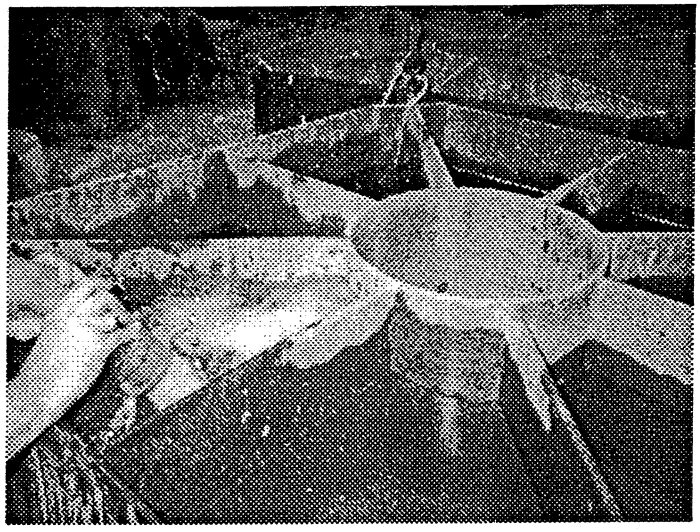

Figure 2.5 Alternatively, cans are filled with water.

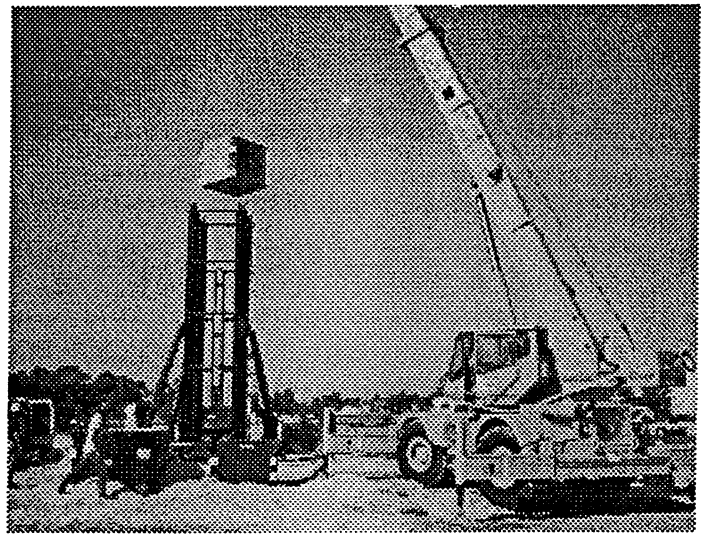

Figure 2.6 Assemble reaction masses (either Option 1 or 2)

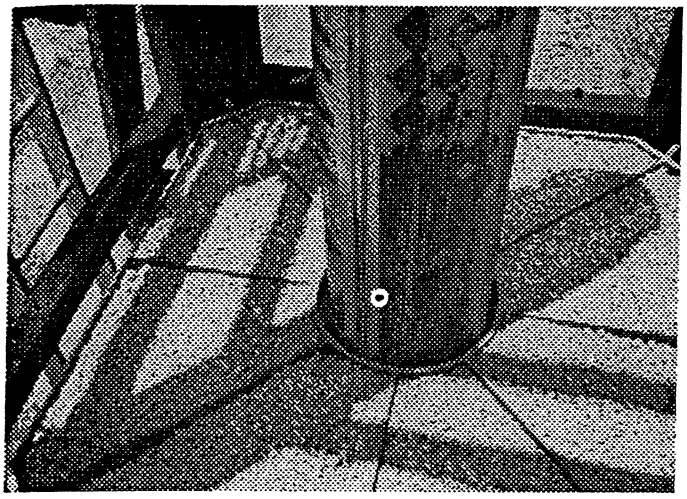

Figure 2.7 Gravel-filled can installed.

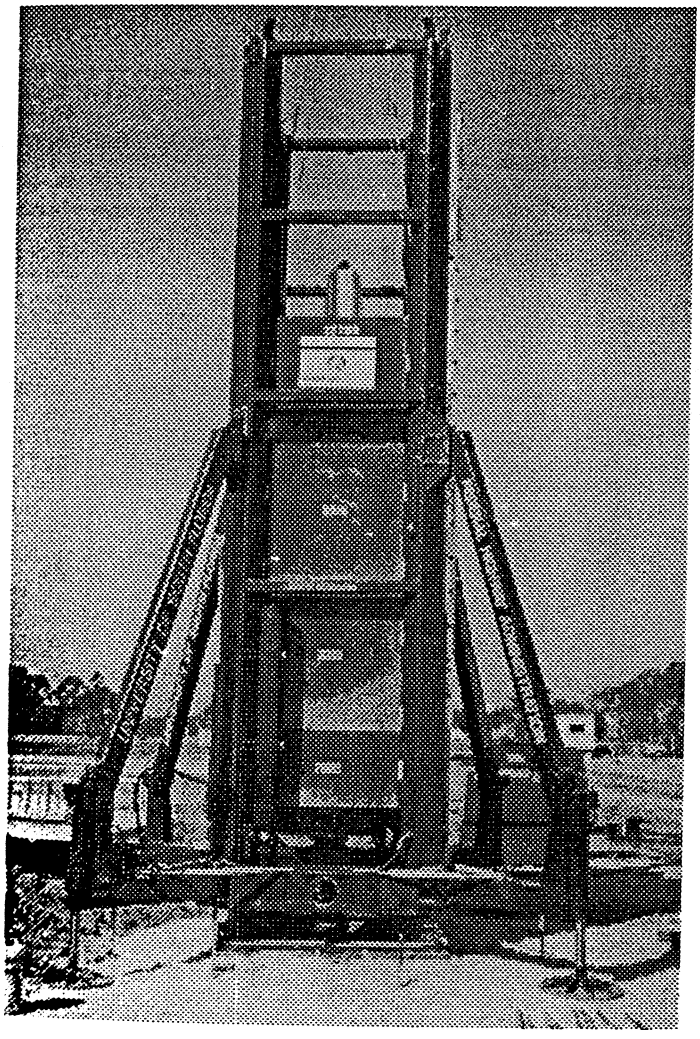

Figure 2.8 Fully assembled mechanism.

Figure 2.9 Statnamic test.

Figure 2.10 Entire mechanism can be placed on the next test pile without disassembly.

3. SHALLOW FOUNDATION TESTING

Researchers at the University of South Florida are currently exploring the correlations between Statnamic and static load testing of shallow foundations. Statnamic testing of shallow foundations has the potential to provide a cost effective alternative to static load testing, and the initial findings have been favorable.

3.1 *Federal Highway Administration Collaboration*

In a series of plate load tests performed in conjunction with the Federal Highway Administration, Statnamic testing was applied to shallow foundations. Three separate yet identical foundations on clean sand were tested in the following manner: (Test 1) incrementally increasing Statnamic load cycles until bearing failure, (Test 2) static load test, and (Test 3) a single Statnamic load test well in excess of the bearing capacity. Using the *Unloading Point Method* (Middendorp et al., 1992), a derived static load-displacement response was obtained for each load cycle, and compared with the static load test in which three load/unload cycles were recorded. Figures 3.1 and 3.2 illustrate the results of these tests.

Shown in Figure 3.1 are the results from the incrementally increasing Statnamic tests (test 1) and the static load test (test 2). The derived static load is shown for each of the four cycles where the peak Statnamic loads were 74, 128, 196, and 262 KN, respectively. Damping coefficients (C) calculated for each cycle were 146, 76, 78, and 92 KN-s/m, respectively. The derived static response slightly over estimates the capacity of the foundation when compared to the true static capacity. This is not altogether surprising based on the probable densification of the soils within the initial cycles. This can be seen from Test 3 (Figure 3.2) which produced a peak load of 219 KN and resulted in more displacement than the fourth cycle of Test 1(262 KN).

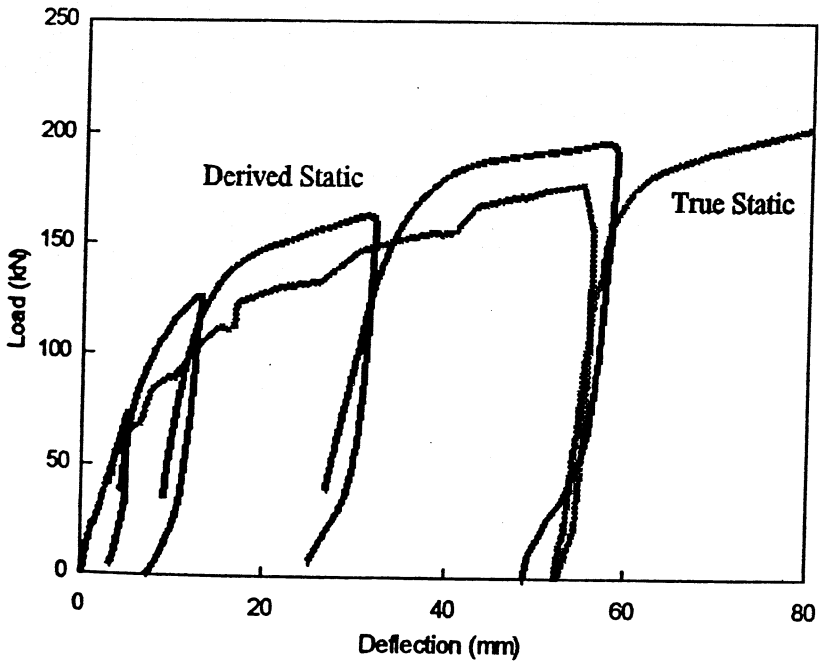

Figure 3.1 Comparison of derived static response from four Statnamic load cycles (test 1) with the true static response (test 2).

Figure 3.2 shows the results of Test 3 and provides an example of a trend that develops wh Statnamic load grossly exceeds the bearing capacity of the foundation. During the linear l stage, Statnamic results indicate a much stiffer system than that of a static test, but once b failure occurs the two test results are similar. Derived static values for shallow foundatio relatively unaffected by inertial forces but seem sensitive to the damping coefficients. The da coefficients calculated from the unloading portion of the

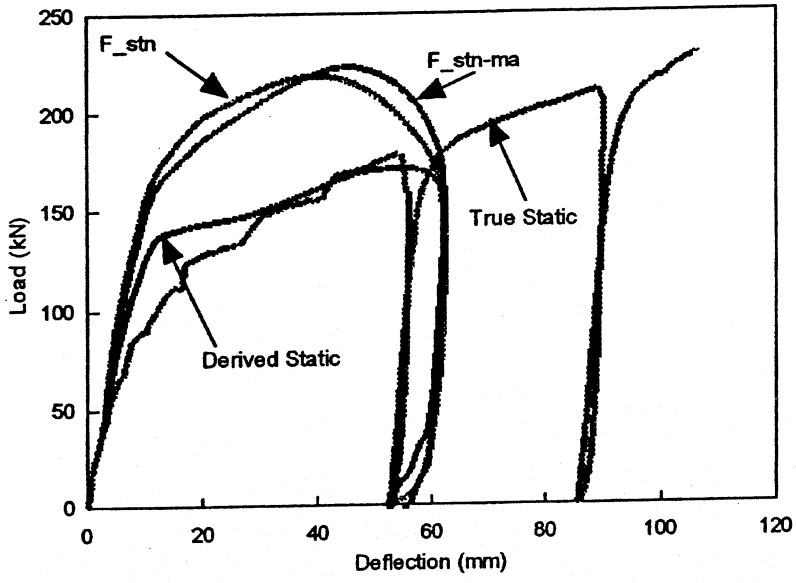

Figure 3.2 Static / derived static comparison of Statnamic test performed well above bearing capacity (tests 2 and 3).

test satisfy the system dynamics in that portion of the loading but fail to do so initially. This i that C varies as the soil strains and is supported by the difference in the calculated da coefficient observed in Test 1 (cycle 1) and Test 3, 146 and 58 KN-s/m, respectively. assumed that the difference between the true static and inertia-corrected Statnamic force is a variable damping coefficient, then the coefficient at any point could be determined for this s site using the following expression:

$$C_x = \frac{F_{stn_x} - F_{ma_x} - F_{static_x}}{V_x}$$

where C, V, F_{stn}, and F_{ma} are the dynamic force parameters at displacement x and F_{static} corre to the true static force at that displacement. Using this expression, Figure 3.3 illustrates the va in the damping coefficient as a function of displacement. It is interesting to note that C, a displacements, is similar to that of Test 1 (cycle 1) and at large displacements similar to Te

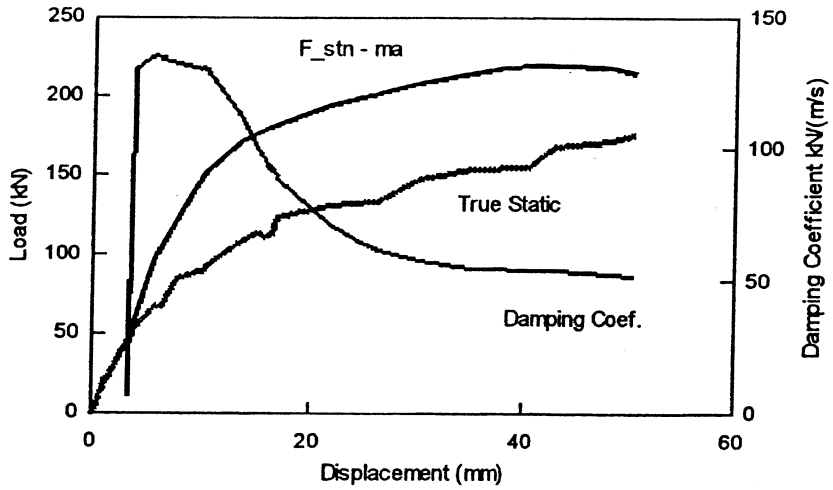

Figure 3.3 Values of the variable damping coefficient calculated using the true static response and the inertia corrected Statnamic force.

3.2 *Testing Foundations on Stone Columns*

Tests performed in conjunction with Hayward Baker using the 4 MN hydraulic catching systen provided the opportunity to investigate the Statnamic response of shallow foundations on ston columns. This program consisted of side by side comparisons of full-scale Statnamic and static loac tests on a 2 m square steel footing. Figures 3.4 and 3.5 show the two test configurations.

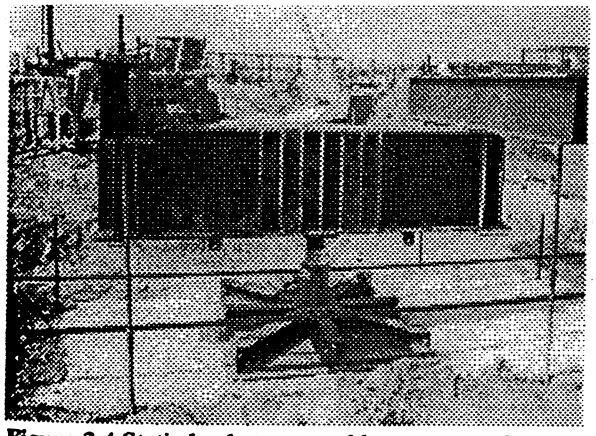

Figure 3.4 Static load test assembly on stone column-reinforced soil.

Shown in Figure 3.6 are the results of the Statnamic testing of the stone column shallow foundations, and the comparison of derived static and true static response of the footing.

As indicated in Figure 3.6, the Statnamic response of the stone column foundation was very similar to the true static response. Because neither test was conducted beyond the bearing capacity of the foundation, the response for both was highly linear. After what appears to be some initial device seating, the Statnamic-derived static load curve has a slope that is nearly identical to the true static. The apparent strain hardening observed in both methods was most likely due to the flexibility

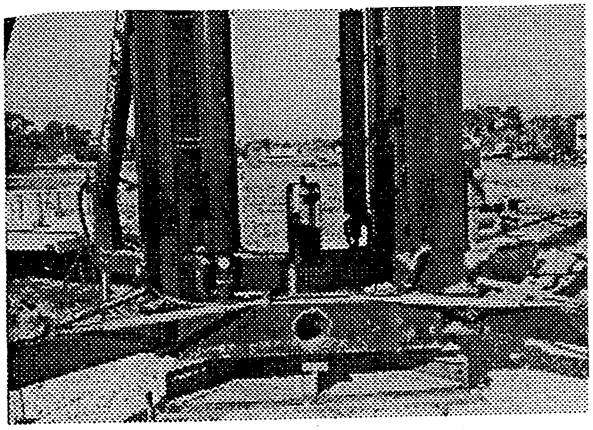

Figure 3.5 4 MN Statnamic piston and HCM frame installed on test plate.

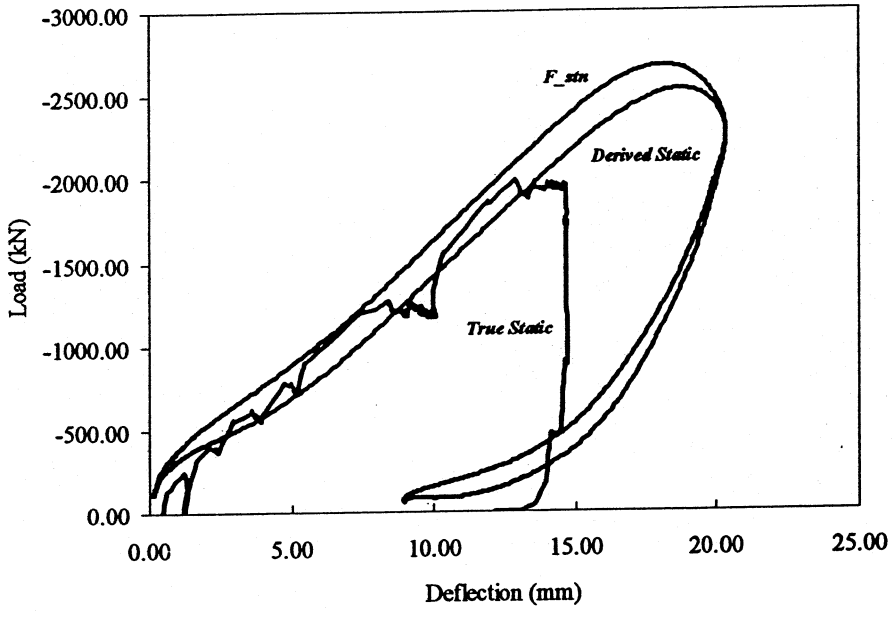

Figure 3.6 Comparison of static and Statnamic test results for shallow foundations on stone columns.

of the plate. Recognizing this as a potential problem, Hayward Baker has agreed to test stiffer, production-type concrete footings in an upcoming test program.

4. DEEP FOUNDATIONS

4.1 *Soft Toe-Constructed Shafts*

In an effort to minimize testing expenses associated with full-scale load testing, drilled shafts with soft toes can be constructed. Such shafts can be tested at loads below that of the their ultimate

capacities. Hence, smaller test equipment can be used as a means of measuring the ultimate skin friction provided by the soil, without having to overcoming tip resistance.

Drilled shafts can be constructed with soft toes by welding a flat plate to the bottom of the reinforcement cage and then attaching a Styrofoam plug to the bottom of the plate. Figure 4.1 shows a typical soft toe-prepared cage. The plug at the tip of the shaft provides virtually no toe resistance when loaded and allows the foundation to fail purely in shear. Strain gauges placed at selected levels can be used to determine unit skin friction for specific soil layers.

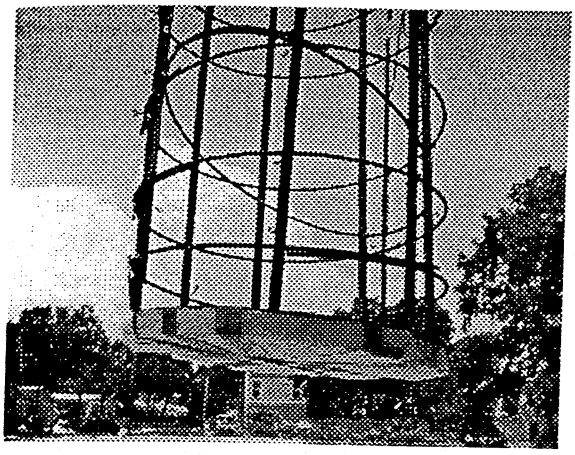

Figure 4.1 Styrofoam soft-toe assembly.

This type of testing requires that load cycling be used to ensure the toe capacity is regained. Because of the need for load cycling the HCM is the perfect device to use in association with soft toes. The initial cycles define the ultimate skin capacity and subsequent cycles develop the toe capacity. Once the plug completely compresses, the toe is seated and the designer can be assured of its capacity.

Figure 4.2 displays the load cycling effects on a 0.9 meter diameter, 7.4 meter long drilled shaft with a soft toe. The shaft was constructed in sand for the upper 3 meters, which was underlain by a 1.5 meter sandy clay layer, and finally tipped in Florida limestone. Foundation testing was completed using USF's 4 MN HCM.

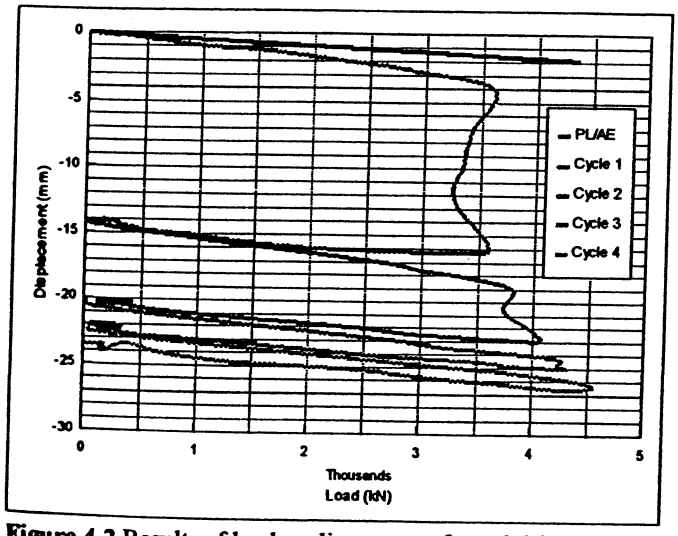

Figure 4.2 Results of load-cycling on a soft-toed drilled shaft.

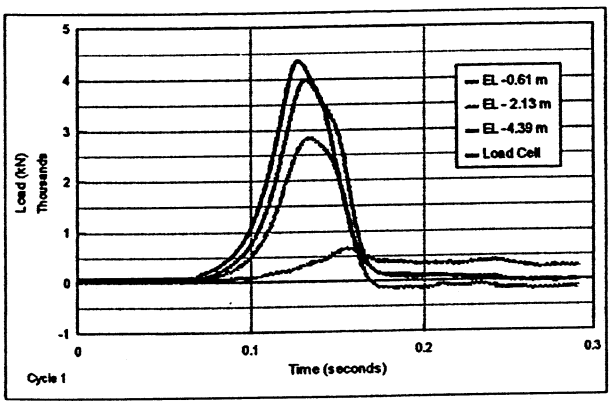

Figure 4.3 Cycle 1: toe load increases late in the test after significant displacement

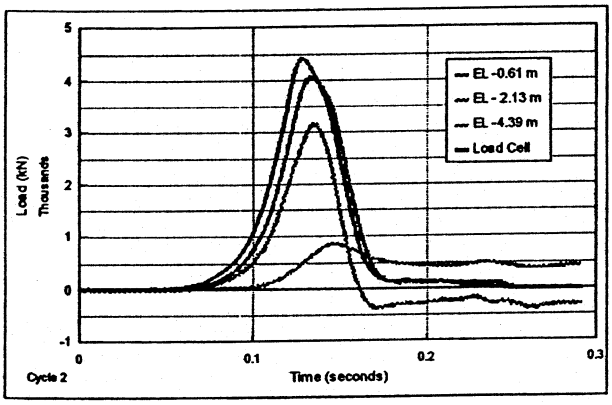

Figure 4.4 Cycle 2: toe load increases, and bottom rock layer fully mobilizes

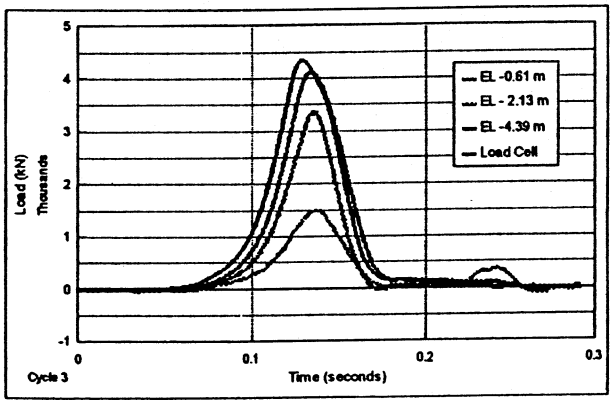

Figure 4.5 Cycle 3: toe load maximizes given the size of the equipment

Shown are four derived static load cycles along with the elastic compression curve. The first load cycle fails the shaft and fully mobilizes the skin friction. In subsequent cycles the toe capacity begins to develop until the third cycle when it has developed enough to exceed the device capabilities. This is confirmed by identical tow response in the fourth cycle. Figures 4.3 through 4.6 display the distribution of load throughout the shaft for cycles 1 through 4 respectively. Shown are the load traces from the Statnamic load cell (upper most) and the embedded strain gauges (lower most being the toe gauge).

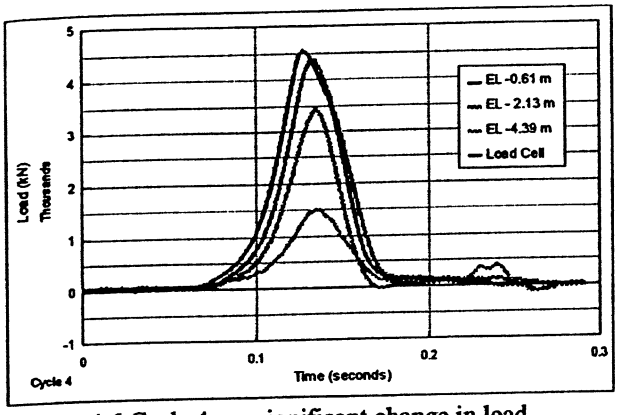

Figure 4.6 Cycle 4: no significant change in load distribution

Soft-toe test shafts allow the engineer to gain an understanding of in-situ soil strengths with smaller, more cost-effective devices.

4.2 *Post-Grouted Drilled Shaft Tips*

Although post-grouting of drilled shaft tips has been adopted in many countries, it is only now being considered for use in the southeastern United States. A program is presently developing to evaluate its effectiveness using Statnamic testing as the primary mechanism of loading. Statnamic testing is ideal for this effort because it is cost-effective and can be implemented without affecting normal construction techniques. Further, the HCM-equipped Statnamic device will allow for multiple staged load cycles that may be required, especially for ungrouted control piles, to fully define the shaft's ultimate end-bearing characteristics.

As a potential side benefit, post-grouting may provide a proof test for all shafts on a project, once the initial Statnamic load testing is completed. This can be accomplished by comparing the pile strain distribution from post-grouting with that of the Statnamic test.

5. DOWN-HOLE LATERAL MOTION SENSOR

5.1 *Background*

Recently, starting in 1996, lateral Statnamic load tests have been performed in addition to static tests to simulate more closely the lateral loads from ship impacts or seismic events. The duration of this test excludes the use of conventional inclinometers which are typically used to measure down-hole lateral displacements for static lateral load tests. Therefore, a dynamic device analogous to the inclinometer has been developed to measure lateral motions beneath the ground surface during a transient lateral load.

5.2 *Concept, Design and Development*

The laterally deflected shape of a steel pile can be estimated from bending strain measurements by double integrating a fitted moment equation. However, the deflected shape of a drilled shaft cannot usually be generated from embedded strain gages due to the changing moment of inertia after tension cracks form in the concrete. The need for displacement measurements during lateral Statnamic tests

gave rise to the *down-hole lateral motion sensor* (DLMS). This device has been designed with several significant features: (1) it can be preset to monitor motion in line with the applied load, (2) it is compatible with standard inclinometer casings, (3) it can be lowered to any desired depth in the casing, and (4) it is retrievable. Additionally, by using several devices in a string, the deflected shape of the casing can be defined.

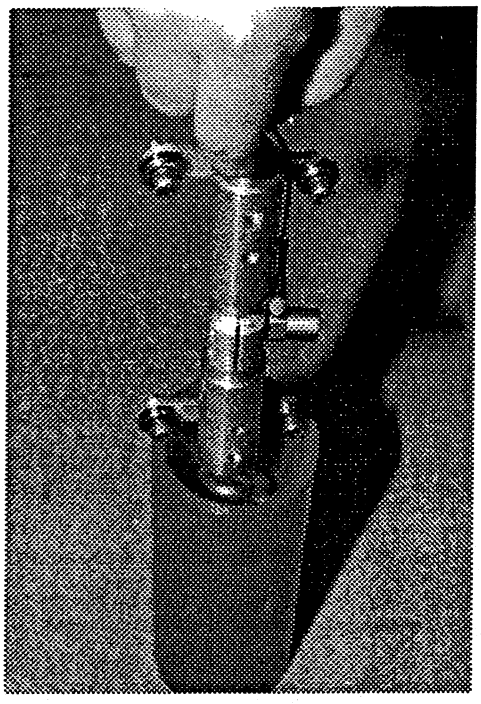

Figure 5.1 Down-hole lateral motion sensor (DLMS) assembly.

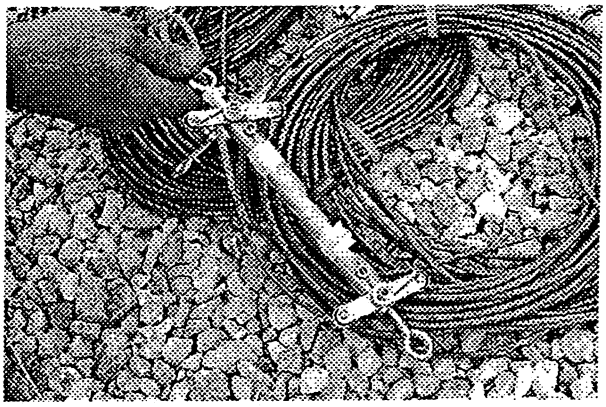

Figure 5.2 Prototype DLMS in Opelika, Alabama.

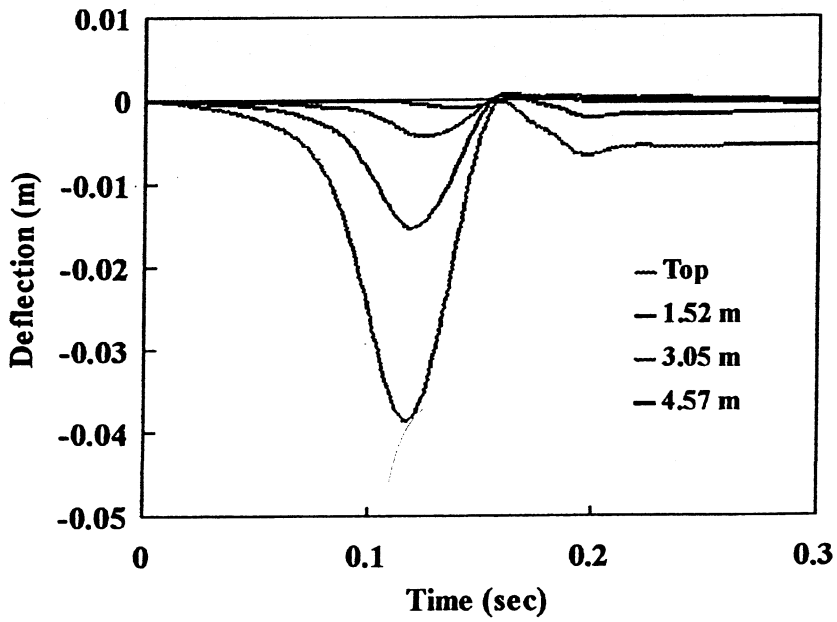

Figure 5.3 Displacement response from four locations along the shaft.

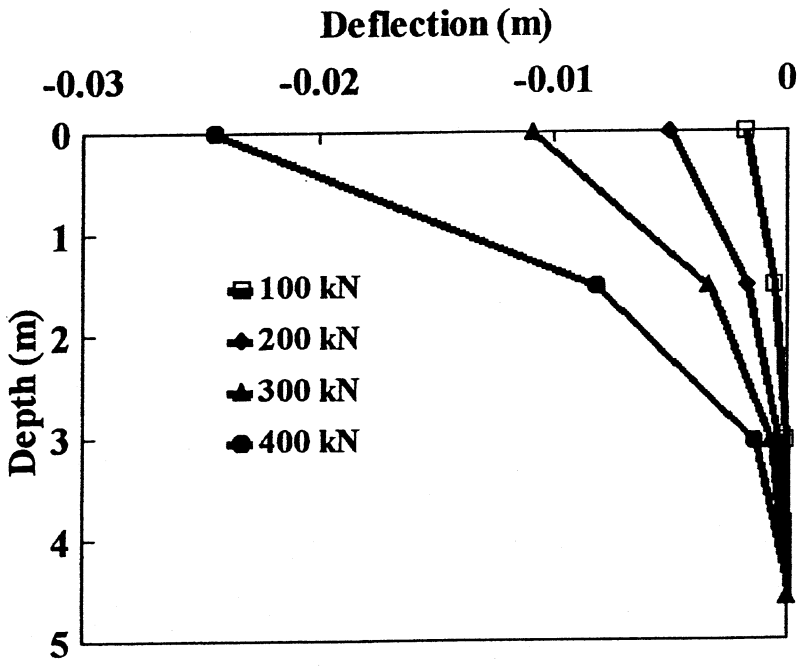

Figure 5.4 Deflected shape of the shaft at 100, 200, 300, and 400 KN.

The device basically uses an accelerometer aligned with the direction of loading. Because the grooves of the inclinometer casing are typically oriented other than that desired, the accelerometer is mounted on an adjustable collar which can be secured in a prescribed direction of loading. This orientation is maintained during installation using spring loaded wheels that snap into the grooves of the inclinometer casing (similar to that of the inclinometer). Figures 5.1 and 5.2 show the DLMS sensor prior to installation.

Several Statnamic load tests have been conducted on drilled shafts where the deflected shape was determined from the down-hole lateral motion sensor data. Each program compared the foundation response of static and Statnamic lateral loads. Full details of these results can be found elsewhere (Brown et al., 1998). Results from data obtained from a string of three devices (1.52, 3.05, and 4.57 meters below the ground surface) are shown in Figure 5.3. This figure shows the displacement trace of a 10 meter, single-shaft lateral load test at the Auburn University site in Opelika, Alabama. Figure 5.5 shows the deflected shape of the shaft from four instances during the Statnamic loading.

6. SUMMARY

In the past two years, the University of South Florida has performed numerous Statnamic tests due to the support received from state and federal agencies, and private industry. As a direct result, an extensive research program has been developed in each of these areas: shallow foundations, deep foundations, lateral testing, and instrumentation. With the purchase of a hydraulic catch mechanism, USF researchers have been able to explore new applications and refine existing procedures. The objective of this paper is to encourage further discussion of these topics. Comments or questions, addressed to gmullins@eng.usf.edu, would be appreciated.

REFERENCES

Bermingham, P. & Janes, M. 1989. An innovative approach to load testing of high capacity piles. *Proc. Int. Conf. On Piling and Deep Foundations*, London, 1: 409-413.

Brown, D., Chakraborty, S., and Mullins, G. 1998. Dynamic measurements and data analysis of statnamic lateral loading. *Second International Statnamic Seminar*, Tokyo, Japan.

Middendorp, P., Bermingham, P., and Kuiper, B. 1992. Statnamic load testing of foundation piles. *Proc. Of the 4th Int. Conf. On the Application of Stress-Wave Theory to Piles*, The Hague, The Netherlands, A.A. Balkema Publishers, 581-588.

The behavior of piles in clay during Statnamic and different static load testing procedures

E.L. Hajduk & S.G. Paikowsky
University of Massachusetts, United States

G. Mullins & C. Lewis
University of South Florida, United States

C.D. Ealy
Federal Highway Administration, McLean, VA, United States

N.M. Hourani
Massachusetts Highway Department, Boston, MA, United States

ABSTRACT: A long-term investigation of pile capacity in the Boston Area was carried out in predominately fine-grained soils at a bridge reconstruction site in Newbury, Massachusetts. This investigation included heavily instrumented piles subjected over a lengthy period of time to different static load and dynamic measurements during driving and restrikes. Staged Statnamic load tests were conducted on two of the test piles following the completion of the capacity gain investigation. A comparison is presented between the final static load tests and the Statnamic testing. Conclusions are drawn regarding (i) the accuracy of the testing, (ii) the Statnamic measurements versus dynamic measurements during testing and (iii) the effect of the testing procedure on the surrounding soil behavior.

1. INTRODUCTION

An investigation of pile capacity gain with time was conducted by the Geotechnical Engineering Research Laboratory of the University of Massachusetts - Lowell (UML). Three full-scale instrumented piles were installed at a bridge reconstruction site along Route 1 in Newbury, MA. Static and dynamic testing were conducted over a period of one year and two of the test piles were subjected to Statnamic testing after the capacity gain investigation had been completed. The presented Statnamic tests are the first to be conducted on deep foundations in the New England area. The Newbury Testing program provided the conditions to examine Statnamic testing in the region (1) the soil profile at the Newbury Site is typical of the Boston, Massachusetts area and a detailed subsurface investigation was carried out at the site and extensive testing was conducted on the test pile cluster and (2) the piles and the soil were well instrumented.

A series of static load tests were performed on each test pile at the end of the pile capacity investigation. The purpose of these tests was to evaluate the final pile capacity as well as to compare various procedures of static load testing. Measurements of the pore pressure along the piles and in the ground piezometer field showed that all excess pore pressure due to driving of the test pile itself or an adjacent pile had completely dissipated at that stage. In addition, a significant amount of time (minimum 4 months) had passed since the last adjacent test pile had been driven, allowing for all pile capacity gain to be completed. Based on this information, it was concluded that these final static load tests would determine the final pile capacity.

The final static load tests are classified as slow maintained, short duration, and static-cyclic, based on the pile loading increments, length of time each load increment was held constant, or loading rate. The slow maintained and short duration tests were conducted according to the of the Massachusetts Highway Department (1995). The static-cyclic tests were conducted according to criteria developed in a concurrent research that is beyond the scope of the present paper (Paikowsky and Operstein, 1999). To minimize the effects of each static load test on each subsequent test, the testing was conducted in the following order: slow maintained, short duration, and static-cyclic. This schedule allowed for the maximum possible time between

loading cycles while allowing the tests to be performed over a short period. Furthermore, the pore pressure measurements along the pile were allowed at or near hydrostatic conditions before the next static load test was conducted. Based on this information, it was assumed that any effect each test may have on another would be negligible.

The results from the various load tests conducted on the two test piles showed that each had reached final capacity. Pore pressure measurements along the piles and in the ground piezometer field before the Statnamic testing indicated that they were at or near hydrostatic conditions. This suggested that the test piles had gained no further capacity.

The Statnamic testing was conducted 6 and 4 months after the completion of static load testing for Test Piles #2 and #3, respectively. A summary of the static and Statnamic testing performed on the two test piles is listed in Tables 1 and 2 for Test Pile #2 and #3, respectively. Each pile was subjected to several Statnamic tests at increasing loads until approximately twice the final static failure load was reached. A total of 10 Statnamic tests were conduccted on the two test piles. Six Statnamic tests at increasing capacities were conducted on TP#3, with the tests being labeled TP#3-1 through 6. After completion of these tests, the Statnamic device was positioned over Test Pile #2. Four Statnamic tests were completed on TP#2 at various capacities. These tests were labeled TP#2-1 through 4. All Statnamic testing for both piles was conducted on the same day within a 10-hour period.

Table 1 Timetable of testing for test pile #2

	TP#2 SLT7	TP#2 SLT8	TP#2 SLT9	TP#2-1 – 4
Type of Test	Slow Maintained	Short Duration	Static-Cyclic	Statnamic
Date of Test	10/22/97 to 10/24/97	10/27/98	10/28/98	4/23/98
Time from End Of Driving (EOD)	8 Months	8 Months	8 Months	14 Months

Table 2 Timetable of testing for test pile #3

	TP#3 SLT3	TP#3 SLT4	TP#3 SLT5	TP#3-1 – 6
Type of Test	Slow Maintained	Short Duration	Static-Cyclic	Statnamic
Date of Test	12/2/97 to 12/4/97	12/4/98	12/5/98	4/23/98
Time from End Of Driving (EOD)	12 Months	12 Months	12 Months	16 Months

2. THE NEWBURY TEST SITE

The Newbury bridge reconstruction site is located along Route 1 on the Newbury - Newburyport border, north of Boston, Massachusetts. The test pile program consisted of three-instrumented test piles laid out in a triangular formation near the north abutment of the bridge. In addition to the test piles, a ground piezometer field consisting of ten vibrating wire piezometers was installed to monitor the piezometric pressures at various elevations and distances away from the test piles. Seven piezometers were located near the center of the clay layer, with an average depth of 11m (36ft). The remaining three ground piezometers were located in a silty sand layer, with an average depth of 29m (69ft). A report describing the test pile cluster, the ground piezometer field, and the testing program is currently being prepared for the Massachusetts Highway Department (Paikowsky and Hajduk, 1998). Figure 1 shows the test pile layout and the ground piezometer field.

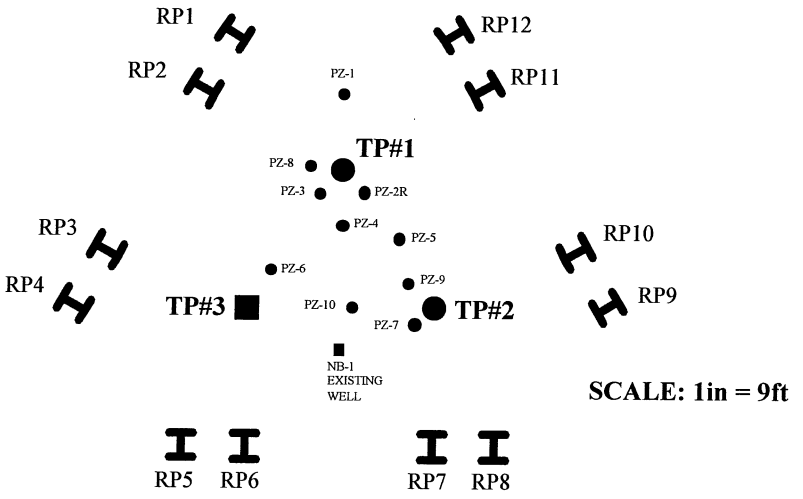

Figure 1. Newbury test site layout (after Paikowsky and Hajduk, 1998).

The soil stratigraphy of the site is typical of the conditions found in the Boston area. The general soil profile at the pile testing location (from ground surface downward) consists of the following soil strata: 8 feet (2.44 meters) of granular fill composed of very dense, brown sand and gravel intermixed with frequent concrete fragments, overlies a thin layer (approximately 1 foot (0.3 meters)) of highly compressible organic silt and peat. In order to protect the test piles, these layers were excavated and cased with steel pipe sections. Below the fill and organics is an approximately 45 feet (13.7 meters) thick deposit of a marine clay, known as Boston Blue Clay. The clay consists of approximately 9 feet (2.7 meters) of very stiff to medium stiff, over-consolidated layer (crust), over 20 feet (6.1 meters) of soft normally consolidated clay and 16 feet (4.9 meters) normally consolidated clay. An interbedded deposit of silt, sand, and clay approximately 9.5 feet (2.9 meters) thick underlies the clay. Below this interbedded deposit is a layer of silty sand approximately 8 feet (2.4 meters) thick.. Another interbedded deposit of silt, sand, and clay approximately 7.5 feet (2.3 meters) thick underlies the silty sand. Below this interbedded deposit is a layer approximately 8 feet (2.4 meters) thick of medium dense to dense, fine to medium sand. Underlying the fine to medium sand is a dense glacial till consisting of medium dense to dense, fine to coarse sand and gravel, with traces of silt and rock fragments. Good quality, unweathered bedrock was encountered at approximately 100 feet below the ground level (elevation 81.7 feet) (Paikowsky and Chen, 1998). A detailed characterization of the subsurface at the site is provided by Paikowsky and Chen, (1998). The typical soil profile of the site and results from a CPT test conducted alongside the configuration of Test Piles #2 and #3 are shown in Figure 2.

3. INSTRUMENTED TEST PILES

Three full-scale instrumented test piles, two friction and one end bearing, were installed at the Newbury test site. Only the two friction piles were selected for additional Statnamic testing. These two piles consisted of a steel pipe pile and a square, pre-stressed concrete pile, designated Test Pile #2 and #3 respectively. A report is currently under preparation detailing the design and construction of these test piles (Paikowsky and Hajduk, 1998).

Test Pile #2 (TP#2) is a 324mm diameter x 13mm x 24.4m long (12.75in diameter x 0.5in thick x 80ft) steel pipe pile. This pile is instrumented with electrical resistance piezometers, vibrating wire piezometers, and strain gages at various depths below the pile top. The piezometers were installed in such a manner that they lie halfway between sets of strain gages. This arrangement allowed for pore pressure measurements to be taken and compared with an

average skin resistance during static load testing. Additional electrical resistance strain gages and piezo-resistive accelerometers were located at the middle and tip of the pile to record dynamic measurements. Over the course of pile capacity gain investigation, an interior water leak damaged the electrical resistance gages of TP#2. These instruments were therefore not available during the Statnamic testing. Pile Driving Analyzer™ (PDA) load transducers and piezo-electric accelerometers were also mounted near the pile top during dynamic and Statnamic testing. A instrumentation layout of TP#2 is shown in Figure 2 relative to the soil profile.

Test Pile #3 is a 356mm square x 23.9m long (14in square x 78.5ft) pre-stressed concrete pile. This pile is instrumented with four vibrating wire piezometers and six vibrating wire strain gages located at various distances from the pile top. As with TP#2, PDA load transducers and piezo-electric accelerometers were also mounted near the pile top during dynamic and Statnamic testing. Figure 2 shows the instrumentation layout of TP#3 in relation to the typical soil profile.

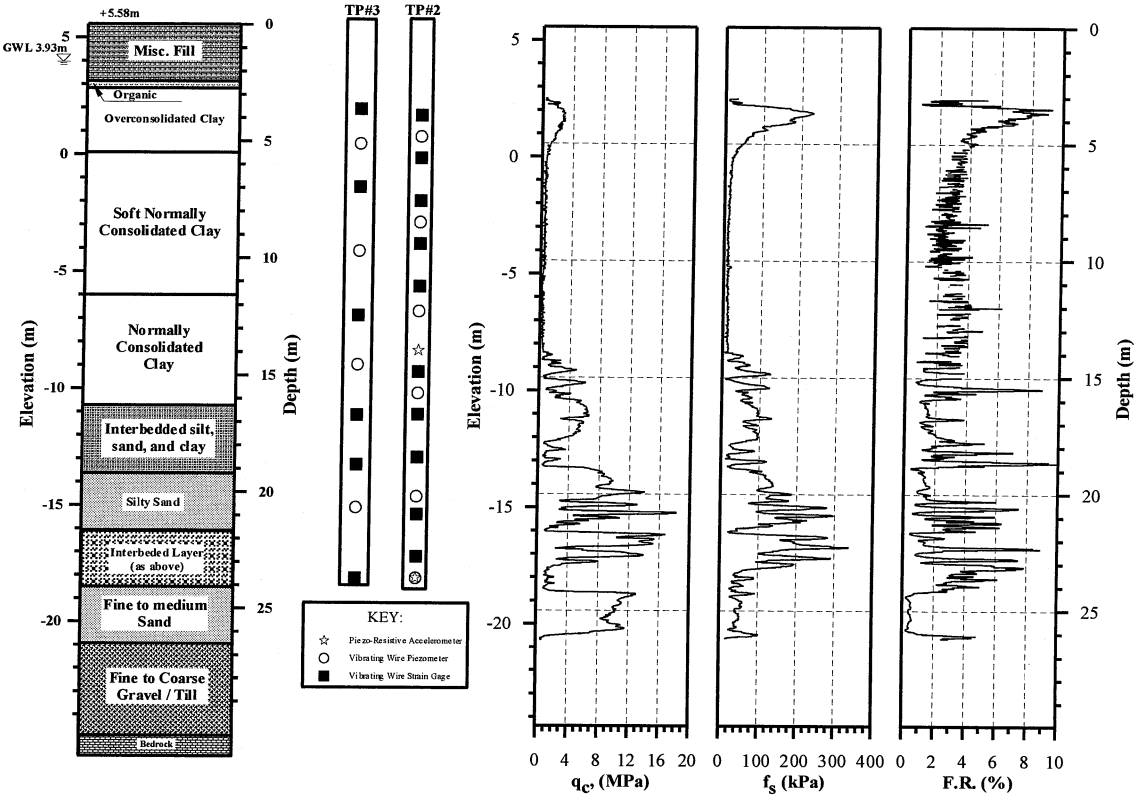

Figure 2. Newbury site soil profile with test piles #2 and #3 layouts and typical CPT test results.

4. LOAD TESTING METHODS

4.1 *Static load tests*

Four HP14x89 reaction piles were driven along each side of the test pile triangle before the installation of the test piles. Each reaction pile was driven to a minimum depth of 18.3m (60ft) and was located a minimum of 2.1m (7ft) from any test pile. This distance was deemed sufficient enough to not disturb the soil at the test pile locations. The triangular layout of the reaction frame allowed for a reaction beam (two W33x201 steel beams) to be placed over any test pile at any time to conduct a static load test. Load was transferred from the reaction beam to the reaction piles with HP14x89 transfer beams. The configuration over each test pile was

identical and produced a 4.4MN (500 ton) test frame. Figure 1 shows the reaction pile layout relative to the test piles. Paikowsky and Hajduk (1998) describe in detail the static load test instrumentation used for TP #2 and #3. All the reaction piles were removed from the site on 1/29/98 to 1/30/98, four months before the Statnamic testing.

4.2 *Statnamic load tests*

A Statnamic load test involves the application of a short duration load (approximately 120ms) to a pile or caisson. Burning a solid fuel inside the Statnamic device produces a high-pressure gas. The attendant force associated with this gas accelerates a reaction mass upward at 20 g's, producing an equal force on the pile. Typically, the reaction mass weighs 5% of the desired load (Justason et al., 1998).

The Statnamic device consists of a reaction mass, a fuel chamber, piston, and silencer. In addition, a gravel chamber or a hydraulic mechanism is used to catch the reaction mass after it is propelled upward. A load cell is placed between the piston and pile to record the load placed on the pile. Displacement is measured by use of a laser sensor. Acceleration is recorded via a servo accelerometer near the load cell. In addition to this instrumentation, Pile Dynamics' load transducers and piezo-electric accelerometers were also attached to the pile to record force and acceleration similar to conventional dynamic pile monitoring during driving. More information on Statnamic testing is provided by the test system manufacturer (Berminghammer, 1997).

A 8MN Statnamic device, owned jointly by the University of South Florida and the Federal Highway Administration, was used at the Newbury Test Site. This device is equipped with a hydraulic catch mechanism, which allows for rapid consecutive testing on one pile. Figure 3 shows the Statnamic testing apparatus on Test Pile #2.

Figure 3. View of Statnamic load test apparatus over test pile #2

4.3 *Pile capacity determination*

In order to standardize the pile capacity determination, Davisson's Failure Criteria was used to determine the pile capacity for the maintained, short duration, and Statnamic load tests. This procedure is consistent with Massachusetts Highway Department specifications and is typically used as the standard method of pile capacity determination. For the static-cyclic tests pile capacity is determined from the points formed by the intersection of the loading and unloading curves. Paikowsky and Operstein (1999) provide details regarding the pile capacity determination under static cyclic test procedures.

5. TEST RESULTS

5.1 *Static load test results*

For the maintained and short duration load tests conducted on Test Pile #2, each test showed a pile capacity of 750kN (84 tons), near a displacement of 14mm (0.55in). The static-cyclic tests showed that a capacity of 670kN (75 tons) was achieved through the recommended analysis procedure. A summary of the results of static load testing conducted on Test Pile #2 is listed in Table 3. The load - displacement curves for all three tests are shown in Figure 4.

Table 3 Summary of static load test results for test pile #2.

	TP#2 SLT7	TP#2 SLT8	TP#2 SLT9
Type of Test	Slow Maintained	Short Duration	Static-Cyclic
Failure Load	750 kN (84 tons)	750 kN (84 tons)	670 kN (75 tons)
Maximum Displacement	33.9 mm (1.333 in)	25.9 mm (1.020 in)	26.8 mm (1.055 in)
Permanent Set	28.5 mm (1.121 in)	20.7 mm (0.815 in)	21.4 mm (0.841 in)

The analysis of the maintained and short duration tests on TP#3 showed a pile capacity of 1150kN (130 tons), near a displacement of 12.3mm (0.48in). The static-cyclic tests showed that a capacity of 1025kN (115 tons) was achieved through the recommended analysis procedure. Table 4 presents the results of the static load tests conducted on Test Pile #3. The load - displacement curves for all three tests are shown in Figure 5.

Table 4 Summary of static load test results for test pile #3.

	TP#3 SLT3	TP#3 SLT4	TP#3 SLT5A
Type of Test	Slow Maintained	Short Duration	Static-Cyclic
Failure Load	1150 kN (130 tons)	1150 kN (130 tons)	1025 kN (115 tons)
Maximum Displacement	34.8 mm (1.371 in)	26.8 mm (1.056 in)	23.7 mm (0.933 in)
Permanent Set	26.9 mm (1.059 in)	21.0 mm (0.828 in)	18.2 mm (0.716 in)

The near identical load-displacement curves of all three static load tests as well as the identical Davisson's failure load for the maintained and short duration load tests for both Test Piles #2 and #3 showed that each pile had achieved its maximum capacity. In addition, this information showed that the repeated loading cycles did not substantially affect each subsequent test.

5.2 *Statnamic test results*

The Statnamic test results conducted on Test Piles #2 and #3 are presented in Figures 4 and 5, respectively. In both figures, the Statnamic load vs. displacement is shown in section (a), while the derived static load vs. displacement is shown in section (b). A summary of the Statnamic test results for Test Pile #2 and #3 are presented in Tables 5 and 6, respectively.

The Unloading Point Method was used to calculate the derived static force, which is the common method of analyzing Statnamic tests. This method determines the static resistance by assuming that the long duration of the Statnamic load allows for modeling of the pile as a concentrated mass and a series of springs (Middendorp and Bielefeld, 1995). The derived static curve shows the load-displacement relationship with the inertia and damping forces removed from the measured Statnamic force (Justason et al., 1997). The mathematical procedure for Unloading Point Method is described by Middendorp et al. (1992).

For the first test conducted on Test Pile #2, the pile experienced small displacements that could not be distinguished from the noise of the data. Data for the third test conducted on Test Pile #3 was not properly collected. These two test results are therefore not presented.

Examination of the Statnamic force - displacement curves (refer to Figures 4(a) and 5(a)) show that the pile load - displacement relations during all tests conducted on both piles was primarily elastic. Each test follows the elastic compression curve of the pile and has little or none permanent set at the end of each Statnamic test. Both piles behave in a similar manner with the elastic behavior being more pronounced in Test Pile #2. Several Statnamic tests were conducted at loads greater than the static failure load on both piles. No trend that could indicate a clear failure of the pile was observed.

The derived static - displacement curves followed the same trend as the Statnamic force - displacement curves (see Figures 4(b) and 5(b) for Test Piles #2 and #3, respectively). The results of the derived static analysis show no indication of failure based on load - displacement relations or as defined by Davisson's criteria, for all the load tests.

In addition to the analysis above, a comparison was conducted between the force measured by the Statnamic load cell and the Pile Dynamic load transducers attached directly to the pile top. The primary purpose of this comparison was to observe if there was any stress wave phenomena present that would affect the measurement of the Statnamic load cell, such as the presence of tension waves. Figures 6 and 7 show the comparison between the average force measured by the load transducers and the Statnamic load cell readings during the Statnamic tests TP#2-2 through 4 and tests TP#3-4 through 6, respectively. The Statnamic force is shifted in time and magnitude (zeroed) to allow for a comparison with the average dynamic load transducer measurements. Both shifts between the two measured force signals is due to the difference in the data acquisition system operations. The Pile Dynamics PDA responds to dynamic forces only (all stationary forces are zeroed) and was triggered based on an increase in the measured force. The Statnamic data acquisition system measures absolute forces and presents an entire time span before and after the event. The time and magnitude shifts are therefore justified and the Statnamic force was adjusted. For each test, an excellent agreement exists between both measurements (see Tables 5 and 6).

Pore water pressure measured along Test Pile #3 during the Statnamic testing are presented in Figure 8. Measurements of the pore water pressure for the ground piezometer field are presented in Figure 9. The decrease in pore water pressure during shearing suggests that the clay along the pile is under over-consolidated clay conditions. A similar behavior was also displayed for the majority of the ground piezometer measurements in the clay layer. An exception was ground piezometer number 7 (Gnd PZ-7), which showed an increase in pore pressure during the testing of Test Pile #2. The proximity of this piezometer to the test pile (less than 3 pile radii) could explain this measurement. For the ground piezometers located in the silty sand layer, any buildup of pore pressure was quickly dissipated.

Table 5 Summary of Statnamic test results for test pile #2.

	TP#2 - 2	TP#2 - 3	TP#2 – 4
Maximum Statnamic Force	572 kN (64 tons)	976 kN (110 tons)	1186 kN (133 tons)
Duration of Test	0.24 sec	0.19 sec	0.18 sec
Maximum PDA Force	531 kN (60 tons)	890 kN (100 tons)	1047 kN (118 tons)
Maximum Displacement	2.6 mm (0.102 in)	10.2 mm (0.402 in)	12.1 mm (0.476 in)
Permanent Set	0.3 mm (0.012 in)	3.0 mm (0.118 in)	3.0 mm (0.118 in)

Table 6 Summary of Statnamic test results for test pile #3.

	TP#3-1	TP#3-2	TP#3–4	TP#3-5	TP#3-6
Maximum Statnamic Force	538 kN (60 tons)	1115 kN (125 tons)	1689 kN (190 tons)	1943 kN (218 tons)	1186 kN (250 tons)
Duration of Test	0.23 sec	0.17 sec	0.15 sec	0.14 sec	0.13 sec
Maximum PDA Force	NA	1257 kN (141 tons)	1869 kN (210 tons)	2010 kN (226 tons)	2303 kN (259 tons)
Maximum Displacement	2.1 mm (0.083 in)	6.1 mm (0.240 in)	11.1 mm (0.437 in)	13.5 mm (0.531 in)	16.1 mm (0.634 in)
Permanent Set	0.1 mm (0.004 in)	1.1 mm (0.043 in)	3.3 mm (0.130 in)	3.3 mm (0.130 in)	3.3 mm (0.130 in)

6. CONCLUSIONS

The Statnamic test produces a compression force wave of a much longer duration (in the order of one order of magnitude) when compared to the typical dynamic impact during driving. This force application cannot however be considered pseudo-static and resulted in a significantly higher response even when compared to a very fast static load test. The static-cyclic tests presented in Figures 4 and 5 were conducted in about 15 minutes per cycle. Their good match to the slow maintained and short duration tests suggest that the impact of the Statnamic test requires dynamic interpretation. The procedures suggested by Middendorp and Bielefeld (1995) seemed to produce excellent results in stiff and/or granular soils. The unfavorable results obtained in the presented tests suggest an influence of soil viscosity alongside buildup of pore pressure in fine-grained soils. These results may require the development of additional analysis tools and experience before the reliable application of the Statnamic test under similar soil conditions.

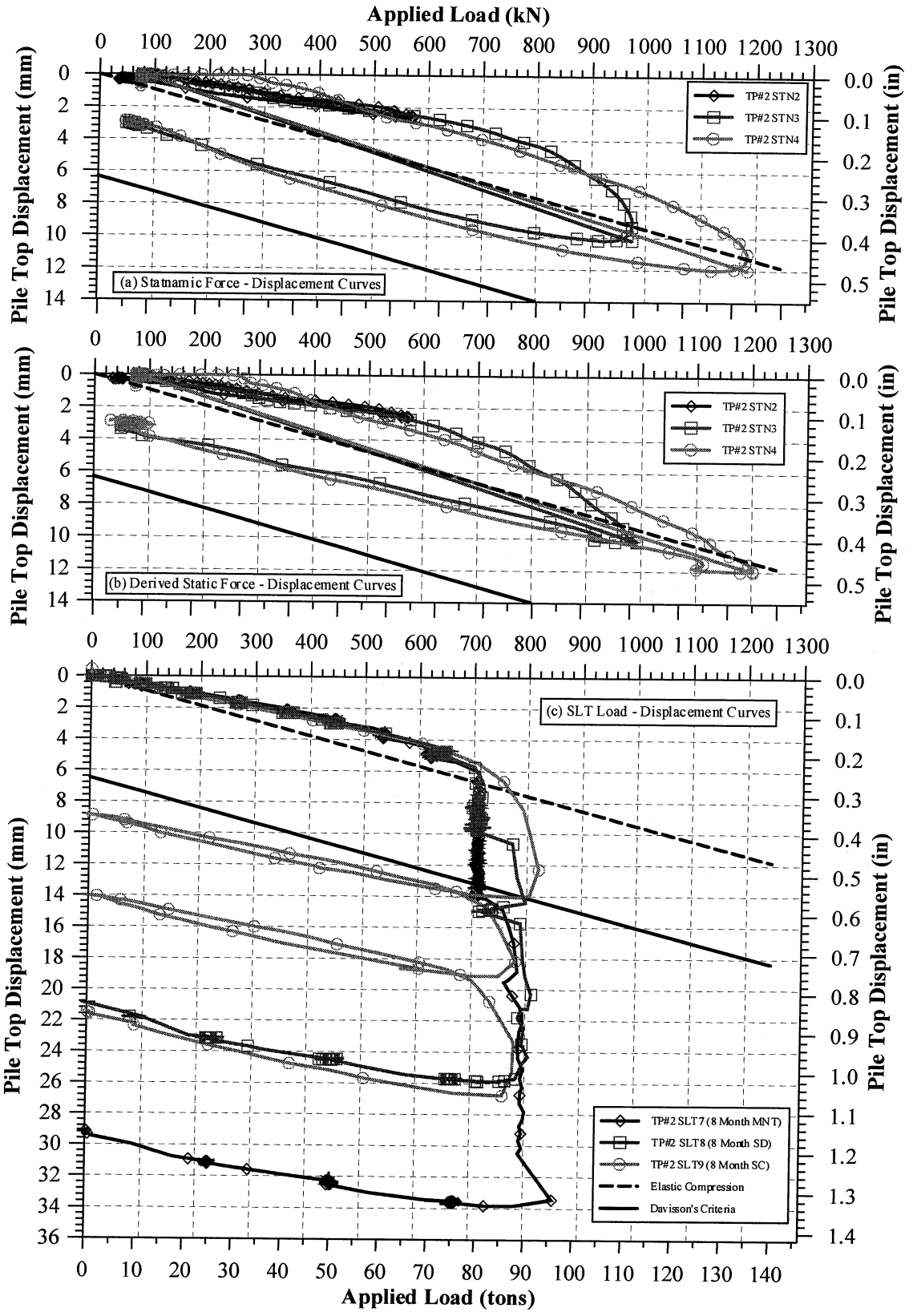

Figure 4. Static and Statnamic test results for test pile #2.

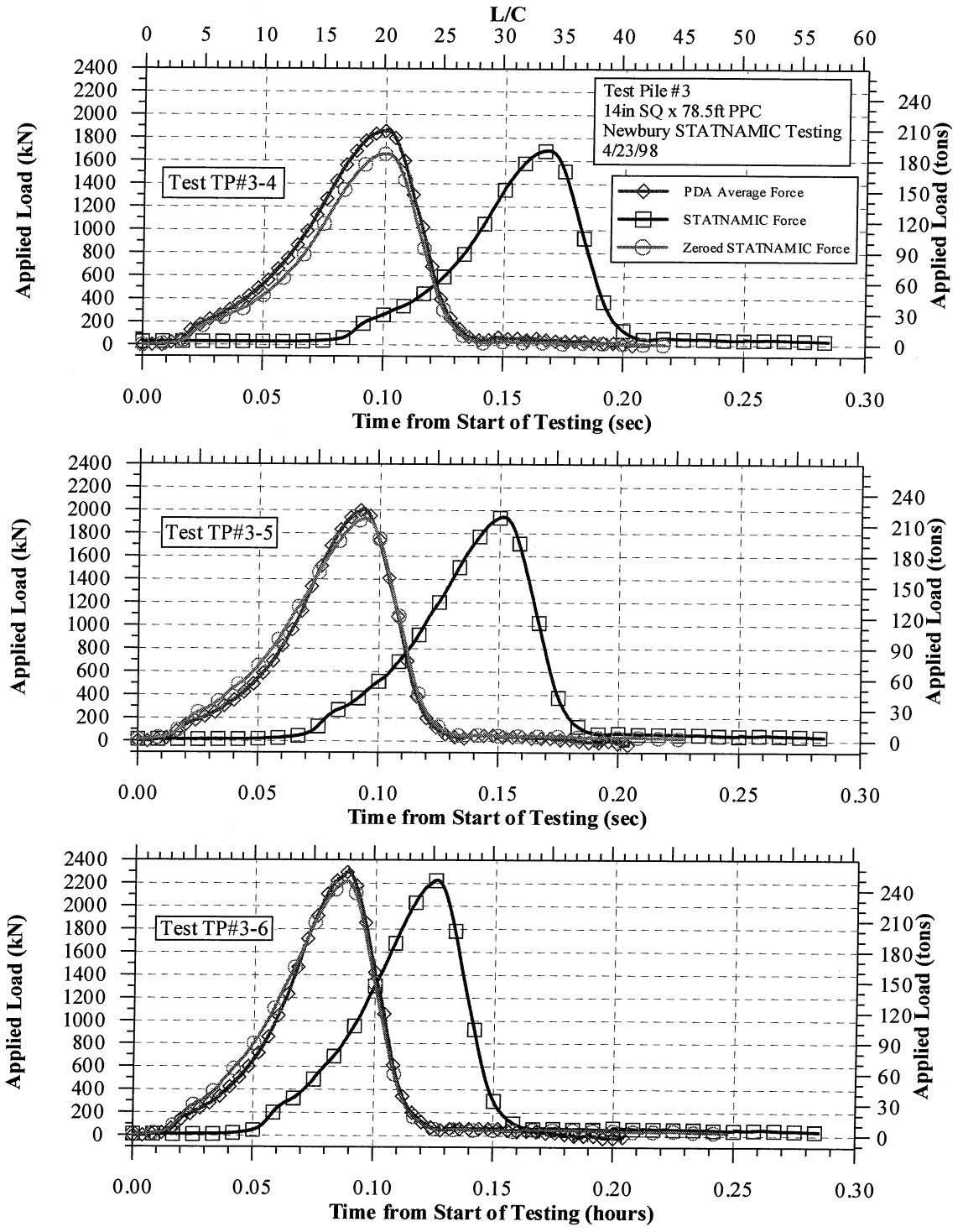

Figure 5. Static and Statnamic test results for test pile #3.

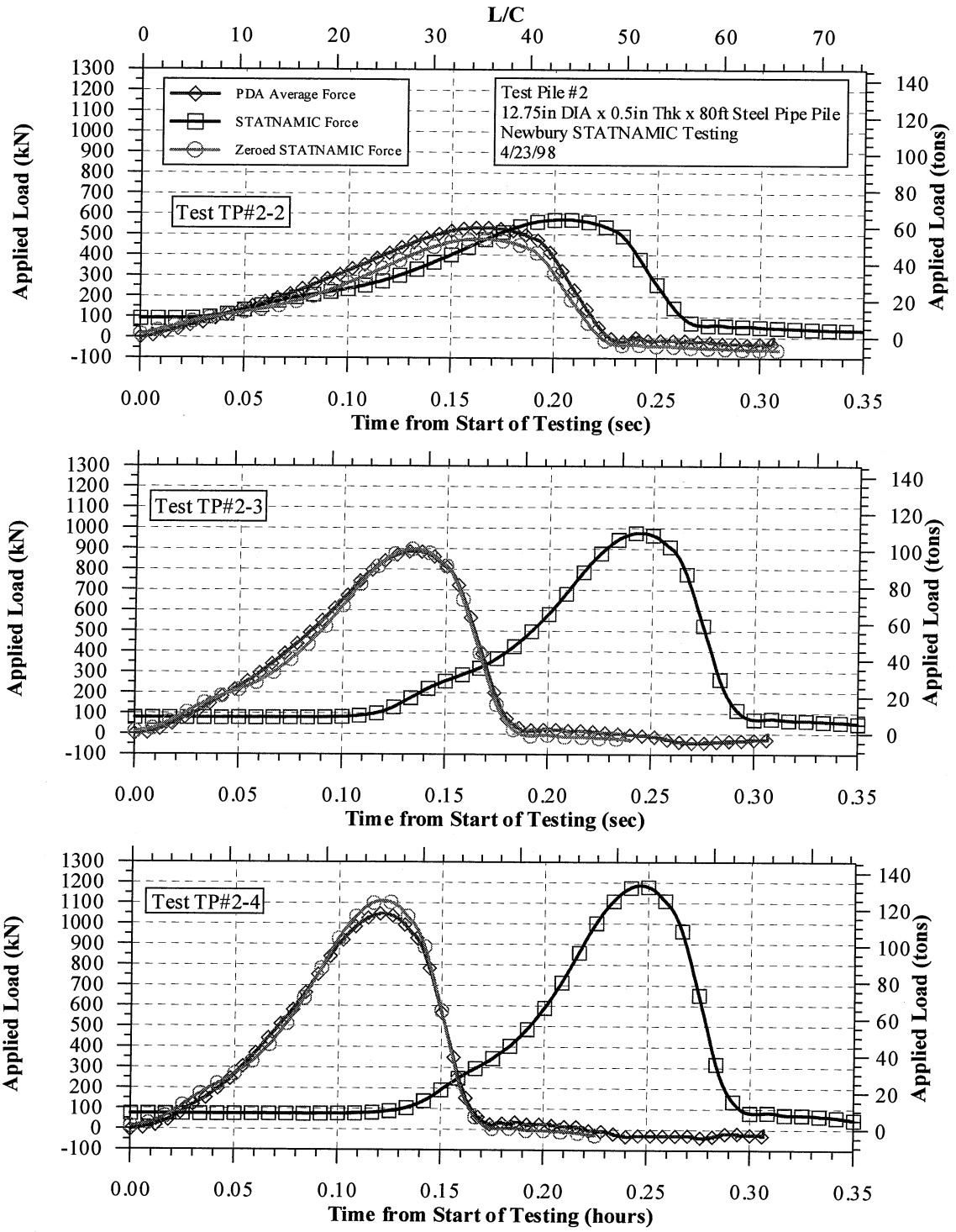

Figure 6. Statnamic and pile dynamic force measurements for test pile #2.

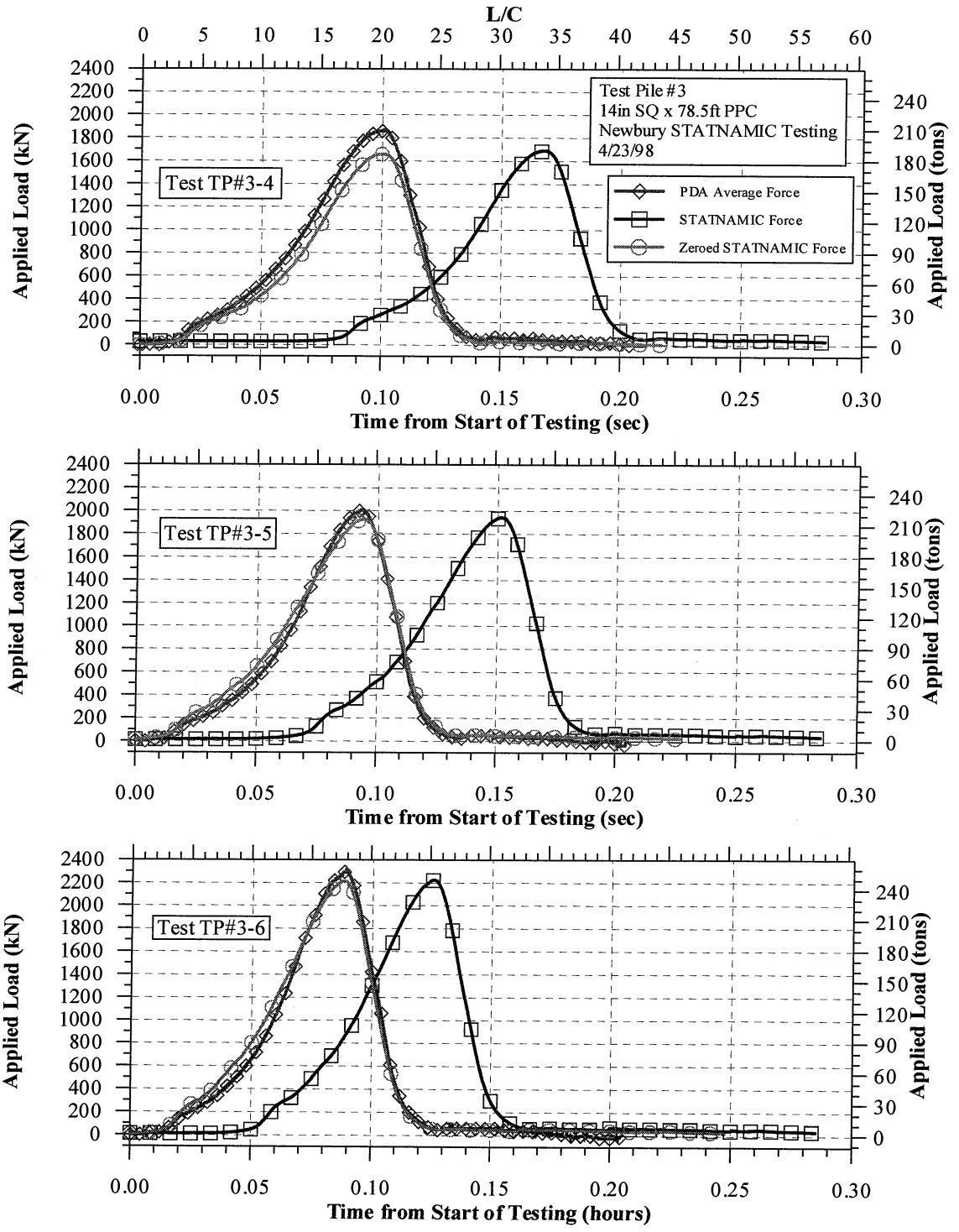

Figure 7. Statnamic and pile dynamic force measurements for test pile #3.

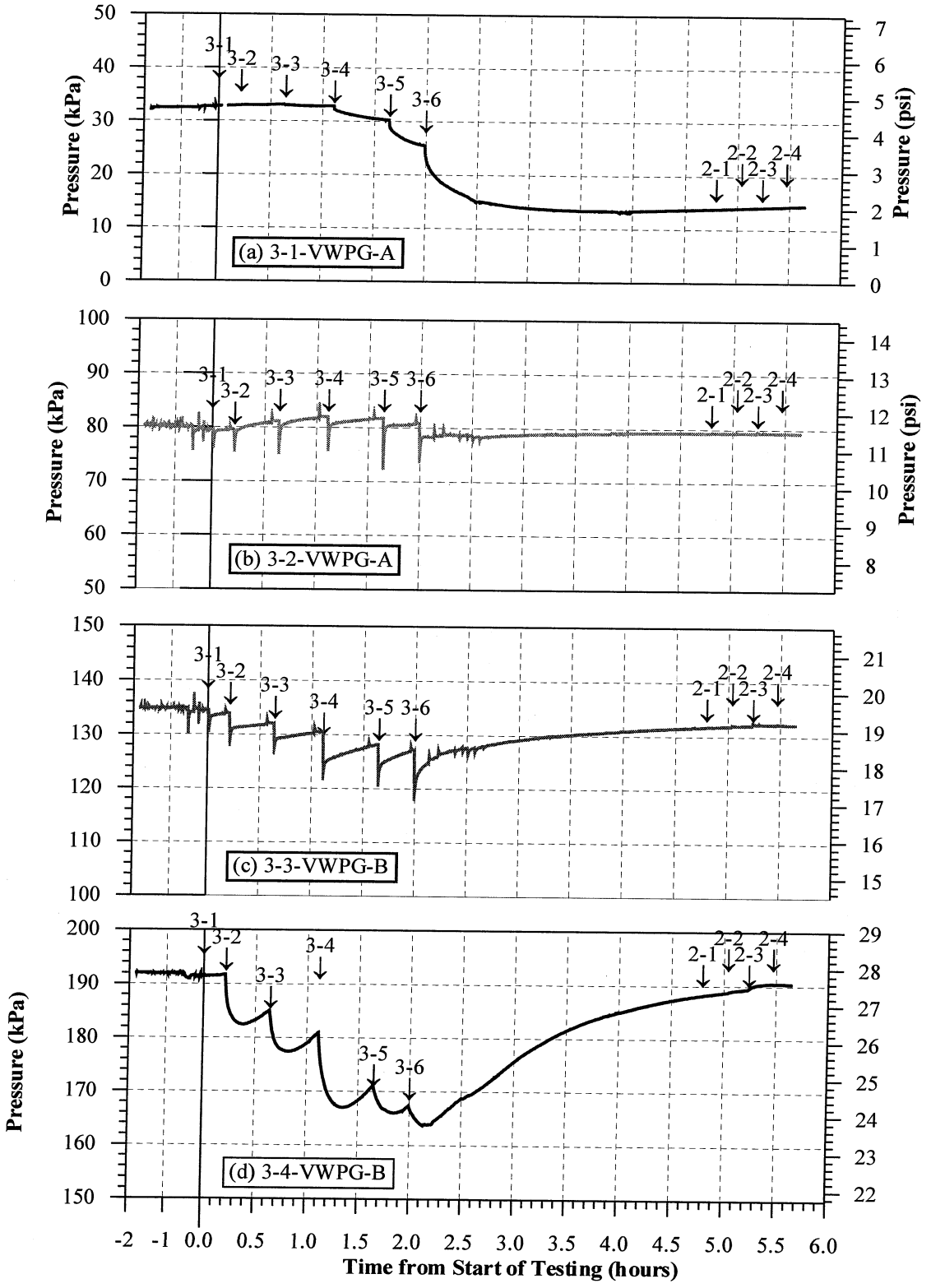

Figure 8. Vibrating wire piezometer measurements during Statnamic testing for test pile #3.

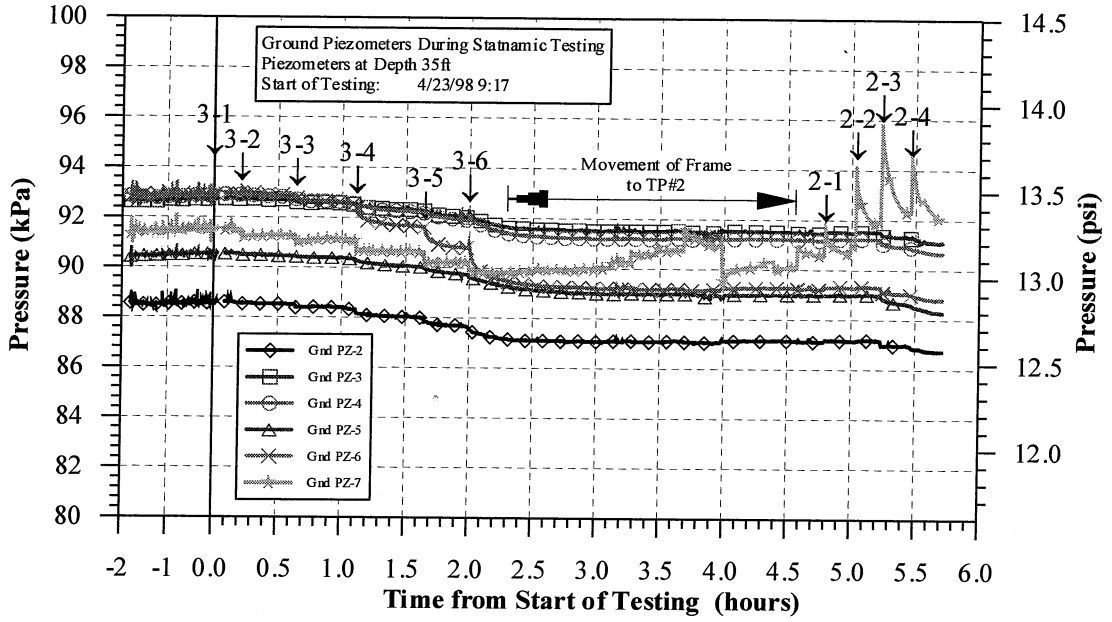

(a) Ground piezometers in the clay layer.

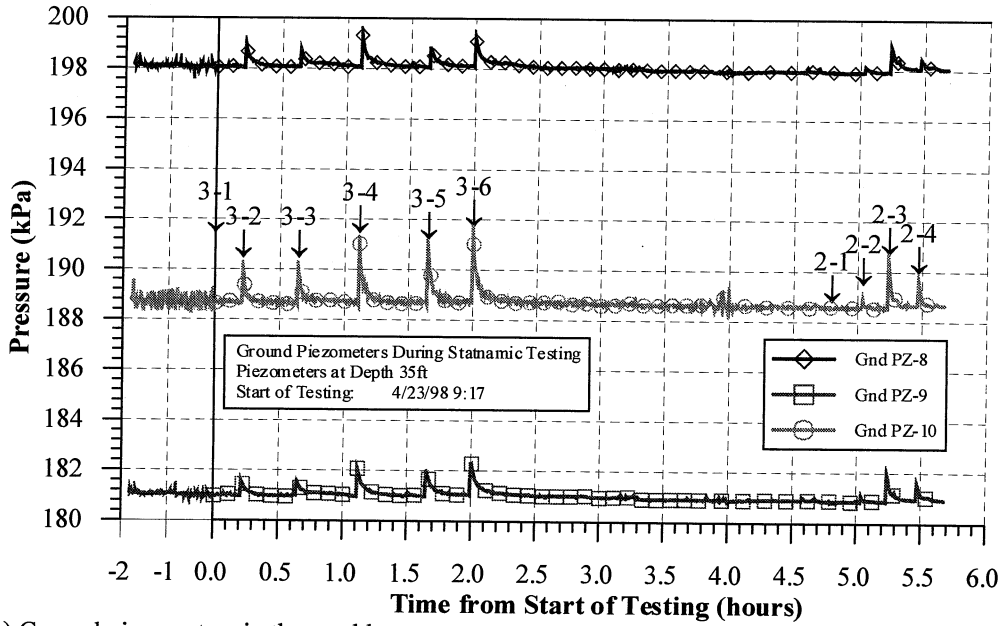

(b) Ground piezometers in the sand layer.

Figure 9. Ground piezometer measurements during Statnamic testing.

ACKNOWLEDGEMENTS

The presented results are a part of a long-term research project supported by the Massachusetts Highway Department (MHD) and assisted by the Federal Highway Administration (FWHA).

The authors would like to acknowledge the assistance of Mr. Al DiMillio of the FHWA and John Pettis of the MHD. Also acknowledged are all the individual and companies associated with this research project, in particular the Graduate Research Students of the Geotechnical Engineering Research Laboratory under the direction of Samuel Paikowsky: Leo Hart, Chris Palmer, John Chen, and Mike Bachand.

The static load testing was conducted by personal from the University of Massachusetts - Lowell Geotechnical Engineering Research Laboratory (UML). The Statnamic testing was conducted by personal from the University of South Florida (USF) in conjunction with the Federal Highway Administration.

REFERENCES

Berminghammer Foundation Equipment. 1997. *Statnamic Load Testing Proposal Notes.*

Janes, M., Berminghammer, P., & White, J. 1995. Work, Velocity, and the Relationship of Shaft Stiffness in Statnamic Load Testing. *Proceedings, First International Statnamic Seminar*, Vancouver, British Columbia, Canada.

Justason, M. D., Mullins, A. G., Robertson, D. T., & Knight, W. F. 1997 A Comparison of Static and Statnamic Load Tests in Sand: A Case Study of the Bayou Chico Bridge in Pensacola, Florida. *Proceedings, Twenty Second Annual Deep Foundations Institute Members Conference*, Toronto, Ontario, Canada.

Massachusetts Highway Department. 1995. *Standard Specifications for Highways and Bridges.*

Middendorp, P., & Bielefeld, M. W. 1995 Statnamic Load Testing and the Influence of Stress Wave Phenomena. *Proceedings, First International Statnamic Seminar*, Vancouver, British Columbia, Canada.

Paikowsky, S. G., & Chen, Y. U. 1998. *Field and Laboratory Study of the Physical Characteristics and Engineering Parameters of the Subsurface at the Newbury Site.* Report submitted to the Massachusetts Highway Department, University of Massachusetts Lowell.

Paikowsky, S. G., & Hajduk, E. L. 1998. *Design and Construction of an Instrumented Test Pile Cluster.* Research report to be submitted to the Massachusetts Highway Department.

Paikowsky, S. G., & Hart, L. J. 1998. *Development and Field Testing of Multiple Deployment Model Pile (MDMP).* Research report submitted to the Massachusetts Highway Department, University of Massachusetts Lowell.

Paikowsky, S. G., & Operstein, V. 1999. *Express Method of Pile Testing by Static-Cyclic Load.* Research report to be submitted to the Massachusetts Highway Department, Geotechnical Research Laboratory, University of Massachusetts Lowell.

Paikowsky, S. G., & Weeks, K. 1997. *Design and Construction of a Pressure Chamber.* Research report under REU submitted to the National Science Foundation.

A comparison of static and Statnamic load tests in sand: a case study of the Bayou Chico bridge in Pensacola, Florida

M.D. Justason
Berminghammer Foundation Equipment, Canada

G. Mullins
University of South Florida, US

D.T. Robertson
Applied Foundation Testing, US

W.F. Knight
Florida Department of Transportation, US

ABSTRACT: This paper details the static and Statnamic load testing on a 600 mm square prestressed concrete pile. The pile was located at Pier 15 on the 20 million-dollar Bayou Chico Bridge Project in Pensacola, Florida. The pile was 10.5 meters long and had a design load of 1.3 MN. Three static load test cycles were performed in November, 1996. The Statnamic load test was performed in January, 1997. The Davisson failure load of the first cycle of the static test was 3.7 MN, and the Davisson failure load of the Statnamic test was 3.2 MN. The load-displacement curves for the two types of tests were similar, indicating that the Statnamic load test performed well in the sandy soils. Strain gauges embedded in the pile showed 35% skin friction and 65% end bearing for both test methods. Strain gauges were located at equal spacing at five elevations in the pile. A toe accelerometer verified the rigid body assumption of the Unloading Point Method currently used in the analysis of Statnamic load tests. The data collected from the pile instrumentation was of excellent quality and represents some of the best research to date comparing static and Statnamic load tests.

1 INTRODUCTION

As part of the 20 million-dollar Bayou Chico Bridge Project, State Road 292, in Pensacola, Florida, the Florida Department of Transportation (FDOT) implemented an extensive load testing program. It included static, Statnamic, and dynamic load tests. The geotechnical consultants for the load testing were Williams Earth Sciences and Applied Foundation Testing, Inc. Berminghammer Foundation Equipment performed the Statnamic load tests. Metric and Beiswenger, Hoch & Associates supplied the design for the bridge structure in cooperation with FDOT. Figg Construction Services provided the construction engineering and inspection, and the contractor was PCL Civil Constructors.

The goal of the test program was firstly, to confirm the design capacity of the piles and secondly, to compare the results obtained by the three test methods. Of the three comparisons made at this site, the results of the static and Statnamic load tests at Pier 15 form the basis of this paper. Testing at two additional locations will be studied in future papers.

Statnamic load testing has been used extensively in Florida for large diameter bored piles. In each case, the Statnamic testing was performed as an alternative to static load testing, or as the only possible testing method. This was due to the high capacity of the shafts and the difficulties associated with static testing. Consequently, previous tests programs were unable to provide static/Statnamic comparisons. The Bayou Chico Project provided an excellent opportunity for a detailed static/Statnamic comparison and also provided the first Statnamic testing on driven piles in Florida.

The test piles were 600 mm concrete piles with lengths between 10.5 and 14.0 meters. Static load tests were performed using a 10.7 MN capacity test frame and eight steel reaction piles (H-piles). The Statnamic tests were performed using a 14MN Statnamic device with a conventional gravel catching system. The design capacity of the piles was 1.3 MN.

The test program recognized the effects of multiple loading cycles on pile capacity and thus alternated the order of static and Statnamic tests for each pile. Three piles were tested, with a total of three static tests and four Statnamic tests. Three static load cycles were performed at Pier 15 on November 26, 1996. The Statnamic test was performed on January 17, 1997.

Each test pile was instrumented with vibrating wire and resistance strain gauges as well as an embedded toe accelerometer. The data obtained at this site was of excellent quality, and is perhaps some of the most revealing data obtained during a Statnamic load test in recent years. The importance of this data is largely due to the presence of the embedded toe accelerometer which provided an opportunity to conduct a detailed investigation of pile top and toe behavior during Statnamic load testing.

The following table summarizes the Bayou Chico test program.

Table 1. Outline of load test program (static and Statnamic)

Location	Test Method
Pier 15	Static, November 26, 1996
	Statnamic, January 17, 1997
Pier 5*	Statnamic, February, 1997
	Static, March, 1997
	Statnamic, April, 1997
Pier 10*	Static, July, 1997
	Statnamic, August, 1997

*Piers 5 and 10 will be discussed in future papers

2 FOUNDATIONS

2.1 *Soil profile and properties*

The soils at the Bayou Chico Bridge were comprised of medium to dense, poorly graded sand with some silty sand. Each of the three test pile locations was investigated using a cone penetrometer and standard boreholes were performed in the immediate area. The results of a typical cone sounding are shown in Figure 1. The Bayou Chico Bridge site was generally uniform in its soil profile.

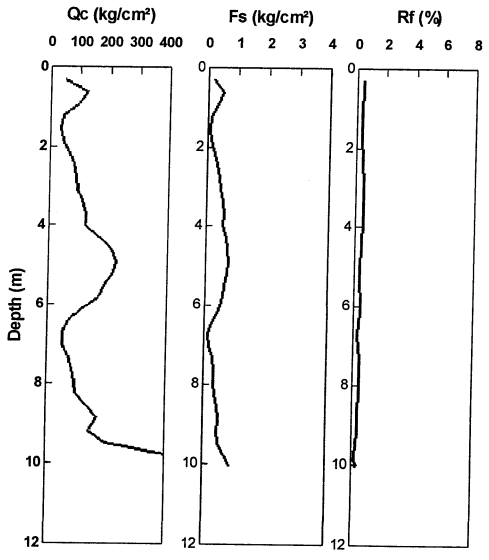

Figure 1 Typical cone sounding

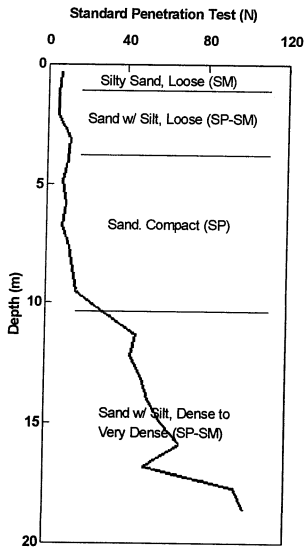

Figure 2 Typical borehole and SPT results

Dense sand layers were present at depths of 10–15 meters, with SPT values in the range of 80–100. A typical borehole log is presented in Figure 2, with SPT values.

2.2 *Pile details*

The piles used at the Bayou Chico Bridge were 600 mm square pre-stressed concrete piles, typical of piles used on FDOT projects. The three test piles ranged from 10.5–14.0 meters in length. The test pile at Pier 15 was 10.5 meters long. A cross-section of the piles is shown in Figure 3. Figure 4 shows a picture of a 5 × 5 pile group.

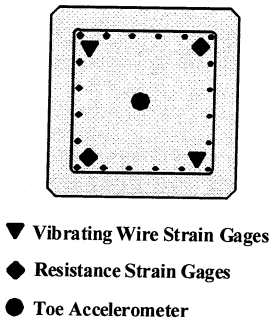

Figure 3 Pile cross-section

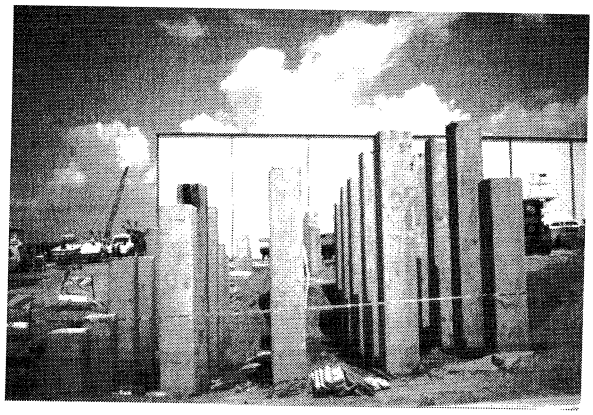

Figure 4 Typical 5 × 5 pile group

2.3 *Instrumentation*

Each of the three test piles was instrumented with 10 resistance and 10 vibrating wire strain gauges, a total of 20 gauges. The vibrating wire gauges were intended as the primary measurement for the static load tests and the resistance gauges were intended for the Statnamic load tests. The pile cross-section in Figure 3 shows the positions of the strain gauges. The strain gauge depths are shown in Figure 5.

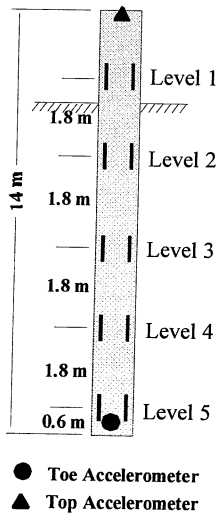

Figure 5 Strain gauge depths

The test data was recorded using a MEGADAC data acquisition and signal-conditioning unit which recorded the load cell, 3 LVDTs, 10 resistance strain gauges, and the hydraulic jack

pressure. An independent recording system was also used to record the vibrating wire gauge response.

Each test pile was equipped with an embedded toe accelerometer (see Figure 3), which was monitored during the Statnamic test by the MEGADAC. A TNO FPDS-5 was used to monitor the Statnamic load cell and laser-activated photo-voltaic displacement transducer. An accelerometer was used as a backup to the laser sensor, in the event that the displacement exceeded the sensor capabilities.

3 LOAD TEST METHODS

3.1 *Static load test*

The static load tests were conducted using a 10.7 MN test frame supplied by FDOT. For each test pile, eight reaction piles were installed around the test pile at a distance of approximately five pile diameters (3 meters). Figure 6 shows the static load test configuration.

The reaction piles at Pier 15 were 350 mm steel H-piles which were installed using a diesel pile hammer. The piles were driven to a depth of approximately 20 meters.

Figure 6 Photo of static load test at Pier 5

3.2 *Statnamic load test*

The Statnamic load test involved the application of a short duration load (about 120 ms). Burning a solid fuel inside the Statnamic device produced high-pressure gas. The attendant force accelerated a reaction mass upwards at 20g. An equal force was applied to the pile. The reaction mass weighed 5% of the desired load.

A schematic diagram of a Statnamic device is shown in Figure 7. The device used at the Bayou Chico Bridge was a 14 MN Statnamic device (see photo in Figure 8). A more detailed description of Statnamic load testing is available in Bermingham, 1989.

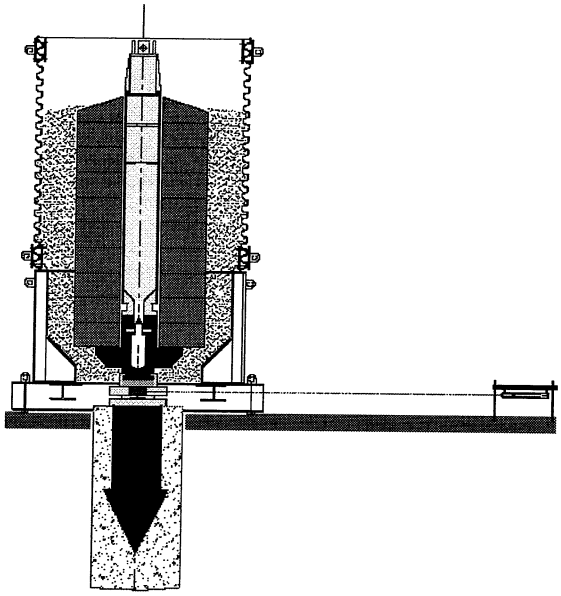

Figure 7 Schematic of a Statnamic load test

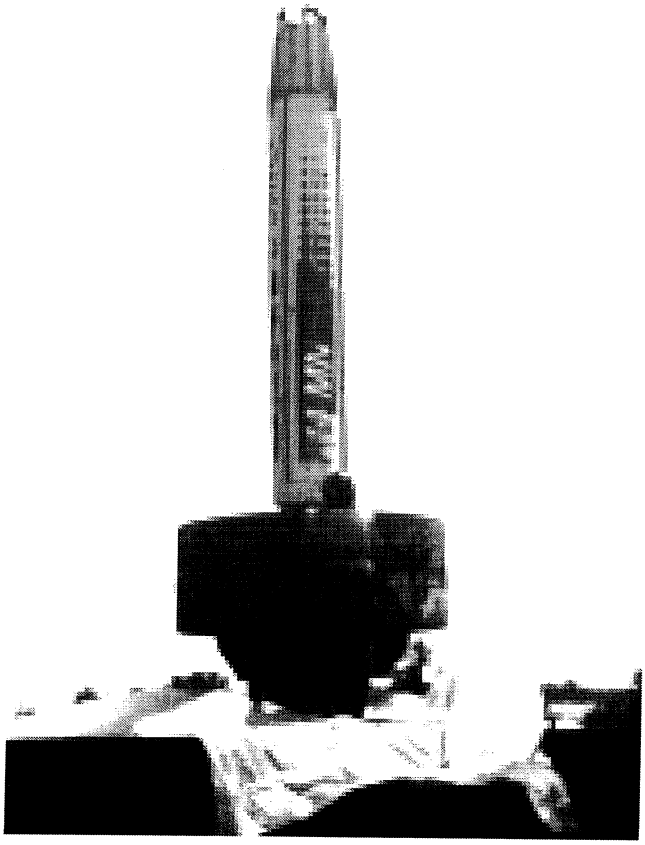

Figure 8 Photograph of the 14 MN Statnamic device

4 TEST RESULTS AND DISCUSSION

4.1 *Static load test at pier 15*

Figure 9 shows the results of the static load test performed on the test pile at Pier 15. The test was performed on November 26, 1996.

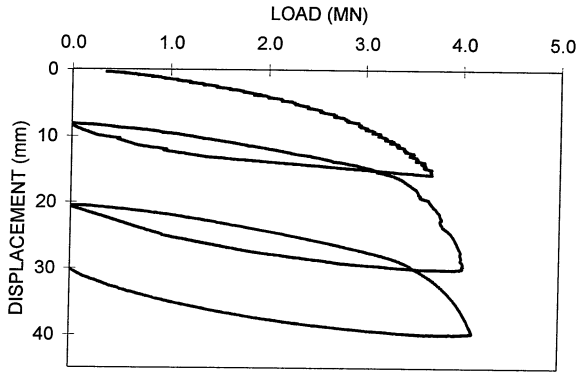

Figure 9 Static load test results

The three static load cycles showed a stiffening trend. The Davisson failure load was 3.7 MN for the first cycle, and increased for subsequent load cycles (3.8 MN and 3.8 MN respectively). The peak load for the three cycles ranged from 3.8 to 4.1 MN, and the peak displacement ranged from 10.2 to 16.0 mm. After the third load cycle, the pile had accumulated 30.0 mm of permanent displacement. None of the three load cycles exhibited a dramatic plunging failure, but rather a gradual softening.

Figure 10 shows the results of the resistance strain gauges vs. time for the 3rd cycle. The vibrating wire gauges yielded similar results for the 1st cycle. The results shown are the average strain values of the gauges at each depth.

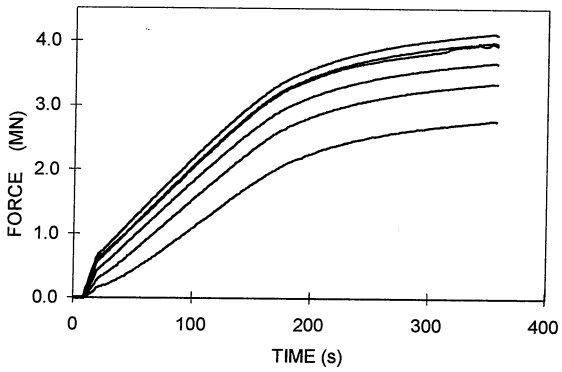

Figure 10 Force vs. time from resistance strain gauges for Pier 15

Near the peak load, approximately 35% of the pile capacity was attributable to skin friction and 65% to end bearing.

4.2 *Statnamic load test at pier 15 and comparison with static test*

Figure 11 shows the results of the Statnamic load test performed on January 17, 1997. The load test was performed by Berminghammer Foundation Equipment with no prior knowledge of the

static load test results. A load of 7.0 MN was targeted. As Figure 11 shows, the actual peak load achieved was 6.3 MN; much more load than was required to achieve the Davisson failure load. The shortfall from the target load was due to the very large pile displacement.

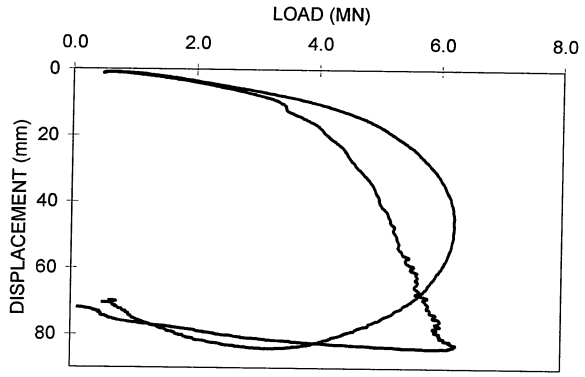

Figure 11 Statnamic and derived static load-displacement

The measured Statnamic curve is the more rounded curve in Figure 11, while the other curve is the calculated static behavior of the pile using the Unloading Point Method (3). Sometimes called the 'derived static' curve, this graph shows the load-displacement relationship with the inertia and damping forces removed from the measured Statnamic force.

Figure 12 shows force vs. time as measured by the load cell, as well as the inertia and damping forces vs. time.

Figures 19 and 20 shown later in this section, depict the acceleration and velocity of the pile. Note that these figures are the same shape as the inertia and damping forces shown in Figure 12.

The inertial forces were calculated by multiplying the pile mass by the measured pile acceleration. The damping forces were calculated by multiplying a damping constant by the velocity. The damping constant was derived using the Unloading Point Method (4). A linear relationship between velocity and damping was assumed. The peak inertial force was –2.8 MN, and the peak damping force was 0.5 MN. These peak values alone are not sufficient to understand the Statnamic loading event. As Figure 12 shows, the full inertial and damping time histories are necessary. This Statnamic load test has unusually high inertia and damping forces due to the large displacement.

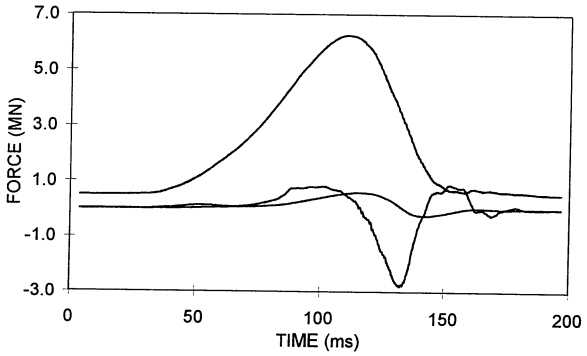

Figure 12 Measured force, inertial force, and damping force vs. time

To find the static soil resistance (or 'derived static') force curve, the damping and inertial forces were subtracted from the measured force. The resulting curve is shown in Figure 13, along with the measured force. This force curve was used to produce the 'derived static' load-

displacement, shown in Figure 11. The 'derived static' curve shows a loading rate that is slower than the measured load, and an unloading rate that is faster.

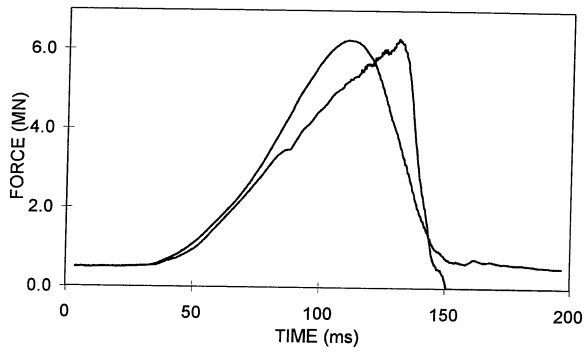

Figure 13 Measured force and derived static force vs. time

When plotted on the same graph the derived static curve and the three static load tests show very similar behavior, as shown in Figure 14.

The static and Statnamic curves appear different due to the large movement of the pile during the Statnamic load test. The loading and unloading portions of the curves are similar.

Figure 15 shows the results from the strain gauges for the Statnamic test at Pier 15. The results shown represent the average strain values of the two gauges at each elevation in the pile.

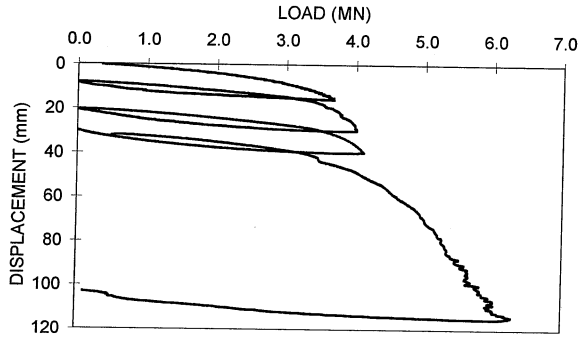

Figure 14 Static and Statnamic derived static

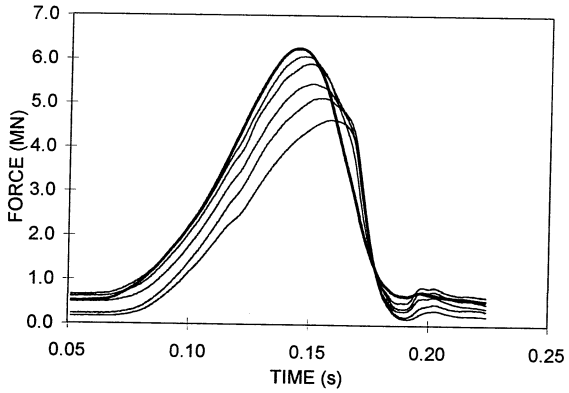

Figure 15 Statnamic force and strain gauge results

The curve showing the highest force in Figure 15 is the force measured by the load cell. The other curves represent the calculated force at each level of strain gauges. To calculate force, the measured voltage signals were converted to micro-strain using the manufacturer-supplied calibration factors, and introducing an elastic modulus of 34.5 GPa and a cross sectional area of 0.37 m^2.

The data displayed in Figure 15 was of interest for many reasons. Firstly, having strain gauges embedded in a pre-cast pile meant that no assumptions were needed for the cross-sectional area. For bored piles, strain gauge results must be interpreted more carefully for this reason. Also, the elastic modulus for the concrete could be checked against the force measured in the load cell. In this case, the first level of strain gauges was only 2.7 m from the load cell, allowing for an accurate 'calibration' of the elastic modulus. The value of 34.5 GPa, may seem higher than expected but is not unreasonable. The rate of loading might also serve to increase the observed elastic modulus, as does the reinforcing steel. In Figure 10, an elastic modulus of only 31 GPa was used. The age of the concrete combined with the faster loading rate of the Statnamic test could have accounted for this difference.

A notable aspect of Figure 15 is the lag between the peak force at the top of the pile and the bottom of the pile. In previous studies, this time lag has been associated with the compressive wave speed in the pile material (2). For this pile, it became apparent that the compressive wave speed was not the cause of the lag.

Assuming a wave speed of 4000 m/s, and given a pile length of 10.5 meters, the time for a compressive wave to travel from the top to the bottom of the pile is only 0.002–3 s. The observed time lag (~0.025 s) is obviously greater so an alternate explanation was necessary.

It is proposed that the time lag was indirectly caused by the large displacement of the pile. Just as a force applied at the top of the pile caused a force distribution downward, the pile penetrating the soil and increasing in capacity caused a force distribution up the pile. This should not be confused with stress wave phenomena, as both the downward and upward forces were distributed at a speed well below the compressive wave speed in the pile material. The resulting superposition of these two force distributions causes the time lag in the strain signals. It has been shown in previous studies that Statnamic tests with smaller displacements do not have time lags as large as those seen in Figure 15 (2).

The displacement at the top of the pile would have normally been measured using the laser sensor, but due to the large displacement, the maximum travel of the sensor was exceeded at approximately 55 mm. The back-up accelerometer was used to derive the displacement at the top of the pile.

The embedded toe accelerometer performed well, and the signal produced a high quality displacement curve. Figure 16 shows both the top and toe displacement curve as well as the force vs. time.

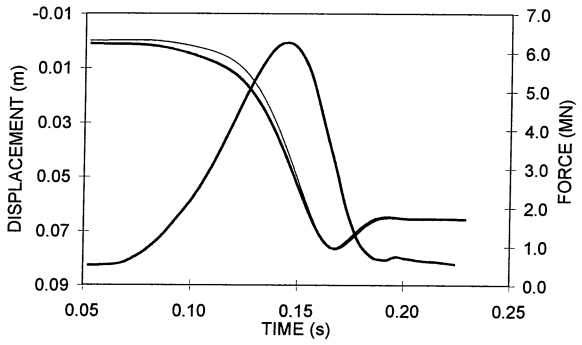

Figure 16 Top and toe displacement and measured force vs. time

Figure 16 shows the time lag between the peak force and the peak displacement. Notice that the peak displacement occurs at nearly the same time as the peak force at the toe of the pile (see Figure 15).

Figure 17 shows the load-displacement curve for the top of the pile, as well as the load-displacement using the toe accelerometer (from Figure 16) and the bottom level of strain gauges (from Figure 15).

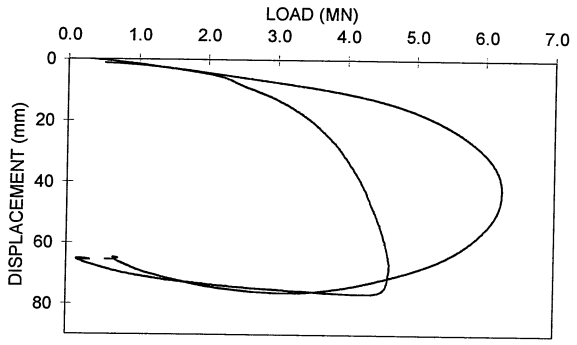

Figure 17 Load-displacement at the top and toe of the pile

Note that the load-displacement at the toe of the pile is very similar in shape to a static load test. This is due to the minimal effects of pile damping and inertia at the pile toe. The load-displacement at the pile toe can also be compared to the 'derived static' load-displacement (see Figure 18).

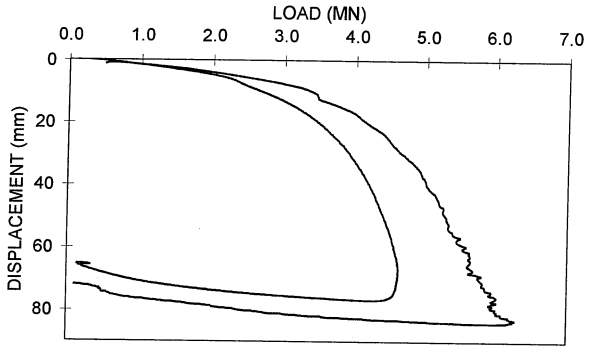

Figure 18 Load-displacement at the pile toe and derived static load displacement

Figures 19 and 20 show the velocity vs. time and the acceleration vs. time at the top and toe of the pile. In each figure, the slightly larger peak values belong to the pile top. Note the similarities between the pile top and pile toe behaviors.

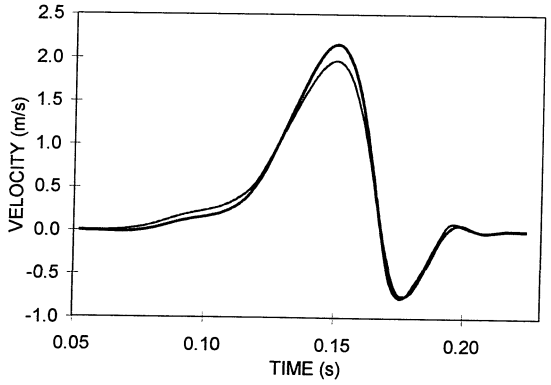

Figure 19 Pile top and toe velocity vs. time

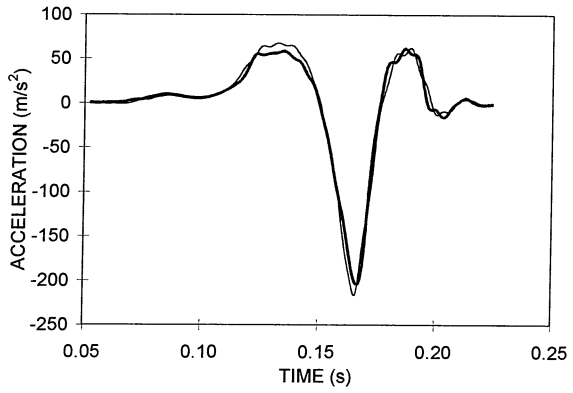

Figure 20 Pile top and toe acceleration vs. time

Figures 19 and 20 support the rigid body assumption of the Unloading Point Method. It also proves the absence of stress wave effects. This assertion may not be true for piles with lengths greater than approximately 50 m (4).

5 CONCLUSIONS

Firstly, it should be concluded that the test pile at Pier 15 achieved the required capacity based on the Davisson failure load of both the static and Statnamic load tests. The required capacity of 2.6 MN (2 times design) was below the capacity determined by the first cycle of the static load test (3.7 MN). The Davisson failure load of the Statnamic test was 3.2 MN.

Secondly, it can be concluded that the static and Statnamic load tests produce similar results. The Statnamic test was taken to a load far exceeding the Davisson failure load and subsequently produced a large permanent displacement (80 mm). The static tests were taken to lesser loads, but the load-displacement behaviors were similar. The first cycle of the static load test produced a somewhat softer response than the subsequent cycles, indicating some increase in capacity due to the testing. The 'derived static' curve from the Statnamic test suggested that the pile was gaining capacity as more load was applied.

Both the static and Statnamic strain gauge results showed that approximately 35% of the pile capacity was skin friction and 65% was end bearing. This indicated that the load distribution in the pile was not affected by the loading rate.

In addition to the above conclusions, the testing on Pier 15 showed that the Unloading Point Method used in the analysis of the Statnamic test was a valid method. The similarity between the movement at the pile top and the pile toe (provided by the toe accelerometer) indicated that the pile essentially moved as a rigid body.

The agreement between the static load test and the 'derived static' curve from the Statnamic test indicated that the effects of loading rate are not significant in this soil.

The testing at Pier 15 of the Bayou Chico Bridge Project supports the use of Statnamic testing for driven piles in sand. Further testing on this site will be explored in future papers.

ACKNOWLEDGMENTS

The authors wish to thank PCL for their work in setting up the static and Statnamic load tests, and Gray Mullins' dog Rudy for his patience and understanding.

REFERENCES

Bermingham, P., & Janes, M., 1989. An Innovative Approach to Load Testing of High Capacity Piles. *Proceedings of the International Conference on Piling and Deep Foundations*, London, May 15-18, 1989, pp.409-413.

Janes, M., 1995. Statnamic Load Testing of Strain Instrumented Large Diameter Bored Shafts. *Proceedings of the First International Statnamic Seminar*, Vancouver, September 27-30, 1995, pp.65-74.

Middendorp, P., Bermingham, P., & Kuiper, B., 1992. Statnamic Load Testing of Foundation Piles. *Proceedings of the 4th International Conference on Application of Stress Wave Theory to Piles*. The Hague, Holland, 1992, pp.581-588.

Middendorp, P., & Bielefeld, M.W., 1995. Statnamic Load Testing and the Influence of Stress Wave Phenomena. *Proceedings of the First International Statnamic Seminar*, Vancouver, September 27-30, 1995, pp.207-221.

Lateral Statnamic load testing: A new method for evaluating lateral load capacity

D. T. Robertson & M. K. Muchard
Applied Foundation Testing, Green Cove Springs, Florida, USA

A. G. Mullins
University of South Florida, Tampa, Florida, USA

ABSTRACT: The Statnamic test method was originally developed as a method for evaluating axial capacity; however, in the last 3 years a new application for the device has been developed. In October 1994, the North Carolina Department of Transportation became the first to perform lateral Statnamic load testing of drilled shafts. Brigham Young University, the Utah DOT and the FHWA followed in 1996 with lateral load tests performed on a group of pipe piles. This testing was done to evaluate foundations under ship impact and earthquake type loading since the force-time pulse generated by the Statnamic device is on the same order of magnitude and frequency. Since that time, the lateral Statnamic test and associated data acquisition systems have been refined and improved. These improvements allow the collection of data in zones of influence while maintaining cost savings over more traditional methods. Tests using these improvements have been most recently performed in Pascagoula, Mississippi as part of a design phase load test program for the Mississippi Department of Transportation.
The paper will describe the test method, describe the equipment utilized to generate the lateral load, describe the data acquisition equipment and present an overview of the results from the most recent test site.

1 INTRODUCTION

Static lateral tests are commonly used to assist in the design of foundations subjected to lateral loads. However, lateral loads are typically generated by various events, which include high wind, earthquakes, impacts from various types of vehicles and numerous other static and dynamic sources. Traditionally, geotechnical and structural engineers have used static lateral test as a guide to the structural response for a dynamic event. Static tests provide data which is used to fine tune computer models such as COM624P, LPILE and Florida PIER. These computer programs estimate the static response of a foundation or structure based on the static properties of the soil and neglect the additional capacity available from the dynamic soil strength and structure response.

Recently, more attention has been placed on the dynamic properties of both soil and the structure. The high costs associated with the construction of foundations and structures to withstand lateral forces have justified more in depth testing and analysis. The Statnamic test method is considered a viable method for generating dynamic lateral loads because of it's ability to impart relatively high loads over a time frame similar to that generated by ship impacts, earthquakes and transient wind loads. Load pulses can last up to 200 milliseconds and are capable of generating lateral forces of 2000 tons. Figure 1 shows a typical force time history for a lateral Statnamic test.

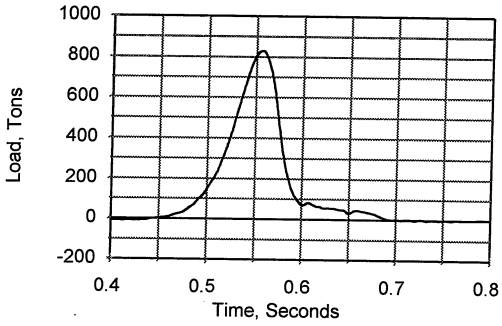

Figure 1. Force-time trace, lateral Statnamic test.

In 1994, the North Carolina Department of Transportation performed the first Statnamic lateral testing. Several tests were performed using a 67-ton Statnamic device on a single drilled shaft during a design phase load test program for the Neuse River Bridge in New Bern, North Carolina. In 1996, Brigham Young University, the Utah Department of Transportation and the FHWA performed lateral Statnamic tests on a group of instrumented pipe piles. This test utilized a 1600-ton device without reaction masses and generated lateral loads of up to 250 tons. Both test programs were performed on land. In 1996, the Mississippi Department of Transportation began planning for a design phase load test program for the US 90 Bridge over the East Pascagoula River. Large lateral load requirements were imposed on this bridge mainly due to vessel impact. Statnamic lateral load testing was specified to better model these conditions. This program included 15 Statnamic tests with loads of up to 823 tons. To the authors knowledge this is the largest lateral test program to date.

Dan Brown, Ph.D., P.E. under a contract with the FHWA and the Alabama Department of Transportation also began investigating the dynamic response of foundations. In April 1997, lateral Statnamic tests were performed at the Auburn University test site located in Opelika, Alabama. Four tests were performed on 36-inch diameter drilled shafts. The tests were performed using a 450-ton Statnamic device on shafts, previously, tested using static methods. The Statnamic tests were performed in the opposite direction of the static test to minimize soil disturbance. During the static tests, care was taken not to induce large permanent plastic deformations, which may have affected the results of the Statnamic tests. Figure 2 shows an example of the 450-ton Statnamic test setup at the 1997 GEOLOGAN conference.

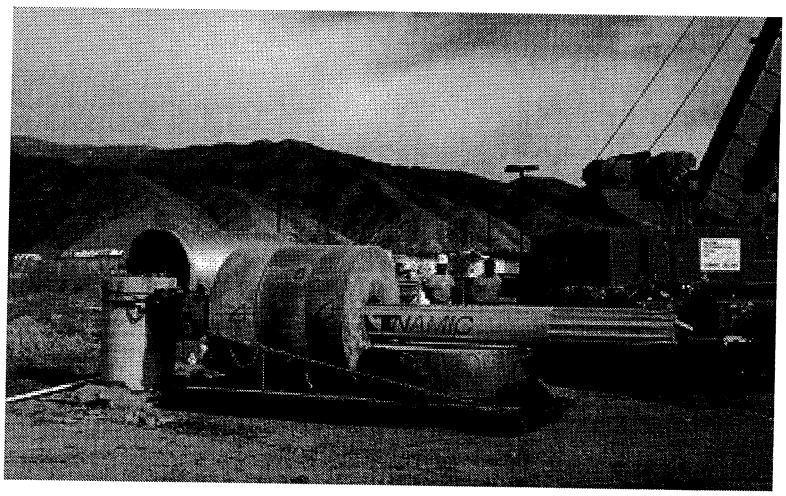

Figure 2. Lateral Statnamic test- 1997 GEOLOGAN conference.

2 STATNAMIC EQUIPMENT

The Statnamic test equipment consists of three essential parts, the piston, the cylinder/silencer assembly, and the reaction masses. Before the test method can be described, the reader must understand the function of each piece.

2.1 *The piston*

The Statnamic piston is the most important part of the system. The piston includes a fuel chamber, where the fuel is ignited and burns, generating a gas, which accelerates the cylinder/silencer assembly away from the piston. The piston also contains a load cell and laser displacement sensor which provide the load and displacement signals. Figure 3 shows a picture of the 1600 ton piston used for the Utah and Mississippi test programs being loaded with fuel.

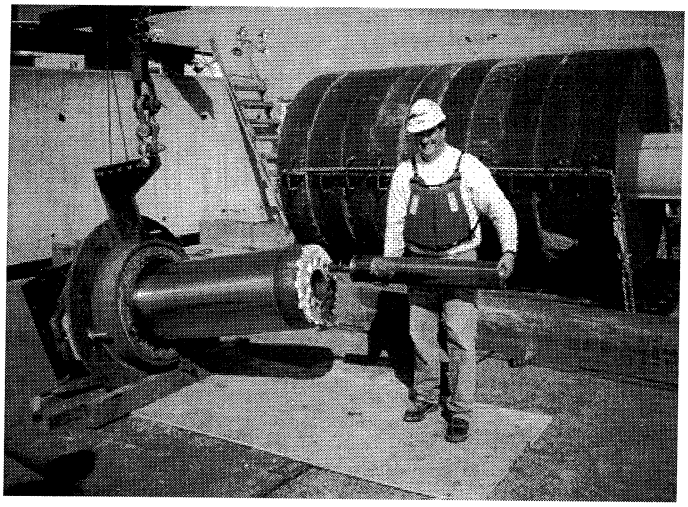

Figure 3. 1600 ton Statnamic piston.

2.2 *The cylinder/silencer assembly*

The cylinder/silencer assembly fits over the piston and forms a pressure chamber. Gas generated in the chamber moves the cylinder off the piston. The base of the cylinder has a large flange, which serves as the support for reaction masses. The silencer portion of this assembly acts as a large muffler. This portion of the device allows the gas to expand and vent in a controlled manner. The silencer reduces the report of the device. Figure 4 shows the 1600-ton cylinder/silencer assembly.

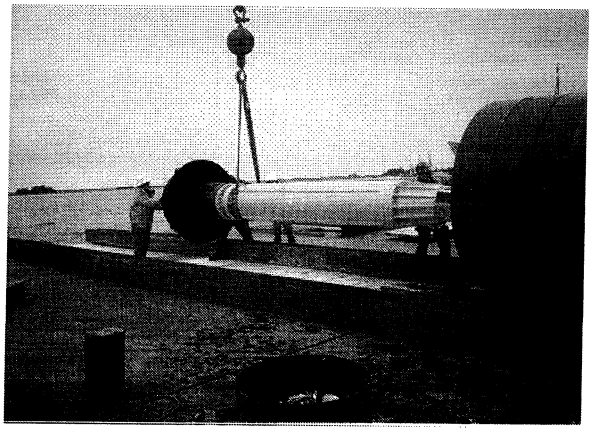

Figure 4. Cylinder/silencer assembly being inserted into masses for lateral testing.

2.3 *The reaction masses*

The "doughnut" shaped rings are constructed of concrete and steel. They typically have a mass equal to 5 to 8 percent of the target maximum load for an axial test. For lateral testing, this ratio can be much greater. Figure 4 shows the cylinder/silencer assembly being inserted into the reaction masses.

3 THE TEST METHOD

3.1 *Basic Statnamic principles*

The Statnamic test method uses two basic principles. The first is that for every action there is an equal and opposite reaction. The second is that force is equal to mass times acceleration. Currently Statnamic equipment can generate test loads of up to 3400 tons.

Fuel is burned inside the piston to generate a gas. The quickly forming gas pressure forces the cylinder/silencer assembly with the reaction masses to accelerate up to twenty times the acceleration of gravity, in turn producing a equal and opposite force acting downward on the foundation. The downward force can be defined as:

$$F = ma \tag{1}$$

where m = the reaction mass and a = the upward acceleration of the reaction masses.

The load cell measures the forces acting on the foundation. As the piston and foundation move, the laser sensor measures this movement relative to a stationary laser beam. A laser projector positioned forty to sixty feet away from the test area generates this laser beam.

An accelerometer is also mounted on the piston or foundation to measure acceleration and to act as a backup to displacement measurement system. During the test, the load cell, laser displacement sensor and accelerometer signals are measured by a data acquisition system interfaced with a laptop computer.

3.2 *The lateral Statnamic test*

The lateral Statnamic test uses these basic principles to generate lateral loads. The only difference between the axial test and the lateral test is working on a horizontal plane instead of a vertical plane. This means that additional reaction mass must be used to make up for the loss of the gravity induced forces (19 g's vs. 20 g's).

To overcome working on a horizontal plane a sled was constructed. This sled supports the reaction masses and cylinder/silencer assembly. The sled is allowed to slide in a runway, which runs on the same axis as the test. Rollers are used under the sled to eliminate soil disturbance near the test shaft due to friction generated between the sled and runway surface. For over water tests the runway can be constructed on a barge. For safety, rails are placed on either side of the sled. However, the large inertia of the sled produces a relatively straight travel path. Figure 5 shows the sled and barge track.

The Statnamic load is transferred to the foundation through a hemispherical bearing. The spherical bearing reduces eccentric loading and corresponding moments. Figure 6, shows the base of the piston and the spherical bearing configured for a lateral Statnamic test at the Pascagoula, Mississippi site.

3.3 Instrumentation

Additional instrumentation is necessary to monitor the lateral displacement at points of interest. This instrumentation can include potentiometers, accelerometers and resistance type strain gauges. To allow the monitoring of displacement of a shaft or pile at various levels, a down hole linear motion sensor was developed by Gray Mullins, Ph.D., P.E. of the University of South Florida. This string of sensors uses traditional slope inclinometer casing. The accelerometers are mounted on specially constructed carriers, which can be tied together and placed at various locations.

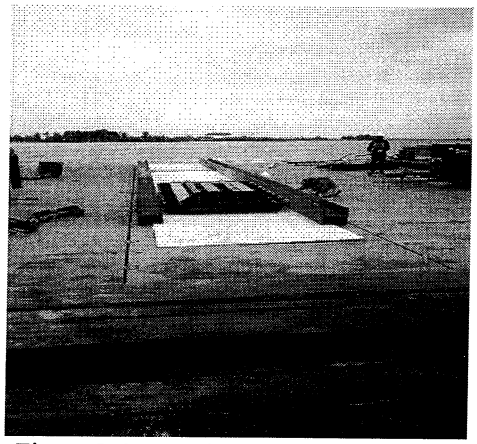

Figure 5. Statnamic sled and runway barge.

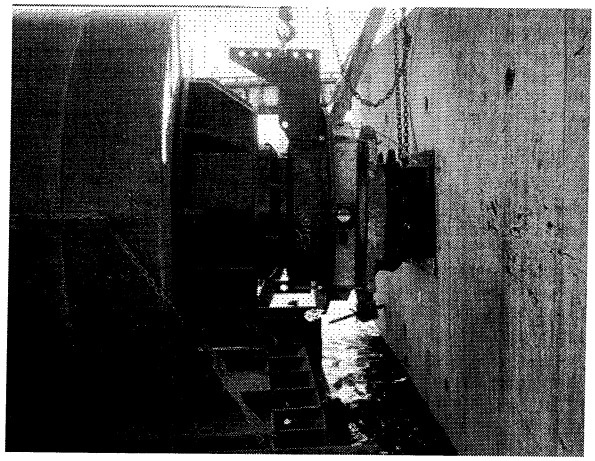

Figure 6. Spherical bearing.

Data from the various sensors is recorded using a high-speed data acquisition system. This system can monitor at rates of 250,000 samples per second. For Statnamic testing, data is normally acquired at rates of 2,000 to 5,000 samples per second. This acquisition rate can vary depending on the numbers of channels that are monitored and the length of sampling.

4 THE US-90 BRIDGE OVER THE PASCAGOULA RIVER LOAD TEST PROGRAM

The lateral Statnamic tests done at this site were part of a design phase test program. The load test program was performed to provide better design information for the foundation of the new US 90 over the Pascagoula River Bridge. The program consisted of the construction and testing of two concrete piers. The first pier was founded on a 2 X 3 pile group. The piles were 30-inch, square, pre-stressed concrete. The second pier was founded on two 84-inch diameter drilled shafts. The piers were constructed to allow a jack system to be placed in between for lateral static testing. Sufficient space was left outside the piers to allow barge access for the lateral Statnamic testing.

In addition to the lateral testing, static tests were performed on one drilled shaft and one 30-inch concrete pile. A 54-inch diameter, post-tensioned, concrete pipe pile was also driven and dynamically tested.

Statnamic testing was performed after all other testing was completed. During static testing, loads were controlled to prevent large permanent plastic deformations. Measurements taken after the completion of static testing show a permanent lateral displacement of ¼ inch for the driven pile group and ¾ inch for the drilled shaft group.

Fifteen lateral Statnamic tests were performed at the Pascagoula site on both the strong and weak axis of each group. Instrumentation for each pier included strain gauges embedded within the piles and shafts, accelerometers mounted at various points of interest around the piers, potentiometers mounted on a fixed reference beam and two strings of down hole linear motion sensors. Applied force was measured using the load cell contained within the Statnamic piston.

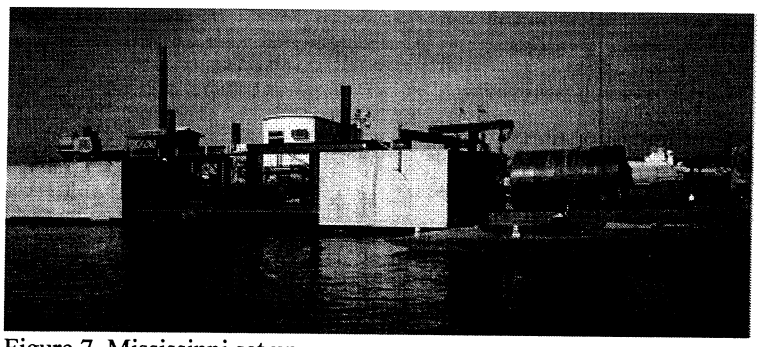

Figure 7. Mississippi set up.

4.1 *Test results*

Analysis of the data obtained during the lateral Statnamic testing is being performed by the Auburn University Highway Research Center under the direction of Dan Brown, Ph.D., P.E. This paper will present some of his initial analysis. The full results are being presented to Mississippi Department of Transportation and should be available in the future.

Figure 8 shows a time history plot of the applied Statnamic load, lateral translation and acceleration for a typical lateral Statnamic test on the strong axis of the drilled shaft pier. The results show a damped harmonic response, which dissipates relatively quickly due to the large damping in the system. This also shows the pier cap was subjected to a maximum force of 823 tons and accelerated to a maximum acceleration of 1.3 g's during the loading. The cap had a maximum displacement of 2.25 inches.

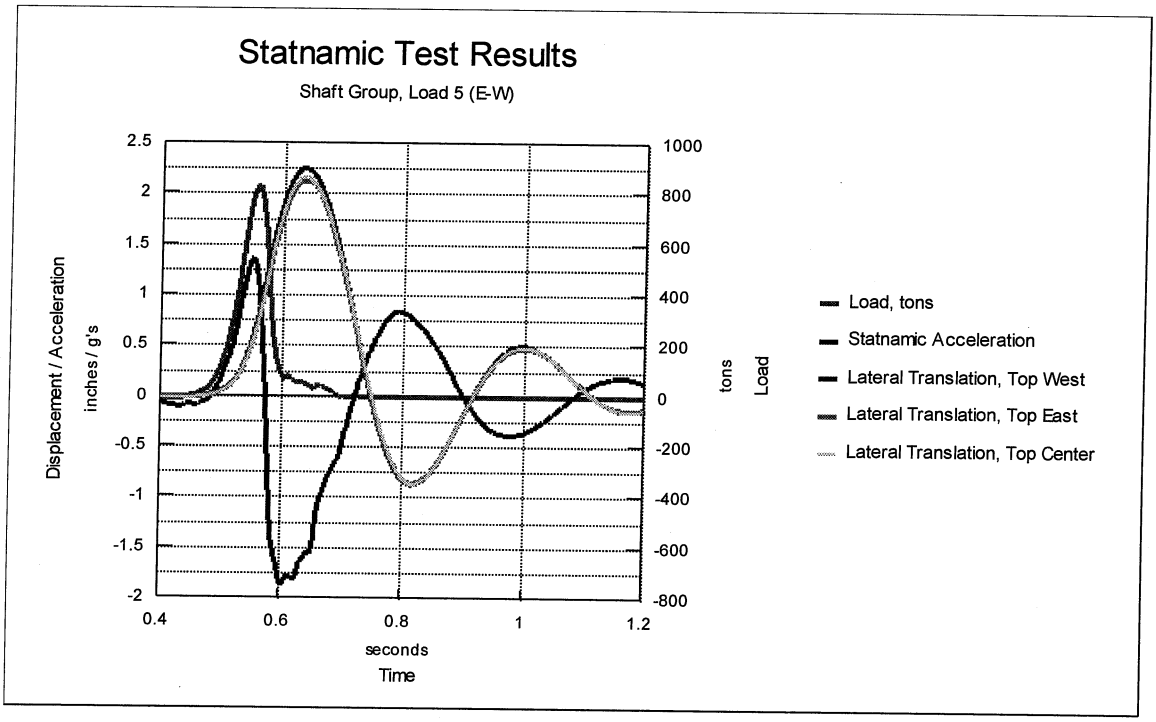

Figure 8. Lateral translation & acceleration.

The resistance to the Statnamic load has three components, which can be modeled as a single degree of freedom system.

The equation of motion is defined as:

$$F = ma + F_d + F_s \tag{2}$$

where, F = applied force, tons; m = mass of the foundation; a = acceleration in g's; F_d = damping force, Cv, tons; F_s = static soil resistance, Ku, tons; C = damping coefficient, ton/ft./sec; v = velocity, ft./sec.; K = static stiffness, tons/in; and u = displacement, in.

Using this model, C and K can be adjusted until a modeled displacement and acceleration response matches the measured response similar to other signal matching techniques. Figure 9, shows the modeled acceleration and displacement response compared to the measured.

Once C and K are calculated, the damping force and static soil resistance can be calculated. Figure 10 shows the Statnamic load, the calculated static soil resistance, the calculated damping force and the calculated inertia force.

The pier translation for the calculated and measured static soil resistance should be similar. Figure 11 shows the peak calculated static soil resistance for the 5 tests done on the shaft group vs. pier translation measured during the static test. This match quality suggests that it is possible to use Statnamic lateral tests to derive static lateral response. The derived static lateral response model is sensitive to the mass used in the computation as well as the subjective fitting of the K and C parameters by the engineer.

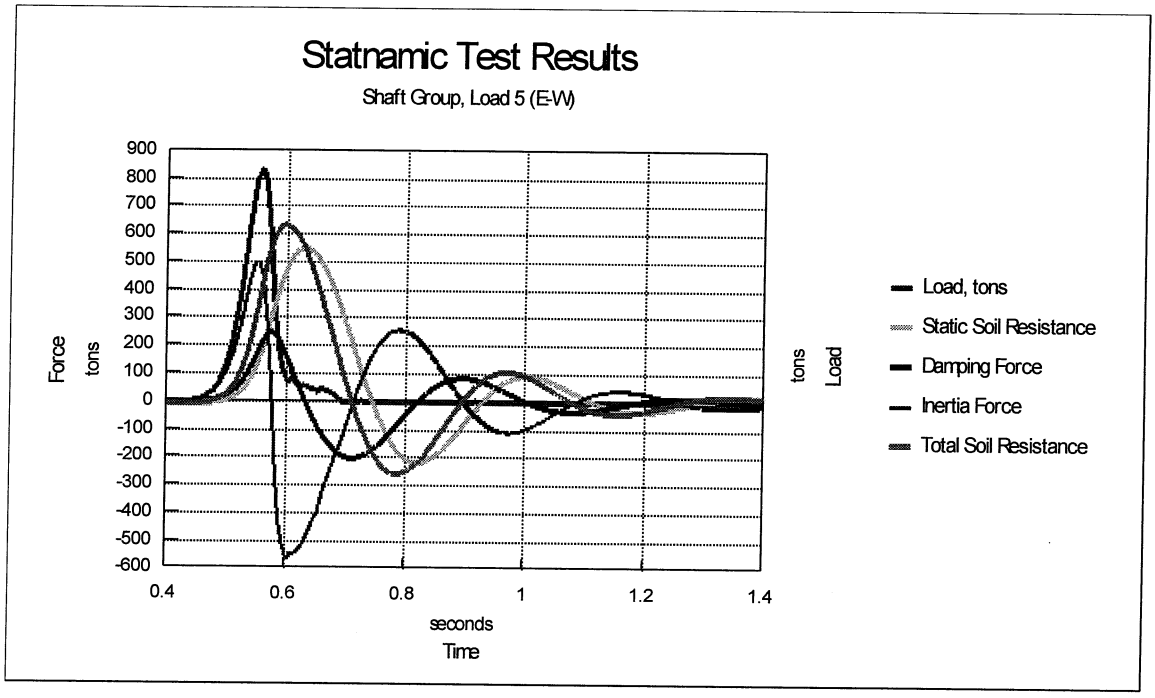

Figure 9. Actual versus model translation & acceleration.

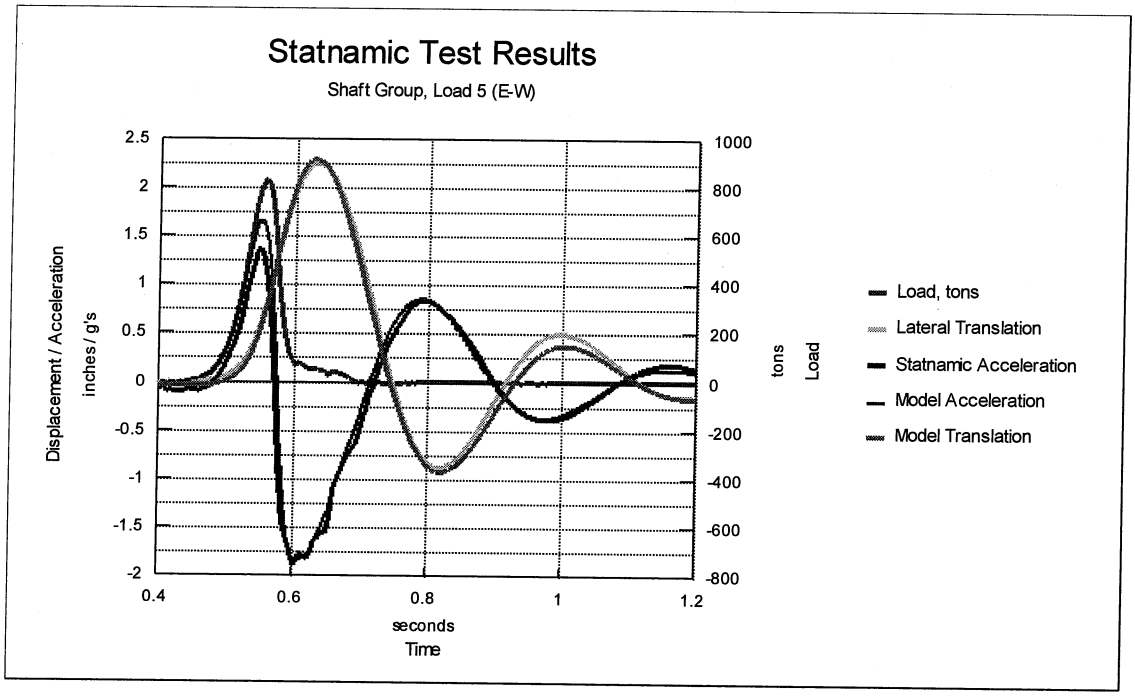

Figure 10. Statnamic forces.

Figure 12 shows a plot of the strain gauge data obtained from an instrumented pile. The Statnamic strain response is taken from a moment in time corresponding to the peak strain. For this loading the maximum total calculated static resistance plus the soil damping was 500 tons. The static strain data shown is taken from the maximum loading of 440 tons. The strain data is of opposite sign because the tests were performed in opposing directions.

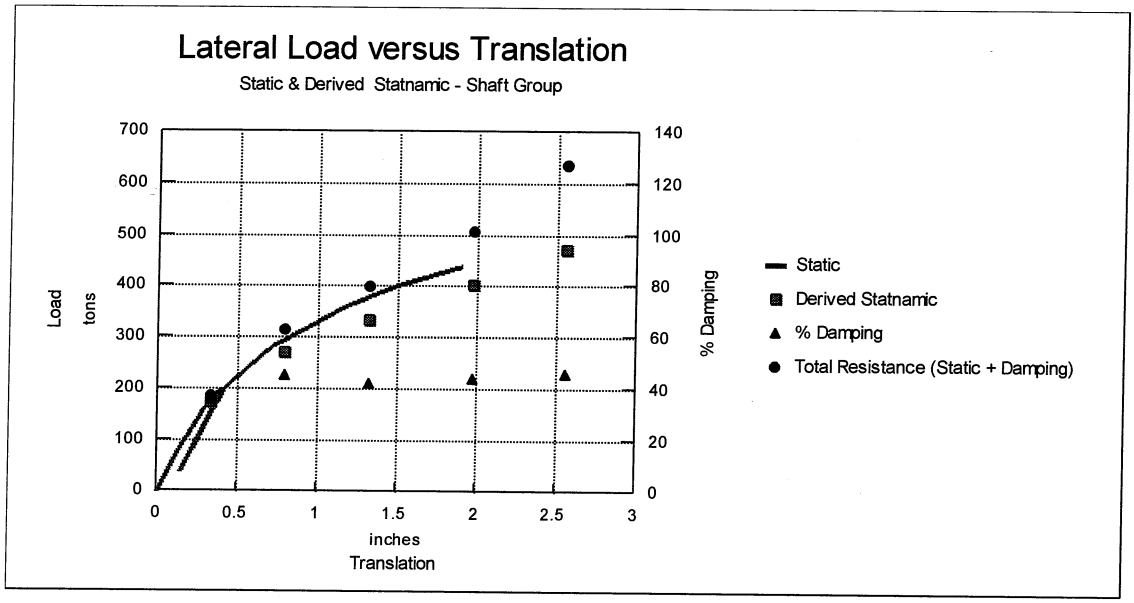

Figure 11. Derived Statnamic & static translation versus lateral load.

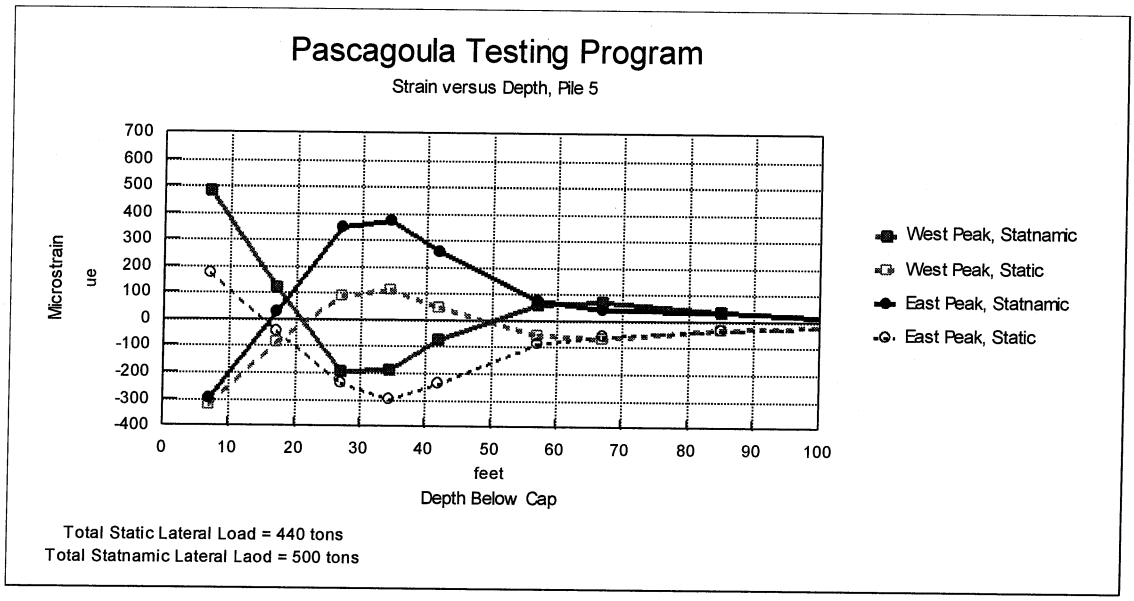

Figure 12. Strain versus depth, Pile 5.

The axial forces in the pile can be derived from the strain gage data. Figure 13 shows the derived axial force in the pile. Once again, the results are similar except for the opposite signs. The bending moment can also be derived as shown in Figure 14. Here the pattern is again similar, but with opposite signs.

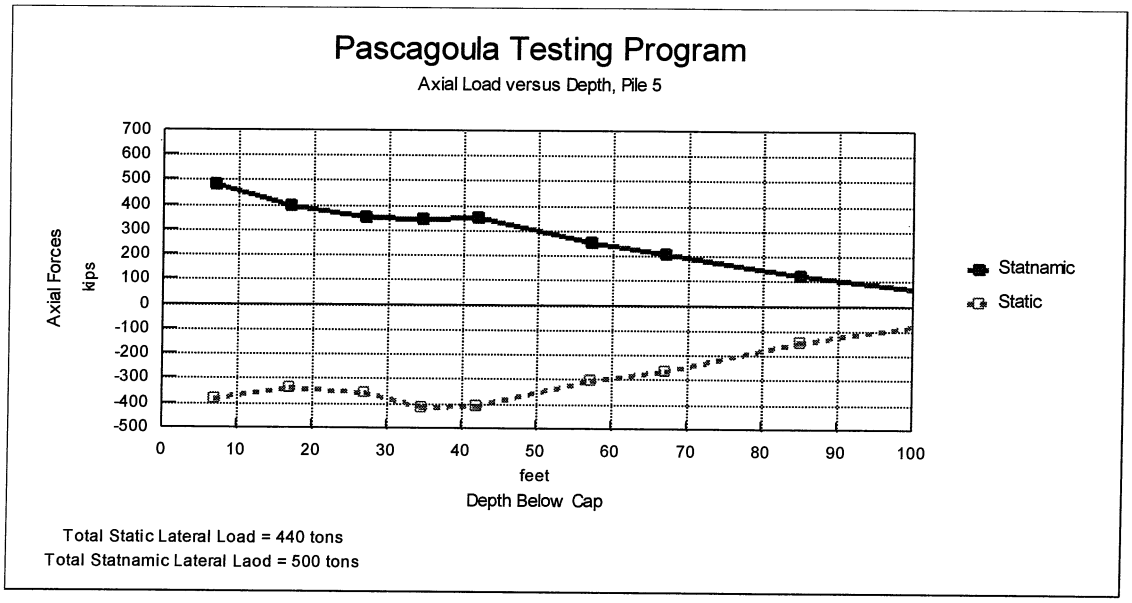

Figure 13. Axial load versus depth, Pile 5.

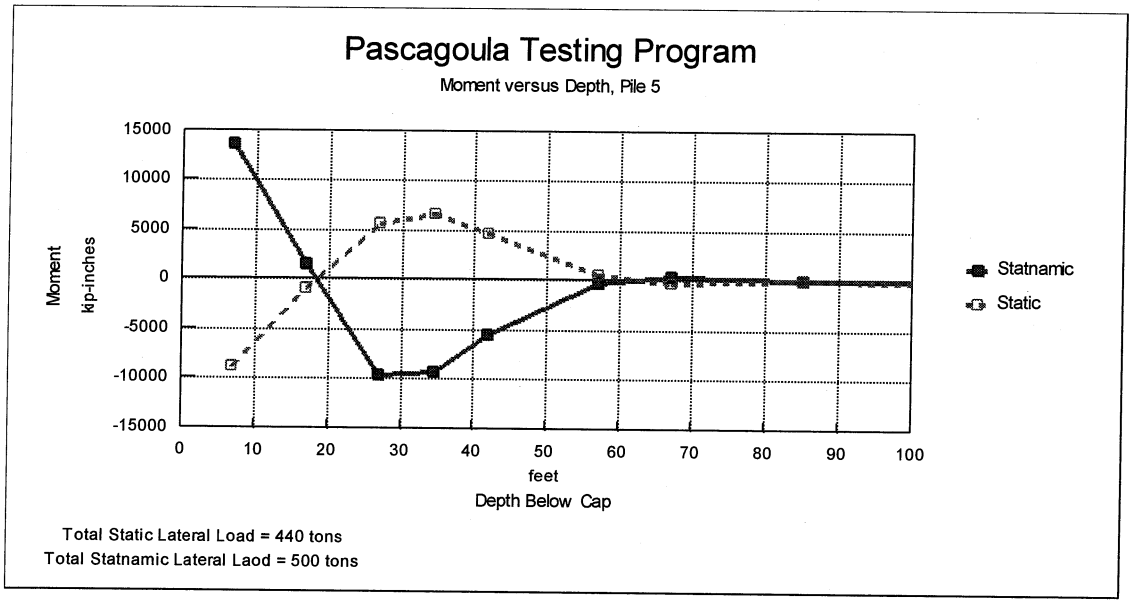

Figure 14. Moment versus depth, Pile 5.

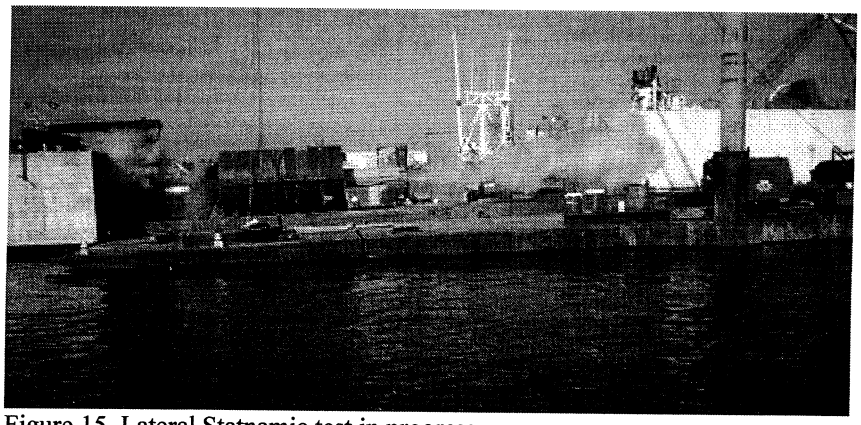

Figure 15. Lateral Statnamic test in progress.

5 CONCLUSIONS

The lateral Statnamic test method has been developed into a viable design and testing tool. The developments of both the loading and data acquisition equipment have progressed beyond the experimental stage. Figure 15 shows a lateral Statnamic test in progress.

Since the lateral Statnamic test method does not require a second foundation on which to react, it is more economical and can be performed in less time then the traditional lateral static method. The lateral Statnamic method can also provide much higher loads than the traditional static load test. The test also provides damping values, which are not provided by a traditional static test.

The calculated static soil resistance appears to provide good agreement with the measured static soil resistance. The lateral Statnamic test also provides dynamic soil response which, to date, has not been examined.

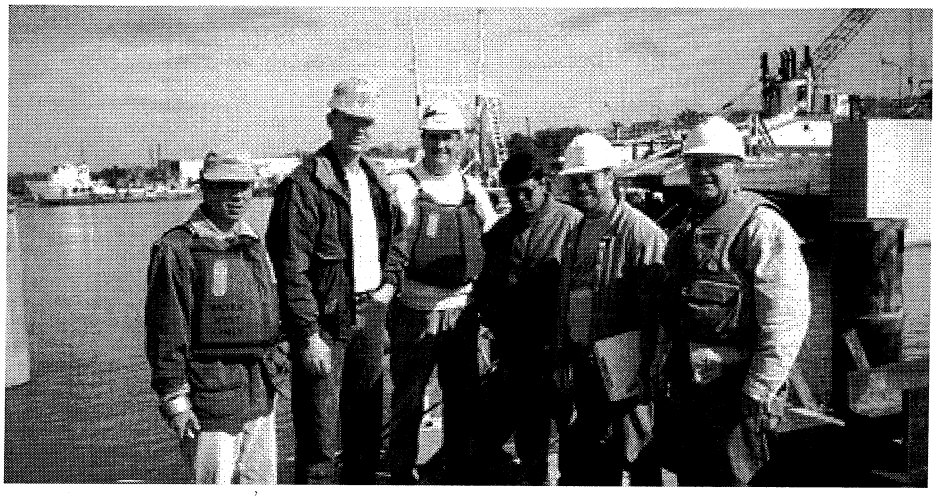

Figure 16. Load testing team.

ACKNOWLEDGEMENTS

The authors wish to thank Dan Brown for supplying the preliminary graphs shown in the report; David Crapps and Dan Brown for designing and implementing this challenging load test program; Bob Hodges and the crew of Warren Paving for providing the strong backs and good equipment; Mike Justason and the personnel at Berminghammer for their technical assistance; and Mike Wright and the staff of the Mississippi Department of Transportation, Geotechnical Branch for allowing us the opportunity to do this project.

REFERENCES

Brown, D.A. 1998. Report of Statnamic Load Testing, US 90 Over the Pascagoula River, Mississippi Department of Transportation.

Berkovitz, B. C. & Hahn, M. 1995. A Review of Statnamic Experiences for Transportation Applications. *Proceedings of the First International Statnamic Seminar*: 243-254. Vancouver.

SECOND INTERNATIONAL CONFERENCE ON COMPOSITES IN INFRASTRUCTURE
H. Saadatmanesh and M.R.Ehsani, Editors, Tucson, AZ 1998

Testing of CFRP/Concrete Bond

G. Mullins, R. Sen, and J. Spain

University of South Florida, Tampa, Florida, U.S.A.

The University of South Florida has investigated the use of two new devices that test the bond between concrete and fiber reinforced plastic (FRP) material under (1) direct and (2) torsional shear stress. Results of tests carried out using these devices on two different unidirectional carbon fiber materials, Tonen Corporation's Forca Tow Sheets (FTS-C1-20) and Fyfe's SCH-41/TYFO™ S, are presented and compared against those on the *same* specimen from a uniaxial tensile test. The tensile tests led to failures in the concrete, implying that the bond was excellent. However, shear tests led to *partial* or *complete* debonding failures at the concrete/carbon fiber interface. The results of the study suggest that torsional shear testing provides the most accurate assessment of bond strength.

INTRODUCTION

Epoxy bonding of fiber reinforced plastic (FRP) material is increasingly being used for strengthening reinforced or prestressed concrete highway structures. As structural performance is reliant on the bond between FRP and concrete, its long term integrity is of critical importance. Tests for measuring bond between concrete and FRP are needed as *acceptance criteria* when the repair is initially carried out. They may also be required during scheduled maintenance to evaluate possible degradation in bond due to prolonged exposure in a hostile environment.

The most common test for measuring bond between FRP and concrete is the *uniaxial tension* test [1]. In this test, a metal disk is epoxied to the FRP surface bonded to concrete. After the epoxy has cured, the force required to pull the metal disk and the bonded material from the concrete surface is measured. The quotient of the applied tensile force (P) and the area of the metal disk (A) bonded to the FRP surface gives the uniaxial tensile bond stress.

The uniaxial tension test is undoubtably a very simple test that can be performed *in situ* or in a laboratory. However, as the bond line is subjected to tensile stresses, the results obtained may not be very meaningful especially for flexural members where load transfer to the FRP material is primarily through shear. Moreover, as the tensile bond strength of the epoxy adhesive is generally greater than the tensile strength of concrete, failures inevitably occur in the concrete. Thus, while the results are very useful in evaluating initial repairs and making appropriate adjustments they maybe less useful in assessing long term performance.

In 1996, the University of South Florida initiated a test program to assess the bond between FRP material and concrete. As part of this program, two new test devices were designed and fabricated to allow measurement of the shear bond stress between FRP material and concrete. This paper provides a description of the test program and a summary of the results obtained.

OBJECTIVES

The principal objectives of the study were: (1) to develop suitable equipment and evaluate test procedures for measuring the bond line shear strength between FRP material and concrete, (2) to determine if the widely used uniaxial tension test is appropriate for testing the bond between FRP and concrete, and (3) to compare the results of three types of tests on identical specimens.

EXPERIMENTAL PROGRAM

To meet the objectives of the study it was necessary to prepare sets of identical specimens whose bond could be measured under both tensile and shear loads. The quality of bond was varied for each set of specimens. The equipment used for the tensile bond testing was based on a design developed by the Virginia Transportation Research Council [2]. Shear bond was evaluated using two new devices that were designed to produce shear stress from either direct shear or torsion.

CFRP Material

Two different types of uni-directional CFRP sheets were tested, FTS-C1-20 provided by the Tonen Corporation of Japan and SCH-41/TYFO^{TM}S provided by the Fyfe corporation.

Specimen Preparation

Forca Tow sheets and Fyfe SCH-41/TYFO^{TM}S sheets were bonded to 300 x 300 x 88 mm concrete slabs. Five sets of slab specimens were prepared: **F1, F2, F3** and **F4** from Forca Tow sheets, and the **H1** series from Fyfe SCH-41/TYFO^{TM}S. Each specimen set varied in its surface preparation: (1) in the **F1** series surface preparation consisted of priming as per manufacturers specifications, (2) slabs **F2, F4,** and **H1** were ground smooth and then primed, and (3) slab **F3** was ground smooth and no primer applied. Following surface preparation, the CFRP sheets were bonded to each slab using the respective manufacturer-supplied proprietary epoxy products.

Test Fixtures

Metal disk test fixtures, also called dollies, were fabricated for each type of test (tension, torsion, and direct shear). These fixtures were 50 mm diameter cold-rolled steel disks drilled and tapped on the upper face with appropriate adaptations for the specific test requirements [3]. Each dolly was bonded to the CFRP surface using a high modulus, low viscosity epoxy, Sikadur 32 (Figure 1).

Scoring

For the uniaxial tension and torsion tests, a water-flushed, diamond-tipped core barrel with an inner diameter of 50-mm was used to score around the metal disk and through the CFRP. This scoring technique was used to minimize micro-cracking damage to the concrete [1]. Direct shear specimens were obtained using the same core barrel by fully coring through the slab. Figures 2 and 3 show the scoring procedure and the test-ready dolly, respectively.

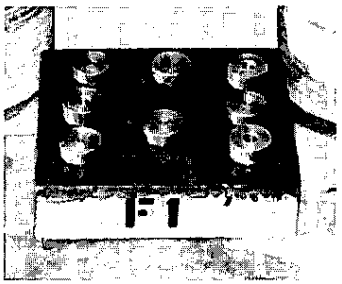

Figure 1. Bonded Test Fixtures (dollies)

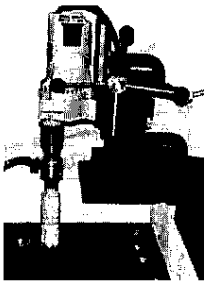

Figure 2. Scoring and Coring Slabs

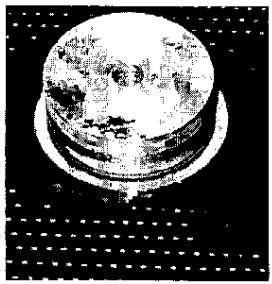

Figure 3. Bonded Dolly and Scored CFRP

TENSILE BOND APPARATUS

The uniaxial tension test apparatus used in the study is shown in Figure 4. It was comprised of a hand operated screw jack mounted to a reaction frame supported by three adjustable legs. The screw jack was used to apply a tensile force to the test dolly via an electronic load cell and a universal joint. The universal joint minimized loading irregularities associated with eccentricities. The load cell and a LVDT were monitored by a MEGADAC data acquisition system. Typical test results are shown in Figure 5.

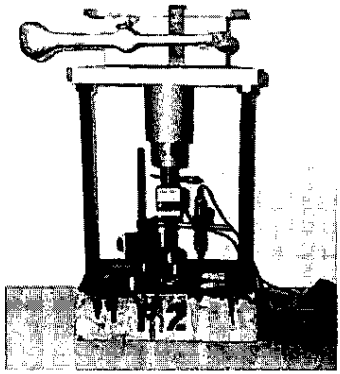

Figure 4. Tension Apparatus

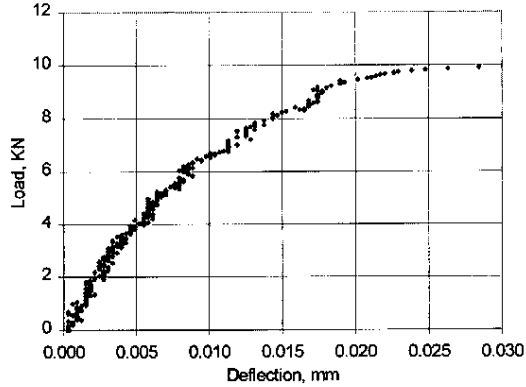

Figure 5. Typical Tension Test Results

DIRECT SHEAR TEST APPARATUS

The direct shear test apparatus was designed to cause shear failure along the CFRP/concrete interface. An average applied shear stress was determined by dividing the peak load (H) by the surface area (A) of the metal disk in contact with the CFRP material.

The essential features of the direct shear apparatus are shown in Figure 6. It consisted of a shear box made in three sections - the main box (top left), a sliding plate with a circular opening to accommodate the metal disk attached to the CFRP specimen (right), and a clamp to secure the specimen inside the box (front left). A 3 mm gap exists between the main section and the sliding plate that forms a predetermined failure plane. The box has appropriate fittings at its top and bottom so that it can be installed in a tension testing machine.

In contrast to the tensile bond test, the direct shear tests involved considerably more setup time and effort. Where tension tests only required the CFRP to be scored, the direct shear test required a cored slab sample be completely removed. Additionally, more precautions were required to eliminate the introduction of bending stresses. Therefore, the slide plate was supported by six sets of linear bearings that prevented out-of-plane rotation of the dolly. Each cored specimen was carefully aligned with the sliding plate and then cast into the direct shear apparatus with quick curing "pour rock" to eliminate stress concentrations on the uneven core surface. The entire assembly was then mounted in an Instron/MTI universal testing machine and a shear force applied to the plane containing the CFRP/concrete bond. Measurements of force vs vertical displacement were recorded throughout the testing. Typical results are shown in Figure 7.

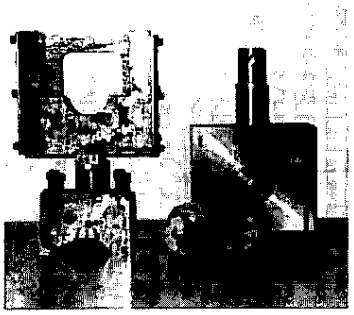

Figure 6. Direct Shear Apparatus

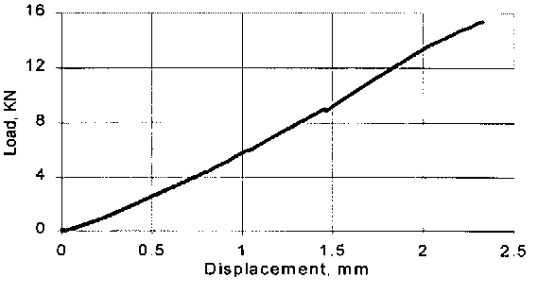

Figure 7. Typical Direct Shear Test Results

TORSION TEST

Apart from direct shear, specimens were also subjected to shear stress as a result of an applied torque. Due to the distribution of shear stresses induced by torsional loading, the failure stress was determined from the maximum measured torque.

Originally, a calibrated torque wrench was used in the testing as in a recent study [5]. However, it was evident that compound stresses were being induced by the manual application of the torque. Therefore, a reaction frame was designed and fabricated that allowed only pure torque to be applied to the specimen (Figure 8). Typical torsion test results are shown in Figure 9 from which peak torque was determined.

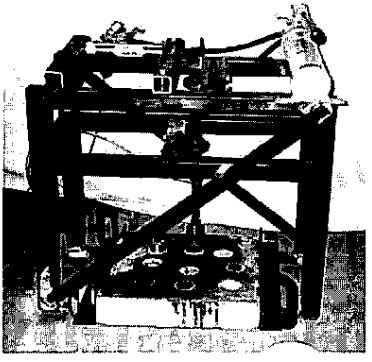

Figure 8. Torsion Test Frame

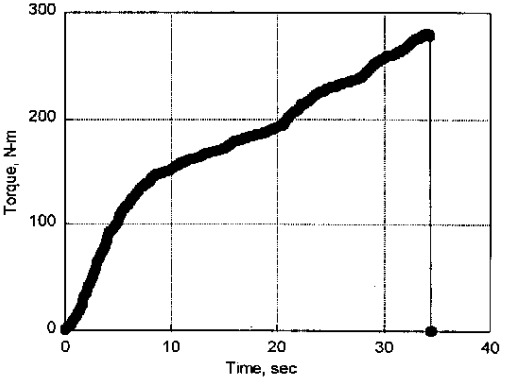

Figure 9. Typical Torsion Test Results

The torsion test frame was fabricated from 50 x 50 x 9.5 mm square tubing. A 25 mm diameter vertical shaft passes through the center of the frame, aligned by two pillow block bearings. At its lower extremity, the shaft is attached to a torque cell. At its upper extremity, the shaft is welded to a lever which pivots about the bearings. The ram of a hydraulic jack (mounted at the top of the frame), presses against the lever arm to apply the torque.

The torque cell was a calibrated shaft instrumented with four strain gages in a full bridge configuration aligned to detect torsional shear stresses. It was calibrated prior to the test to directly convert strains into torques.

The slab specimen is immobilized below the shaft in the reaction frame. A 19 mm hardened steel bolt was threaded and seated into the top of the torsion dolly. A socket placed on the head of the bolt completed the connection from the torque cell to the specimen. During testing, the torque cell was connected to a data acquisition system that recorded the peak applied torque (T). The maximum shear stress was calculated using the outer fiber radius (r) and the polar moment of inertia ($J = \pi r^4/2$).

TEST RESULTS

Results from uniaxial tension, direct shear and torsional shear tests are summarized for all five slab specimens in Table 1. The table lists the average failure stresses for each of the five slabs and the percentage of dolly area that debonded (italicized). This data was compiled from 45 tension, torsion and direct shear tests.

Table 1. Summary of Average Failure Stresses and Percent of Area Debonded

Slab ID	Average Failure Stress, MPa (ksi) and *Percent of Area Debonded %*					
	Tension (P/A)		Torsion (Tr/J)		Direct Shear (H/A)	
F1	5.2 (0.76)	*0%*	7.2 (1.04)	*0%*	7.2 (1.04)	*0%*
F2	5.1 (0.74)	*0%*	8.0 (1.27)	*33%*	6.6 (0.95)	*0%*
F3	5.1 (0.73)	*0%*	6.1 (0.89)	*85%*	5.8 (0.84)	*50%*
F4	4.3 (0.63)	*0%*	7.3 (1.06)	*20%*	6.2 (0.90)	*3%*
H1	4.3 (0.62)	*0%*	8.1 (1.27)	*65%*	6.0 (0.87)	*50%*
Average of All Slabs						
All	4.8 (0.70)	*0%*	7.3 (1.11)	*41%*	6.4 (0.92)	*20.6%*

Inspection of Table 1 shows tension failures occurred in the concrete in all five slabs even in series **F3** (specimen prepared with poor bond). In contrast, when defective specimens were tested in direct shear or torsion, partial debonding occurred in some tests (Figure 10). This suggests that in situations where bond is suspect, tensile tests may provide a misleading picture. The results also indicate that tensile bond stress values are about 30-40% lower than those from the shear bond tests. This trend is consistent with observations from similar tests carried out on repaired concrete [6].

In the torsional tests, only perfectly prepared specimens (**F1**) developed the full shear strength of the concrete. Although the direct shear tests exhibited less debonding than torsion, the failure stress was consistently lower than that produced on similar torsion samples. This implies that the torsion test can more effectively stress the bond line without affecting the base concrete.

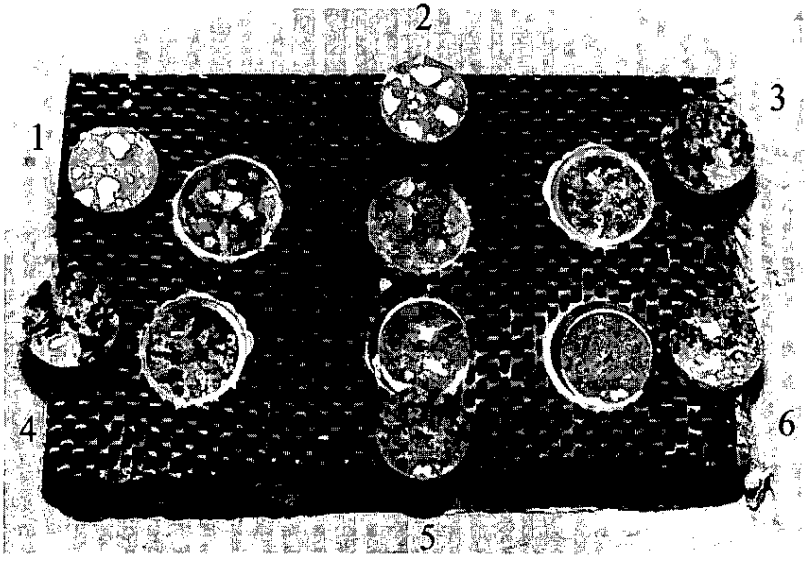

Legend: 1, 2 Tension
3, 4 Torsion
5, 6 Direct Shear

Figure 10. Failure Surfaces from Tension, Torsion, and Direct Shear Tests

CONCLUSIONS

The uniaxial tension test is widely used for assessing the bond between FRP and concrete. Unfortunately, in most applications the bond line is subjected to shear not tension making the uniaxial tension results of limited value. Moreover, as concrete has a very low tensile strength compared to the epoxy, failures generally occur in the concrete making it impossible to assess degradation in bond under service conditions unless the bond is disastrously weak. The alternative shear tests described in the paper lead to higher induced bond line stresses that do not necessarily lead to failure in concrete. Of these tests, the torsion test is the easiest to conduct, produces the highest bond line stresses, and better assesses the bond quality. However, when FRP is bonded correctly, none of the tests truly test the full strength of the epoxy bond due to the relatively lower strength of concrete.

ACKNOWLEDGMENTS

The authors gratefully acknowledge the advice and support of Dr. Howard Kliger. Materials tested were donated by Tonen Corporation of Japan and by Mr. Duane J. Gee of Fyfe Co. LLC. This support is gratefully acknowledged.

REFERENCES

1. Steele, J. (1994). "Testing Adhesion of Coatings Applied to Concrete", Materials Performance, Vol 33, No 11, pp. 33-36.

2. Sprinkel, M. (1995). Private Communication with R. Sen, August 11.

3. American Concrete Institute (1995). "Manual of Concrete Practice", Section 503R-95, Use of Epoxy Compounds with Concrete, Farmington Hills, MI.

4. Gere, J.M. and Timoshenko, S.P. (1984). Mechanics of Materials, Second Edition, PWS Publisher, Boston, MA.

5. Vaysburd, A.(1996). "External Carbonfiber Reinforcement Bond to Concrete". Presentation, ACI Fall Convention, New Orleans, November.

6. Knab, L.I., Sprinkel, M.M. and Lane, O.J. (1989). "Preliminary Performance Criteria for the Bond of Portland Cement and Latex Modified Concrete Overlays", NISTIR 89-4156, National Institute of Standards and Technology, MD.

Manjriker Gunaratne,[1] *Pamela Stinnette,*[1] *A. Gray Mullins,*[1] *Ching L. Kuo,*[2] *and Wayne F. Echelberger, Jr.*[1]

Compressibility Relations for Peat and Organic Soil

REFERENCE: Gunaratne, M., Stinnette, P., Mullins, A. G., Kuo, C. L., and Echelberger, W. F., Jr., **"Compressibility Relations for Peat and Organic Soil,"** *Journal of Testing and Evaluation*. JTEVA, Vol. 26, No. 1, January 1998, pp. 1–9.

ABSTRACT: A new technique is formulated to predict the ultimate settlement (primary and secondary) of normally consolidated organic soils on the basis of the organic content. Data from a large number of oedometer tests on samples collected from organic soil deposits in Central Florida exhibit a definitive relationship of ultimate settlement versus organic content. These laboratory test results are analyzed using the Gibson and Lo rheological model to develop expressions for primary and secondary compressibilities in terms of organic content and consolidation pressure. It is shown how the compressibility relations predicted by the authors' approach concur with extensive data collected by other researchers. The usefulness of the authors' analytical relations is displayed by showing how the expected ultimate settlement of an organic soil subjected to a given pressure increase can be computed readily by using them.

KEYWORDS: consolidation, organic soil, peat, ultimate settlement

Of the total area of organic soils in North America, an area of two million acres is in a single deposit in Florida known as the Everglades (Thomas 1965). These organic-rich soils are generally referred to as "muck," and when they contain more than 75% organics, as "peat." When this organic material is encountered within proposed roadway alignments, it is often regarded as an undesirable foundation material for highways because of its high compressibility and poor strength. Surcharging is one technique used to preconsolidate and stabilize such material. When surcharging is impractical, complete excavation or "demucking" is sought. However, in some situations, such costly construction practices can be avoided if the ensuing ultimate settlement can be estimated accurately and determined to be tolerable for the intended structure. Thus, analytical expressions for settlement estimation based on laboratory test results are invaluable for highway construction operations on natural organic soil deposits.

Although research findings on compressibility of peats are commonplace in the literature, data for natural amorphous organic deposits are scarce. Moreover, in spite of the recent application of rheological models to explain the settlement behavior of organic soils [*1,2*], definitive expressions for evaluating the model parameters have not been developed in terms of basic organic soil properties. Hence, the objective of this research is to present simple expressions to predict the ultimate, one-dimensional (1-D) settlement of natural organic soils with reasonable accuracy, using their basic index properties. Researchers have shown that the most significant basic index property of a normally consolidated organic soil is its organic content. Consistency limits such as the plasticity index and liquid limit are not practically meaningful when dealing with fibrous organic soils with a granular mineral soil component. Even in the case of amorphous organic samples in which a liquid limit can be experimentally found, a plasticity index may be difficult to obtain, a fact clearly seen by the position of organic soils in the Casagrande plasticity chart.

A number of consolidation tests run on normally consolidated Florida organic soil samples show definitive trends of ultimate settlement variations with organic content and with consolidation pressure. The ultimate laboratory settlements also agree reasonably well with the predictions of the Gibson and Lo [*8*] long-term solution for Merchant and Taylor's (1940) consolidation theory. Hence, using this theory, analytical relations are generated for primary and secondary compressibilities in terms of the organic content and the consolidation pressure. These relations enable one to determine simply the ultimate 1-D compression of an organic soil, precluding the need to differentiate the primary and the secondary settlements on a time scale.

Sample Classification and Consolidation Testing

Classification of the organic rich soils is generally done based on two classification systems. They are the Von Post System and the Kearns and Davison [*5*] System (Table 1). In the latter, the chemical and physical properties of organic soils at organic contents greater than 35% are dominated by the organics; therefore, the IT is placed in parentheses after the organic term. The appropriate IT term will depend on the dominant inorganic component (sand, silt or clay) of the soil. This method of classification agrees

TABLE 1—*Kearns and Davison* [5] *classification of organic rich soils.*

Organic Content, %	Classification
<5	IT
5–15	mucky IT
15–35	IT muck
35–55	muck (IT)
55–75	peaty muck (IT)
>75	peat (IT)

Manuscript submitted 11/30/95; accepted for publication 4/12/97.

[1]Department of Civil Engineering, University of South Florida, Tampa, FL.

[2]Senior engineer, Professional Services Industries (PSI), Tampa, FL.

with that of the American Society for Testing and Materials (ASTM) which defines true peat as containing more than 75% organic material.

Table 2 shows the classification and index properties of a number of Shelby tube organic soil samples recovered from various districts in South Central Florida, at depths of 0.3 to 0.5 m. These are identified by the designation of highways closest to the site where they were retrieved such as US 27, SR 597, etc. The inorganic portion of the samples was predominantly coarse grained or silty and the fiber contents were very low, making them mostly amorphous material. Furthermore, none of the samples indicated any appreciable overconsolidation during conventional consolidation testing performed on them [*6*]. Thus, all the samples were adjudged to be normally consolidated (NC) for all practical purposes, which can be attributed to the shallow depths where they were retrieved. This assertion is further verified by the compressibility relations formulated in this study, which portray all of the samples tested as being in the same family (NC) of soils, as far as the ultimate settlement behavior is concerned. Since there is no traceable stress history, such as reported previous loadings, there was no need to include that factor, except to emphasize that the developed relations are valid for NC organic soils. Retrieval of significantly overconsolidated samples and modifying the relations with the overconsolidation ratio (OCR) parameter can be an extension to this project.

Analysis of Laboratory Consolidation Tests

In Florida organic soil deposits, which are often completely saturated, the main causes of settlement due to a stress increase are expulsion of pore fluids and simultaneous compression of the organic soil structure. These causes, classically separated into primary and secondary compression, respectively, have been postulated to occur concurrently. Researchers [*1*] have often sought rheological models to predict the settlement behavior of organic soils.

A commonly adopted parameter to express the secondary settlement behavior of organic soils is the coefficient of secondary consolidation ($\mathbf{C}_\alpha$), which is defined as the slope of the linear portion of a vertical strain versus logarithm-of-time plot. Although convenient for settlement rate predictions, such a linear plot does not adequately explain any termination in secondary compression. Berry and Poskitt (1972) used a rheological model to provide an analytical base to the above approach and validate the $\mathbf{C}_\alpha$ concept for both amorphous and fibrous peats. Their theoretical formulation is based on linking the primary and secondary compression to discrete void ratio changes in the soil skeleton, a concept that is utilized in the current work as well. More recently, Fox et al. [*7*] showed that $\mathbf{C}_\alpha/\mathbf{C}_c$ concept does not apply to peat. This empirical concept also suffers from its inability to predict the ultimate settlement.

TABLE 2—*Classification of Florida organic soil samples.*

Location	Water Content, (%)	Organic Content, (%)	Wet Density, (kN/m^3)	Specific Gravity	Initial Void Ratio	Classification
SR 951B	116	8.6	13.5	2.40	2.8	mucky sand
SR 951A	97	10.8	13.1	2.63	2.9	mucky sand
SR 597A	61	12.4	14.9	2.40	1.5	mucky silt
S 951B	165	15.8	13.3	2.41	3.7	muck
S 951A	292	37.0	11.0	2.13	6.5	muck
S 951C	326	43.5	10.6	1.95	6.7	clayey muck
SR 597B	291	57.4	10.8	2.09	6.4	peaty muck
US 27B	686	81.7	9.9	1.58	11.3	silty peat
US 27A	726	88.9	9.8	1.34	10.1	silty peat
SR 46E	654	92.1	10.1	1.45	9.6	sandy peat

Out of all the above-mentioned techniques, the Gibson and Lo [*8*] model based on Merchant and Taylor's theory was found to be more applicable for the organic soils tested in this project. The main attractiveness of the Merchant and Taylor theory lies in its generalization of Terzaghi's 1-D primary consolidation theory to include creep effects, as seen in Eq 1.

$$C_v \frac{\partial^2 u}{\partial z^2} = \frac{\partial u}{\partial t} - \frac{\lambda}{ab}\left[(a + b)(u_o - u) + \frac{e - e_o}{1 + e_o}\right] \quad (1)$$

where

a = primary compressibility = $\delta\epsilon_p/\delta\sigma$
b = secondary compressibility = $\delta\epsilon_s/\delta\sigma$
λ/b = secondary compression rate factor
ϵ_p = primary component of strain
ϵ_s = secondary component of strain
e_o, u_o = initial void ratio and pore pressure
C_v = conventional coefficient of consolidation

The above theory simulates the reality where both pore pressure dissipation and creep take place simultaneously. Hence, although the theory acknowledges different mechanisms as causing the two types of settlement and treats them accordingly, the following solutions derived for Eq 1 by Gibson and Lo [*8*] do not differentiate the two phenomena on a time scale.

For small time periods,

$$\epsilon = 2\sqrt{\frac{kt}{\pi a \gamma_w}}\frac{\Delta\sigma}{a}\left[1 + \frac{\lambda t}{3a} + \text{Order}\left(\frac{\lambda t}{a}\right)^2\right] \quad (2)$$

For large time periods,

$$\epsilon = \Delta\sigma[a + b(1 - e^{-\frac{\lambda t}{b}})] \quad (3)$$

where

$\Delta\sigma$ = effective stress increment
k = coefficient of permeability

It should be noted that a, k, and C_v are considered constants. Equation 3 predicts the settlement at $t \rightarrow \infty$ as $(a + b)\Delta\sigma$. This would be the settlement after both primary and secondary settlements are completed. From the original Merchant and Taylor's solution it can be shown that a is the commonly used coefficient of primary compressibility, m_v.

The Gibson and Lo model has been used successfully to represent the laboratory and field compression curves for organic soils that exhibit significant secondary compression behavior [*1*]. However, the model does not take into account certain nonlinearities that may result from finite strains, stress level, and strain rate. In spite of these drawbacks, this model yields reasonable results in predicting the rate and magnitude of settlement when compared to field measurements [*1*]. However in a latter study, Edil and Simon-Gilles [*2*] report limitations of the above model in predicting field settlement. The authors address this issue in a section of this paper where their model predictions are compared with published laboratory results.

Comparison of Laboratory Results with the Gibson and Lo Model Predictions

Since Eq 3 expresses the combined 1-D strain of a soil undergoing concurrent pore pressure dissipation and creep during large time intervals, the authors applied it for predicting the combined (ultimate) settlement of Florida organic soil. Hence, although the pore pressures were monitored, the more common approach of indicating the EOP on the settlement plots was unnecessary for development of this model. In evaluating the parameters a, b, and λ for each consolidation test, the technique developed by Edil and Dhowian [9] was used. This technique employs a plot of the logarithm of strain rate versus time [(log $(\Delta\epsilon/\Delta t)$) versus t]. By simple manipulation of Eq 3, it can be shown to be linear for the time range corresponding to secondary compression if the soil agrees with the basic assumptions made in the model. The slope and intercept of the best-fit line yield the values of a, b, and λ as follows:

$$\text{Slope} = -0.434(\lambda/b) \tag{4}$$

$$\text{Intercept} = \log_{10}(\Delta\sigma\lambda) \tag{5}$$

$$a = \frac{\epsilon(t_k)}{\Delta\sigma} - b + be^{-(\lambda/b)t_k} \tag{6}$$

where t_k is equal to the last time a reading of compression was taken [1].

Edil et al. [2] also state that long-term compression tests performed on fibrous peats do not show a linear ln ϵ versus t tendency when the load increments are permitted to remain on a specimen for up to six months. This further supports the Gibson and Lo model for large time intervals (Eq 3), which predicts a nonlinear relationship between ln ϵ and time.

Figure 1 shows the logarithm of strain rate versus time plots obtained from a sample taken from US 27B for six different consolidation stages. A pronounced departure from linearity is seen in the initial stages. This is because Eq 3 is a specific solution valid only for relatively large time periods. On the other hand, the perfect matching of Eq 3 with actual data for large time periods is remarkable, as indicated by Fig. 1. Similar results were obtained for all the samples tested [6].

Moreover, the predicted ultimate settlement also agreed very well with the asymptotic value established by tracing the deflection versus time curves for each test [6]. Thus, it was concluded that the above rheological approach is suitable for modeling the ultimate compression of Florida organics. As the model also offers the added advantage of yielding primary and secondary compressibilities, it was determined to be ideal for the development of compressibility relations.

Compressibility Relations

The a and b coefficients found using Eqs 4–6 from plots (such as Fig. 1) corresponding to all of the samples are seen in Table 3. a and b are seen to vary with consolidation pressure (σ) and the organic content (oc). The following formulation describes the derivation of explicit relationships for a and b, based on the experimental data in Table 3.

To decouple the discrete void ratio changes due to primary and secondary compressions, the authors assumed the void ratio to constitute primary compression and secondary compression components of the soil skeleton. For each consolidation load step, these components correspond to the void volumes that can be separately closed by exhaustive primary and secondary compressions, respectively. In this paper, they will be referred to as $(\Delta e)_p$ and $(\Delta e)_s$, which correspond to one-dimensional strains $\Delta\epsilon_p$ and $\Delta\epsilon_s$ identified in relation to Eq 3.

When the initial void ratios (e_0) of the samples are plotted against their organic contents (Table 2), the following linear relation is obtained (Fig. 2):

$$e_0 = 1.79 + 9.72(oc) \tag{7}$$

Equation 7 is in concurrence with the Andersland et al. [3] conclusion for fibrous organic samples.

Next, the authors expressed basic compressibility relationships in terms of e_p and e_s, which are the equilibrium (final) void ratios for a given loading under purely primary and purely secondary compressions, respectively:

$$e_p = e_0 - (\Delta e)_p = f_1(oc, \sigma) \tag{8}$$

$$e_s = e_0 - (\Delta e)_s = f_2(oc, \sigma) \tag{9}$$

Thus, the actual equilibrium void ratio under any loading is given by:

$$e = e_0 - (\Delta e)_p - (\Delta e)_s \tag{10}$$

It should be noted that the primary and secondary compressibilities are separated in Eq 10 on a magnitude basis and not on a time scale. The combination of Eqs 8–10 produces the useful relationship,

$$e = e_p + e_s - e_0 \tag{11}$$

The authors then employed the following methodology to synthesize the functions f_1 and f_2 utilizing the data in Table 3. During the jth loading step of 1-D consolidation of a given organic soil sample:

$$a_j = -\frac{1}{1 + e_j}\frac{(\Delta e)_{j,p}}{\Delta\sigma_j} \tag{12}$$

where $(\Delta e)_{j,p}$ is the change in primary void ratio of the sample and e_j is the initial void ratio during that step.

Therefore, at the end of a consolidation test with $n - 1$ load increments, the final void ratio due to primary compression alone is:

$$e_{n,p} = e_0 - \sum_{j=1}^{j=n-1} a_j(\Delta\sigma)_j(1 + e_j) \tag{13}$$

which is the equilibrium void ratio due solely to primary compression (Eq 8) of the particular sample at a consolidation pressure σ given by:

$$\sigma = \sum_{1}^{n-1} \Delta\sigma_j \tag{14}$$

Using similar reasoning, the equilibrium void ratio due to secondary compression (Eq 9) of a sample with a specified organic content, oc, at a consolidation pressure, σ, (Eq 14) is given by

$$e_{n,s} = e_0 - \sum_{j=1}^{j=n-1} b_j(\Delta\sigma)_j(1 + e_j) \tag{15}$$

The above steps illustrate how e_p and e_s can be evaluated using a, b, and e_0 values in Tables 2 and 3 as well as Eq 10, which

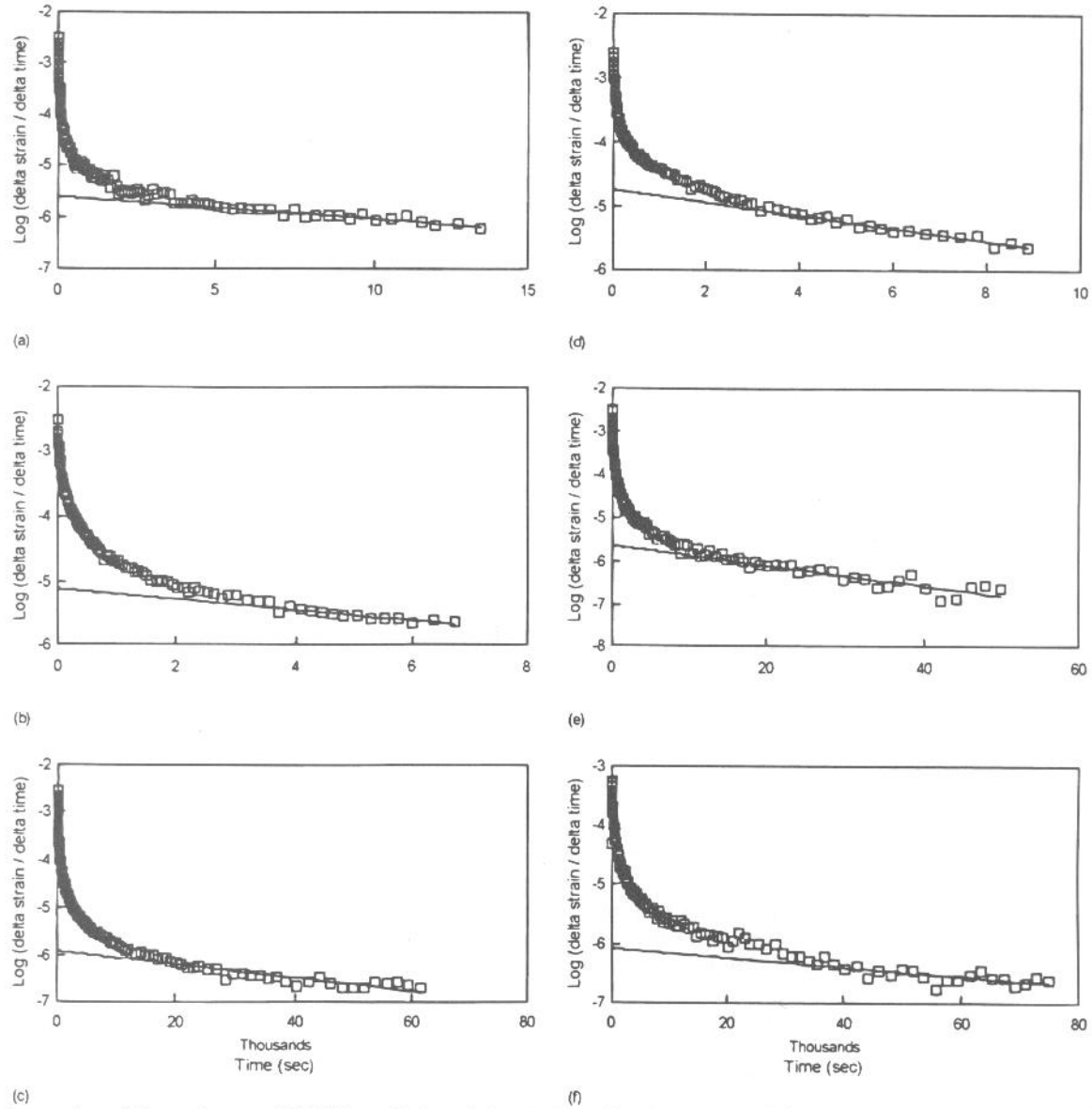

FIG. 1—*Comparison of the settlement of US 27 sample B with the rheological predictions. Applied pressures are (a) 31.9 kPa, (b) 63.79 kPa, (c) 127.59 kPa, (d) 255.18 kPa, (e) 510.35 kPa, (f) 1020 kPa.*

computes the actual void ratio e_j in each loading step. At this stage of the formulation, functions f_1 and f_2 in Eqs 8 and 9 can be illustrated graphically by plotting e_p and e_s values for each sample against its organic content at different consolidation pressures σ. As seen in Figs. 3 and 4, these individual plots are linear with respect to the organic content. It is realized that e_p and e_s are imaginary void ratios back-calculated based on the a and b values in Table 3 that relate to the final void ratio, e, through Eq 1. It can be deduced from the above linear relations that the resultant equilibrium void ratio due to both primary and secondary compressions should also be linear with respect to the organic content, which confirms Andersland et al. [*3*] observations.

Now, following the Andersland et al. [*3*] approach, expressions 8 and 9 can be rewritten as:

$$e_p = I_p(\sigma) + M_p(\sigma).oc \tag{16}$$

$$e_s = I_s(\sigma) + M_s(\sigma).oc \tag{17}$$

where $I(\sigma)$ and $M(\sigma)$ are intercepts and slopes corresponding to any given consolidation pressure σ of Figs. 3 and 4. Derivation of expressions for $I(\sigma)$ and $M(\sigma)$ values will be discussed in the following section. Since the expressions must accommodate the lower and the upper boundaries of σ which are (1) $\sigma = 0$—the unloaded condition and (2) $\sigma \rightarrow \infty$—the infinite pressure condition, the following 3-parameter rectangular hyperbolic equation $F(\sigma)$ was fitted for all four I and M expressions in Eqs 16 and 17:

$$F(\sigma) = A - \frac{\sigma}{B\sigma + C} \tag{18}$$

It is obvious from Eq 18 that when $\sigma = 0$, $F(\sigma)$ should provide the value of A. Hence, inspection of Eq 7 and comparison with Eqs 16 and 17 reveal that the A term for both I and M functions will be 1.79 and 9.72, respectively.

With the A parameter known, the following rearranged linear

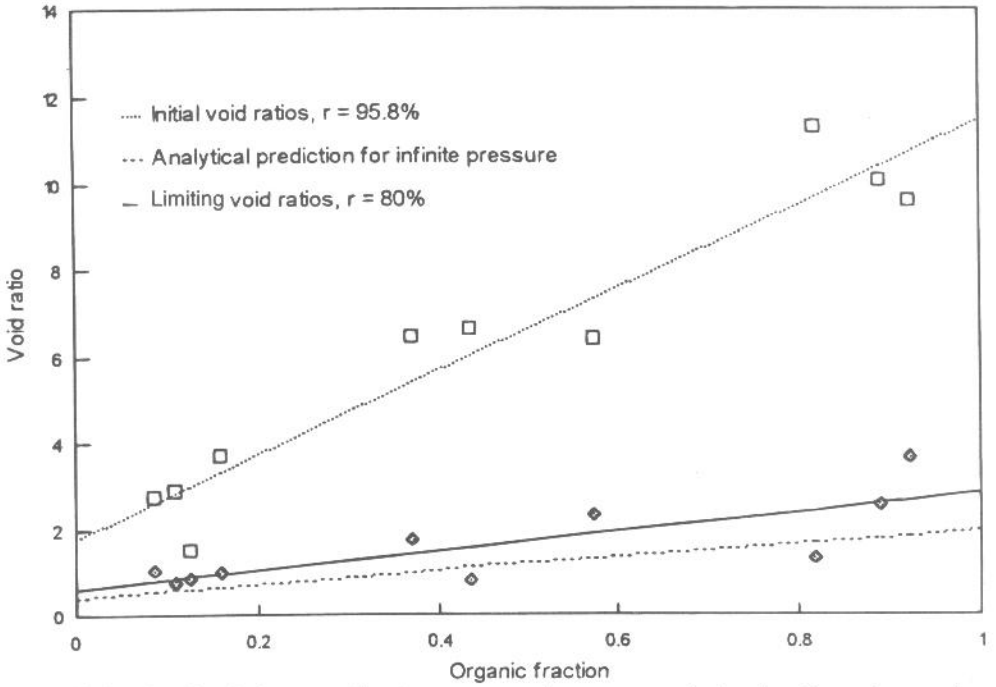

FIG. 2—*Initial and ultimate void ratio versus organic content correlations for all samples tested.*

form of Eq 18 was used to find B and C using linear regression analysis:

$$\frac{\sigma}{A - F(\sigma)} = B\sigma + C \tag{19}$$

It is realized that $F(\sigma)$ values are obtained from the slopes or intercepts of Fig. 3 (for primary compression) and Fig. 4 (for secondary compression), depending on whether F represents M or I. The resulting expressions and the corresponding correlation coefficients (r) are given in Eqs 20–23, in which the pressure is measured in kPa.

TABLE 3—*Experimental compressibility values* a *and* b *(in parentheses) in* 10^{-5} m^2/kN.

Organic Content, (%)	Stress (kPa)					
	31.9	63.8	127.6	255.2	510.4	1020.8
8.6	170	96	89	25	19	7
	(23)	(32)	(13)	(10)	(4)	(1)
10.8	303	106	99	28	24	9
	(59)	(52)	(22)	(13)	(4)	(2)
12.4	144	34	32	14	11	5
	(16)	(8)	(6)	(3)	(2)	(1)
15.8	416	116	79	41	15	8
	(118)	(74)	(28)	(14)	(4)	(2)
37.0	456	116	69	33	15	3
	(172)	(142)	(86)	(25)	(6)	(4)
43.5	276	146	138	68	27	9
	(169)	(163)	(63)	(28)	(22)	(7)
57.4	97	81	82	30	28	12
	(93)	(36)	(21)	(16)	(6)	(3)
81.7	548	219	163	52	46	23
	(81)	(63)	(29)	(31)	(8)	(5)
88.9	366	53	153	52	36	11
	(94)	(63)	(26)	(21)	(6)	(3)
92.1	160	78	64	59	21	8
	(235)	(52)	(38)	(12)	(4)	(2)

$$I_p(\sigma) = 1.79 - \frac{\sigma}{1.27\sigma + 97.79} \qquad r = 99.95\% \tag{20}$$

$$M_p(\sigma) = 9.72 - \frac{\sigma}{0.16\sigma + 23.13} \qquad r = 99.95\% \tag{21}$$

$$I_s(\sigma) = 1.79 - \frac{\sigma}{1.86\sigma + 360.17} \qquad r = 96.2\% \tag{22}$$

$$M_s(\sigma) = 9.72 - \frac{\sigma}{0.52\sigma + 40.61} \qquad r = 99.95\% \tag{23}$$

When the ultimate deflection of all the samples was plotted against the consolidation pressure over the entire range of pressures (Fig. 5), the ultimate settlement tends to diminish gradually with increasing pressure as one would anticipate, until what appears to be a limiting settlement is reached at very high pressures. Based on the

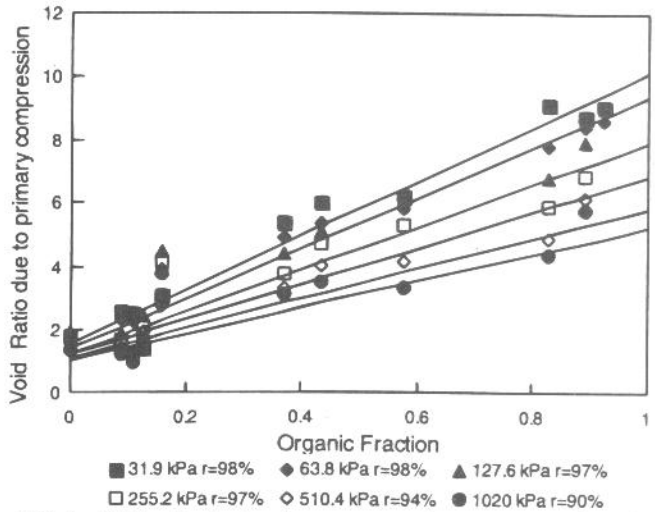

FIG. 3—*Void ratio due to primary compression versus organic content correlation for all of the samples.*

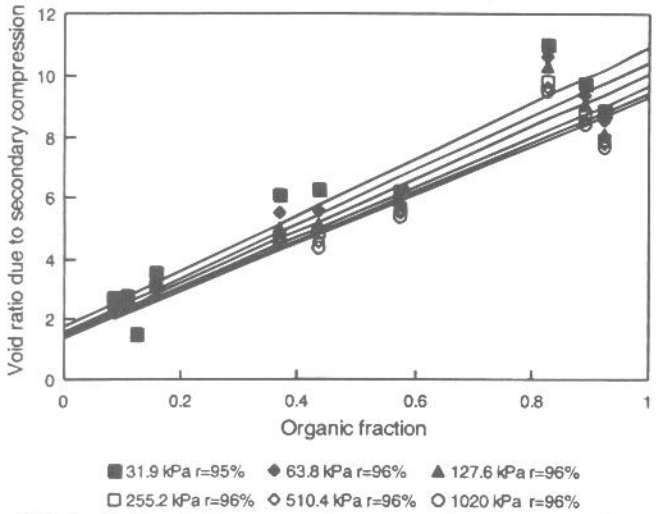

FIG. 4—*Void ratio due to secondary compression versus organic content correlations for all of the samples.*

limiting settlement value for each sample in Fig. 5, the authors estimated the corresponding limiting void ratios (for $\sigma \rightarrow \infty$) for each sample and extracted the ultimate void ratio versus organic content curve, which is the upper pressure boundary of the family of e versus oc plots in Fig. 2.

The above limiting void ratio versus organic content curve can also be obtained by using the authors' analytical relation by setting $\sigma \rightarrow \infty$ in Eqs 20–23 and substituting in Eqs 16, 17 and 11 as

$$e_\infty = 0.46 + 1.55(oc) \tag{24}$$

When plotted on Fig. 2, Eq 24 matches well with its experimental counterpart, thus further confirming the validity of the relationships in the entire range of pressure values from zero to infinity.

Determination of *a* and *b* Compressibility Parameters

It is known that a can be determined by the continuous form of Eq 12 as

$$a = -\frac{1}{(1 + e)} \frac{\partial e_p}{\partial \sigma} \tag{25}$$

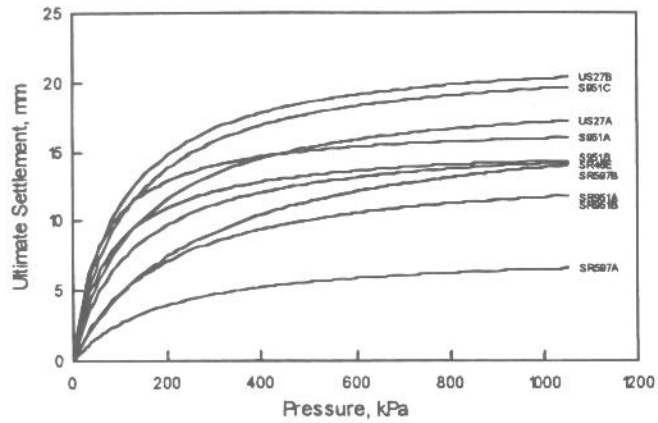

FIG. 5—*Ultimate settlement versus consolidation pressure curves for all of the samples.*

Then, by substitution for e_p from Eq 16:

$$a = -\frac{1}{(1 + e)} \left[\frac{d}{d\sigma} \overline{I_p(\sigma)} + oc \frac{d}{d\sigma} \overline{M_p(\sigma)} \right] \tag{26}$$

The actual equilibrium void ratio e in the denominator in Eq 6 can also be represented with a hyperbolic relation on its own as in the cases of e_p and e_s. Finally, by introducing the first derivatives of Eqs 20 and 21 in Eq 26, the expression for a can be obtained as (σ in kPa)

$$a = \frac{\dfrac{97.79}{(1.27\sigma + 97.79)^2} + \dfrac{23.13.oc}{(0.16\sigma + 23.13)^2}}{F(oc, \sigma)} \tag{27}$$

Similarly for b, one can deduce

$$b = \frac{\dfrac{360.17}{(1.86\sigma + 360.17)^2} + \dfrac{40.61.oc}{(0.52\sigma + 40.61)^2}}{F(oc, \sigma)} \tag{28}$$

where

$$F(oc, \sigma) = \left[2.79 - \frac{\sigma}{(0.78\sigma + 74.28)} \right] + oc \left[9.72 - \frac{\sigma}{(0.12\sigma + 15.33)} \right]$$

The above primary and secondary compressibility expressions can be used to evaluate the 1-D ultimate strain from Eq 3 as:

$$\epsilon_{ult} = \Delta\sigma[a + b] \tag{29}$$

Sometimes it is common practice to characterize an organic soil deposit based on its moisture content rather than the organic content. Hence, a useful relationship was developed between the initial moisture content, w_o (%), and the organic content, oc (%), [6] as:

$$oc = w_o * 0.136 + 2.031 \qquad r = 93\% \tag{30}$$

Equation 30 can be used to estimate the ultimate strain from Eqs 27–29 when the organic content is not available.

Verification of the Compressibility Relation

Figure 6 shows a plot of the predictions of a and b from the above expressions compared with the experimental values for the

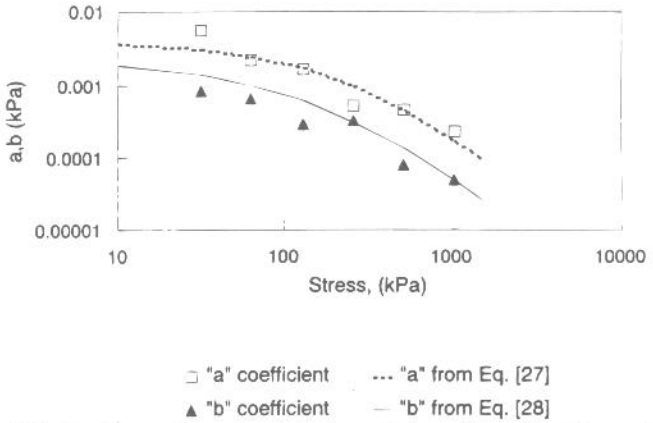

FIG. 6—*Comparison of analytical predictions of* a *and* b *with experimental values for US 27 sample B.*

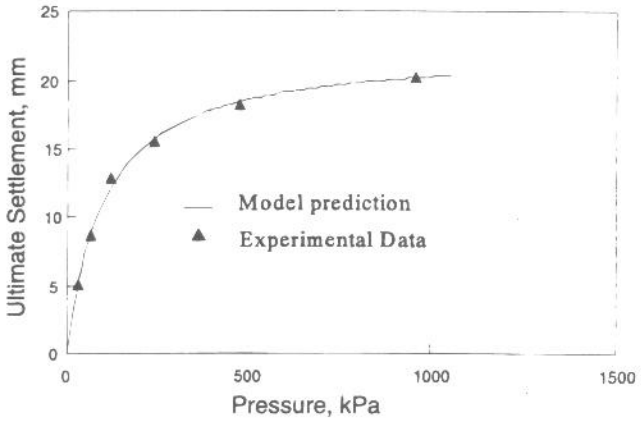

FIG. 7—*Comparison of the model predictions and experimental data for US 27 sample B.*

US 27 sample B found in Table 3. For the same sample (US 27 sample B) in Fig. 7, the authors also plotted the ultimate settlement obtained from the above expressions against the experimental values shown in Fig. 5. Reasonable agreement is observed in both Figs. 6 and 7. An additional consolidation test on a similar sample of organic soil (oc = 95%) was also performed for a much longer period of time. Figure 8 shows the settlement versus time plot for the new test up to a period of 18 days. It is seen how the secondary settlement continued at the end of the observation period, at a reduced rate. Figure 8 also shows the model prediction of the ultimate settlement and one can observe the agreement between the extrapolated (extended) settlement curve and the model prediction.

Comparison with Published Laboratory Results

The authors scrutinized the validity of their model for laboratory tests conducted by independent sources [*1*]. Figures 9 and 10 are plots of a and b values obtained by Eqs 27 and 28 against the pressure for different organic contents. A proposed average experimental correlation suggested by Edil and Mochtar [*1*] based on a large base of laboratory data is plotted on Figs. 9 and 10 as well. The agreement between the authors' predictions for organic contents in the range of 50% to 90% and Edil's laboratory results is encouraging. Furthermore, when comparing the authors' predictions with Edil and Mochtar's [*1*] plots, one realizes that the scatter in the latter group of data can be due predominantly to the variability of organic contents of the peats and the OCRs in the case of OC peat samples.

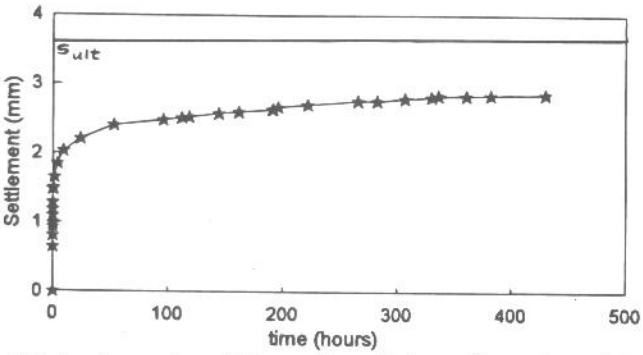

FIG. 8—*Comparison of the model prediction and experimental data for the I-4 sample.*

Application to Field Organic Soil Deposits

The Edil and Mochtar [*1*] field database for peat shown in Fig. 10 shows a deviation from the laboratory results. Edil and Mochtar [*1*] attribute this departure in the field results to differences in strain rates.

One can attribute part of the above deviation to lateral strains that can occur in the field as well. Gruen and Lovell [*10*] also state that settlement resulting from lateral movement under load have been found to be relatively large and report that in the field, lateral strains can contribute up to 30% of the total settlement. The authors' 1-D model can be modified by incorporating 3-D field effects arising from lateral strains to show that magnitudes of measured a and b values can vary between laboratory and field conditions [*6*]. Therefore, Eqs 27 and 28 may also be applied to predict the settlement behavior of organic soil deposits where the lateral strains are insignificant. These conditions can typically occur in the middle of loads, such as roadway fills, covering an extensive area. It should also be noted that field primary consolidation is usually estimated based on 1-D consolidation tests.

Numerical Example

The following numerical example illustrates the significance and the use of Eqs 27 and 28. Assume that based on the laboratory consolidation test results, one wishes to predict the ultimate 1-D settlement expected in a 1 m thick organic soil layer (oc = 50% and current overburden stress 50 kPa) due to an extensively placed surcharge of 50 kPa.

Since there is no significant stress attenuation within 1 m due to an extensive surcharge, the final pressure will be 100 kPa throughout the layer. Then, by applying Eq 29, one obtains

$$\epsilon_{ult} = \int_{50}^{100} [a(\sigma) + b(\sigma)]\, d\sigma \tag{31}$$

where $a(\sigma)$ and $b(\sigma)$ are obtained from Eqs 27 and 28 using an oc value of 0.5.

Finally, when Eqs 27 and 28 are substituted in Eq 31 and numerically integrated, primary and secondary compressions of 0.107 m and 0.041 m are predicted. Hence, an ultimate settlement of 0.148 m can be anticipated. The numerical integration can be easily performed using *Mathcad* or a similar package.

Conclusion

Results of laboratory tests conducted on Florida's natural normally consolidated organic soils indicate that the ultimate settlement can be predicted accurately by the Gibson and Lo [*8*] rheological model. Using laboratory correlations, closed-form expressions useful for predicting analytically the ultimate 1-D settlement of normally consolidated organic soils have been developed and experimentally verified for a wide range of organic contents. The close agreement between the authors' analytical predictions and the results collected elsewhere [*1*] suggests a possible extension of these relations to other natural organic soils with coarse-grained inorganic components.

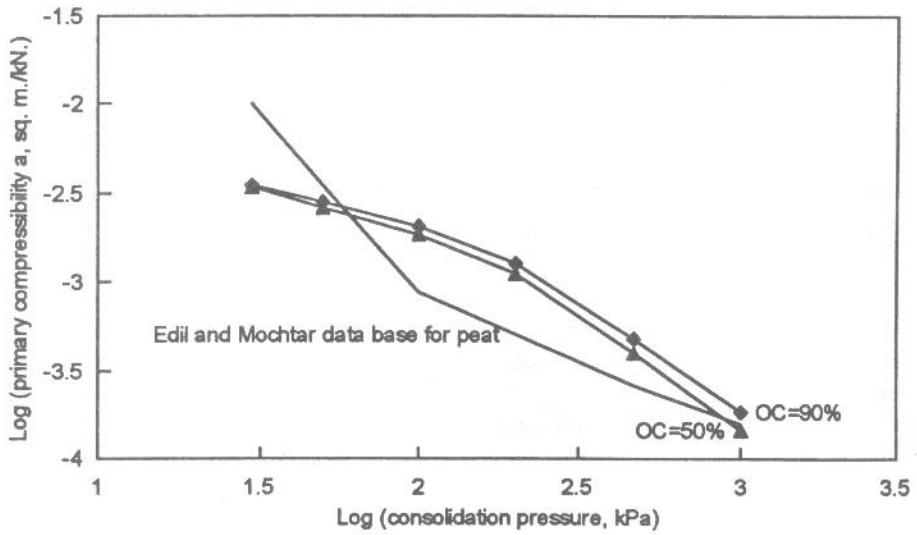

FIG. 9—*Variation of primary compressibility with consolidation pressure and organic content compared with Edil and Mochtar's* [1] *database for peat.*

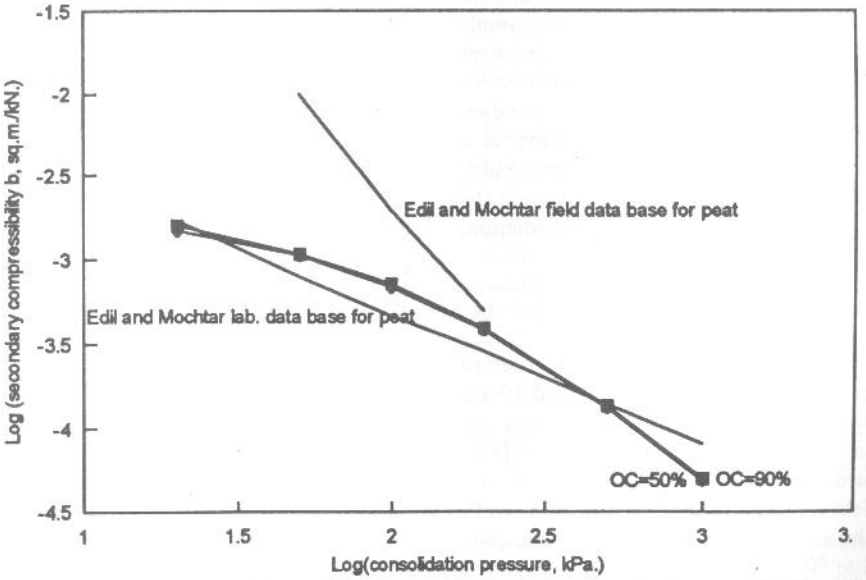

FIG. 10—*Variation of secondary compressibility with consolidation pressure and organic content compared with Edil and Mochtar's* [1] *database for peat.*

The inclusion of zero pressure and infinite pressure boundary conditions in formulating e versus σ plots allows these relations to be applicable for a wide consolidation pressure range. This feature makes it a unique model compared to existing consolidation models that do not accommodate extreme pressure conditions, leading to undefined void ratios at extremely low and extremely high pressures. Another significant outcome of this study is that the frequently observed nonlinearity of e versus log σ curves for most organic soils is explained by the hyperbolic nature of the newly-developed e versus σ curves.

Acknowledgments

The authors wish to thank Dr. Rajaram Janardhanam, professor of civil engineering at the University of North Carolina, Charlotte, for review of this manuscript.

References

[1] Edil, T. B. and Mochtar, N. E., "Prediction of Peat Settlement," *Sedimentation Consolidation Models Predictions and Validation*, Proceedings of a symposium sponsored by the ASCE Geotechnical Engineering Division in conjunction with the ASCE Convention in San Francisco, CA, October 1, 1984, R. N. Young and F. C. Townsend, Eds., American Society of Civil Engineers, New York, 1984, pp. 411–424.

[2] Edil, T. B. and Simon-Gilles, D. A., "Settlement of Embankments on Peat: Two Case Histories," *Proceedings*, Conference on Advances in Peatlands Engineering, National Research Council of Canada, 1986.

[3] Andersland, O. B. and Al-Khafaji, A. A. W. N., "Organic Material and Soil Compressibility," *ASCE Journal of the Geotechnical Engineering Division*, Vol. GT7, July 1980, p. 749.

[4] Holtz, R. D. and Kovacs, W. D., *An Introduction to Geotechnical Engineering*, Prentice-Hall, Inc., 1981.

[5] Kearns, F. L. and Davison, A. T., "Field Classification of Organic Rich Soils," *Proceedings*, Mineral Matter in Peat: Its Occurrence, Form and

Distribution, R. Raymond, Jr. and M. J. Andrejko, Eds., Los Alamos National Laboratory, Los Alamos, NM, 1983, pp. 147–157.

[6] Stinnette, P., "Engineering Properties of Florida Organic Material," Masters thesis, University of South Florida, Tampa, FL, 1992.

[7] Fox, P. J., Edil, T. B., and Li-Tus, L., "C∝/Cc Concept Applied to Compression of Peat," *Journal of Geotechnical Engineering*, Vol. 118, No. 8, 1992.

[8] Gibson, R. E. and Lo, K. Y., "A Theory of Consolidation of Soils Exhibiting Secondary Compression," *Acta Polytechnical Scandinavia*, Ci 10 296: Scandinavian Academy of Science, 1961.

[9] Edil, T. B. and Dhowian, A. W., "Analysis of Long-Term Compression of Peats," *Journal of Geotechnical Engineering*, Vol. 10, 1979, pp. 159–178.

[10] Gruen, H. A. and Lovell, C. W., "Use of Peats as Embankment Foundations," Joint Highway Research Project IN/JHRP-83/3, 1983, p. 43.

Geotechnical and Geological Engineering, 1997, **15** 283–302

A quality control programme for performance evaluation of dynamic replacement of organic soil deposits

P. STINNETTE*, M. GUNARATNE, G. MULLINS and S. THILAKASIRI

Department of Civil and Environmental Engineering, University of South Florida, 4202 E. Fowler Avenue, Tampa, FL 33620, USA

Received: 18 March 1996
Accepted: 19 August 1997

Summary

Dynamic replacement (DR) is a relatively new ground-modification technique that has been used successfully to stabilize organic soil deposits by replacing the organic soil with sand columns. A full-scale DR field study was conducted in order to assess its effectiveness on Florida organic soils. A computer-based quality control system was developed using data-acquisition-management techniques to evaluate the degree of improvement of the organic soil layer at a given stage of treatment. One of the DR drop locations was instrumented in order to select technical criteria such as the print spacing and the number of blows per print for effective DR implementation, and to facilitate monitoring of the improvement of soil properties. The new quality control system evaluates the effects of treatment by computing the dynamic settlement modulus (DSM) from the impact acceleration data collected during the treatment period. This paper presents the results obtained from the pilot study and their subsequent use in establishing evaluation criteria for the test programme. It is also shown how the DSM-based treatment criteria are in agreement with those obtained from conventional methods. Hence, it is concluded that with the use of the quality control system presented, the implementation of any DR programme can be effectively monitored.

Keywords: Dynamic replacement; organic soil; data acquisition; data management.

Introduction

Organic soils are abundant in Florida, with two million acres existing in a single deposit known as the Everglades (Thomas, 1965). These organic-rich soils are generally referred to as ‘muck’, and when high in organic levels ($>75\%$) as ‘peat’. When this organic material is encountered within proposed roadway alignments, it is often regarded as an

* To whom correspondence should be addressed at: Hillsborough Community College, 1206 N. Park Road, Plant City, FL 33566, USA.

undesirable foundation material for highways due to its high compressibility and poor strength. Surcharging is one technique used to preconsolidate and stabilize such material. However, when surcharging is deemed impractical, complete excavation or 'demucking' is sought. Clearly, a timely and cost-effective treatment alternative is desirable.

The commonly used dynamic compaction is typically confined to loose natural soil deposits and miscellaneous fill materials (Lukas, 1992). However, several dynamic replacement (DR) case studies have been reported that involve the application of low- and high-energy impacts onto organic soil deposits that are overlain with sand surcharges. Lo *et al*. (1990) report that, by using a combination of low-energy impacts followed by high-energy ones, a peaty clay deposit can be transformed into an upper sand raft with pockets of peaty sand underlain by a fairly uniform layer of mixed sand and peat. They further report that both layers exhibit relatively insignificant secondary compression characteristics. In an earlier study on peaty clay, Ramaswamy *et al*. (1979) report improvements in both strength and consolidation characteristics of the site studied as a result of high-energy impacts. Ramaswamy *et al*. (1979) also note the procedure's cost effectiveness over other alternatives and estimate potential savings of 30%.

Field study site

The DR field study site selected is located in Plant City, Florida, USA. The site, owned by the Florida Department of Transportation (FDOT), is adjacent to Interstate I-4 in Eastern Hillsborough County. In order to conduct the study, an area of the site of 0.2 ha was cleared and filled with approximately 1–1.5 m of sandy fill material (approximately 7% fines). This material acted as a foundation for the crane and cone truck and as initial replacement material for the dynamic replacement process. The cleared study site with the fill material placed is shown in Fig. 1. The extent of the organic deposit at the site satisfied the requirements of the project, being representative of what is typically encountered in highway construction alignments. In fact, the site itself is expected to become a part of a scheduled I-4 on-ramp (slip road) to be constructed in the summer of 1996.

The thickness of the surficial organic deposit at the site varied from approximately 0.91 m to 1.83 m. The site was characterized as primarily amorphous in nature having an organic content of 95%.

Dynamic replacement programme

The dynamic replacement testing programme was conducted using two drop weights. One – specifically designed for the DR process – was fabricated out of 25 square steel plates 4.93 cm high; its total height was 1.26 m with a square base of width (b) 0.61 m and it weighed 3.64 tonnes. The other weight which was used for the final smoothing pass was 1.22 m in diameter and weighed 5.09 tonnes. Hayward-Baker, Inc. acted as technical advisor and provided the contractorial services for this project, including the second weight, crane and crane operator. The crane used to lift the weights was a model 50 manufactured by Northwest Engineering; it had a 23.5 m boom and a lifting capacity of

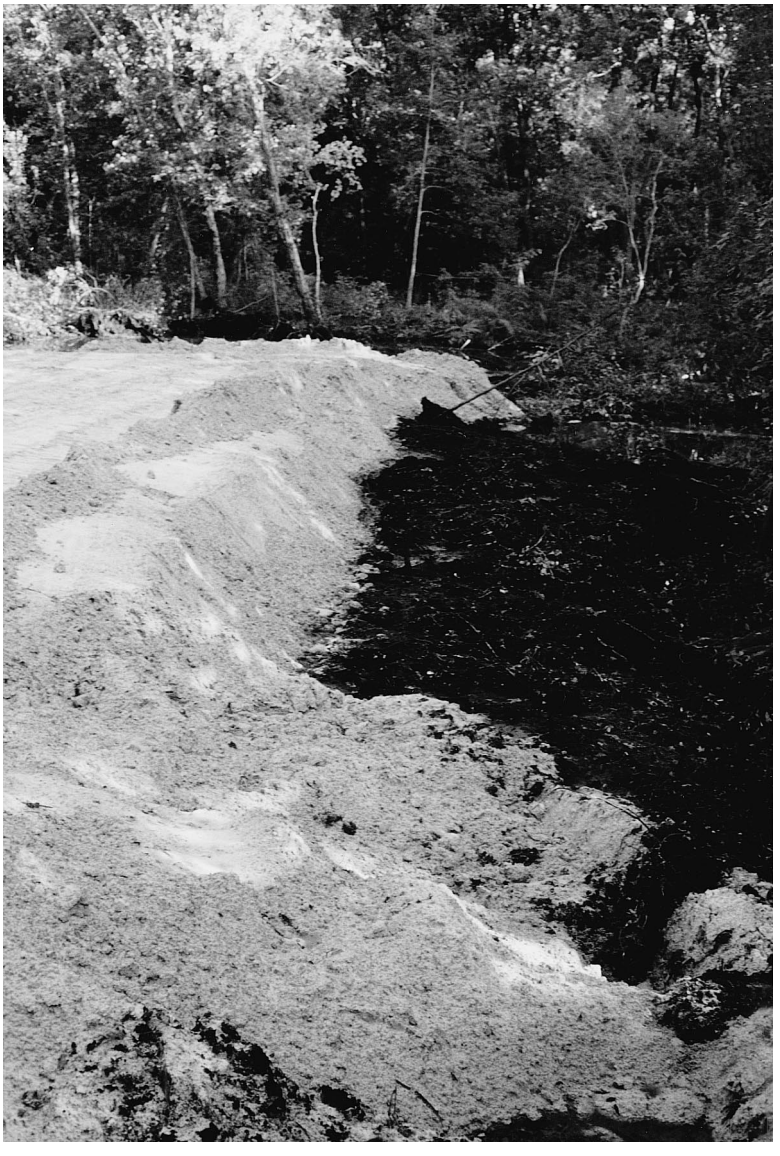

Fig. 1. Cleared and filled study site in Plant City, Florida.

90.91 tonnes. The drop location pattern was hexagonal so as to maintain a constant spacing between the drop locations. The centreline spacing between the drop locations was determined to be 2.44 m, which corresponds to 4 times the hammer base ($4 \times b$). The rationale for the selection of this spacing will be addressed later in the paper. The pattern consisted of 19 drop locations identified by coordinates, (0,0), (0,1), set with respect to two sides as shown in Fig. 2. Drop location (1,3) was selected as the point to be fully instrumented. The instruments included: (1) an accelerometer attached to the falling drop weight, (2) three laser diode photoelectric cells to determine velocity and drop hammer

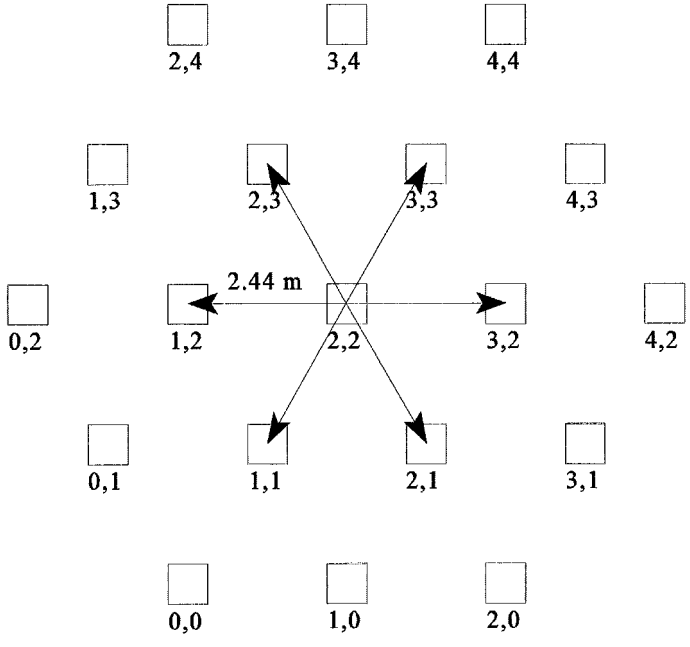

Fig. 2. Hexagonal test pattern with the drop locations identified by coordinates.

efficiency, and (3) five inclinometers to show lateral deflection and provide guidelines for spacing criteria. Additionally, cone penetration tests were performed before and after each impact. Figure 3 shows a boring log, typical of the site, taken at the pilot study location (1,3) after the fill was placed. The pilot study testing programme, instrumentation and monitoring schemes employed will be discussed in the following section.

Pilot study instrumentation and monitoring programme

Test programme

Dynamic replacement of the pilot study location consisted of two passes – the first with a relatively low energy and the second pass with a higher energy. However, in order to ensure that the drop weight would not be irrecoverable due to excessive penetration and the subsequent development of suction forces, it was decided to employ a lower drop height during the first pass, the result of which is a low applied energy. The initial drop height selected for the first series of drops was 6.1 m. This choice was based on a new approach that predicts the crater depth of a dynamic replacement drop hammer after the first impact (Mullins *et al.*, 1996).

After each impact, clean sandy fill was used to fill the resulting crater. After five drops it was seen that the drop weight was easily recoverable, and the drop height was raised to 12.2 m. The drops were continued until the energy (number of blows) required to reach the

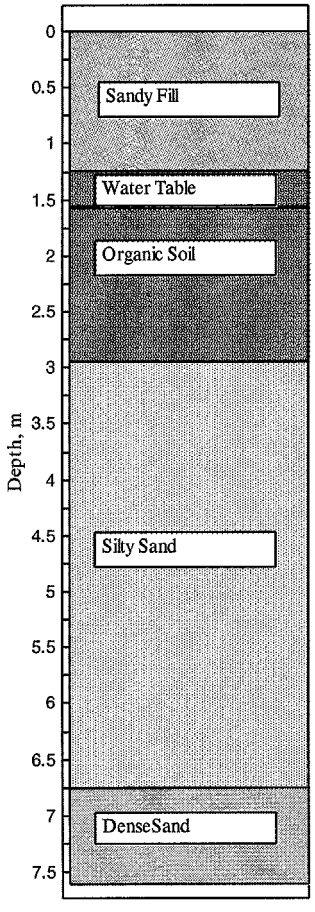

Fig. 3. Boring log taken at pilot study location (1,3).

desired level of improvement was identified. The analytical techniques used to monitor the improvement and the associated computer data acquisition system are discussed below.

Computer interface and programming

The data acquisition and analysis system used includes a 486–33 MHz microcomputer with 20 megabytes of random access memory (RAM). The computer interface with the transducers was by a AT-MIO-16F-5 multifunction interface board. It contains a 12-bit analogue to digital converter (ADC) which can sample up to 16 separate single-ended (SE) analogue inputs or eight channels of differential input (DI) at 200 kilo-samples per second.

Visual Basic 3.0 Windows-based programming software was used to interface the data acquisition board to the microcomputer. Visual Basic communicates with the selected data acquisition board through the use of NI-DAQ Windows. NI-DAQ Windows is a *Windows 3.1* Dynamic Link Library (DLL) that includes functions for controlling the data

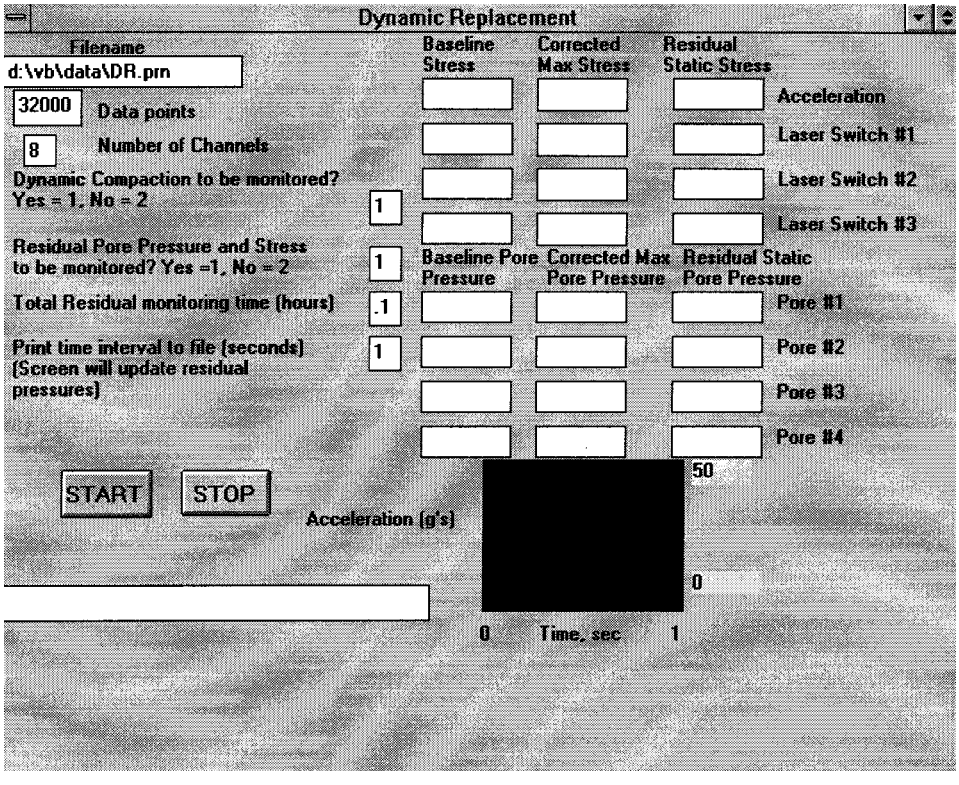

Fig. 4. Dynamic replacement data acquisition screen.

acquisition board for the AT microcomputer. Through the use of this DLL, executable programs were developed using *Visual Basic* for the field DR tests performed.

A data-management system for organic soil (DMSOS) was developed to enable the acquisition, management and analysis of organic soil data as well as the presentation of results to be conducted effectively through a common interface. It is through this interface that data acquisition is initiated. The interface was also written in Visual Basic and incorporates data management through interaction with ACCESS, a relational data base (RDB), and analysis and presentation through Excel, a programmable spreadsheet. Details of the DMSOS structure and its operation are found in Stinnette (1996). Figure 4 shows the data-acquisition–user interface. It is on this screen that the user provides pertinent test information such as an output filename and sets the test options desired for the specific test.

All test results obtained at the study site, by manual observation or by manipulating the stored digital data file, are stored in the ACCESS database where they can be easily retrieved, analysed and graphically presented through the combined interactive use of Visual Basic programming and Excel macro programming.

The computer containing the outlined data acquisition and monitoring system was operated from a truck on the site. All of the instruments were battery operated. The computer was powered by a gas generator and was also equipped with a back-up battery power supply.

Fig. 5. Weight positioned between poles with mounted laser photocells.

Instrumentation of pilot study location

Drop hammer velocity determination. To determine the velocity of the drop hammer at impact, three laser diode photoelectric cells were used, mounted along two vertical poles at predetermined heights. This configuration is shown in Fig. 5. The drop weight obstructs the photocell beams at these predetermined heights and since the photocell beams are located at a known distance apart and the time interval between the breaks are recorded by the data-acquisition system, the instant velocity, *V*, can be determined.

The efficiency factor, η, for the crane can be defined as the ratio of the present kinetic energy to the original potential energy as follows:

$$\eta = \frac{E_k}{E_p} = \frac{V^2}{2\boldsymbol{g}h} \tag{1}$$

where η = efficiency factor, E_k = kinetic energy at impact, E_p = potential energy at start, $\boldsymbol{g}$ = acceleration due to gravity (m s^{-2}), h = drop height (m), and V = velocity at impact (m s^{-1}).

Then η can be computed from Equation 1, knowing V. The average efficiency factor for the crane was determined to be 81%. The reduction of efficiency may be attributed to cable drag, drum resistance and sheave resistance. However, the above value agrees with reported values of 80–90% for that of typical production cranes (McMullin, 1994).

Impact velocity was also determined by video-recording the impact. Standard video cameras capture frames at the rate of 30 per second. Once the video footage was taken, the measured velocity can be ascertained by determining the number of video frames required to capture the complete impact process. Then, with the drop height (h) known, and letting each frame represent 1/30th of a second, the velocity, V, can be calculated as:

$$V = \frac{2h}{t} \tag{2}$$

where h = drop height (m) and t = drop time interval (s). The efficiency (Equation 1) was determined to be 83% by this method. This is in strong agreement with the value previously determined through the use of the laser diode photoelectric cells.

Acceleration determination. The 3.64 tonne drop weight had a piezoelectric accelerometer attached to its top. The transducer was connected by wire to the data-acquisition system described previously. When the first photoelectric cell beam sensed the falling drop weight, the data-acquisition system was initiated. Measurements were recorded during the impact for 1 s and were then stored in the computer. During testing, the acceleration *versus* time graph was automatically plotted on the screen (Fig. 4). The values of acceleration, velocity and displacement *versus* time were calculated and plotted using an Excel spreadsheet. Figure 6 shows those graphs for a typical high-energy impact (12.1 m drop height).

As seen in Fig. 6, there are irregularities in the deceleration record. These irregularities have been previously reported during dynamic compaction and most probably reflect the reverberation of seismic waves bouncing through the drop weight (Mayne and Jones, 1983). This phenomenon was probably amplified due to the fact that the drop weight was composed of 25 separate plates which, although welded along the edges, had their own degrees of freedom.

Shear-resistance by cone penetration tests (CPTs). The FDOT provided use of their cone truck for the cone resistance comparisons for the pilot study location. CPT's were taken to a maximum depth of 7.6 m, initially and after each impact for the pilot study location. The first profile, CPT-0, represents the initial conditions at the pilot study location. Values for CPT-1 to CPT-5 were obtained after a total of five low-energy blows, and for CPT-6 to CPT-20 after 15 high-energy ones. For ease of comparison, Fig. 7 shows the resulting plots

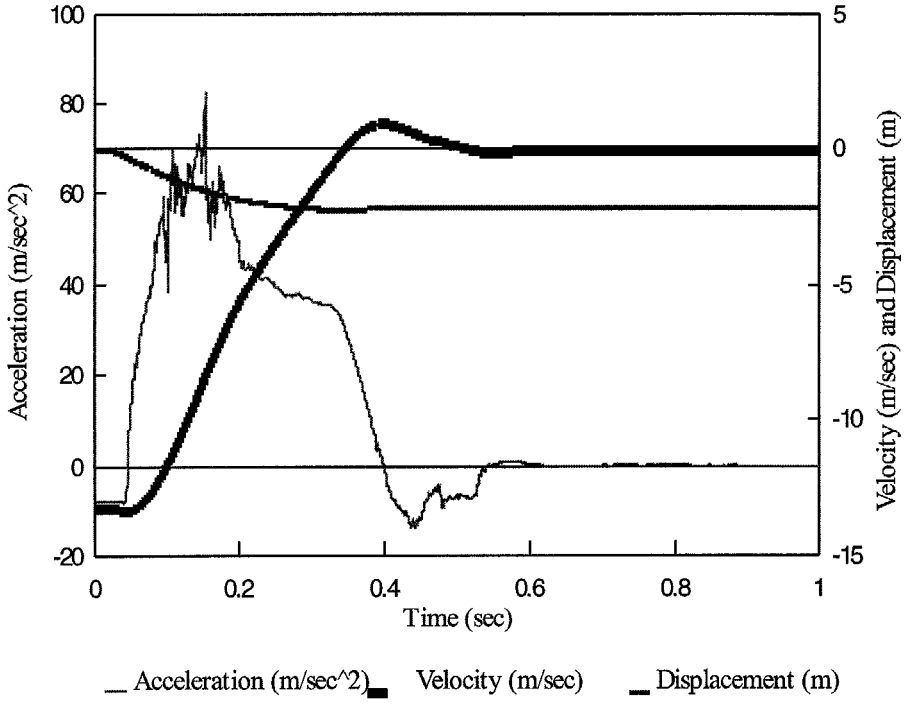

Fig. 6. Acceleration, velocity and displacement graphs for a typical high-energy impact (12.1 m drop height).

when CPT-0 to CPT-20 are plotted on a single graph. Only the first 3.0 m of the cone profiles are shown in the graph so as to emphasize the position of the organic layer. The top horizontal line on the graph represents the measured crater depth before each CPT. The second and third horizontal lines delineate the limits of the organic layer. As can be seen in Fig. 7, the organic layer was initially 1.7 m deep, but by the 20th blow it had diminished to 0.12 m deep. This is attributable to (1) the vertical compression of the organic layer, and (2) the lateral expulsion and compression of organic material into the area surrounding the impact zone. Lateral compression of the organic layer can be more clearly observed by means of the inclinometer data taken at the test site.

Inclinometer/settlement monitoring systems. Four inclinometer casings, I/S-1, I-4, I/S-2, and I-4 were installed at radial centreline distances of 1.22 m, 1.83 m, 2.44 m and 3.66 m, respectively, from the pilot study location (1,3). Figure 8 shows the position of each of these systems around the pilot study location. Each of these casings were installed to a depth of 9.14 m. Two of these systems, I/S-1 and I/S-2, were also instrumented with magnetic settlement monitoring systems.

The inclinometers were read initially and after each of the 20 impacts. Figure 9 shows the final inclinometer results for each of the four inclinometers. Figure 9 demonstrates the amount of lateral ground compression and hence the extent of overall improvement as a result of the 20 applied impacts. Inclinometer I-1, located at a distance of twice the hammer base (*b*) from the centreline of the pilot study location, is seen to have deflected

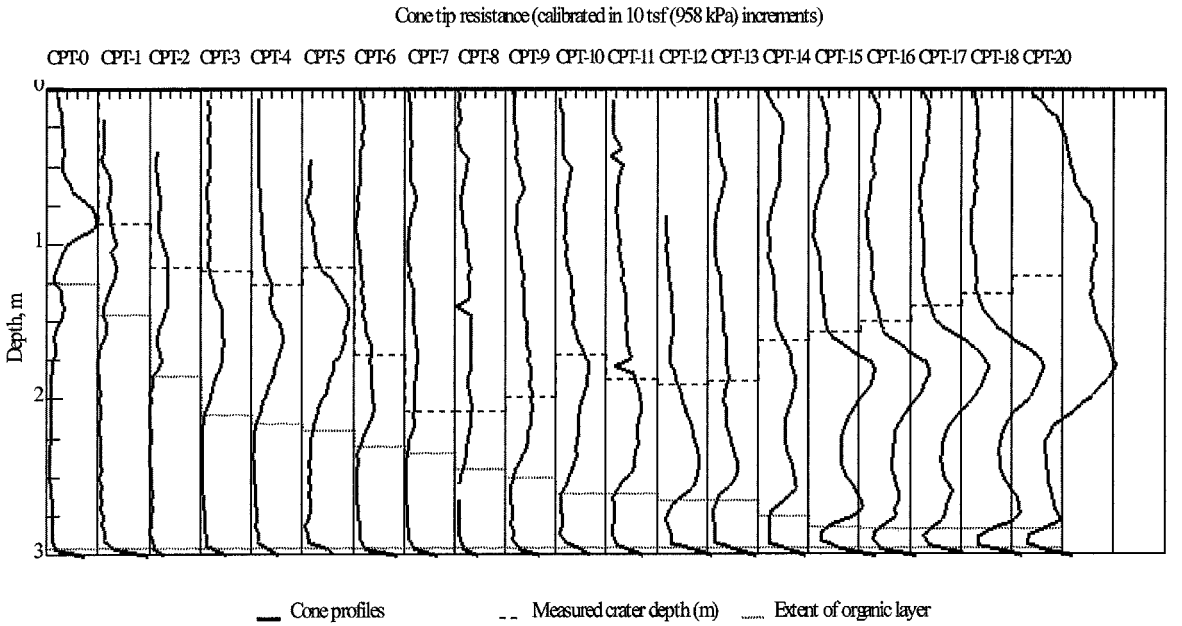

Fig. 7. All cone penetration tests taken at pilot study location (1,3) (initially and after each blow).

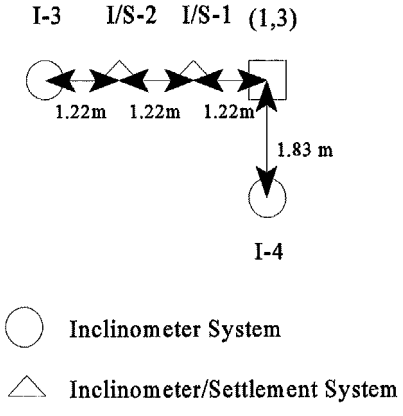

Fig. 8. Plan view of positions of instrumentation systems around the pilot study location.

0.20 m. Hence, the test pattern spacing criterion of four times the hammer base (or 2.44 m) was selected to allow for the development of an interference zone of laterally compressed organic soil of approximately 0.4 m at the midpoints between successive print positions. This magnitude of an interference zone will ensure substantial treatment of the intermediate ground as well.

Analysis of pilot study results

As mentioned in the preceding text, a spacing of $4 \times b$ or 2.44 m was selected. It was also determined that an initial low-energy pass was required to avoid excessive penetrations and alleviate the development of suction forces, which could make the drop weight potentially unrecoverable. However, a more in-depth analysis and comparison of the pilot study results led to the decision to use a minimum of 10 high-energy impacts. The primary quality-control criterion used to evaluate the improvement of the organic soil layer was the computation of the dynamic stiffness of the soil based on the dynamic settlement modulus (DSM). Concurrent inspection of the change in measured crater depth per blow also provides insight as to when the desired level of improvement has been reached. These criteria were independently verified by examining the gradual compression of the organic soil layer as indicated by the CPT profiles. The method of analysis used for determining the DSM and a comparison of the various test results obtained for the pilot study location follows.

Dynamic settlement modulus (DSM) approach

As described in the subsection ‘Acceleration determination’, by employing data acquisition techniques and the DMSOS, magnitudes of velocity and displacement can be calculated from the digitally stored acceleration impact record. This procedure is processed by the EXCEL spreadsheet as follows. First, the acceleration record is integrated once with respect to time to obtain the impact velocity record, V, as

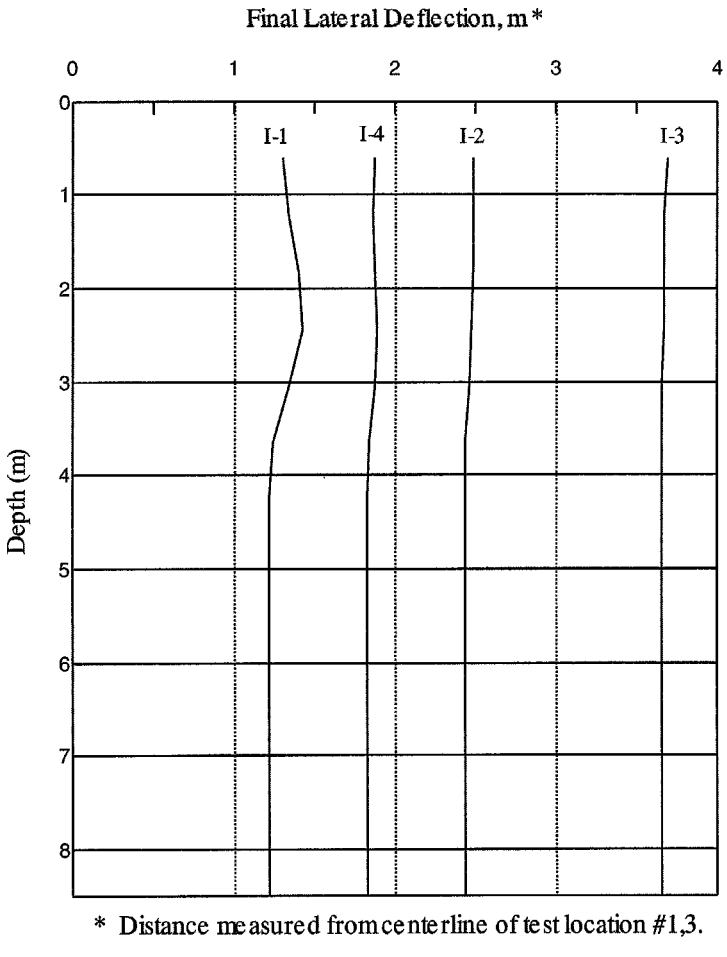

Fig. 9. Final lateral deflections at depth measured with inclinometers at 1.22 m, 1.83 m, 2.44 m, and 3.66 m from the pilot study location.

$$V = \int_0^t a \, dt + \sqrt{\eta} V_{th} \tag{3}$$

where a = acceleration, V_{th} = theoretical velocity at moment of impact ($t = 0$) and η = system efficiency (Equation 1).

The impact velocity record is then integrated to obtain the displacement record. The record of impact stress, σ, is then calculated from the acceleration record, a, as

$$\sigma = \frac{ma}{A} \tag{4}$$

where m = mass of the drop weight, and A = base area of the drop weight.

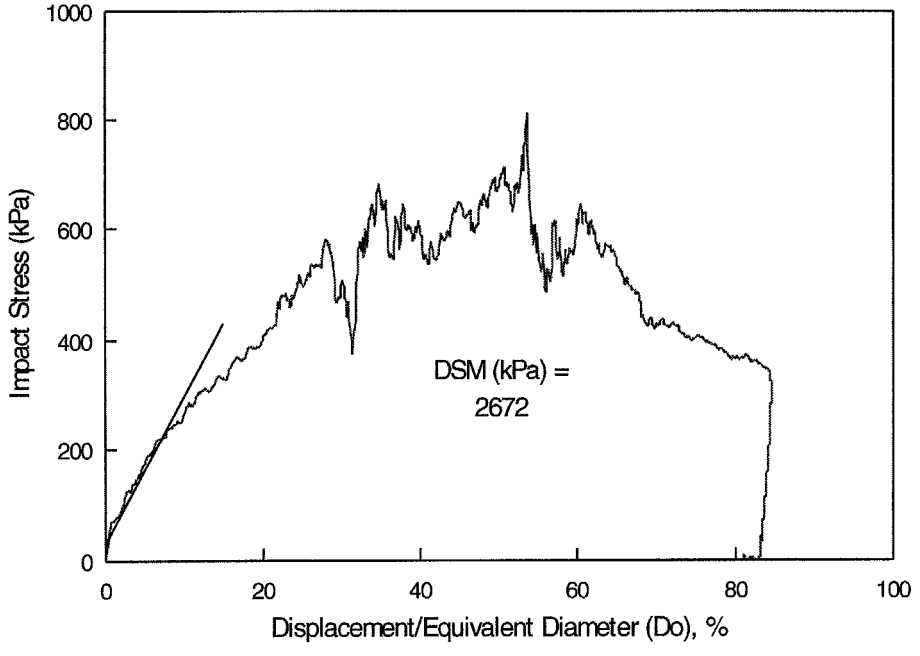

Fig. 10. Impact stress *versus* relative displacement.

The ratio of the instant displacement to the drop weight's equivalent diameter, D_o, (relative displacement) was then plotted against impact stress, σ. The dynamic settlement modulus, DSM, is defined as the slope of the tangent of the loading portion of the impact-stress–relative-displacement curve and is given by

$$\mathrm{DSM} = \frac{\Delta\sigma}{\Delta\left(\frac{d}{D_o}\right)} \tag{5}$$

Figure 10 shows the resulting impact stress versus relative displacement plot and the value of the DSM for a typical high energy impact.

Poran *et al*. (1992a) outlined the use of this technique for the quality control of dynamic compaction on dry sand, and report that the DSM values obtained from experimental tests conducted in the laboratory have shown good correlation to soil densities and that the relative change in DSM values was found to be proportional to the rate of densification (density increase as a function of number of drops).

The values of the DSM versus blow number are plotted for the pilot study location in Fig. 11. As can be seen from the Figure, the DR was more effective in the first 15 drops, while after that there is a small relative increase in the DSM, corresponding to little additional improvement. The same trend was seen by Poran *et al*. (1992a).

In order to correlate the DSM results to the improvement of the organic layer, the organic layer thickness obtained from the CPT profiles and measured crater depth were plotted against the blow number (Fig. 12). It can be seen that the thickness of the organic layer, initially 1.70 m, is reduced to only 12 cm after 15 blows. No additional compression

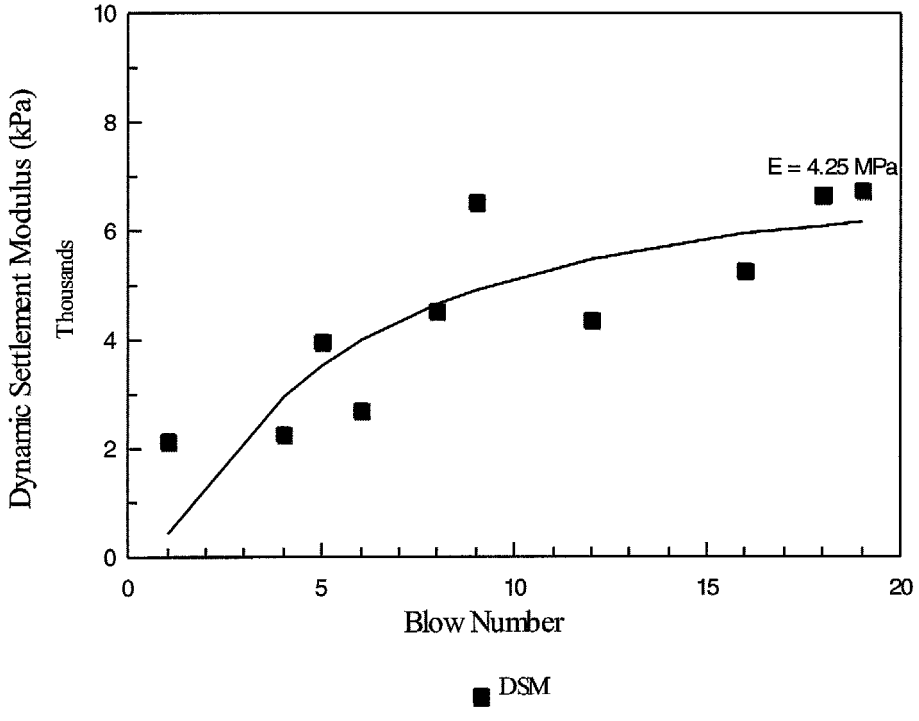

Fig. 11. DSM *versus* blow number for the pilot study location.

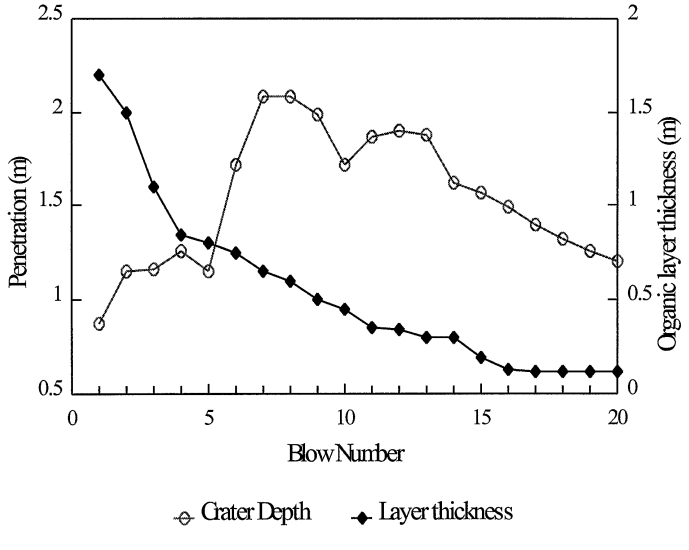

Fig. 12. Measured crater depth and depth of organic layer *versus* blow number.

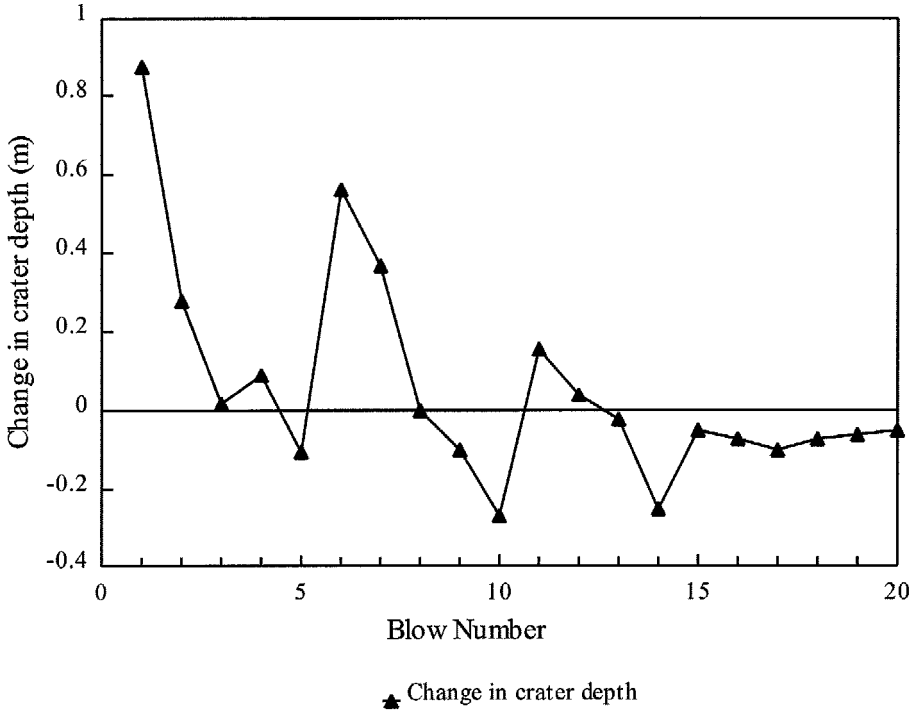

Fig. 13. Change in crater depth *versus* blow number for the pilot study location.

of the organic layer is seen to occur as a result of the last five blows. This observation is in agreement with the improvement shown by the DSM approach where there is very little improvement after the 15th blow (Fig. 11).

The measured crater depth is seen to increase initially during both the low-energy impacts (blows 1–5) and the high-energy ones (blows 6–20). However, after reaching a peak value, the crater depth decreases with each additional blow. This behaviour corresponds to a gain in the density of the sand column and is shown by the soil resistance to penetration (Fig. 12). In order to observe this trend more clearly, a plot of the change in crater depth per blow is shown in Fig. 13. The soil density is seen to increase as the change in crater depth approaches an asymptotic value near zero around the 15th blow. This trend is also in agreement with the DSM results.

Hence, by comparing Figs 11, 12 and 13 it can be seen that the DSM in fact provides an alternative parameter for DR quality control. Another advantage of using the DSM approach is that DSM can be used to monitor the improvement of soil properties by means of available correlations.

Correlation of DSM to elastic modulus

Poran *et al*. (1992a) report correlations of DSM to elastic properties. The dynamic stiffness of the soil at impact, K' (in kN m^{-1}) may be related to the DSM as

$$K' = \frac{\pi(D_o)}{4}\ \text{DSM} \tag{6}$$

Then, by examining the stiffness of a circularly loaded area with diameter D_o on an elastic half space, K', was expressed by Gazetas (1991) as

$$K' = \frac{1.135E\ D_o}{(1-\nu^2)}\ k(\omega) \tag{7}$$

where K' = dynamic system stiffness (kN m^{-1}), $K(\omega)$ = dynamic stiffness coefficient, ν = Poisson's ratio, E = elastic modulus (kN m^{-2}), and D_o = equivalent diameter of the loaded area (m).

The dynamic system stiffness, K', computed from experimental data in Equation 6 should be the same as that in Equation 7. By equating Equation 6 to Equation 7, E may be expressed in terms of the DSM and $k(\omega)$ as

$$E = 0.692\ (1-\nu^2)\ k(\omega)\ \text{DSM} \tag{8}$$

Poran *et al*. (1992a) report that, based on the frequency content of the dynamic pulses found in the laboratory, a $k(\omega)$ value of approximately 1.0 may be assumed for loose and medium-dense sandy soils with $\nu < 0.4$. Poran *et al*. (1992a) conclude that the dynamic stiffness coefficient, $k(\omega)$, is practically equal to the static value.

If a Poisson's ratio of 0.25 is assumed for the fill material used to build the sand columns in the current test, and a value of 1 is assumed for $k(\omega)$, then the final asymptotic value of E for the last impact was calculated to be 4.25 MPa (Fig. 11) – a low value that can be attributed to the loosened soil state after the high-energy blows. However, after the high-energy pass was completed, four additional low-energy blows (two 3.048 m drops and two 1.524 m drops) were applied to densify this loosened top stratum of soil. Although acceleration data was not taken for these four blows, plate load tests conducted afterwards indicate a secant subgrade modulus, k_s, for the pilot study location of 12 818 kN m^{-3}. The elastic modulus, E, may be estimated from a plate load test by

$$E = k_s B(1-\nu^2) \tag{9}$$

where k_s = subgrade modulus (kN m^{-3}), and B = footing width (equivalent plate width, 0.675 m).

Knowing the subgrade modulus and assuming the same Poisson's ratio of 0.25 for the fill material, the elastic modulus is calculated to be 8 MPa. On the other hand, the DSM correlation predicts the elastic modulus to be approximately 4 MPa prior to the upper layer being densified by the additional low-energy drops. This discrepancy may also arise from the fact that the DSM reflects the properties of a larger volume of material than that of the plate load test.

Based on the results obtained by the DMSOS, a decision was made to apply a minimum of five low-energy blows and 10 high-energy blows to each of the remaining 18 print positions in the study pattern. Thus, the DMSOS was effectively utilized in the field implementation of dynamic replacement.

Energy considerations

It was determined by means of the DSM approach, and verified by CPTs, that the sand columns were sufficiently developed in the organic layer after five low-energy drops ($h = 6.1$ m) and 10 high-energy drops ($h = 12.2$ m). However, this same level of improvement could have been obtained by using a different combination of low and high energy, including the use of a different drop weight – provided that the drop weight satisfies the slenderness ratio (height/diameter) of approximately 1.83:1.

The different combinations of applied energy needed to achieve the desired level of improvement can be addressed by the following analysis. The cumulative specific energy (WH/Ad_c) *versus* d_c/D_o for the pilot study are plotted in Fig. 14, where A is the contact area of the drop weight, W is its weight and d_c is the sand-column depth in the organic soil stratum determined from the CPTs. It is noted that a unique linear relationship is obtained in Fig. 14. Linear regression of the above data yields the best fit line of:

$$\sum_{1}^{n} \frac{WH}{Ad_c} = 4423.18 \, \frac{d_c}{D_o} \qquad r^2 = 0.94 \tag{10}$$

It should be noted that Equation 10 depends on soil properties and is therefore site specific.

Hence, Equation 10 can conveniently be used to select the energy requirements for forming a sand column by DR at this site. The following example will illustrate the application of this concept. First, determine the required cumulative specific energy to build a sand column through the 1.7 m organic layer using the previous drop weight. In this case $d_c = 1.7$ m and $D_o = 0.6879$ m, so $d_c/D_o = 2.47$. Then, from Fig. 14 (or Equation 10), the required cumulative specific energy is determined to be 10 932 kN-m m^{-3}. The

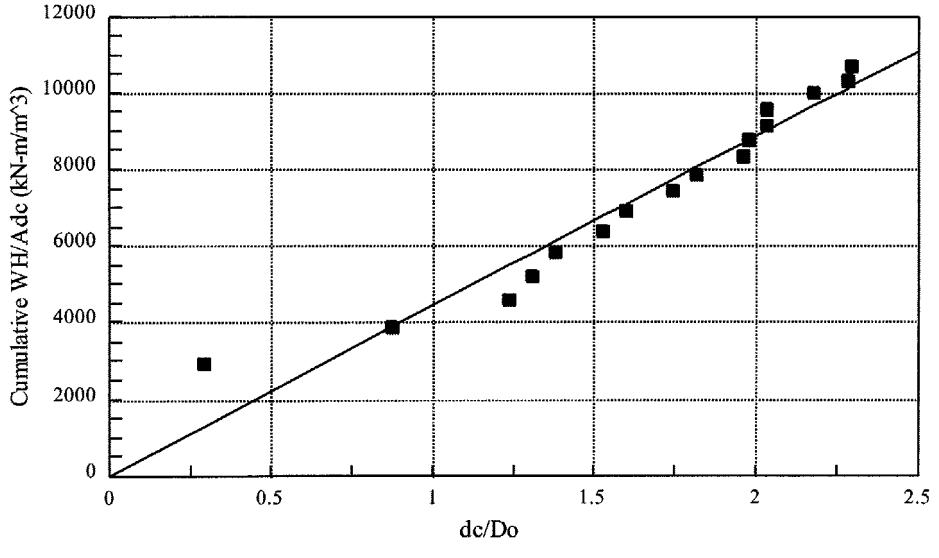

Fig. 14. Cumulative specific energy per blow *versus* normalized strain.

unit energy, Σ *WH/A*, independent of d_c, is then computed to be 18 583.71 kN m^{-1}. Since it is desired to use a low initial energy to alleviate excessive penetration problems at the beginning, the following initial low-energy pass is assumed; No. of blows (n) = 5, $h = 4.57$ m, $W = 35.59$ kN, $A = 0.3716$ m^2, $D_o = 0.6879$ m. Then, solving for d_c in Equation 10 yields $d_c = 0.58$ m. Therefore, the portion of total unit energy exhausted for these five low-energy blows is

$$\frac{nWh}{A} = 2188.46 \text{ kN m}^{-1} \tag{11}$$

The required cumulative unit energy for the high-energy drops is then determined as the difference between the total cumulative required unit energy and the total unit energy for the low-energy blows as 16 395.25 kN m^{-1}.

Selecting a high-energy drop height, h, of 9.144 m, the unit energy per blow is:

$$\frac{Wh}{A} = 875.75 \text{ kN m}^{-1} \tag{12}$$

Hence, the number of high-energy blows required will be approximately 19.

It is seen how different combinations of low and high drop energies may be selected to achieve a given column depth by using this approach. Thus, this approach will be useful when multiple cranes or drop weights are in use at a single site or if a relatively low 'high' energy level is desirable due to the proximity of adjacent structures. Moreover, the approach would be invaluable if a variation in depth of the organic layer is noted on different boring logs at the same site. Then by simply adjusting d_c in the preceding analysis to reflect the height of the organic layer at a specific location, one can select a combination of appropriate energy levels for that location.

Poran *et al*. (1992b) outlined a similar rational design method for dynamic compaction (DC) of dry sand based on correlations between the normalized impact energy and the resulting densification measured in terms of normalized volumetric strain.

Discussion

The goal of this research was to achieve a desired degree of improvement in an organic soil stratum by introducing sand columns. The study site consisted of 19 drop locations, one of which was fully instrumented. The optimum print spacing, drop height and the number of blows required to yield the desired level of improvement was determined based on the test results of this location. The DSM method stands out among the several criteria used to identify the level of improvement. These results were then used as a guide for treating the remaining locations, as a similar soil profile was seen to exist at the entire study site. However, in larger projects, the ground profile may vary significantly, in which case representative boring logs for the site to be modified should be obtained at many locations. Thus, potential pilot-study locations can then readily be identified from the soil profiles. Depending on the necessity, acceleration data may be obtained for some or all of the drop locations. However, if only a few of the drop locations are instrumented, then the trend in the change in crater depth can be used as an indicator of densification at the non-instrumented drop locations.

Field implementation of the computerized data-acquisition system proved to be very reliable in general. However, in several instances, the acceleration record registered by the data acquisition system was unusable. This can be attributed to the delayed actuation of data acquisition due to the late response of the laser diode photoelectric cells. This problem can be easily overcome by using an additional laser diode photoelectric cell as a backup, to initiate data acquisition.

The cost of setting up such a system which includes the computer, associated software, data acquisition board, and instruments (accelerometer and laser diode photocells) is in the range of US$8000, which makes it cost-effective.

Conclusion

A quality-control system has been developed for evaluation of dynamic replacement (DR) of organic soils. It is incorporated in an existing database management system for organic soils (DMSOS) that stores and retrieves all acquired test data from both field and laboratory tests. The system also facilitates analysis and graphical presentation of the test results. These include the plots of acceleration, velocity and displacement of the drop weight for each impact. The dynamic settlement modulus (DSM) parameter was computed and plotted for each impact. From this plot, the optimum energy level can be obtained when the change in the DSM per blow becomes relatively insignificant. Once the final DSM value is available, the elastic modulus, *E*, may also be computed to identify the level of improvement achieved. Furthermore, the plot of the change in crater depth *versus* blow number provides yet another way of observing maximum improvement. Post-DR ground testing using CPTs and plate load tests further verified the DSM prediction of the level of improvement achieved. Based on the findings of this field study, it appears feasible to use the DSM-based quality-control system to evaluate the degree of improvement and select the optimum DR technical criteria such as the number of blows and drop print spacing.

Acknowledgements

We thank Mr Brian Jory and Ms Terry Puckett of the Florida Department of Transportation for their support during the study. The FDOT grant funding this research under contract No. 99700–7572–119 is gratefully acknowledged.

References

Gazetas, G. (1991) Foundation vibrations, in *Foundation Engineering Handbook*, Fang, H.Y. (ed.) Van Nostrand Reinhold, pp. 571–5.

Lo, H.W., Ooi, P.L. and Lee, S.L. (1990) Dynamic replacement and mixing of organic soils with sand charges, *ASCE Journal of Geotechnical Engineering*, **116**, 1463–82.

Lukas, R.G. (1992) Dynamic compaction engineering considerations, in *Grouting, Soil Improvement and Geosynthetics*, Geotechnical Special Publication No. 30, ASCE, New York, pp. 940–53.

Mayne, P.W. and Jones, J.S. (1983) Impact stresses during dynamic compaction, *ASCE Journal of Geotechnical Engineering*, **109**, 1342–6.

McMullin, S.R. (1994) Evaluation of dynamic compaction of low level waste burial trenches containing B-25 boxes, in *In-Situ Deep Soil Improvement*, Geotechnical Special Publication No. 45, ASCE, New York, pp. 44-54.

Mullins, A.G., Gunaratne, M., Stinnette, P. and Thilakasiri, S. (1996) Prediction of crater depth from dynamic compaction using CPT, submitted to *ASCE Journal of Geotechnical Engineering*,

Poran, C.J., Heh, K.S. and Rodriquez, J.A. (1992a) A new technique for quality control of dynamic compaction, in *Grouting, Soil Improvement and Geosynthetics*, Geotechnical Special Publication No. 30, ASCE, New York, pp. 915–26.

Poran, C.J., Heh, K.S. and Rodriquez, F.A. (1992b) Impact behavior of Sand, *Soils and Foundations*, **32** (4), 81–92.

Ramaswamy, S.D., Aziz, M.A., Subrahamanyam, R.V., Khader, M.H. and Lee, S.L. (1979) Treatment of peaty clay by high energy impact, *ASCE Journal of the Geotechnical Engineering Division*, **105** (No. GT8), 957–67.

Stinnette, P. (1996) Geotechnical Data Management and Analysis System for Organic Soil, PhD Thesis, University of South Florida.

Thomas, F.H. (1965) Subsidence of peat and muck soils in Florida and other parts of the United States – A review, *Proc. of the Soil and Crop Society*, **25**, 153–160.

INTERNATIONAL JOURNAL FOR NUMERICAL AND ANALYTICAL METHODS IN GEOMECHANICS, VOL. 20, 753–767 (1996)

INVESTIGATION OF IMPACT STRESSES INDUCED IN LABORATORY DYNAMIC COMPACTION OF SOFT SOILS

H. S. THILAKASIRI, M. GUNARATNE, G. MULLINS, P. STINNETTE AND B. JORY[†]

Department of Civil and Environmental Engineering, University of South Florida, Tampa, FL 33647, U.S.A.

SUMMARY

The majority of currently available analytical tools to predict ground stresses due to impact are based on linear spring-dashpot dynamic models. Although these simple models adequately represent stiff ground possessing linear visco-elastic behaviour, they suffer from two striking limitations when applied to relatively softer ground; (1) the inability to account for the permanent deformation resulting from impact, (2) failure to incorporate stiffness changes of softer soil within the impact duration. In this paper, the authors present an improved analytical approach formulated on the basis of a series of laboratory impact tests, to address the shortcomings of the current dynamic models in relation to soft soils. In this procedure, the impact zone is modelled as three distinct zones; (1) a zone beneath the falling weight undergoing non-linear axial deformation while being in vertical motion, (2) an inner zone immediately surrounding zone 1 with non-linear shear deformation, and (3) an outer zone undergoing a relatively lower degree of (linear) shear deformation. The soil constitutive parameters pertinent to the model are obtained from a modified dynamic compression test that simulates the impact conditions. It is shown that analytical predictions of the impact stress history and penetration are in agreement with test results. The findings are useful in the exploration of dynamic compaction techniques that will be effective in soft soil improvement.

KEY WORDS: dynamic; compaction; soil; damping; non-linear stressing

1. INTRODUCTION

A number of analytical models have been proposed by several researchers[1–4] in recent years to estimate surface stresses during dynamic compaction. In these models, it is assumed that the soil behaviour is linear elastic, isotropic and hence can be modelled by a linear spring and a linear dashpot. However, it is a common observation made during dynamic compaction of soft soil that the soil mass close to the surface is subjected to a very high strain level resulting in permanent deformation. Obviously a model that employs a linear spring and a linear dashpot is unable to simulate these observations because non-linearity is clearly exhibited by soils at high strain levels. Apart from the above-mentioned simplified models, Chow *et al.*[3] proposed a different analytical approach where the one-dimensional wave equation model for pile-driving analysis is modified by replacing the pile with a soil column extending to at least the anticipated depth of improvement. In this method, the soil surrounding the soil column is represented by linear elastic springs and linear dashpots. Furthermore, they adopted an implicit finite element method to solve the equation of motion of the soil column.

[†]Present address: Florida Department of transportation, Bartow, FL, U.S.A.

CCC 0363–9061/96/100753–15

Received 9 September 1994
Revised 12 January 1996

An improved analytical model is proposed in this paper to estimate the surface stress and the surface deformation, accounting for non-linearity of soil immediately below the drop hammer as well as that of the immediate neighbourhood of the hammer. In this procedure, equations of motion are separately written for three zones distinguished by their mode and degree of deformation while satisfying compatibility. A numerical procedure is adopted to solve these equations of motion because of complexity arising from the constitutive model that accounts for non-linearity. The solution procedure uses an explicit direct time integration together with lumped mass formulation for computational efficiency. Finally, analytical predictions of the impact surface stress history and penetration are compared with laboratory measurements.

2. EXPERIMENTAL OBSERVATIONS

Figure 1 shows a typical plot of the impact surface stress history recorded during the authors' experiments on a wet organic soil by employing a falling hammer instrumented with sensitive pressure transducers. The sensitivity of the data acquisition system is discussed in the ensuing Section 4 on the experimental set-up. The stress–time plot such as that shown in Figure 1 obtained from a series of tests consistently demonstrate the existence of two distinct regions:

(1) An immediate peak followed by rapidly diminishing stress. This phase of the stress history usually lasts only an extremely small time (1–2 ms) thus possibly eluding detection without a sensitive data acquisition system. This could be one reason why such an instantaneous peak has not been documented in previous experimental studies.
(2) A subsequent oscillatory stress pattern. This phase of the stress pulse on the other hand has been the subject of most previous experimental and analytical investigations.

3. MATHEMATICAL IDEALIZATION

From the perspective of deformation, the soil mass in the impact vicinity can be considered as being comprised of three distinct zones (Figure 2):

Zone 1: soil under the falling hammer in the zone of influence undergoing significant vertical deformation that permits it to be considered as a moving or participating soil mass,
Zone 2: soil in the immediate neighbourhood undergoing excessive shear deformations that can only be characterized by non-linear models,

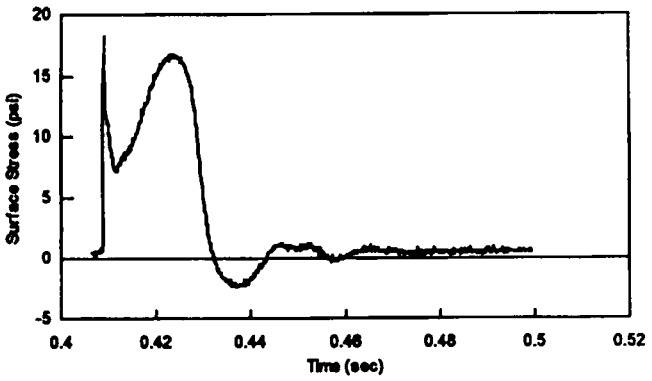

Figure 1. Typical experimental impact stress history

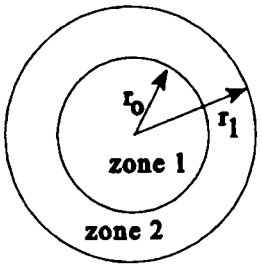

Figure 2. Plan view of the impact vicinity

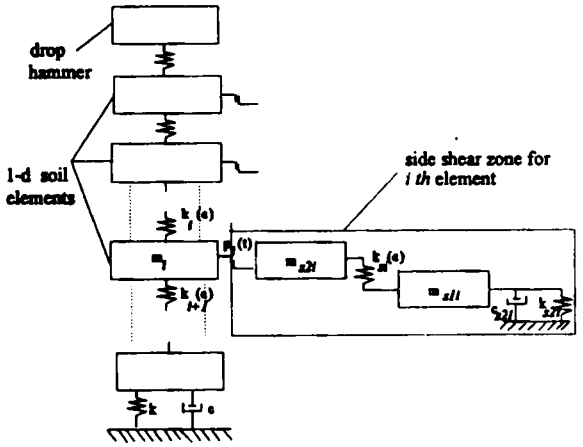

Figure 3. Dynamic model (shear zone is shown only for the ith element)

Zone 3: soil in the outer region undergoing limited shear deformations within linear elastic limits.

The authors' analytical formulation discussed here is founded on consideration of the mechanics of these three zones. The analytical formulation is kept simple by replacing the soil in the above zones with equivalent lumped masses. Researchers have observed that the depth of the zone of influence (z) during dynamic compaction varies in the range of $\sqrt{(W_1 h)} \geqslant z \geqslant 1/2\sqrt{W_1 h)}$,[6,7] where W_1 and h are drop weight in tonnes and drop height in meters, respectively. Hence, in their formulations the authors suggest that the vertical depth (z) of the above non-linear zones should at least extend to a depth of $\sqrt{(W_1 h)}$. In the mathematical discretization, zones 1 and 2 up to the depth of influence are divided into elements of equal thickness as shown in Figure 3. Since the vertical strain within each element is assumed to be uniform, their thickness should be decided by a sensitivity analysis.

Since the strains in zone 1 are large, it is logical to expect non-linear behaviour. Thus, the soil elements in that zone are replaced in the current model by moving solid lumped masses (m_i) having the same cross-sectional area as that of the drop weight and are connected by non-linear

springs of stiffness $k_i(\varepsilon)$ as shown in Figure 3. $k_i(\varepsilon)$ can be expressed by $M_i(\varepsilon)A/L$ where $M_i(\varepsilon)$, A and L are the constrained modulus corresponding to the current strain (ε) (Section 3.1), cross-sectional area of the element and the current length of the element, respectively. The soil half-space beneath the immediate vicinity of the non-linear soil column is modelled by a linear spring (k) and a linear dashpot in parallel having a spring stiffness of $4G_s r_0/(1-\nu)$ and a dashpot coefficient of $3{\cdot}4Gr_0^2/(1-\nu)$ as proposed by Lysmer and Richart[8] in which r_0, G and ν are the radius of the soil column, initial shear modulus and the Poisson ratio, respectively. In the case where there is a stiff layer present within the zone of influence, the displacement of the last element is set to zero to account for it. In such a situation, the spring and the dashpot are not required.

On the other hand, the elements in annular zone 2, represented by two masses (m_{s1i} and m_{s2i}) of radius (r_1) surrounding zone 1 are also subjected to high strain levels. Therefore, its effect on the impact zone must also be modelled by non-linear shear stiffness properties (k_{si}). In this regard, the stiffness expression developed by El Naggar and Novak[9] would be appropriate. The expression for k_{si} is derived in the Appendix. The mass of the ith element in zone 2 is equally distributed to lumped masses m_{s1i} and m_{s2i} as shown in Figure 3. The elements in zone 2 interact with the corresponding elements in zone 1 through rigid plastic sliders $p_i(t)$ as shown in Figure 3.

Outside zone 2, the shear strains are small enough to permit the application of linear elastic constitutive relations. Thus, the shearing resistance of zone 3 is simulated by a linear spring (k_{s2i}) and a dashpot (c_{s2i}) having a stiffness of $2{\cdot}75G_s\,dz_i$ and a damping constant of $2\pi r_1\sqrt{\rho_s G_s}\,dz_i$, respectively, as proposed by Novak et al.[10] in which G_s, ρ_s and dz_i are the initial shear modulus, initial density and vertical thickness of elements in zone 2, respectively. Hence, zone 3 provides shear resistance to the vertical movement of elements in zone 2 through the parallel combination of spring k_{s2i} and c_{s2i}.

It is assumed that slipping can occur at the interface between the deforming soil elements in zone 1 and the elements in the surrounding zone 2 when the shear stress in the rigid plastic sliders $p_i(t)$ exceeds the maximum static resistance which is taken to be $k_0\sigma'_v \tan\Phi$; where, k_0, σ'_v and ϕ are coefficient of lateral earth pressure at rest, current vertical effective stress and angle of internal friction of the soil, respectively. It is accepted that the coefficient of lateral earth pressure depends on the over consolidation ratio (OCR) of the soil. Hence, in the proposed model k_0 is taken to be equal to $(1-\sin\phi)\sqrt{(\text{OCR})}$. Except for fully saturated low permeable soils with multiple impacts, the generation of pore water pressure in zone 1 is comparatively small[6] resulting in increased vertical effective stress in zone 1 during an impact. Therefore, it is important to note here that the maximum shear resistance changes during an impact even for a normally consolidated soil as the effective vertical stress changes with deformation of the soil column.

Finally, Newmark's explicit time step integration is employed to solve the equations of motion of the soil elements. The impacting hammer is disconnected from the numerical solution when the contact stress becomes less than zero.

If the depth of the non-linear zone is insignificant such as in the case of a small amplitude vibration, it is clear that the present model approaches the already accepted visco-elastic models, in which linear spring and a dashpot are in parallel (Figure 3). Further, the thickness of the influence zone can decrease with decrease in the drop weight and the drop height according to the aforementioned effective zone criterion ($\sqrt{Wh}$).

3.1. Determination of non-linear stiffness values

Figure 4 shows a typical axial stress–strain curve obtained for loading and unloading during a dynamic impact. The experimental procedure used to obtain Figure 4 is highlighted in Section 4. A unique feature of the stress–strain curve is a distinct yielding stage as shown in Figure 4 after

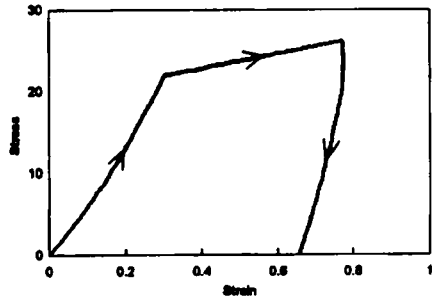

Figure 4. Experimental stress–strain curve

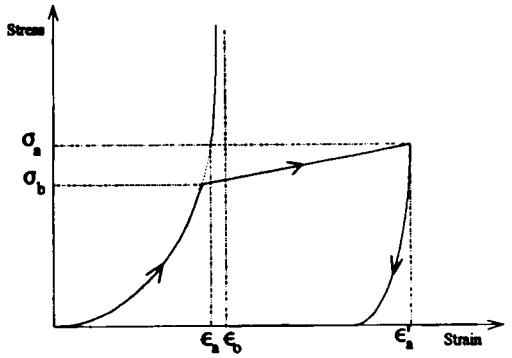

Figure 5. Typical theoretical stress–strain graph with symbols used in mathematical expressions

which a major portion of the axial strain is irrecoverable. This sudden change of the stiffness can be attributed to plastic flow resulting from shear failure. It was found that the pre-bearing capacity region of the curve can be conveniently expressed by the mathematical expression given by Ginsberg[11] for one-dimensional dynamic loading (equations (1) and (2)). Moreover, Ginsberg's[11] expression for the unloading phase correctly represented the unloading curve obtained by the authors as well (equations (5)–(6)). However, it should be noted that the post bearing capacity failure portion of the curve is linear with a small slope instead of being flat, indicating some strain hardening. Hence, based on Figure 4, the axial force in zone 1 can be determined by employing a constitutive relationship similar to that proposed by Ginsburg[11] for non-linear uniaxial dynamic compression. During each time step, the incremental strain in a given element is calculated based on the shortening of the element during the period and the current length of the element. Then, those incremental strains are summed up to estimate the total strain in the element and the corresponding axial stress from Figure 4. While the shape of the stress–strain curve proposed for loading and unloading is shown in Figure 5, the related mathematical relationships modified from the original Ginsburg model to include plastic flow, are expressed below.

For the loading stage

Up to the bearing capacity

$$\sigma = \frac{M_0 \varepsilon \varepsilon_0}{\{\varepsilon_0 - \varepsilon\}} \tag{1}$$

$$M(\varepsilon) = \frac{M_0 \varepsilon_0^2}{\{\varepsilon_0 - \varepsilon\}^2} \tag{2}$$

Beyond the bearing capacity

$$\sigma = k\{\varepsilon - \varepsilon_b\} + \sigma_b \tag{3}$$

$$M(\varepsilon) = k \tag{4}$$

For the unloading state

$$\sigma = M_0 \varepsilon_* \varepsilon_0 / \{\varepsilon_0 - \varepsilon_*\} \tag{5}$$

$$\varepsilon_* = (\varepsilon - (\varepsilon_a' - \varepsilon_a) - \varepsilon_a \eta / 1 - \eta \tag{6}$$

$$M(\varepsilon) = M_0 \varepsilon_0^2 / \{1 - \eta\}\{\varepsilon_0 - \varepsilon_*\}^2 \tag{7}$$

$$\varepsilon_a = \varepsilon_0 \sigma_a / (\sigma_a + M_0 \varepsilon_0) \tag{8}$$

where

M_0 = initial constrained modulus,
$M(\varepsilon)$ = constrained modulus at strain ε,
ε_0 = asymptotic value of strain corresponding to the pre-bearing failure portion,
η = a material constant,
ε_a' = strain at the beginning of the unloading phase,
σ_a = stress at the beginning of the unloading phase,
σ_b = bearing capacity,
k = modulus after the bearing capacity failure.

As mentioned in the mathematical idealization, the following expression for stiffness developed by El Naggar and Novak[9] assuming a plane strain condition are used for zone 2.

For loading

$$k_{s/i} = \frac{2\pi G_s}{\ln \dfrac{r_1/r_2 - \eta_0}{1 - \eta_0}} \tag{9}$$

For unloading

$$k_{s/i} = \frac{2\pi G_s}{\ln(r_1/r_0)} \tag{10}$$

where

r_1 = outer radius of the inner zone,
r_0 = radius of the soil column,
G_s = initial shear modulus,
τ_0 = shear stress at the axial element and shear element interface,
τ_f = ultimate shear strength,
$\eta_0 = \tau_0/\tau_f$.

3.2. Kinematic equations of the system

Using the notation indicated in Figure 6, the following equations of motion can be written for various components of the system:

For the drop hammer

$$w_1 - q_1(t) = \frac{w_1}{g} d_1''(t) \tag{11}$$

For the ith axial element (in Figure 6)

$$q_i(t) - q_{i+1}(t) - p_i(t) = m_i d_i''(t) \tag{12}$$

For ith shear element (in Figure 6)

$$p_i(t) - q_{si}(t) = m_{s1i} d_{s1i}''(t) \tag{13}$$

$$q_{si}(t) - k_{s2i} d_{s2i}(t) - c_{s2i} d_{s2i}'(t) = m_{s2i} d_{s2i}''(t) \tag{14}$$

where

$$k_{s2i} = 2{\cdot}75 G_s \, \mathrm{d}z_i, \tag{15}$$

$$c_{s2i} = 2\pi r_1 \sqrt{(\rho_s G_s)} \, \mathrm{d}z_i, \tag{16}$$

$\mathrm{d}z_i$ = thickness of the ith element in zone 2.

Newmark's explicit time step integration can be used to solve the equations (11)–(14) in combination with equations (17) and (18) as previously mentioned. For an element with a displacement $d(t)$ at any time t, Newmark's classical explicit time step integration algorithm (14) involves following recurrence relationships:

$$d_{n+1}(t) = d_n(t - \Delta t) + \Delta t \, d_n'(t - \Delta t) + \frac{\Delta t^2}{2} d_n''(t - \Delta t) \tag{17}$$

$$d_{n+1}'(t) = d_n'(t - \Delta t) + \Delta t(1 - \beta_1) d_n''(t - \Delta t) + \Delta t \beta_1 d_{n+1}''(t) \tag{18}$$

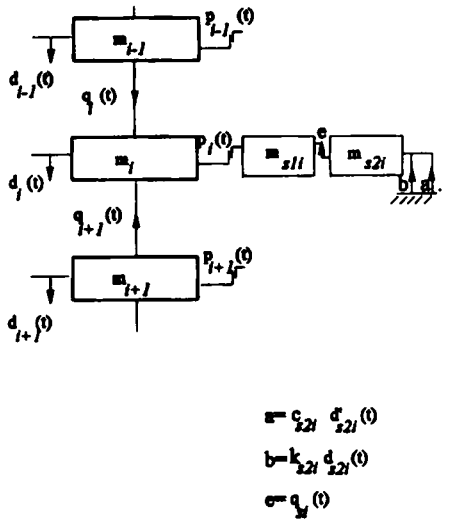

Figure 6. Free body diagrams for the ith axial and shear elements

where β_1 is Newmark's parameter, the value of which can be chosen for effective implementation of the particular algorithm.

Equation (17) can be used to explicitly obtain the current displacement $d_{n+1}(t)$ knowing the displacement, velocity and the acceleration of the element during the previous time step, while equation (18) enables one to express the current velocity of the element in terms of the current acceleration.

Thus, when equations (17) and (18) are separately applied to the elements in motion in Figure 3, it will facilitate the solution of equations (11)–(14) by evaluating the current displacement and the acceleration of each element based on the state of motion of the entire system at the preceding time step. Furthermore, at the end of each time step, element thicknesses and soil properties are upgraded according to the current strains, using the non-linear constitutive model described in the previous section. By repeating this procedure for a number of time steps, the numerical solution procedure can be successfully implemented. The explicit direct time integration algorithm is conditionally stable and the stability is governed by the magnitude of the time step size. It is found from the literature that the maximum size of the time step for a stable solution is related to the time required for an elastic wave to propagate across the shortest element of the mesh. In contrast to implicit algorithms, explicit algorithms require a large number of small time steps to avoid the solution of a large matrix equation which is typical of implicit methods at each time step.

4. EXPERIMENTAL SET-UP

The experimental set-up shown in Figure 7 was used to determine the dynamic impact stress due to a drop weight and the related stress–strain behaviour of an organic soil in the laboratory. The organic soil had a water content of 378 per cent, a we density of 1064 kg/m^3 (66 pcf) and an

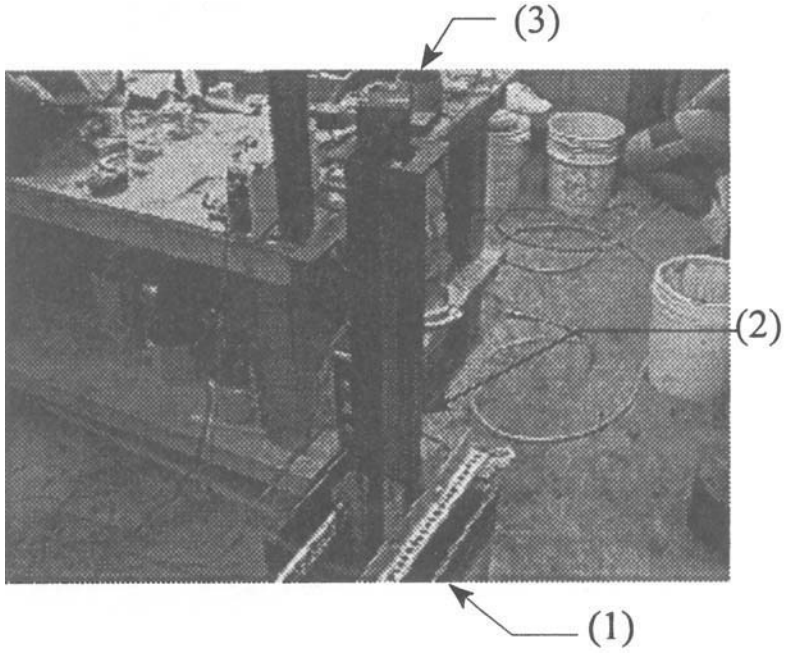

Figure 7. Experimental set-up

organic content of 80 per cent. The soil was compacted in a PVC lined 0·03 m^3 (one cubic foot-1′ × 1′ × 1′) container to a final bed depth of 10·16 cm (4 in) for the test used to get the surface stress history while a reduced depth of 2·6cm (1 in) was used for the test to determine the stress–strain relationship. A 0·923 m (3 ft) tall guide rail system (2) was placed on top of the box. A 2·27 kg (5 lb) steel weight with a 7·62 cm (3 in) square base (3) was held by an electro-magnet at the top of the guide rail. The weight was instrumented with five pressure transducers that were installed in such a manner that they were flush with the surface of the bottom of the weight. An accelerometer was also attached to the top of the weight so that its position was in line with the centre of gravity of the weight. The pressure transducers and the accelerometer were interfaced to a 486-33 MHz microcomputer through the use of a AT-MIO-16F-5 interface board.

Programs are written in Visual Basic to facilitate multiple channel data acquisition. A remote relay was used to simultaneously release the weight from the electro-magnet and initiate data acquisition. The impact stress was sampled at a rate 10 000 samples/s for each of the five

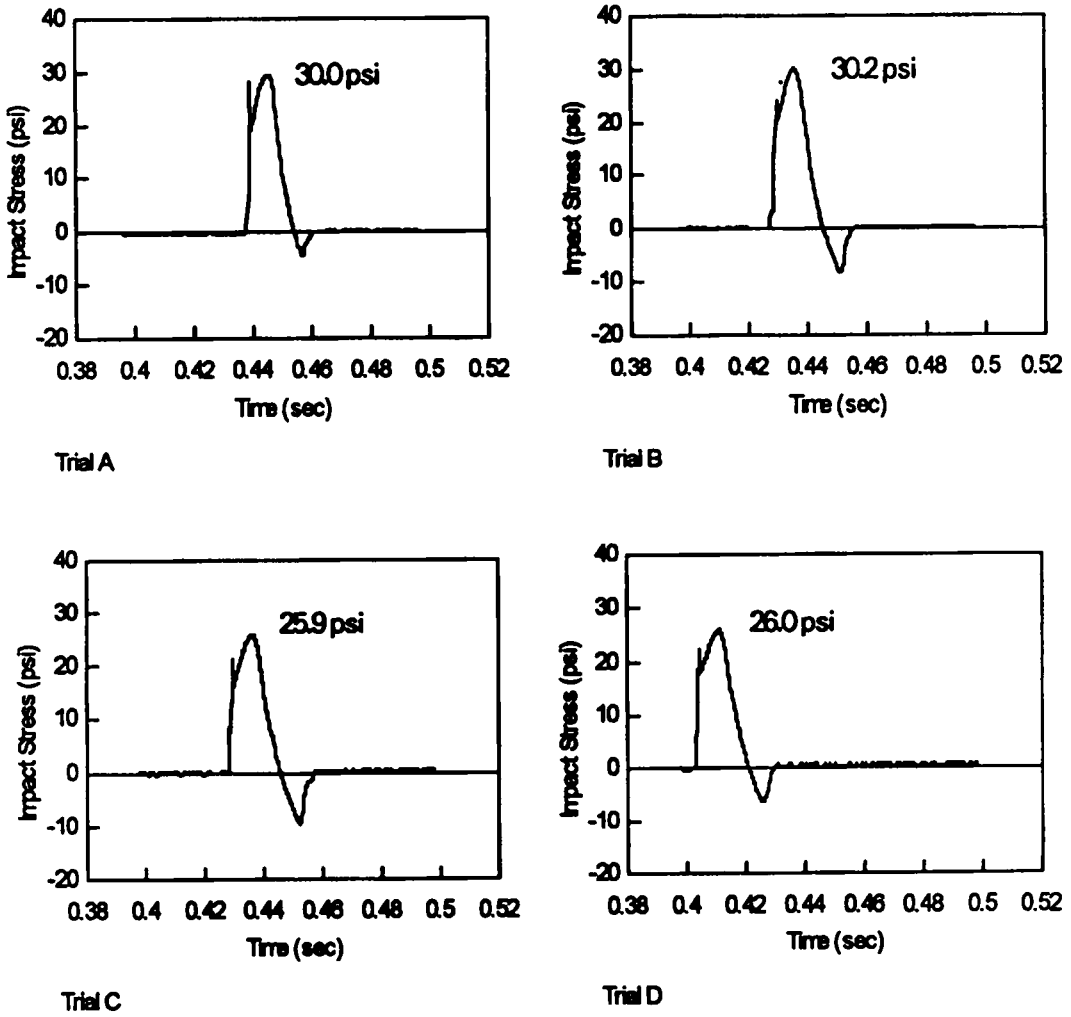

Figure 8. Impact stress versus time graphs for trials A–D

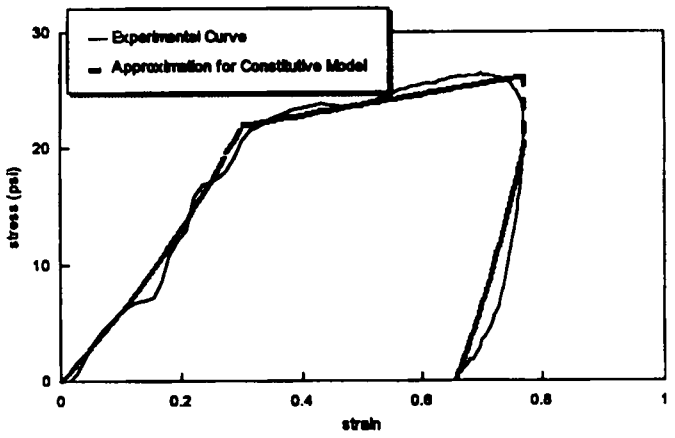

Figure 9. Experimental and simulated stress–strain curves

Table I. Model parameters for organic soil

Parameter	Assigned value
Outer radius of zone 2 (r_1)	8·56 cm ($2r_0$)
Initial modulus (M_0)	379 572 N/m^2
Poisson ratio	0·37
Angle of internal friction	35°
ε_0 (equations (1)–(8))	1·25
η (equations (6) and (7))	0·06
$K_0 = (1 - \sin\Phi)\sqrt{(\text{OCR})}$	0·4264
k (equations (3) and (4))	7·0 N/m^2

transducer channels in order to register the initial stress peak. Acceleration data was also sampled at a rate of 10 000 samples/s. Once data had been acquired and stored on the computer, data analysis was performed using LOTUS-123.

In order to verify reproduceability, four separate trials (A–D) were conducted using the same experimental set-up described above. Figure 8 shows the resulting impact stress versus time plot for each trial and the magnitude of the peak average impact stress. As seen from Figure 8, the peak average impact stress as well as the duration of impact are in agreement for all the trials.

By employing the accelerometer readings, the authors used the same test set-up with a thin soil layer to establish a non-linear stress–strain relationship for soil in zone 1 in the following manner. The vertical strain history can be deduced by converting the accelerometer results to displacements and then to corresponding strains assuming uniform strain throughout the thin layer of soil (2.5 cm) used in that test. Then, by comparing the average stress and strain histories at different stages of time in the soil layer, the dynamic stress–strain plot shown in Figure 9 was created.The constitutive parameters extracted from Figure 9 are shown in Table I.

5. EXPERIMENTAL VERIFICATION

In order to compare the analytical predictions with the experimental results, the authors discretized the 10 cm thick peat layer used in the experiment into 10 elements of equal thickness.

The steel bottom of the container was assumed to be infinitely stiff. Hence, the displacement and the velocity of the 10th element were set to zero. In addition, the outer radius of zone 2 was assumed to be $2 \times r_0$ (8·56 cm) where r_0 is the radius of the soil column (zone 1) (Table I). In order to scrutinize the sensitivity of the selected number of elements and the radius of zone 2 on the analysis, variation of the final penetration with the above parameters were plotted as shown in Figures 10 and 11. It is seen that the values of the above parameters can be determined based on Figures 10 and 11 so that a computationally efficient analysis could be performed.

Figure 11 shows that the hammer penetration responds significantly to the change of the radii ratio (zone 2 to zone 1) up to a value of 3·5. It also shows that under the present impact conditions, introduction of the non-linear zone changes the final penetration by only a factor of 0·97. This is mainly due to the fact that during the small-scale laboratory impact considered here, the *in situ* shear strength of the elements in zone 1 is inadequate to enforce the formation of a non-linear zone that provides a transition between the participating soil mass (zone 1) and the stationary zone 3. In case of field dynamic compaction where the influence zone extends to deeper layers with higher lateral stresses, the presence of the non-linear zone will be more significant. Hence Figure 11 by no means indicates an insignificant role of the non-linear transition zone.

In a trial run of the numerical algorithm with $\beta_1 = 0{\cdot}5$, it was found that the results were insensitive to the selected time interval, at time intervals smaller than 0·00005 s for the parameters indicated in Table I. The corresponding analytical prediction of the stress history is plotted against the experimental results in Figure 12, where the agreement between them with respect to the magnitude and time seems to be reasonable.

Furthermore, the penetration predicted from the ultimate value of d_1 was 12 mm while experimentally it was observed to be 7 mm.

Figures 12 and 8 show the eventual introduction of tension at the bottom of the weight mainly due to the suction created by pore water. Although the current analytical technique can predict tensile stresses, due to its inability to incorporate the pore pressure behaviour and tensile soil

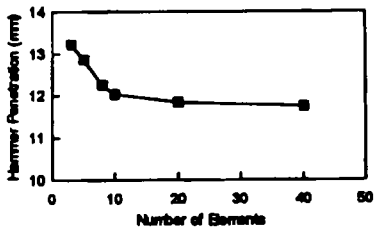

Figure 10. Variation of penetration with element thickness

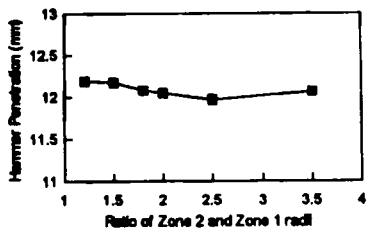

Figure 11. Variation of penetration with the ratio of zone 2 to zone 1 radii

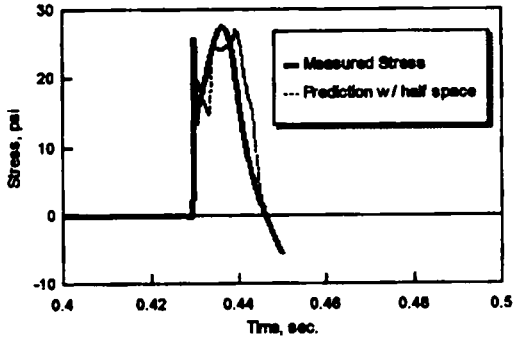

Figure 12. Comparison of measured and predicted stress pulses

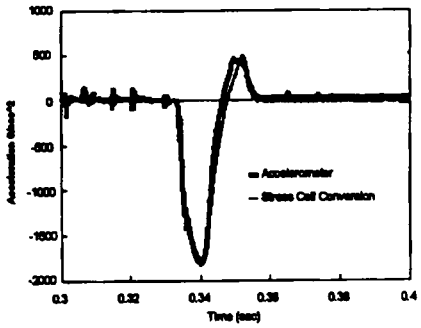

Figure 13. Comparison of the accelerometer and converted stress cell readings

properties, the predicted stress pulse was truncated after the compression wave. It is apparent that a major portion of the penetration descrepancy could be attributed to the rebound of soil during the tension stress pulse.

The authors further verified the accuracy of the measured stresses by comparing the accelerometer reading with the converted average stress cell readings according to the following equation, for another trial impact in the same experimental set-up.

$$a = \frac{[-\sigma_{avg}A + mg]}{m}$$

where

A = base area of the drop weight,
a = acceleration,
m = mass of drop weight,
σ_{avg} = average of stress cell readings.

Figure 13 shows excellent agreement between the accelerometer and converted stress cell readings verifying the accuracy of the above measurements.

6. GUIDELINES FOR USE OF THE MODEL

Reliability of any analytical model depends upon appropriate mathematical idealization of a given engineering problem and accurate determination of the model parameters. Estimation of the zone of influence, element thickness and the radius of the inner zone are the main tasks in the idealization phase of this specific problem. On the other hand, the parameters needed for this specific model are those associated with the constitutive relationship. As previously mentioned, the $\sqrt{(Wh)}$ criterion can be used to estimate the zone of influence while the thickness of individual elements should be decided after a sensitivity analysis using different trial element thicknesses. The outer radius of the non-linear shear zone (zone 1) is usually considered as a multiple of the inner soil column radius and should be based on past experience of the extent of deformation around the hammer. Moreover, in the case of a rectangular or a square hammer, the use of an equivalent radius is advocated.

The parameters needed for the constitutive relationship include initial constrained modulus (M_0), asymptotic strain (ε_0) and the material dependent constant (η). The constrained modulus (M) and the shear modulus (G) are related to the Young's modulus (E) and the Poisson's ratio (ν) by the following expressions:

$$M = \frac{E(1-\nu)}{(1-2\nu)(1+\nu)}$$

$$G = \frac{M(1-2\nu)}{2(1-\nu)}$$

Phillips and Baladi[12] and Nelson[13] suggested that, for loose granular soil, η takes values between 0·80 and 0·90 while ε_0 is between 0·40 and 0·50 for ideal one-dimensional dynamic compression. On the other hand, in loose soils like peat, the authors observed that ε_0 goes up to 1.25 and η takes the value of 0·06 under simulated dynamic compaction. Thus, especially for soft soils, it is advisable to find the parameters using laboratory tests where soils are subjected to similar conditions as that of dynamic compaction. The yield point (σ_b) in the stress–strain curve can be found from the standard bearing capacity equations.

CONCLUSIONS

The stress history of impact loading of soft soils has been studied using analytical and experimental techniques. When the falling weight was instrumented with pressure transducers and an accelerometer, two distinct stress peaks were consistently observed during the dynamic compaction of soft materials like organic soils. Furthermore, as one would anticipate, these impact produce relatively large strains during dynamic compaction leading to permanent deformations.

The above observations cannot be explained by any of the currently available analytical models for impact loading since they incorporate linear stiffness and damping properties. In the improved methodology advanced in this work, the stiffness and damping properties of the entire impact vicinity are modelled using spring and dashpot elements which appropriately represent the deformation modes of the individual zones. Moreover, the different degrees of deformation of the distinct zones are also considered in the model by utilizing nonlinear stiffness properties whereever necessary. On the other hand, when the impact is relatively mild, the non-linear zone becomes insignificant, thus appropriately reducing the model to currently available linear models.

Finally, it was displayed that the current technique posseses the capability of predicting the entire surface stress history including the two distinct peak stresses to a reasonable accuracy. In

addition, its ability to predict the approximate permanent penetration is indeed another advantage of the model.

APPENDIX

A.1. Derivation of the stiffness expression[9] of zone 2

The following stress–strain relationship is used for zone 2:

$$\gamma/\gamma_r = \beta/(1-\beta)$$

$$\beta = \tau/\tau_f$$

$$\gamma_r = \tau_f/G_s \text{where}$$

τ_0 = shear stress at the soil column interface,
τ_f = ultimate shear strength,
G_s = initial tangent shear modulus,
τ = shear stress at radius r from the centre of the impact area.

By assuming plane strain conditions, the displacement at soil column surface (w_0) is obtained by direct integration of the angular distortion from the radius of the zone 1 (r_0 to the radius of the zone 2 r_1).

$$w_0 = \int_{r_0}^{r_1} \gamma \, dr$$

$$w_0 = \int_{r_0}^{r_1} \frac{dr}{\dfrac{1}{\beta\gamma_r} - \dfrac{1}{\gamma_r}}$$

But for the equilibrium of zone 2

$$2\pi r_0 \tau_0 \, dx = 2\pi r \tau \, dx$$

By substituting the above condition and simplifying

$$w_0 = \int_{r_0}^{r_1} \frac{dr}{\left\{\dfrac{G_s r}{\tau_0 r_0} - \dfrac{1}{\gamma_r}\right\}}$$

Then by integrating and simplifying the above equation, it can be proved that $k_3 = \tau_0/w_0$

$$k_{s1i} = \frac{2\pi G_s}{\ln\left[\dfrac{(r_1/r_0) - (\tau_0/\tau_f)}{1 - (\tau_0/\tau_f)}\right]}$$

REFERENCES

1. P. Mayne and J. Jones, 'Impact stresses during dynamic compaction, *J. of Geotechnical Engineering, ASCE* **109**, 1342–1346 (October 1983).
2. R. A. Scott and R. W. Pearce, 'Soil compaction by impact', *Geotechnique*, **25**(1), 19–30 (1975).
3. J. H. Qian, 'Dynamic consolidation from practice to theory', *Proc 8th Asian Regional Conf. on Soil Mechanics and Found. Engrg.*, Vol. 2 Japanese Society for Soil Mechanics and Foundation Engineering, 1986, pp. 213–217.

4. J. W. Roesset, E. Kausel, V. Cuellar, J. L. Monte and Valerio, 'Impact of weight falling onto the ground, *J. Geotech. Eng. Div., ASCE*, **120**, 1395–1412 (1994).
5. Y. K. Chow, D. M. Yong, K. Y. Yong, and S. L. Lee, 'Dynamic compaction analysis', *J. Soil Mech. Found. Div. ASCE*, **118**(8), (1992).
6. L. Menard and Y. Broise, 'Theoretical and practical aspects of dynamic consolidation', *Geotechnique*, London, **25**(1), 3–18 (1975).
7. G. A. Leonards, W. A. Cutter and R. D. Holtz, 'Dynamic compaction of granular soil', *J. Geotech. Eng. Div. ASCE*, **106**(1), 35–44 (1980).
8. J. Lysmer and F. E. Ricart, 'Dynamic response of footings to vertical loading", *J. Soil Mech. Found. Div. ASCE* **92**(1), 65–91 (1966).
9. M. H. E. I. Naggar and M. Novak, 'Non-linear model for dynamic axial pile response', *J. Soil Mech. Found. Div. ASCE*, **120**(2), 308–329 (1994).
10. M. Novak, T. Nogami and F. Aboul-Ella, 'Dynamic soil reactions for plane strain case', *J. Eng. Mech. Div. ASCE* **104**, EM4 953–959 (1978).
11. T. Ginsburg, 'Propagation of shock waves in the ground', *J. Soil Mech. Found. Div. ASCE*, **90**(1), 125–163 (1964).
12. B. R. Phillips and G. Y. Baladi, 'Results of two free-field code calculations versus field measurements for the distant plain 1A event', Misc. Paper S-73-2I, U.S. Army Engr. Waterways Experiment Station, Vicksburg, Ms, 1973.
13. I. Nelson, 'Numerical solution of problems involving explosive loading, in '*Proc. Dynamic Methods in Soil and Rock Mechanics, Vol. 2: Plastic and Long Term Effects in Soils*, A. A. Balkema, Rotterdam, The Netherlands, 1977.
14. O. C. Zienkiewicz, '*The Finite Element Method Vol. 2*, McGraw-Hill New York.

INTERNATIONAL JOURNAL FOR NUMERICAL AND ANALYTICAL METHODS IN GEOMECHANICS, VOL. 20, 753–767 (1996)

INVESTIGATION OF IMPACT STRESSES INDUCED IN LABORATORY DYNAMIC COMPACTION OF SOFT SOILS

H. S. THILAKASIRI, M. GUNARATNE, G. MULLINS, P. STINNETTE AND B. JORY[†]

Department of Civil and Environmental Engineering, University of South Florida, Tampa, FL 33647, U.S.A.

SUMMARY

The majority of currently available analytical tools to predict ground stresses due to impact are based on linear spring-dashpot dynamic models. Although these simple models adequately represent stiff ground possessing linear visco-elastic behaviour, they suffer from two striking limitations when applied to relatively softer ground; (1) the inability to account for the permanent deformation resulting from impact, (2) failure to incorporate stiffness changes of softer soil within the impact duration. In this paper, the authors present an improved analytical approach formulated on the basis of a series of laboratory impact tests, to address the shortcomings of the current dynamic models in relation to soft soils. In this procedure, the impact zone is modelled as three distinct zones; (1) a zone beneath the falling weight undergoing non-linear axial deformation while being in vertical motion, (2) an inner zone immediately surrounding zone 1 with non-linear shear deformation, and (3) an outer zone undergoing a relatively lower degree of (linear) shear deformation. The soil constitutive parameters pertinent to the model are obtained from a modified dynamic compression test that simulates the impact conditions. It is shown that analytical predictions of the impact stress history and penetration are in agreement with test results. The findings are useful in the exploration of dynamic compaction techniques that will be effective in soft soil improvement.

KEY WORDS: dynamic; compaction; soil; damping; non-linear stressing

1. INTRODUCTION

A number of analytical models have been proposed by several researchers[1–4] in recent years to estimate surface stresses during dynamic compaction. In these models, it is assumed that the soil behaviour is linear elastic, isotropic and hence can be modelled by a linear spring and a linear dashpot. However, it is a common observation made during dynamic compaction of soft soil that the soil mass close to the surface is subjected to a very high strain level resulting in permanent deformation. Obviously a model that employs a linear spring and a linear dashpot is unable to simulate these observations because non-linearity is clearly exhibited by soils at high strain levels. Apart from the above-mentioned simplified models, Chow *et al.*[3] proposed a different analytical approach where the one-dimensional wave equation model for pile-driving analysis is modified by replacing the pile with a soil column extending to at least the anticipated depth of improvement. In this method, the soil surrounding the soil column is represented by linear elastic springs and linear dashpots. Furthermore, they adopted an implicit finite element method to solve the equation of motion of the soil column.

[†]Present address: Florida Department of transportation, Bartow, FL, U.S.A.

CCC 0363–9061/96/100753–15

Received 9 September 1994
Revised 12 January 1996

An improved analytical model is proposed in this paper to estimate the surface stress and the surface deformation, accounting for non-linearity of soil immediately below the drop hammer as well as that of the immediate neighbourhood of the hammer. In this procedure, equations of motion are separately written for three zones distinguished by their mode and degree of deformation while satisfying compatibility. A numerical procedure is adopted to solve these equations of motion because of complexity arising from the constitutive model that accounts for non-linearity. The solution procedure uses an explicit direct time integration together with lumped mass formulation for computational efficiency. Finally, analytical predictions of the impact surface stress history and penetration are compared with laboratory measurements.

2. EXPERIMENTAL OBSERVATIONS

Figure 1 shows a typical plot of the impact surface stress history recorded during the authors' experiments on a wet organic soil by employing a falling hammer instrumented with sensitive pressure transducers. The sensitivity of the data acquisition system is discussed in the ensuing Section 4 on the experimental set-up. The stress–time plot such as that shown in Figure 1 obtained from a series of tests consistently demonstrate the existence of two distinct regions:

(1) An immediate peak followed by rapidly diminishing stress. This phase of the stress history usually lasts only an extremely small time (1–2 ms) thus possibly eluding detection without a sensitive data acquisition system. This could be one reason why such an instantaneous peak has not been documented in previous experimental studies.
(2) A subsequent oscillatory stress pattern. This phase of the stress pulse on the other hand has been the subject of most previous experimental and analytical investigations.

3. MATHEMATICAL IDEALIZATION

From the perspective of deformation, the soil mass in the impact vicinity can be considered as being comprised of three distinct zones (Figure 2):

Zone 1: soil under the falling hammer in the zone of influence undergoing significant vertical deformation that permits it to be considered as a moving or participating soil mass,
Zone 2: soil in the immediate neighbourhood undergoing excessive shear deformations that can only be characterized by non-linear models,

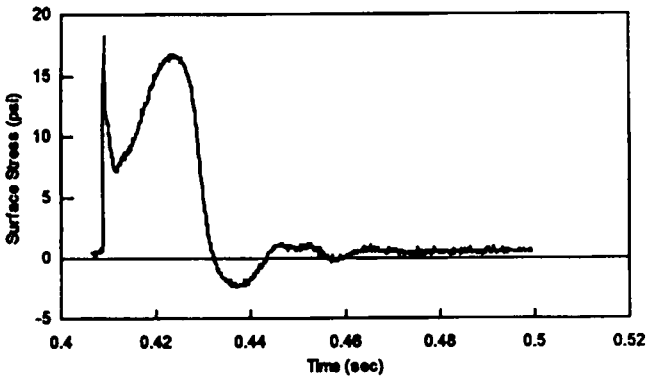

Figure 1. Typical experimental impact stress history

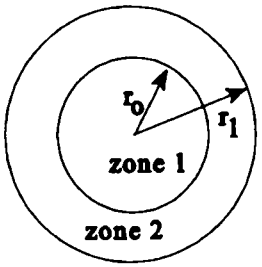

Figure 2. Plan view of the impact vicinity

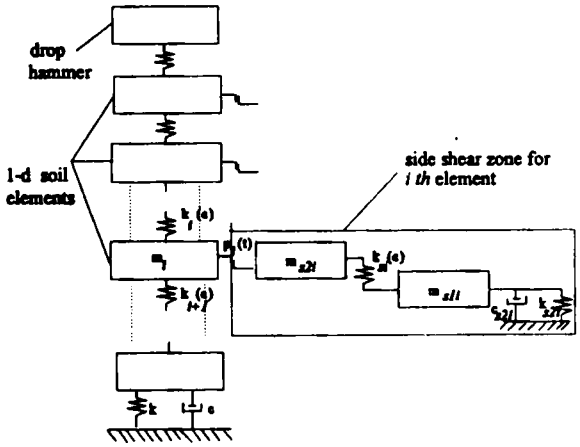

Figure 3. Dynamic model (shear zone is shown only for the ith element)

Zone 3: soil in the outer region undergoing limited shear deformations within linear elastic limits.

The authors' analytical formulation discussed here is founded on consideration of the mechanics of these three zones. The analytical formulation is kept simple by replacing the soil in the above zones with equivalent lumped masses. Researchers have observed that the depth of the zone of influence (z) during dynamic compaction varies in the range of $\sqrt{(W_1 h)} \geqslant z \geqslant 1/2\sqrt{W_1 h}$),[6,7] where W_1 and h are drop weight in tonnes and drop height in meters, respectively. Hence, in their formulations the authors suggest that the vertical depth (z) of the above non-linear zones should at least extend to a depth of $\sqrt{(W_1 h)}$. In the mathematical discretization, zones 1 and 2 up to the depth of influence are divided into elements of equal thickness as shown in Figure 3. Since the vertical strain within each element is assumed to be uniform, their thickness should be decided by a sensitivity analysis.

Since the strains in zone 1 are large, it is logical to expect non-linear behaviour. Thus, the soil elements in that zone are replaced in the current model by moving solid lumped masses (m_i) having the same cross-sectional area as that of the drop weight and are connected by non-linear

springs of stiffness $k_i(\varepsilon)$ as shown in Figure 3. $k_i(\varepsilon)$ can be expressed by $M_i(\varepsilon)A/L$ where $M_i(\varepsilon)$, A and L are the constrained modulus corresponding to the current strain (ε) (Section 3.1), cross-sectional area of the element and the current length of the element, respectively. The soil half-space beneath the immediate vicinity of the non-linear soil column is modelled by a linear spring (k) and a linear dashpot in parallel having a spring stiffness of $4G_s r_0/(1-\nu)$ and a dashpot coefficient of $3{\cdot}4Gr_0^2/(1-\nu)$ as proposed by Lysmer and Richart[8] in which r_0, G and ν are the radius of the soil column, initial shear modulus and the Poisson ratio, respectively. In the case where there is a stiff layer present within the zone of influence, the displacement of the last element is set to zero to account for it. In such a situation, the spring and the dashpot are not required.

On the other hand, the elements in annular zone 2, represented by two masses (m_{s1i} and m_{s2i}) of radius (r_1) surrounding zone 1 are also subjected to high strain levels. Therefore, its effect on the impact zone must also be modelled by non-linear shear stiffness properties (k_{si}). In this regard, the stiffness expression developed by El Naggar and Novak[9] would be appropriate. The expression for k_{si} is derived in the Appendix. The mass of the ith element in zone 2 is equally distributed to lumped masses m_{s1i} and m_{s2i} as shown in Figure 3. The elements in zone 2 interact with the corresponding elements in zone 1 through rigid plastic sliders $p_i(t)$ as shown in Figure 3.

Outside zone 2, the shear strains are small enough to permit the application of linear elastic constitutive relations. Thus, the shearing resistance of zone 3 is simulated by a linear spring (k_{s2i}) and a dashpot (c_{s2i}) having a stiffness of $2{\cdot}75G_s\,dz_i$ and a damping constant of $2\pi r_1\sqrt{\rho_s G_s}\,dz_i$, respectively, as proposed by Novak et al.[10] in which G_s, ρ_s and dz_i are the initial shear modulus, initial density and vertical thickness of elements in zone 2, respectively. Hence, zone 3 provides shear resistance to the vertical movement of elements in zone 2 through the parallel combination of spring k_{s2i} and c_{s2i}.

It is assumed that slipping can occur at the interface between the deforming soil elements in zone 1 and the elements in the surrounding zone 2 when the shear stress in the rigid plastic sliders $p_i(t)$ exceeds the maximum static resistance which is taken to be $k_0\sigma'_v \tan\Phi$; where, k_0, σ'_v and ϕ are coefficient of lateral earth pressure at rest, current vertical effective stress and angle of internal friction of the soil, respectively. It is accepted that the coefficient of lateral earth pressure depends on the over consolidation ratio (OCR) of the soil. Hence, in the proposed model k_0 is taken to be equal to $(1-\sin\phi)\sqrt{(\text{OCR})}$. Except for fully saturated low permeable soils with multiple impacts, the generation of pore water pressure in zone 1 is comparatively small[6] resulting in increased vertical effective stress in zone 1 during an impact. Therefore, it is important to note here that the maximum shear resistance changes during an impact even for a normally consolidated soil as the effective vertical stress changes with deformation of the soil column.

Finally, Newmark's explicit time step integration is employed to solve the equations of motion of the soil elements. The impacting hammer is disconnected from the numerical solution when the contact stress becomes less than zero.

If the depth of the non-linear zone is insignificant such as in the case of a small amplitude vibration, it is clear that the present model approaches the already accepted visco-elastic models, in which linear spring and a dashpot are in parallel (Figure 3). Further, the thickness of the influence zone can decrease with decrease in the drop weight and the drop height according to the aforementioned effective zone criterion ($\sqrt{Wh}$).

3.1. Determination of non-linear stiffness values

Figure 4 shows a typical axial stress–strain curve obtained for loading and unloading during a dynamic impact. The experimental procedure used to obtain Figure 4 is highlighted in Section 4. A unique feature of the stress–strain curve is a distinct yielding stage as shown in Figure 4 after

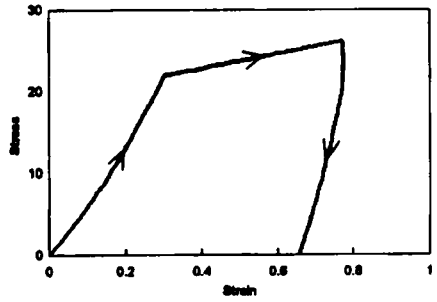

Figure 4. Experimental stress–strain curve

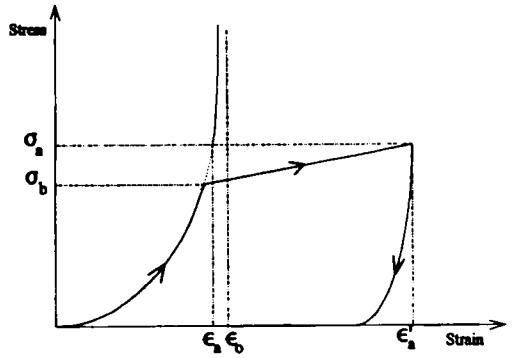

Figure 5. Typical theoretical stress–strain graph with symbols used in mathematical expressions

which a major portion of the axial strain is irrecoverable. This sudden change of the stiffness can be attributed to plastic flow resulting from shear failure. It was found that the pre-bearing capacity region of the curve can be conveniently expressed by the mathematical expression given by Ginsberg[11] for one-dimensional dynamic loading (equations (1) and (2)). Moreover, Ginsberg's[11] expression for the unloading phase correctly represented the unloading curve obtained by the authors as well (equations (5)–(6)). However, it should be noted that the post bearing capacity failure portion of the curve is linear with a small slope instead of being flat, indicating some strain hardening. Hence, based on Figure 4, the axial force in zone 1 can be determined by employing a constitutive relationship similar to that proposed by Ginsburg[11] for non-linear uniaxial dynamic compression. During each time step, the incremental strain in a given element is calculated based on the shortening of the element during the period and the current length of the element. Then, those incremental strains are summed up to estimate the total strain in the element and the corresponding axial stress from Figure 4. While the shape of the stress–strain curve proposed for loading and unloading is shown in Figure 5, the related mathematical relationships modified from the original Ginsburg model to include plastic flow, are expressed below.

For the loading stage
Up to the bearing capacity

$$\sigma = \frac{M_0 \varepsilon \varepsilon_0}{\{\varepsilon_0 - \varepsilon\}} \tag{1}$$

$$M(\varepsilon) = \frac{M_0 \varepsilon_0^2}{\{\varepsilon_0 - \varepsilon\}^2} \tag{2}$$

Beyond the bearing capacity

$$\sigma = k\{\varepsilon - \varepsilon_b\} + \sigma_b \tag{3}$$

$$M(\varepsilon) = k \tag{4}$$

For the unloading state

$$\sigma = M_0 \varepsilon_* \varepsilon_0 / \{\varepsilon_0 - \varepsilon_*\} \tag{5}$$

$$\varepsilon_* = (\varepsilon - (\varepsilon_a' - \varepsilon_a) - \varepsilon_a \eta / 1 - \eta \tag{6}$$

$$M(\varepsilon) = M_0 \varepsilon_0^2 / \{1 - \eta\}\{\varepsilon_0 - \varepsilon_*\}^2 \tag{7}$$

$$\varepsilon_a = \varepsilon_0 \sigma_a / (\sigma_a + M_0 \varepsilon_0) \tag{8}$$

where
M_0 = initial constrained modulus,
$M(\varepsilon)$ = constrained modulus at strain ε,
ε_0 = asymptotic value of strain corresponding to the pre-bearing failure portion,
η = a material constant,
ε_a' = strain at the beginning of the unloading phase,
σ_a = stress at the beginning of the unloading phase,
σ_b = bearing capacity,
k = modulus after the bearing capacity failure.

As mentioned in the mathematical idealization, the following expression for stiffness developed by El Naggar and Novak[9] assuming a plane strain condition are used for zone 2.

For loading

$$k_{s/i} = \frac{2\pi G_s}{\ln \dfrac{r_1/r_2 - \eta_0}{1 - \eta_0}} \tag{9}$$

For unloading

$$k_{s/i} = \frac{2\pi G_s}{\ln(r_1/r_0)} \tag{10}$$

where
r_1 = outer radius of the inner zone,
r_0 = radius of the soil column,
G_s = initial shear modulus,
τ_0 = shear stress at the axial element and shear element interface,
τ_f = ultimate shear strength,
$\eta_0 = \tau_0/\tau_f$.

3.2. Kinematic equations of the system

Using the notation indicated in Figure 6, the following equations of motion can be written for various components of the system:

For the drop hammer

$$w_1 - q_1(t) = \frac{w_1}{g} d_1''(t) \tag{11}$$

For the ith axial element (in Figure 6)

$$q_i(t) - q_{i+1}(t) - p_i(t) = m_i d_i''(t) \tag{12}$$

For ith shear element (in Figure 6)

$$p_i(t) - q_{si}(t) = m_{s1i} d_{s1i}''(t) \tag{13}$$

$$q_{si}(t) - k_{s2i} d_{s2i}(t) - c_{s2i} d_{s2i}'(t) = m_{s2i} d_{s2i}''(t) \tag{14}$$

where

$$k_{s2i} = 2{\cdot}75 G_s \, \mathrm{d}z_i, \tag{15}$$

$$c_{s2i} = 2\pi r_1 \sqrt{(\rho_s G_s)} \, \mathrm{d}z_i, \tag{16}$$

$\mathrm{d}z_i$ = thickness of the ith element in zone 2.

Newmark's explicit time step integration can be used to solve the equations (11)–(14) in combination with equations (17) and (18) as previously mentioned. For an element with a displacement $d(t)$ at any time t, Newmark's classical explicit time step integration algorithm (14) involves following recurrence relationships:

$$d_{n+1}(t) = d_n(t - \Delta t) + \Delta t \, d_n'(t - \Delta t) + \frac{\Delta t^2}{2} d_n''(t - \Delta t) \tag{17}$$

$$d_{n+1}'(t) = d_n'(t - \Delta t) + \Delta t(1 - \beta_1) d_n''(t - \Delta t) + \Delta t \beta_1 d_{n+1}''(t) \tag{18}$$

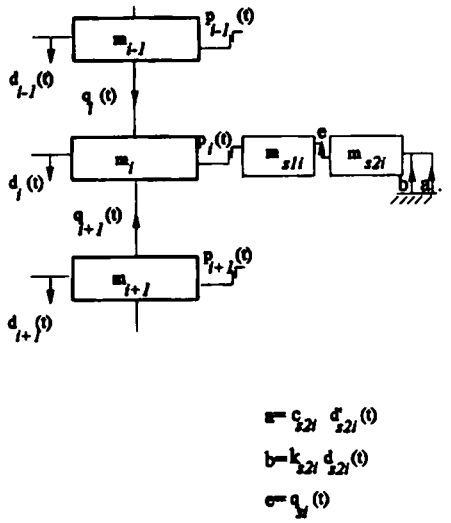

Figure 6. Free body diagrams for the ith axial and shear elements

where β_1 is Newmark's parameter, the value of which can be chosen for effective implementation of the particular algorithm.

Equation (17) can be used to explicitly obtain the current displacement $d_{n+1}(t)$ knowing the displacement, velocity and the acceleration of the element during the previous time step, while equation (18) enables one to express the current velocity of the element in terms of the current acceleration.

Thus, when equations (17) and (18) are separately applied to the elements in motion in Figure 3, it will facilitate the solution of equations (11)–(14) by evaluating the current displacement and the acceleration of each element based on the state of motion of the entire system at the preceding time step. Furthermore, at the end of each time step, element thicknesses and soil properties are upgraded according to the current strains, using the non-linear constitutive model described in the previous section. By repeating this procedure for a number of time steps, the numerical solution procedure can be successfully implemented. The explicit direct time integration algorithm is conditionally stable and the stability is governed by the magnitude of the time step size. It is found from the literature that the maximum size of the time step for a stable solution is related to the time required for an elastic wave to propagate across the shortest element of the mesh. In contrast to implicit algorithms, explicit algorithms require a large number of small time steps to avoid the solution of a large matrix equation which is typical of implicit methods at each time step.

4. EXPERIMENTAL SET-UP

The experimental set-up shown in Figure 7 was used to determine the dynamic impact stress due to a drop weight and the related stress–strain behaviour of an organic soil in the laboratory. The organic soil had a water content of 378 per cent, a we density of 1064 kg/m^3 (66 pcf) and an

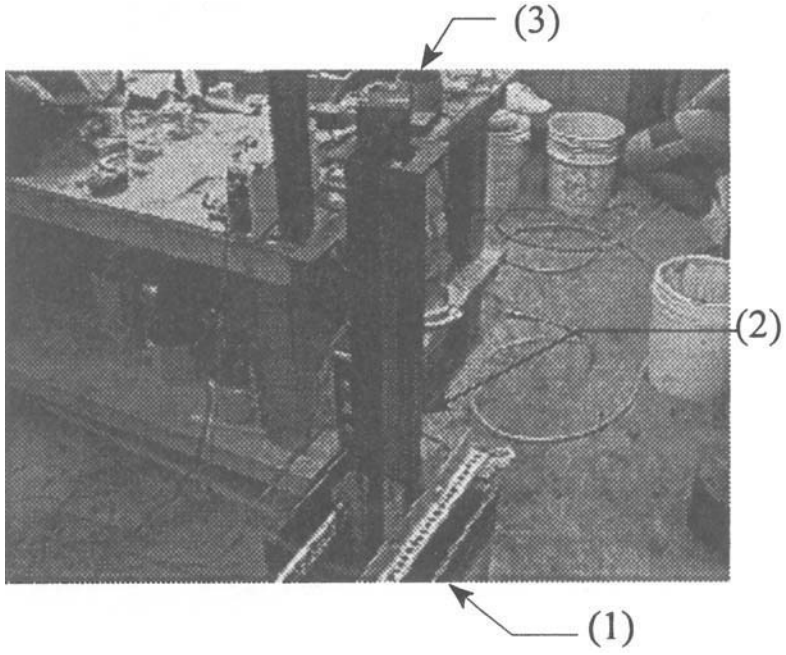

Figure 7. Experimental set-up

organic content of 80 per cent. The soil was compacted in a PVC lined 0·03 m^3 (one cubic foot-1′ × 1′ × 1′) container to a final bed depth of 10·16 cm (4 in) for the test used to get the surface stress history while a reduced depth of 2·6cm (1 in) was used for the test to determine the stress–strain relationship. A 0·923 m (3 ft) tall guide rail system (2) was placed on top of the box. A 2·27 kg (5 lb) steel weight with a 7·62 cm (3 in) square base (3) was held by an electro-magnet at the top of the guide rail. The weight was instrumented with five pressure transducers that were installed in such a manner that they were flush with the surface of the bottom of the weight. An accelerometer was also attached to the top of the weight so that its position was in line with the centre of gravity of the weight. The pressure transducers and the accelerometer were interfaced to a 486-33 MHz microcomputer through the use of a AT-MIO-16F-5 interface board.

Programs are written in Visual Basic to facilitate multiple channel data acquisition. A remote relay was used to simultaneously release the weight from the electro-magnet and initiate data acquisition. The impact stress was sampled at a rate 10 000 samples/s for each of the five

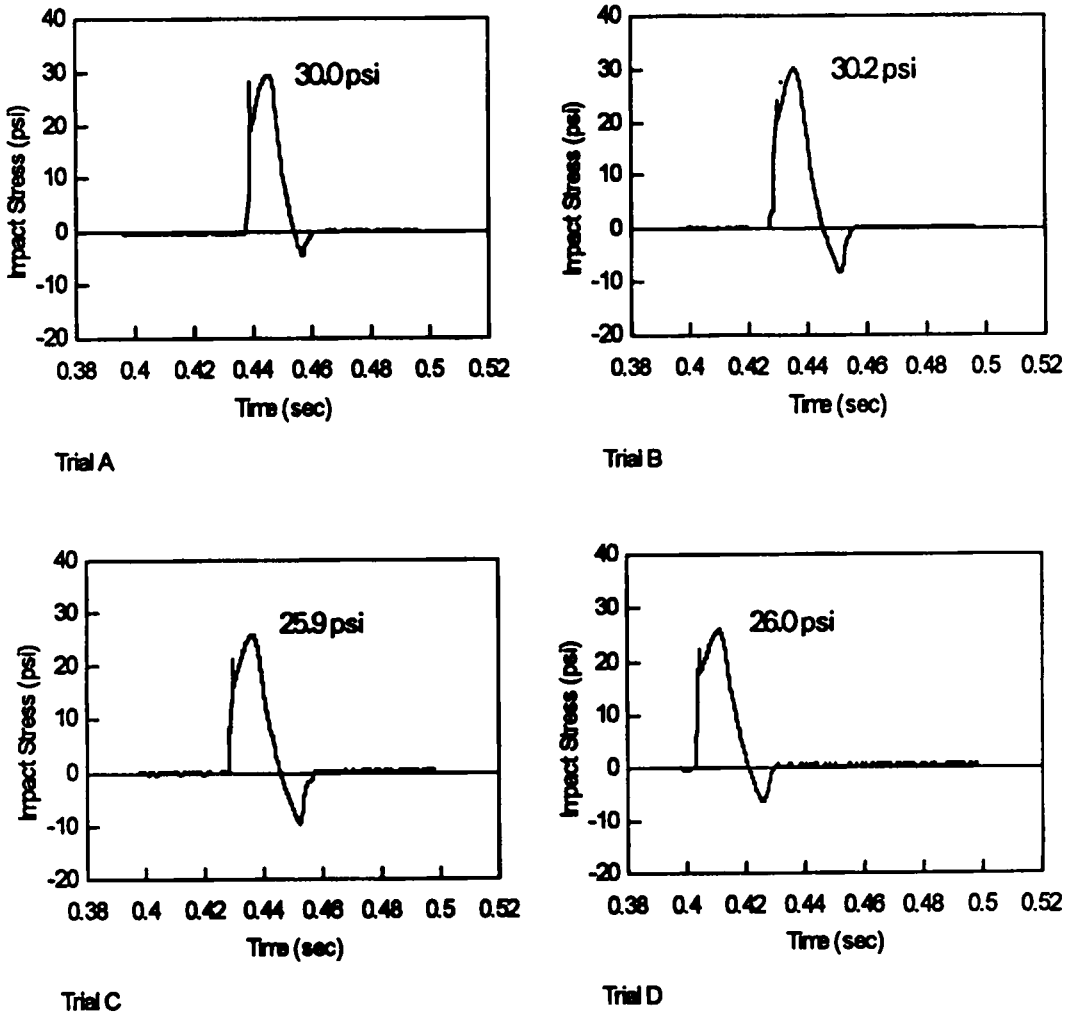

Figure 8. Impact stress versus time graphs for trials A–D

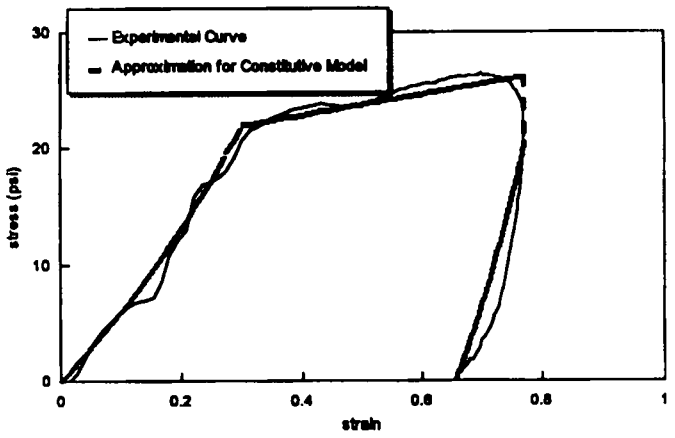

Figure 9. Experimental and simulated stress–strain curves

Table I. Model parameters for organic soil

Parameter	Assigned value
Outer radius of zone 2 (r_1)	8·56 cm ($2r_0$)
Initial modulus (M_0)	379 572 N/m^2
Poisson ratio	0·37
Angle of internal friction	35°
ε_0 (equations (1)–(8))	1·25
η (equations (6) and (7))	0·06
$K_0 = (1 - \sin\Phi)\sqrt{(\text{OCR})}$	0·4264
k (equations (3) and (4))	7·0 N/m^2

transducer channels in order to register the initial stress peak. Acceleration data was also sampled at a rate of 10 000 samples/s. Once data had been acquired and stored on the computer, data analysis was performed using LOTUS-123.

In order to verify reproduceability, four separate trials (A–D) were conducted using the same experimental set-up described above. Figure 8 shows the resulting impact stress versus time plot for each trial and the magnitude of the peak average impact stress. As seen from Figure 8, the peak average impact stress as well as the duration of impact are in agreement for all the trials.

By employing the accelerometer readings, the authors used the same test set-up with a thin soil layer to establish a non-linear stress–strain relationship for soil in zone 1 in the following manner. The vertical strain history can be deduced by converting the accelerometer results to displacements and then to corresponding strains assuming uniform strain throughout the thin layer of soil (2.5 cm) used in that test. Then, by comparing the average stress and strain histories at different stages of time in the soil layer, the dynamic stress–strain plot shown in Figure 9 was created.The constitutive parameters extracted from Figure 9 are shown in Table I.

5. EXPERIMENTAL VERIFICATION

In order to compare the analytical predictions with the experimental results, the authors discretized the 10 cm thick peat layer used in the experiment into 10 elements of equal thickness.

The steel bottom of the container was assumed to be infinitely stiff. Hence, the displacement and the velocity of the 10th element were set to zero. In addition, the outer radius of zone 2 was assumed to be $2 \times r_0$ (8·56 cm) where r_0 is the radius of the soil column (zone 1) (Table I). In order to scrutinize the sensitivity of the selected number of elements and the radius of zone 2 on the analysis, variation of the final penetration with the above parameters were plotted as shown in Figures 10 and 11. It is seen that the values of the above parameters can be determined based on Figures 10 and 11 so that a computationally efficient analysis could be performed.

Figure 11 shows that the hammer penetration responds significantly to the change of the radii ratio (zone 2 to zone 1) up to a value of 3·5. It also shows that under the present impact conditions, introduction of the non-linear zone changes the final penetration by only a factor of 0·97. This is mainly due to the fact that during the small-scale laboratory impact considered here, the *in situ* shear strength of the elements in zone 1 is inadequate to enforce the formation of a non-linear zone that provides a transition between the participating soil mass (zone 1) and the stationary zone 3. In case of field dynamic compaction where the influence zone extends to deeper layers with higher lateral stresses, the presence of the non-linear zone will be more significant. Hence Figure 11 by no means indicates an insignificant role of the non-linear transition zone.

In a trial run of the numerical algorithm with $\beta_1 = 0{\cdot}5$, it was found that the results were insensitive to the selected time interval, at time intervals smaller than 0·00005 s for the parameters indicated in Table I. The corresponding analytical prediction of the stress history is plotted against the experimental results in Figure 12, where the agreement between them with respect to the magnitude and time seems to be reasonable.

Furthermore, the penetration predicted from the ultimate value of d_1 was 12 mm while experimentally it was observed to be 7 mm.

Figures 12 and 8 show the eventual introduction of tension at the bottom of the weight mainly due to the suction created by pore water. Although the current analytical technique can predict tensile stresses, due to its inability to incorporate the pore pressure behaviour and tensile soil

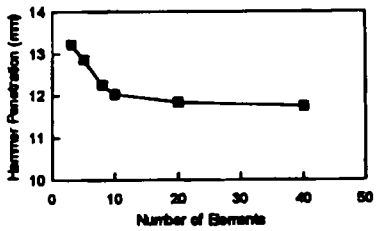

Figure 10. Variation of penetration with element thickness

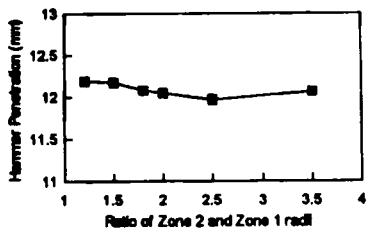

Figure 11. Variation of penetration with the ratio of zone 2 to zone 1 radii

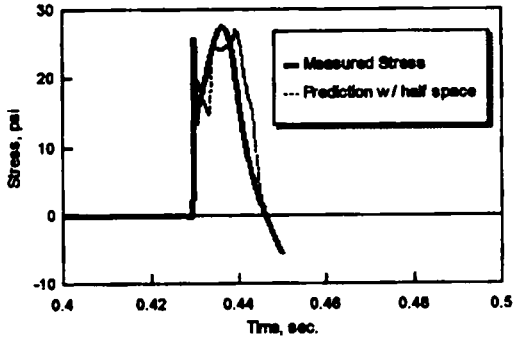

Figure 12. Comparison of measured and predicted stress pulses

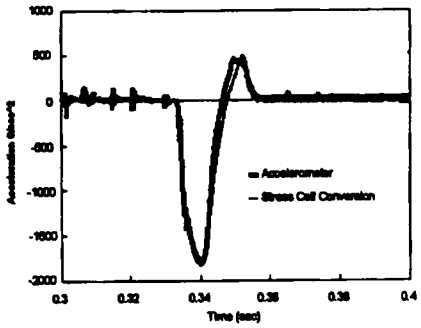

Figure 13. Comparison of the accelerometer and converted stress cell readings

properties, the predicted stress pulse was truncated after the compression wave. It is apparent that a major portion of the penetration descrepancy could be attributed to the rebound of soil during the tension stress pulse.

The authors further verified the accuracy of the measured stresses by comparing the accelerometer reading with the converted average stress cell readings according to the following equation, for another trial impact in the same experimental set-up.

$$a = \frac{[-\sigma_{avg}A + mg]}{m}$$

where

A = base area of the drop weight,
a = acceleration,
m = mass of drop weight,
σ_{avg} = average of stress cell readings.

Figure 13 shows excellent agreement between the accelerometer and converted stress cell readings verifying the accuracy of the above measurements.

6. GUIDELINES FOR USE OF THE MODEL

Reliability of any analytical model depends upon appropriate mathematical idealization of a given engineering problem and accurate determination of the model parameters. Estimation of the zone of influence, element thickness and the radius of the inner zone are the main tasks in the idealization phase of this specific problem. On the other hand, the parameters needed for this specific model are those associated with the constitutive relationship. As previously mentioned, the $\sqrt{(Wh)}$ criterion can be used to estimate the zone of influence while the thickness of individual elements should be decided after a sensitivity analysis using different trial element thicknesses. The outer radius of the non-linear shear zone (zone 1) is usually considered as a multiple of the inner soil column radius and should be based on past experience of the extent of deformation around the hammer. Moreover, in the case of a rectangular or a square hammer, the use of an equivalent radius is advocated.

The parameters needed for the constitutive relationship include initial constrained modulus (M_0), asymptotic strain (ε_0) and the material dependent constant (η). The constrained modulus (M) and the shear modulus (G) are related to the Young's modulus (E) and the Poisson's ratio (ν) by the following expressions:

$$M = \frac{E(1-\nu)}{(1-2\nu)(1+\nu)}$$

$$G = \frac{M(1-2\nu)}{2(1-\nu)}$$

Phillips and Baladi[12] and Nelson[13] suggested that, for loose granular soil, η takes values between 0·80 and 0·90 while ε_0 is between 0·40 and 0·50 for ideal one-dimensional dynamic compression. On the other hand, in loose soils like peat, the authors observed that ε_0 goes up to 1.25 and η takes the value of 0·06 under simulated dynamic compaction. Thus, especially for soft soils, it is advisable to find the parameters using laboratory tests where soils are subjected to similar conditions as that of dynamic compaction. The yield point (σ_b) in the stress–strain curve can be found from the standard bearing capacity equations.

CONCLUSIONS

The stress history of impact loading of soft soils has been studied using analytical and experimental techniques. When the falling weight was instrumented with pressure transducers and an accelerometer, two distinct stress peaks were consistently observed during the dynamic compaction of soft materials like organic soils. Furthermore, as one would anticipate, these impact produce relatively large strains during dynamic compaction leading to permanent deformations.

The above observations cannot be explained by any of the currently available analytical models for impact loading since they incorporate linear stiffness and damping properties. In the improved methodology advanced in this work, the stiffness and damping properties of the entire impact vicinity are modelled using spring and dashpot elements which appropriately represent the deformation modes of the individual zones. Moreover, the different degrees of deformation of the distinct zones are also considered in the model by utilizing nonlinear stiffness properties whereever necessary. On the other hand, when the impact is relatively mild, the non-linear zone becomes insignificant, thus appropriately reducing the model to currently available linear models.

Finally, it was displayed that the current technique posseses the capability of predicting the entire surface stress history including the two distinct peak stresses to a reasonable accuracy. In

addition, its ability to predict the approximate permanent penetration is indeed another advantage of the model.

APPENDIX

A.1. Derivation of the stiffness expression[9] of zone 2

The following stress–strain relationship is used for zone 2:

$$\gamma/\gamma_r = \beta/(1-\beta)$$

$$\beta = \tau/\tau_f$$

$$\gamma_r = \tau_f/G_s \text{where}$$

τ_0 = shear stress at the soil column interface,
τ_f = ultimate shear strength,
G_s = initial tangent shear modulus,
τ = shear stress at radius r from the centre of the impact area.

By assuming plane strain conditions, the displacement at soil column surface (w_0) is obtained by direct integration of the angular distortion from the radius of the zone 1 (r_0 to the radius of the zone 2 r_1).

$$w_0 = \int_{r_0}^{r_1} \gamma \, dr$$

$$w_0 = \int_{r_0}^{r_1} \frac{dr}{\dfrac{1}{\beta\gamma_r} - \dfrac{1}{\gamma_r}}$$

But for the equilibrium of zone 2

$$2\pi r_0 \tau_0 \, dx = 2\pi r \tau \, dx$$

By substituting the above condition and simplifying

$$w_0 = \int_{r_0}^{r_1} \frac{dr}{\left\{\dfrac{G_s r}{\tau_0 r_0} - \dfrac{1}{\gamma_r}\right\}}$$

Then by integrating and simplifying the above equation, it can be proved that $k_3 = \tau_0/w_0$

$$k_{s1i} = \frac{2\pi G_s}{\ln\left[\dfrac{(r_1/r_0) - (\tau_0/\tau_f)}{1 - (\tau_0/\tau_f)}\right]}$$

REFERENCES

1. P. Mayne and J. Jones, 'Impact stresses during dynamic compaction, *J. of Geotechnical Engineering, ASCE* **109**, 1342–1346 (October 1983).
2. R. A. Scott and R. W. Pearce, 'Soil compaction by impact', *Geotechnique*, **25**(1), 19–30 (1975).
3. J. H. Qian, 'Dynamic consolidation from practice to theory', *Proc 8th Asian Regional Conf. on Soil Mechanics and Found. Engrg.*, Vol. 2 Japanese Society for Soil Mechanics and Foundation Engineering, 1986, pp. 213–217.

4. J. W. Roesset, E. Kausel, V. Cuellar, J. L. Monte and Valerio, 'Impact of weight falling onto the ground, *J. Geotech. Eng. Div., ASCE*, **120**, 1395–1412 (1994).
5. Y. K. Chow, D. M. Yong, K. Y. Yong, and S. L. Lee, 'Dynamic compaction analysis', *J. Soil Mech. Found. Div. ASCE*, **118**(8), (1992).
6. L. Menard and Y. Broise, 'Theoretical and practical aspects of dynamic consolidation', *Geotechnique*, London, **25**(1), 3–18 (1975).
7. G. A. Leonards, W. A. Cutter and R. D. Holtz, 'Dynamic compaction of granular soil', *J. Geotech. Eng. Div. ASCE*, **106**(1), 35–44 (1980).
8. J. Lysmer and F. E. Ricart, 'Dynamic response of footings to vertical loading", *J. Soil Mech. Found. Div. ASCE* **92**(1), 65–91 (1966).
9. M. H. E. I. Naggar and M. Novak, 'Non-linear model for dynamic axial pile response', *J. Soil Mech. Found. Div. ASCE*, **120**(2), 308–329 (1994).
10. M. Novak, T. Nogami and F. Aboul-Ella, 'Dynamic soil reactions for plane strain case', *J. Eng. Mech. Div. ASCE* **104**, EM4 953–959 (1978).
11. T. Ginsburg, 'Propagation of shock waves in the ground', *J. Soil Mech. Found. Div. ASCE*, **90**(1), 125–163 (1964).
12. B. R. Phillips and G. Y. Baladi, 'Results of two free-field code calculations versus field measurements for the distant plain 1A event', Misc. Paper S-73-2I, U.S. Army Engr. Waterways Experiment Station, Vicksburg, Ms, 1973.
13. I. Nelson, 'Numerical solution of problems involving explosive loading, in '*Proc. Dynamic Methods in Soil and Rock Mechanics, Vol. 2: Plastic and Long Term Effects in Soils*, A. A. Balkema, Rotterdam, The Netherlands, 1977.
14. O. C. Zienkiewicz, '*The Finite Element Method Vol. 2*, McGraw-Hill New York.

Discussion by S. Thilakasiri,[7] G. Mullins,[8] P. Stinnette,[9] and M. Gunaratne[10]

The authors present a closed-form solution to predict impact stress in soil due to a falling weight using a linear-elastic

---

[7]Dept. of Civ. Engrg. and Mech., Univ. of South Florida, Tampa, FL 33620.
[8]Dept. of Civ. Engrg. and Mech., Univ. of South Florida, Tampa, FL.
[9]Dept. of Civ. Engrg. and Mech., Univ. of South Florida, Tampa, FL.
[10]Dept. of Civ. Engrg. and Mech., Univ. of South Florida, Tampa, FL.

spring and dashpot model. It should be noted that very similar models, such as those proposed by Scott and Pearce (1975) and Qian (1982), have previously been used to predict impact stresses in soil. However, the authors have advanced the mass-spring-dashpot model further by not overlooking the significance of overdamped and critically damped conditions, as opposed to Scott and Pearce (1975) and Qian (1982).

The discussers have also investigated the same problem, both analytically and experimentally. Accordingly, impact tests on soil were designed by the discussers to understand the effects of drop height, drop weight, and impact area on the contact stress. One series of tests in this experimentation involved dropping a 2.27 kg, 7.62 cm square drop hammer on compacted sandy soil from various drop heights. Stress measurements, recorded at a sampling rate of 10,000 Hz, were obtained using stress cells embedded in the surface of the hammer at the corners and center. The input parameters required to execute the authors' model, such as the shear wave velocity and Poisson's ratio, were back-calculated from the experimentally observed peak stress and contact time from the first trial of a previous test series on compacted sand. This prevented possible uncertainties in the precise measurement of the shear wave velocity, which is an important parameter in the authors' model. The values of shear wave velocity and Poisson's ratio were suitable for the compacted sand tested. These parameters were then utilized to predict the impact stresses and contact times for the consequent drops.

Fig. 19 shows the comparison of predicted peak stresses and those measured from experimentation, while Fig. 20 shows the stress-time history for the predicted and experimental stress for the 0.61 m drop. Although the peak stress and the contact time are predicted reasonably well, the shape of the curve, and hence the area under the curve vary significantly from the experimental results. This deviation, which invariably affects the prediction of the impulse applied to the ground, may be attributed to the deformations in the participating soil mass and the nonlinearity of soil even at low strains. As the authors

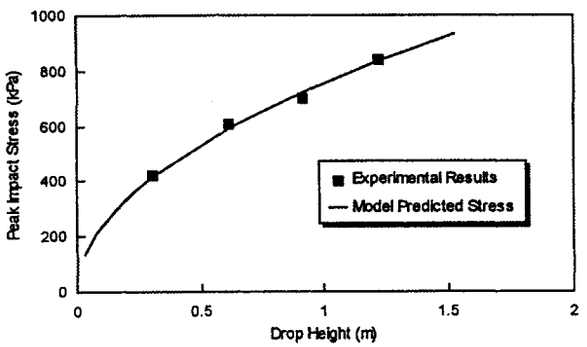

FIG. 19. Peak Stress versus Drop Height for 2.27 kg Drop Weight

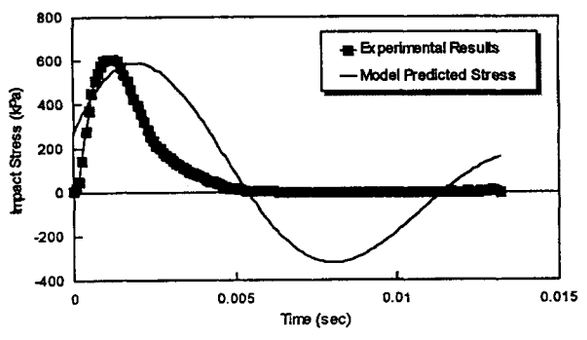

FIG. 20. Stress-Time History for 2.27 kg Drop Weight with 0.61 m Drop Height

point out, the contact time is comparable to the travel time of waves within the participating soil mass; however, the extent of the participating soil mass changes during the contact time thereby changing the parameters related to the soil half-space during that time period. Fig. 20 also indicates that the initial damping stress predicted by the authors' model is not observed in the tested soil. Similar discrepancies were reported by Scott and Pearce (1975) and Qian (1982).

The writers, on the other hand, had to formulate a nonlinear spring and dashpot model to explain the experimental observations (Thilakasiri et al. 1994). However, the complexity involved in a more realistic model certainly prohibits a closed-form solution such as that presented by the authors.

Furthermore, in most cases, drop weights permanently deform the ground surface. Nonlinear models such as the one formulated by the writers are needed to predict the permanent ground indentation. This limits the applicability of the authors' model to situations involving a low energy impact on a relatively stiff soil, which is certainly not illustrated by the example provided in the paper where a 125.7 kg weight is dropped from 5 m on a stiff soil. Moreover, the contact stress of 6,000 kPa produced in the authors' example is likely to induce a bearing capacity failure in the soil, thus invariably exceeding the limiting strain levels for elastic behavior.

Generally, elastic total stress techniques are also inadequate for saturated or partially saturated soils where pore pressure generation and dissipation govern the soil behavior under dynamic conditions. Within the limitations described previously, the authors' analytical model does provide an accurate closed-form prediction of the magnitude of peak stress induced by a rigid mass dropped on soil.

APPENDIX. REFERENCES

Qian, J. H. (1982). "Dynamic consolidation from practice to theory." *8th Asian Regional Conf. on Soil Mech. and Found. Engrg.*, Japanese Soc. for Soil Mech. and Found. Engrg., 2, 213–217.

Scott, R. A., and Pearce, R. W. (1975). "Soil compaction by impact." *Géotechnique*, London, England, 25(1), 19–30.

Thilakasiri, S., Mullins, G., Stinnette, P., Gunaratne, M., and Jory, B. (1994). "Investigation of impact stresses induced in laboratory dynamic compaction of soft soil." Under rev. by the *Int. J. for Analytical and Numer. Methods in Geomech.*

Closure by Jose M. Roesset,[11] Member, ASCE, Eduardo Kausel,[12] Member, ASCE, Vicente Cuellar,[13] Jose L. Monte,[14] and Julian Valerio[15]

The writers wish to thank the discussers for bringing to their attention some earlier works containing additional material relevant to the topic at hand, of which they were not aware. Of these, only the paper by Scott and Pearce (1975) is readily available to us for immediate consultation. We are also indebted to the discussers for presenting some actual test results for drop masses, which they used to highlight aspects where simple models fall short.

We are impressed by Thilakasiri et al.'s excellent agreement

[11]Prof., Dept. of Civ. Engrg., Univ. of Texas, Austin, TX 78712.

[12]Prof., Dept. of Civ. Engrg., Massachusetts Inst. of Technol., Cambridge, MA 01239.

[13]Head, Geotech. Engrg. and Testing Div., CEDEX, Alfonso XII-3, 28014 Madrid, Spain.

[14]Head, Special Testing Program, CEDEX, Alfonso XII-3, Madrid, Spain.

[15]Head, Dynamic Methods Program, CEDEX, Alfonso XII-3, Madrid, Spain.

ELSEVIER

Computers and Geotechnics, Vol. 18, No. 2, pp. 127–143, 1996

0266-352X(95)00023-2 0266-352X/96$15.00+0.00

Study of Pore Pressures Induced in Laboratory Dynamic Consolidation

M. Gunaratne, M. Ranganath, S. Thilakasiri, G. Mullins, P. Stinnette & C. Kuo†

Department of Civil and Environmental Engineering, University of South Florida, Tampa, FL 33620, U.S.A.

(Received 28 July 1994; revised version received 8 December 1994; accepted 14 February 1995)

ABSTRACT

Knowledge of the pore pressure behavior during dynamic impacts on moderately low permeability soils is essential in averting possible liquefaction and effective field implementation of dynamic consolidation. Although field observations of dynamically induced pore pressures are abundant in the literature, analytical or numerical approaches for pore pressure prediction are scarce. Herein, the authors advance a simple technique to analytically model the laboratory dynamic consolidation by modifying the classical Terzaghi's static consolidation theory. Since the analytical prediction of dynamic surface stress and experimental verification are performed in a companion paper, the surface stress due to a dynamic impact is assumed to be known in this work. Then, the time dependent stress pulse is de-synthesized into a number of constant load steps to predict the subsequent pore pressure behavior. Since this methodology accounts for even the dynamic stress attenuation within the soil sample, a rigorous closed form solution has to be replaced by a numerical solution. It is shown how this solution rapidly converges when the load steps are made sufficiently small. Finally, the analytical predictions of dynamic pore pressure are verified by well controlled laboratory experiments performed on a special apparatus set up at the University of South Florida.

INTRODUCTION

Since its first introduction by Menard, dynamic consolidation has been successfully applied in stabilizing soils with poor drainage and consolidation properties. In spite of the extensive field application, analytical or numerical

†Formerly District Geotechnical Engineer, Florida Department of Transportation, Bartow, FL.

methods to predict the rate of pore pressure dissipation are scarce in the literature. One reason for this may be the inability to adequately address the dynamically induced stress problem in its entirety.

In a companion paper [1], the authors describe their analytical model to predict the dynamic surface stresses observed in laboratory dynamic consolidation. Therefore, in the work presented here, the investigation is extended to explore the pore pressure behavior due to such dynamic impacts on relatively impervious soil. The authors also experimentally show that the dynamic stress attenuation with depth is in close agreement with the static elastic stress distribution. Due to the analytical complexity involved in predictions at off-centerline positions, the current investigation is limited to the locations on the load centerline where the most severe condition of pore pressure is registered on any horizontal plane. It is also theoretically shown that drainage can be expected to be vertical under the centerline of the impact especially close to the impact region. Hence, a modified version of Terzaghi's 1-D consolidation equation is utilized to predict the induced pore pressure behavior based on a load step method.

It is also shown how the numerical solution can be made to rapidly converge by considering sufficiently small load steps. Finally, the numerical predictions are compared to the results of an experimental setup developed at the University of South Florida.

DYNAMIC SURFACE STRESS

Several researchers have attempted to analytically examine the surface stresses induced during dynamic compaction. Scott and Pierce's [2] approach using basic stiffness and damping properties of the soil and Mayne and Jones' [3] technique based on the deceleration of the hammer during penetration are some of them. The former researchers predict a dynamic stress pulse producing a significant initial stress value due to the instantaneous damping. However, early experimental observations within the soil mass have revealed no such initial instantaneous stress value [2,3]. On the other hand, Mayne and Jones [2] introduced an analytical approach which complies with the experimental observation of a zero initial stress.

One drawback of the latter approach is that it does not model the continued but less severe stress pulses observed in more recent laboratory studies conducted by the authors utilizing stress cells placed at different locations in the sample. Moreover, the authors' tests indicate very high initial instantaneous stresses close to the surface especially under saturated conditions. In the companion paper [1], the authors address the shortcomings of the aforementioned theories by advancing a new analytical approach that can explain

the observed dynamic stress history and the vibration behavior of the soil upon dynamic impact, addressing the shortcomings of the aforementioned theories. Hence, in this paper, the discussion is limited to the pore pressure predictions using the dynamic stresses observed in the authors' experiments (Fig. 1).

DISTRIBUTION OF STRESSES BELOW THE IMPACT SURFACE

During their experimental program, the authors conducted a series of experiments to investigate the dynamic stress attenuation. Both the vertical and horizontal stress distributions below the impact center were seen to be in agreement with the elastic theory. Figure 2 exhibits a comparison of stress distributions from the authors' results and other experimental evidence, with the elastic theory.

Thus, if $\Delta\sigma_0$ is the contact dynamic stress developed under a falling weight of radius r_0, then the vertical stress at any depth z vertically below the center of the weight can be expressed using elastic theory as:

$$\Delta\sigma_v = \Delta\sigma_0 \left[1 - \frac{1}{[1 + (r_0/z)^2]^{3/2}} \right] \tag{1}$$

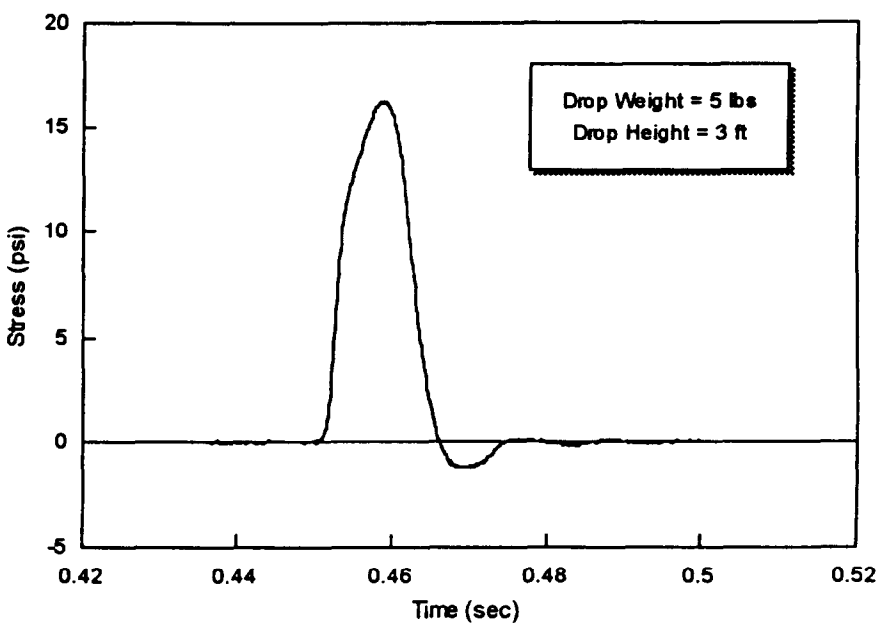

Fig. 1. Impact stress measured at a depth of three (3) inches.

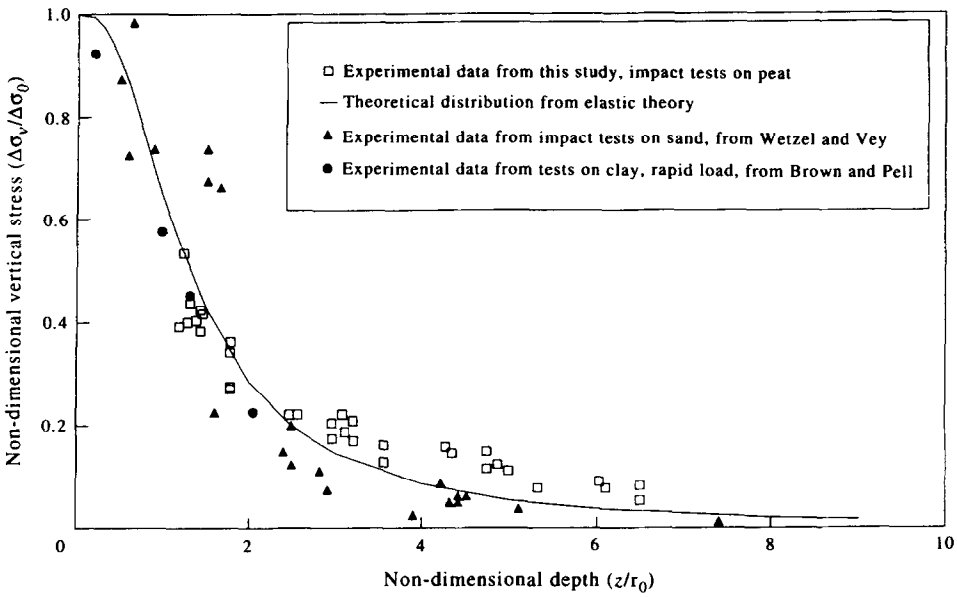

Fig. 2. Comparison of dynamic vertical stress distribution with elastic predictions.

DRAINAGE CONDITIONS

On impact, the pore pressure will increase instantaneously under the hammer inducing drainage in the radial and vertical directions. However, if a water particle is considered at any depth beneath the center of the weight, under isotropic soil conditions, clearly it cannot acquire a velocity in any preferential radial direction due to symmetry. Hence, the pore pressure variation contributing to the response of a transducer placed at any location under the centerline of the impact is theoretically a result of the vertical drainage only. This is especially the case when the observation point is located in the vicinity of the surface. This fact can be mathematically illustrated as follows.

Consider the volumetric changes induced by the drainage conditions due to a centerline radial velocity of v and a vertical velocity of u as shown in Fig. 3. If the net flow out of the element having a radius of dr is equated to the volume reduction in the element, one would obtain the following expression:

$$\pi(\mathrm{d}r)^2\left[\frac{\partial u}{\partial z}\mathrm{d}z + u - u\right] + 2\pi(\mathrm{d}r)(\mathrm{d}z)\left[v + \frac{\partial v}{\partial r}\mathrm{d}r\right] = -\frac{1}{1+e}\frac{\partial e}{\partial t}[\pi(\mathrm{d}r)^2\mathrm{d}z]$$

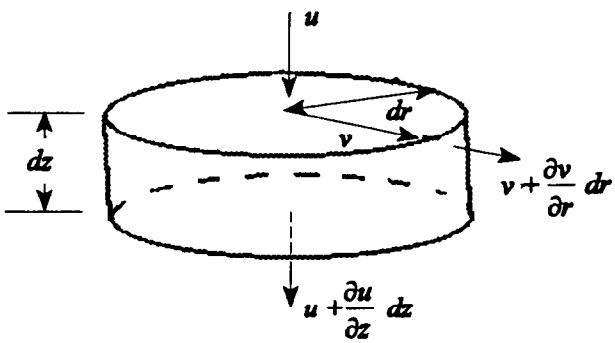

Fig. 3. Consolidation of a small cylindrical element.

which when simplified produces

$$\frac{\partial u}{\partial z}\mathrm{d}r + 2v + 2\frac{\partial v}{\partial r}\mathrm{d}r = -\frac{1}{1-e}\frac{\partial e}{\partial t}\mathrm{d}r$$

It is seen that as the radius dr becomes smaller, the centerline radial velocity v approaches zero.

The above conclusion can be further verified by theoretically illustrating that there is no radial pore pressure gradient on the centerline. As it will be shown later [eqn (13)], the instantaneous pore pressure generated at any depth z (u_z) is proportional to the total vertical stress induced at that depth ($\Delta\sigma_z$). On the other hand, the authors extended their dynamic stress monitering program to obtain the radial distribution of $\Delta\sigma_z$ as well, as shown in Fig. 4. Hence, the radial distribution of pore pressure (u_z) will also be a similar distribution. It is obvious from Fig. 4 that:

$$\left[\frac{\partial(\Delta\sigma_z)}{\partial r}\right]_{r=0} = 0$$

thus it follows that:

$$\left[\frac{\partial u_z}{\partial r}\right]_{r=0} = 0$$

which supports the assumption of no radial drainage conditions on the centerline. Furthermore, since the radial pore pressure gradient increases only gradually as r increases (Fig. 4), it is also reasonable to assume that the radial flow is insignificant even in the immediate neighborhood of the centerline. Accordingly, in the testing program, the authors utilized a very fine

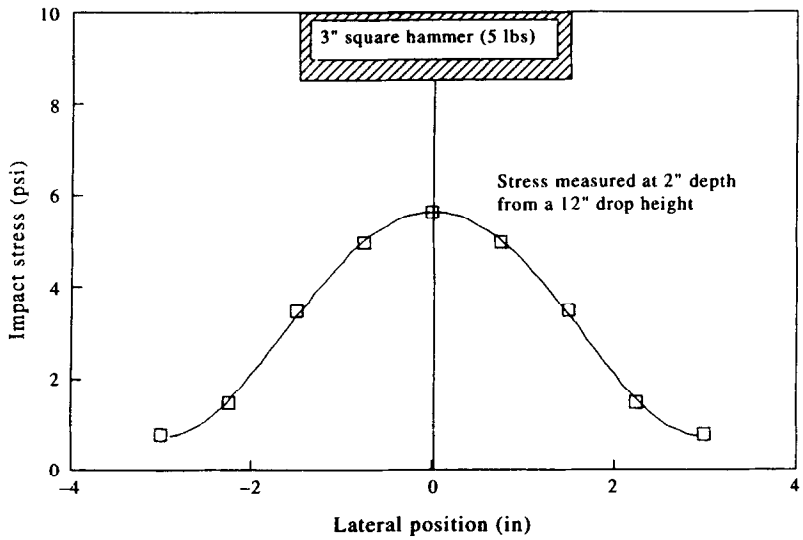

Fig. 4. Vertical stress variation with lateral (r) position.

pore pressure probe with a negligible diameter compared to the base width of the drop weight, to monitor the pore pressure at the centerline.

As for the boundary conditions, a free draining boundary is assumed at the top of the compacting soil layer while the bottom of the soil layer or the transducer soil interface is assumed to be perfectly impervious.

PORE PRESSURE MODEL

Under 1-D drainage conditions, the pore pressure dissipation in a saturated medium at any depth z due to a constant load can be analyzed starting from the following initial step of Terzaghi's formulation [4]:

$$\frac{a_v}{(1+e)}\frac{\partial \sigma'}{\partial t} = -\frac{k}{\gamma_w}\frac{\partial^2 u}{\partial z^2} \tag{2}$$

where a_v, k and e are the compressibility of the soil skeleton, the hydraulic conductivity and the void ratio of the soil, respectively.

If the water compressibility is assumed to be C_w, unlike in Terzaghi's formulation where it is neglected, the water pressure and the total stress can be introduced to the above equation as:

$$\frac{a_v}{(1+e)}\left[\frac{\partial \sigma}{\partial t} - \frac{\partial u}{\partial t}\right] - \frac{e}{1+e}C_w\frac{\partial u}{\partial t} = -\frac{k}{\gamma_w}\frac{\partial^2 u}{\partial z^2} \tag{3}$$

The above expression can be simplified to

$$\frac{\partial u}{\partial t}\left(1+\frac{eC_w}{a_v}\right)-\frac{\partial \sigma}{\partial t}=C_v\frac{\partial^2 u}{\partial z^2} \tag{4}$$

which is a general 1-D consolidation equation, applicable for static as well as dynamic loading, and C_v is the coefficient of consolidation of the soil. Under a static total stress (no variation of total stress with time) and negligible water compressibility, eqn (4) simplifies to the classical Terzaghi's 1-D consolidation equation which expresses solely the dissipation behavior of pore pressure with no generation.

$$\frac{\partial u}{\partial t}=C_v\frac{\partial^2 u}{\partial z^2} \tag{5}$$

On the other hand, for undrained loading or unloading conditions which can be simulated by setting the hydraulic conductivity k or C_v to zero, eqn (4) reduces to:

$$\frac{\partial u}{\partial t}\left(1+\frac{eC_w}{a_v}\right)=\frac{\partial \sigma}{\partial t}$$

which can be rearranged in the more common form as

$$\frac{\partial u}{\partial t}=B\frac{\partial \sigma}{\partial t} \tag{6}$$

where B is the Skempton's pore pressure parameter relevant to isotropic stress increments as expressed below.

$$B=\frac{1}{(1+eC_w/a_v)} \tag{7}$$

In fact, it can be shown using the generalized Hooke's law that the stress condition is isotropic for 1-D undrained loading which induces zero strains in all directions. It is noted that eqn (6) is applicable to generation of pore pressure without any dissipation.

By blending B with C_v, eqn (4) can be rewritten as:

$$\frac{\partial u}{\partial t}=B\frac{\partial \sigma}{\partial t}+C_v\frac{\partial^2 u}{\partial z^2} \tag{8}$$

From the above discussion, it is obvious that eqn (8) encompasses both pore pressure generation and dissipation components during dynamic loading.

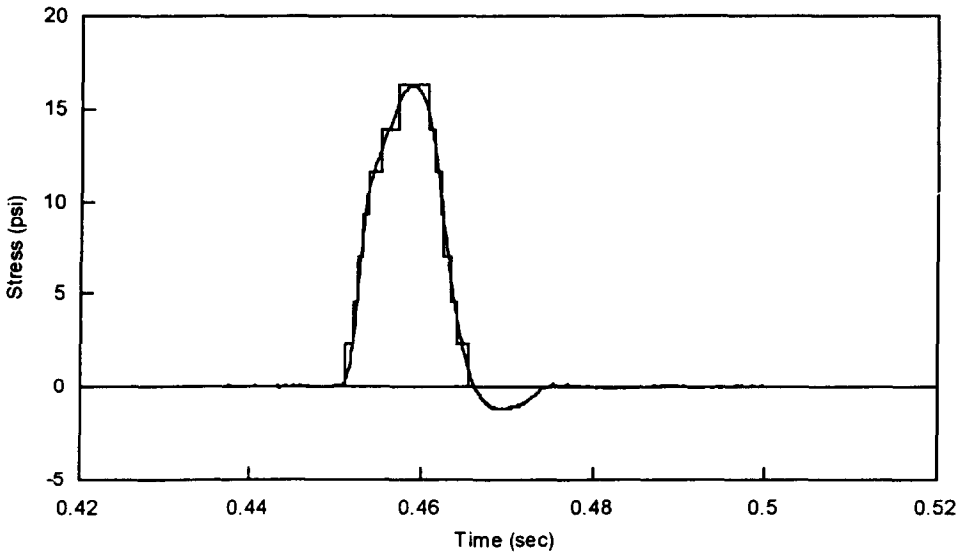

Fig. 5. Approximation of dynamic loading with constant stress increments.

This can be further illustrated by applying eqn (8) during a time interval Δt to depict the individual magnitudes of the pore pressure components at any depth z as:

$$\Delta u = B\Delta\sigma + \left(C_v \frac{\partial^2 u}{\partial z^2}\right)\Delta t \tag{9}$$

The above concept is utilized in the ensuing formulation to isolate the generation and dissipation components of pore pressure during sufficiently small time intervals (Fig. 5). In summary, the pore pressure generation is treated as a boundary condition by utilizing eqn (6) and the dissipation during the same time is expressed by Terzaghi's expression in eqn (5).

SOLUTION OF PORE PRESSURE EQUATION

Since the vertical stress has been experimentally verified to be distributed according to elastic theory, the classical Terzaghi solution which is valid for uniform or linear vertical stress distributions has to be replaced by a fresh solution. A solution of the following general form is possible for eqn (5).

$$u = (P\cos Az + Q\sin Az)e^{Dt} \tag{10}$$

By substitution in eqn (5), one finds that,

$$D = -A^2 C_v$$

Hence eqn (10) can be modified to,

$$u = (P\cos Az + Q\sin Az)e^{-A^2C_v t} \tag{11}$$

At this stage, the previously discussed spatial boundary conditions can be utilized as follows:

Free draining surface at the top

$$u = 0 \quad \text{at} \quad z = 0 \quad \text{for} \quad t > 0^+$$

Rigid boundary at the bottom

$$\frac{\partial u}{\partial z} = 0 \quad \text{at} \quad z = H$$

to find expressions for P and A as:

$$P = 0$$

and

$$A = (2n - 1)\frac{\pi}{2H}$$

where n is any integer. This modifies the solution in eqn (11) to

$$u_{z,t} = \sum_{n=1}^{\infty} Q_n \sin[(2n - 1)\frac{\pi}{2H}z]e^{-[(2n-1)\pi/2]^2 T} \tag{12}$$

where

$$T = \frac{C_v t}{H^2}$$

If the soil medium is saturated, the initial pore pressure u_z at any point below the impact center due to a total stress increase $\Delta\sigma_z$ can be expressed using eqn (6) as:

$$u_z = B.\Delta\sigma_z \tag{13}$$

Substituting from eqn (1) in the above equation, a third boundary condition for $t = 0$ can be written as:

$$u_{z,0} = \Delta\sigma_0 B\left[1 - \frac{1}{[1 + (r_0/z)^2]^{3/2}}\right] \tag{14}$$

At $t = 0^+$, eqn (12) becomes

$$u_{z,0} = \sum_{n=1}^{\infty} Q_n \sin[(2n-1)\frac{\pi}{2H}z] \tag{15}$$

By comparing eqns (14) and (15), Q_n can be found using the Fourier half-range expansion as:

$$Q_n = \frac{2}{H}\int_0^H u_{z0} \sin[(2n-1)\frac{\pi z}{2H}]\mathrm{d}z \tag{16}$$

In order to extend the above concepts to the dynamic stress increment shown in Fig. 1, the latter was considered as being composed of a series of equal positive stress increments i ($i = 1, m_1$) of magnitude $\Delta\sigma_0$ (or $Q_{\max}/m_1$) imposed at time t_i followed by a similar series of negative stress increments i ($i = m_1 + 1, m_2$) of the same magnitude (Fig. 5). It is realized that this approximation should yield the exact dynamic solution at the limit where the stress increment, $\Delta\sigma_0$, approaches zero. However, one limitation of this approach is that it does not account for the time lag between the actual impact and the arrival of the consequent stress wave at the considered depth z, as stress and pore pressure increments at that depth [eqn (14)] are considered to be static.

According to eqns (12), (14) and (16), the pore pressure variation in space and time due to the first total stress increment $\Delta\sigma_0$ imposed at the time t_1, can be expressed as,

$$u_{z,t} = \frac{2B.\Delta\sigma_0}{H}\sum_{n=1}^{n=\infty}\left[\int_0^H k(z)\sin\frac{Nz}{H}\mathrm{d}z\right]\sin\frac{Nz}{H}\mathrm{e}^{-\frac{C_v N^2}{H^2}(t-t_1)} \tag{17}$$

where

$$k(z) = \left[1 - \frac{1}{[1+(r_0/z)^2]^{3/2}}\right]$$

and

$$N = (2n-1)\pi/2$$

Therefore, the pore pressure distribution at a subsequent time t due to all of the increments up to t_{m1} can be expressed as

$$u_{z,t} = \frac{2B.\Delta\sigma_0}{H} \sum_{n=1}^{n=\infty} \left[\int_0^H k(z) \sin \frac{Nz}{H} dz \right] \sin \frac{Nz}{H} \sum_{i=1}^{m_1} e^{-\frac{C_v N^2}{H^2}(t-t_i)} \tag{18}$$

Similarly, the pore pressure distribution at any time t due to a load removal of equal magnitude at a time t_j ($> t_{m1+1}$) will be:

$$u_{z,t} = \frac{B^*.2.\Delta\sigma_0}{H} \sum_{n=1}^{n=\infty} \left[\int_0^H k(z) \sin \frac{Nz}{H} dz \right] \sin \frac{Nz}{H} e^{-\frac{C_v^* N^2}{H^2}(t-t_j)} \tag{19}$$

where C_v^* represents the coefficient of swelling (reverse consolidation) and B^* is the isotropic pore pressure parameter [eqn (7)] relevant to unloading. From the basic definition of the coefficient of consolidation, it can be shown that

$$\frac{C_v}{C_v^*} = \frac{a_v^*}{a_v} = r$$

where

a_v^* = coefficient of recompression
a_v = coefficient of compression

and thus r is a factor representing the ratio of the soil compressibilities (a_v) under unloading and loading.

Since eqn (7) exhibits that a difference in a_v values in loading and unloading should reflect a corresponding difference in the B parameter as well, another factor R can be defined to account for the difference in the pore pressure parameter during loading and unloading as

$$R = \frac{B^*}{B}$$

Finally, the pore pressure variation for the combination of the loading and unloading sequence (Fig. 5) is determined by the following equation:

$$u(z,t) = \frac{2B.R.\Delta\sigma_0}{H} \sum_{n=1}^{n=\infty} \left[\int_0^H k(z) \sin \frac{Nz}{H} dz \right] \sin \frac{Nz}{H} \sum_{i=1}^{m_2} e^{-\frac{rC_v N^2}{H^2}(t-t_i)} \tag{20}$$

under conditions stated below:

Positive stress increase

$$\text{If} \quad i \leqslant m_1, \quad \text{then} \quad R = 1, \; r = 1$$

Negative stress increase

$$\text{If} \quad i > m_1, \quad \text{then} \quad \Delta\sigma_0 = -\Delta\sigma_0$$

A computer program was written to execute eqn (20) and determine the variation of pore pressure with time due to a single impact. In order to illustrate that the numerical solution rapidly converges to what can be assumed to be the exact dynamic solution when $\Delta\sigma$ approaches zero, a hypothetical pore pressure distribution due to the stress history in Fig. 1 is predicted and plotted for different magnitudes of stress increments ($\Delta\sigma_0$ = 2.11, 4.23 and 8.46) in Fig. 6.

The following data have been used in the example:

Coefficient of consolidation	=	0.002 in.^{2}/s
Depth of soil sample	=	3 in.
Base diameter of weight	=	3.4 in.
R	=	0.95
r	=	1.3
B	=	0.95

Moreover, the authors utilized the above computer program to perform a parametric study of the impact of C_v on the dissipation of pore pressure

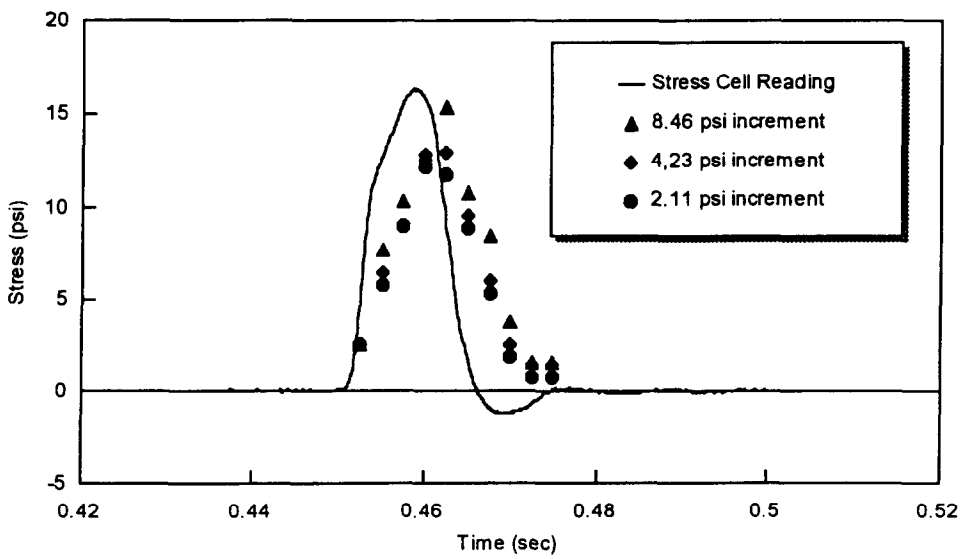

Fig. 6. Convergence of numerical solution with small stress increments.

during the short impulse stress duration. From the results, it was concluded that the need for "coupled analysis" [eqn (9)] clearly depends on the magnitude of the coefficient of consolidation, C_v and hence indirectly on the hydraulic conductivity, k. As one would expect, the authors also found that C_v values corresponding to coarse grained soils do not allow significant pore pressure generation, whereas C_v values that represent clayey soils typically exhibit undrained behavior during impact loading. Hence, consideration of pore pressure dissipation during the impact stress is unnecessary for the above soil types. However, the numerical values revealed that modeling of dissipation is essential for moderately pervious soils (with approximately $10^{-2} > C_v > 10^{-4}$ in.^{2}/s).

As illustrated in the following section on experimental verification, C_v value for the organic soil tested in this research was approximately 0.002 in.^{2}/s. This value yields an equivalent hydraulic conductivity of 10^{-5} cm/s from the following basic relationship:

$$C_v = \frac{k(1+e)}{a_v \gamma_w}$$

The coefficient of compressibility (a_v) and void ratio (e) values were obtained from the authors' previous work on this organic soil [5]. Although the above k value indicates a "moderately" low permeability, it does not fall in the range of much more impervious clayey soils ($k < 10^{-6}$–10^{-7} cm/s) which are known to exhibit typical undrained behavior. Classification tests on the tested organic soil also supported the above determination, since it was found to consist of a course grained mineral fraction mixed with 50–80% mostly amorphous organic matter. Even experimentally, all of the monitored impacts on this organic soil revealed partially drained behavior under impact loading. Hence, it can be concluded from the computational and experimental results that the assumption of "undrained" behavior is too idealistic for moderately low permeability soils.

EXPERIMENTAL VERIFICATION

The experimental set-up shown in Fig. 7 was used to simulate dynamic consolidation in the laboratory. A 5 lb weight having a 3 in. square base was held by an electro-magnet the height of which was adjustable along the length of a support. A switching relay was used to simultaneously release the weight from the electro-magnet and initiate a computerized data acquisition system. The impact stress history was registered by means of a stress cell attached to the base of the drop weight.

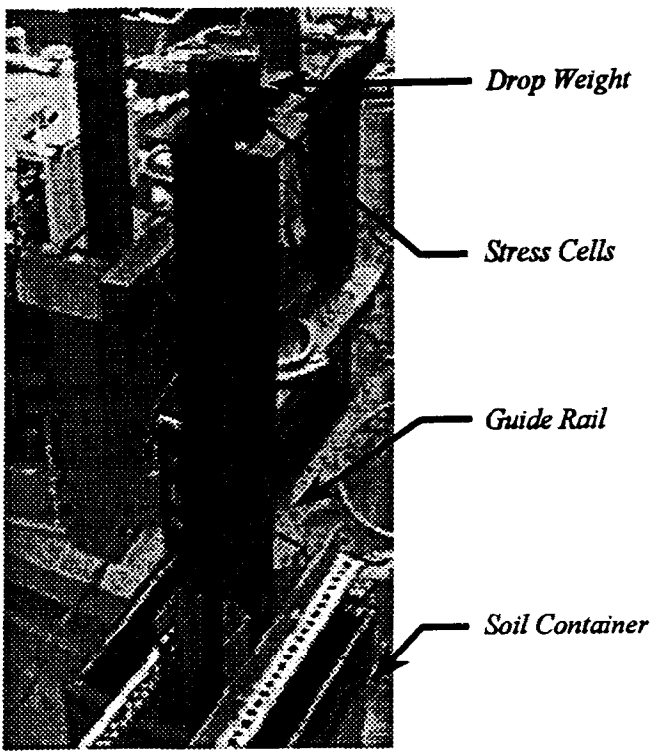

Fig. 7. Dynamic impact apparatus.

The soil sample was prepared in a one cubic foot container. The container (Fig. 7) was placed below the weight so that the weight would impact the soil directly above the pore pressure transducer. Before performing each test, the position of the container was clearly marked on the ground to achieve this condition. Then, the box was filled with an organic soil having a relatively low hydraulic conductivity up to the required height and compacted using a vibratory process which also insured higher saturation. After the pore pressure transducer connections were saturated with water, the surface stress and the pore pressure variation at the bottom of the sample were monitored by the data acquisition system.

The most commonly used values for A and B parameters in organic soils are 0.65 and 1.0, respectively [6]. The authors verified the above values using conventional triaxial testing. The stress cell reading indicating the dynamic surface stress and the pore pressure variation at the bottom plate initially placed one (1.0) inch below the impact is plotted in Fig. 8. The final clearance between the weight and the bottom plate after the impact induced penetration was 0.69 in. as indicated. The corresponding pore pressure variation

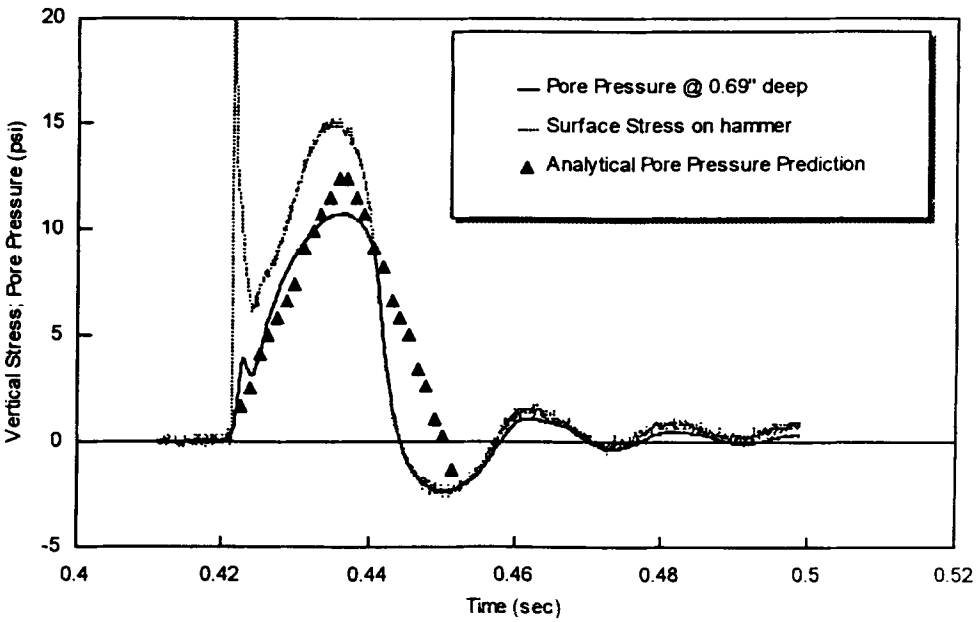

Fig. 8. Comparison of predicted and measured pore pressure variation.

predicted from the stress cell reading using the authors' theoretical formulation is also depicted in Fig. 8 for comparison. An initial depth of 1 in. was selected to obtain a significant pore pressure response in the transducer and to ensure that the centerline drainage is mostly vertical as stipulated in the analysis. The average C_v value of the organic soil was determined from separate laboratory consolidation tests to be approximately 0.002 in.^{2}/s using the Casagrande's fitting method.

The slight deviation of the predictions from the measurement can be attributed to two main reasons. A number of consolidation tests performed on the same organic material yielded a range of C_v values indicating the sensitivity of this parameter to sample preparation, natural texture and the stress level. Thus, the average C_v value used in the prediction may not have accurately represented that of the sample tested. Secondly, the measurement depth varied from an initial value of 1 in. to a final value of 0.69 in. thereby introducing some uncertainty in the actual depth to be used in eqn (1). The authors chose to use an average depth of 0.85 in. for this prediction.

CONCLUSIONS

A procedure was developed to predict the variation of pore pressure directly beneath the impact location during laboratory dynamic consolidation,

using a known dynamic contact stress. The technique was based on substituting a step-wise varying function for the dynamic stress history. When the stress steps are made sufficiently small, the numerical solution is shown to converge rapidly. An important feature of this formulation is that it can accommodate the possible differences in the soil compressibility under loading and unloading conditions. Furthermore, the vertical distribution of dynamic stress within an organic soil is experimentally shown to follow the predictions of the elastic theory thus confirming the same conclusion reached by previous researchers for other soil types.

As anticipated, a computational parametric study resulting from the developed numerical model clearly exhibited that the time variation of induced pore pressure is predominantly dependent on the coefficient of consolidation or the hydraulic conductivity of the treated soil. Within the short duration of the impact load, free draining soils with relatively high C_v values show no significant pore pressure development while impervious soils with much lower C_v values behave in an undrained fashion. Thus, the presented theoretical model is useful for moderately impervious soils such as this amorphous organic soil which induce partial drainage under dynamic loading. The authors also found other published research on field dynamic consolidation [7] in which the *in situ* soil types have been distinctly characterized as pervious, semi-pervious and impervious, depending on the monitored pore pressure behavior.

Finally, the authors demonstrated that the laboratory pore pressure measurements reasonably corroborate the analytical procedure in terms of the pore pressure magnitude and the dissipation time. Hence, it is concluded that the pore-pressure model presented in this paper is adequate to predict the dynamic pore pressure behavior of semi-pervious (moderately low permeability) soils.

REFERENCES

1. Thilakasiri, S., Mullins, G., Stinnette, P., Gunaratne, M. & Jory, B., Analytical and experimental investigation of dynamic compaction induced stresses. To be published in *Int. J. Numer. Anal. Meth. Geomech.*
2. Scott, R. A. & Pearce, R. W., Soil compaction by impact. *Geotechnique*, **25**(1), (1975) 19–30.
3. Mayne, P. W. & Jones, J. S. Jr, Impact stresses during dynamic compaction. *J. Geotech. Engng Div.*, **109**(10), (1983) 1342–1346.
4. Holtz, R. & Kovacs, R., *An Introduction to Geotechnical Engineering*. Prentice–Hall, Englewood Cliffs, NJ, 1981.
5. Gunaratne, M., Stinnette, P., Mullins, G., Kuo, C. & Echelberger, W., Compressibility relations for Florida organic soils. Submitted to *Can. Geotech. J.*
6. Andersland, O. B., Khattak, A. S. & Al-Khafaji, A. W. N., Effect of organic material on soil shear strength. *Laboratory Shear Strength of Soil*, ASTM STP 740, 1981.

7. FHWA, *Dynamic Compaction for Highway Construction, Vol. I, Design and Construction Guidelines.* FHWA/RD 86-/133, 1986.
8. Wetzel, R. A. & Vey, E., Axisymmetric stress wave propagation sand. *J. Soil Mech. Foundation Div., ASCE*, **96**(SM5), (1970) 1763–1786.
9. Brown, S. F. & Pell, P. S., Subgrade stress and deformation under dynamic load. *J. Soil Mech. Foundation Div., ASCE*, **93**(SM1), Proc. Paper 5057 (1967) 17–46.

FIELD MEASUREMENT OF TRANSFER LENGTH

Rajan Sen[1], Jose Rosas[2], Gray Mullins[1], Larry Liby[3], Satya Sukumar[4] and Ken Spillett[5]

[1] Department of Civil & Environmental Engineering, University of South Florida, Tampa, FL

[2] David Volkert & Associates, Tampa, FL, formerly graduate student, University of South Florida, Tampa, FL

[3] Department of Civil Engineering, University of Texas, Austin, TX , formerly graduate student, University of South Florida, Tampa, FL

[4] American Consulting Engineers PLC, Land O'Lakes, FL, formerly graduate student, University of South Florida, Tampa, FL

[5] Parsons Brinckerhoff Construction Services, Atlanta, GA, formerly graduate student, University of South Florida, Tampa, FL

Abstract: Five aramid fiber reinforced plastic (AFRP) and five carbon fiber reinforced plastic (CFRP) beams, cast in adjacent 122 m beds in a commercial pretensioning facility, were field instrumented to determine their transfer length. The rods were jacked to 55% and 60% of the characteristic strength of the AFRP and CFRP material respectively. A total of twelve strain gages - five at each end and two in the middle - were attached to the top surface of the beams. The prestressing force in the rods was monitored using load cells located at the live and dead ends. Following release, concrete strains were recorded by a computerized data acquisition system. Reconciliation of test results with finite element analysis indicated that the transfer lengths for the sand coated AFRP rod and the grit coated CFRP rod were very similar - equal to about 30 times the rod diameter - in broad agreement with results reported previously.

Keywords: Aramid, ARAPREE, AFRP, beam, carbon, CFRP, field, finite element analysis, FRP, grit coated, kevlar, pretensioned, sand coated, transfer length

Introduction

Transfer length is the length at the end of pretensioned members over which the prestressing force is transferred to the concrete. Because large eccentricities are the norm in prestressing, high tensile stresses develop at release. Since the transfer length determines the location where these stresses must be checked, knowledge of its magnitude is of obvious importance.

In 1992, the University of South Florida, Tampa, FL utilized commercial pretressing facilities to cast a total of 33 aramid fiber reinforced plastic (AFRP) and 33 carbon fiber reinforced plastic (CFRP) beams that were used in a long term durability study. The beams were cast side-by-side in adjacent 122 m prestressing beds normally used for fabricating 25 cm x 25 cm piles, by inserting appropriately sized wood forms. The opportunity was also taken to instrument five AFRP and five CFRP beams to determine their transfer length. This paper presents the results obtained from this study.

Experimental program

Materials

Circular AFRP and CFRP rods were used for pretensioning the test specimens. The material properties of these rods and the target jacking force, as given by their manufacturers, are listed in Table 1.

Table 1. Short term properties of AFRP and CFRP rods.

Property	AFRP	CFRP
Diameter, mm	5.7	5.8
Breaking Load, kN	33.7	43.0
Ultimate Tensile Stress, MPa	3,000[1]	2,250
Elastic Modulus, GPa	125-130[1]	121
Failure Strain, %	2.3	1.5
Jacking Force (% of ultimate)	55	60

[1] Values relate to the effective fiber cross-section

The surface of the AFRP rods, tradename ARAPREE, had sand particles impregnated to improve its bond with concrete. The surface of the CFRP rod (manufactured by NDI, the Netherlands) was similarly provided with a special grit finish.

Fabrication

The beams fabricated were 114 mm x 150 mm in cross-section. Each beam was pretensioned with two AFRP or two CFRP rods at an eccentricity of 50 mm. The length of the beam was 2.44 m to match the size of available plywood sheeting. A complete description of the fabrication is presented elsewhere [1].

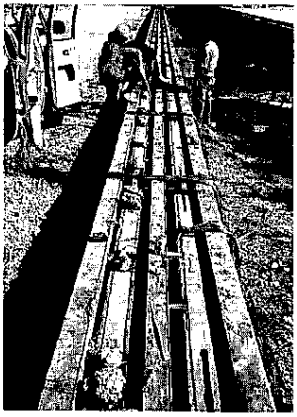

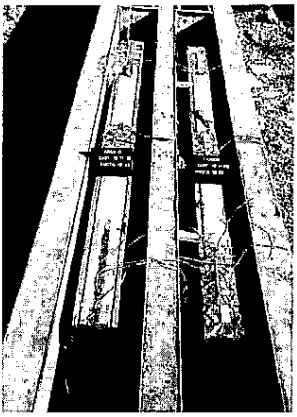

Figure 1. (Left) Overview of field instrumentation for transfer length.
(Right) Instrumentation of adjacent AFRP and CFRP beams.

Instrumentation

The logistics involved in outdoor experimentation limited the number of beams that could be instrumented. The two most important constraints were the number of strain gage channels available in the data acquisition system and the length of wiring needed. Based on these considerations, only five of the thirty three AFRP and CFRP specimens cast could be instrumented.

The *location* of the AFRP and CFRP specimens in the pretressing bed was the primary basis for selecting specimens for instrumentation. *Adjacent* AFRP and CFRP specimens were selected (see Figure 1) to allow the same wires to be used for measuring strains in either beam.

Since load cells were mounted at both the live and dead ends, the AFRP or CFRP specimens closest to these locations were instrumented. These were specimens AR-1 or CA-1 (nearest to the live end) and AR-33 or CA-33 (closest to the dead end). Their selection enabled the accuracy of the strain measurements to be assessed relative to that of the load cell readings. Moreover, it also provided an index of the instantaneous elastic shortening losses. The three remaining specimens selected were located near the middle of the bed where uniform conditions were expected. These were AR-16 or CA-16, AR-17 or CA-17 and AR-18 or CA-18. More importantly, their proximity to the data acquisition system, (housed in the van in Figure 1) greatly reduced the length of wiring needed.

To capture the strain variation, five gages were attached to the concrete surface at each end spaced 5 cm apart. This meant that strains were measured at 2.5 cm, 7.5 cm, 12.5 cm, 17.5 cm and 22.5 cm (from each end). In addition, two further gages were placed symmetrically 119.4 cm from each end.

Test procedure

Just prior to release, the prestressing force was estimated by averaging readings of the four load cells connected to each prestressing rod at both the dead and live ends. An electric grinding wheel (see Figure 2) was then used to cut the prestressing rod and release the prestressing force.

After each rod was cut, strain readings were taken using the computerized data acquisition system that was located in a van near the middle of the prestressing bed. This operation was repeated until the prestressing force had been released in all 33 beams.

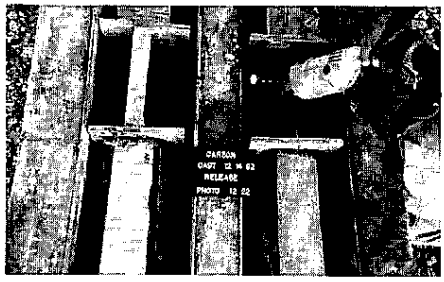

Figure 2. Release of prestressing force.

Since the instrumentation for the AFRP and CFRP beams was identical and they were cast in adjacent beds (see Figure 1), it was possible to conduct the testing expeditiously even though it had to be carried out sequentially.

After all measurements for the CFRP beams had been concluded, the wires leading from the (CFRP) beams to the data acquisition system were dis-connected at the beam site and immediately re-hooked to the corresponding locations in the AFRP beams. The procedure for determining transfer length outlined before was then repeated.

Results

The target jacking force was 55% and 60% of the reported ultimate tensile capacities of the AFRP and CFRP rods respectively (see Table 1). Based on load cell measurements just prior to release, the average prestressing force was 50.6% of ultimate in the AFRP beams [2] and 51% of ultimate in the CFRP beams [3].

Since the strain gages were attached to the top surface of the beams, the concrete strain, ϵ (tension positive), should reach a terminal value approximately given by Eq. 1

$$\epsilon = -\frac{P}{AE} + \frac{Pe}{SE} - \frac{M}{SE} \qquad (1)$$

In Eq. 1, P is the prestressing force, M the self weight bending moment, A the beam cross-section, S its section modulus and E the Young's Modulus for concrete.

By substituting appropriate values for all the variables in Eq. 1, the expected strain variations for the AFRP and CFRP beams may be calculated. At the ends, where the effects of self weight bending moments are minimal, the concrete strains were 64$\mu\epsilon$ (tension) and 81$\mu\epsilon$ (tension) in the AFRP and CFRP beams respectively. The corresponding strains at mid-span, where bending moment effects are important, were 42$\mu\epsilon$ (tension) and 59$\mu\epsilon$ (tension). The strain variation between these locations is parabolic to match the variation in strains due to self weight bending moments.

Typical results for the representative beams are shown in Figures 3-4. These show the strain variation in AFRP and CFRP beams located near the live end (AR-1 and CA-1 in Figure 3) and those located near the middle of the prestressing bed (AR-17 and CA-18 in Figure 4). Tensile strains are assumed positive in these figures.

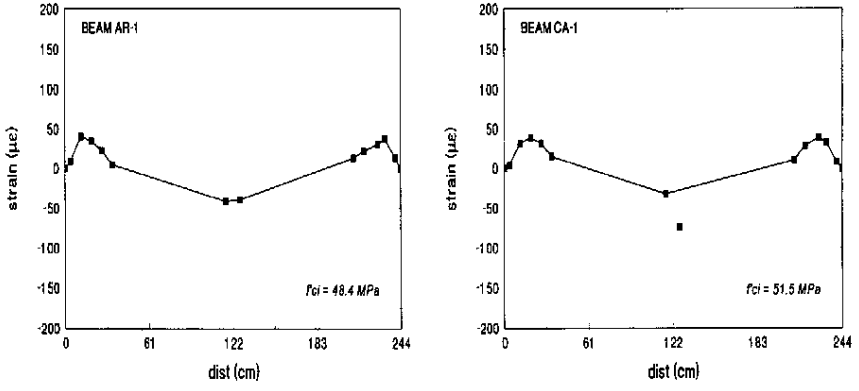

Figure 3. Strain variation in AFRP and CFRP beams located near live end.

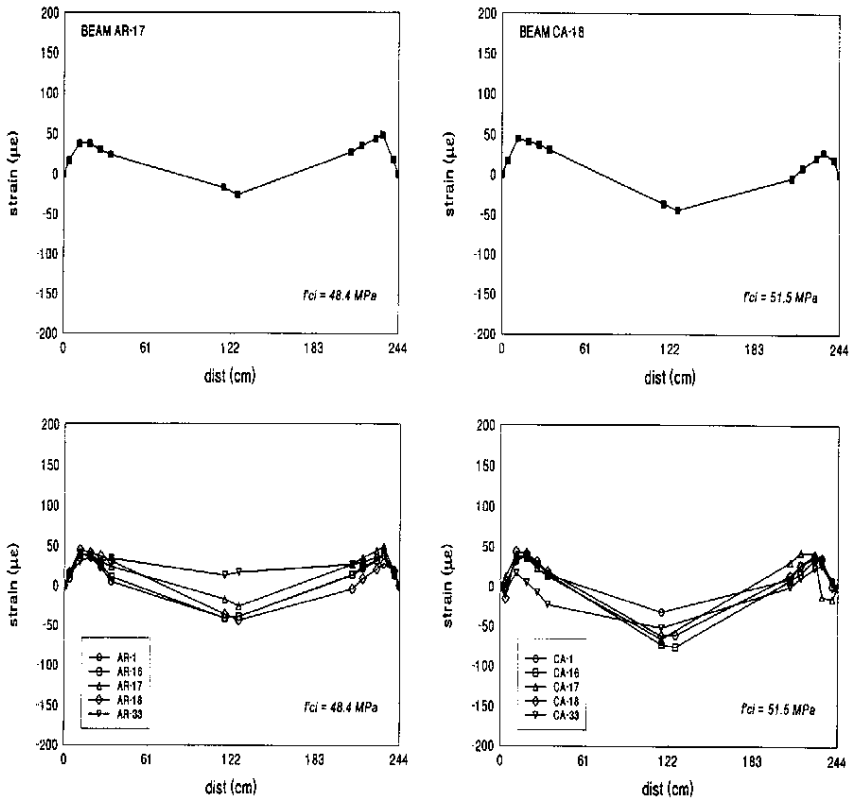

Figure 4. Strain variation in AFRP and CFRP beams.

Inspection of Figures 3-4 shows that while the distribution of strains is more or less symmetrical, the magnitudes of the maximum and minimum strains depart significantly from that predicted by Eq. 1. While minor variations could be attributed to inaccuracies in the estimate of the prestressing force or in the assumed modulus of concrete, this cannot be used to explain why mid-span strains were compressive rather than tensile.

Since this pattern was observed in all the beams tested (see Figure 4), instrumentation error was ruled out. Instead, it was hypothesized that when the prestressing force was released, the upward movement of the beams was impeded by frictional type forces that developed between the wood forms and the concrete. This was believed to be due to the presence of concrete that had been inadvertently placed in the narrow space between the sides of the steel form and the wood insert (see Figure 5).

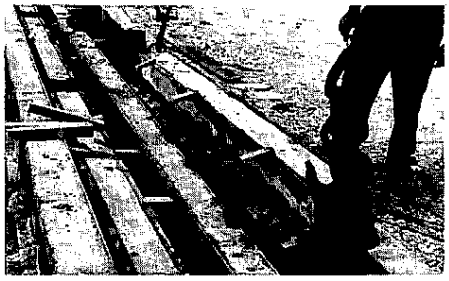

Figure 5. Concrete sticking to sides of wood form.

Normal forces required for the frictional force to develop were due in part to bending about the weak axis caused by the unsymmetric placement of the prestressing rods in the beam and the unequal magnitude of the forces in the two rods [2,3]. Consequently, finite element analyses were carried out to determine the theoretical transfer length and also to establish the kind of frictional force needed to match the test results.

Finite element analysis

Three dimensional finite element analyses were carried out using ANSYS 5.0. The beams were modeled using SOLID95 type elements. These are 3-D structural elements defined by twenty nodes - eight at each face and four intermediate nodes. Each node had three translation degrees of freedom. Two separate analyses were carried out. The first attempted to determine the theoretical transfer length; the second, to re-produce the results that were obtained from the testing.

To determine the theoretical transfer length, the idealization assumed perfect symmetry. Thus, the location of the AFRP and CFRP rods was assumed to be symmetrical with respect to *both axes* with the force in each prestressing rod assumed to be *identical*. In the second analysis, the actual locations of the prestressing rods in the cross-section and the actual forces obtained from load cell readings were used to reconcile the results obtained from the testing. For the former case, symmetry allowed the problem size to be greatly reduced. Because the results for transfer length were found to be insensitive to the exact location of the AFRP or CFRP rods, only one representative mesh was used for analyzing all the beams in the latter analysis. The finite element mesh for the cross-section for both analyses is shown in Figure 6a, b.

The discretization along the length was kept the same for the two analyses (Figure 6c). Since the prestressing force was assumed to be unchanged over the length of the specimen it was only necessary to model half the length. To obtain agreement with the theoretical transfer strain (see Eq. 1), a very fine discretization was needed. A total of 48 elements each 2.5 cm long were used to model half the length. Because of the discretization of the cross-section this meant that six layers of 48 elements were provided along the length. A total of 2,592 elements and 12,817 nodes were used in the discretization. In the cross-section, 193 nodes were present.

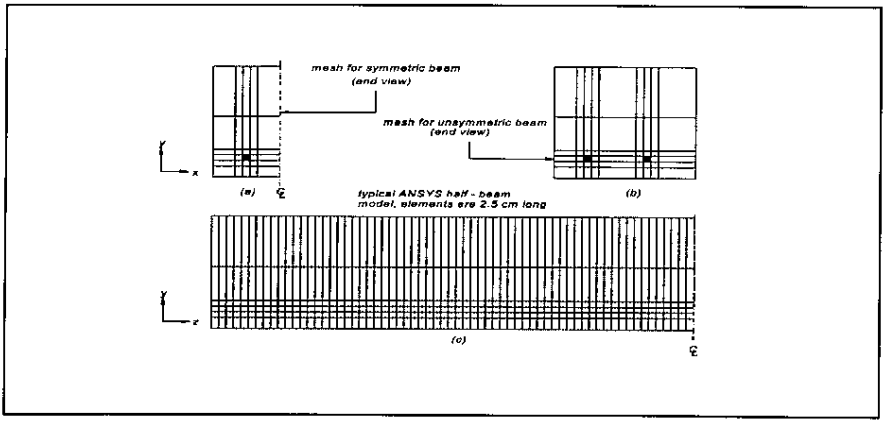

Figure 6. Finite element mesh for transfer length analysis.

Since prestress forces are transferred to the concrete by the *Hoyer* effect, the Poisson's ratio of the two materials is an important variable. For concrete, a value of 0.2 given in design specifications was used. For the AFRP and the CFRP material, values were different in the axial and radial directions. In the axial direction, the AFRP used a value of 0.36. For CFRP it was taken as 0.28. In the radial directions, the resin value of 0.35 was used for both materials.

To determine the theoretical transfer length ideal conditions were assumed. Thus, the beam was assumed to be free to move longitudinally because of elastic shortening (z) and upward (y) because of eccentricity of the prestressing force. However, the ends were assumed to be simply supported and restrained to prevent out of plane movement (x direction). The prestressing force was equally distributed among each of the corners of the element(s) representing the AFRP and CFRP rods (see darkened element(s) in Figure 6a, b).

The results from the finite element analyses for the theoretical transfer length for AFRP and CFRP are shown in Figure 7. As stated earlier, the transfer length (also referred to as the *transmission length* [7]) is the distance measured from the end face over which

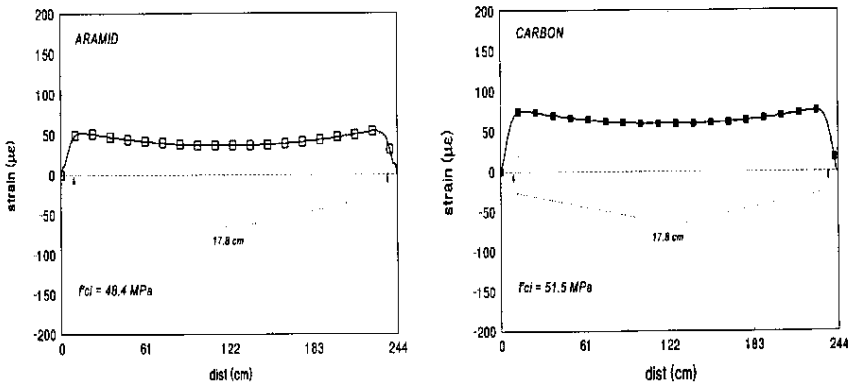

Figure 7. Transfer length prediction from finite element analysis.

the full initial stress is developed. The transfer length predicted is about 17.8 cm for both AFRP and CFRP. The corresponding concrete strains are 59με for AFRP and 81με for CFRP. These compare favorably with strains of 64με (AFRP) and 81με (CFRP) obtained by appropriate substitutions in Eq. 1. This suggests that the finite element discretization was satisfactory.

The transfer length of 17.8 cm predicted by the finite element analyses corresponds to about 30 diameters for both AFRP and CFRP. This falls broadly within the range reported by other researchers [4-6], though it is somewhat larger for the aramid rods in comparison to results reported recently by Belgian researchers [7].

Friction forces

As noted earlier, the discrepancy between the field results (Figures 3-4) and expected results (Figure 7) was attributed to friction forces that impeded the upward movement of the beam at transfer. The normal forces needed for these friction forces developed at the locations along the length where spacers had been provided (see Figure 1) and also where hardened concrete prevented movement of the beam (see Figure 5).

The assumptions made in the finite element analysis for modeling the frictional force are illustrated in Figure 8. The eccentricity of the prestressing force (e_1 and e_2), and their unequal magnitude (P_1 and P_2), gave rise to bending moments (M) about the weak axis. This moment caused only a part of the tensile surface to press against the wood forms, described as the *contact surface* in Figure 8. The compression face moved away from the form and was therefore not subject to any friction force.

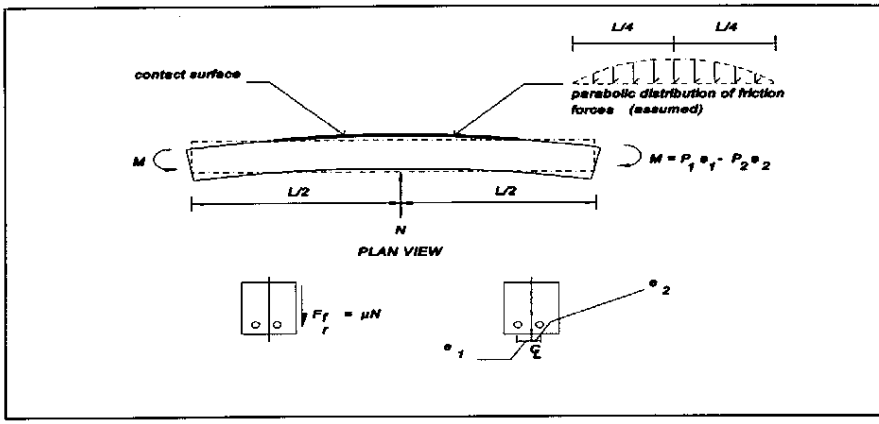

Figure 8. Idealization of frictional force in finite element analysis.

The frictional force was assumed to have a parabolic distribution that extended from quarter point to quarter point. This is consistent with the upward movement which is greater in the middle and smaller near the ends. This force was additionally assumed to act only on the tension face as shown in Figure 8.

Trial and error was used to obtain correlation between test results and predictions from ANSYS. Since the frictional forces were not identical in each beam, the magnitude of this force varied from beam to beam. These ranged from 0.9 kN to 1.9 kN for the AFRP specimens and from 2.3 to 3.2 kN for the CFRP beams. Using a very simplified model, this suggests a large friction coefficient [2,3].

Figure 9 compares the predictions from finite element analysis incorporating frictional forces and test results. The overall agreement is close and appears to confirm the validity of the hypothesis.

Conclusions

This paper presents results of field measurements carried out to determine the transfer length of beams pretensioned using AFRP and CFRP rods. The surfaces of these rods were provided with sand or grit to improve bond with concrete. A total of ten 2.44 m long beams were instrumented by strain gages that were bonded to the top surface of the beam at both ends and also at the middle.

The strain distributions obtained from the tests were consistent yet inexplicable (see

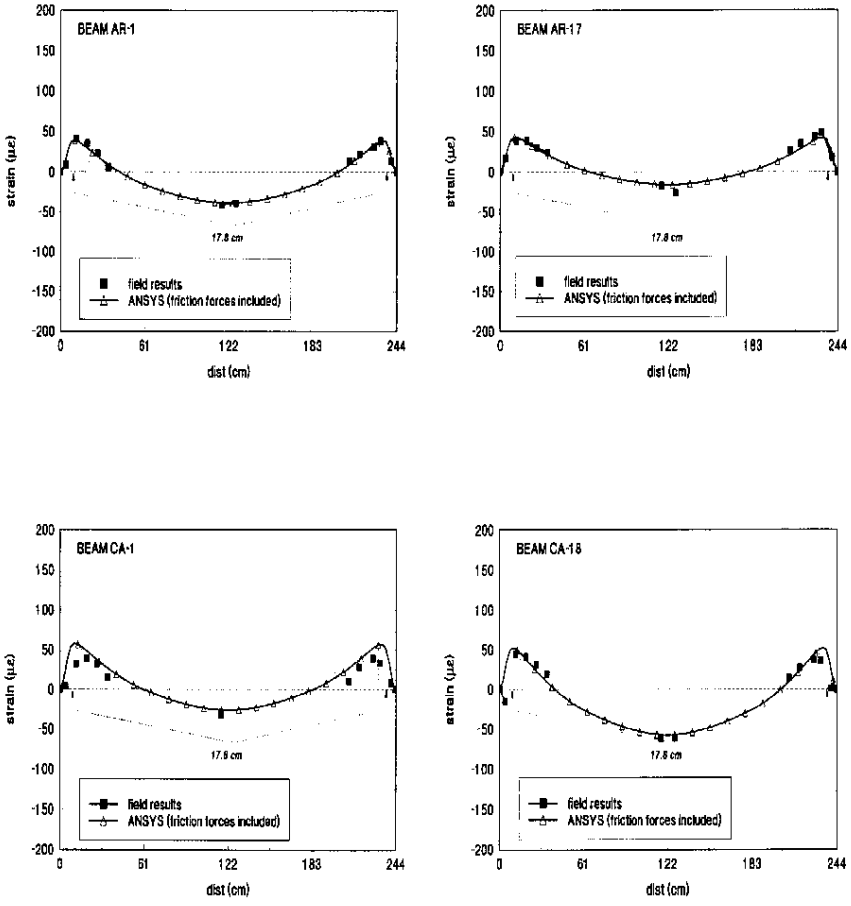

Figure 9. Comparison of test results and predictions from finite element analysis.

Figures 3-4). Finite element analysis appeared to confirm the hypothesis that frictional forces impeding movement along the length were responsible for this variation. The results of the finite element analysis incorporating frictional forces provided close correlation with the test results. The analysis also indicated that the transfer length for the beams tested was about 30 diameters, in broad agreement with results reported previously [4-6].

Acknowledgments

The investigation reported in this paper was carried out with the financial support of a research contract from the US and Florida Department of Transportation. The authors gratefully acknowledge the many contributions of Dr. Mohsen Shahawy, Director, Florida Department of Transportation in this study. However, the opinions, findings and conclusions expressed in this paper are those of the writers and not necessarily those of the Florida or US Department of Transportation.

References

1. Sen, R., Spillett, K. and Shahawy, M. (1994). "Fabrication of aramid and carbon fiber reinforced plastic pretensioned beams." *Concrete International, Vol 16, No. 6, pp. 45-47.*

2. Rosas, J. (1995). "Studies in durability of AFRP pretensioned piles." MSCE Thesis submitted to Department of Civil Engineering & Mechanics, University of South Florida, Tampa, FL, May.

3. Sukumar, S. (1995). "Studies in durability of CFRP pretensioned piles." MSCE Thesis submitted to Department of Civil Engineering & Mechanics, University of South Florida, Tampa, FL, May.

4. Machida, A. (1993). Editor, "State-of-the-art-report on continuous fiber reinforcing materials." *Japanese Society of Civil Engineers*, Tokyo, Japan, October.

5. McKay, K.S. and Erki, M.A. (1993). "Flexural behaviour of concrete beams pretensioned with aramid fiber reinforced plastic tendons", *Canadian Journal of Civil Engineering*, Volume 20, Number 4, August, pp. 688-695.

6. Arockiasamy, M. and Sandepudi, K.S. (1994). "Active deformation of bridges prestressed with aramid FRP cables." Final report submitted to Florida Department of Transportation, August.

7. Taerwe, L. and Pallemans, I. (1995). "Force transfer of AFRP bars in concrete prisms." *Non-Metallic (FRP) Reinforcement for Concrete Structures*, Proceedings of the Second International RILEM Symposium (FRPRCS-2) Edited by L. Taerwe, F & FN Spon, London, UK, pp. 154-163.

STRENGTHENING CONCRETE BLOCK WALLS USING CARBON FIBER

Dan Engebretson[1], Rajan Sen[2], Gray Mullins[3], and Alfred Hartley[4]

Abstract

The University of South Florida is conducting full scale tests to assess the feasibility of using uni-directional carbon fiber sheet material in repairing damaged concrete masonry walls. The damage under investigation was from in-plane loads resulting from soil subsidence--a common problem in the Southeastern United States. A finite element study was undertaken as part of this research. This paper presents the results obtained using the finite element program FEM/I developed under the joint U.S.-Japan Coordinated Program for Masonry Research. The predictions from the finite element analysis show reasonable agreement with the test results for both plain and strengthened walls. Interestingly, the analysis also suggests that comparable strengthening could have been achieved with narrower strips than those evaluated in the tests.

Introduction

Concrete blocks are used predominantly in the Southeastern United States where wind rather than seismic forces govern design. Historically, residential masonry structures in this region are only partially reinforced because the design loads are relatively small and ductility is less important. Vertical reinforcement has typically been provided only at the corners in conjunction with horizontal reinforcement in the bond beam. While such construction has adequately resisted out-of-plane bending due

[1] Graduate Research Assistant, Department of Civil & Environmental Engineering, University of South Florida, Tampa, FL 33620
[2] Professor, Department of Civil & Environmental Engineering, University of South Florida, Tampa, FL 33620
[3] Assistant Professor, Department of Civil & Environmental Engineering, University of South Florida, Tampa, FL 33620
[4] Structural Engineer, Ayres & Associates, Tampa, FL 33619

to hurricane force winds, it is incapable of withstanding in-plane bending resulting from settlement loads.

In 1995, the University of South Florida commenced a systematic study to investigate the feasibility of using carbon fiber sheets to repair concrete block walls damaged by foundation settlement. Four full-sized test walls representative of the practices stipulated by the prevailing Standard Building Code over the past thirty years were built. Two of the walls were damaged under simulated subsidence loads and then repaired using Forca Tow sheets from Tonen Corporation of Japan (Hartley et al. 1996). The second phase of the research involves numerical analyses which will be used to validate the available finite element programs.

The analysis of unreinforced masonry walls is complicated by the presence of horizontal and vertical mortar joints which are significant planes of weakness. Specialist programs for unreinforced masonry that use interface elements to model the joints (e.g., Manzouri et al. 1995) are still in development. In view of this, the program FEM/I, a finite element program developed under the joint U.S.-Japan Coordinated Program for Masonry Research (Ewing et al. 1990), was used for the preliminary analysis. It was developed to analyze *reinforced* masonry building components but surprisingly provided reasonable agreement for both the plain and strengthened partially reinforced test walls.

Test program

Four 5.9 m (232 in.) x 2.4 m (96 in.) test walls were constructed using 194 mm (7.63 in.) nominal blocks atop a 203 mm (8 in.) x 406 mm (16 in.) concrete footer. The steel reinforcement consisted of two 15M (#5) rebars in the footer and one vertical 15M (#5) rebar at the following spacings: 1.2 m (4 ft.), 2.4 m (8 ft.), or rebars only at the corners. All specimens included a reinforced bond beam at roof level. The walls were cantilevered over half their length, fully supported over the rest, and a concentrated load was placed on the end to simulate severe ground settlement. The plain walls were loaded to failure and repaired with a uni-directional carbon fiber tow sheet. Three horizontal oriented strips, each 51 cm (20 in.) wide, were applied to one side of each specimen. The strips were bonded from the top down and overlapped such that each wall was repaired with an approximately 152 cm (60 in.) wide strip across the full 5.9 m length of the wall. Each repaired wall was tested in the same manner as the plain walls

Figure 1. - One of Four Repaired Test Specimens

and the increase in strength was determined. Two of the four specimens (Wall #1 and Wall #2) have been tested (Hartley 1995).

Finite Element Analysis

The PC based finite element program, FEM/I, was used to analyze the test specimens. This program models the reinforcement and the underlying masonry matrix separately using appropriate stress-strain relationships. The two elements are assumed to share the same nodes and remain fully bonded. The resulting smeared hybrid element is an overlay, or layered, model where the computed strains are assigned to both materials. This approach lends itself well to carbon fiber sheets but, as discussed above, the program has a major drawback: it was designed for the analysis of fully grouted, reinforced masonry structures. It therefore employs stress-strain relationships where the effects of the masonry joints are averaged rather than modeled specifically. Grouting provides continuity across the mortar joints and reduces the degree of anisotropy in the masonry. It has been found to significantly increase the tensile and shear strengths relative to the bed joint (Drysdale et al. 1994). The program only allows one value for tensile strength which implies that the masonry is considered as isotropic. The mortar joints are a significant area of weakness for unreinforced masonry, and the tensile strength of masonry normal to the bed joint is typically half of that normal to the head joint. To compound the potential inaccuracies the program includes several models which are based on concrete research. A before-cracking constitutive model based on the Darwin-Peckhold model is used, and the modeling of strength enhancements due to lateral confinement and decreases due to compression softening are also derived from concrete research.

A program that perhaps better addresses the effects of the mortar joints on the overall strength of unreinforced or partially reinforced masonry was developed by Manzouri et al. (1995). It also uses a smeared-crack approach for the concrete blocks but uses the interface element developed by Lotfi and Shing (1994) to model the mortar joints. This interface element better represents the shear dominated behavior of the masonry joints.

Unfortunately, the program developed by Manzouri et al. was not readily available at the time of the initial analysis. The researchers decided to use the FEM/I program for the following reasons: i) to provide generalized results; ii) the test specimens were full-sized walls rather than masonry assemblages and the approach utilized by FEM/I may be suitable; and iii) the cracking pattern, which FEM/I cannot accurately predict, is not as important for this study.

Idealization of Test Specimens

Masonry Properties

The masonry is modeled as a material with bimodular orthotropy, and with tensile cracking modeled using a non-coaxial rotating smeared crack approach. The secant moduli E_1 and E_2 are determined from the compressive stress-strain relationships specified by six parameters: f'_m, ε_0 (at peak uniaxial stress), A_1, A_2, A_3, and A_4. The parameters A_1 through A_4 specify the shape and attachment points of the three functions which define the stress-strain curve. The tensile stress-strain curve is assumed to be linear up to cracking and is defined by four parameters: F_{cr}, E_m, B_1, and α. The tensile cracking strain is derived from the cracking stress (F_{cr}) and Young's Modulus (E_m) for masonry which is assumed to be equal to the initial linear portion of the compression stress-strain curve. Debonding of the reinforcement from the masonry is modeled as a material property and is reflected in the tensile stress-strain curve. Table 1 summarizes the parameters used to model the compressive stress-strain curves for unreinforced masonry, reinforced masonry (i.e., grouted cells), and concrete (i.e., footer). The properties were determined via actual materials testing when economically feasible or from the literature (Drysdale et al. 1979; Guo 1991; Hamid and Drysdale 1988) when it was reasonable to do so. These and all other parameter values were validated using an extensive parametric study and sensitivity analysis. It was found that the parameters F_{cr}, f'_m, ε_0, and E_m had the greatest impact on the predicted results while the others had little or no impact.

Parameter	Unreinforced Masonry	Reinforced Masonry	Concrete Footer
f'_m or f'_c (MPa) (psi)	11.43 (1657)	9.3 (1341)	30.6 (4442)
ε_0	0.0018	0.0016	0.0019
A_1	2.0	2.0	2.0
A_2	1.2	1.4	2.3
A_3	0.1	0.1	0.1
A_4	0.6	0.6	0.6
F_{cr} (kPa) (psi)	517.1 (75.0)	827.4 (120.0)	2937.3 (426.0)
E_m or E_c (GPa) (psi x 10^{-6})	11.99 (1.74)	10.83 (1.57)	30.54 (4.43)
B_1	n/a	0.50	n/a
α	n/a	0.18	n/a
ν	0.175	0.175	0.190

Table 1. - Summary of Material Parameters
(Hollow masonry is based on net area; reinf. masonry on gross area)

Steel Properties

The program uses a bilinear model for the reinforcement stress-strain curve and is determined by three parameters: F_y, E_s, and ζ. The plastic modulus is derived by multiplying the elastic modulus (E_s) by the parameter, ζ, which estimates the effects of strain hardening. Its value had no impact on the results since the steel did not reach yielding. The reinforcement may be specified in both horizontal or vertical orientations. It is also considered smeared over the element but is uni-directional per the orientation specified.

CFRP Properties

The carbon fiber sheet used was Tonen's FORCA Tow Sheet (FTS-C1-20). It is uni-directional providing high tensile strength in the longitudinal fiber direction, and is almost perfectly linear elastic up to the ultimate stress. For a 152 cm (60 in.) wide sheet, the Forca Tow sheet displays an ultimate stress of 3.48 GPa (504,825 psi) and a tensile modulus of 231.0 GPa (33.5×10^6 psi) (Tonen 1995).

Results

Preliminary analyses have been completed for Wall #1 and Wall #2. FEM/I provided promising results when compared with actual test results. Figures 2 and 3 show the comparisons of horizontal strains measured from Wall #1 without the Forca Tow sheet (plain) and after being repaired with a 152 cm (60 in.) wide strip across the top (repaired). The strains were measured along two vertically aligned gage positions: one at 193 cm (76 in.) from the cantilevered end and the other at 335 cm (132 in.) from the end. With the exception of the uppermost bond beam gages in Figure 3, the predicted results yielded reasonable values and similar strain variation patterns. The large disparity in the top gages was due to the program's assumption of compatibility of strains between nodes at the joint interface (in absence of a discretized joint element) and its inability to model shear behavior along the joint. The bond beam of Wall #1 was formed by using a 152 mm (6 in.) wide felt cap applied along the length of the wall before the last course of bond beam units were mortared in place. The felt cap prevented the grout from falling through the cells below and was typical of older style construction. Unfortunately, it reduced the effective width of the mortar bed from 32 mm (1.25 in.) to 21 mm (0.813 in.) for each face shell. A separation was observed along this weaker interface for almost the full length of the wall. In addition, it was suspected that a separation occurred along the interfaces between the face shells and grout core of the bond beam. This resulted in the grout core being able to strain relatively independently to the rest of the wall. The uppermost strain gage was attached to the bond beam's grout core while the Forca Tow sheet was bonded to one of the face shells of the bond beam. The lack of connectivity would result in the actual recorded strains being significantly less that the predicted values.

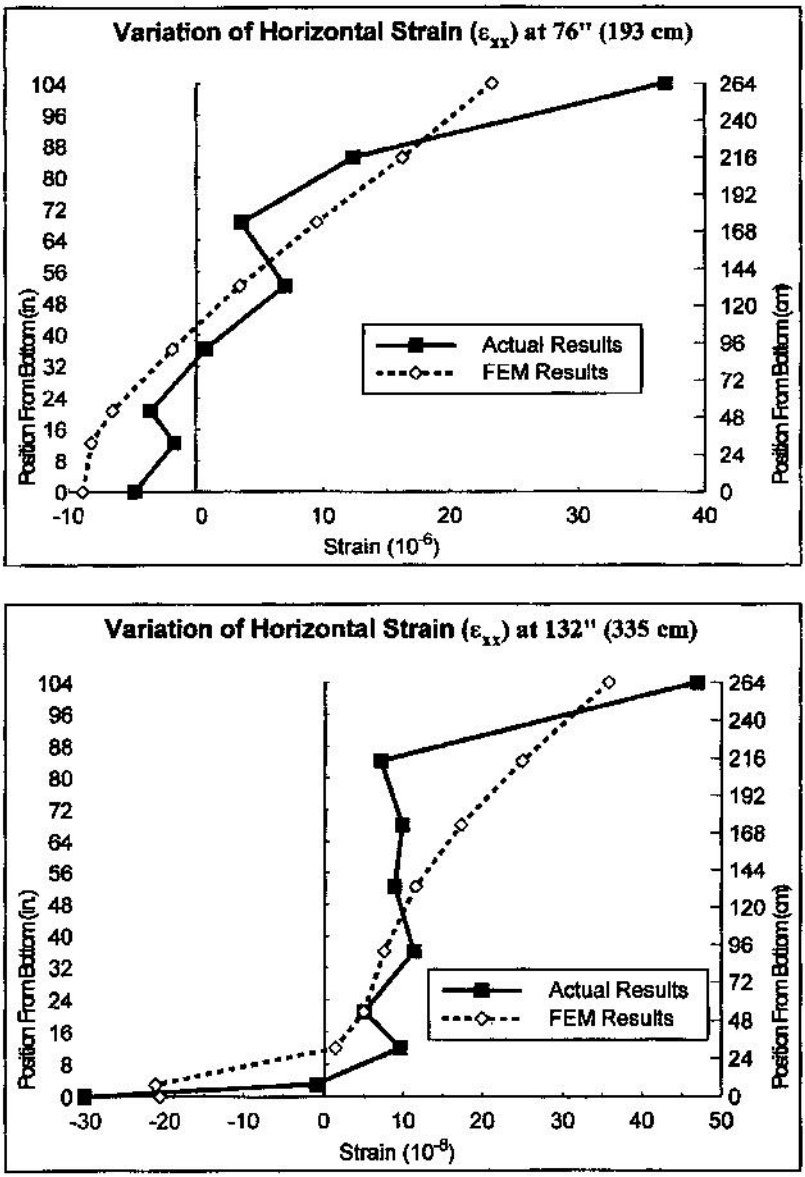

Figure 2. - Variation of Horizontal Strain (ε_{xx}) for Wall #1 (Plain)

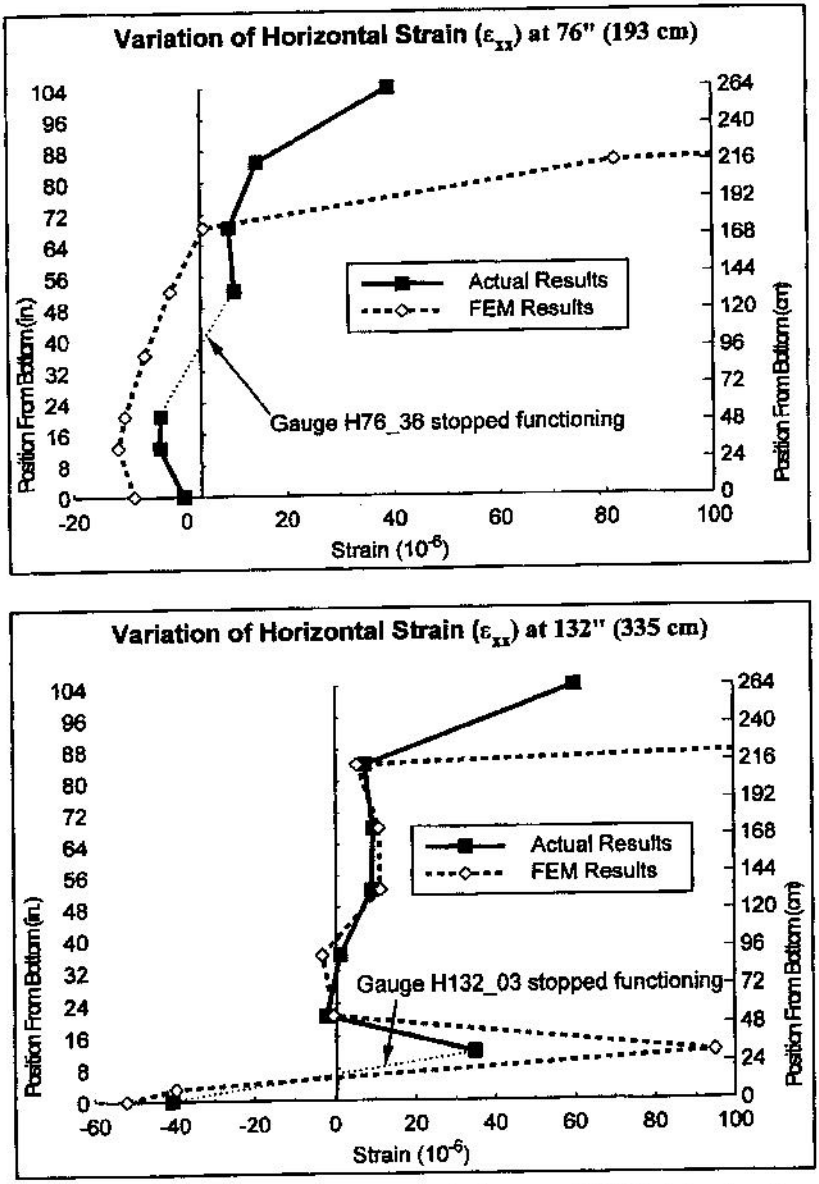

Figure 3. - Variation of Horz. Strain (ε_{xx}) for Wall #1 (Repaired)

FEM/I did not accurately predict the crack pattern as was expected. Such disparities are not uncommon because smeared crack models are unable to accurately model the type of shear dominated behavior apparent during testing. Although the predicted deflections at the peak recorded load were reasonable, especially for the plain Wall #1, the program yielded a predicted load-deflection curve which took a significantly different path from the actual curve.

Because the agreement between predicted and actual results were satisfactory, FEM/I was used to examine the correlation of tow sheet width and strength gains. Additional analyses were conducted for repairs of Wall #1 using 31 cm (12 in.), 51 cm (20 in.), and 102 cm (40 in.) wide tow sheet strips. The respective predicted deflections were 549.7 μm (0.02164 in.), 507.0 μm (0.01996 in.), and 530.6 μm (0.02089 in.) versus an actual deflection of 697.5 μm (0.02167 in.) for 152 cm (60 in.) at an arbitrary load of 32.2 kN (7232 lbs.). This arbitrary load was the peak load for Wall #1 (plain) and was chosen in order to provide a basis of comparison between the plain and strengthened configurations. In addition to the deflections, the analyses yielded similar plots of stress trajectories for the different tow sheet strip widths. The plots indicated that the carbon fiber applied along the bond beam consistently provided the greatest tensile strength while the portions of the tow sheet applied below the bond beam had little impact. The implications are that narrower, less costly strips could have been used with no commensurate strength reduction.

Conclusions

This paper presents comparisons of results obtained from the finite element program FEM/I with data from full-scale tests on walls which were damaged by foundation settlement. The walls used different reinforcement configurations and were subsequently repaired with carbon fiber Forca Tow sheets to assess strengthening capabilities.

Obvious problems arise when analyzing unreinforced or partially reinforced masonry structures with programs that are based on fully grouted masonry. Although FEM/I is intended for analyzing fully grouted walls, the correlation between the test results and the predictions of strain and deflections was surprisingly good--despite an inability to accurately predict the cracking pattern.

The analysis indicates that similar strength enhancements could be achieved with overall narrower tow sheet strips rather than the 152 cm (60 in.) width originally evaluated in this study. The ability to strengthen damaged masonry walls, and to do so with narrower strips, would be a significant cost savings to the home owner.

This study is on-going and the next phase will include analyses with finite element programs that better model the shear dominated behavior of the mortar joints.

Acknowledgments

The authors gratefully acknowledge the contributions of Mr. Bob Ewing, Mr. Howard Kliger, and the Tonen Corporation of Japan to this study.

References

Drysdale, R., Hamid, A., and Heidebrecht, A. (1979). "Tensile strength of concrete masonry." *Journal of the Structural Division*, ASCE, 105(ST7), 1261-1275.

Drysdale, R., Hamid, A., and Baker, L. (1994). *Masonry structures: behavior and design*. Prentice-Hall, Englewood Cliffs, N.J.

Ewing, R., El-Mustapha, A., Kariotis, J. (1990). "A finite element computer program for the nonlinear static analysis of reinforced masonry building components." *Report No. 2.2-1*, Ewing and Associates, Rancho Palos Verdes, CA.

Guo, P. (1991). "Investigation and modeling of the mechanical properties of masonry." Ph.D. thesis, McMaster University, Hamilton, Ontario.

Hamid, A. and Drysdale, R. (1988). "Flexural tensile strength of concrete block masonry." *Journal of Structural Engineering*, ASCE, 114(1), 50-66.

Hartley, A. (1995). "Strengthening of concrete masonry walls using CFRP material," Masters Thesis, University of South Florida, Tampa, FL.

Hartley, A., Mullins, G., and Sen, R. (1996). "Repair of concrete masonry block walls using carbon fiber," Second International Conference on Advanced Composite Materials in Bridges and Structures, Montreal, P.Q., Canada.

Lotfi, H., and Shing, P.B. (1994). "Interface model applied to fracture of masonry structures," *Journal of Structural Engineering*, ASCE, 120 (1), 63-80.

Manzouri, T., Shing, P.B., Amadei, B., Schuller, M., and Atkinson, R. (1995). "Repair and retrofit of unreinforced masonry walls: experimental evaluation and finite element analysis," University of Colorado at Boulder, CO.

"FORCA Tow sheet technical notes." (1995). Tonen Corp., Japan.

ADVANCED COMPOSITE MATERIALS IN BRIDGES AND STRUCTURES
M.M. El-Badry, Editor; Canadian Society for Civil Engineering, Montreal, Quebec, 1996

MATÉRIAUX COMPOSITES D'AVANT-GARDE POUR PONTS ET CHARPENTES
M.M. El-Badry, éditeur; Société canadienne de génie civil, Montréal, Québec, 1996

REPAIR OF CONCRETE MASONRY RLOCK WALLS USING CARBON FIBER

Alfred Hartley, Gray Mullins and **Rajan Sen**
University of South Florida
Tampa, Florida, USA

ABSTRACT

The University of South Florida has embarked on an outdoor test program to investigate the feasibility of using uni-directional carbon fiber sheets for repairing settlement damaged block walls used in home construction. For the initial phase of the study, four 200 mm (8 in.) thick concrete block walls each 2.44 m (8 ft) high and 6.1 m (20 ft) long have been designed and built. Vertical steel reinforcement has been varied to meet past and present requirements of the Standard Building Code. In the testing, the walls are subjected to simulated foundation settlement to replicate observed cracking and then repaired by bonding carbon fiber tow sheets *on only one wall face*. The repaired walls are then loaded identically to assess the efficacy of the repair. Preliminary results are very encouraging and suggest that this technique may be economically viable for repairing damaged homes.

INTRODUCTION

Sixty-five percent of all residential structures in the state of Florida are constructed from concrete masonry units, making Florida the biggest user of concrete blocks in the United States. Because loads on single family dwellings are small, such structures were not required to be engineered; however, damage by successive hurricanes has led to new requirements currently enshrined in "*deemed to comply*" rules (SBC 1993). For typical 200 mm (8 in.) walls, these rules require (a) one 15M (#5) vertical rebar at the corners and every 9.14 m (30 ft), and (b) 200 mm (8 in.) deep bond beam reinforced (horizontally) by one 15M (#5) bar. Construction must also ensure continuity of the horizontal and vertical steel so that the entire structure acts in concert to resist hurricane force winds.

Apart from high winds and their attendant uplift problems, external masonry walls in homes may also be subjected to foundation movement. This is a common problem that affects large numbers of homeowners nationwide. Since foundation subsidence subjects walls to *in-plane* loading, vertical reinforcing steel provided to resist out-of-plane bending is largely ineffective; the resulting damage, calls for expensive repairs. Unfortunately, relatively little is known about the response of such lightly reinforced walls under settlement loading. As such, repair methods, e.g. use of micro-piles combined with grouting of cells, may be both inappropriate and costly. Instead, more effective repairs may be achieved through the use of advanced composites.

OBJECTIVES

The overall objectives of the study are twofold: (1) to determine the response of typical concrete block walls built for residential construction in accordance to the Standard Building Code (*the prevailing code in the Southeastern United States and parts of Texas*) under settlement loading (2) to repair the damaged walls using advanced composites and to assess the extent of the strengthening. Although the focus of the study is largely experimental, numerical analyses will also be conducted. These will be directed towards calibrating finite element models developed for masonry construction in seismic zones, e.g. Ewing 1993, and also to identify simplified idealizations that can be used by consulting engineers to obtain reasonably accurate predictions.

TEST PROGRAM

A careful survey was made of subsidence damage to masonry block homes in the Tampa Bay area prior to the design of the test specimens. Based on this inspection, and interviews with consulting engineers, the representative wall length was determined to be 6.1 m (20 ft). The wall height was taken as 2.4 m (8 ft) as this is typical for residential construction.

For the initial phase, four 200 mm (8 in) concrete block walls each 2.4 m (8 ft) x 6.1 m (20 ft) were designed and built. The spacing of vertical reinforcement was varied from 6.1 m (20 ft) to 1.22 m (4 ft) to reflect changing provisions in code specifications. A typical wall elevation is shown in Fig. 1.

Settlement Simulation

Each wall is supported by 200 mm (8 in.) x 400 mm (16 in.) concrete footings reinforced by two 15M (#5) rebars - typical of residential construction as shown in Fig. 1. It may be seen that over half its length, the footing is supported on compacted fill 0.91 m (3 ft) above grade; in the remaining half it is supported on a W10 x 49 steel beam. The steel beam is simply supported above grade between a keystone screw jack at the free end of the wall and on an on-

grade beam at the center of the wall. During construction, a plastic sheet was used to completely separate the footing from the steel beam to prevent any composite action. By unscrewing the jack with a wrench the wall can be made to settle.

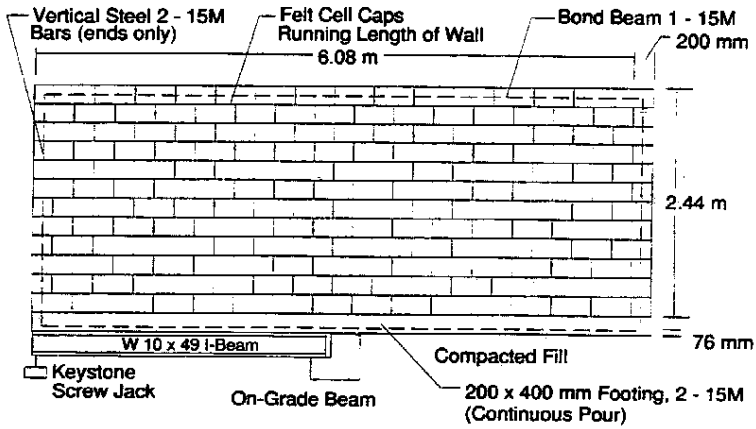

Fig. 1. Concrete block details, Wall #1

The settlement loads are equivalent to the cantilevered weight of the wall. Additional loads, simulating the weight of other materials that bear on the wall and actual roof loads, can also be applied at the top of the wall by a 27 tonne ENERPAC hydraulic jack. This is jacked against a steel beam that is chained to ground anchors bored into the ground. The reaction frame geometry and the location of the ground anchors permit loads of up to 9 tonnes to be applied to any location along each wall (see Fig. 2a).

Instrumentation

The test specimens were instrumented using load cells, LVDT's, and strain gages. Two load cells placed at the free end measure the self weight during subsidence and the magnitude of the simulated roof load. LVDT's measure deflections in both the vertical and horizontal directions; strain gages are used to record strains in both the wall and the footing.

Strain gages were provided along three vertical lines across the subsiding portion of the wall: at the support, at mid-span in the cantilevered section, and at the free end. A battery powered MEGADAC 3108 DC data acquisition system is used for recording data.

Test Procedure

The wall is initially subjected to several load-unload cycles in the elastic range to verify its stiffness. Following completion of these tests, it is loaded past its cracking load. The wall is then repaired using advanced composites and tested as before. All data is automatically recorded during testing using the data acquisition system.

Repair of Wall

In the initial phase, walls damaged due to subsidence will be repaired using uni-directional carbon fiber Force Tow Sheets (FTS-C1-120) developed by Tonen Corporation of Japan. This is a lightweight, high strength material that is epoxy bonded to the wall surface. The Forca Tow Sheet was designed and developed for structural rehabilitation and has been primarily used for repairing concrete structures (Kobayashi et al. 1995).

The application of the tow sheets generally involves six steps (1) surface preparation, (2) application of a primer coating, (3) application of epoxy adhesive after the primer surface has dried, (4) placement of the tow sheet (5) removal of excess resin and air bubbles with a putty knife, and (6) application of a second epoxy coating. Because of the nature of the intended application, surface preparation was kept to a minimum and essentially consisted of only removing any mortar that was protruding from the wall surface. No attempt was made to grind the mortar joints.

To expedite placement, the Forca Tow Sheets were cut to lengths of approximately 6.1 m (20 ft) to match the wall length. More importantly, the sheets were then *re-rolled* inside out. This greatly simplified placement since the tow sheet could then be unrolled directly onto the wall as epoxy was being applied. Since the carbon fiber was only intended to increase bending resistance, it was oriented parallel to the length of the wall. Three sheets, each 500 mm (20 in.) wide, were attached *only to one face* as shown in Fig. 2b.

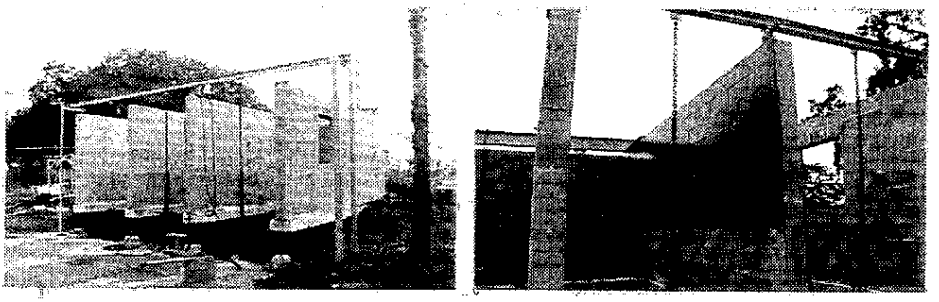

(a) (b)

Fig. 2. (a) View of walls and reaction frame (b) Repaired wall.

RESULTS

The study is on-going and only preliminary results from two of the walls are available, Hartley 1995. However, many additional tests are planned. Since the aim of the investigation is also to assess long term performance, the repaired walls were not loaded to failure. Because the specimens are outdoors, all testing is restricted to pre-dawn hours when constant conditions prevail.

In the tests, the original wall referred to here as the *'plain wall'* was loaded and unloaded several times to verify its elastic response prior to the application of the final cracking load. Under this load, the wall developed step cracks along horizontal and vertical mortar joints as was observed in actual buildings. It was then repaired using carbon fiber Forca Tow sheets (see Fig. 2b).

Tests results obtained from Wall #1 (for wall details see Fig. 1) appear in Figs. 3-6. Similar trends were observed from Wall #2, Hartley 1995. Fig. 3 compares the vertical load versus vertical displacement for the plain and repaired walls. The loads shown exclude the self-weight of the wall. Under the applied vertical load, the plain wall cracked at a load of 30.2 kN (6.78 kips). The repaired wall was then tested in the identical manner. The test on this wall was stopped when the load reached 55.6 kN (12.5 kips), an increase of over 80% of the original load. No evidence of cracking could be detected in this wall.

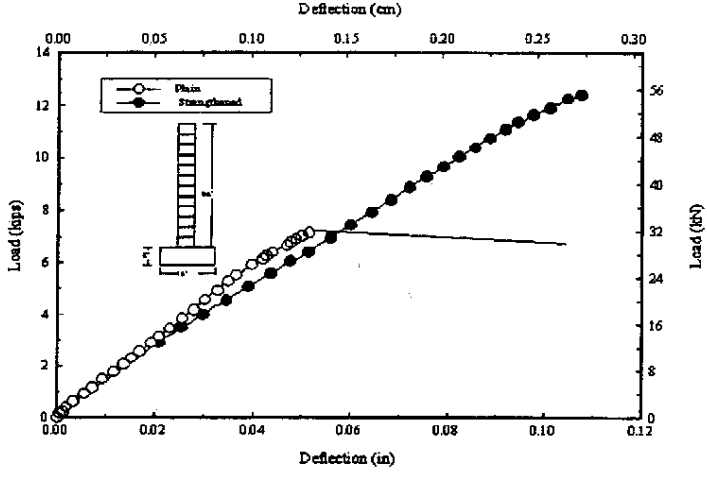

Fig. 3. Wall #1: Load vs. Deflection

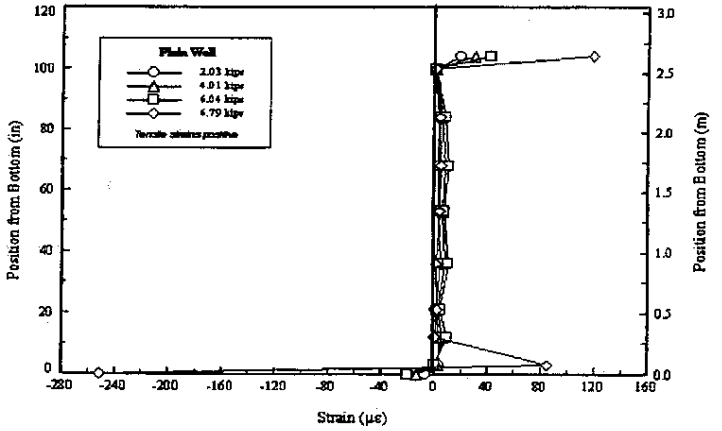

Fig. 4. Wall #1 (Plain): Variation of strain down wall

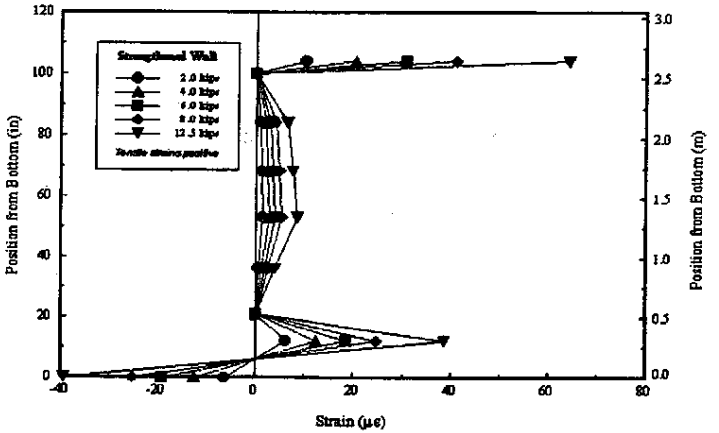

Fig. 5. Wall #1 (strengthened): Variation of strain down wall

Fig. 4 shows the strain variation with load in the plain wall. No strains were recorded on gages that were positioned at mid-height of the bond beam when the load was varied. This suggests that the grout is not bonded to the sides of the masonry unit forming the bond beam. Inspection of Fig. 4 also shows that the overall strains are relatively small until cracking. The strain variation with depth for the strengthened wall is shown in Fig. 5. The larger strains recorded show the effect of the carbon fiber. A comparative plot of strains in the plain and strengthened walls under selected loads is shown in Fig. 6.

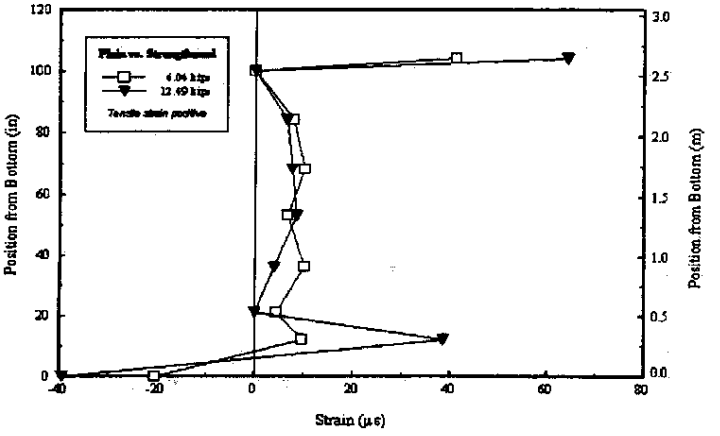

Fig. 6. Wall #1: Comparison of strain for both plain and strengthened

CONCLUSIONS

Homes damaged by foundation settlement are traditionally repaired by preventing further movement through the use of micro-piles/grade beams followed by repair of the damaged walls. While these solutions are undoubtably effective, they are costly, time consuming and very disruptive. The alternative examined in this paper is the use of carbon fiber sheets to *only* strengthen damaged walls so as to make them capable of sustaining additional loads or movement without further deterioration. While this technique may not be suitable for all situations, e.g. sinkholes, the results from preliminary tests reported clearly show that the strength of damaged walls can be significantly increased. Moreover, since the repairs need only be carried out on the outside of the home, disruptions are minimized. This study is still in the preliminary stage; however, the results obtained are encouraging and suggest that carbon fiber sheets may offer a viable and economical alternative for repairing concrete block walls damaged by ground subsidence.

ACKNOWLEDGMENTS

The authors gratefully acknowledge the support and contribution of the Tampa Bay Chapter of the Masonry Contractors Association of Florida. We also wish to thank Howard Kliger for much useful technical advice and for providing the carbon fiber Forca Tow Sheets and resin used in the testing.

REFERENCES

Ewing, R. (1993). "Nonlinear Static Finite Element Analysis of Reinforced Masonry Walls in Tall Buildings,". *The Structural Design of Tall Buildings*, Vol. 2, pp. 133-152.

Hartley, A. (1995). "Strengthening of Concrete Masonry Walls using CFRP Material,". Thesis submitted in partial fulfillment of MSCE degree, Department of Civil and Environmental Engineering, University of South Florida, Tampa, FL, December, pp. 215.

Kobayashi, A., Ohori, N. and Kuroda, H. (1995). "Repair and Reinforcement of Concrete Structure with Carbon Fiber Tow Sheet," *Non-metallic (FRP) Reinforcement for Concrete Structures (Editor L. Taerwe)*, E & FN Spon, London, England, pp. 688-695.

Southern Building Code Congress International, Inc. (1993). "*Standard for Hurricane Resistant Residential Construction SSTD 10-93*," Birmingham, AL.

STRENGTHENING STEEL COMPOSITE BEAMS WITH CFRP LAMINATES

Rajan Sen[1], Larry Liby[2], Gray Mullins[3] and Ken Spillett[4]

Abstract

The University of South Florida completed an experimental and numerical study in which wide flange steel beams acting compositely with concrete slabs, were strengthened using carbon fiber reinforced plastic (CFRP) laminates. This paper presents an overview of the research project and also compares the material cost of providing equivalent strengthening using conventional means, i.e. by welding steel plates.

Introduction

Steel stringer bridges are very common in the United States and make up almost a third of all bridges with spans exceeding 6.1 m. Since many were constructed just prior to World War II, they are nearing the end of the average 65-70 year useful service life. Strengthening steel members in these bridges using bonded CFRP laminates offers the prospect of speedy and economical repair with minimal disruption to traffic.

[1]Professor, Dept. of Civil & Environmental Engineering, University of South Florida, Tampa, FL 33620
[2]Graduate Student, Texas A&M University, College Station, TX 77843
[3]Assistant Professor, Dept. of Civil & Environmental Engineering, University of South Florida, Tampa, FL 33620
[4]Operations Manager & Professional Associate, Parsons Brinckerhoff Construction Services, Tampa, FL 33607

In 1993, the University of South Florida completed an experimental and numerical study to examine the feasibility of using CFRP laminates for strengthening steel composite beams typically used in highway construction. This paper presents a brief overview of the study. Additional information may be found elsewhere Sen et al 1994a, 1995.

Test Specimens

The specimens tested were obtained from two composite bridge models from a separate study, Sen et al 1994b. The concrete deck slab was reinforced longitudinally and transversely and stud shear connectors were welded to the top flange of the steel beams to ensure composite action. The yield stresses of the steel in the two bridge models were 310 MPa and 370 MPa.

The test specimens were obtained by cutting the 6.1 m long by 2.13 m wide concrete deck slab longitudinally. Since each bridge had three equi-spaced steel beams, each bridge provided three specimens so that a total of six specimens were tested. Each test section comprised a W8 x 24 steel section attached to a 0.71 m wide, 0.114 m thick reinforced concrete slab.

CFRP laminates were used to strengthen the composite sections. The 0.165 m width of the 3.65 m long CFRP laminates was the same as the steel flange. The average tensile strength parallel to the unidirectional laminates' fiber orientation was reported as 1839 MPa and the tensile modulus, 114 GPa. Fiber Resin Corporation's two part epoxy adhesive, FR-1272, was used to bond the CFRP laminate to the steel surface, augmented by bolts for some tests.

Test Results

A total of 13 tests were carried out in three series of tests. In the initial series, plain composite beams were loaded past yield of the tension flange to simulate severe distress under service loading. In the next series, the damaged specimens were strengthened by bonding the CFRP laminate to the tension flange and loaded to failure. In the final series, a plain composite beam was loaded to failure to assess its actual strength. Comparison of the relative performance of the unreinforced and strengthened beams provided a measure of the efficacy of the CFRP laminate.

Typical results obtained from the testing are shown in Figs 1 and 2. Fig. 1 shows the comparison of the load displacement response of a beam strengthened using 2 mm thick CFRP laminate with that of a plain composite beam.

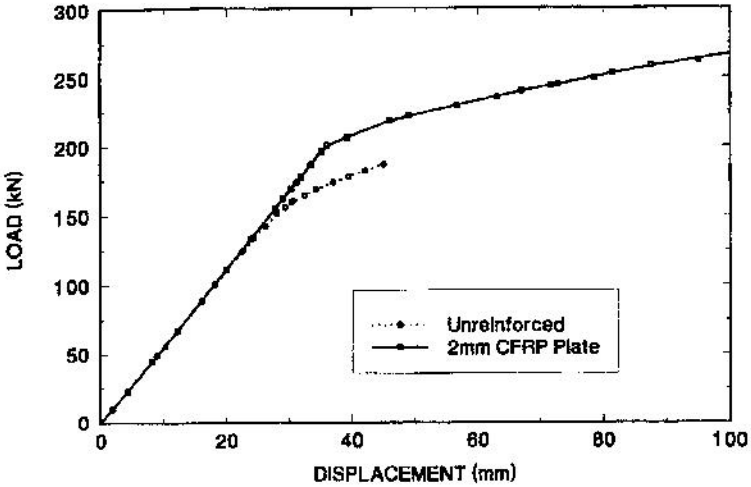

Fig. 1. Load Displacement 370 MPa - 2mm (epoxy only).

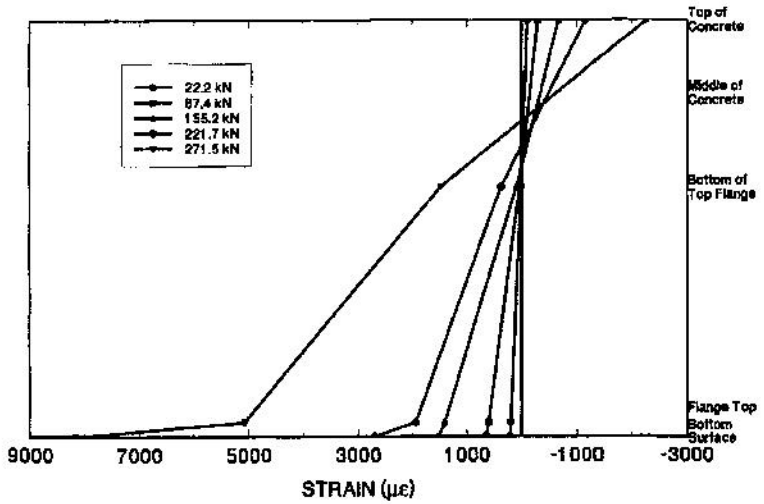

Fig. 2. Strain Variation at Mid-Span 370 MPa - 2-mm (epoxy only).

Inspection of Fig 1. shows that the use of the CFRP laminate leads to an increase in both the elastic and ultimate capacity though there is practically no increase in stiffness. However, in other tests using 5 mm thick CFRP laminates, substantial stiffness increases were realized.

The strain variation with depth for the same strengthened beam is shown in Fig. 2. It may be seen that until the steel yields, there is relatively little load transfer to the CFRP laminate.

Table 1 summarizes the test results. The percentage increases in this table are relative to the load at which the tension flange yielded and range from 19% to 109% depending on the yield stress of the steel and the thickness of the CFRP laminates. The larger increases correspond to the thicker CFRP laminate and the weaker steel.

Table 1. Summary of Strengthening Results.

Steel	Test	Yield	2-mm CFRP		5-mm CFRP	
(MPa)		Load (kN)	Load (kN)	% Gain	Load (kN)	% Gain
310	1	141.9	236.6	66.7	-	-
	2	142.3	-	-	298.0	109.4
	3	141.9	-	-	169.0	19.1
370	1	186.4	271.3	45.5	-	-
	2	186.8	271.3	44.8	-	-
	3	187.3	-	-	329.1	76.2

The opposite combination, i.e. thinner CFRP laminate and stronger steel, gave smaller increases as can be anticipated. Since these increases are relative to the yield load, they are somewhat misleading. Absolute increases, i.e. relative to the failure strength of the unstrengthened were smaller for the one beam that was tested in this manner. The increase for this beam was substantial and compared favorably with average strength increases of 22% reported from tests on reinforced concrete members, Meier et. al 1992.

Prototype Bridge Section

The bridge sections tested were not however, representative of prototype sections since the deck slab was deliberately kept larger to ensure that concrete failure would not occur prior to yielding of the steel wide flange shapes. A quarter scale model bridge called for a 50 mm concrete slab reinforced with No. 6 gage wire placed 150 mm on center instead of the 114 mm slab reinforced by 20M (#6) bars that was tested.

To determine if the more typical bridge section would also benefit from strengthening using CFRP laminates, non-linear finite element analyses were carried out. The predicted response of the bridge sections with 310 MPa steel wide flange beams showed strength gains of 40% and 75% when strengthened by 2-mm and 5-mm CFRP laminates, respectively. The corresponding gains for the prototype model bridge section with 370 MPa steel were 30% and 60%. These strength gains are in line with those obtained from the ultimate load capacity tests of the model bridge sections.

Equivalent Steel Plate

In order to compare costs, bridge sections based on a prototype bridge were analyzed to determine the thickness of steel cover plates that would provide strengthening that was equivalent to that provided by 2-mm and 5-mm CFRP laminates.

The non-linear finite element analyses revealed that to provide the same strengthening, the 2-mm CFRP laminate would need to be replaced by 6.3 mm thick steel plates and the 5-mm CFRP laminate by 11.1 mm thick steel plates. At $0.20/N, the 6.3 mm steel plate would cost $58.70 and the 11.1 mm plate, $103.20. This compares with the CFRP laminate cost of $560 for the 2-mm CFRP laminate and $780 for the 5-mm CFRP laminate. Thus, the CFRP laminate is roughly 8-10 times more expensive than the steel plate for this configuration. Complete results may be found in Liby 1993.

Conclusions

This paper provides a brief summary of a study conducted to investigate the feasibility of strengthening steel composite bridge members using CFRP laminates. Although the CFRP laminates are less stiff than the steel flange to which it was attached and the shear strength of the epoxy adhesive orders of

magnitude smaller than steel, substantial strength gains were realized. Moreover, since the majority of the load transfer to the CFRP laminate occurred only after the steel flange had yielded, failures were preceded by large deflections.

Cost comparisons are presented which compare the actual cost of the CFRP laminates used in the study with that of steel plates required to provide the same strengthening. This shows that the CFRP material costs were between 8-10 times that of steel. Since the CFRP laminates are much lighter than the equivalent steel plates, the repair can be carried out speedily with minimal disruption to traffic. Thus, the overall cost differential will be lower especially in busy urban areas.

The study indicates that it is feasible to use CFRP laminates to strengthen steel composite bridges provided durability of the adhesive is assured and measures are taken to ensure that there is no galvanic action due to the direct contact between the CFRP laminate and steel. At the present time, however, such repairs are likely to be more costly though this may change in the future.

Acknowledgements

This investigation was carried out with the financial support of the Florida Department of Transportation and the US Department of Transportation. The authors thank Dr. Mohsen Shahawy for this support. They also wish to express their appreciation to Composite Horizons, Covington, CA for their many contributions to the study. However, the opinions, findings and conclusions expressed in this publication are those of the writers and not necessarily those of the Florida Department of Transportation or the US Department of Transportation.

References

Liby, L. (1993) Steel Composite Bridge Sections Strengthened by CFRP Laminates. Master's Thesis submitted to Department of Civil Engineering & Mechanics, University of South Florida, Tampa, FL, November, pp.353.

Meier, U., Deuring, M., Meier, H. and Schwegler, G. (1992) Strengthening of Structures with CFRP laminates: Research and Applications in Switzerland, *Advanced Composite Materials in Bridges and Structures* (Ed. K.W. Neale and P. Labossiere), CSCE, Montreal, P.Q., pp. 243-251.

Sen, R. and Liby, L. (1994a) Repair of Steel Composite Bridge Sections using CFRP Laminates. Final Report submitted to the US and Florida Department of Transportation, National Technical Information Service, VA, August, pp. 95.

Sen, R. and Spillett, K. (1994b) Restraint Effect of Bridge Bearings. Final Report submitted to the US and Florida Department of Transportation, National Technical Information Service, VA, January, pp. 118.

Sen, R., Liby, L., Spillett, K. and Mullins, G. (1995) Strengthening Steel Composite Bridge Members using CFRP Laminates. *Non-metallic (FRP) Reinforcement for Concrete Structures (Editor L. Taerwe)*, E & FN Spon, London, England. pp. 551-558.